ROB BONTA
Attorney General of California
TRACY L. WINSOR
Senior Assistant Attorney General
SIERRA ARBALLO
EVAN EICKMEYER
Supervising Deputy Attorneys General
KATE D. FRITZ, SBN 336966
LINDSAY N. DERIGHT GOLDASICH, SBN 344649
KRISTIN K. MCCARTHY, SBN 328196
DAVID M. MEEKER, SBN 273814
L. ELIZABETH SARINE, SBN 285631
*STEPHEN A. SUNSERI, SBN 207030
Deputy Attorneys General
600 West Broadway, Suite 1800
P.O. Box 85266
San Diego, CA 92186-5266
Telephone: (619) 738-9625
Fax: (619) 645-2271
E-mail: Stephen.Sunseri@doj.ca.gov

Attorneys for Respondent and Defendant California Department of Water Resources

Exempt from Filing Fees Under Government Code § 6103

SUPERIOR COURT OF THE STATE OF CALIFORNIA

COUNTY OF SACRAMENTO

COUNTY OF SACRAMENTO, a California county,

Petitioner and Plaintiff,

v.

CALIFORNIA DEPARTMENT OF WATER RESOURCES, a California State Agency,

Respondent and Defendant.

DOES 1 through 50,

Real Parties in Interest.

Case No. 24WM000014

(Related to 24WM000006; 24WM000008; 24WM000009; 24WM000010; 24WM000011; 24WM000012; 24WM000017; 24WM000062; 24WM000076)

COMPENDIUM OF EVIDENCE IN SUPPORT OF CAL. DEPT. OF WATER RESOURCES' EX PARTE APPLICATION FOR ORDER TO MODIFY OR STAY THE PRELIMINARY INJUNCTION – VOLUME I OF IV

(CEQA case: California Environmental Quality Act, Pub. Resources Code, § 21000 et seq.)

Dept: 36
Judge: Hon. Stephen Acquisto
Action Filed: January 22, 2024

Respondent California Department of Water Resources (DWR) hereby submits the following evidence in support of the DWR's ex parte application for order to modify or stay the preliminary injunction (Ex Parte Application). For ease of reference, DWR's Ex Parte Application contains citations to both the declarations themselves (and any exhibits, where relevant), and to the Bates numbered pages referenced in this Compendium of Evidence in Support of DWR's Ex Parte Application (COE). This is DWR's second Compendium of Evidence, and the Bates numbered pages continue from DWR's first Compendium of Evidence in Support of DWR's Opposition to All Petitioners' Motions for Preliminary Injunction.

Volume	Declaration	Exhibit	Exhibit Description	Bates Nos.
I	Decl. of Graham Bradner			291-305
I		A	2024 Cost Estimate, titled "Total Project Cost Summary Memorandum"	306-371
I		B	Finch, M. 1985. Earthquake Damage in the Sacramento–San Joaquin Delta, Sacramento and San Joaquin Counties. February. California Geology 38(2):39–44	372-380
I		C	Tsai, Y. 2018. Characterizing Seismic Performance of Levees on Peaty Organic Soils from Case Histories and Simulations. PhD dissertation. University of California, Los Angeles. Los Angeles, CA	381-715
II		D	U.S. Geological Survey. 2016. Earthquake Outlook for the San Francisco Bay Region 2014–2043. Fact Sheet 2016-3020. Version 1. August	716-722
II		E	California Department of Water Resources, October 2018, Supplement C – Water Project Export Disruptions for Multiple-Island Breach Scenarios using the Delta Emergency Response Tool	723-804
II		F	California Department of Water Resources, February 2009, Delta Risk Management Strategy, Phase 1, Executive Summary	805-837
II		G	Sunding, D. and Browne, O. 2024. Benefit-Cost Analysis of the Delta Conveyance Project. Berkeley Research Group	838-913

Volume	Declaration	Exhibit	Exhibit Description	Bates Nos.
III		H	California Department of Water Resources, December 2023, Delta Conveyance Project Final Environmental Impact Report, Chapters 6, 7, 10, 25, 26 and 30	914-1260
III	Decl. of Carolyn Buckman			1261-1267
III		A	Map of 2024-2026 Proposed Geotechnical Activities that are subject to temporary entry permits voluntarily entered by landowners to date or are located on DWR-owned property	1268-1269
III		B	Map of 2024-2026 Proposed Geotechnical Activities that will require court-ordered entry, assuming additional landowners do not enter temporary entry permits	1270-1271
III		C	Delta Conveyance Project - Modernizing California's Water Infrastructure - 2024 Fast Facts	1272-1274
III		D	Facts About the Economic Value of the Delta Conveyance Project	1275-1283
III		E	Sunding, D. and Browne, O. 2024. Benefit-Cost Analysis of the Delta Conveyance Project. Berkeley Research Group	1284-1359
IV	Decl. of Andrew Finney			1360-1364
IV		A	Map of 2024-2026 Proposed Geotechnical Activities that are subject to temporary entry permits voluntarily entered by landowners to date or are located on DWR-owned property	1365-1366
IV		B	Map of 2024-2026 Proposed Geotechnical Activities that will require court-ordered entry, assuming additional landowners do not enter temporary entry permits	1367-1368
IV	Decl. of Jeff Henderson			1369-1371
IV		A	Delta Stewardship Council's "Delta Plan's regulatory policies in PDF format"	1372-1382

Volume	Declaration	Exhibit	Exhibit Description	Bates Nos.
IV		B	"Draft Determination Regarding Appeals of the Certification of Consistency by the California Department of Water Resources for California WaterFix" (November 8, 2018)	1383-1539
IV	Decl. of Katherine Marquez			1540-1557
IV		A	Delta Stewardship Council's "Administrative Procedures Governing Appeals, Statutory Provisions Requiring Other Consistency Reviews, and Other Forms of Review or Evaluation by the Council"	1558-1581
IV		B	Delta Stewardship Council's December 16, 2022, comment letter on the Delta Conveyance Project Draft Environmental Impact Report	1582-1620
IV		C	2024-2026 Exploratory Planning and Design Field Investigations - Environmental Compliance, Clearance, and Monitoring Plan	1621-1704
IV		D	Tribal Cultural Resources Management Plan: Phase I (updated July 2024)	1705-1722
IV	Decl. of Demetri Polyzos			1723-1736
IV		A	Facts About the Economic Value of the Delta Conveyance Project	1737-1745
IV		B	Delta Conveyance Project - Modernizing California's Water Infrastructure - 2024 Fast Facts	1746-1748
IV	Decl. of Craig Wallace			1749-1755
IV		A	Facts About the Economic Value of the Delta Conveyance Project	1756-1764
IV		B	Delta Conveyance Project - Modernizing California's Water Infrastructure - 2024 Fast Facts	1765-1767

Dated: July 24, 2024

Respectfully submitted,

ROB BONTA
Attorney General of California
SIERRA ARBALLO
EVAN EICKMEYER
Supervising Deputy Attorneys General

David Meeker

DAVID M. MEEKER
Deputy Attorney General
Attorneys for Respondent and Defendant
California Department of Water Resources

SA2024300372
38257919.docx

SUPERIOR COURT OF THE STATE OF CALIFORNIA
COUNTY OF SACRAMENTO
Department 36
Judge: Hon. Stephen P. Acquisto

Related Case Nos. 24WM000006; 24WM000008; 24WM000009; 24WM000010; 24WM000011; 24WM000014; 24WM000012; 24WM000017; 24WM000062; 24WM000076

DECLARATION OF GRAHAM BRADNER IN SUPPORT OF CALIFORNIA DEPARTMENT OF WATER RESOURCES' EX PARTE APPLICATION

1. I, GRAHAM BRADNER, make this declaration in support of the Department of Water Resources' (DWR) Ex Parte Application for Modification or Stay of Preliminary Injunction. I have personal knowledge of the below, and if called to serve as a witness, I would and could testify to the following. The following statements are based upon my personal knowledge, my review of scientific papers and reports, and upon my review of records kept by the Delta Conveyance Design and Construction Authority (DCA). I have personal knowledge of the manner in which DCA's records are kept. Each of the records upon which I rely was made in the ordinary course of business at or near the time of the act, condition, or event. The sources of information at the time of preparation are such that I believe the records to be trustworthy.

Background

2. I am the principal of Bradner Consulting, LLC and currently serve as the Executive Director of the DCA. I am a certified engineering geologist, certified hydrogeologist, and professional geologist registered in the State of California. I received a bachelor's of science degree with a major in environmental geology and a master's of science degree in hydrogeology both from Clemson University. I have over twenty-five years of experience in engineering geology, program management, and water supply projects. Prior to my experience with the DCA, I managed large, multi-discipline flood and water supply projects including screening studies and feasibility studies through project design and construction. During and before my time with the DCA, I regularly review scientific papers and reports regarding relevant subject matters, including the Sacramento-San Joaquin River Delta, geology, tunneling, and other matters discussed below.

3. The DCA is a joint powers agency formed by sixteen local public water agencies that receive water from the State Water Project (SWP), which is owned and operated by DWR. These public water agencies include those agencies that have committed funds to DWR to pay for Delta Conveyance Project (DCP) planning, permitting, and design efforts. Once project design is finalized and all of the permitting is obtained, the DCA will construct the DCP for DWR.

4. I have served on the DCA engineering team since 2019 and have acted as the Executive Director since April 2021. As Executive Director of the DCA, I am the chief

administrative officer responsible for the proper and efficient administration of the DCA. I report directly to the DCA's Board of Directors and supervise all DCA contractors and consultants, excepting the DCA's legal counsel and treasurer.

5. I am familiar with DWR's DCP and have a detailed understanding of the DCP's components. The DCP, based on the alternative selected by DWR in certifying the DCP Final Environmental Impact Report (FEIR) on December 21, 2023, will generally involve the construction of two new intakes on the Sacramento River near the town of Hood that will convey water through an underground tunnel to a pumping plant that will discharge water into the Bethany Reservoir. I am familiar with the DCP and its proposed facilities based on DCA's ongoing efforts to assist DWR in the design and planning of the DCP.

The DCA is Charged with Conducting Geotechnical Investigations Necessary for DCP Design, Permitting, and other Inter-Agency Authorizations

6. The DCA currently provides engineering and technical support for the design and planning efforts necessary for DWR to obtain permits and approvals. DCA provides these services to DWR as set forth in the parties' Amended and Restated Joint Exercise of Powers Agreement, as amended in those First through Eighth Amendments (collectively, the JEPA). The DCA's current services are those services occurring during the "Planning Phase" as defined in the JEPA. The entire JEPA is available on the DCA's public website at https://www.dcdca.org/info-center/document-library/#DCA-Governance-Documents.

7. As part of the DCA's services to DWR during the Planning Phase, DWR has directed DCA to conduct a series of geotechnical investigations and activities to inform planning and design work, which commenced in May 2024 and which stopped when DWR received the June 20, 2024, Sacramento Superior Court's ruling granting motions to enjoin geotechnical investigations.

8. To support DWR's Ex Parte Application for Modification or Stay of Preliminary Injunction, DCA has proposed geotechnical activities that will be referred to as the "2024–2026 Proposed Geotechnical Activities" that DWR may conduct if the court modifies or stays the injunction. The specifics of the currently-proposed "2024–2026 Proposed Geotechnical

Activities" are more particularly described in the Declaration of Andrew Finney submitted concurrently with this declaration in support of DWR's Ex Parte Application for Modification or Stay of Preliminary Injunction.

9. From a program-level, the 2024–2026 Proposed Geotechnical Activities will generate necessary information to: 1) refine project feature layouts and configurations, and to develop design and engineering criteria for DCP facilities; and 2) support applications and requests to other agencies for permits, authorizations, conditional approvals, or project modifications; both of which are necessary to maintain the overall program design and construction schedule. The 2024–2026 Proposed Geotechnical Activities, are essential to evaluating subsurface conditions to support continued analyses of design assumptions as part of the ongoing conceptual design phase; and developing design criteria for structure and bridge foundations, new or modified levee cross-sections, ground improvement (including seepage cutoff walls,[1] liquefaction mitigation,[2] and foundation strengthening), selecting tunnel boring machine methods, dewatering methods and quantities, and below grade construction methods (such as at the shafts, pumping plant, and aqueducts).

10. Soil samples obtained from soil borings will be analyzed to determine the engineering properties of the soil to validate, and if needed modify, conceptual design and layout of project features. Soil and water quality tests will be conducted to determine the existence of high concentrations of metals, organic compounds, or other possibly hazardous constituents, to determine whether such constituents can be avoided. Soil and water quality tests are also necessary to ensure project features and infrastructure are designed and planned to allow for required treatment and/or disposal methods in consideration of the constituents identified.

[1] Seepage cutoff walls prevent water seepage through levees and dams.

[2] In relevant part, liquefaction occurs when loose soil sediments behave like a liquid in response to an earthquake such that the surface above the sediment is no longer structurally sound.

2024–2026 Proposed Geotechnical Activities are Necessary to Obtain Permits and Authorizations from Other Agencies

11. The geotechnical investigation data will be necessary to support DWR's request to the U.S. Army Corps of Engineers (USACE) for modification to federal facilities pursuant to Section 14 of the Rivers and Harbors Act of 1899 codified in 33 USC 408 (Section 408) to address intake construction and the tunneled crossing of the Stockton Deep Water Ship Channel.

12. As explained below, additional geotechnical data would also inform the substantial evidence supporting DWR's certification of the DCP's consistency with the Delta Plan.

13. At DWR's request, the DCA is currently evaluating a series of potential design or construction innovations that could reduce the construction footprint, construction timeline, and improve constructability—which in turn would reduce related impacts to biological resources, land uses, traffic, noise, and air quality compared to the expected impacts in the FEIR. Additional subsurface data provides important information for these potential refinements and further definition of the DCP relevant to future consideration by regulatory agencies. The Project Planning Schedule shown below provides the timeline for additional major permit activities continuing through 2026 and is available on the DCA's publicly available website at https://www.deltaconveyanceproject.com/about-the-delta-conveyance-project/dwr-updates-delta-conveyance-project-schedule-charts-permitting-pathway.

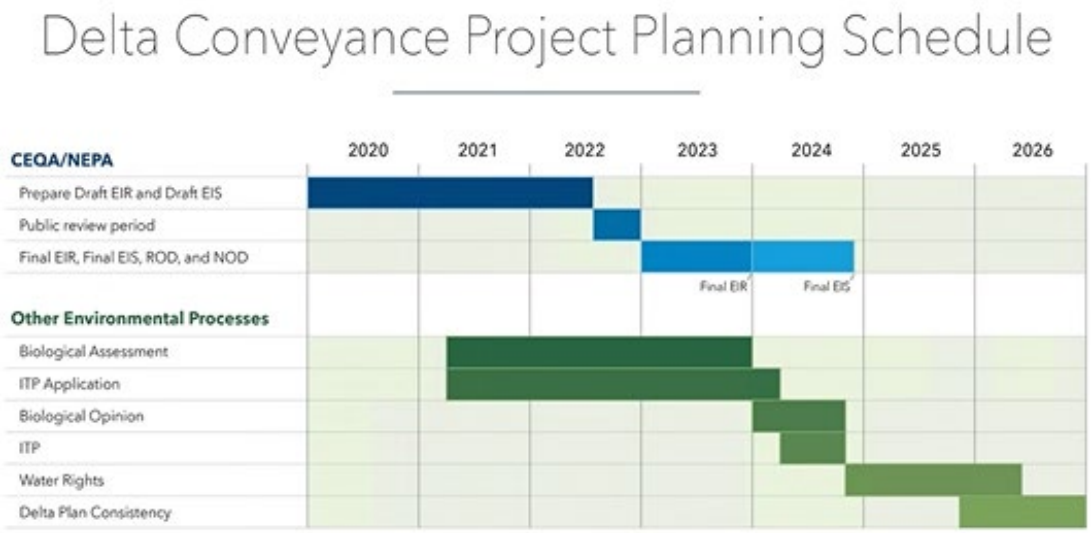

14. Additional geotechnical data will be used to inform concept and design work submitted to the Delta Stewardship Council in the certification of the DCP's consistency with the Delta Plan. The DCP project area spans nearly the entire North-South limits of the Delta, extending approximately 48 miles from the intakes on the Sacramento River to the Bethany Reservoir. Subsurface conditions in the Delta are highly variable as an interwoven network of historic stream channels overlain in many areas by thick deposits of peat and highly organic soils. More consolidated competent soil deposits[3] are present at depths approximately coinciding with the intended DCP tunnel profile. The exact conditions along the project alignment can only be confirmed through site-specific field investigations, which will be used to refine all aspects of below grade construction, as well as surface configurations for a more thorough and refined representation of the DCP. Additionally, the conceptual designs prepared to support DWR's evaluation of alternatives as documented in the DCP FEIR were based on limited information available at the time resulting in the use of appropriately conservative design assumptions regarding ground conditions and construction approaches that must be verified on the ground.

15. Based on this, the 2024–2026 Proposed Geotechnical Activities will inform the refinement of important project features. These refinements would inform the record evidence that the Delta Stewardship Council will review for substantial evidence when adjudicating any appeal of DWR's certification of the DCP's consistency with the Delta Plan. For example, the current plan for the tunnel alignment may shift within the corridor identified in the FEIR depending on soil and other conditions. These modifications may result in new or different parcels or areas within parcels being affected by permanent land easements required for the tunnel or associated with modification of existing features from the ground surface that would require new site access.

16. The tunnel alignment analyzed in the FEIR included considerations to minimize the time and distance that tunnel construction activities would occur under critical surface infrastructure, such as levees. Where the tunnel crossing beneath a levee cannot be avoided, the alignment has been configured to minimize the parallel orientation (i.e. tunnel crossing passes

[3] Competent soils are more stable and more capable of withstanding heavy loads.

beneath the levee over the shortest practical distance). Adjustments or curvature added to the tunnel alignment to avoid unforeseen underground conditions would also require reconsideration of these crossings, which may further expand the effects of a changing alignment relative to surface and land use impacts.

17. The addition of curves within the tunnel alignment beyond what is included in the FEIR would increase the overall tunneling distance, thereby increasing the overall construction schedule. An increase in overall tunneling distance would also affect the amount of soil excavated and the ultimate size of permanent soil stockpiles at the tunnel launch sites.

18. For the purposes of the environmental analysis, the DCA has assumed the DCP would be constructed using Earth Pressure Balance Tunnel Boring Machine technology, which is well suited for clayey, or soft ground conditions. This assumption requires the largest surface footprint at the tunnel launch site, since the saturated soil is conveyed back to the launch site and to the ground surface on open conveyors and then tested, dried and stockpiled at the site. For each of the double-launch sites analyzed in the EIR, more than 400 acres of the approximate total 600 acres needed for construction is dedicated to the management, drying, storage of highly saturated excavated soil associated with Earth Pressure Balance tunneling method. Alternatively, Slurry Tunnel Boring Machines, which are also entirely appropriate for soft ground but excel in cohesionless soils (sand, silt, gravel), convey the excavated soil suspended in fluid contained within conveyance pipes. The soil is removed from the slurry at the ground surface through a mechanical process contained within a slurry plant at the launch sites where the fluid is recycled within the tunnel system, while the soil is removed through centrifuges and presses before being discharged directly to the stockpile. The resulting soil stockpiles at the surface have significantly less water content and do not require supplemental drying at the surface before permanent stockpiling. The use of this alternative tunneling technology can only be determined based on site-specific information but would result in significant reductions in temporary construction land acreage at each launch site (i.e. 75 acres reduction for each tunnel boring machine; or up to 150 acres per double launch shaft site).

19. Similarly, the FEIR uses relatively conservative estimates of soil conditions and properties necessary for the analysis of required ground stabilization at tunnel shaft locations. These assumptions are the basis for the environmental analyses of construction equipment, duration, and impacts (i.e. emissions, traffic, noise, dust). If the 2024–2026 Proposed Geotechnical Activities determine that this work is not required or can be reduced, the amount of construction traffic and related land use and quality of life impacts will be reduced. This is relevant to Delta Plan Policy DP P2, which requires that "water management facilities . . . be sited to avoid or reduce conflicts with existing uses."

20. In addition, and related to the paragraph above, some of the 2024–2026 Proposed Geotechnical Activities are anticipated to occur in the vicinity of the intake sites. This work is less extensive than the geotechnical work planned at the shaft locations and along the tunnel alignment. However, the data from this work may demonstrate that the ground stabilization work is not required, or a lesser amount of ground stabilization is required. Such a result would reduce the amount of construction traffic, land use, and quality of life impacts. This is also relevant to Delta Plan Policy DP P2.

21. Another way to consider the importance of the 2024–2026 Proposed Geotechnical Activities is in their ability to progress the design of DCP. The current stage of design is "conceptual" and would generally be considered a 10% design level. The Association for the Advancement of Cost Engineering (AACE) uses a classification system to provide an approximate representation of the relationship between the level of project design and accuracy of project cost estimates to, in part, assist stakeholders in project decision making. The AACE classification system includes five classes, Class 1 to 5. A "project maturity" table from AACE's International Recommended Practice No. 17R-97, Cost Estimate Classification System, Rev. August 7, 2020, outlines the class of a project to its level of project definition (i.e., design). Below is a table that is adapted from and summarizes relevant portions of the AACE project maturity table:

ESTIMATE CLASS	MATURITY LEVEL OF DCP PROJECT DEFINITION
Class 5	0% to 2%
Class 4	1% to 15%
Class 3	10% to 40%
Class 2	30% to 75%
Class 1	65% to 100%

With relation to the planning process for the DCP, when DWR commenced preparation of the EIR in January 2020, project design was within the Class 5, 0% to 2%, range for each of the proposed project alternatives. Field investigations completed during preparation of the DCP EIR, in reliance on the 2020 Soil Investigation Project Initial Study/Mitigated Negative Declaration (2020 IS/MND), enabled DWR to reach an overall approximate 10% design level for each of the proposed project alternatives by December of 2023 when DWR certified the EIR and selected the Bethany Reservoir Alignment Alternative (DCP EIR Alternative 5) for further planning and design. However, the majority of tunnel reaches remain at a lower level of design development (i.e. 2%) due to lack of subsurface information. Therefore, the facility layouts presented in the FEIR conservatively overestimate acreage to allow for ground improvement areas to strengthen weak soils, peat soil remediation to reduce greenhouse gas emissions, and methods to address potential water quality issues. If the 2024–2026 Proposed Geotechnical Activities are allowed to and continue to proceed, it is anticipated that the Bethany Reservoir Alignment Alternative will be between Class 4 and Class 3 by the end of 2026—at which point the DCP planning will have progressed to overall approximate 15 to 30% design level. This design level will provide greater specificity regarding all DCP features, including refining the tunnel route and location and design of aboveground facilities for a project construction footprint and duration that reflects potential reductions in disturbance to biological resources, land uses, traffic, air quality, and noise. If the 2024–2026 Proposed Geotechnical Activities are allowed to proceed, while DCP will remain in the early stages of planning and design in 2026, it is anticipated that DWR would have more

project details to inform DWR's evaluation and written certification of the DCP's consistency with the Delta Plan in a more complete manner.

If 2024–2026 Proposed Geotechnical Activities are Delayed, DWR and The Public Will be Harmed

22. Any delay in the DCP's projected timeline will result in foreseeable harms to both DWR and the public. DWR's harms include, but are not limited to, a substantial increase in the estimated cost of the project, due at least to inflation. Harms to the public include, but are not limited to, threats to water security as climate change and seismic events amplify the risks to an already unstable source of freshwater in the Delta.

23. In addition to estimating the cost of DCP, the DCA has evaluated potential project schedules. Assuming the DCA conducts the planning and design field investigations on the timeline discussed above, the DCA estimates commencing DCP construction in approximately 2029 and completing the project in approximately 2044. (See DCP Cost Estimate (as defined below), Exhibit A, p. 6.) The project needs to reach 100% design before commencement of construction. If the 2024–2026 Proposed Geotechnical Activities are delayed until after 2026, construction would likely be delayed until the investigative and accompanying design work can be completed in order for the DCP to progress from the current "conceptual" 10% design level to 100% design. This is anticipated to delay the commencement of construction by potentially one to two years. Under this delayed-schedule scenario, construction could be completed around 2045–2046. This would necessarily increase the cost of DCP due to inflationary pressures and associated cost escalation with delayed completion.

24. It is industry standard to apply reliable trends and indices to estimate the cost of a given construction project. For typical project planning and construction, an industry standard approach uses average annual construction cost increases based on the United States Bureau of Reclamation Construction Cost Trends (USBR CCT) and the Engineering News Record Construction Cost Index (ENR CCI) for the latest time period of 1985 to 2019 to estimate annual escalation to apply towards future years (Source: Bureau of Reclamation [USBR], Technical Service Center-Construction Cost Trends, April 2024; Engineering News Record Construction

Cost Index 20 City Average). USBR CCT annual increases range from 2.6% to 3.2% and ENR CCI ranges from 2.8% to 3.2%; as such, an escalation of 3% is assumed for future years. However, based on USBR CCT there has been significant actual inflation observed since the 2020 cost assessment was released resulting in construction industry cost increases of 26.8% over the years of 2021 to 2023. Applying this 26.8% inflationary factor to the 2020 cost assessment prepared for DCP by DCA translates to an updated cost of approximately $20.2 billion in 2023 dollars. The DCA recently released an updated cost estimate ("2024 Cost Estimate") for DCP of $20.1 billion in 2023 dollars. This $20.1 billion estimate is consistent with the inflated 2020 estimate. The updated 2024 Cost Estimate for DCP includes an analysis of costs by project feature (material prices, labor rates, equipment rates, productivity of construction crews, schedule, indirect costs, sales tax, contractor markup and profit, and other add-on costs like insurance and bonds), allowances for known but undefined requirements for an individual activity or work item, risk treatment costs, and contingency. The 2024 Cost Estimate, titled "Total Project Cost Summary Memorandum," is available at <https://www.dcdca.org/wp-content/uploads/2024/05/2023-Bethany-Total-Project-Cost-Estimate.pdf> (last accessed, July 12, 2024). A true and correct copy of the 2024 Cost Estimate is attached as **Exhibit A**.

25. Based on the above, delaying the 2024–2026 Proposed Geotechnical Activities will delay the completion of DCP by approximately one to two years, resulting in up to approximately $1.2 billion in increased costs. This estimate is based on the current estimated schedule and approach. As explained below, the DCA may consider future project innovations that would have correlative and independent effects on this estimate of schedule impacts.

26. Subject to DWR direction and as discussed above in Paragraph 13, DCA is considering potential innovations for DCP that are not currently part of the Project. If implemented, these innovations have the potential to reduce total project costs by $1.23 billion as outlined in the 2024 cost estimate, as well as for most innovations related reductions in construction duration, traffic, noise, and air quality emissions. The development and potential inclusion of these innovations in DCP would be affected by the ability to conduct the 2024–2026 Proposed Geotechnical Activities. First, with the 2024–2026 Proposed Geotechnical Activities,

these innovations can be refined and considered on the currently proposed schedule. This would inform DWR's planning efforts and would assist in determining consistency with the Delta Plan as explained above. As an example, innovations may reduce the amount of land needed for a launch shaft, which is relevant to and can inform DWR's certification of DCP's consistency with Delta Plan Policy DP P2.

27. For every year of delay to the commencement of construction, the threat to millions of Californians' water security is exacerbated. For example, should an earthquake in the Delta trigger strong shaking that leads to catastrophic failure of levee embankments in the Delta, operations of the existing SWP could be disrupted for a year or more while levee repairs are completed and then upstream releases are able to flush out poor quality water before resuming operations. (DCP FEIR, Ch. 6 [Water Supply]; Ch. 10 [Geology and Seismicity].) This example assumes there is sufficient upstream storage to flush out poor quality water in the Delta, which would not necessarily be the case after multiple years of prolonged drought. Disruption to SWP operations of a year or more, likely would be calamitous to the State, its communities, and its economy. In addition, constructing the DCP earlier results in significant benefits. As sea levels rise, salinity will intrude further into the Delta, reducing the ability to divert from the existing south Delta pumps. As the climate changes, there likely will be wetter wet periods and drier dry periods. The additional operational flexibility from DCP with its intakes in the north Delta may help mitigate the water supply losses that otherwise may occur. Even without any seismic events, side effects from climate change—including rising sea levels and saltwater intrusion[4]—can similarly undermine levees in the Delta and contaminate fresh water that would have otherwise been securely stored if the DCP had been timely constructed. (*Id*., Ch. 30 [Climate Change].) This is my professional opinion based on firsthand experience working in the Delta as well as from my review of the scientific literature, including the exhibits listed below and attached to this Declaration.

[4] Saltwater intrusion occurs when saltwater moves into freshwater sources, causing contamination. Intrusion is due to a number of factors, including overusing groundwater sources as well as rising sea levels.

a. **Exhibit B**: Finch, M. 1985. Earthquake Damage in the Sacramento–San Joaquin Delta, Sacramento and San Joaquin Counties. February. California Geology 38(2):39–44. Available upon request at https://www.conservation.ca.gov/cgs/publications/cg-magazine (last accessed: July 10, 2024). In relevant parts, this article discusses (1) the liquefaction risk for Delta levees due to their construction from unstable peat and sand sediments; and (2) damage to Delta islands/tracts and levees attributable to moderate earthquakes ranging in magnitude from 3.6–6.7.

b. **Exhibit C**: Tsai, Y. 2018. Characterizing Seismic Performance of Levees on Peaty Organic Soils from Case Histories and Simulations. PhD dissertation. University of California, Los Angeles. Los Angeles, CA. Available at <https://escholarship.org/uc/item/2wg7b13s> (last accessed: July 11, 2024). In relevant part, the research in this dissertation concluded that levees in the Delta are comparatively fragile, and more susceptible to liquefaction and damage from earthquakes due to their unstable peat foundations.

c. **Exhibit D**: U.S. Geological Survey. 2016. Earthquake Outlook for the San Francisco Bay Region 2014–2043. Fact Sheet 2016-3020. Version 1. August. Available at <https://pubs.usgs.gov/fs/2016/3020/fs20163020.pdf> (last accessed: July 11, 2024). In relevant parts, this U.S.G.S. survey mapped historical earthquakes for the San Francisco Bay Region—which abuts and directly impacts the Delta—to forecast there is a 72% probability of one or more magnitude 6.7 or greater earthquakes in the region between 2014 and 2043. Many of the faults that were mapped and used for modeling extend through the Delta.

d. **Exhibit E**: California Department of Water Resources, October 2018, Supplement C – Water Project Export Disruptions for Multiple-Island Breach Scenarios using the Delta Emergency Response Tool. I received

this document from DWR in the regular course of business as part of my work as DCA Executive Director. It is also publicly available from DWR upon request. In relevant parts, this Supplement to the Delta Flood Emergency Management Plan addresses various levee breach scenarios as well as estimates the level of disruption in terms of time to repair, cost of repair, and reduced water exports associated with each scenario.

e. **Exhibit F**: California Department of Water Resources, February 2009, Delta Risk Management Strategy, Phase 1, Executive Summary. Available at < https://www.waterboards.ca.gov/waterrights/water_issues/programs/bay_delta/california_waterfix/exhibits/docs/SJRECWA/sjrecwa_3.pdf> (last accessed July 12, 2024). In relevant parts, this analysis of the Delta concluded that seismic events, high water conditions, sea level rise, and land subsidence all threaten Delta levees, with earthquakes posing the greatest risk. A major seismic event could result in more than $15 billion dollars in damages (using 2005 dollars); fatalities; and has a 62 percent probability of occurring between 2003 and 2032. [See p. 2, 10.]

f. **Exhibit G**: Sunding, D. and Browne, O. 2024. Benefit-Cost Analysis of the Delta Conveyance Project. Berkeley Research Group. Available at < https://water.ca.gov/-/media/DWR%20Website/Web%20Pages/Programs/Delta%20Conveyance/Public%20Information/DCP%20Benefit-Cost%20Analysis%202024-05-13__ADA.pdf> (last accessed July 12, 2024). Within larger benefit-cost analysis of the DCP, this report discusses the economic and social risks, as well as likelihood, of service disruptions stemming from Delta levee damage due to climate change and seismic events.

g. **Exhibit H**: California Department of Water Resources, December 2023, Delta Conveyance Project Final Environmental Impact Report, Chapters 6,

7, 10, 25, 26 and 30. Available at <https://www.deltaconveyanceproject.com/planning-processes/california-environmental-quality-act/final-eir/final-eir-document> (last accessed: July 12, 2024). These chapters address the above-described issues and more.

I declare under the penalty of perjury under the laws of the State of California that the foregoing is true and correct. Executed this _19th__ day of July 2024.

GRAHAM BRADNER

EXHIBIT A
TO BRADNER DECLARATION

Total Project Cost Summary Memorandum

Document History

Project Feature: Projectwide
Document version: Version 02
Date: May 14, 2024
Reference no.: EDM_PW_CE_MEM_Total-Project-Cost-Summary_001326_V02_F_20240514

Contents

Delta Conveyance Design and Construction Authority
980 9th Street, Suite 2400
Sacramento, CA 95814

Subject	**Total Project Cost Summary**
Project feature	Projectwide
Prepared for:	Delta Conveyance Project (DCP) File
Prepared by:	Delta Conveyance Design and Construction Authority (DCA)
Copies to	California Department of Water Resources (DWR) / Delta Conveyance Office (DCO)
Date/Version	May 14, 2024 / Version 2
Reference no.	EDM_PW_CE_MEM_Total-Project-Cost-Summary_001326_V02_F_20240514

Executive Summary

The Delta Conveyance Design & Construction Authority (DCA) prepared this memorandum to document the updated estimate of total project costs for the Bethany Reservoir Alignment of the Delta Conveyance Project. The updated estimate is being prepared to support strategic and feasibility evaluations being performed by the California Department of Water Resources (DWR) and participating Public Water Agencies. This document includes the rationale, assumptions, pricing sources, and other inputs to the estimating process that were used to develop the total project cost estimate.

The estimate is presented in 2023 dollars and is "undiscounted", an economic term meaning the value does not account for the time value of money. Reporting the estimate in 2023 dollars provides a base cost that allows DWR and participating Public Water Agencies to perform further economic analyses of costs and benefits in a manner that ensures consistency and comparability.

Total project costs include construction and other program costs associated with the following primary features:

- Two intakes (maximum 3,000 cfs each)
- Main Tunnel & Shafts
  - 36-foot-inside-diameter tunnel, 45 miles long
  - 11 Shafts including two double-launch shafts
- A 6,000-cfs Bethany Reservoir Pumping Plant (BRPP)
- Aqueduct from the BRPP to Bethany Reservoir
  - Includes four 15-foot-diameter pipelines
  - Tunneled crossing of Jones Penstocks and the Bethany Conservation Easement
- Discharge Structure to Bethany Reservoir
- Logistics works for access, levee improvements, power, utilities, communication, and site restoration

The total project cost estimate has been prepared in accordance with Association for the Advancement of Cost Engineering (AACE) guidelines and considers items such as labor, materials, equipment, level of effort, and other relevant cost items for a defined scope of work as described in the Environmental Impact Report (EIR) prepared by DWR and the supporting Engineering Project Report (EPR) prepared by the DCA. The updated cost estimate includes an appropriate level of contingency and risk treatment costs to manage uncertainty at the current conceptual stage of project development.

Following project approval, DWR directed DCA to consider potential design or construction innovations to further reduce community or environmental disturbances, schedule, and/or costs or improve constructability. This evaluation resulted in a set of potential reasonable and credible innovations which indicate potential savings when compared to the total project cost estimate. The innovations discussed herein do not represent changes to the project description presented in the EPR and analyzed in the EIR, but rather provide an indication of how normal design development processes can help manage costs for large infrastructure projects. As the innovation concepts advance, DWR will determine and document the need for any revisions to the project description, which will be used by DWR to determine if additional reviews will be required under CEQA and/or for project permitting.

Table ES-1 summarizes the total project costs for the 6,000-cfs Bethany Reservoir Alignment and potential reduced total project costs associated with the innovation concepts.

Table ES-1. Delta Conveyance Project Summary of Total Project Costs

Cost Category	Total Project Cost Estimate ($M[a])	Total Project Cost with Innovations ($M[a])
Construction Cost	$15,012	$14,008
Other Program Costs[b]	$5,108	$4,886
Total Project Cost	**$20,120**	**$18,894**

[a] Costs are in 2023 dollars and are undiscounted.

[b] Other Program Costs represent: Planning, Design, Construction Management, Land Acquisition, Environmental Mitigation, Settlement Agreement, and Community Benefits.

The total project cost estimate presented is primarily intended to support project financial and economic analysis and to provide guidance for further project development. The final costs of the project once constructed will depend on actual labor and material costs, competitive market conditions, actual site conditions, final project scope, implementation schedule, continuity of personnel and engineering, and other variable factors.

1. Introduction

On December 21, 2023, California Department of Water Resources (DWR) approved the Delta Conveyance Project (DCP) and selected the Bethany Reservoir Alignment for further engineering, design, and permitting necessary to be completed prior to initiating implementation. DWR completed extensive environmental review and certified the Environmental Impact Report (EIR) (DWR, 2023) as compliant with the California Environmental Quality Act (CEQA).

This memorandum provides an estimate of total costs for the project to support strategic and feasibility evaluations being performed by DWR and participating Public Water Agencies. The updated cost estimate is presented in two primary categories: (1) Construction Costs, and (2) Other Program Costs. The costs presented are inclusive of all activities and work required for the project and provide the rationale, assumptions, pricing sources, and other inputs to the estimating process used to develop the cost estimate.

The estimate is presented in 2023 dollars, which provides a base cost that allows DWR and participating Public Water Agencies to evaluate potential costs and benefits using their own agency-specific approaches and methodologies and avoids potential conflicts with DCA escalation assumptions.

2. Project Scope of Work

This section describes the facilities and elements of work included in the estimate. The project scope of work aligns with the 6,000-cfs Bethany Reservoir Alignment as presented in the *Delta Conveyance Final Draft Engineering Project Report, Bethany Reservoir Alternative* (DCA, 2022) and updates to the Engineering Project Report (EPR) issued in November 2023 (DCA, 2023).

2.1 Layout

Figure 2-1 shows the following proposed conveyance facility features:

- **Intake C-E-3 and Intake C-E-5:** Two 3,000-cfs intakes located along the Sacramento River
- **Main Tunnel and Shafts:** 36-foot-inside-diameter tunnel, approximately 45 miles long, connecting C-E-3 and C-E-5 to the Bethany Reservoir Pumping Plant (BRPP) with 11 shafts along the alignment used for launching, reception, and maintenance (including the Surge Basin shaft)
- **Surge Basin Shaft and Surge Basin:** The Surge Basin Shaft is used as a reception shaft connecting the Main Tunnel to the Surge Basin and providing connection to the BRPP wet well inlet conduit
- **Bethany Reservoir Pumping Plant:** A 6,000-cfs pumping plant with wet well and dry pit structures housing 14 vertical centrifugal end suction type pumps
- **Aqueduct**: Four 15-foot-diameter parallel pipelines approximately 2.5 miles long each, which include 2 tunneled sections and vertical shafts at the connection to the Discharge Structure
- **Discharge Structure:** Located at Bethany Reservoir to discharge flow delivered from the Aqueduct into Bethany Reservoir which delivers water to the California Aqueduct
- **Logistics Works**: Includes access, levee improvements, power, utilities, communication, and site restoration to support construction of the project

Figure 2-1. Schematic of Project Features

Figure 2-2 shows the total alignment extending from the Intake facilities to the discharge structure facilities in Bethany Reservoir for delivery to the existing State Water Project.

The 6,000-cfs-project includes two river intake facilities on the Sacramento River, with on-bank intake structures and sedimentation basins that connect to the main tunnel via drop shafts. The main tunnel would be 36-foot-inside-diameter and approximately 45 miles long and would be constructed as four reaches driven in opposite directions from the Twin Cities Complex and Lower Roberts Island double-launch shafts. The tunnel drives would end at reception shafts at Intake 3, Terminous Tract, and the Surge Basin located at the BRPP. The other shafts would be used as maintenance shafts during tunnel construction and for future project operations and maintenance. The Surge Basin and BRPP at the southern end of the alignment connect to a four-pipeline aqueduct and discharge structure at Bethany Reservoir.

Figure 2-2. Project Map
Data Source: DCA, DWR

2.2 Project Schedule

A project schedule was developed to represent major phases of the project that includes permits, procurement, design, construction, and startup. The schedule was developed by estimating the duration of time required to complete the design and construction of each major project element along with the logical sequencing of activities required to complete the entire project such that testing and startup can occur in years 2043 and 2044 with the project becoming fully operational at the beginning of year 2045. Figure 2-3 shows the overall DCP schedule and logical sequences of the major project elements.

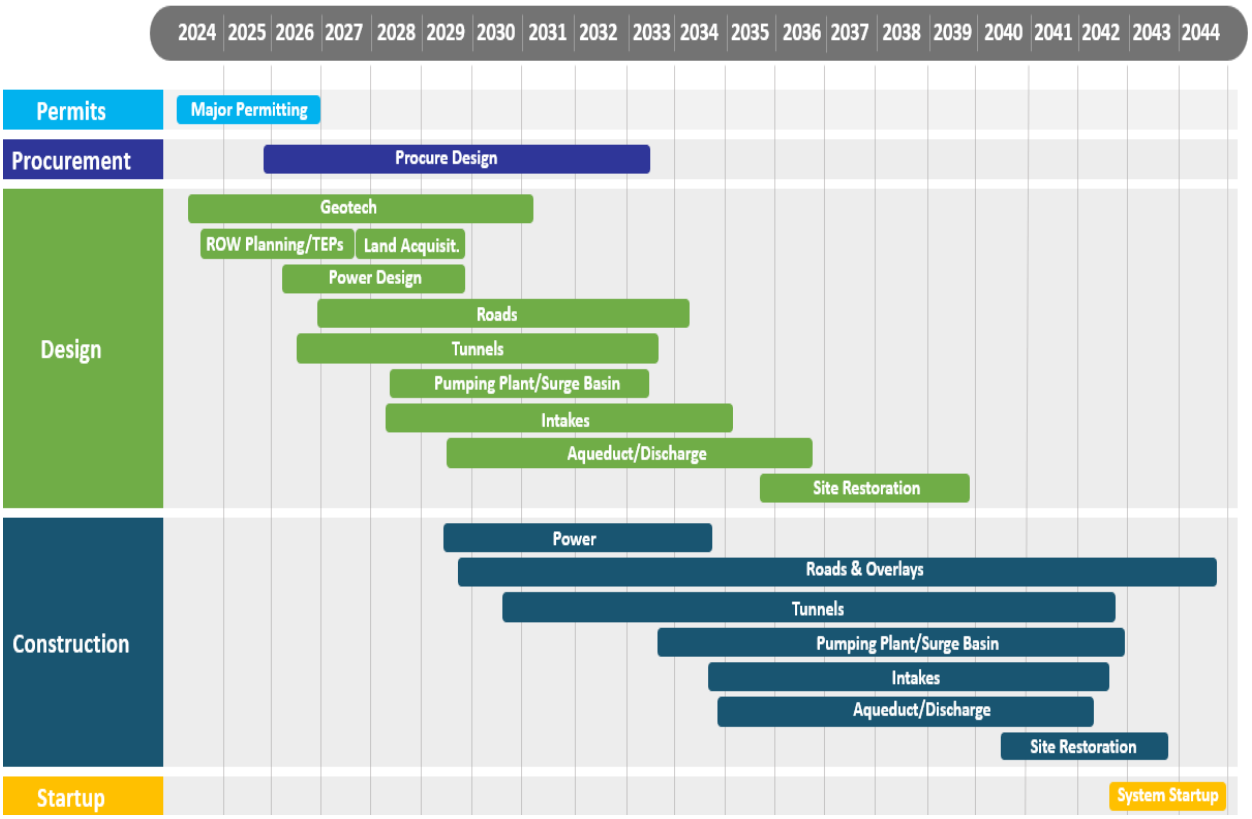

Figure 2-3. Delta Conveyance Project Schedule

3. Methodology and Estimate Classification

Total project costs for this estimate are divided into two categories: Construction Costs and Other Program Costs. The methodology used for developing the estimate and the estimate classification are presented below.

3.1 Methodology

The construction cost estimate has been prepared with quantities taken from drawings and other information contained in the EPR documents and, where applicable, has been adjusted to reflect the commitments described in the EIR. The construction cost estimate has been prepared with a crew-based estimating approach that uses materials, labor, and equipment crew estimates to complete work activities at the lowest level of detail for the anticipated method of construction as described in the EPR and EIR. Because of the scale and complexity of the project, a rigorous estimating approach was used to develop

the construction costs which included development of concept level drawings and technical memorandums, obtaining deterministic costs for unit rates and materials, replacing most of the cost allowances with actual estimates and material price quotes, and estimating the work based on the current understanding of subsurface ground conditions.

The other program costs were developed by considering the planning, design, and construction management labor costs (soft costs) and include all anticipated activities associated with delivering the project. Soft costs were developed by estimating the labor and level of effort over a given duration of time to complete the work, and other associated costs with these activities. The other program costs category of the estimate also includes costs for land, mitigation, power, the Contra Costa Water District (CCWD) Settlement Agreement, and the Community Benefits Program, which can be a mixture of direct, indirect, and labor costs.

Details of the construction costs are further presented in Section 4 and details of the other program costs are further presented in Section 5.

3.2 Estimate Classification

The DCA used the guidance provided in *17R-97: Cost Estimate Classification System Recommended Practice* (AACE, 2020) to determine the class of estimate. Based on the design stage and maturity, the project construction cost estimate generally categorizes as a Class 4 estimate, although some areas are considered Class 5. Appendix A, *Basis of Estimate-Construction Costs,* attached to this memorandum includes an Estimate Maturity Checklist that qualitatively evaluates the design maturity for individual project features. According to AACE 17R-97, estimate classification progresses down from Class 5 to Class 1 as project definition improves coinciding with improved expected accuracy (see Figure 3-1).

AACE guidelines provide anticipated accuracy ranges based on general and industry-specific benchmarking and empirical data. The total project cost estimate provides the DCA's opinion of the most probable cost. Due to the uncertainty associated with ground conditions along the tunnel alignment and industry experience with underground tunneling projects, DCA has assigned an accuracy range between +80% and -55% to the current cost estimate, but the far ends of the range have a much lower probability of occurrence than the most probable value. As illustrated on Figure 3-1, the accuracy range is expected to decrease as project definition improves and the estimate classification shifts towards Class 1.

The Class 4 estimate for the DCP is primarily presented to support project financial and economic analysis and to provide guidance for further project development. In general, the end use of cost estimates evolve over time – as the project definition increases from early conceptual design stages to final design, the end usage shifts from supporting strategic evaluations to funding authorizations and budgets to project control purposes. The final costs of the project once constructed will depend on actual labor and material costs, competitive market conditions, actual site conditions, final project scope, implementation schedule, continuity of personnel and engineering, and other variable factors.

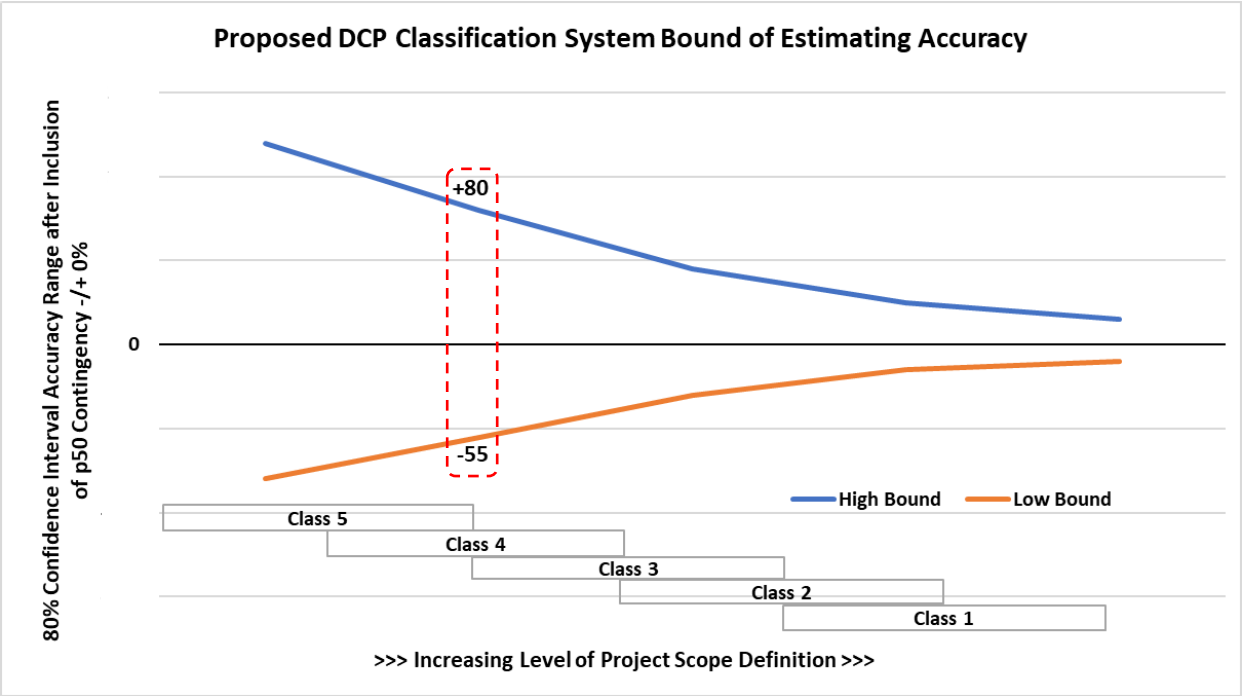

Figure 3-1. DCA Estimate Class within Range of Accuracy Modified from AACE 17R-97

4. Construction Cost Estimate

This section presents the construction cost estimate for the project including summaries of the major components and items considered while developing the estimate. Appendix A provides a more detailed breakdown and understanding of the construction cost estimate.

- **Cost Basis** – A variety of elements serve as the cost basis for the construction cost estimate, such as material prices, labor rates, equipment rates, productivity of construction crews, schedule, indirect costs, sales tax, contractor markup and profit, and other add-on costs (such as insurance and bonds). The estimate does not include escalation for the construction period and for future start dates. The prices in this estimate are in 2023 dollars.
- **Allowances** – Allowances are resources included in the estimate to cover the costs of known but undefined requirements for an individual activity or work item. The estimate recognizes the following allowances associated with the project:
  - Allowance for all diesel/gas-powered equipment to become zero emissions by 2035
  - Allowance for testing and commissioning of mechanical and electrical equipment before the systemwide commissioning
- **Risk Treatment Costs** – Risk treatment costs are included to account for identified risks associated with design and construction of the project and reflect potential costs beyond those developed by direct interpretation of the concept designs. Risk treatment costs also help manage potential risks by reducing threats and improving opportunities and have been developed based on industry standards, professional judgement and experience, and an assessment of uncertainties and potential risks for each major project feature.
- **Contingency** – In addition to risk treatment costs for each project feature, an overall construction contingency is applied to all project features beyond those directly accounted for in the estimate.

Contingency is an amount added to a construction cost estimate to account for uncertain items, conditions, or events that are likely to result in additional project costs. An assessment of project design maturity (i.e. approximately 10% level of design maturity overall) was completed along with an assessment of potential risks to determine the appropriate amount of contingency. An overall estimated construction cost contingency of 30% was included in the total project cost estimate.

4.1 Summary of Construction Estimate

Table 4-1 summarizes the construction costs and the risk treatment costs for each project feature. The 30% contingency is then applied to the summation of the estimated construction and risk treatment costs which results in an overall construction cost estimate for the project. Appendix A provides more details and a breakdown of the construction cost estimate.

Table 4-1. Summary of Construction Costs

Feature	Construction Estimate ($M[a])	Risk Treatment ($M[a])	Total Cost ($M[a])
Intakes	$1,660	$54	$1,714
Main Tunnels and Shafts	$6,018	$335	$6,353
Pumping Plant & Surge Basin	$2,496	$40	$2,536
Aqueduct Pipe & Tunnels	$541	$22	$563
Discharge Structure	$95	$4	$99
Access Logistics & Early Works	$241	$12	$253
Communication	$13	-	$13
Restoration	$17	-	$17
Subtotal Construction Costs [b]	**$11,081**	**$467**	**$11,548**
Construction Contingency (30%)			$3,464
Total Construction Cost Estimate [b]			**$15,012**

[a] Costs are in 2023 dollars and are undiscounted.
[b] The Total Construction Cost estimate excludes provision of electrical power supply and associated infrastructure to deliver power to work sites – these costs are included with the Other Program Costs.

5. Other Program Costs

In addition to construction costs, there are a series of other program costs that need to be included in the total project cost estimate. These have been grouped into two sub-categories:

1) Planning, design, and construction management costs (soft costs)
2) Other costs

Following is a summary of these other program costs.

5.1 Planning, Design, and Construction Management Costs

Planning, design, and construction management costs (soft costs) include labor and other direct and indirect costs associated with delivering the project. These represent what is often referred to as non-

construction professional services-related costs, or soft costs, of the project. Table 5-1 summarizes the categories and elements that represent the planning, design, and construction management activities.

Table 5-1. Planning, Design, Construction Management Cost Basis Categories

2023 Cost Basis Categories – Planning/Design/Construction Management
DWR Permitting & Oversight: • Engineering Standards Compliance • Program Controls Monitoring (Schedule and Budget) • Invoice Processing and Payment • Startup and Commissioning Support • Ongoing Environmental Permitting & Compliance Monitoring
DCA Permits & Agency Coordination: • Permit Coordination • Agency Coordination • Mitigation Monitoring & Reporting Coordination
DCA Program Management: • Executive Office (Human Resources, Legal, Finance, Program Office Direct Costs) • Program Management Leadership • Program Support (Assurances, Program Controls, Contracts/Procurement, Community Engagement)
DCA Engineering, Design, and Construction Management: • Engineering (Design Project Management/Technical Support, Construction Project Management/Technical Support, Geotechnical Exploration, Survey, Property Acquisition/Right-of-Way, Startup/Commissioning, Supplemental Programmatic Technical Services – Value Engineering, Hydraulic Modeling) • Design (Project Management, Basis of Design Reports, 30% Design, 60% Design, 90% Design, 100% Design, Independent Technical Review Coordination, Engineering Services During Construction, Startup/Commissioning Support) • Construction Management (Construction Project Management, Construction Oversite Services, Startup/Commissioning Support)

5.2 Other Costs

Other costs include items such as land acquisition, mitigation requirements, power, the settlement agreement and community benefits that are included as part of the overall cost of the project. Table 5-2 shows the different categories for these other costs.

Table 5-2. Other Cost Basis Categories

2023 Cost Basis Categories – Other Costs
Land: • Easements • Land Purchase
DWR Mitigation: • Tribal Monitoring • Mitigation Plans • Habitat Restoration Projects • Other Significant Mitigation
Power: • Design Services for Power Provided by Utility • Procurement/Construction of Infrastructure to Provide Power (SMUD, PG&E, WAPA) • Power Utilization Cost During Construction
Contra Costa Water District Settlement Agreement: • Agreed Cost Share (50-cfs pumping capacity)
Community Benefits: • Allowance for Community Benefits Program

The following points summarize the development and basis of the other costs:

- **Land Acquisition** – The land acquisition estimate is based on an estimate of costs to purchase the property and right-of-way to construct and operate the project. In addition to the property and rights-of-way costs, the estimate includes relocation assistance, utility relocation land costs, legal, and consulting fees.
- **Mitigation** – This estimate covers the environmental mitigation requirements outlined in the EIR and provided by DWR. These costs include items for Tribal monitoring, mitigation plan development, habitat mitigation (including compensatory mitigation), and other significant mitigation, as described in the EIR.
- **Power** – This item includes the costs for the design, procurement, and construction of the electrical infrastructure required to bring power to each project site from the major power utility companies in the project area. This item also includes the estimated cost associated with the electrical power consumption during construction. Primarily, this includes electrical consumption costs at the Intakes, Pumping Plant, and the Twin Cities Complex and the Lower Roberts Island double-launch shafts, where power is supplied for the tunnel boring machines. It also includes the power used during the commissioning and start-up of the overall conveyance system.
- **Contra Costa Water District (CCWD) Settlement Agreement** – This item includes the agreed cost share of $47 million for a 50-cfs pump station to be located at the Union Island Maintenance Shaft to transfer water to CCWD's existing facilities on Victoria Island.
- **Community Benefits Program** – This item is an allowance of $200 million to fund a community benefits program that would provide tangible benefits to local communities potentially effected by DCP construction approximately equal to 1% of the total project cost. Total actual benefits to the

community associated with implementation of the project are ultimately likely to represent a value beyond this funding commitment due to additional benefits associated with project leave behinds, job training and employment, local business participation, and other local and regional economic gains.

5.3 Summary of Other Program Costs

Table 5-3 summarizes the estimated cost associated with the other program costs. As noted in the table, an appropriate contingency between 15% to 30% has been added to each item based on whether it was a services-related or construction-related cost.

Table 5-3. Other Program Costs

Item	Estimated Cost ($M[a])
Planning, Design, Construction Management (Soft Costs)	
DWR Permitting & Oversight[b]	$426
DCA Program Management Office[b]	$668
DCA Engineering Management / Detailed Design / Construction Management[b]	$2,167
DCA Permitting and Agency Coordination[b]	$67
Other Costs	
Land[c]	$158
Mitigation[b,c]	$960
Power[c]	$415
CCWD Settlement Agreement	$47
Community Benefits Program	$200
Total Other Program Costs	**$5,108**

[a] Costs are in 2023 dollars and are undiscounted.

[b] Other Program Costs including soft costs and portions of the mitigation costs include a 15% contingency.

[c] Land and the construction related elements of Mitigation and Power costs include a 30% contingency.

6. Total Project Cost Summary

Table 6-1 summarizes the total project cost estimate for the project.

Table 6-1 Total Project Cost Summary

Feature	Total Cost ($M[a])	Percent of Construction (%)
Construction Costs		
Intakes	$1,714	Not Applicable
Main Tunnels	$6,353	
Pumping Plant & Surge Basin	$2,536	
Aqueduct Pipe & Tunnels	$563	
Discharge Structure	$99	
Access Logistics & Early Works	$253	
Communication	$13	
Restoration	$17	
Construction Subtotal	**$11,548**	
Contingency (30%)	$3,464	
Total Construction Cost	**$15,012**	
Other Program Costs		
DCO Oversite	$426	2.84%
Program Management Office	$668	4.45%
Engineering / Design /Construction Management	$2,167	14.44%
Permitting and Agency Coordination	$67	0.45%
Total Planning/Design/Construction Management	**$3,328**	**22.17%**
Land	$158	Not Applicable
DWR Mitigation	$960	
Power	$415	
CCWD Settlement Agreement	$47	
Community Benefits Program	$200	
Total Other Costs	**$1,780**	
TOTAL PROJECT COSTS	**$20,120**	

[a] Costs are in 2023 dollars and are undiscounted.

7. Total Project Costs with Innovations

Following project approval, DWR directed DCA to further evaluate several project features presented in the EPR/EIR and consider potential design or construction innovations to improve constructability or further reduce community or environmental disturbances, schedule, and/or costs. This evaluation resulted in a set of potential innovations at this early conceptual stage of the project that are considered by the DCA to be reasonable and credible based on industry experience. The innovations discussed herein do not represent changes to the project description presented in the EPR and analyzed in the EIR, but rather provide an indication of how normal design development processes can help manage costs for large infrastructure projects. As the innovation concepts advance, DWR will determine and document the need for any revisions to the project description, which will be used by DWR to determine if additional reviews will be required under CEQA and/or for project permitting. Appendix B summarizes the considered innovations.

Innovation concepts were initially developed by the DCA through a screening process that evaluated compatibility and appropriateness given the current level of project definition. The resulting 19 innovation concepts were then advanced into initial concept design to support an analysis of potential cost savings compared to those taken from drawings and other information contained in the EPR and EIR documents.

Table 7-1 presents the estimated construction cost savings for the combined set of innovations, grouped by project feature, reflecting reductions in construction quantities, crews, and equipment. The total construction cost savings includes a proportionally scaled portion of risk treatment cost (see Table 4-1).

Table 7-1 Construction cost savings from recommended combined set of innovations

Feature	Construction Cost Savings ($M[a])	Risk Treatment Cost Savings ($M[a,b])	Total Construction Cost Savings ($M[a])
Intakes	$35	$1	$36
Tunnels & Shafts	$211	$12	$223
Pumping Plant & Surge Basin	$370	$6	$376
Aqueducts	$75	$3	$78
Discharge Structure	$40	$1	$41
Logistics	$18	$1	$19
Total	**$749**	**$24**	**$773**

[a] Costs are in 2023 dollars and are undiscounted.

[b] Risk treatment cost savings are estimated as a scaled proportion of construction cost savings relative to the Total Project Cost estimate for the Bethany Reservoir Alignment as depicted in the EIR/EPR.

Table 7-2 compares the total project cost estimate described in Section 6 to a potential total project cost estimate associated with these early innovation concepts. The cost reductions associated with the innovations (see Table 7-1) only account for potential reductions in construction costs including risk treatment costs. In order to provide an indication of the potential full cost savings of innovations as described in Appendix B, contingencies and other program costs were applied proportionally to the revised construction costs. The costs for land acquisition, mitigation, power, the CCWD settlement

agreement, and the community benefits program were not adjusted from the total project cost estimate described in Section 6 of this memorandum.

Table 7-2. Summary of Total Project Cost and Total Project Cost with Innovations

Feature	Total Project Cost ($M[a])	Percent of Construction (%)	Total Project Cost with Innovations ($M[a])
Construction Costs			
Intakes	$1,714	Not Applicable	$1,678
Main Tunnels	$6,353		$6,130
Pumping Plant & Surge Basin	$2,536		$2,160
Aqueduct Pipe & Tunnels	$563		$485
Discharge Structure	$99		$58
Access Logistics & Early Works	$253		$234
Communication	$13		$13
Restoration	$17		$17
Construction Subtotal	**$11,548**		**$10,775**
Contingency (30%)	$3,464		$3,233
Total Construction Cost	**$15,012**		**$14,008**
Other Program Costs			
DCO Oversite[b]	$426	2.84%	$398
Program Management Office[b]	$668	4.45%	$623
Engineering/ Design /Construction Management[b]	$2,167	14.44%	$2,022
Permitting and Agency Coordination[b]	$67	0.45%	$63
Total Planning/Design/Construction Management[b]	**$3,328**	**22.17%**	**$3,106**
Land	$158	Not Applicable	$158
DWR Mitigation	$960		$960
Power	$415		$415
CCWD Settlement Agreement	$47		$47
Community Benefits Program	$200		$200
Total Other Program Costs	**$1,780**		**$1,780**
TOTAL PROJECT COSTS	**$20,120**		**$18,894**

[a] Costs are in 2023 dollars and are undiscounted.

[b] DCO Oversite, Planning, Design, and Construction Management costs are assumed to be the same percentage of construction as the total project cost estimate.

As shown in Table 7-2, reductions in construction effort associated with a set of reasonable and credible innovations identified at this early stage of design has the potential to reduce the total cost of the project

by $1.23B, or approximately 6%. Cost savings shown in Table 7-2 are limited to just those derived from changes in construction cost and proportional reductions in risk treatment costs and labor associated with planning, design, and construction management. Potential additional cost savings associated with innovations that were not considered in the analysis include:

- Reduced schedule durations for individual project features could reduce overhead costs and escalation impacts associated with individual components of the project.
- Reduced schedule durations for project features that affect the overall project schedule (i.e. "critical path" features) could potentially expedite the overall project construction timeline resulting in reduced overhead costs and escalation impacts. Expediting the overall project schedule could also bring the project into operation sooner.
- Innovations may reduce the impact of uncertainty within the cost estimate currently captured by risk treatment costs and project contingencies.
- Innovations may reduce the land required for construction and operations of the project, which could reduce land acquisition costs.
- Innovations may reduce the impacts of construction and operations, which could reduce mitigation requirements associated with the project.

The potential benefits of the identified innovations or future innovations should be further analyzed as project definition improves. Additional benefits of potential design or construction innovations to improve constructability or further reduce community or environmental disturbances, schedule, and/or costs savings associated with potential innovations could be realized but would require further analyses in coordination with DWR.

8. References

AACE International (AACE). 2020. 17R-97: Cost Estimate Classification System Recommended Practice. August 7.

California Department of Water Resources (DWR). 2023. Delta Conveyance Project Final Environmental Impact Report. December 2023. SCH# 2020010227.

Delta Conveyance Design and Construction Authority (DCA). 2022. Delta Conveyance Final Draft Engineering Project Report. Bethany Reservoir Alternative. May 2022.

Delta Conveyance Design and Construction Authority (DCA). 2023. Delta Conveyance Final Draft Engineering Project Report Update Bethany Reservoir Alternative. November 2023.

Appendix A
Bethany Reservoir Alignment Basis of Estimate – Construction Costs

Subject	**Bethany Reservoir Alignment Basis of Estimate – Construction Cost**
Project Feature	Project-wide
Prepared For:	Delta Conveyance Project (DCP) File
Prepared By:	Delta Conveyance Design and Construction Authority (DCA)
Copies To	California Department of Water Resources (DWR) / Delta Conveyance Office (DCO)
Date/Version	May 8, 2024 / Version 2
Reference No.	EDM_PW_CE_MEM_Bethany-Construction-Cost-BoE_001324_V02_D_20240508

1. Introduction

This memorandum prepared by the Delta Conveyance Design and Construction Authority (DCA) describes construction cost development methods and procedures for the Delta Conveyance Project Bethany Reservoir Alignment (Project). The documentation includes the rationale, assumptions, pricing sources, and other inputs to the estimating process used by the team in development of the construction cost estimate.

1.1 Purpose

The purpose of this document is to provide a construction cost estimate for the project as defined in the Final Environmental Impact Report (EIR) prepared by the California Department of Water Resources (DWR) and the supporting Engineering Project Report (EPR) prepared by the DCA. This document is in the form of a Basis of Estimate (BOE) and describes how construction costs have been developed for the Bethany Reservoir Alignment (6,000-cubic-foot-per-second [cfs] capacity) with the rationale, assumptions, pricing sources, and other inputs to the estimating process DCA used to develop the cost estimate. This estimate is presented in 2023 dollars and is "undiscounted", meaning the value does not account for the time value of money.

This BOE complies with Association for the Advancement of Cost Engineering International (AACE) *34R-05: Basis of Estimate Recommended Practice* (AACE, 2021). The estimate has been prepared using a standard process for a defined scope, as discussed within this report. DCA understands the assumed facility arrangements are at a conceptual planning level. As design development progresses, any potential changes are expected to be within the expected range of accuracy of the construction estimate.

Section 15 summarizes the total construction cost, and Attachments 1 and 2 provide more detailed breakdowns of the cost components.

Contingency has not been included and is being developed separately as part of the project cost management process.

This BOE is limited to the development of construction costs and excludes other program costs, such as planning, design, and construction management labor costs (soft costs), or other activities associated with delivering the project beyond the direct construction costs. This document also excludes the costs for providing electrical power and transmission to support the project, because those costs are being coordinated with the utility provider. All of these other program costs will be reported separately in the total project cost summary document, and thus are not included in this BOE.

1.2 Organization

This document is organized as follows:

- Introduction
- Project Scope of Work
- Estimate Methodology
- Estimate Classification
- Design Basis
- Planning Basis (Schedule)
- Cost Basis
- Allowances
- Assumptions
- Exclusions and Exceptions
- Program Risks
- Risk Treatment Costs
- Contingency
- Estimate Checking and Review
- Summary
- References
- Document History and Quality Assurance

1.3 Background

DCA completed Engineering Project Reports (EPRs) that presented conceptual engineering information for three potential conveyance alignments for the project: Central alignment, Eastern alignments, and Bethany Reservoir alignment (DCA, 2022a and DCA, 2022b). Updates to these reports were prepared in late 2023 (DCA, 2023a and DCA, 2023b). On December 21, 2023, DWR approved the project and certified the Environmental Impact Report (EIR) (DWR,2023). Based upon an extensive environmental review, as documented in the EIR, DWR selected the Bethany Reservoir Alignment for further engineering, design, and permitting.

This report provides the BOE for construction costs associated with the Bethany Reservoir Alignment for the 6,000-cfs flow capacity, as presented in the EPR and EIR.

1.4 Approach

This BOE complies with AACE *34R-05: Basis of Estimate Recommended Practice* (AACE 2021). It has been developed using a buildup of quantities for the key features where drawings and quantity information are available. Other less-defined elements of work have been developed with stochastic methods using judgment and experience, and these have been added to the estimate either as built-up or allowance items. The structure of the estimate assigns the work elements into a work breakdown structure (WBS) based on anticipated works contracts that are broadly based on the main discipline features and key site locations. The feature and WBS groupings are subject to revision as the project definition is further developed.

This BOE presents the key elements in a general north to south sequence, followed by the early site development and logistics works. Section 3 provides details about the construction estimate methodology. Note the following comments regarding the estimate:

- The estimate was prepared using 2023 prices.
- A preliminary set of construction activities has been developed in conjunction with the cost estimate for assessment of activity durations and interfaces.
- Lump sum allowances are included for elements of work where no design information was available or if the estimates were provided for items not included in the DCA scope.

2. Project Scope of Work

This section describes the facilities and elements of work included in this BOE. The project scope of work aligns with the 6,000-cfs Bethany Reservoir Alignment as presented in the *Delta Conveyance Final Draft Engineering Project Report, Bethany Reservoir Alternative* (DCA 2022b) and updates to the EPR issued in November 2023 (DCA 2023).

2.1 Layout

Figure 2-1 shows the following proposed conveyance facility features:

- **Intake C-E-3 and Intake C-E-5:** Two 3,000-cfs intakes located along the Sacramento River.
- **Main Tunnel and Shafts:** 36-foot internal diameter tunnel, approximately 45 miles long, connecting C-E-3 and C-E-5 to the Bethany Reservoir Pumping Plant (BRPP) with 11 shafts, inclusive of the surge basin shaft, along the alignment used for launching, reception, and maintenance.
- **Surge Shaft and Surge Basin:** Shaft is used as a reception shaft connecting the Main Tunnel to the Surge Basin and providing connection to the BRPP wet well inlet conduit.
- **Bethany Reservoir Pumping Plant:** A 6,000-cfs pumping plant with wet well and dry pit structures housing fourteen vertical centrifugal end suction type pumps.
- **Aqueduct**: Four 15-foot-diameter parallel pipelines approximately 2.5 miles long each, which include 2 tunneled sections and vertical shafts at the connection to the Discharge Structure.
- **Discharge Structure:** Located at Bethany Reservoir to discharge flow delivered from the Aqueduct.
- **Logistics works**: Including access, power, and utilities.

Figure 2-1. Schematic of Project features

The total alignment is illustrated on the project map (Figure 2-2), extending from the Intake facilities to the discharge facilities in Bethany Reservoir for delivery to the existing State Water Project.

The 6,000-cfs-project includes two river intake facilities on the Sacramento River, with on-bank intake structures and sedimentation basins that connect to the main tunnel via drop shafts. The main tunnel at 36-foot-inside-diameter (ID) and approximately 45 miles long, would be constructed as four reaches driven in opposite directions from the Twin Cities Complex and Lower Roberts Island double launch shafts. The tunnel drives would end at reception shafts at Intake 3, Terminous Tract, and the Surge Basin located at the BRPP, with all other shafts used as maintenance shafts during construction of the tunnel and for future project operations and maintenance. The Surge Basin and BRPP at the southern end of the alignment connect to a four-pipeline aqueduct and the discharge structure at Bethany Reservoir.

Figure 2-2. Project Map
Data Source: DCA, DWR

2.2 Features

2.2.1 Intakes

The intakes, C-E-3 (Intake 3 [or B per the EIR]) and C-E-5 (Intake 5 [or C per the EIR]), and associated sedimentation facilities are designed to divert up to 6,000 cfs (3,000 cfs maximum per intake) from the Sacramento River. Each intake consists of the following major components:

- Intake structure
- Thirty fish screens (T-screen option)
- Thirty 60-inch-diameter discharge pipes from Intake to Sedimentation basin
- Sedimentation basin
- Flow control and isolation gate structure
- Four sediment drying lagoons
- Appurtenant features

The two intake sites, along with sedimentation basin facilities, are located in the northern Delta along the Sacramento River near the town of Hood.

Figure 2-3 provides a conceptual rendering of one of the on-bank intake and sedimentation facilities. The intakes have on-bank cylindrical tee fish screens. The various control gates would be used to comply with the approach velocity of 0.2 foot per second (fps) at the fish screens and the 3,000 cfs maximum flow per intake. The sedimentation basins would be designed to remove sand-sized settleable solids before entering the conveyance system.

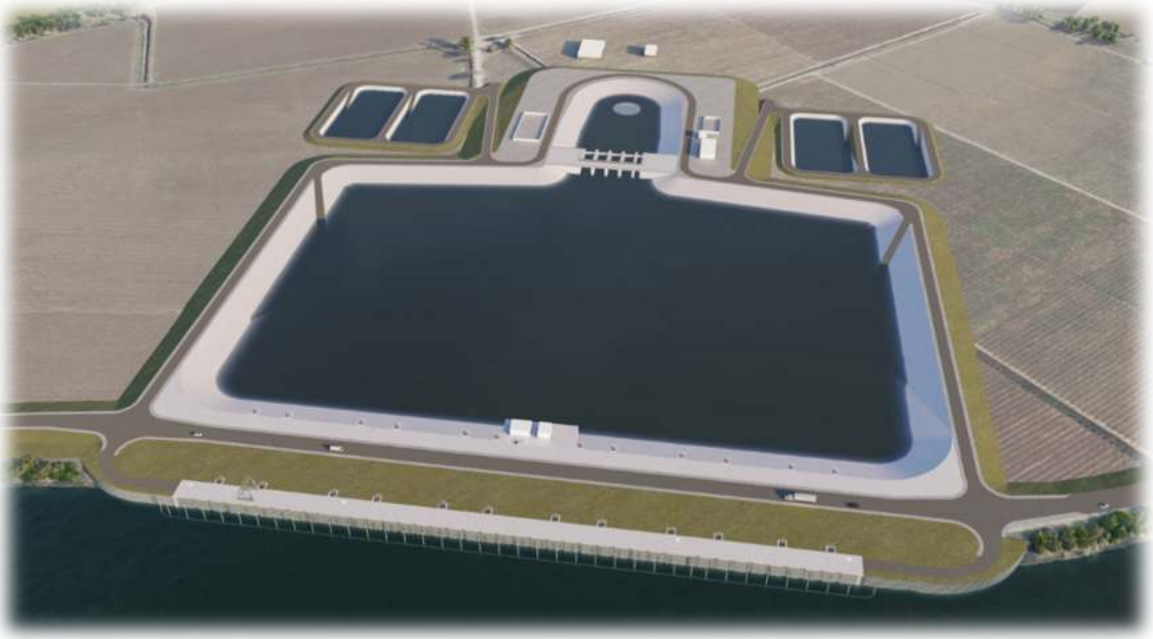

Figure 2-3. Conceptual On-bank Intake and Sedimentation Facilities

2.2.2 Tunnel and Shafts

The single main tunnel alignment is a 36-foot-ID tunnel, approximately 45 miles long and composed of four tunnel reaches. Each tunnel reach is driven between a launch and a reception shaft using a tunnel

boring machine (TBM). From Figure 2-2, there are two double launch shafts and three reception shafts. The launch shafts consist of two double launch shafts with interlocking 115-foot-ID shafts, named the Twin Cities Double Launch Shaft, and the Lower Roberts Island Double Launch Shaft. The reaches heading south from the Twin Cities Double Launch Shaft and north from the Lower Roberts Island Double Launch Shaft terminate into the Terminous Tract Reception Shaft with a 70-foot ID. The reach heading north from the Twin Cities Double Launch Shaft terminates at the C-E-3 Intake Reception Shaft with an 83-foot ID; this shaft also serves as an outlet shaft for Intake 3. The fourth tunnel reach, heading south from Lower Roberts Island Double Launch Shaft, terminates into the Surge Basin Reception Shaft with a 120-foot ID.

Between each launch and reception shaft, intermediate maintenance shafts, each at a 70-foot ID, are provided approximately every 5 miles, for a total of 6 maintenance shafts (Figure 2-2). These shafts are provided for TBM maintenance and temporary access during construction. The C-E-5 Intake Maintenance Shaft also serves as an outlet shaft for Intake 5 and is sized at 83-foot-ID.

The average shaft depth is approximately 180 feet, with an average tunnel invert depth of approximately 140 feet below existing grade (refer to the EPR conceptual drawings for detailed dimensions). These shafts would be constructed to a top elevation about 25 to 45 feet above existing grade for flood protection during tunnel construction and during operations. The shafts are also constructed to a top elevation to maintain the maximum water surface elevation expected within the shaft during a surge event caused by sudden stoppage of the pumping station.

Tunnel construction includes installing 6-foot-long precast concrete segmental lining rings. Each ring would consist of seven segments plus the key, with a thickness of about 18 inches.

2.2.3 Bethany Reservoir Pumping Plant Complex

The BRPP Complex covers all the works within the project area north of Kelso Road and before the aqueduct continues south toward the Bethany Reservoir. The main features included in the BRPP Complex include the Surge Basin Reception Shaft, Surge Basin, BRPP, inlet conduit connecting the reception shaft to the wet well within the BRPP, and the main deep box pumping plant with the aqueduct pipes between the box and the aqueduct interface at Kelso Road.

2.2.3.1 Surge Basin Reception Shaft

The Surge Basin Reception Shaft is a 120-foot-ID and 205-foot-deep structure that would first serve as the Main Tunnel reception shaft from the southern Lower Roberts Island Double Launch Shaft reach. Once the TBM is removed and the tunnel reach completed, the shaft would be modified to become the Surge Basin overflow structure and the connection to the inlet conduit to the pumping plant. The Main Tunnel connects to the base of the shaft and the inlet wet well conduit connects on the opposite side, approximately 65 feet higher in elevation.

2.2.3.2 Surge Basin

The Surge Basin structure is an open-top, rectangular, below-ground-level basin. The top of the basin would be at existing grade and the bottom elevation (top of floor slab) at about 30 or 40 feet below the ground surface (Figure 2-4).

The Surge Basin would be located immediately to the east of Mountain House Road and would contain an access ramp that would connect to an access road to Mountain House Road to facilitate the removal of the TBM and vehicle access during the construction and operation of the Surge Basin.

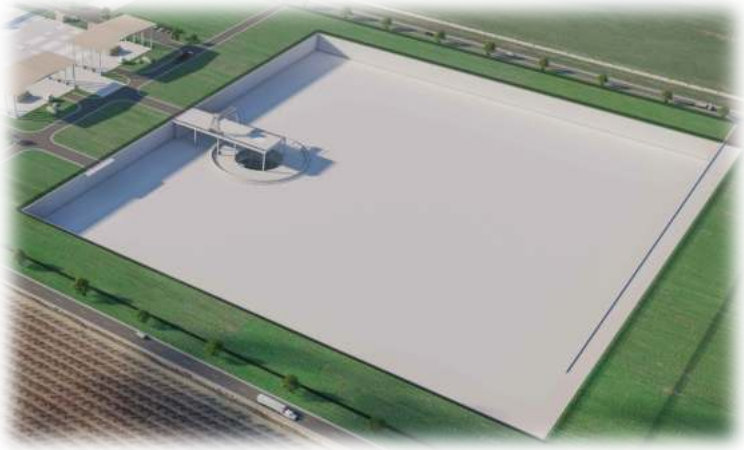

Figure 2-4. Surge Basin (Bethany)

The Surge Basin would normally be empty and would be used during infrequent hydraulic transient-surge events created by power failure or sudden stoppage to the pump station. Under these conditions, surge flows in the Main Tunnel would flow into the Surge Basin through the Surge Basin Reception Shaft. A circular weir wall with gates would be located around the top outlet of the shaft to allow water to overflow into the Surge Basin and prevent these overflows from immediately re-entering the tunnel.

The Surge Basin would include a gantry crane on a bridge structure between the southern edge of the basin and the vertical reception shaft. The bridge structure would include a removable panel, centered over the reception shaft, and a rail-mounted gantry crane that would be used to install portable submersible pumps and connect discharge piping into the reception shaft to dewater the tunnel.

2.2.3.3 Inlet Wet Well Conduit

The inlet wet well conduit would convey water from the Surge Basin Reception Shaft to the BRPP wet well. The inlet wet well conduit would be approximately 400 feet long, and 60 feet wide. Two sets of isolation bulkhead gates and openings would be provided in the inlet wet well conduit to isolate water flowing through the conduit and entering the BRPP wet well during inspection or maintenance, with double isolation provisions for the safety of the workers. The overhead-mounted gantry crane on the Surge Basin bridge structure would be used to install and remove the bulkhead panels.

2.2.3.4 Pumping Plant

The BRPP facilities would be adjacent to the surge basin (refer to Figure 2-5). The pumps lift water from a wet well hydraulically connected to the surge shaft via the inlet wet well conduit. The pumps would be operated to maintain the flow rate supplied into the tunnel at the northern Sacramento River intakes. The desired flow of the pumping plant would range from a minimum of 600 cfs to a maximum of 6,000 cfs, which would be achieved with fourteen 500-cfs pumps (12 duty pumps and 2 standby pumps).

The major components of the BRPP include the below-ground pumping plant and wet well, above-ground water surge tanks (open to atmosphere), electrical building, heating and air conditioning mechanical equipment yard, transformer yard, electrical substation adjacent to the electrical building, standby engine

generator building, equipment storage building, offices, welding shop, machine shop, storage area, and a walled enclosure/storage facility and two separate dry-pit pump bays adjacent to the wet well.

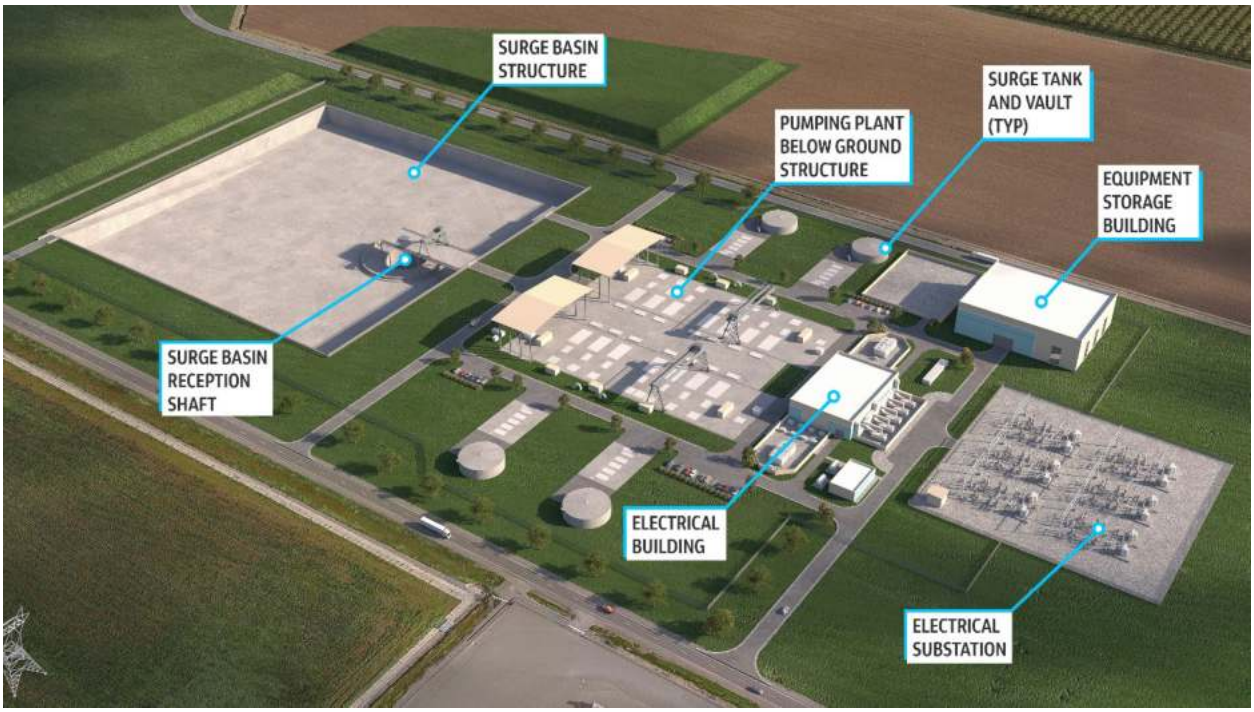

Figure 2-5. Bethany Reservoir Pumping Plant

2.2.4 Aqueduct

For the Bethany Reservoir Alignment, the aqueduct would convey water from the BRPP to Bethany Reservoir Discharge Structure located along the bank of the existing State Water Project Bethany Reservoir. The Bethany Reservoir Aqueduct would consist of four pressurized 180-inch-ID welded steel pipes. Each pipeline would convey up to 1,500 cfs. The aqueduct pipelines would be constructed using open-cut and backfill trench methods, except where the aqueduct pipelines crossed beneath the existing C. W. “Bill” Jones Pumping Plant discharge penstocks and the existing Bethany Reservoir Conservation Easement near Bethany Reservoir, where tunneling methods would be used for aqueduct construction (Figure 2-6).

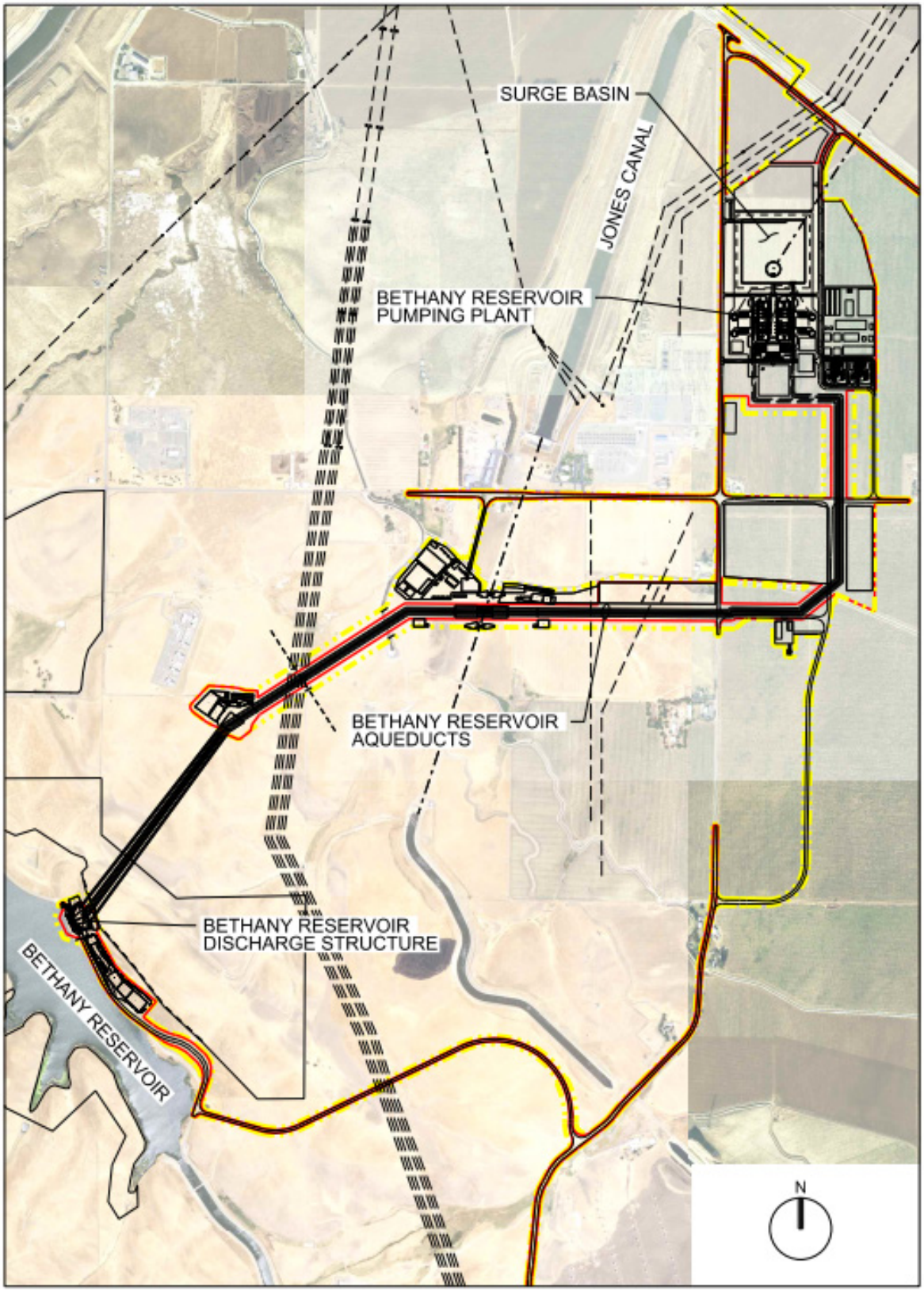

Figure 2-6. Bethany Aqueduct pipeline

2.2.5 Early Works Access Logistics

This section describes the works identified to support the main works contracts. These items include provision of access, levee protection, power, and utilities that would be available at the start of a main construction activities. The work elements defined in this section include roads and rail.

2.2.5.1 Early Works – Logistics – Roads and Levee

Early works for roads include the following provisions:

- Sacramento County Roads
  - Employee Park & Ride facility at Hood Franklin Road
  - Hood Franklin Road Snodgrass Slough bridge widening
  - Intakes 3 & 5 access roads
  - Lambert Road widening
- Twin Cities Complex Access Roads and Levees
  - Dierssen Road paving
  - Franklin Boulevard improvements at Dierssen Road
  - Twin Cities Road widening (East)
  - Twin Cities Complex ring levee
- San Joaquin County Roads
  - New Hope Tract Blossom Road widening
  - Canal Ranch access road construction
  - Terminous Tract Highway 12 widening
  - King Island access road construction
  - Lower Roberts Island access road construction
  - Lower Roberts Island levee protection work
  - Upper Jones Tract access road construction
  - Union Island access road
- Bethany Complex Access Roads
  - Byron Highway Lindemann Rd intersection
  - Byron Highway frontage road
  - Kelso Road widening
  - Mountain House Road widening
  - Mountain House Road shaft access
  - Mountain House Road by-pass
  - Bethany Reservoir access road
- Bethany Reservoir Access Road
  - Bethany Reservoir access road

2.2.5.2 Early Works – Logistics – Rail

Early works for rail include the Lower Roberts Island Rail Yard construction and extension of the rail line from the Port of Stockton.

2.2.6 Early Works Power and Utilities

2.2.6.1 Power

Power supplies to the main works sites are not included in the base construction cost estimate because this provision is being developed by DWR in coordination with the power providers (SMUD, PG&E, WAPA). These costs will be included in the other program cost element of the total project cost estimate. The power costs for each individual project do include the costs for both temporary and permanent requirements at each project site, as necessary.

2.2.6.2 Utilities

Work to provide or protect utilities is included in the mobilization and site preparation estimates for each contract. This includes:

- General allowances where no details are available
- Water supply to Bethany Complex
- Protection works for the East Bay Municipal Utility District (EBMUD) aqueduct tunnel

2.2.7 Systemwide

2.2.7.1 Communications and Control

Systemwide communications systems include fiberoptic cable for each site. Control panel equipment at each facility is included within the individual feature projects.

2.2.7.2 Testing and Commissioning

Testing and commissioning for the project, which follows all construction, is not included in this construction estimate but is included in the total project cost estimate. An allowance for contractor participation and assistance with testing and commissioning equipment within each facility is included in the feature project costs.

3. Estimate Methodology

This estimate has been prepared with quantities taken from drawings and other information contained in the EPR documents and, where applicable, adjusted to reflect the conclusion set out in the EIR. The cost estimate has been prepared using the Heavy Construction Systems Specialists (HCSS) Heavy Bid estimating software platform. This is a crew-based estimating system that uses labor and equipment crew estimates to complete work activities for the anticipated method of construction and anticipated durations. Because of the scale and complexity of the project, a more rigorous estimating approach was used to develop the construction costs which included development of concept level drawings and technical memorandums, obtaining deterministic costs for unit rates and materials, replacing most of the cost allowances with actual estimates and material price quotes, and estimating the work based on the current understanding of subsurface ground conditions.

Surface facilities include the Intakes, Surge Basin, BRPP, Aqueduct pipelines, and Discharge Structure. Early works for access logistics and levee protection are also included in the surface works estimate and are separated into the individual work packages required.

Tunnel and shaft estimates have been prepared for the main 36-foot-internal-diameter tunnels, the pipejack tunnels at the intakes, and the tunneling and shaft work required for the aqueduct section from the BRPP to the Discharge Structure located at the Bethany Reservoir.

The WBS in Table 3-1 has been used to code cost items and is based on an assumed number of works contracts with associated construction elements. This WBS is used to assess the number of contractor setups required for the overall estimate. The contract grouping and total number of contracts are subject to change as the project develops.

Table 3-1. Work Breakdown Structure, and Estimate Coding

Feature Code	Feature Name	Contract Code	Contract Name
1	Intakes	13	Intake 3 Facilities
		15	Intake 5 Facilities
2	Tunnels and Shafts	21	Reach 1 Shafts & Tunnel (Twin Cities to Intake 3)
		22	Reach 2 Shafts & Tunnel (Twin Cities to Terminous)
		23	Reach 3 Shafts & Tunnel (Lower Roberts to Terminous)
		24	Reach 4 Shafts & Tunnel (Lower Roberts to Bethany Complex)
3	Pumping Plant	33	BRPP, Surge Basin, and Reception Shaft
5	Aqueduct	55	Bethany Aqueduct including Tunnels and Shafts
6	Discharge	66	Bethany Discharge Structure
7	Logistics	71	Sacramento County Access Roads – Intakes Access Roads and Park & Ride
		72	Twin Cities Advanced Sitework – Access Roads & Levees
		73a	Lower Roberts Island Access Roads and Park & Ride
		73b	State Route 12 Road
		74a	Bethany Complex Access Roads – Byron Hwy & Interchange
		74b	Bethany Complex Access Roads – BRPP area & Roundabout
		75	Bethany Reservoir Access Road
		76	Projectwide Road Maintenance
		77	Lower Roberts Island Rail & Rail Yard
		78	Lower Roberts Island Levee improvements advanced work
8	Communications & Power	83	SCADA Projectwide
		86	Power (SMUD)
		87	Power (PG&E)
		88	Power (WAPA)

Table 3-1. Work Breakdown Structure, and Estimate Coding

Feature Code	Feature Name	Contract Code	Contract Name
9	Environmental	91	Bouldin Island Compensatory Mitigation
		92	I-5 Pond Compensatory Mitigation
		93	Projectwide Restoration & Site Establishment

SMUD = Sacramento Municipal Utility District
PG&E = Pacific Gas and Electric Company
WAPA = Western Area Power Administration

4. Estimate Classification

DCA used the guidance provided in *17R-97: Cost Estimate Classification System Recommended Practice* (AACE, 2020) to determine the class of estimate. The engineering information available for these estimates is assessed to determine the maturity class of estimate as shown in Table 4-1. Based on this information, the project construction cost estimate falls generally within Class 4, although with some areas still at Class 5. The Class 4 designation should be considered an overall classification level; individual project features would have different levels of design maturity that contribute to this judgement.

Table 4-1. Estimate Maturity Checklist

General Project Information	Class 5 Initiation	Class 4 Planning
Project Scope Description	Preliminary	**Advanced** [a]
Plant Capacity	Assumed	**Advanced** [a]
Site Location	Assumed	**Specific** [a]
Site Layout	None required	**Preliminary** [a]
Earthwork Quantities	None required	**Preliminary** [a]
Process Selection and Criteria	None required	**Preliminary** [a]
Design Discipline Criteria and Standards	None required	**Preliminary** [a]
Equipment Lists	**None required** [a]	Preliminary
Geotechnical Information	**None required** [a,b,c]	**Preliminary** [a,b,c]
Permitting Requirements	**Assumed** [a]	Preliminary
Site Environmental Survey	**None required** [a,b]	**Preliminary** [a,b]
Site Hazards Survey	**None required** [a]	Preliminary
Aerial Photography	None required	**Preliminary** [a]
Site Survey	**None required** [a,b]	**Preliminary** [a,b]
Building Programming	**None required** [a]	Preliminary
Architectural Material Boards	None required	**None required** [a]
Traffic Plan	None required	**None required** [a]
Acoustical Study	None required	**None required** [a]
Contract Packaging Strategy	**None required** [a]	Advanced

Table 4-1. Estimate Maturity Checklist

General Project Information	Class 5 Initiation	Class 4 Planning
Equipment Procurement Approach	**None required** [a]	Preliminary
Calculations	None required	**Preliminary** [a]
Project Schedule	Assumed	**Preliminary** [a]
Project Risk Log	Assumed	**Preliminary** [a]

Notes:
[a] **Bold and underline** text represents the current class of information available.
[b] Information levels may vary for project features where both columns are **bold and underline**
[c] Majority of tunnel alignment has no Geotechnical information

The accuracy of the estimate is proportionally impacted by considering different project elements such as underground tunneling requirements, the project's location in an environmentally sensitive area, limited geotechnical information, permitting requirements, a site environmental survey, and a site hazards survey. The additional uncertainty associated with defining these elements should also be reflected in the project risk management approach and associated consideration of contingency costs allowance that are not included in this construction cost estimate.

Figure 4-1 shows the class location of this estimate within the varying limits of accuracy. The range of accuracy will decrease as the class of estimate becomes more definitive (decreasing class number) from left to right according to AACE 17R-97 (AACE, 2020). The construction cost estimate provides the DCA's opinion of the most probable cost. Due to the uncertainty associated with ground conditions along the tunnel alignment and industry experience with underground tunneling projects, DCA has assigned an accuracy range between +80% and -55% to the current cost estimate. The zero axis represents the current total construction estimate including appropriate contingency with the 80% confidence interval range represented by percentage increase or decrease on that value.

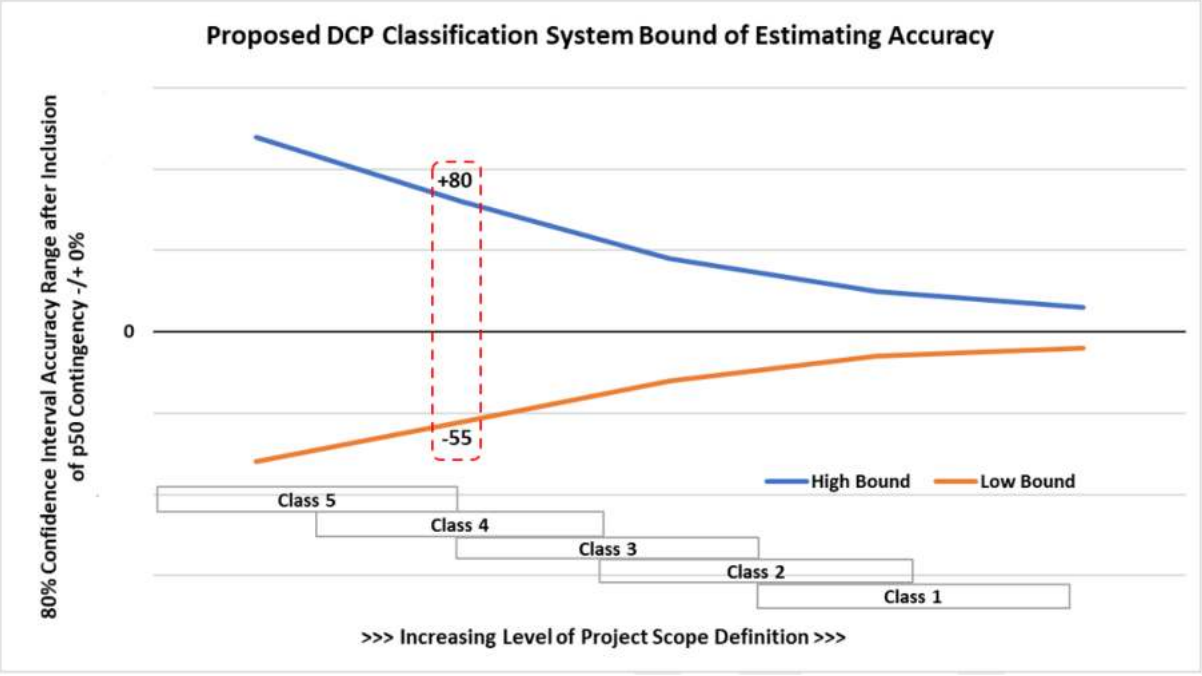

Figure 4-1. DCA Estimate Class within Range of Accuracy Modified from AACE 17R-97

The Class 4 estimate for the DCP is primarily presented to support project financial and economic analysis and to provide guidance for further project development. The final costs of the project once constructed will depend on actual labor and material costs, competitive market conditions, actual site conditions, final project scope, implementation schedule, continuity of personnel and engineering, and other variable factors.

5. Design Basis

The scope of the project used for this estimate is as defined in the EPRs (DCA 2022a, 2022b) and the EPR Update (DCA 2023a, DCA 2023b). These documents contain summaries for the Central and Eastern Alignments and for the Bethany Reservoir Alignment, as well as concept-level engineering drawings and supporting technical memoranda. This BOE document only considers the 6,000-cfs capacity option for the Bethany Reservoir Alignment together with the tee-screen option for the intake structures.

6. Planning Basis

This section describes the basis for developing the sequence of activities used in conjunction with the construction estimate. The sequence has been used to support the development of duration-related costs in the estimate. Refer to the construction portion of the DCP summary schedule presented in Figure 6-1.

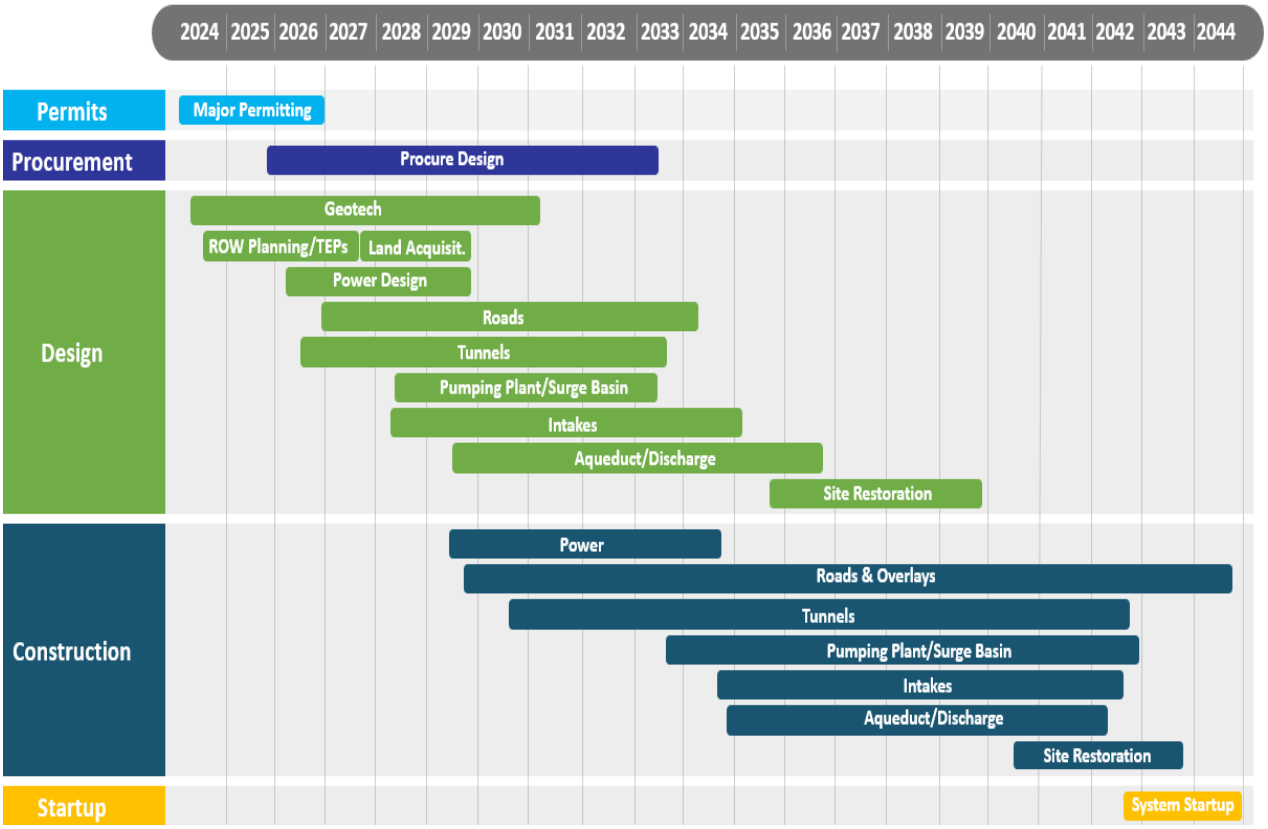

Figure 6-1. Delta Conveyance Project Summary Schedule

6.1 Preconstruction Activities

For this BOE, the preconstruction activities are assumed to include all activities required to achieve the start of early works construction, followed by main works construction.

6.2 Construction Sequence

Preliminary construction sequences were developed using the activities from the HCSS estimate. The estimate includes the allocated resources required to perform each task to complete the work. These tasks would include labor, equipment, materials, and, in some cases, subcontracts. The estimators calculated the time that would be required to perform each individual task for a given crew. The arrangement of activities is based on this effort, and depending on the type of work performed, the durations were adjusted to reflect likely work sequences. The durations were also adjusted to accommodate multiple crews working concurrent where necessary.

7. Cost Basis

Following is a summary of the cost element considerations. In general, all costs are based on 2023 dollars reflecting local area rates.

- Material Prices – material prices in the estimate are using 2023 prices. Concrete prices are based on supply from commercial or onsite batch plants and the estimate considers the cost of construction and operations of the batch plant to be included in the concrete unit rates.
- Labor Rates – labor rates are based on prevailing wage rate determination for the local area with fringe benefits and are fully burdened to include tax, insurance, and overtime, and are adjusted for the anticipated shift pattern. Typical fringes vary and may include health & welfare, pension, vacation & holiday, and training.
- Equipment Rates – equipment rates are sourced from established and industry accepted databases reflecting the nature of the work, such as U.S. Army Corps of Engineers and Equipment Watch Cost Reference Guide, or from quotes obtained from suppliers. Rates used could be overall hourly hire rates, or operating rates and ownership costs if the equipment is purchased.
- Productivity – crews were developed for each type of work based on either labor or equipment-based production, and generally using a 5-days-per-week, 24-hour schedule for tunneling and some shaft work elements, and single 10-hour shifts for other surface works.
- Indirect Costs – indirect costs are generally project specific overhead costs that are not associated with a specific work element. Their value can be spread over the project duration and often determined by the duration of the works. Typical types of indirect cost include:
  - Management and supervision salaries
  - Engineering salaries
  - Administrative salaries
  - Automobile and other miscellaneous expenses
  - General plant and facilities costs
- Sales Tax – sales tax rates of 9.25% were used on equipment and materials required for the project. Duty fees were applied where applicable.
- Escalation – the estimate does not include escalation for the construction period and for future start dates. The prices are in 2023 dollars.

- Contractor Mark-up and Profit – industry accepted contractor overheads and profits reflective of the nature of the work are applied.
- Add-on Costs – insurance, bonds, and other add-on costs are included in the estimates.

8. Allowances

Allowances are resources included in estimates to cover the costs of known but undefined requirements for an individual activity, work item, account, or subaccount. This estimate recognizes the following allowances associated with the project:

- Allowance for all diesel-/gas-powered equipment to become zero emissions by 2035.
- Allowance for testing and commissioning of mechanical & electrical equipment before the systemwide commissioning.

With the development of the design, these allowances would become incorporated into future revisions of the main estimates and design drawings.

9. Assumptions

As is normally the case, certain assumptions were made to reflect the conceptual level of design development. These assumptions may be related to the scope of the work where the design documents do not provide full details, or related to the pricing where the buildup of the cost may require specific experience-based assumptions. As the design progresses, these assumptions will be confirmed or refined.

10. Exclusions and Exceptions

Exclusions and exceptions are costs that might normally be considered part of the estimate but have not been included because they are not part of the scope or are included in other non-construction parts of the project. This construction estimate does not include the following items.

- Construction cost contingency
- Electrical power supply and associated infrastructure to deliver power to work sites, which are being incorporated in the overall project estimate as part of the other program costs noted below
- Other program-related costs, including:
  - DWR oversight costs
  - DWR EIR mitigations costs
  - DCA planning, design, and construction management costs
  - DCA permitting and other administrative cost
  - Power costs (power supply to the work sites and consumption during construction)
  - Land-right-of-way costs
  - Settlement Agreements
  - Community Benefits Program

11. Program Risks

A program-level evaluation of potential risks is ongoing and will be used to identify areas of potential additional costs and potential saving opportunities.

12. Risk Treatment Cost

Risk treatment costs have been assessed as part of the risk evaluation process and are considered for each feature type. These risk treatment costs are considered containment costs to help manage potential risks by reducing threats and improving opportunities and are included in this construction cost estimate assigned to each project element based on the associated features and value of the project. Attachment 3 provides details about this distribution.

13. Contingency

As noted above, the construction estimates presented in this document include risk treatment costs but do not include contingency. Contingency is an amount added to a construction cost estimate to account for uncertain items, conditions, or events that are likely to result in additional project costs. An assessment of the construction contingency would be derived by an assessment of the current state of design development, evaluation of program risks and judgement. Together, these assessments would be used to establish an appropriate construction contingency amount that would be added to the construction cost. Contingency is included and documented as part of the total project cost estimate.

14. Estimate Checking and Review

The estimating review and validation process included the following:

- Internal checks by the estimating team
- Design review with estimating team and design team
- Independent estimate and reconciliation with the DCA program management support team
- Management review with executive managers within DCA

As indicated above, the DCA program management support team completed an independent check estimate. A reconciliation process was completed comparing the DCA's Engineering Design Management team's estimate to the check estimate following industry recognized guidelines (Sundaram, 2024).

Using the EPR (2022b) and updates to the EPR (2023b) to prepare both estimates, a cost comparison was performed at the project level of the WBS. The independent check did not include some elements of work, such as the compensatory mitigation and power supply projects. Items with significant variances were reconciled through a series of meetings between the lead estimators for the relevant features, and appropriate modifications to the estimate were agreed upon. Through this process, an overall reconciled cost difference was obtained.

15. Summary

Table 15-1 summarizes the updated 2023 construction cost estimate. More detailed summaries are provided in Attachments 1 and 2, which show the buildup of cost types and bid items respectively.

Table 15.1. Bethany Reservoir Alternative – Direct Construction Cost Estimate Summary

Feature	Contract/Element	Construction Estimate ($M[a])	Risk Treatment ($M[a])	Total Construction Cost ($M[a])
Intakes	13- Intake 3 Facilities	855	28	882
	15- Intake 5 Facilities	806	26	832
Main Tunnels	21- Reach 1 Shafts & Tunnel (Twin Cities to Intake 3)	1,033	60	1,093
	22- Reach 2 Shafts & Tunnel (Twin Cities to Terminous)	1,735	95	1,830
	23- Reach 3 Shafts & Tunnel (Lower Roberts to Terminous)	1,292	69	1,362
	24- Reach 4 Shafts & Tunnel (Lower Roberts to Bethany Complex)	1,958	111	2,068
Pumping Plant	33- BRPP, Surge Shaft and Basin	2,496	40	2,536
Aqueduct	55- Bethany Aqueduct Pipeline, Tunnels and shafts	541	22	563
Discharge	66- Bethany Reservoir Discharge Structure	95	4	99
Access Logistics	71- Sacramento County Access Roads – Intakes and Park & Ride	30	1.6	32
	72- Twin Cities Advanced Sitework – Access Roads & Levees	20	1.0	21
	73a – San Joaquin County Access Roads Lower Roberts Island and Park & Ride	46	2.3	48
	73b – State Route 12 Access Road – Terminus Site	2	0.1	2
	74a – Bethany Complex Access Roads – Byron Hwy & Interchange	60	3.1	63
	74b – Bethany Complex Access Roads – BRPP area & Roundabout	21	1.1	22
	75- Bethany Reservoir Access Road	10	0.5	11
	76- Projectwide Road Maintenance	25	1.3	26
	77- Lower Roberts Island Rail & Rail Yard	16	0.8	17
	78- Lower Roberts Island Levee improvements advanced work	10	0.5	11
Communication	83- SCADA Projectwide	13	-	13

Table 15.1. Bethany Reservoir Alternative – Direct Construction Cost Estimate Summary

Feature	Contract/Element	Construction Estimate ($M[a])	Risk Treatment ($M[a])	Total Construction Cost ($M[a])
Restoration	93 - Projectwide Restoration & Site Establishment	17	-	17
Total Direct Construction[b, c, d]		**11,081**	**467**	**11,548**

[a] Costs are in 2023 dollars and are undiscounted
[b] Total excludes provision of electrical power supply and associated infrastructure to deliver to work sites
[c] Total includes Risk Treatment costs
[d] Total excludes contingency

Note that Attachments 1 and 2 include costs for several compensatory mitigation projects that have not been included in Table 15-1. The estimates for these elements are as follows:

- Bouldin Island Compensatory Mitigation = $36.4 M
- I-5 Pond Compensatory Mitigation = $54.3 M

The costs associated with these compensatory mitigation projects will be incorporated in the total project cost estimate as part of the DWR Mitigation other program cost item.

16. References

AACE International (AACE). 2021. 34R-05: *Basis of Estimate. Recommended Practice*. October 5.

AACE International (AACE). 2020. 17R-97: Cost Estimate Classification System Recommended Practice. August 7.

California Department of Water Resources (DWR). 2023. Delta Conveyance Project Public Final Draft Environmental Impact Report. December 2023. SCH# 2020010227.

Delta Conveyance Design and Construction Authority (DCA). 2022a. *Delta Conveyance Engineering Project Report – Central and Eastern Options*. Final Draft.

Delta Conveyance Design and Construction Authority (DCA). 2022b. *Delta Conveyance Engineering Project Report – Bethany Reservoir Alternative*. Final Draft.

Delta Conveyance Design and Construction Authority (DCA). 2023a. *Engineering Project Report Update – Central and Eastern Corridor Options.* Final Draft.

Delta Conveyance Design and Construction Authority (DCA). 2023b. *Engineering Project Report Update - Bethany Reservoir Alternative.* Final Draft.

Sundaram, R. n.d. *Construction cost estimates: reconciling, comparing and relating your estimate to another independent estimate*." Accessed February 2024. https://www.curriebrown.com/media/a3df2mtr/short-feature-piece_2017-11nov13-v2.pdf.

United States Bureau of Reclamation (USBR). 2023. Bureau of Reclamation Construction Cost Trends 2020 through 2023. https://www.usbr.gov/tsc/techreferences/mands/cct-pdfs/cct20-23.pdf

17. Document History and Quality Assurance

The reviewers listed here have completed an internal quality control (QC) review and approval process for deliverable documents that is consistent with procedures and directives identified by the Engineering Design Manager and the DCA.

Rev.	Date	Version Description	Approval Names and Roles			
			Prepared by	Internal QC Review by	Consistency Review by	Approved for Submission by
0	02/29/2024	Initial submission	Martin Ellis / Cost & Schedule Lead	Shaun Firth / QC Reviewer	Adam Murdock / Engineering Design Manager	Terry Krause / Engineering Project Manager
1	04/01/2024	Revised draft	Martin Ellis / Cost & Schedule Lead	Shaun Firth / QC Reviewer	Adam Murdock / Engineering Design Manager	Terry Krause / Engineering Project Manager
2	05/08/2024	Revised draft	Martin Ellis / Cost & Schedule Lead	Shaun Firth / QC Reviewer	Adam Murdock / Engineering Design Manager	Terry Krause / Engineering Project Manager

Attachment 1
Project Cost Summary Table

Bethany Reservoir Alternative Basis of Estimate - Construction

Attachement 1 - Estimate Cost Summary

A	B	C	D	E	F	G	H	I	J
PROJECT	**Man Hours**	**Labor cost**	**Permanent Materials**	**Construction Materials**	**Equipment Cost**	**Subcontractor Costs**	**Estimate Total**	**Risk Mitigation Total**	**Project Total**
13 - Intake 3 Facilities	2,884,849	$ 278,941,337	$ 277,487,055	$ 203,171,550	$ 94,090,290	$ 1,135,019	$ 854,825,251	$ 27,647,192	$ 882,472,443
15 - Intake 5 Facilities	2,728,882	$ 263,386,005	$ 263,306,867	$ 188,741,805	$ 88,988,082	$ 1,105,663	$ 805,528,421	$ 26,052,808	$ 831,581,230
21 - Reach 1 Shafts & Tunnel (Twin Cities to Intake 3)	1,330,971	$ 208,433,785	$ 495,859,696	$ 100,900,590	$ 195,745,000	$ 31,669,380	$ 1,032,608,451	$ 60,335,345	$ 1,092,943,796
22 - Reach 2 Shafts & Tunnel (Twin Cities to Terminous)	2,414,995	$ 366,966,472	$ 826,724,333	$ 160,733,395	$ 328,889,339	$ 51,463,336	$ 1,734,776,876	$ 95,159,675	$ 1,829,936,551
23 - Reach 3 Shafts & Tunnel (Lower Roberts to Terminous)	1,894,724	$ 283,279,054	$ 604,771,308	$ 121,429,839	$ 245,863,385	$ 37,069,474	$ 1,292,413,060	$ 69,221,103	$ 1,361,634,163
24 - Reach 4 Shafts & Tunnel (Lower Roberts to Bethany Complex)	2,980,572	$ 440,657,237	$ 948,104,596	$ 183,589,965	$ 324,296,568	$ 61,089,231	$ 1,957,737,597	$ 110,583,877	$ 2,068,321,474
33 - Bethany Pumping Plant, Surge Shaft and Basin	7,486,564	$ 751,954,884	$ 845,359,805	$ 435,342,562	$ 338,840,061	$ 124,242,938	$ 2,495,740,250	$ 40,000,000	$ 2,535,740,250
55 - Bethany Aqueduct Pipeline, Tunnels and shafts	938,518	$ 111,073,090	$ 273,393,252	$ 73,923,203	$ 62,803,909	$ 19,630,952	$ 540,824,406	$ 21,775,643	$ 562,600,049
66 - Bethany Discharge Structure	370,460	$ 36,061,254	$ 31,644,354	$ 19,553,873	$ 7,976,161	$ 27,732	$ 95,263,374	$ 3,724,357	$ 98,987,731
71 - Sacramento County Access Roads - Intakes, Batch plant & P&R	84,485	$ 7,282,941	$ 14,374,707	$ 6,029,690	$ 2,251,437	$ 351,000	$ 30,289,775	$ 1,561,699	$ 31,851,474
72 - Twin Cities Advanced Sitework - Access Roads & Levees	72,988	$ 7,048,034	$ 5,081,051	$ 3,459,007	$ 3,794,908	$ 855,136	$ 20,238,135	$ 1,043,450	$ 21,281,586
73a - Lower Roberts Island Access Roads & P&R	151,484	$ 13,625,048	$ 15,167,853	$ 13,648,528	$ 2,781,566	$ 351,000	$ 45,573,995	$ 2,349,732	$ 47,923,727
73b - State Route 12 Access Road - Terminus Site	2,565	$ 234,710	$ 1,444,662	$ 3,354	$ 125,497	$ -	$ 1,808,224	$ 93,230	$ 1,901,453
74a - Bethany Complex Access Roads - Byron Hwy & Interchange	228,472	$ 19,988,238	$ 20,213,517	$ 15,819,619	$ 3,149,309	$ 326,311	$ 59,496,993	$ 3,067,583	$ 62,564,576
74b - Bethany Complex Access Roads - PP area & Roundabout	24,229	$ 2,289,023	$ 13,704,118	$ 105,916	$ 1,656,647	$ 3,309,643	$ 21,065,347	$ 1,086,100	$ 22,151,447
75 - Bethany Reservoir Access Road	11,712	$ 1,125,293	$ 6,115,714	$ 108,273	$ 1,493,524	$ 1,462,662	$ 10,305,466	$ 531,336	$ 10,836,801
76 - Projectwide Road Maintenance	30,688	$ 2,794,080	$ 17,525,833	$ 3,748,997	$ 1,007,134	$ -	$ 25,076,044	$ 1,292,886	$ 26,368,930
77 - Lower Roberts Rail & Rail Yard	28,237	$ 2,492,579	$ 8,904,451	$ 2,974,747	$ 1,103,423	$ 829,732	$ 16,304,932	$ 840,660	$ 17,145,592
78 - Lower Roberts Levee improvements advanced work	35,303	$ 3,575,866	$ 2,492,965	$ 1,789,996	$ 2,386,736	$ 98,457	$ 10,344,020	$ 533,323	$ 10,877,344
83 - SCADA Projectwide	49,851	$ 5,784,645	$ 1,039,279	$ 2,411,342	$ 4,213,011	$ -	$ 13,448,276	$ -	$ 13,448,276
93 - Projectwide Restoration & Site Establishment	87,807	$ 7,978,351	$ 2,042,640	$ 121,547	$ 6,854,544	$ -	$ 16,997,083	$ -	$ 16,997,083
Grand Total	**23,838,357**	**$ 2,814,971,925**	**$ 4,674,758,056**	**$ 1,537,607,798**	**$ 1,718,310,532**	**$ 335,017,666**	**$ 11,080,665,979**	**$ 466,900,000**	**$ 11,547,565,979**

PROJECT	Man Hours	Labor cost	Permanent Materials	Construction Materials	Equipment Cost	Subcontractor Costs	Estimate Total	Risk Mitigation Total	Project Total
91 - Bouldin Island Compensatory Mitigation	172,384	$ 16,222,171	$ 4,958,073	$ 8,309,306	$ 6,949,439	$ -	$ 36,438,989	$ -	$ 36,438,989
92 - I-5 Pond Compensatory Mitigation	252,751	$ 24,490,107	$ 3,832,616	$ 12,862,323	$ 12,989,515	$ 98,457	$ 54,273,017	$ -	$ 54,273,017
Grand Total	**425,135**	**$ 40,712,278**	**$ 8,790,688**	**$ 21,171,629**	**$ 19,938,954**	**$ 98,457**	**$ 90,712,006**	**$ -**	**$ 90,712,006**

Note: Contractors indirect costs and mark ups are distributed and included with cost columns C through G for each project identified in column A

Attachment 2
Estimate Bid Item Summary Cost Table

Bethany reservoir Alternative Basis of Estimate - Construction
Attachement 2 - Estimate Bid Item Prices

Project/Contract	Bid Item	Unit	Quantity	Total 2023$
13 - Intake 3 Facilities				
	113317105 - Mobilization / Site Setup Intake 5 Pipe Jacking	LS	1	346,670
	113317110 - Purchase 60" WSP AWWA C300	LF	7650	6,166,818
	113317115 - Off Load 60" WSP AWWA C300	LF	7650	12,469
	113317136 - Plant & Equipment	LS	1	6,883,773
	113317137 - Indirects	MO	12	3,549,342
	113317139 - Demob & Clean Up	LS	1	231,114
	113317220 - Setup Akkerman MTBM Equipment	EA	30	286,308
	113317230 - Pipe Jack 60" WSP AWWA C300	LF	7650	1,334,466
	113317231 - Weld 60" AWWA C300 Joints	EA	383	350,545
	113317232 - Pipe Reception Pit	EA	30	361,657
	113317235 - Muck Excavation & Truck Haul Off	CY	5562	250,568
	133001000 - Int 3 Ph M Contractors Profit & Burden	LS	1	112,728,000
	133002000 - Int 3 Environmental Protection	LS	1	14,635,224
	133002100 - Int 3 Tire Wash Station	EA	1	53,845
	133003000 - Int 3 Ph 1Contractor Mobilization	LS	1	1,024,164
	133005000 - Int 3 Ph M Contractor Mngt & Admin., Technica	MO	85	91,029,164
	133007000 - Int 3 Ph M Contractor's Temporary Facilities	LS	1	16,506,406
	133008000 - Int 3 Ph M Lost Labor Time	LS	1	2,091,140
	133009000 - Int 3 Ph M Cont Temporary Facility Operations	MO	85	21,200,533
	133010000 - Int 3 Owners Office Facilities	LS	1	217,191
	133013000 - Int 3 Ph 1 Erect Rebar & Metal Fab Shop	SF	8000	2,973,727
	133014000 - Int 3 Ph M Dismantle Metal & Rebar Fab Shop	LS	1	417,403
	133016000 - Int 3 Ph M Operate Metal & Rebar & Fab Shop	TON	36682	6,726,071
	133305000 - Int 3 Ph 1 Site Work	LS	1	57,693,487
	133306000 - Int 3 Ph 2 Site Work	LS	1	80,397,434
	133307000 - Int 3 Ph 2 Cofferdam	LS	1	29,152,086
	133308000 - Int 3 Ph 2 Erect Work Trestle	LF	1034	6,969,554
	133309000 - Int 3 Ph 3 Final Site Work	LS	1	43,574,192
	133311000 - Int 3 Ph 2 Jet Grout Under Intake	CY	102600	14,273,606
	133313000 - Int 3 Ph 2 Excavate Inside Intake Cofferdam	CY	74978	3,277,784
	133314000 - Int 3 Ph 2 Install Training Wall Anchors & Backfil	LS	1	7,458,395
	133315000 - Int 3 Ph 2 Drilled Piers	EA	1215	85,622,077
	133317000 - Int 3 Ph 2 Tremie Concrete Under Intake Structure	CY	8547	3,466,176
	133319000 - Int 3 Ph 2 Dewater Intake C'dam & Place Xbra	LS	1	8,251,635
	133319500 - Int 3 Ph 2 Prep & Leveling Slab Concrete	CY	2142	2,285,765
	133321000 - Int 3 Ph 2 Intake Structural Concrete	CY	30673	41,241,753
	133322000 - Int 3 Ph 2 Intake Gate Shaft & outlet Structures	EA	30	14,066,767
	133322600 - Int 3 Ph 3 Jack 60" Dia Pipe	LF	0	-
	133323000 - Int 3 Ph 2 5'x5' Gates, Frames & Opera	EA	60	9,724,118
	133324000 - Int 3 Ph 2 8'x8' Gates, Frames & Opera	EA	30	5,908,178
	133324400 - Int 3 Ph 2 Set Guides for Screens & Stoplogs	LF	2700	850,757
	133324500 - Int 3 Ph 2 Intake Stoplogs	EA	5	1,545,074
	133325000 - Int 3 Ph 3 Fish Screens & Panels	LS	30	43,620,484
	133327000 - Int 3 Ph 3 Intake Structure MEP	LS	1	12,173,390
	133329000 - Int 3 Ph 3 Finish Out	LS	1	3,431,129
	133355000 - Int 3 Ph 2 Sediment Basin Drilled Piers	EA	400	6,949,828
	133357000 - Int 3 Ph 2 Radial Gate Flow Control Structure	CY	20908	22,732,867
	133359000 - Int 3 Ph 3 Sediment Basin Radial Gates & Stoplogs	LS	1	22,915,022
	133361000 - Int 3 Ph 3 Sediment Basin MEP & Finish Work	LS	1	1,895,589
	133901100 - Int 3 Ph 3 Purchase & Store Equip for Ops	LS	1	4,746,799
	133901400 - Int 3 Ph 3 Start up and Commissioning	LS	1	3,390,000
	21400510 - Build Slurry Wall Receiving Shaft at Intake C-E-3	LS	1	16,316,309
	21400515 - Reach 1 Receiving Shaft at Intake C-E-3	LS	1	11,518,400
13 - Intake 3 Facilities Total				854,825,251

Project/Contract	Bid Item	Unit	Quantity	Total 2023$
15 - Intake 5 Facilities				
	115517145 - Mobilize / Site Setup Intake 3 Pipe Jacking	LS	1	346,670
	115517150 - Purchase 60" WSP AWWA C300	LF	7980	6,432,838
	115517155 - Offload 60" WSP AWWA C300	LF	7980	11,651
	115517176 - Plant & Equipment	LS	1	6,803,413
	115517177 - Indirects	MO	12	3,547,146
	115517190 - Demob & Clean Up	LS	1	231,114
	115517260 - Setup Akkerman MTBM Equipment	EA	30	286,308
	115517270 - Pipe Jack 60" WSP AWWA C300	LF	7980	1,392,031
	115517271 - Weld 60" AWWA C300 Joints	EA	399	365,189
	115517272 - Pipe Reception Pit	EA	30	361,657
	115517274 - Muck Excavate & Haul Off	CY	5825	262,533
	155001000 - Int 5 Ph M Contractors Profit & Burden	LS	1	105,768,000
	155002000 - Int 5 Ph M Environmental Protection	LS	1	13,685,133
	155002100 - Int 5 Tire Wash Station	EA	1	53,845
	155003000 - Int 5 Ph 1Contractor Mobilization	LS	1	1,024,164
	155005000 - Int 5 Ph M Contractor Mngt & Admin., Technica	MO	85	85,290,142
	155007000 - Int 5 Ph M Contractor's Temporary Facilities	LS	1	17,974,141
	155008000 - Int 5 Ph M Lost Labor Time	LS	1	1,898,080
	155009000 - Int 5 Ph M Cont Temporary Facility Operations	MO	85	21,200,533
	155010000 - Int 5 Owners Office Facilities	LS	1	522,238
	155015000 - Int 5 Ph 1 Erect Rebar & Metal Fab Shop	SF	8000	2,973,727
	155015100 - Int 5 Ph M Dismantle Metal & Rebar Fab Shop	LS	1	417,403
	155016000 - Int 5 Ph M Operate Metal & Rebar & Fab Shop	TON	35354	6,485,757
	155205000 - Int 5 Ph 1Site Work	LS	1	51,387,815
	155206000 - Int 5 Ph 2 Site Work	LS	1	67,764,500
	155207000 - Int 5 Ph 2 Cofferdam	LS	1	28,067,147
	155208000 - Int 5 Ph 2 Erect Work Trestle	LF	1064	6,969,554
	155209000 - Int 5 Ph 3 Final Site Work	LS	1	40,738,041
	155211000 - Int 5 Ph 2 Jet Grout Under Intake	CY	34200	7,052,349
	155213000 - Int 5 Ph 2 Excavate Inside Intake Coffertam	CY	74978	3,277,784
	155214000 - Int 5 Ph 2 Install Training Wall Tiebacks & Backfi	LS	1	7,076,782
	155215000 - Int 5 Ph 2 Drilled Piers	EA	1215	83,374,231
	155217000 - Int 5 Ph 2 Tremie Concrete Under Intake Stru	CY	8547	3,466,176
	155219000 - Int 5 Ph 2 Dewater Intake C'dam & Place Xbra	LS	1	8,264,383
	155219500 - Int 5 Ph 2 Prep & Leveling Slab Concrete	CU	2142	2,285,765
	155221000 - Int 5 Ph 2 Structural Concrete	CY	30256	40,649,033
	155222000 - Int 5 Ph 2 Intake Gate Shaft & outlet Structures	EA	30	13,671,165
	155222600 - Int 5 Ph 3 Jack 60" Dia Pipe	LF	0	-
	155223000 - Int 5 Ph 2 5'x5' Gates, Frames & Opera	EA	60	9,724,118
	155224000 - Int 5 Ph 2 8'x8' Gates, Frames & Opera	EA	30	5,908,178
	155224400 - Int 5 Ph 2 Set Guides for Screens & Stoplogs	LF	2700	850,757
	155224500 - Int 5 Ph 2 Intake Stoplogs	EA	5	1,545,074
	155225000 - Int 5 Ph 3 Fish Screens & Panels	EA	30	43,620,484
	155227000 - Int 5 Ph 3 Intake Structure MEP	LS	1	12,173,390
	155229000 - Int 5 Ph 3 Finish Out	LS	1	2,978,442
	155255000 - Int 5 Ph 2 Sediment Basin Drilled Piers	EA	400	6,949,828
	155257000 - Int 5 Ph 2 Radial Gate Flow Control Structure	CY	20723	22,262,756
	155259000 - Int 5 Ph 2 Sediment Basin Radial Gates & Stoplogs	LS	1	22,914,901
	155261000 - Int 5 Ph 3 Sediment Basin MEP & Finish Work	LS	1	1,896,305
	155901100 - Int 5 Ph 3 Purchase & Store Equip for Ops	LS	1	1,802,531
	155901400 - Int 5 Ph 3 Startup & Commissioning Support	LS	1	3,300,000
	21600530 - Build Slurry Wall Pass Through Maint. Intake C-E-5	LS	1	15,809,869
	21600535 - Pass Through Maintenance Shaft Intake C-E-5	LS	1	12,413,351
15 - Intake 5 Facilities Total				**805,528,421**
21 - Reach 1 Shafts & Tunnel (Twin Cities to Intake 3)				
	21100425 - Twin Cities Reach 1 Launch Shaft Construction Site	LS	1	7,377,330
	21300440 - Reach 1 Tunnel	LF	42849	1,006,146,367
	21300445 - Remove TBM	EA	1	2,086,446
	21300450 - Remove Shaft Utilities & Conveyor Belt	LS	1	357,683
	21300455 - Remove Tunnel Conveyor Belt	LS	1	798,168
	21300460 - Remove Tunnel Utilities & Cleanup	LS	1	787,025
	21300462 - Instrumentation Shafts & Tunnel	LS	1	10,185,045
	21300465 - Indirects Reach 1	LS	1	-
	21300470 - Plant & Equipment Reach 1	LS	1	-
	22200531 - RTM Pads	LS	1	4,870,387
21 - Reach 1 Shafts & Tunnel (Twin Cities to Intake 3) Total				**1,032,608,451**

Bethany reservoir Alternative Basis of Estimate - Construction
Attachement 2 - Estimate Bid Item Prices

Project/Contract	Bid Item	Unit	Quantity	Total 2023$
22 - Reach 2 Shafts & Tunnel (Twin Cities to Terminous)				
	22100515 - Twin Cities Reach 2 Launch Shaft Construction Site	LS	1	8,191,815
	22200519 - Build Slurry Wall Reach 2 Launch Shaft	LS	1	27,082,082
	22200520 - Reach 2 Launch Shaft Twin Cities	LS	1	22,846,607
	22200523 - RTM Pads	LS	1	4,870,387
	22300530 - Reach 2 Tunnel 36 Foot	LF	66807	1,580,495,955
	22300535 - Remove TBM	LS	1	2,086,446
	22300540 - Remove Shaft Utilities & Conveyor Belt	LS	1	357,683
	22300545 - Remove Tunnel Conveyor Belt	LS	1	1,076,394
	22300550 - Remove Tunnel Utilities & Cleanup	LS	1	1,057,297
	22300552 - Instrumentation Shafts & Tunnel	LS	1	17,823,829
	22300555 - Reach 2 Indirects	LS	1	-
	22300560 - Reach 2 Plant & Equipment	LS	1	-
	22500610 - Build Slurry Wall Pass Through New Hope Shaft	LS	1	14,675,297
	22500615 - Pass Through Maintenance Shaft New Hope	LS	1	12,828,242
	22500621 - Furnish & Place Shaft Cover	LS	1	355,200
	22500630 - Pass Through Maint Shaft New Hope Work Area	LS	1	7,399,057
	22600625 - Build Slurry Wall Pass Through Canal Ranch Tract	LS	1	14,397,806
	22600630 - Pass Through Maintenance Canal Ranch Tract	LS	1	12,970,273
	22600636 - Furnish & Place Shaft Cover	LS	1	370,049
	22600640 - Pass Through Maint. Shaft Canal Ranch Tract Work A	LS	1	5,365,801
	731710000 - New Hope Tract Road	MI	0.28	167,919
	731770000 - Canal Ranch Tract	MI	1.17	212,496
	760000000 - Project Wide Road Maintenance	LS	1	146,241
22 - Reach 2 Shafts & Tunnel (Twin Cities to Terminous) Total				**1,734,776,876**
23 - Reach 3 Shafts & Tunnel (Lower Roberts to Terminous)				
	23100005 - Lower Roberts Reach 3 Launch Shaft Construct Site	LS	1	13,642,772
	23300020 - Reach 3 Tunnel 36 Foot	LF	49975	1,169,490,462
	23300025 - Remove TBM	LS	1	2,082,941
	23300030 - Remove Shaft Utilities & Conveyor Belt	LS	1	357,683
	23300035 - Remove Tunnel Conveyor Belt	LS	1	1,319,639
	23300040 - Remove Tunnel Utilities & Cleanup	LS	1	1,300,542
	23300042 - Instrumentation Shafts & Tunnel	LS	1	12,731,306
	23300045 - Reach 3 Tunnel Indirects	LS	1	-
	23300050 - Reach 3 Tunnel Plant & Equipment	LS	1	-
	23400014 - Terminous Tract Slurry Wall Reception Shaft	LS	1	11,858,585
	23400015 - Terminous Tract Reception Shaft	LS	1	12,807,556
	23400021 - Furnish & Place Shaft Cover	LS	1	370,049
	23400095 - Terminous Tract Reception Shaft Construction Site	LS	1	8,427,432
	23500096 - Build Slurry Wall Pass Through Maint.Kings Island	LS	1	14,735,734
	23500097 - Pass Through Maint Shaft Kings Island	LS	1	13,257,462
	23500103 - Furnish & Place Shaft Cover	LS	1	370,049
	23500110 - Pass Through Maint. Kings Island Work Area	LS	1	7,001,664
	24200127 - RTM Pad	LS	1	22,114,325
	731870000 - Kings Island Access Road	MI	3	544,858
23 - Reach 3 Shafts & Tunnel (Lower Roberts to Terminous) Total				**1,292,413,060**
24 - Reach 4 Shafts & Tunnel (Lower Roberts to Bethany Complex)				
	24100115 - Lower Roberts Reach 4 Launch Shaft Construct Site	LS	1	15,952,706
	24200118 - Slurry Wall Reach 4 Launch Shaft Lower Roberts	LS	1	27,922,450
	24200120 - Reach 4 Launch Shaft Lower Roberts	LS	1	23,184,163
	24200121 - RTM Pad	LS	1	22,114,325
	24200125 - Furnish & Install Shaft Cover	LS	1	370,049
	24300125 - Reach 4 Tunnel 36 Foot	LF	76697	1,767,845,909
	24300130 - Remove TBM	LS	1	2,037,822
	24300135 - Remove Shaft Utilities & Conveyor Belt	LS	1	357,683
	24300140 - Remove Tunnel Conveyor Belt	LS	1	1,157,476
	24300145 - Remove Tunnel Utilities & Cleanup	LS	1	1,209,130
	24300150 - Reach 4 Tunnel Indirects	LS	1	-
	24300155 - Reach 4 Tunnel Plant & Equipment	LS	1	-
	24300190 - Instrumentation Shafts & Tunnels	LS	1	20,370,090
	24500199 - Build Slurry Wall Pass Through Upper Jones Tract	LS	1	15,173,003
	24500200 - Pass Through Shaft Upper Jones Tract	LS	1	13,476,934
	24500206 - Furnish & Place Shaft Cover	LS	1	370,049
	24500220 - Pass Through Shaft Upper Jones Tract Work Area	LS	1	5,499,181
	24600225 - Build Slurry Wall Pass Through Union Island	LS	1	15,344,697
	24600230 - Pass Through Shaft Union Island	LS	1	13,647,623
	24600235 - Furnish & Place Shaft Cover	LS	1	370,049
	24600240 - PassThrough Shaft Union Island Work Area	LS	1	8,450,304
	731820000 - Upper Jones Tract Road	MI	2	441,979
	731880000 - Union Island Access Road	MI	2	2,441,978
24 - Reach 4 Shafts & Tunnel (Lower Roberts to Bethany Complex) Total				**1,957,737,597**

Project/Contract	Bid Item	Unit	Quantity	Total 2023$
33 - Bethany Pumping Plant, Surge Shaft and Basin				
	24400205 - Slurry Wall Reach 4 Reception Shaft Surge Basin	LS	1	19,917,361
	24400210 - Reach 4 Tunnel Reception Shaft Surge Basin	LS	1	25,071,914
	331001000 - Pump Plant/Surge Basin Contractors Profit & Burden	LS	1	338,442,637
	331002000 - Environmental Protection - Pump Plant/Surge Basin	LS	1	13,894,039
	331007000 - SB Temp. Construction Facilities Build	LS	1	3,612,219
	331007500 - Lost Labor Time - Pump Plant/Surge Basin	LS	1	5,906,869
	331015000 - Dismantle Rebar & Metal Fab Shop	SF	8970	369,428
	331103000 - Mobilize Pump Plant/Surge Basin Contractor	LS	1	1,737,286
	331105000 - Pump Plant Contractor Mngt & Admin., Technica	MO	84	128,709,210
	331109000 - Pump Plant Temp. Faciltities Build	LS	1	11,981,994
	331110000 - Owners Office Facilities	LS	1	522,238
	331112500 - Temporary Fire/EMT Station	LS	1	1,370,115
	331115000 - Pump Plant/SB Temporary Facility Operate	MO	84	28,419,811
	331117500 - Pump Plant/SB Erect Rebar & Metal Fab Shop	SF	8970	3,761,077
	331117800 - Pump Plant/Surge Basin- Rebar Shop Operation	TON	92633	43,999,895
	331120000 - Construction Water Supply from Banks Canal	LS	1	5,225,302
	331400000 - PP Substation Civil & Structural Work	LS	1	8,894,969
	332005000 - Surge Basin Clear & Grub/Demolition	LS	1	252,672
	332010000 - Surge Basin E xcavation & Demo'n	LS	1	12,294,677
	332015000 - Surge Basin Ramp Construction	LS	1	1,586,680
	332105000 - Pump Plant Initial Earthwork	LS	1	4,952,147
	332105100 - Pump Plant Final Site Work	AC	38	6,619,979
	332105200 - Pumping Plant SWPPP	ACRE	130	17,360,409
	332115000 - Diaphragm Wall Construction	SF	1221343	455,364,278
	332120000 - Excavate Pump Plant Phase 1 Below Floor El 42.0	CY	224000	6,819,266
	332121000 - Excavate Pump Plant Phase 2 Below Floor El 3.0	CY	129422	4,053,741
	332122000 - Excavate Pump Plant Phase 3 Below Floor El (-)22	CY	129422	4,457,492
	332123000 - Excavate Pump Plant Phase 4 Below Floor El (-)47	CY	129422	5,054,542
	332125000 - Excavate Pump Plant Phase 5 Below Floor El (-)72.0	CY	75911	3,304,984
	332126000 - Excavate Pump Plant Phase 6 Below Floor El (-)86.2	CY	105778	4,770,500
	332130000 - Excavate Pump Plant Inlet Conduit All Levels	CY	141423	6,659,150
	332135000 - Excavate PP Mech(E-W) & Elect(N-S) Rooms	0	260817	4,474,294
	332136000 - Excavate Surge Vault & Tank Inlet	CY	106053	9,373,773
	332145000 - 36" Drilled Piers Pump Plant & Surge Vaults	EA	154	4,717,654
	332150000 - 15' Dia Bethany Res. Pipe to Conn. with AQUE.PIPE	LF	6608	46,098,923
	332175000 - Remove Sec of Diaph. Walls - WW, Pipe. Elect. Cond	SF	11493	569,923
	333010000 - 36" Diaphragm Walls	SF	422000	93,426,542
	333020000 - Tiebacks	EA	1088	6,774,041
	333030080 - Rebar in Surge Basin Drilled Shafts	TON	16269	42,268,607
	333035000 - Drilled Tiedown Shafts	0	2589	155,203,479
	333100000 - PP Storage Areas & Yards	SF	11000	29,560
	333105000 - Generator Building	SF	3500	3,651,656
	333106000 - HVAC Mechanical Equipment Yard	SF	10200	2,043,848
	333110000 - Foundation Slab @ El. -110.50	CY	51543	38,251,986
	333111000 - Intermediate Slab @ El. -86.25	CY	18436	15,188,003
	333112000 - Intermediate Slab @ El. -72.00	CY	18436	15,419,969
	333113000 - Intermediate Slab @ El. -47.00	CY	18846	16,821,433
	333114000 - Intermediate Slab @ El. -22.00	CY	18436	16,018,288
	333115000 - Operation Deck Conc. @ El. 3.00	CY	18436	14,650,915
	333116000 - Roof Deck Concrete @ El. 47.00	CY	18508	16,933,124
	333116500 - PC Concrete Hatches @ El. 47.00	CY	2557	3,414,757
	333119000 - Concrete - Interior Column Facing	CY	6174	9,428,343
	333120000 - Structure Concrete Vert. Wall Liners	CY	38680	45,441,186
	333121000 - Interior Conc. Walls (Stairwells, Doghouses, etc.)	CY	23723	61,259,752
	333122000 - Pump Plant Conc. Fill around Pump Inlets/Housing	CY	3460	2,935,223
	333123000 - Mechanical Room Conc. Inv. Slab @ El. 3.00	CY	4988	4,610,843
	333124000 - Mechanical Room Conc. Walls	CY	4497	6,336,645
	333125000 - Mechanical Room Conc. Roof Slab	CY	4584	5,931,378
	333130000 - Surge Tanks Valve Vault - Inv. Slab Conc.	CY	2152	2,066,302
	333131000 - Surge Tanks Valve Vault - Conc. Walls	CY	2944	5,094,036
	333132000 - Surge Tanks Valve Vault - Conc. Roof Slab	CY	780	1,883,459
	333135000 - Surge Tanks - Inv. Slab Conc.	CY	1628	1,687,956
	333136000 - Surge Tanks - Conc. Walls	CY	1501	3,251,783
	333137000 - Surge Tanks - Conc. Roof Slab	CY	764	1,966,906
	333140000 - Wet Well Inlet Conduit Invert Slab	CY	9472	7,439,373
	333141000 - Wet Well Inlet Conduit Intermediate. Slabs	CY	16720	15,357,998
	333142000 - Wet Well Conduit Walls	CY	19367	26,010,244
	333143000 - Wet Well Conduit Top Deck Conc. @ El. 3.00	CY	4021	3,900,148
	333143100 - Isolation Gates - Wetwell Conduit	LS	1	7,910,626
	333144000 - Pump Plant Miscellaneous Metals	LS	1	13,475,089
	333145000 - 500 CFS Pumps & Motors (14 ea)	EA	14	92,767,168
	333147000 - 108" Dia. Steel Pipe, Valves, to 15' Dia. RW Conn.	LF	2700	90,556,635
	333149000 - PP Wet Well Bulkheads	LS	1	17,324,228
	333150000 - Pump Plant Overhead Gantry Cranes	LS	1	7,069,575

Bethany reservoir Alternative Basis of Estimate - Construction
Attachement 2 - Estimate Bid Item Prices

Project/Contract	Bid Item	Unit	Quantity	Total 2023$
33 - Bethany Pumping Plant,	333152000 - Service Elevators	EA	6	5,041,636
	333155000 - Pump Plant Structural Canopies (2 ea)	SF	30000	1,174,825
	333157000 - Wet Well Dewatering Pumps	EA	2	22,243,603
	333160000 - HVAC Mechanical Systems	LS	1	5,464,433
	333165000 - Valve Vault Piping & Valves	LS	1	26,509,076
	333166000 - Surge Tank Piping & Valves	LS	1	2,110,917
	333190000 - PP Electrical Building - Civil & Structural Work	SF	45500	20,929,321
	333195000 - PP Equipment Storage Building	SF	45800	15,653,055
	334010000 - Surge Basin Concrete Slabs	LS	1	78,043,685
	334020000 - Surge Basin Structures	LS	1	2,269,020
	334030000 - Surge Basin Gantry Crane Bridge	LS	1	5,139,366
	334040000 - Dewatering System	LS	1	3,229,175
	334050000 - Surge Basin Site Restoration	LS	1	830,208
	336120005 - PP Substation - Electrical Distribution	LS	1	80,751,532
	336120007 - Pump Plant Buildings - Electrical	LS	1	57,717,516
	336140009 - Pump Plant - Electrical System	LS	1	15,992,669
	336150005 - Pump Plant - Site Electrical System	LS	1	26,640,940
	336160005 - SCADA System - Pump Plant Only	LS	1	1,875,715
	337111000 - Start-up & Commissioning - Pumping Plant	LS	1	9,701,000
33 - Bethany Pumping Plant, Surge Shaft and Basin Total				**2,495,740,250**
55 - Bethany Aqueduct Pipeline, Tunnels and shafts				
	552001000 - Aqueduct Pipes - Contractors Profit & Burden	LS	1	53,493,856
	552005000 - Mobilization - DCA AQUEDUCT PIPES - Section 1	LS	1	278,056
	552006000 - Dewatering Treatment & Disposal	LS	1	518,776
	552006500 - Traffic Control	LS	1	342,448
	552006700 - Environmental Protection - Aqueduct Pipe Contract	LS	1	8,918,594
	552007000 - Lost Labor Time - Aqueduct Pipe Inst. Contract	LS	1	309,892
	552008000 - NEW DISCHARGE STRUCTURE - Site Preparation	LS	1	5,559,113
	552010000 - Clear & Grub - Section 1	AC	81	758,296
	552015000 - Strip & Stockpile Topsoil - Section 1	LF	6307.8	837,837
	552020000 - Trench Excavation - Section 1	CY	317497	2,606,962
	552025000 - Place Trench Stabilization Material - Section 1	CY	15412	1,109,584
	552030000 - Furnish Pipe Support Cradles - Section 1	EA	1448	841,462
	552035000 - Backfill - Section 1	LS	1	27,171,889
	552040000 - Compact and Finish - Section 1	LS	1	251,289
	552045000 - Dewatering - Section 1	LS	1	973,591
	552047000 - Add Dewatering Wells @ Kelso, BBID, Mtn. House Rd.	LS	1	613,279
	552050000 - General Support Crew - Section 1	LS	1	2,033,906
	552055000 - Site Restoration & DeMobilization - Section 1	LS	1	29,588
	553005000 - Mobilization - DCA AQUEDUCT PIPES - Section 2	LS	1	278,056
	553006000 - Dewatering Treatment & Disposal	LS	1	518,776
	553006500 - Traffic Control	LS	1	342,448
	553010000 - Clear & Grub - Section 2	AC	62	477,340
	553015000 - Strip & Stockpile Topsoil - Section 2	LS	1	497,282
	553020000 - Trench Excavation - Section 2	CY	189000	1,525,153
	553025000 - Place Trench Stabilization Material - Section 2	CY	7892	624,128
	553030000 - Furnish Pipe Support Cradles - Section 2	LS	1	429,818
	553035000 - Backfill - Section 2	LS	1	15,953,684
	553040000 - Compact and Finish - Section 2	LS	1	150,501
	553045000 - Dewatering - Section 2	LS	1	747,796
	553046000 - Bridges at Jones Penstocks	LS	1	1,911,129
	553047000 - Bridges at BBID	LS	1	1,429,741
	553048000 - Bridges at Gas LIne Crossing	LS	1	1,429,741
	553050000 - General Support Crew - Section 2	LS	1	1,207,632
	553055000 - Site Restoration & DeMobilization - Section 2	LS	1	29,588
	555010000 - Purchase and Transport Pipes	LS	1	147,200,051
	555015000 - Unload & Store Pipes at Storage Yard	LS	1	3,182,620
	555020000 - Installation of Pipes at Open Cut	LF	9971.5	6,126,287
	555040000 - Internal Lining	LF	57200	20,447,646
	555045000 - Cathodic Protection	LS	1	647,036
	555050000 - Installation of Pipes at Crossings	LF	920	34,135,119
	555055000 - Installation of Pipes at Tunnels & Shafts	LF	3408.5	25,204,308
	555056000 - Install Pipe at Disch Structure Vertical Shafts	EA	4	2,169,775
	555060000 - General Support Crew	LS	1	3,257,427
	555065000 - Geotechnical Monitoring and Instrumentation	LS	1	351,536
	555070000 - Indirect Cost - Section 1, 2, Tunnels & Shafts	LS	1	10,256,608
	85101000 - Mobilize Portals	LS	1	1,702,180
	85102000 - Excavate East Penstock Portal	CY	160245	2,738,587
	85102500 - Excavate West Penstock Portal	CY	224321	3,227,979
	85103000 - Excavate Conservation Easement Portal	CY	239336	4,116,579
	85103100 - Portal Headwall Cut Support	LS	1	518,086
	85103150 - Staging Areas Portals	LS	1	3,023,838
	85103500 - Plant & Equipment	LS	1	-
	85104000 - Indirect Cost	LS	1	-

Bethany reservoir Alternative Basis of Estimate - Construction
Attachement 2 - Estimate Bid Item Prices

Project/Contract	Bid Item	Unit	Quantity	Total 2023$
55 - Bethany Aqueduct Pipel	85201000 - Mobilize Tunnels & Shafts	LS	1	662,974
	85201500 - Site Setup Tunnels & Shafts	LS	1	404,143
	85202000 - Excavate Jones PenstockTunnel 1	LF	200	1,721,806
	85202500 - Excavate Jones Penstock Tunnel 2	LF	200	1,721,806
	85203000 - Excavate Jones Penstock Tunnel 3	LF	200	1,721,806
	85203500 - Excavate Jones Penstock Tunnel 4	LF	200	1,721,806
	85203550 - Staging Areas Penstock Tunnels	LS	1	3,023,838
	85204000 - Excavate Conservation Easement Tunnel 1	LF	3064	22,994,554
	85204500 - Excavate Conservation Easement Tunnel 2	LF	3064	22,994,554
	85205000 - Excavate Conservation Easement Tunnel 3	LF	3064	24,496,527
	85205500 - Excavate Conservation Easement Tunnel 4	LF	3064	24,496,527
	85205550 - Staging Areas Conservation Easement Tunnels	LS	1	6,047,676
	85205600 - Shaft Access Excavation	LS	1	2,392,667
	85206000 - Excavate Shaft 1	LS	1	5,601,227
	85206500 - Excavate Shaft 2	LS	1	5,601,227
	85207000 - Excavate Shaft 3	LS	1	5,601,227
	85207500 - Excavate Shaft 4	LS	1	5,601,227
	85207550 - Staging Areas Shafts	LS	1	1,511,919
	85208000 - Plant & Equipment	LS	1	-
	85208500 - Indirect Cost	LS	1	-
55 - Bethany Aqueduct Pipeline, Tunnels and shafts Total				**540,824,406**
66 - Bethany Discharge Structure				
	663005000 - Discharge Structure - Contractors Profit & Burden	LS	1	13,411,795
	663010000 - Mobilize for Bethany Reservoir Discharge Structure	LS	1	212,419
	663011000 - Discharge Structure Contr. Management Tech.	MO	24	13,248,456
	663015000 - Discharge Structure - Temp. Faciltities Build	LS	1	2,736,027
	663016000 - Discharge Structure - Temporary Facility Operate	MO	24	2,371,824
	663016500 - Lost Labor Time - Beth. Discharge Structure Cont.	LS	1	280,827
	663016700 - Environmental Protection - Disch. Struct.	LS	1	5,144,531
	663018000 - SITE WORK - Bethany Discharge Structure	LS	1	2,108,963
	663019000 - Cofferdam @ Discharge Structure	LS	1	5,446,342
	663021000 - Slab 1 East Section - Discharge Structure	CY	9342	6,620,099
	663022000 - Slab 2 Middle Section - Discharge Structure	CY	6593	4,761,282
	663023000 - Slab 3 West Section - Discharge Structure	CY	3420	2,784,841
	663026000 - Conc. Structural Walls - Bethany Discharge Struct.	CY	11400	16,010,938
	663050000 - Soil Nail Retaining Wall	SF	7689	1,172,630
	663055000 - Radial Gates & Stoplogs - Bethany Disch. Struct.	LS	1	15,089,082
	663060000 - Embankment Fill from Site Excavation	FCY	38266	145,435
	663062000 - Discharge Structure - Mech./Elect.	LS	1	2,591,734
	663064000 - Stop Log Struct. and Fuel Storage	LS	1	393,648
	663070000 - Discharge Structure - Finish Out	LS	1	732,501
66 - Bethany Discharge Structure Total				**95,263,374**
71 - Sacramento County Access Roads - Intakes, Batch plant & P&R				
	711001000 - Contractors Overhead and Profit	LS	1	4,393,006
	711002000 - Contractor Site Management & Facilities	MO	18	6,574,060
	711003000 - Mobilization	LS	1	169,935
	711120000 - Hood Franklin Road	MI	2.5	54,059
	711130000 - Intakes Access Road	MI	3.93	11,125,403
	711140000 - Intake #3 Access Road	MI	0.18	392,734
	711150000 - C-E-5 Intake Access Road	MI	1	2,032,299
	711315000 - Employee Park & Ride - Hood Franklin	LS	1	1,893,570
	711460000 - Lambert Road Widening	MI	3.39	3,654,711
71 - Sacramento County Access Roads - Intakes, Batch plant & P&R Total				**30,289,775**
72 - Twin Cities Advanced Sitework - Access Roads & Levees				
	721001000 - Contractors Overhead and Profit	LS	1	3,134,787
	721002000 - Contractor Site Management & Facilities	MO	8	3,463,476
	721003000 - Mobilization	LS	1	135,252
	721410000 - Twin Cities Site Development & Ring Levee	LS	1	9,742,205
	721420000 - Diersen Road Paving	MI	0.8	835,203
	721430000 - Franklin Blvd Improvements at Dierrsen	MI	0.49	1,277,522
	721470000 - Twin Cities Road Widening (East)	MI	1.01	1,649,690
72 - Twin Cities Advanced Sitework - Access Roads & Levees Total				**20,238,135**

Bethany reservoir Alternative Basis of Estimate - Construction
Attachement 2 - Estimate Bid Item Prices

Project/Contract	Bid Item	Unit	Quantity	Total 2023$
73a - Lower Roberts Island Access Roads & P&R				
	711313000 - Employee Park & Ride - Charter Way	LS	1	1,064,525
	731001000 - Contractors Overhead and Profit	LS	1	11,158,598
	731002000 - Contractor Site Management & Facilities	MO	28	11,585,468
	731003000 - Mobilization - Both	LS	1	169,935
	731830000 - Lower Roberts Island Road	MI	5.93	21,595,469
73a - Lower Roberts Island Access Roads & P&R Total				**45,573,995**
73b - State Route 12 Access Road - Terminus Site				
	731730000 - Highway 12 /Terminous Tract Widening	MI	0.82	1,808,224
73b - State Route 12 Access Road - Terminus Site Total				**1,808,224**
74a - Bethany Complex Access Roads - Byron Hwy & Interchange				
	741001000 - Contractors Overhead and Profit	LS	1	12,753,303
	741002000 - Contractor Site Management & Facilities	MO	45	19,625,790
	741003000 - Mobilization	LS	1	197,246
	741900000 - Byron Hwy Frontage Rd	MI	1.18	2,511,984
	741910000 - Byron Hwy	MI	1.05	4,816,936
	741920000 - Byron Hwy - Lindermann Rd Interchange	MI	1.82	19,591,735
74a - Bethany Complex Access Roads - Byron Hwy & Interchange Total				**59,496,993**
74b - Bethany Complex Access Roads - PP area & Roundabout				
	741930000 - Mountain House Shaft Access Road	MI	2.4	7,470,635
	741940000 - Kelso Road Widening	MI	1.48	2,343,254
	741950000 - Mountain House Road Widening	MI	3.74	6,854,429
	741970000 - Mountain House By-pass Rd	MI	0.78	4,397,029
74b - Bethany Complex Access Roads - PP area & Roundabout Total				**21,065,347**
75 - Bethany Reservoir Access Road				
	741960000 - Bethany Road	MI	1.57	9,782,459
	751001000 - Contractors Overhead and Profit	LS	1	72,569
	751002000 - Contractor Site Management & Facilities	MO	1	112,880
	751003000 - Mobilization	LS	1	21,242
	751960000 - Bethany Road	MI	0.16	316,315
75 - Bethany Reservoir Access Road Total				**10,305,466**
76 - Projectwide Road Maintenance				
	133305000 - Int 3 Ph 1 Site Work	LS	1	220,565
	155205000 - Int 5 Ph 1Site Work	LS	1	181,351
	760000000 - Project Wide Road Maintenance	LS	1	24,674,129
76 - Projectwide Road Maintenance Total				**25,076,044**
77 - Lower Roberts Rail & Rail Yard				
	770000000 - Lower Roberts Rail & Rail Yard	LS	1	16,304,932
77 - Lower Roberts Rail & Rail Yard Total				**16,304,932**
78 - Lower Roberts Levee improvements advanced work				
	781410000 - Lower Roberts Levee Improvement advanced work	LS	1	10,344,020
78 - Lower Roberts Levee improvements advanced work Total				**10,344,020**
83 - SCADA Projectwide				
	836160020 - Bethany Complex Communications (Contra Costa/Almed	MI	52.59	13,448,276
83 - SCADA Projectwide Total				**13,448,276**

Bethany reservoir Alternative Basis of Estimate - Construction
Attachement 2 - Estimate Bid Item Prices

Project/Contract	Bid Item	Unit	Quantity	Total 2023$
93 - Projectwide Restoration & Site Establishment				
	133901500 - Int 3 Ph 2 Site Restoration	ACRE	110	1,450,973
	133901600 - Int 3 Establishment Period	YR	5	703,974
	155901500 - Int 5 Ph 2 Site Restoration	ACRE	120	1,450,201
	155901600 - Int 5 Establishment Period	YR	5	582,668
	221015000 - Twin Cities - Launch Shaft Site Restoration	LS	1	6,398,179
	223015000 - Lower Roberts Island - Launch Shaft Site Restore	LS	1	2,289,747
	334050000 - Surge Basin Site Restoration	LS	1	302,759
	334050010 - Surge Basin Establishment Period	YR	5	155,383
	721410000 - Twin Cities Site Development & Ring Levee	LS	1	2,197,919
	781410000 - Lower Roberts Levee Improvement advanced work	LS	1	1,465,279
93 - Projectwide Restoration & Site Establishment Total				**16,997,083**
Grand Total				**11,080,665,979**

Project/Contract	Bid Item	Unit	Quantity	Total 2023$
91 - Bouldin Island Compensatory Mitigation				
	911017000 - Mitigation Bouldin Island Site B-1	LS	1	25,682,772
	911018000 - Mitigation Bouldin Island Site B-2	LS	1	5,627,733
	911019000 - Mitigation Bouldin Island Site B-3	LS	1	5,128,484
91 - Bouldin Island Compensatory Mitigation Total				**36,438,989**
92 - I-5 Pond Compensatory Mitigation				
	921015000 - Mitigation I-5 Pond 6	LS	1	17,319,832
	921016000 - Mitigation I-5 Ponds 7&8	LS	1	32,490,700
	921017000 - SR 12 Wildlife Crossing Culvert	LS	1	4,462,485
92 - I-5 Pond Compensatory Mitigation Total				**54,273,017**
Grand Total				**90,712,006**

Attachment 3
Risk Treatment Costs

Bethany reservoir Alternative Basis of Estimate - Construction
Attachement 3 - Distribution of Risk Treatment Costs

PROJECT	Total	Risk Treatment Cost	Percentage of total
HCSS bid item name	(All)		
Sum of Bid Total			
PROJECT	Total	Risk Treatment Cost	Percentage of total
13 - Intake 3 Facilities	$ 854,825,251	$ 27,647,192	3%
15 - Intake 5 Facilities	$ 805,528,421	$ 26,052,808	3%
21 - Reach 1 Shafts & Tunnel (Twin Cities to Intake 3)	$ 1,032,608,451	$ 60,335,345	6%
22 - Reach 2 Shafts & Tunnel (Twin Cities to Terminous)	$ 1,734,776,876	$ 95,159,675	5%
23 - Reach 3 Shafts & Tunnel (Lower Roberts to Terminous)	$ 1,292,413,060	$ 69,221,103	5%
24 - Reach 4 Shafts & Tunnel (Lower Roberts to Bethany Complex)	$ 1,957,737,597	$ 110,583,877	6%
33 - Bethany Pumping Plant, Surge Shaft and Basin	$ 2,495,740,250	$ 40,000,000	2%
55 - Bethany Aqueduct Pipeline, Tunnels and shafts	$ 540,824,406	$ 21,775,643	4%
66 - Bethany Discharge Structure	$ 95,263,374	$ 3,724,357	4%
71 - Sacramento County Access Roads - Intakes, Batch plant & P&R	$ 30,289,775	$ 1,561,699	5%
72 - Twin Cities Advanced Sitework - Access Roads & Levees	$ 20,238,135	$ 1,043,450	5%
73a - Lower Roberts Island Access Roads & P&R	$ 45,573,995	$ 2,349,732	5%
73b - State Route 12 Access Road - Terminus Site	$ 1,808,224	$ 93,230	5%
74a - Bethany Complex Access Roads - Byron Hwy & Interchange	$ 59,496,993	$ 3,067,583	5%
74b - Bethany Complex Access Roads - PP area & Roundabout	$ 21,065,347	$ 1,086,100	5%
75 - Bethany Reservoir Access Road	$ 10,305,466	$ 531,336	5%
76 - Projectwide Road Maintenance	$ 25,076,044	$ 1,292,886	5%
77 - Lower Roberts Rail & Rail Yard	$ 16,304,932	$ 840,660	5%
78 - Lower Roberts Levee improvements advanced work	$ 10,344,020	$ 533,323	5%
83 - SCADA Projectwide	$ 13,448,276	$ -	0%
93 - Projectwide Restoration & Site Establishment	$ 16,997,083	$ -	0%
Grand Total	**$ 11,080,665,979**	**$ 466,900,000**	4%

Appendix B
Total Project Costs with Innovations

Title:	**Project Wide Innovations Summary**
Prepared for:	Delta Conveyance Project (DCP) File
Prepared by:	Delta Conveyance Design and Construction Authority (DCA)
Copies to:	Files
Date/Version:	May 8, 2024 / Version 1
Reference no.:	EDM_PW_CE_MEM_Projectwide-Innovations-Summary_001325_V01_D_20240508

1. Introduction

1.1 Context and Purpose

On December 21, 2023, California Department of Water Resources (DWR) approved the Delta Conveyance Project (DCP) and selected the Bethany Reservoir Alignment for further engineering, design, and permitting necessary to be completed prior to initiating implementation. DWR completed extensive environmental review and certified the Environmental Impact Report (EIR) (DWR, 2023) as compliant with the California Environmental Quality Act (CEQA).

Following project approval, DWR directed DCA to further evaluate several project features presented in the Bethany Reservoir Alignment Engineering Project Report (EPR) and consider potential design or construction innovations to further reduce community or environmental disturbances, schedule, and/or costs or improve constructability. This evaluation resulted in a set of potential innovations that at this early conceptual stage of the project are considered by the DCA to be reasonable and credible based on industry experience. The innovations discussed herein do not represent changes to the project description presented in the EPR and analyzed in the EIR, but rather provide an indication of how normal design development processes can help manage costs for large infrastructure projects.

As the innovation concepts are further advanced, DWR will review the innovation concepts to determine and document if the innovation concepts would result in a change in the project description presented in the EPR and analyzed in the EIR. The results of these reviews will be used by DWR to determine if additional reviews will be required under the CEQA and for project permitting.

1.2 Summary of Innovations

This memorandum summarizes the process used to identify and select innovation concepts for evaluation and compares the potential cost and schedule savings to the project as described in the EIR/EPR. A summary of these innovations and their assessment related to cost and schedule is shown in Table 1-1.

Table 1-1. Summary of Innovations

Innovation ID	Innovation Title	Potential Cost Savings[a] ($M[b])	Potential Schedule Savings[c] (Days)
Intakes			
INV-I2	Intake Fish Screen Barrier System	$ 1.07	14
INV-I3	Raise Intake 3 and 5 Tee Screen Elevation	$ 4.13	28
INV-I4/I5	Intake Structure Configuration	$ 29.81	26
Tunnels and Shafts			
INV-T1	Provide Separate Access to Double Launch Shafts	($ 0.63)	No Change
INV-T2	Tunnel Lining Optimization	$ 45.85	No Change
INV-T3	Planning for Semi Continuous Mining	$ 70.35	184
INV-T4	Optimizing Tunnel Profile and Shaft Sizes	$ 95.43	192
Pumping Plant and Surge Basin			
INV-P1	Optional Pumping Plant Belowground Configuration	$ 138.72	981
INV-P3	A) Surge Basin Slab Uplift Resistance B) Surge Basin Wall Configuration	P3A: $ 178.44 P3B: $ 52.39	P3A: 280 P3B: 237
Aqueducts			
INV-A1/A5	Reduce Pipe Diameter and Trench Section	$ 60.38	79
INV-A4	Bethany Conservation Easement Tunnel/Shaft Considerations	$ 14.36	222
Discharge Structure			
INV-D1	Reconfigure Discharge Structure Retaining Wall	$ 1.39	No Change
INV-D2	Refine Bethany Reservoir Discharge Structure Configuration	$ 38.50	554
Hydraulics and Operations			
INV-H1/H2	Reduce Diameter of Intake Shafts and Maintenance Shafts	$ 40.11	No Change
Logistics			
INV-L1	Eliminate Rail-Served Materials Depot – Lower Roberts Island	$ 16.30	128
INV-L2	Hood Franklin Road Intersection Innovation	$ 2.05	No Change

[a] Potential Cost Savings refers to reductions associated with potential innovations compared to the Construction Cost estimate for the Bethany Reservoir Alignment as depicted in the EPR. Values in () represent a potential increase in costs.

[b] Costs are in 2023 dollars and are undiscounted.

[c] Schedule savings represent the number of physical construction days that could be saved for the feature studied. The potential schedule savings would reduce the overall project schedule only if the schedule for that feature impacts the overall project critical path.

As shown in Table 1-1, each innovation concept is identified with an ID number and grouped by project feature (i.e. Intakes, Tunnels and Shafts, etc.). The innovation concepts presented in Table 1-1 are mutually exclusive and have been analyzed as independent concepts except for the following:

- Innovation T4 considers the cost differential associated with adjusting the tunnel profile and assumes the reduced shaft diameter included with innovation H1/H2.
- Innovation A4 considers a revised profile of the tunnel under the Bethany Reservoir Conservation Easement and incorporates the reduced diameter of the aqueduct pipelines as presented in innovation A5.

A summary of the potential cost savings by major project feature is presented in Table 1-2.

Table 1-2. Potential cost savings from combined set of innovations

Feature	Potential Construction Cost Savings[a] ($M[b])	Potential Risk Treatment Cost Savings[a,c] ($M[b])	Total Potential Cost Savings[a] ($M[b])
Intakes (I2, I3, I4, I5)	$35	$1	$36
Tunnels & Shafts (T1, T2, T3, T4, H1/H2)	$211	$12	$223
Pumping Plant & Surge Basin (P1, P3)	$370	$6	$376
Aqueducts (A1, A4, A5)	$75	$3	$78
Discharge Structure (D1, D2)	$40	$1	$41
Logistics (L1, L2)	$18	$1	$19
Total	**$749**	**$24**	**$773**

[a] Potential Cost Savings refers to reductions associated with potential innovations compared to the construction cost estimate for the Bethany Reservoir Alignment as depicted in the EPR. Values in () represent a potential increase in costs.

[b] Costs are in 2023 dollars and are undiscounted.

[c] Risk treatment cost savings are estimated as a scaled proportion of construction cost savings relative to the Total Project Cost estimate for the Bethany Reservoir Alignment as depicted in the EIR/EPR.

As shown in Table 1-2, the innovations evaluated for the tunnels and shafts and the pumping plant and surge basin present the greatest potential savings and make up the majority of the combined innovation savings. The potential benefits of the identified innovations or future innovations should be further analyzed as project definition improves. Additional benefits of potential design or construction innovations to improve constructability or further reduce community or environmental disturbances, schedule, and/or costs savings associated with potential innovations could be realized but would require further analyses in coordination with DWR.

2. Development and Screening of the Innovations

The purpose of identifying and developing innovations at this early stage of conceptual design was to demonstrate the potential project benefits associated with industry innovation, constructability improvements, and eventual value engineering activities that will likely occur in future design phases. Initially, 167 innovative ideas were identified with potential to improve the project. The DCA analyzed the ideas and categorized them into 51 potential innovations that were then advanced through additional

feasibility-level analyses and reviewed in a series of workshops with DCA and DWR staff. The result of this screening and evaluation process was the identification of 19 reasonable innovation concepts that could result in potential cost and/or schedule reductions, which are summarized in this memorandum.

3. Analysis of the Innovations

The DCA determined a variety of potential improvements, or innovations, to the EPR conceptual design based on additional engineering and design consideration and additional geotechnical subsurface information not available at the time of completing the EPR conceptual design. When deciding which innovations might be considered for further evaluation, the innovation concept was compared to the EPR conceptual design in terms of cost and schedule.

3.1 Cost Considerations

To evaluate the cost savings, a high-level concept design and subsequent cost estimate for the innovations was compared to the baseline construction cost estimate for the project described in the EPR/EIR. For some innovations, the basic design remained the same, but with a change to the quantities, and hence cost. For other innovations, new potential construction approaches associated with the concepts were evaluated and compared using the same unit costs as presented in the baseline construction cost estimate to determine the potential construction cost savings.

Cost evaluations resulted in either a cost increase, cost decrease, or minimal change compared to the baseline cost estimate prepared for the EPR concept design. The cost evaluation also considered how each innovation could either reduce or optimize construction materials, labor hours, and construction sequencing to ultimately reduce the cost and schedule duration while still meeting the overall functional requirements of the project. The construction cost savings presented for the innovations include the same cost basis used to develop the baseline construction cost estimate as related to materials, labor and equipment, taxes, contractor markup and profit, and other add on costs such as insurance and bonds. This analysis does not re-evaluate risk treatment costs associated with design and construction of the project features, but rather applies a proportionally scaled portion of the risk treatment costs as described for the baseline construction cost estimate for the project.

Innovation construction cost savings presented in this memorandum do not currently include contingency. However, it is recommended that the same contingency be applied to the innovation construction costs savings as used for the baseline total project cost estimate when comparing the cost impacts. Innovations may reduce the impact of uncertainty within the cost estimate currently captured by risk treatment costs and project contingencies and should be further evaluated in the future.

Labor costs associated with design and construction of the project features were not re-evaluated for this evaluation, so any comparison with the baseline total project cost estimate should use a proportionally scaled labor cost to indicate the total costs of the project including potential innovations. Cost savings discussed in this memorandum do not include effects related to the reduced schedule durations for each individual construction project nor for the reduction of the overall project schedule. Labor cost and schedule cost savings should be further evaluated during future design stages.

3.2 Schedule Considerations

Each innovation was individually assessed to determine the impact on the construction schedule compared to the EPR schedule. Where quantities of materials changed, the same production rates were

applied to ascertain new activity durations. Where new activities were introduced, production rates from similar activities were used wherever possible to determine the new activity duration.

The schedule savings referenced in this memorandum are in terms of construction days for each individual feature and not overall project schedule. The potential schedule savings for each individual feature would reduce the overall project schedule only if the schedule for that feature impacts the overall project critical path. An evaluation of overall project schedule savings should be completed as part of future design phases.

4. Description of the Innovations

This section summaries each innovation and compares it with the EPR design, including an assessment of the impacts on potential cost and schedule.

4.1 Intakes

4.1.1 INV-I2 Intake Fish Screen Barrier System

EPR Concept	
The EPR concept for the fish screen barrier system at the intakes included a combination of thirty three 24-inch-diameter pipe piles with approximately 1,015 feet of floating fabricated steel log booms affixed in front of the piles spaced at approximately 35 feet.	
Innovation Concept	
This innovation concept includes a combination of twelve 24-inch-diameter piles with approximately 995 feet of floating HDPE log booms in between the piles using proprietary vendor-fabricated floating “pile sliders” attached to each pile spaced at 100 feet maximum	
Cost Savings:	$1,070,000
Schedule Savings:	14 construction days

4.1.2 INV-I3 Raise Intake 3 and 5 Tee Screen Elevation

EPR Concept	
The EPR concept for both Intake 3 and Intake 5 places the bottom of the tee screens at EL -13 feet, which provides approximately 8.6 feet of submergence below the design (low) water surface elevation at Intake 5, and approximately 8.7 feet of submergence at Intake 3. The minimum recommended tee screen submergence is one half of the screen diameter, or 4 feet for the current 8-foot-diameter tee screen units. At the same time, the EPR concept places the screen sill at EL -17 feet, which is equal to the average river bottom elevation.	
Innovation Concept	
This innovation proposes to increase the separation between the river bottom and the bottom of the Intake 5 tee screens by up to 4.6 feet (up to 4.7 feet at Intake 3) and reduce the screen submergence to the minimum 4 feet. The height of the structure is reduced by up to 4.6 feet (up to 4.7 feet at Intake 3).	
Cost Savings:	$4,133,000
Schedule Savings:	28 construction days

4.1.3 INV-I4 and INV-I5 Intake Structure Configuration

EPR Concept	
The EPR intake structure configuration concept includes thirty 60-inch-diameter discharge pipes, each with a separate gate structure located along the discharge pipe alignment near the sedimentation basins.	
Innovation Concept	
Combined, these two innovations include replacing the thirty 60-inch-diameter discharge pipes with fifteen 84-inch-diameter discharge pipes and combines the gate box structures with the intake structure. In addition, structural elements are added to each bay of the intake structure to resist tunnel jacking forces from construction of each of the 84-inch-diameter discharge pipes.	
Cost Savings:	$29,810,000
Schedule Savings:	26 construction days

4.2 Tunnels and Shafts

4.2.1 INV-T1 Provide Separate Access to Double Launch Shafts

EPR Concept	
In the EPR, access to the raised launch shaft pads is via ramps that are shared by two potential contractors, each responsible for driving a tunnel from the double shaft in opposite directions.	
Innovation Concept	
This innovation adds two additional ramps together with a slightly larger top of pad area that would enable each contractor to access their respective halves of the double launch shaft and with an effective dividing wall between them. Reorganization of the equipment and access routes would mean that each contractor could be entirely responsible for maintaining their own construction roads.	
Cost Savings:	($630,000)
Schedule Savings:	No change to schedule

4.2.2 INV-T2 Tunnel Lining Optimization

EPR Concept	
The reinforcement details for the tunnel lining in the EPR concept was based on the maximum net pressure that could be encountered for the entire 45-mile-long tunnel being applied to all tunnel reaches. The design accounted for internal and external water pressure but assumed no soil loads acting on the tunnel to counteract the internal pressures.	
Innovation Concept	
This innovation reduces the amount of reinforcement required in the tunnel lining by considering the maximum net internal pressure that will be encountered within each tunnel reach individually and accounting for an effective soil pressure to counteract the internal pressures.	
Cost Savings:	$45,850,000
Schedule Savings:	Reduced construction time but no impact to the overall schedule

4.2.3 INV-T3 Planning for Semi-continuous Mining

EPR Concept	
The EPR assumed tunnel excavation using a TBM with separate phases for excavation and tunnel lining installation. In this manner, a full precast concrete segmental tunnel lining ring is installed before the TBM rams push the machine forward from the leading edge of the lining to excavate the next section.	
Innovation Concept	
This innovation concept considers the latest TBM technology that allows a TBM to thrust forward from a partially completed segmental lining ring such that excavation and lining installation can happen concurrently.	
Cost Savings:	$70,350,000
Schedule Savings:	101 construction days for Reach 1 160 construction days for Reach 2 118 construction days for Reach 3 184 construction days for Reach 4

4.2.4 INV-T4 Optimize Tunnel Profile and Shaft Sizes

EPR Concept	
The tunnel profile in the EPR slopes continuously from north to south at a constant slope of about 0.01% and is excavated to a depth of approximately 200 feet. The diaphragm walls and final linings of the shafts are shown as 5 feet and 3 feet thick respectively and the shafts invert slabs are 30 feet thick.	
Innovation Concept	
This innovation considers optimizing the vertical tunnel profile and the configuration of the reception and maintenance shafts by reducing the depth of the tunnel between Intake No. 3 and the Stockton Deep Ship Channel Crossing and then increasing the depth of the tunnel from Lower Roberts Island Launch Shaft to the Surge Basin Reception Shaft to provide clearance underneath the future East Bay Municipal Utility District (EBMUD) Mokelumne Aqueducts Resiliency Project (MARP) tunnel. It also considers reducing diameter of the reception and maintenance shafts along with the thickness of the diaphragm walls, final lining and invert slab of the reception and maintenance shafts.	
Cost Savings:	$95,430,000
Schedule Savings:	192 construction days

4.3 Pumping Plant and Surge Basin

4.3.1 INV-P1 Optional Pumping Plant Belowground Configuration

EPR Concept	
In the EPR, the Bethany Reservoir Pumping Plant (BRPP) is a below ground structure with vertical rectangular diaphragm walls and consists of dry-pit pump bays housing the pumping plant equipment and piping plus an adjoining rectangular concrete wet well and wet well inlet conduit connected to the reception shaft located within the Surge Basin. Separate dry pit pump structures would be connected to both sides of the wet well that would be located along the center of the overall structure.	
Innovation Concept	
This innovation would replace the vertical, deep box diaphragm wall arrangement with interlinking shafts of diaphragm wall construction that would house the pumping plant equipment and piping and a tunnel that would replace the wet well and wet well inlet conduit	
Cost Savings:	$138,720,000
Schedule Savings:	981 construction days

4.3.2 INV-P3A/B- Surge Basin Base Slab Uplift Resistance/Surge Basin Wall Configuration

EPR Concept	
In the EPR, uplift resistance to the surge basin base slab is provided by an array of six-foot diameter passive (not pre-stressed) drilled shafts. The surge basin perimeter walls are constructed using concrete diaphragm walls consisting of an upper structural section with two rows of tieback anchors and a lower unreinforced, cut off wall section.	
Innovation Concept	
This innovation considers tiedown anchors for the base slab instead of the drilled shafts (P3A) and a conventional tied-back sheetpile/concrete wall system for the surge basin walls (P3B).	
Cost Savings:	$230,830,000
Schedule Savings:	P3A: 280 construction days P3B: 237 construction days

4.4 Aqueducts

4.4.1 INV-A1 and INV-A5 Reducing Pipe Diameter and Trench Section

EPR Concept	
The EPR concept includes four 180-inch-diameter parallel aqueduct pipelines installed from the BRPP to the Bethany Reservoir Discharge Structure with the parallel pipes spaced at 30 feet on center constructed partially below ground (0.7 x pipeline diameter) and partially above ground (0.3 x pipeline diameter) backfilled with Controlled Low Strength Material (CLSM) from the bottom of the excavated trench to the ground surface and soil cover to 6 feet above the top of pipes.	
Innovation Concept	
This innovation reduces the diameter of the four aqueduct pipelines to 166-inch-diameter, and spaces the pipelines at 21 feet on center while maintaining the backfill and soil cover dimensions.	
Cost Savings:	$60,380,000
Schedule Savings:	79 construction days

4.4.2 INV-A4 Bethany Conservation Easement Tunnel/Shaft Considerations

EPR Concept	
In the EPR, the Bethany Conservation Easement tunnels and Bethany Reservoir Discharge Structure shafts were designed for a 180-inch-diameter pipeline. The tunnel had a constant 0.65% gradient and the shafts consisted of four circular shafts with an internal diameter of 55-feet.	
Innovation Concept	
This innovation considers the reduced aqueduct pipeline diameter proposed in INV-A5 to reduce the size of the excavated tunnel and shafts. It also considers raising the gradient of the tunnel which reduces the depth of the discharge structure shafts and reduces the diameter of the shafts from 55-feet to 32-feet.	
Cost Savings:	$14,360,000
Schedule Savings:	222 construction days

4.5 Discharge Structure

4.5.1 INV-D1 Reconfigure Discharge Structure Retaining Wall

EPR Concept	
In the EPR, shoring during construction of the discharge structure to support hillside excavation would be required and would provide a 10-foot minimum buffer from the closest edge of the Bethany Reservoir Conservation Easement. It was assumed that the shoring system included a combination of soil-nail reinforced wall and excavations sloped between 2H:1V and 1.5H:1V.	
Innovation Concept	
This innovation involves construction of a steepened slope excavation, with soil nail reinforcement to decrease the total area of the cut and volume of excavation. This will also increase the ten-foot buffer from the Bethany Reservoir Conservation Easement and provide an access road for maintenance.	
Cost Savings:	$1,387,000
Schedule Savings:	No change

4.5.2 INV-D2 Refine Bethany Reservoir Discharge Structure Configuration

EPR Concept	
The discharge structure concept in the EPR includes four 55-foot-diameter shafts and four separate channels to convey flow from each shaft to the Bethany Reservoir. Each flow channel would be isolated from the reservoir when not in operation using two radial gates.	
Innovation Concept	
This innovation proposes raising the discharge elevation of each aqueduct pipeline just above the crest of the dam spillway which provides isolation from the reservoir and eliminates the need for the isolation radial gates.	
Cost Savings:	$38,500,000
Schedule Savings:	554 construction days

4.6 Hydraulics and Operations

4.6.1 INV-H1 and INV-H2 Reduce Diameter of Intake Shafts and Maintenance Shafts

EPR Concept	
The EPR design includes 83-foot-diameter shafts at Intake Structures 3 and 5 and five 70-foot-diameter maintenance shafts.	
Innovation Concept	
This innovation reduces the shafts at Intake 3 and Intake 5 to 70-foot-diameter and reduces the maintenance shafts to 66-foot-diameter.	
Cost Savings:	$40,110,000
Schedule Savings:	No change to schedule

4.7 Logistics

4.7.1 INV-L1 Eliminate Rail-Served Materials Depot – Lower Roberts

EPR Concept	
The EPR included new rail access to Lower Roberts Island from the Port of Stockton's rail network via a new bridge over Burns Cut and a new rail-served materials depot on Lower Roberts Island.	
Innovation Concept	
This innovation maintains the construction of the Burns Cut bridge while deferring the construction of the rail-served materials depot on Lower Roberts Island as a future option.	
Cost Savings:	$16,305,000
Schedule Savings:	128 construction days

4.7.2 INV-L2 Hood Franklin Road Intersection Innovation

EPR Concept	
The EPR concept involves the widening of an existing bridge over Snodgrass Slough on Hood-Franklin Road to accommodate left and right turn pockets onto the Intake Haul Road from Hood-Franklin Road leading to the two intake construction sites.	
Innovation Concept	
This innovation involves the installation of a single-lane roundabout that would eliminate the need to widen the bridge and would provide efficient traffic movement.	
Cost Savings:	$2,050,000
Schedule Savings:	No change to schedule

5. Summary and Future Considerations

Compared to the EPR project description, the proposed set of 19 combined innovations are estimated to reduce the construction cost of the project by up to $773M (without contingency) and save a combined total of 2,925 construction days on the various projects. These proposed innovation concepts are recommended for further study as the project develops. Further evaluation of these potential innovations should be fully coordinated with other innovations, environmental impact considerations, risk elements, and other changes that might result from additional future project development.

6. References

California Department of Water Resources (DWR). 2023. Delta Conveyance Project Final Environmental Impact Report. December 2023. SCH# 2020010227.

Delta Conveyance Design and Construction Authority (DCA). 2024. Bethany Reservoir Alternative Basis of Estimate – Construction Cost, February 2024

Delta Conveyance Design and Construction Authority (DCA). 2022a. Delta Conveyance Final Draft Engineering Project Report, Central and Eastern Options. May 2022.

Delta Conveyance Design and Construction Authority (DCA). 2022b. Delta Conveyance Final Draft Engineering Project Report. Bethany Reservoir Alternative. May 2022.

Delta Conveyance Design and Construction Authority (DCA). 2023a. Delta Conveyance Final Draft Engineering Project Report Update Central and Eastern Corridor Options. November 2023.

Delta Conveyance Design and Construction Authority (DCA). 2023b. Delta Conveyance Final Draft Engineering Project Report Update Bethany Reservoir Alternative. November 2023.

EXHIBIT B
TO BRADNER DECLARATION

CALIFORNIA GEOLOGY

February 1985

50¢

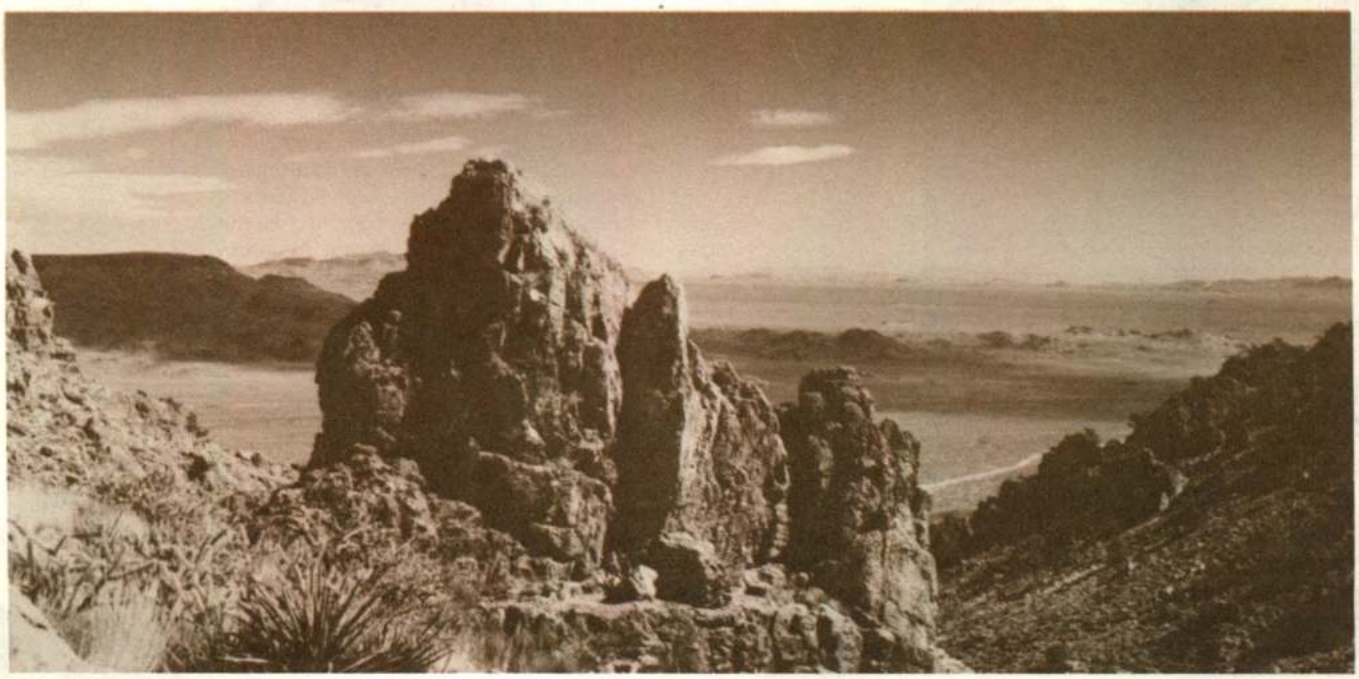

Understanding California's Geology - Our Resources - Our Hazards

CALIFORNIA GEOLOGY

A PUBLICATION OF THE
DEPARTMENT OF CONSERVATION
DIVISION OF MINES AND GEOLOGY

State of California — GEORGE DEUKMEJIAN, *Governor*

The Resources Agency — GORDON K. VAN VLECK, *Secretary for Resources*

Department of Conservation — DON L. BLUBAUGH, *Director*

Division of Mines & Geology — JAMES F. DAVIS, *State Geologist*

CALIFORNIA GEOLOGY staff

Editor-in-chief: Mary C. Woods
Editor: Don Dupras
Editorial assistance: Carole R. Johnson
Graphics and design: Louise Huckaby
Publications Supervisor: Merl Smith

Typeset: Department of Conservation
Word Processing Center
Printed: Department of General Services
Office of State Printing

Division Headquarters: 1416 Ninth Street, Room 1341, Sacramento, CA 95814
(Telephone: 916-445-0514)

Los Angeles Office: 107 South Broadway, Room 1065, Los Angeles, CA 90012
(Telephone: 213-620-3560)

Sacramento Office: 2815 "O" Street, Sacramento, CA 95816
(Telephone: 916-445-5716)

Pleasant Hill Office: 367 Civic Drive, Pleasant Hill, CA 94523
(Telephone: 415-671-4941)

CALIFORNIA GEOLOGY (ISSN 0026 4555) is published monthly by the Department of Conservation, Division of Mines and Geology. The Publication Office is at 1721-20th Street, Sacramento, CA 95814. Second class postage is paid at Sacramento, CA. Postmaster: Send address changes to CALIFORNIA GEOLOGY (USPS 350 840), Box 2980, Sacramento, CA 95812.

Reports concerning Division of Mines and Geology projects and articles and news items related to the earth sciences in California are included in the magazine. Contributed articles, photographs, news items, and geological meeting announcements are welcome.

The conclusions and opinions expressed are solely those of the authors and are not necessarily endorsed by the Department of Conservation.

Correspondence should be addressed to Editor, CALIFORNIA GEOLOGY, 1416 Ninth Street, Room 1341, Sacramento, CA 95814.

Subscriptions: $5.00 per year. Single copies: 50¢ each at DMG offices. Send subscription orders and change of address information to CALIFORNIA GEOLOGY, P.O. Box 2980, Sacramento, CA 95812

February 1985/Volume 38/Number 2

CGEOA 38 (2) 25-48 (1985)

In This Issue

COVER PHOTOS:

TOP: Providence Mountains, San Bernardino County, view toward the eastern face of the mountains rising above Clipper Valley in foreground. *Photo by Joe Engbeck.*

BOTTOM: Weathered rhyolite on crest of Providence Mountains in the foreground. View looking northeast across Clipper Valley in foreground and Fenner Valley in background. *Photo by Joe Engbeck.*

CMA Annual Meeting

The California Mining Association will hold an Annual Meeting March 6-8, 1985 in San Diego, California. The conference theme is Mining's Alive in 85.

The Safety and Health, the Environmental, the SMARA, and the Public Lands Committees will hold workshops, panel discussions, and forums focusing on Bureau of Land Management Wilderness program, management policies for the California desert, and mineral resources zones or mineral assessment procedures on public lands.

For more information contact: California Mining Association, P.O. Box 3, Jackson, CA 95642, (209) 223-1129.

MOUNT ST. HELENS: 5 YEARS LATER

A symposium on the physical and social consequences of Mount St. Helens' eruptive activity and the ramifications for volcanology will be held May 16-18, 1985 at Eastern Washington University, Cheney, Washington.

For information contact: Michael M. Folsom or Sarah A.C. Keller, Department of Geography and Anthropology, Eastern Washington University, Cheney, WA 99004 (509) 359-2433.

EARTHQUAKE DAMAGE in the SACRAMENTO – SAN JOAQUIN DELTA

SACRAMENTO AND SAN JOAQUIN COUNTIES

By
MICHAEL FINCH
California Department of Water Resources
Sacramento, California

INTRODUCTION

The Sacramento-San Joaquin Delta is located at the confluence of the Sacramento and the San Joaquin river systems (Figure 1). Nearly one-half of California's total river volume from one-third of the state's land area drains through the Sacramento-San Joaquin Delta (U.S. Army Corps of Engineers, 1982).

Before 1850 the Delta was a tidewater swamp with low, tule covered islands that were awash at high tide (Thompson, 1982). With the passage of the Arkansas Swamp Act in 1850, the federal government granted to the states all swamp and tidelands within their borders that could be reclaimed and drained. In California the State Legislature passed the Green Act (1868), which removed all controls to the reclamation process, and widespread reclamation began in the Delta. Private citizens gained title to Delta islands by constructing low levees around them and reclaiming the land. After the islands were drained and their protective native vegetation stripped off, the land began to subside. Subsidence continues today because of oxidation, dewatering, and wind erosion of the Delta's peat soils. The surface of some islands lose up to 3 inches of peaty soil per year (Newmarch, 1981). At present, an estimated 200,000 acres of the Delta are below sea level at elevations as low as minus 25 feet (California Assembly Office of Research, 1982). As the land sank, higher levees were built. Today, some Delta levees are 30 feet high (U.S. Army Corps of Engineers, 1983).

PREVIOUS STUDIES

Until recently, the earthquake safety of Delta levees was ignored. In a 1982 report, the Task Force on California's Water Future dismissed the idea of levee damage due to earthquakes because no known levee failure could be directly attributed to earthquakes. However, another report, the 1980 "Seismicity hazards in the Sacramento-San Joaquin

Levee damage on Bacon Island (Site 2). A 250-foot landside rotational slip-out dropped several feet during the January 24, 1980 Livermore earthquake.

Part of the 500-foot crack that opened on the north levee of Webb Tract (Site 4) during the May 2, 1983 Coalinga earthquake. The crack was still visible two months after the earthquake when this photograph was taken.

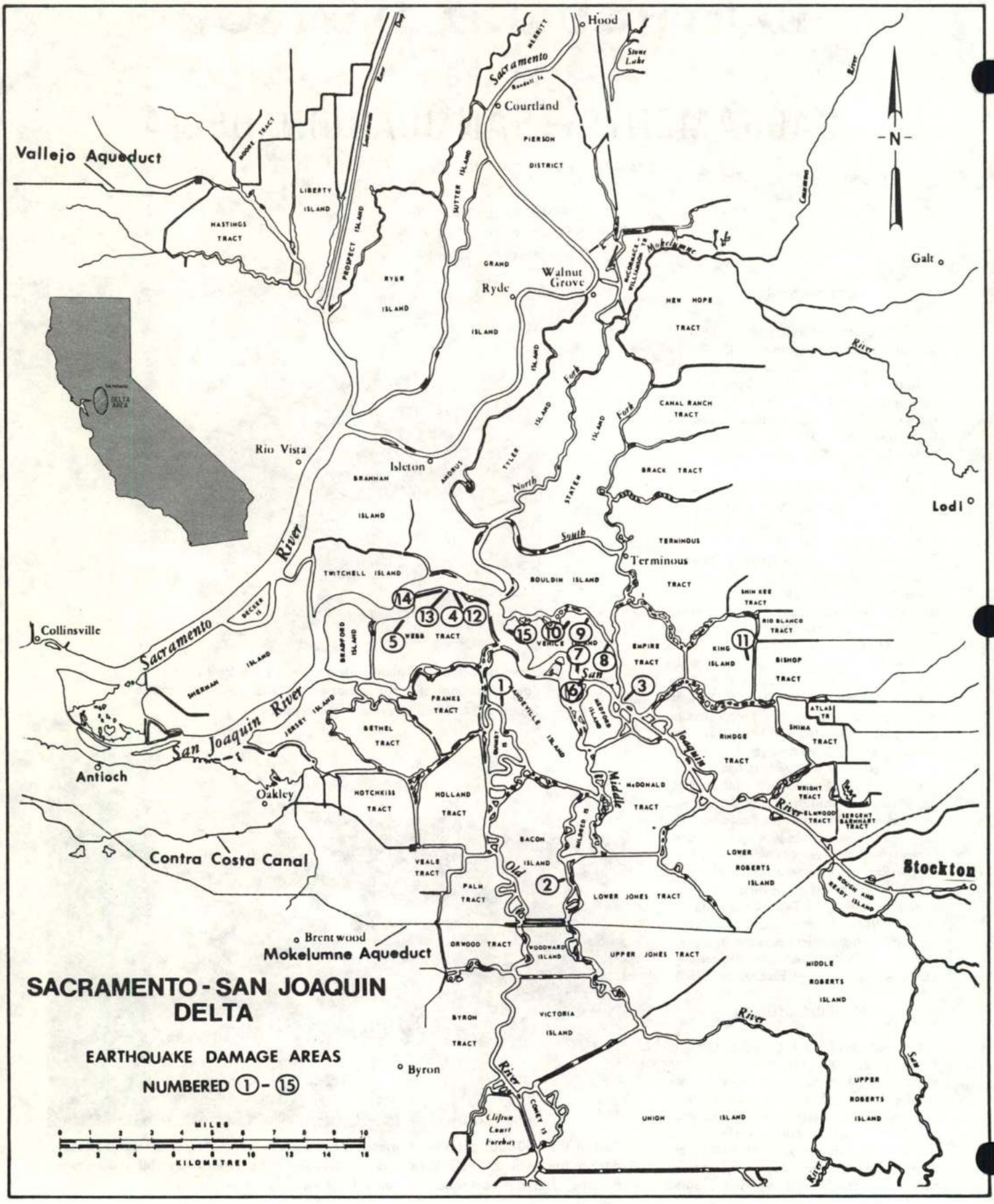

Figure 1. Sacramento-San Joaquin Delta, showing earthquake damage on levees. Damaged sites are numbered 1 through 15.

TABLE I. EARTHQUAKE RELATED DAMAGE, SACRAMENTO-SAN JOAQUIN DELTA.

Map No.	Epicenter	Date	Magnitude	Delta Island or Tract	Distance to epicenter in miles	Damage
1	Coyote Lake	8-06-79	5.9	Mandeville	65	A 500-foot section of the west levee moved landward several feet. It was noticed independently by two people, and first seen minutes after the earthquake.
2	Livermore	1-24-80	5.9	Bacon	15	A 250-foot land-side rotational slip-out dropped several feet. This damage was cited by the 1980 DWR Delta seismicity hazards report as possible earthquake related damage.
3				Empire	20	A 200-foot land-side rotational slip-out dropped 6 inches. It was reported by a local resident and a DWR employee.
4	Coalinga	5-02-83	6.7	Webb	150	A 500-foot crack opened along levee crown up to 5 feet wide. Four or five land-side rotational slip-outs caused a bulldozer to fall off levee. Several eyewitnesses were present.
5				Webb	150	The "Garratt Well," an abandoned artesian well, and the site of seepage for many years, stopped flowing. This claim is supported by DWR photographs taken both before and after the earthquake.
6				Venice	150	A 500-foot crack opened on land-side toe of levee and dropped from several inches to over 2 feet. The damage was noticed minutes after the earthquake.
7				Venice	150	An area of persistent seepage into a drainage ditch for many years. The seepage stopped after the earthquake.
8				Venice	150	Several cracks opened at the site of the 1982 levee break. One crack was 400 feet long and 10 to 20 feet deep; another crack had water pouring out of it.
9				Venice	150	A 1000-foot crack ran along the levee toe. It was up to 3 feet wide and 10 to 15 feet deep.
10				Venice	150	At this site 14 wooden pilings popped up in a field that had been mowed the day before. The tops of the pilings were evenly 9 feet above the ground surface. The pilings were the foundations of an abandoned horse barn.
11				King	160	The concrete floor of a shed cracked for a length of 25 feet and settled about 8 inches.
12	Pittsburg	6-05-83	3.6	Webb	15	Several minor cracks were noticed at the Coalinga damage area. These cracks were at right angles to those produced by the Coalinga earthquake.
13	Morgan Hill	4-24-84	6.2	Webb	60	Six parallel cracks one inch wide and 75 feet long were noticed minutes after the earthquake. They were not present the day before the earthquake.
14				Webb	60	A 25-foot long crack one inch wide was noticed the same time as site no. 13.
15				Venice	60	A pre-existing 25-foot long crack lengthened 75 feet and the land side of levee dropped 2 inches. This site was inspected by the island caretaker and DWR employees before and after the earthquake.

Delta" by the Department of Water Resources (DWR), identified the Delta as an area of definite earthquake hazard. This report concluded that no serious earthquake had occurred near the Delta since 1906, but a large earthquake today could result in the widespread loss of Delta levees.

In June 1980, two SMA-1 triaxial strong motion accelerographs were installed in the central Delta by the Department of Water Resources. An accelerograph is an instrument which records ground acceleration at a point on the earth during an earthquake. These instruments were located along the west levee of Grand Island and along the east levee of Bouldin Island. The accelerographs were removed in December 1983 after funding for the project ended. No earthquake shaking was strong enough to trigger either instrument and no data was recorded (Newmarch, 1984).

EFFECTS OF THE 1906 EARTHQUAKE

Much of the Delta was already below sea level during the April 1906 San Francisco earthquake. Prior to 1906, Delta levees were either small or nonexistent (Department of Water Resources, 1980). The levees were still relatively new in 1906 and low in height. Maps of the Delta from the 1906 era showed the land to be at or near sea level with minimum elevations of about minus 5 feet.

Although no levee damage is known due to the 1906 earthquake, several bridges sank in the Delta due to the ground shaking. The Santa Fe railroad bridge at Middle River sank 3 feet and twisted out of line (Salinas Daily Index, 1906). Another bridge over the San Joaquin River on the eastern fringe of the Delta near Stockton sank several inches (New York Tribune, 1906). The bed of the Mokelumne River near Lodi dropped 12 feet (San Francisco Chronicle, 1906). These embankments were similar in composition to present Delta levees.

The San Francisco earthquake may have weakened Delta levees and led to failures during the following wet season. In 1907, a single flood during the first high water after the earthquake flooded 53 of the 60 major islands (U.S. Bureau of Reclamation, 1964).

RECENT EARTHQUAKE DAMAGE

After the May 2, 1983 Coalinga earthquake, local residents reported levee damage on Webb Tract in the Delta. Further investigation revealed that the damage occurred in the presence of witnesses, who were working on the levee at the time of the earthquake. The damage was immediately repaired. Subsequent interviews with other Delta residents revealed 14 other reports of damage believed to be

View of some of the cracks that opened up on the north levee of Webb Tract (Site 13) during the April 24, 1984 Morgan Hill earthquake. Photographs taken the day after the earthquake.

A 25-foot crack (obscured by blowing sand) opened on Webb Tract (Site 14) during the April 24, 1984 Morgan Hill earthquake. This site illustrates the wide use of sand in the Delta for levee maintenance.

earthquake related from five earthquakes (Figure 1, Table 1). Most of these accounts were supported by information obtained from Damage Survey Reports to the Federal Emergency Management Agency, DWR personnel, and other sources.

COMPOSITION OF DAMAGED LEVEES

Of the known earthquake-damaged levees in the Delta, most of those that were in the vicinity of surface ruptures were made of coarse-grained sediments that generally had no clay content. All of the known earthquake-damaged levees contained large amounts of sand (Table 2).

Sand is used today for Delta levee maintenance because traditionally used channel deposits of peat and mud have become depleted. The use of suction dredges, to obtain sand from the channel bottom, and the use of imported sand has become common practice in the Delta over the past 10 years. Saturated sandy sediments are particularly susceptible to liquefaction during earthquakes. The continued use of sandy sediments for maintenance of Delta levees may pose a serious earthquake hazard.

TABLE 2. PREDOMINANT SURFACE SEDIMENTS AT EARTHQUAKE DAMAGE SITES ON DELTA LEVEES.

Site No. from Table 1	Predominant surface sediments
(1)	unknown at time of damage
(2)	unknown at time of damage
(3)	unknown at time of damage
(4)	silty sands, poorly graded sand-silt mixtures
(6)	silty sands, poorly graded sand-silt mixtures
(8)	well graded gravelly sands, sands; little or no fines
(9)	silty sands, poorly graded sand-silt mixtures
(12)	silty sands, poorly graded sand-silt mixtures
(13)	silty sands, poorly graded sand-silt mixtures
(14)	poorly graded sands, gravelly sands; little or no fines
(15)	well graded gravelly sands, sands; little or no fines

DIRECTION OF EPICENTER AND LEVEE DAMAGE

Apparently levees are more susceptible to damage when earthquake waves strike broadside. When a line is drawn from the earthquake epicenter to the damaged levee, the acute angle between this line and the levee crown (top) line ranges from 40 to 90 degrees with an average of 60 degrees (Figure 2). Weak levees that were parallel to the epicenter line and perpendicular to the earthquake waves, remained unaffected. The May 2, 1983 Coalinga earthquake, for example, did not affect the east levee of Webb Tract, the west levee of Twitchell Island, the east levee of Bacon Island, or the west levee of Upper Liberty Island. These levees were all weak but the acute angles between the epicenter line and levee crown are less than 40 degrees.

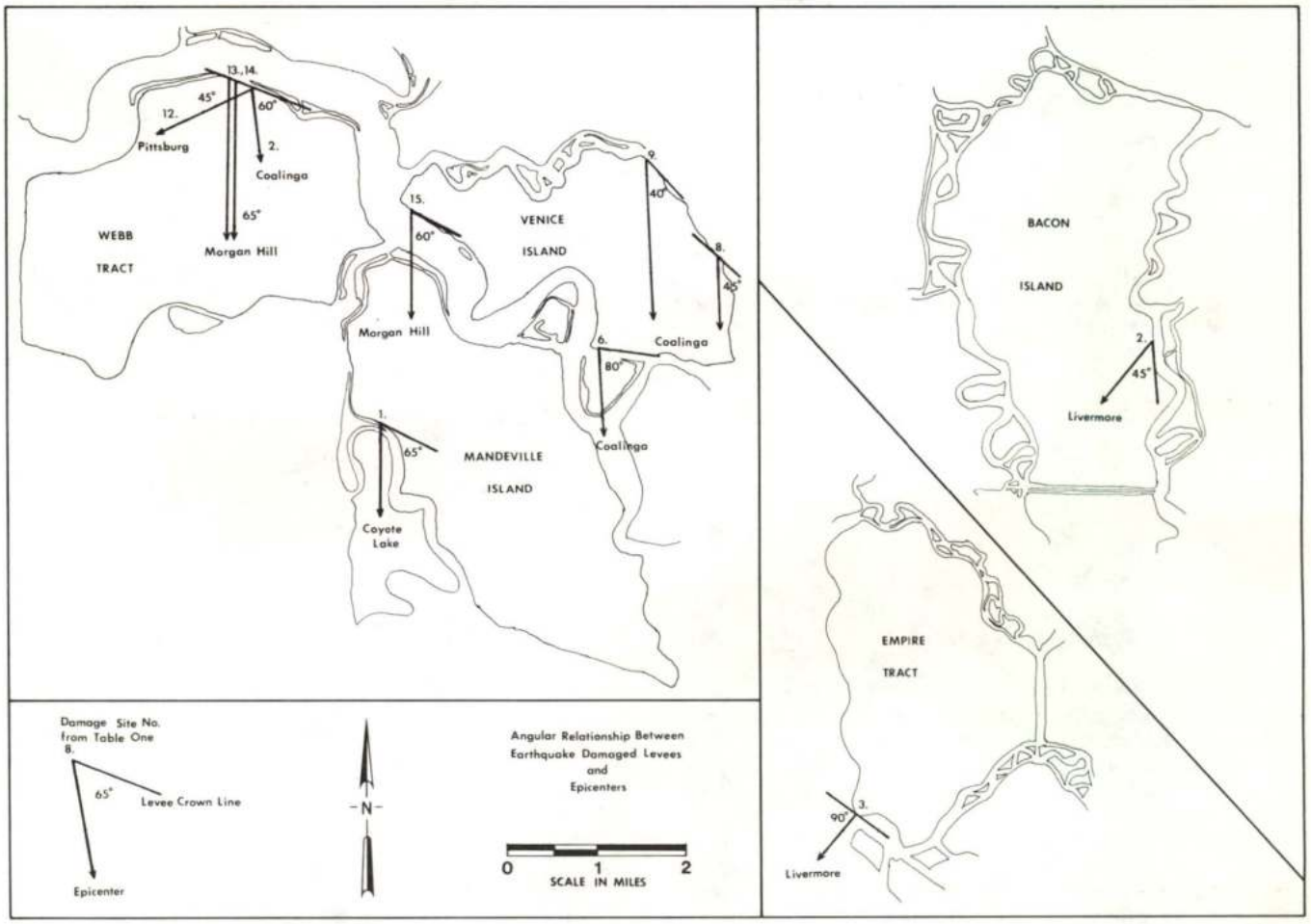

Figure 2. Angular relationship between earthquake damaged levees and epicenters, Sacramento-San Joaquin Delta. Numbers represent damage sites, Table 1. Letters keyed to locations on Figure 1.

CONCLUSIONS

The Sacramento-San Joaquin Delta was once assumed to be "seismically safe," but it now appears to have the potential for widespread damage in even a moderate earthquake. Delta levees that contain large amounts of sand are most likely to be affected by earthquakes, particularly if the earthquake waves hit the levee broadside at an angle from 40 to 90 degrees. The practice of using sand and other dredged material for levee maintenance in the Delta may contribute to earthquake instability in the future. Water pumped from the Delta directly serves two-thirds of California's population and nearly one-quarter of the state's land area. Earthquake induced levee failure in the Delta may lead to salt water intrusion from San Francisco Bay and dramatically affect California's water supply.

View of a pre-existing crack on Venice Island (Site 15) that lengthened 50 feet and dropped 2 inches during the April 24, 1984 Morgan Hill earthquake. Photograph taken the day after the earthquake.

REFERENCES

California Assembly Office of Research, 1982, Sacramento-San Joaquin Delta dilemma, p. iii.

Department of Water Resources, 1980, Seismicity hazards in the Sacramento-San Joaquin Delta, p. 2 and 3.

New York Tribune, 1906: Ruin and death widespread: April 19, 1906, v. 66, no. 21,704, p.1.

Newmarch, G., 1981, Subsidence of organic soils, Sacramento-San Joaquin Delta: CALIFORNIA GEOLOGY, v. 34, no. 7, p. 135-141.

Newmarch, G., 1984, Personal communication.

Salinas Daily Index, 1906: Latest earthquake news, the Santa Fe's condition: April 20, 1906, v. 19, no. 124, p. 3.

San Francisco Chronicle, 1906: River changed by trembler: May 1, 1906, v. 88, no. 106, p. 1.

Thompson, J., 1982, Discovering and rediscovering the fragility of levees and land in the Sacramento-San Joaquin Delta, 1870-1879 and today, California Department of Water Resources, Central District, p. 3.

U.S. Army Corps of Engineers, 1982, Draft Feasibility Report and Draft Environmental Impact Statement, Sacramento-San Joaquin Delta, p. 27 and 30.

U.S. Army Corps of Engineers, 1983, Salinity impact study for levee failures flooding Sacramento-San Joaquin Delta model islands: Report no.1, p.5.

U.S. Bureau of Reclamation, 1964, CVP CA: Delta lowlands service area investigations, Report Area DL-2, Courtland to Rio Vista and Vicinity: Grand Island, p. 2.

RETIREMENTS

Mary Louise Burgess Retires

After 39 years with the Division of Mines and Geology, Mary Louise Burgess has retired from State service. The occasion was marked by a lively gathering of over 100 people for a dinner party in her honor.

Mary Louise joined the division in 1945 when the Division of Mines and Geology (DMG) was part of the Department of Natural Resources. During her career she was Executive Secretary to seven State Geologists—Olaf P. Jenkins, Gordon B. Oakeshott (interim), Ian Campbell, Wesley G. Bruer, James E. Slosson, Thomas E. Gay, Jr. (interim), and James F. Davis.

When she retired, Mary Louise was Senior Information Clerk at the DMG's Sacramento District office, which receives more public inquiries than any other Division office. Mary Louise developed many informational packets and procedures to provide the public with prompt responses to information queries. In May 1984 she received the Department of Conservation certificate of award for Sustained Superior Accomplishment in recognition of her work.

At her retirement dinner Mary Louise was awarded a Letter of Appreciation from Governor George Deukmejian, a Resolution from the State Legislature (signed by Senator Green and Assemblyman Isenberg), and a Letter of Appreciation from the Department of Conservation.

Mary Louise celebrated her retirement by taking a trip to Hawaii.

Charles C. Bishop Retires

Charles Bishop, Senior Geologist and Assistant District Geologist for the San Francisco office, has retired after nearly 23 years of state service with the Division of Mines and Geology.

Charles received a B.S. degree in geology from the University of California at Berkeley in 1948. Subsequently, he worked for both Texaco and Intex oil companies in oil and gas exploration before joining the staff of the Division of Mines and Geology (DMG) in 1961.

As a staff member of DMG, Charles was responsible for many geologic studies and related publications. He was either author or co-author of reports on such diverse topics as Upper Cretaceous stratigraphy (Special Report 104), the mineral resources of the Ione area (Special Report 117), the Needles sheet of the Geologic Map of California, and a seismic safety and environmental resource study of the Tri-Cities area (Preliminary Report 19). He also represented DMG on the COSUNA project (correlation of stratigraphic units of North America) which was sponsored by the American Association of Petroleum Geologists.

Charles hopes to be spending much of his time in the future on the golf course, but he also plans to continue work with DMG on problems related to his special fields of interest which include stratigraphy and stratigraphic correlation in California.

EXHIBIT C
TO BRADNER DECLARATION

Title
Characterizing Seismic Performance of Levees on Peaty Organic Soils from Case Histories and Simulations

Author
Tsai, Yi Tyan

Publication Date
2018

Peer reviewed|Thesis/dissertation

UNIVERSITY OF CALIFORNIA

Los Angeles

Characterizing Seismic Performance of Levees on Peaty Organic Soils from Case Histories and Simulations

A dissertation submitted in partial satisfaction of

the requirements for the degree of Doctor of Philosophy

in Civil Engineering

by

Yi Tyan Tsai

2018

ABSTRACT OF THE DISSERTATION

Characterizing Seismic Performance of Levees on Peaty Organic Soils from Case Histories and Simulations

by

Yi Tyan Tsai

Doctor of Philosophy in Civil Engineering

University of California, Los Angeles, 2018

Professor Scott Joseph Brandenberg, Co-Chair

Professor Jonathan Paul Stewart, Co-Chair

Levee systems along Kushiro and Tokachi Rivers in Hokkaido, Japan, rest on significant deposits of peat and organic soils in downstream regions. Both levee systems were subjected to strong shaking during the 1993 **M** 7.6 Kushiro-oki and 2003 **M** 8.2 Tokachi-oki earthquakes. Local levee staff with the Japan Ministry of Land, Infrastructure, and Tourism (MLIT) performed thorough inspections of the full length of these levee systems after both events, which documented the location and severity of damages. This record of field performance presents a valuable dataset for investigating the factors that given rise to different levels of seismic performance. To my knowledge, this is the only such data set world-wide of levee performance when founded on peaty organic soils and subjected to strong earthquake shaking.

A crucial requirement for an investigation of the seismic performance of these levee systems is to understand the levels of seismic shaking they experienced. This is accomplished using a Kriging routine that operates on event-adjusted residuals between observed ground motions from local recording stations and ground motion models. Two ground motion models are considered, with some accommodations made to the path and site components of the ground motion models.

The site response component of the ground motion models is not able to capture the effect of the local geologies in the downstream regions, where the soft peat and organic soils are outside of the range present in global site databases. Accordingly, a regional site amplification model is developed using recordings from the downstream portion of the Tokachi River system in combination with nonlinear ground response analyses (GRA) with representative profiles. The profiles are based on information from the literature, local field offices, and a subsurface exploration program conducted as part of this research using the spectral analysis of surface waves (SASW) method and ambient noise measurements at 21 sites. The fundamental site period is estimated from the horizontal to vertical spectra ratio (HVSR) of the ambient noise and used as a predictive parameter for the empirical site response model. Dispersion curves are inverted to obtain shear wave velocity profiles for GRA and estimates of V_{S30} along the levees. The empirical amplification is higher and exhibits less nonlinearity than the amplification model derived from simulations. The regional model is used in place of the ergodic site terms in the ground motion models for predicting PGA at the levee segments with similar foundation conditions.

Seismic levee fragility is expressed as the probability of exceeding a damage level given the peak ground acceleration. The levee system is discretised into 50 m segments, each of which is assigned damage levels based on crack depth, crack width and subsidence from the MLIT reconnaissance.

Around a third of the 9,768 levee segments have peat within the foundations. Within the levee systems examined, levees on peat are found to be significantly more fragile than levees on inorganic soils.

Detailed analyses were performed for ten cross sections along the Tokachi River where strong motion recordings on the levees are available for the 2003 earthquake. Typical geotechnical performance assessment methods (liquefaction susceptibility, triggering, and consequence) are applied to examine the degree to which the observed field performance can be predicted. 2-D limit equilibrium models are constructed to evaluate slope displacements from Newmark analysis. A composite prediction framework considering both liquefaction severity indices and slope displacements is proposed to account for damage from multiple failure mechanisms and the consequence of liquefaction in the foundation and/or body of the levee.

The dissertation of Yi Tyan Tsai is approved.

Henry Burton

Robert Kayen

An Yin

Scott Joseph Brandenberg, Committee Co-Chair

Jonathan Paul Stewart, Committee Co-Chair

University of California, Los Angeles

2018

TABLE OF CONTENTS

LIST OF FIGURES

LIST OF TABLES

ACKNOWLEDGEMENTS

This project was funded by the Department of Water Resources under Contract No. 4600010406. Any opinions, findings, conclusions and recommendations expressed here are those of the author and do not necessarily reflect the views of the DWR. The Department of Civil and Environmental Engineering at UCLA supported me through fellowships and teaching apprenticeships, the latter of which provided a wonderful opportunity to interact with the undergraduate students.

This dissertation came to fruition through the guidance and help rendered by numerous individuals in all imaginable shapes and forms. A small fraction of which is described here:

I am deeply indebted to Professor Atsushi Mikami from Tokai University for procuring the reconnaissance reports and requesting permission for the field investigation, as well as Takashi Sato from the Civil Engineering Research Institute for obtaining the recordings from the Obihiro stations. I also acknowledge the National Research Institute for Earth Science and Disaster Prevention (NIED), Ministry of Land, Infrastructure, Transportation and Tourism (MLIT) and Japanese Meteorological Agency (JMA) for making their data readily available online.

Much gratitude to my committee, whose expertise spans the breadth of geology to structural engineering, for their thoughtful and challenging feedback. I owe my initial interest in geology to Professor An Yin for mistakenly letting me into his Yosemite Fiat Lux, and greatly enjoyed our discussions as well as the endless supply of tea. The geophysical investigation performed in Japan would have been impossible without Professor Robert Kayen, whose experience with the testing procedures and unflappable calm make the field work a pleasure. Thank you for bringing me to places I have never been, working on things I have never done.

I also won the advisor lottery – twice! Scott Brandenberg and Jonathan Stewart are extraordinary educators and exemplary advisors. Their dedication to detail and commitment to each student while juggling numerous other responsibilities is inspiring and humbling. Thanks Jon for opening up your home and hosting us for various celebrations and holidays – I now have a rudimentary understanding of American football and know to stay away from eggnog. Thanks Scott for always having your door open to questions big and small, and believing in me through all the rough patches. It was a distinct privilege to work with and learn from both of you.

A large portion of my doctorate work transpired within the collaborative environment of the geotechnical family at UCLA. I was blessed with several "older siblings" who were always happy to help, thank you Dong Youp for starting me off on the project and sharing several ; Mandro for sharing your teaching notes; Paolo and Margo for their excellent life advice and graciously hosting me in Italy, I look back very fondly on that trip. Special thanks to Sean, who did most of the heavy lifting (literally) for the geophysical field work, and Pengfei with the statistical analysis for the linear site response model. I am also grateful to have the mutual support of Sean and Grace as we wrapped up our dissertations together. And Ben, Sam, Ali, Kioumas, Claudia, Victor, Yang Yang and Ebuka for your companionship and insights.

I am also grateful for help from the departmental staff, Reba, Ben and Jesse, with all manners of paperwork and requirements. I am particularly grateful for Jesse Dieker - from lending a listening ear to wheeling over extra pizza to our office, you went far above and beyond to serve the students.

Beyond my academic circle, I am incredibly thankful to spend many normal days with my housemates, Alice, Maggie[2], Devin, Jennifer and Joanna; Prisca for all our remote study sessions, Grace[2] for all the prayers and Susan for understanding my Ph.D struggles and listening to me practice for my major presentations.

xx

Finally, the uttermost appreciation goes to my family – my Dad for giving me a firm foundation in the sciences and encouraging me to study abroad, my sister for balancing me and cheering me on. Xiaoguma for warmly welcoming me whenever I am back. Even though the distance and time difference are a challenge, your unwavering support made it possible for me to finish this marathon.

CURRICULUM VITA

2012	B.S. in Civil and Environmental Engineering, University of California - Los Angeles
2013	M.S. in Civil Engineering, University of California - Los Angeles
2014-2018	Graduate Research Assistant, Department of Civil and Environmental Engineering University of California - Los Angeles
2015	Teaching Assistant, Samueli School of Engineering, University of California - Los Angeles
2016-2018	Teaching Assistant, Department of Civil and Environmental Engineering University of California - Los Angeles

Publications

Brandenberg, S. Stewart, J., Shafiee, A., Tsai, Y.T., Wang, P and Mikami, A. (2018). "Seismic Deformation Potential of Peaty Organic Soils Underlying Delta Levees", Project Report for California Department of Water Resources, Civil & Environmental Engineering Dept., UCLA.

Tsai, Y.T., Brandenberg, S., Kayen, R., Mikami, A. Sato, T., Stewart, J. (2017) "Dataset for Empirical Assessment of Seismic Performance for Levees Founded on Peaty Organic Soils", 6th International Symposium on Geotechnical Safety and Risk, Denver, CO. Geo-Risk 2017.

Tsai, Y.T., Brandenberg, S., Stewart, J., (2016) "Estimating Ground Motions for Levees Founded Upon Soft Soils," Proc. Association of State Dam Safety Officials Annual Conference, Philadelphia.

Presentations

Tsai, Y.T., Brandenberg, S.J., "Case Studies of the Seismic Performance of Levee Segments on Peat Foundation Soil", Dam Safety 2018, Seattle, September 2018

Tsai, Y.T., Brandenberg, S.J., Stewart, J.P. "Developing fragility functions for levees on peat from case histories", Le Val Lund Student Symposium - Lifeline Infrastructure and Community Resilience, California Institute of Technology, April 2017.

Tsai, Y.T., Kayen, R.E., "Site characterization using non-invasive surface wave tests in Hokkaido, Japan", Bremen University, Germany, March 2017

Tsai, Y.T., "Seismic vulnerability of levee systems", Temple University, September 2016

1 INTRODUCTION

Levees are earthen embankments elevated from the surrounding land. They can occur naturally from deposition during flood events, or can be constructed as infrastructure to protect costal or riverside communities during high water events. Earthquakes pose a serious hazard to levees in seismically active regions, since they are frequently founded on loose alluvial deposits with shallow groundwater, and are therefore prone to liquefaction and softening from cyclic loading. This is concerning for the San Francisco Bay-Delta region in California, where the levees continuously impound water and rest on peaty foundation soils, the seismic response of which is poorly understood.

This study aims to characterize the seismic performance of levees by developing empirical fragility functions from field performance data and by performing geotechnical analysis of individual levee cross sections with well-understood ground motion demands and field performance. Following a similar approach to that introduced by Kwak et al. (2016) for the Shinano River levees, fragility functions are developed for four damage states conditioned on ground motion intensity using a combined data set from the Kushiro and Tokachi levee systems in Hokkaido. Both systems have portions of the levee system founded on peaty organic soils, as well as the occurrence of widespread and well-documented levee failures during the 1993 Kushiro-oki and 2003 Tokachi-oki earthquakes (Sasaki 2009).

The dissertation contains 6 main body chapters and progresses through the dataset development to the final fragility function development in the following manner:

Chapter 2 introduces the study region and summarizes the dataset collected, which includes geology, subsurface conditions, soil properties within and beneath the levees. The two earthquakes considered, ground motion recordings, and station information are also presented. Documentation of observed

damage and conversion to damage levels are described. Based on the dataset assembled, shear wave velocity profiles are identified to be lacking, and Chapter 3 summarizes the geophysical site investigations performed and the interpretation of the data collected with the spectral analysis of surface waves (SASW) method and ambient noise measurements to obtain additional shear wave velocity profiles and to estimate site frequencies. The site investigation revealed an additional local network of seismic stations directly on the levees in Obihiro, and subsequent collaboration with the network administrators secured additional recordings.

Chapter 4 describes the analysis performed for ten levee cross sections close to Obihiro recording stations for the 2003 Tokachi-oki earthquake. Damage severity predicted using liquefaction severity indices, as well as slope stability and deformation analyses, are compared with observed performance. The section analyses provide insight on the mechanisms driving the failure, and complement the fragility functions by providing insights to the behaviors observed.

Recognizing differences in site amplification within the downstream areas relative to predictions of ergodic site response models, Chapter 5 and 6 describe the development of site amplification functions specific to the downstream region. Chapter 5 discusses the derivation of the site amplification function empirically by examining recordings from the Obihiro stations on the levees. I provided the recordings and station properties, and Pengfei Wang performed the statistical analysis to develop the site amplification function from the within-event residuals. Chapter 6 lays out the development of representative soil profiles and ground response analysis that were performed in *DEEPSOIL* to constrain the nonlinear behavior at strong shaking. The work in Chapter 5 is previously unpublished and included here for completeness for comparison with the simulation-based site amplification functions.

In Chapter 7, the shaking intensity, represented by the PGA at the levee sites, is estimated using a combination of ground motion models and Kriging of the residuals. The resulting dataset consists of 9,768 segments for each of the events, with around a third having peat in the foundation. Failure probability and median demands are developed from binned data, and a lognormal cumulative distribution function is fitted for varying damage levels, which comprises the recommended fragility function. Comparison within the same systems show that levees on peat are much more fragile than those on inorganic soils.

Finally, Chapter 8 summarizes the findings from the work and provides recommendations for future research.

2 STUDY REGION AND DATASET

2.1 REGIONAL GEOLOGY AND CONSTRUCTION HISTORY

The environment in Hokkaido is favorable for peat formation, and prior investigations have found continuous peat deposits in the downstream region. We focused on two levee systems along the Kushiro and Tokachi Rivers on the eastern coast of Hokkaido, Japan. These levees have experienced strong shaking from large magnitude subduction earthquakes occurring directly offshore. The Hokkaido Development Bureau (HDB), under the Ministry of Land, Infrastructure, Transportation and Tourism (MLIT), manages both systems through local offices.

The Kushiro River originates from Lake Kusshаro, flowing south for 154 km through several towns and Kushiro City before discharging into the Pacific Ocean. The first levees were constructed in response to the devastating flood in 1920, with expansions and upgrades continuing until 1981. The original levees were trapezoidal and around half the height of the current levees. Expansions were made in stages through a combination of raising the levee height and widening the levee on the landward side, while retaining the original levees at the core. The current levees are benched and have a 1V:2H slope, with a crest elevation of around 9 m, crest width of 8 m and a base width of around 45-50 m in the downstream sections (Sasaki, 2009). The levees can be broadly divided into two continuous stretches: within the first 15km through Kushiro City and surrounding the Kushiro Marsh, and between 38 to 75 km along the towns of Shibecha and Teshikaga, totaling around 74 km of levees. Levees are absent between these two stretches as the neighboring areas are mostly uninhabited and surrounded by hills that naturally confine the river flow.

The Tokachi River originates from the Taisetsu Mountains and has a length of 156 km. Unlike the Kushiro River which is mostly linear, many subsidiary rivers join the Tokachi River in the Tokachi

Plains and the flood plain consists of alluvial fans and stream terraces. The steep gradient between the surrounding mountains and the plains contribute to frequent flooding. A flood control plan was established in 1918 and initial levees are constructed along the Tokachi, Otohuke, Sastunai and Urahoro Rivers. The levees along the main Tokachi River were significantly broadened in the early 2000s to remedy settlements due to the soft peaty organic soils. The peat extend to a depth of 2-6 m and are underlain by alluvial deposits of sandy, silty and clayey sediments. Under the levees, the peat layer is typically 0.5-1.0 m thinner than in the free-field. Penetration resistance measured during CPTs and SPTs, as well as shear wave velocities are low in the area. Relatively firm material, likely Pleistocene in age, is located at greater depths generally around 35-40 m.

The levees are delineated based on satellite imagery and the flood control maps compiled by the Geospatial Information Authority of Japan (2009). Levees designated as temporary on the official maps are not included as they may not be inspected after earthquakes.

2.2 EARTHQUAKE RECORDINGS

Two large magnitude earthquakes are selected based on the extensive damage that was observed, the availability of detailed damage documentation, and a wide spectrum of shaking intensities along the levee systems. Both occurred off the eastern coast of Hokkaido. The 1993 **M** 7.6 Kushiro-oki earthquake occurred on January, 15, 1993, and is an intra-slab earthquake with a hypocentral depth of 107 km. The geometry and the slip distribution of the fault plane for Kushiro-oki was obtained from the inversion of near-field strong ground motion records and aftershock distribution (Ide & Minoru 1996). Substantial lengths of levees were damaged in both system, though the more severe damage is confined to Kushiro. The 2003 **M** 8.2 Tokachi-oki earthquake occurred on September, 26, 2003, and is an inter-slab earthquake, with a hypocentral depth of 23.3 km. The finite fault model is inverted

using a combination of ground motion records and geodetic data by Koketsu et al. (2004). The hypocenter was located offshore and further south, and mainly damaged levees along the Tokachi River. Figure 2.1 shows the hypocenter, focal mechanism, slip distribution and surface projection of the finite fault planes for both events.

Ground motion recordings are obtained from the Japan Meteorological Agency (JMA), Port and Airport Research Institute (PARI), and National Research Institute for Earth Science and Disaster Prevention (NIED) and the Hokkaido Development Bureau (HDB). The NIED maintains two strong-motion seismograph networks – the Kyoshin Network (K-NET) and the Kiban Kyoshin Network (KiK-net) (NIED, 2015) and has stations deployed at approximately 20 km intervals throughout Japan. The network was established after 1995, hence limited recordings are available for the 1993 event. Obihiro Development and Construction Department (ODCD), which is a local branch of the Hokkaido Regional Development Bureau (HDB) under MLIT maintains a local network on the levees in the downstream region of Tokachi River. This is particularly valuable and discussed in more detail in Chapter 4. The number of stations active during the two earthquakes are listed in Table 2.1 for each network.

Table 2.1 Active strong motion recording stations from each network

Network	1993 Kushiro-oki	2003 Tokachi-oki
JMA	20	55
PARI	13	9
NIED	-	553
HDB (WISE)	15	120
ODCD	-	6
Total	48	737

Figure 2.1. The fault plane and the focal mechanisms for the 1993 Kushiro-oki (top) and the 2003 Tokachi-oki (bottom) earthquake.

Site condition at the stations, typically represented by the time-averaged shear-wave velocity in the upper 30 m (V_{S30}), is of interest for site response considerations. The degree of site characterization varies among the networks, with NIED stations possessing the most complete data, which includes P and S-wave velocity profiles from downhole measurements, SPT blow counts, soil type and bulk density. For stations without measured velocity profiles, V_{S30} is estimated from the geomorphology, elevation, slope and distance to hill/mountains at the station location (Wakamatsu & Matsuoka 2011). With assistance from T. Kishida, all recordings are filtered and corrected following standard PEER procedures.

2.3 SITE CHARACTERIZATION

Geotechnical data collected during routine site investigations include Cone Penetration Tests (CPTs), boring logs with Standard Penetration Tests (SPTs), and index laboratory tests on retrieved samples for soil classification purposes. Ground water levels are reported when encountered in borings, and is an important parameter for considering liquefaction susceptibility.

For the Kushiro River, subsurface information is obtained from borings and geotechnical investigations performed by the Kushiro Development and Construction Office (KDCO) for design and maintenance. Additional site investigations performed at damaged sections to evaluate suitable repair measures are also collected (KDCO, 1994). These include open-cuts and excavation pits for investigating cracks and deformation, during which soil samples are also retrieved for testing and stratigraphy of underlying layers are noted. A total of 181 borings were performed between 1980 and 2004 along Kushiro River, with the majority located in the downstream region close to Kushiro City and Kushiro Marsh. The graphical representations of the borings and an interpreted cross-section are available in an AutoCAD file, from which individual logs are extracted and digitized. Each boring is identified by the year and

the order of the investigation (i.e., S56-16 refers to the 16th boring performed in 1981), and includes groundwater depth, raw blow counts from standard penetration tests (SPT), and soil classification. The drilling method and sampler used for the borings are not specified. Figure 2.2 shows the cross section along the levees from the river mouth to around 50 km upstream. Peat, abbreviated as A_p and colored purple, is present throughout the downstream region and tapers out at around 38 km upstream. Beyond that, the foundation material consists mostly of Holocene alluvial sand or gravel deposits.

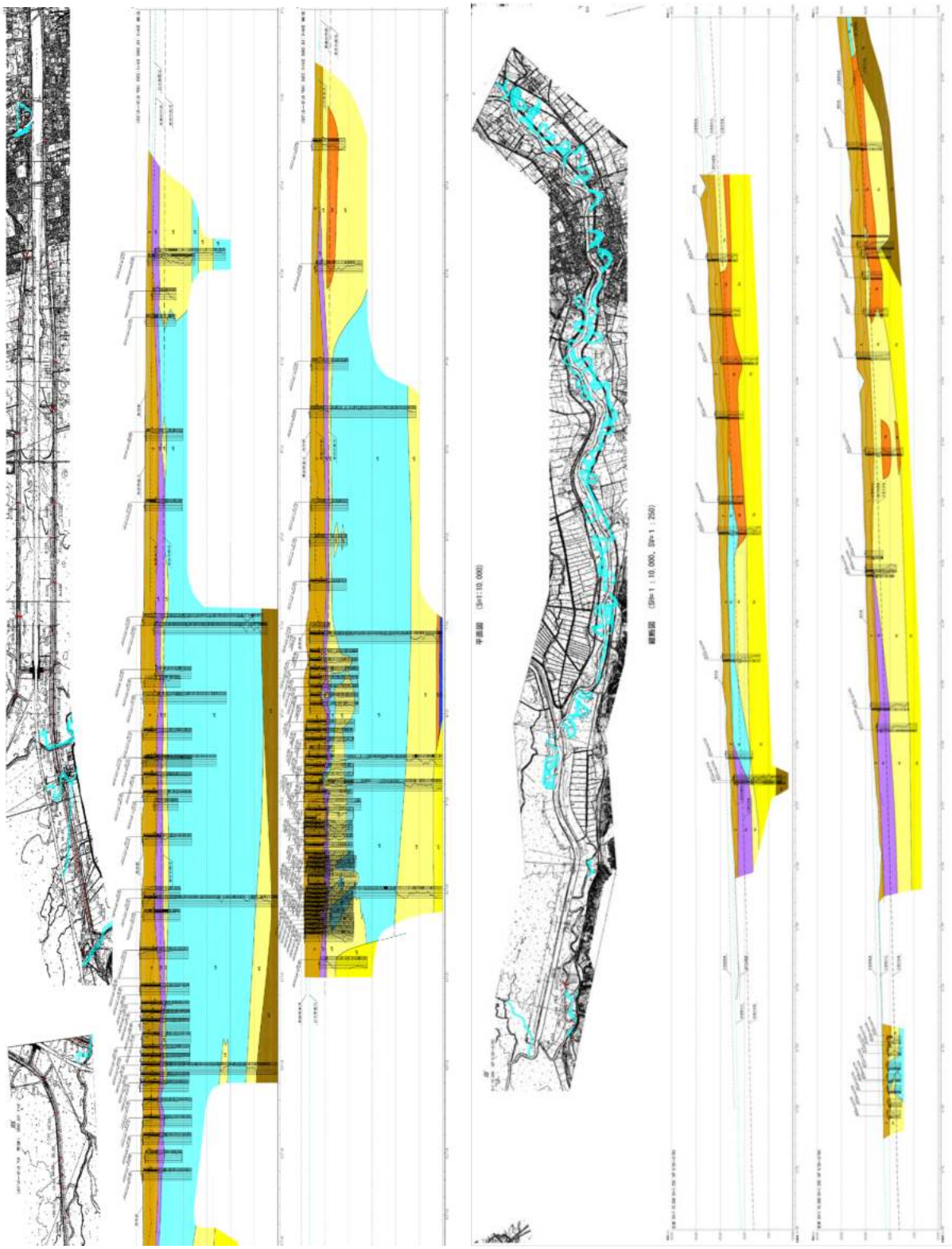

Figure 2.2. Longitudinal cross section along Kushiro River from the river mouth to 15 km (left), and 30-50 km (right). A consistent layer of peat (purple) is present under the levees in the downstream region and tapers out around 38 km upstream.

For Tokachi, the original field reports for at 21 sites investigated after the 2003 Tokachi-oki earthquake were available and includes layer descriptions according to the Japanese soil classification system, layer boundary depths, groundwater depths, raw SPT blow counts and CPT cone tip resistance. The SPTs are accompanied by stratigraphy description and soil type classified based on the composition by weight, with the major fraction exceeding 50%, the secondary fraction exceeding 15%, and the minor fraction between 5 - 15%. Thick peat deposits are present in the downstream region of Tokachi, ranging from 1-6 m. The ground water levels tend to be elevated within the levees in the downstream region.

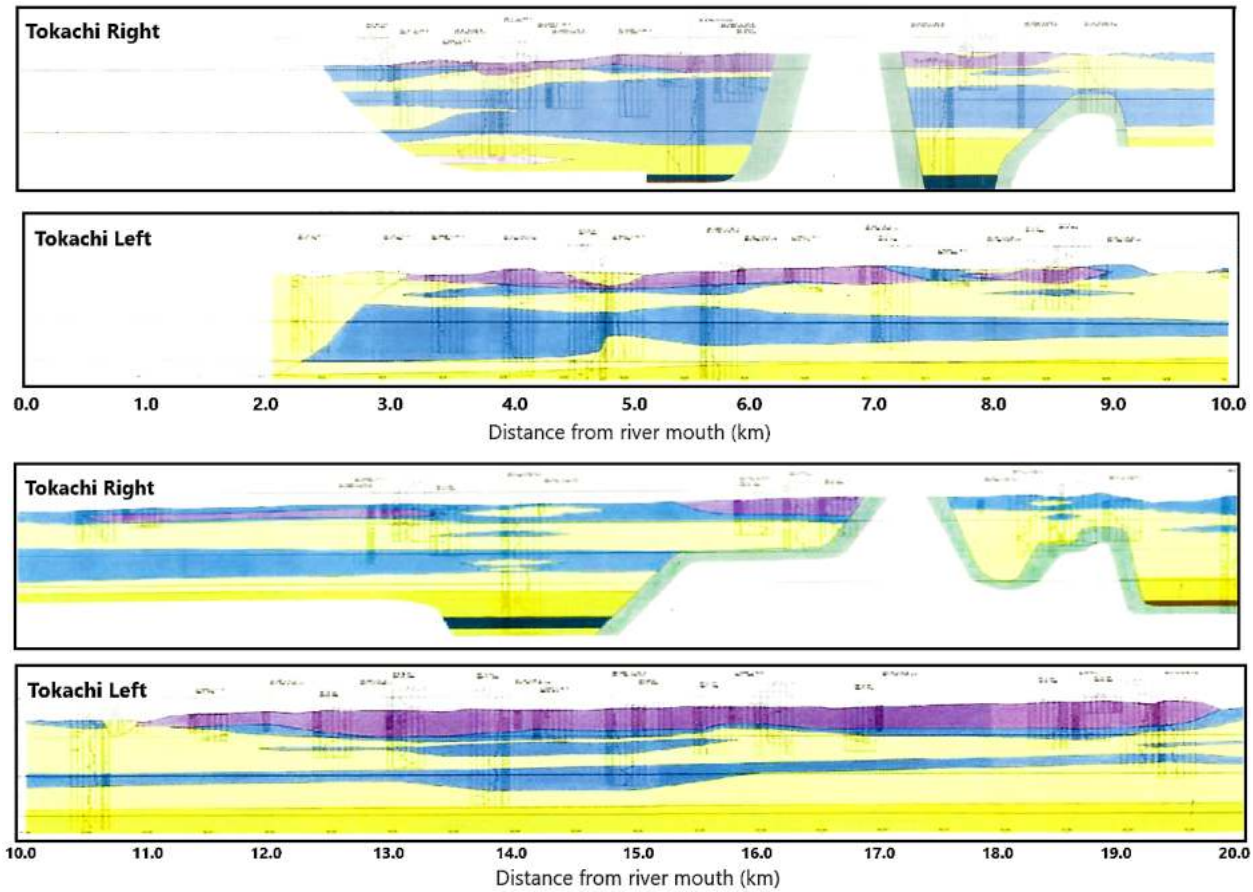

Figure 2.3 Longitudinal cross section along Tokachi River from the river mouth to 20 km. A consistent layer of peat (purple) is present under the levees.

2.4 DAMAGE DOCUMENTATION

After a strong seismic event, levees along major rivers are inspected by teams from the regional HDB offices. During the post-event reconnaissance, engineers visually inspect the entire length of the levees, documenting any signs of distress. The entire levee system is inspected and is a crucial detail indicating 1) segments without reported damage are confirmed null cases rather than unobserved performance, and 2) the performance data collected is not biased towards sections with distress. Levee sections with damage are noted, and accompanied by measurements of subsidence, differential settlement, and crack depth and width where applicable. Evidence of liquefaction, such as sand boils, are also noted where present. The information is collected from reports published by the Kushiro Development and Construction Office (KDCO) (1994, 2004), Civil Engineering Research Institute (CERI) (1993), and the Hokkaido River Disaster Prevention Research Center (2004, 2005).

The levees are discretized into 50 m segments as the basic unit. The performance, soil properties, and seismic demand is assumed to be constant within a segment. The occurrence of lack of damage for each segment is established from the reconnaissance reports, starting from the most general description of damage at the sectional level. Sections span tens to a few hundred meters, across which the range of crest settlement, width and depth of cracks, subsidence and differential settlement are given. All segments within the section are interpreted as damaged. This is followed by localized measurements based on cross-section surveys and plan views of crack distribution, as well as crack dimensions inferred from photographs. The local description supersedes the general descriptions. Levee segments without any observations are interpreted as having no damage.

The descriptions from the reconnaissance reports are mapped to damage levels (DL) indicative of overall performance based the metrics summarized in Table 2.2 (Kwak et al., 2016). If multiple observations are available and correspond to different damage levels, the most severe level is assigned.

The same scheme is adopted to allow meaningful comparison between the fragility function derived from the two studies. Figure 2.4 shows the distribution of damage levels for levees with and without peat in the foundations. Levees with peat foundations were shaken more strongly than levees on inorganic soil further upstream (and further from the earthquake source), therefore Figure 2.4 alone is inadequate to assess the relative fragility of levees on peat compared with levees on inorganic soil. The ground shaking level must also be considered. Figure 2.5 shows photographs for perspective on the severity of each damage level (KDCO, 1994).

Table 2.2 Damage level assignment

Damage Level	Crack depth (cm)	Crack width (cm)	Subsidence (cm)	Description
0	0	0	0	No damage reported
1	0-100	0-10	0-10	Slight damage, small cracks
2	100-200	10-50	10-30	Moderate damage, cracks or small lateral spreading
3	200-300	50-100	30-100	Severe damage, lateral spreading
4	> 300	> 100	> 100	Levee collapse

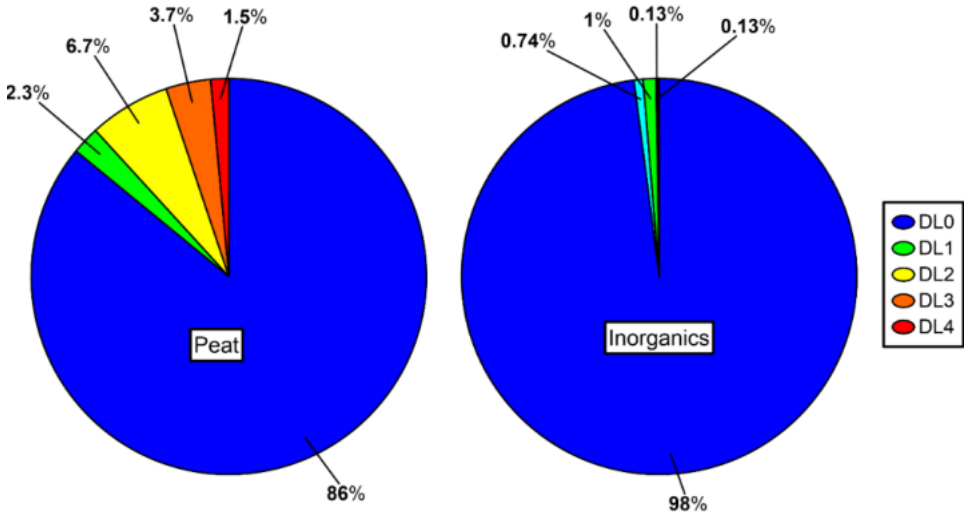

Figure 2.4 Distribution of damage levels for segments with peat or inorganic foundation material for both earthquakes.

Figure 2.5 Photographs after the 1993 and 2003 earthquakes showing the various damage levels. (a) Level 1, with minor cracking and no subsidence, (b) Level 2, with 20-30 cm of subsidence and cracks on the exterior face (c) Level 3, with subsidence of over 30 cm and (d) Level 4, with 60-225 cm of subsidence and 6 m wide cracks (KDCO 1994, 2004).

3 GEOPHYSICAL SITE INVESTIGATION

3.1 INTRODUCTION

Measurements of shear wave velocity at the levees are not routinely performed in Japan, but is crucial for performing site-specific ground response analysis. In addition, the effect of shallow soil layers on earthquake ground motions is typically represented by the time-averaged shear wave velocity in the upper 30 meters (V_{S30}) in Ground Motion Models (GMMs). Professor Robert Kayen, Sean Ahdi and I performed geophysical measurements at 21 sites along Kushiro and Tokachi Rivers from 20 June to 4 July 2016. We focused on the downstream regions where peat is expected based on prior subsurface investigations and geology maps, and with the following considerations:

- Availability of nearby borings to provide stratigraphy information to guide inversion of dispersion curves to obtain shear wave velocity (V_S) profiles;
- Prioritizing strong motion stations near/on levees without prior site characterization;
- Adequate spatial coverage representing full range of observed damage from both earthquakes.

We collected ambient noise for developing horizontal-to-vertical (H/V) spectral ratios to estimate site period, and spectral analysis of surface waves (SASW) measurements for developing dispersion curves for inversion. Original plans included drilling and sampling at the levee sites, but permissions could not be secured, and geophysical investigation is performed instead. A total of 23 ambient vibration measurements were made, with 10 along Kushiro River and the 13 along Tokachi River. A total of 21 SASW tests were conducted, with 10 along Kushiro River and the remaining 11 along Tokachi River. The SASW test and ambient noise recordings would ideally be co-located, but due to time constraints, they were performed concurrently. Each test location have a pair of ambient noise and SASW test,

except for 1048HK and 1049HK where two ambient noise measurements were made. The tests are spaced apart by 200-300 m to minimize the disturbance from footsteps and machinery from the SASW testing on the recordings. The test sites are shown in Figure 3.1 and 3.2.

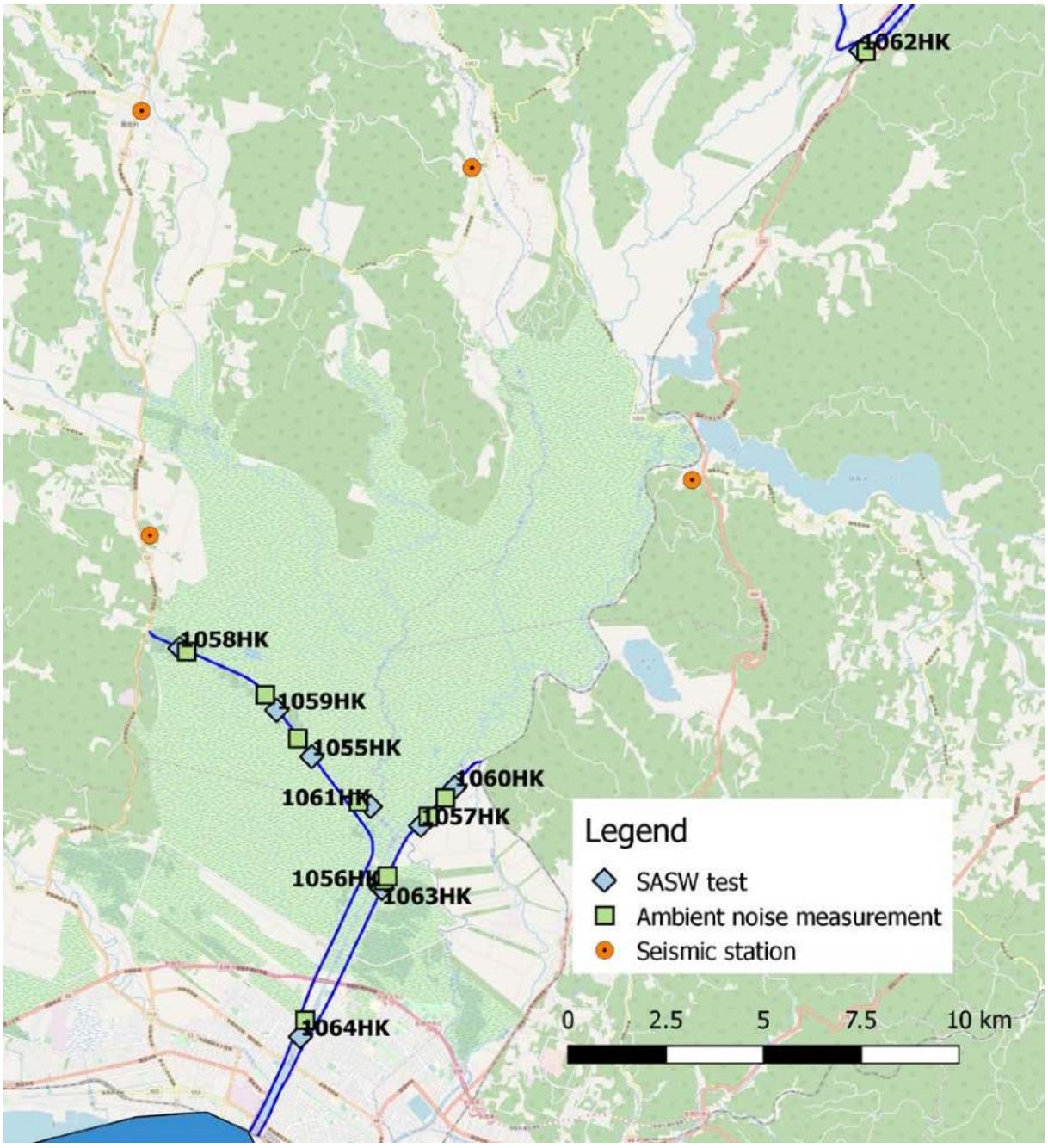

Figure 3.1 Test sites along Kushiro River are concentrated within the downstream basin, where peat deposits are present. Ambient noise measurements are performed close to SASW tests.

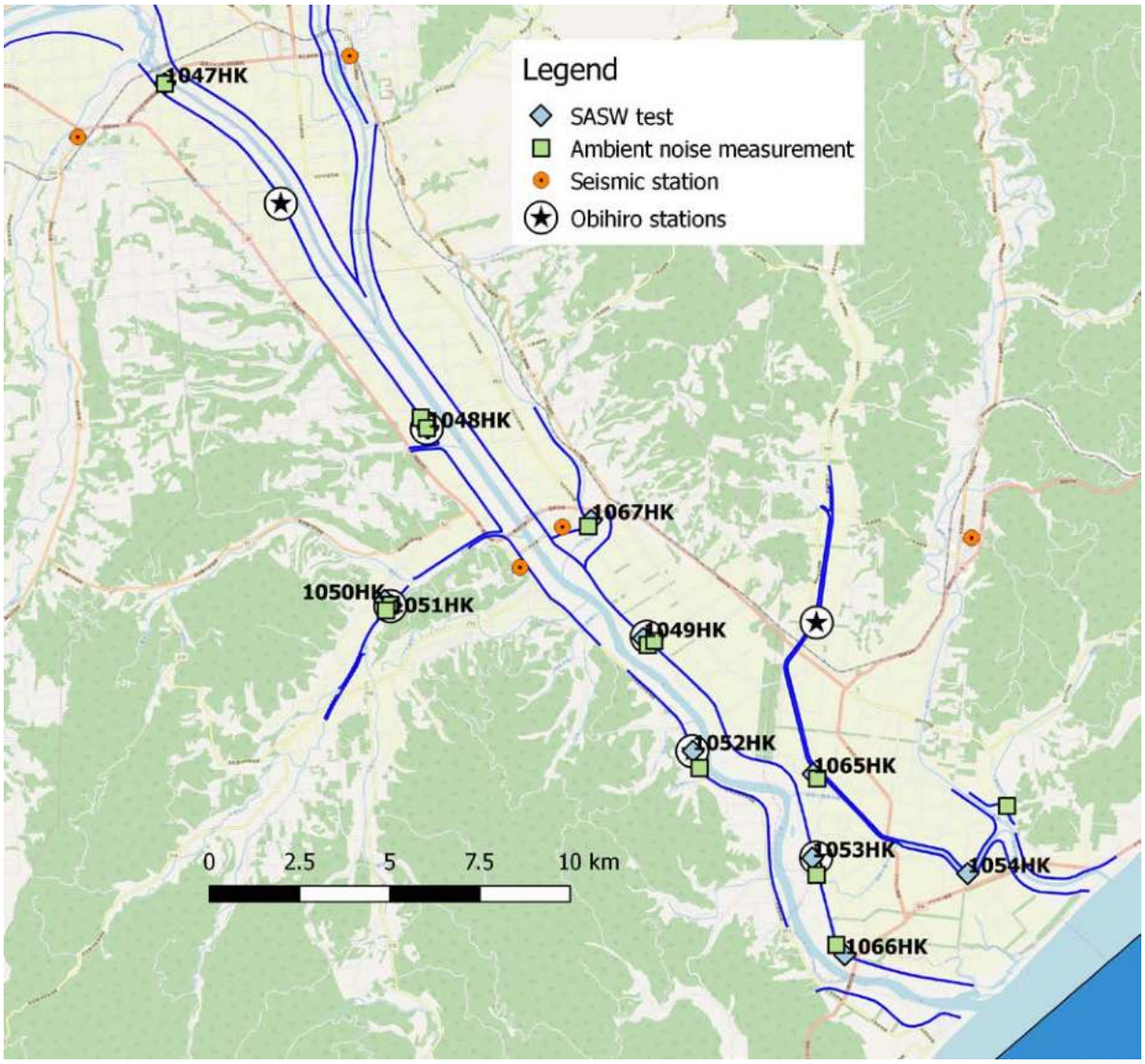

Figure 3.2 Test sites along Tokachi River. A local network of recording stations installed on the levees and are prioritized for testing.

3.2 AMBIENT NOISE RECORDINGS AND SITE PERIOD

The principal motivation for considering H/V spectral ratios is to identify the site period and possible resonance effects in the site amplification. The ambient vibrations were recorded using a triaxial seismometer and a Trimble REF TEK 130 data acquisition unit, and each record lasts between 60-120 minutes. The frequency at which the fundamental-mode resonance occurs in the site response (f_{peak}) is

estimated from the peaks in plots of H/V spectral ratio against frequency. Shorter windows within the main record are selected to exclude transient signals (e.g., footsteps, passing vehicles and wind) in the open-source program Geopsy (www.geopsy.org). Figure 3.3 shows ambient vibrations recorded at site 1050HK. Fourier spectra are computed for each time window and subsequently averaged. f_{peak} at each site are summarized in Table 3.1 and are generally lower along the Kushiro River than along the Tokachi River. The plots of the HV spectra and selected f_{peak} are presented in Appendix A. The peak frequency is used as a predictive variable for a region-specific ergodic site amplification model in Chapter 5.

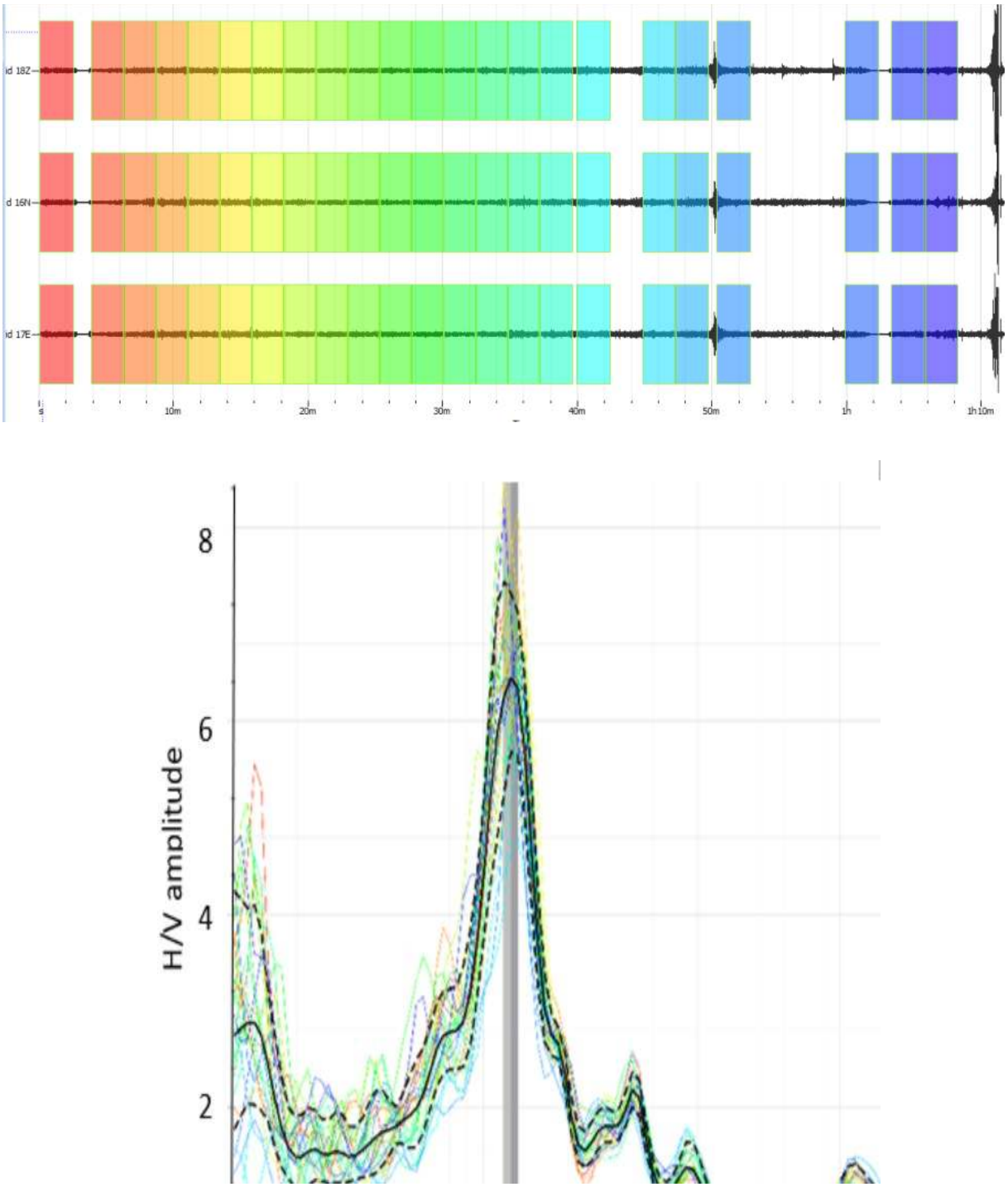

Figure 3.3 Ambient vibrations recorded at 1050HK site (top). Shorter segments are selected to exclude transient excitations. The H/V spectra ratio is computed for each windowed interval and the averaged spectra shown by the solid black line with a distinct peak around 1.2 Hz (bottom).

Table 3.1 Fundamental frequencies estimated from HVSR

Test Site	River	Date	Latitude	Longitude	Position	f_0 (Hz)
1047HK	Tokachi	6/25/2016	42.921	143.386	Riverside	0.27
1048HK-a	Tokachi	6/26/2016	42.839	143.472	Landside	1.50
1048HK-b	Tokachi	6/26/2016	42.836	143.474	Landside	1.60
1049HK-a	Tokachi	6/26/2016	42.782	143.549	Riverside	1.54
1049HK-b	Tokachi	6/26/2016	42.783	143.551	Landside	1.66
1050HK	Ushi	6/27/2016	42.792	143.462	Landside	1.19
1051HK	Ushi	6/27/2016	42.791	143.461	Crest	1.18
1052HK	Tokachi	6/27/2016	42.751	143.567	Riverside	1.08
1053HK	Tokachi	6/28/2016	42.725	143.606	Crest	0.87
1054HK	Urahoro	6/28/2016	42.742	143.671	Landside	2.30
1055HK	Kushiro	6/29/2016	43.089	144.374	Landside	0.32
1056HK	Kushiro	6/29/2016	43.057	144.401	Riverside	0.49
1057HK	Kushiro	6/29/2016	43.071	144.415	Landside	0.49
1058HK	Kushiro	6/30/2016	43.109	144.339	Landside	1.24
1059HK	Kushiro	6/30/2016	43.099	144.364	Landside	0.29
1060HK	Kushiro	6/30/2016	43.076	144.420	Landside	0.50
1061HK	Kushiro	7/1/2016	43.075	144.393	Marsh	0.39
1062HK	Kushiro	7/1/2016	43.247	144.552	Riverside	1.25
1063HK	Kushiro	7/2/2016	43.058	144.402	Crest	0.49
1064HK	Kushiro	7/2/2016	43.025	144.376	Riverside	0.59
1065HK	Shita	7/3/2016	42.749	143.607	Landside	1.75
1066HK	Tokachi	7/3/2016	42.708	143.613	Riverside	0.97

3.3 SPECTRAL ANALYSIS OF SURFACE WAVES

The SASW test measures surface wave dispersion data of near-surface layers, which is then inverted to profile the subsurface conditions. An active continuous swept-sine wave source is used with a notch-filter, which allows control over the frequencies generated and improves signal to noise ratio (Kayen et al. 2004). Our test setup consists of an electro-mechanical harmonic shaker driven by a signal

generator and two uniaxial seismometers arranged in a linear array. The instruments and the setup are pictured in Figure 3.4.

During each run, the shaker sweeps through a range of frequencies in stepped increments for a set number of cycles. The wavelength range of the dispersion curve was constrained by the source receiver and the inter-receiver distances. The frequency range and step size for each run depend on the thickness and stiffness of the underlying soil layers. A thick, soft soil layer requires lower frequencies to produce waves with sufficiently long wavelengths to penetrate and image it. The separation of the seismometers is increased after each run. Portions of the data with low coherence (low signal to noise ratio) is masked, and the phase angle between the seismometers is determined from the cross-power spectrum. The Rayleigh wave velocity through the underlying soil is given by:

$$V_R = f \times \frac{2\pi}{\emptyset} \times s \tag{3.1}$$

where *f* is the frequency of the shaker, $\emptyset$ is the unwrapped, cumulative phase angle in radians, and *s* is the separation distance between the sensors. This is performed at all frequencies for each sensor separation.

Figure 3.4 The mass shakers for generating harmonic stepped waves (top left) and the seismometer (top right). The spacing between the seismometers are changed after each sweep by the mass shakers (bottom).

Ideally the individual dispersion curve for a single sensor spacing would overlap with curves for other sensor spacings to form a single composite curve as shown in Figure 3.5a. A few sites have scattered, non-overlapping curves as seen in Figure 3.5b, which may arise from unusual subsurface conditions present at the test site. Several of the ill-behaved test are measured on the levee crest where the presence of the stiffer levee material over the softer underlying peat may result in higher modes in the dispersion curve data. 11 sites have excellent data, and 5 sites have a subset of the measurements at select separations that are excluded. The remaining 5 sites have very scattered data and a composite curve cannot be reasonably fitted. Table 3.2 summarizes the test locations, with site photos and dispersion curves presented in Appendix A.

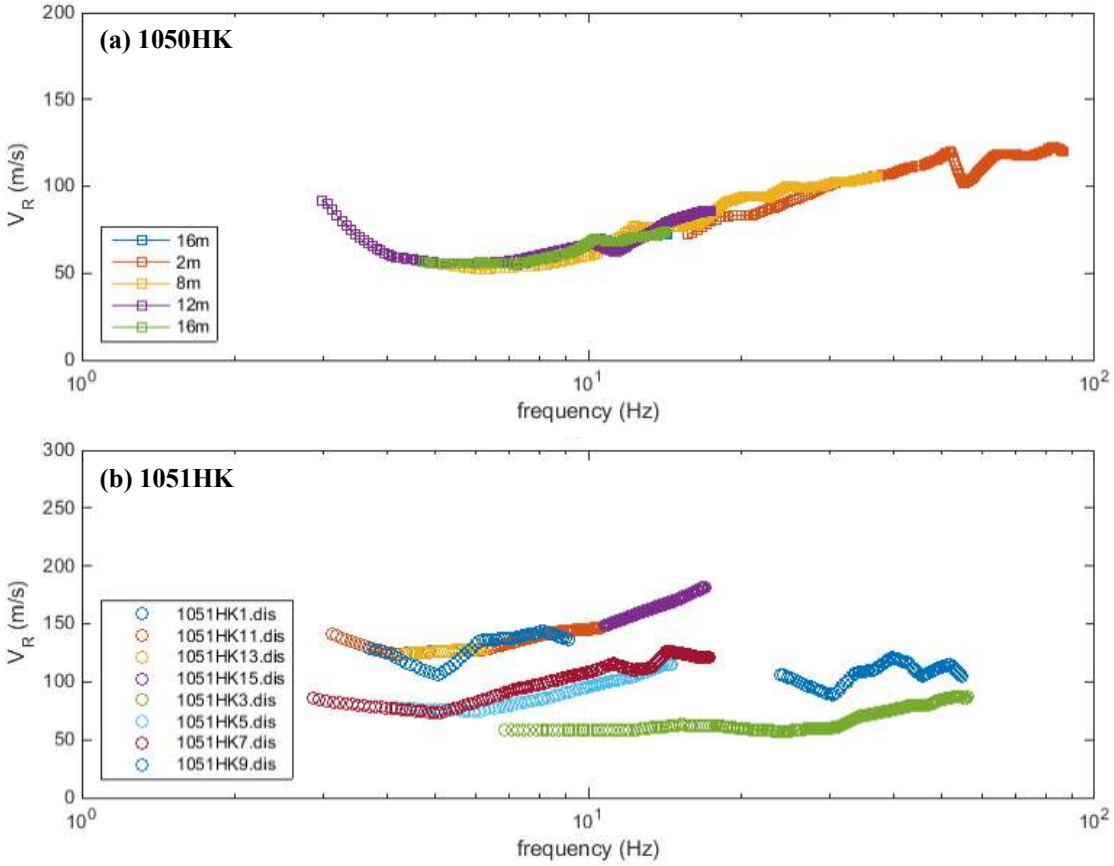

Figure 3.5 Experimental dispersion curves obtained from two adjacent SASW tests, a) is in the free-field and the individual curves are overlapping, b) is on the levee crest and the data is scattered with multiple modes.

Table 3.2 SASW test sites and data

Test Site	River	Position	Latitude	Longitude	Data Quality[(a)]	Nearest Boring[(b)]
1047HK	Tokachi	Riverside	42.9214	143.3857	Bad	-
1048HK	Tokachi	Crest	42.8359	143.4747	Bad	B-12-1
1049HK	Tokachi	Riverside	42.7837	143.5477	Excellent	B-2-2
1050HK	Ushi	Landside	42.7932	143.4602	Excellent	B-11-2
1051HK	Ushi	Crest	42.7920	143.4623	Excellent	B-11-1
1052HK	Tokachi	Crest	42.7557	143.5645	Excellent	B-5-1
1053HK	Tokachi	Riverside	42.7291	143.6049	Excellent	P-7-5
1054HK	Urahoro	Landside	42.7252	143.6575	Excellent	P-17-2
1055HK	Kushiro	Landside	43.0852	144.3782	Bad	H4-28
1056HK	Kushiro	Riverside	43.0553	144.3998	Excellent	H5-1
1057HK	Kushiro	Landside	43.0695	144.4124	Good	H2-72
1058HK	Kushiro	Landside	43.1100	144.3367	Good	H5-77
1059HK	Kushiro	Landside	43.0959	144.3672	Excellent	H5-69
1060HK	Kushiro	Landside	43.0782	144.4231	Excellent	H5-33
1061HK	Kushiro	Marsh	43.0738	144.3966	Excellent	H5-56
1062HK	Kushiro	Riverside	43.2467	144.5506	Good	H13-4
1063HK	Kushiro	Crest	43.0550	144.4003	Bad	H5-1
1064HK	Kushiro	Riverside	43.0210	144.3746	Good	H11-1
1065HK	Shita	Landside	42.7500	143.6052	Bad	P-20-2
1066HK	Tokachi	Riverside	42.7050	143.6159	Excellent	P-7-5
1067HK	Tokachi	Riverside	42.8130	143.5300	Good	P-14-2

[(a)]Condition of the composite experimental dispersion curve; "bad" denotes cases where the individual curves cannot be reasonably combined into a single curve and inversion is not performed.

[(b)]SPTs with stratigraphic information used to guide inversion.

The experimental dispersion curves are inverted to obtain the shear-wave velocity profiles, with layering constrained by the stratigraphy of neighboring borings. Robert Kayen applied the direct simplified inversion method (SIM) to obtain the V_S profiles (Pelekis and Athanasopoulos, 2011). The SIM directly inverts the surface wave dispersion data by considering the shape (i.e., slope, curvature) of the dispersion curve, and a penetration depth coefficient which is a function of the Poisson's ratio.

For 1050HK and 1056HK, the inversion is also performed using the Geopsy program. The approach differs from the SIM method in that a suite of trial layered earth models are generated and their resulting dispersion curves are compared with the experimental dispersion data. The forward computations for each trial earth model are based on the work originally developed by Thomson (1950) and Haskell (1953) and later modified by Dunkin (1965) and Knopoff (1964). A dispersion misfit value is computed for each trial model (Wathelet et al. 2004), and the "best" profile with the lowest misfit is selected.

The resulting V_S profiles are used to define soil profiles for ground response analysis in Chapter 6 and to estimate the time averaged shear wave velocity in the upper 30 m, V_{S30}, along the levees. V_{S30} is commonly used to represent site condition, and is calculated as,

$$V_{S30} = \frac{30}{\sum \frac{h_i}{V_{s,i}}} \tag{3.2}$$

where h_i and $V_{s,i}$ are the thickness and shear wave velocity of the ith layer, to a depth of 30 m. The profiles at the majority of the sites tested extended to depths less than 30 m as the shear wave velocities in the surficial layers are low. For those cases, extrapolation to V_{S30} is based on Midorikawa and Nogi (2015):

$$\log(V_{S30}) = c_0 + c_1 \log(V_{SZ}) + c_2 \log(V_s(z_p)) \tag{3.3}$$

where z_p is the profile depth, $V_S(z_p)$ is the V_S at the base of the profile, and V_{SZ} is the time-average shear wave velocity to depth z_p.

The inversion procedures utilized only considered the fundamental mode of propagation. 3-D effective mode forward analysis may be more appropriate given the inversely dispersive velocity structure present at some of the sites, particularly where measurements are performed atop the levees. The

uncertainties of inverting the dispersion curves are not addressed in this study but recognized as an important consideration. V_{S30} is an averaged parameter and is likely stable, but as discussed in Chapter 6, the amplification characteristic of a soil column is sensitive to the boundaries and impedance contrasts in the V_S profile.

4 DETAILED ANALYSIS OF LEVEE SECTIONS

4.1 INTRODUCTION

A local network of strong motion stations located on levees implemented in Obihiro recorded ground motions during the 2003 **M** 8.2 Tokachi-oki earthquake. Japanese engineers provided detailed observations of levee damage induced by this event, and performed a total of 22 site investigations at various locations along the levees. The combination of ground motion measurements, detailed subsurface information, and observations of levee damage make this an unprecedented set of case histories.

In this chapter, typical methods of levee performance assessment (liquefaction susceptibility, triggering, and consequence) are applied to 10 selected levee cross sections having good performance and varying severity of damage. Recorded ground motions are presented first, followed by subsurface conditions and observations of damage. I analyzed the slope stability of the levee sections and estimated slope displacements for a rigid sliding block with the 2D limit equilibrium analysis software SLIDE (Rocscience, 2017). Liquefaction severity indices and Newmark displacements are considered in conjunction to predict a representative damage level and compared to the observed performance.

4.2 GROUND MOTIONS DURING THE 2003 TOKACHI-OKI EARTHQUAKE

The Obihiro Development and Construction Department (ODCD) maintains a local network of seven strong motion recording stations to assess potential for damage and plan emergency responses after earthquakes. Each station has a pair of triaxial sensors on the crest and at the land-side toe of the levee, with the horizontal components oriented parallel and perpendicular to the levees as diagramed in Figure 4.1. The levees are within the active channel and sited on recent soft alluvial deposits, the V_{S30} are low.

Two additional stations were in the vicinity of the levees further inland. Details of the fault and rupture for the 2003 Tokachi-oki earthquake are described in Section 2.2. All recordings were filtered and processed according to PEER standards. The RoTD50 peak accelerations from the horizontal channels are summarized in Table 4.1with the site properties of the stations. These recordings provide estimates of ground shaking intensities, as well as time histories to be used with the subsurface investigations to assess performance at nearby levee segments. The time series and acceleration response spectra for each station are shown in Figures 4.2-4.7. In general, the motion at the levee crest was higher than that at the levee toe, and the peak in the acceleration response spectrum on the crest tended to occur at an oscillator longer than or equal to that at the toe.

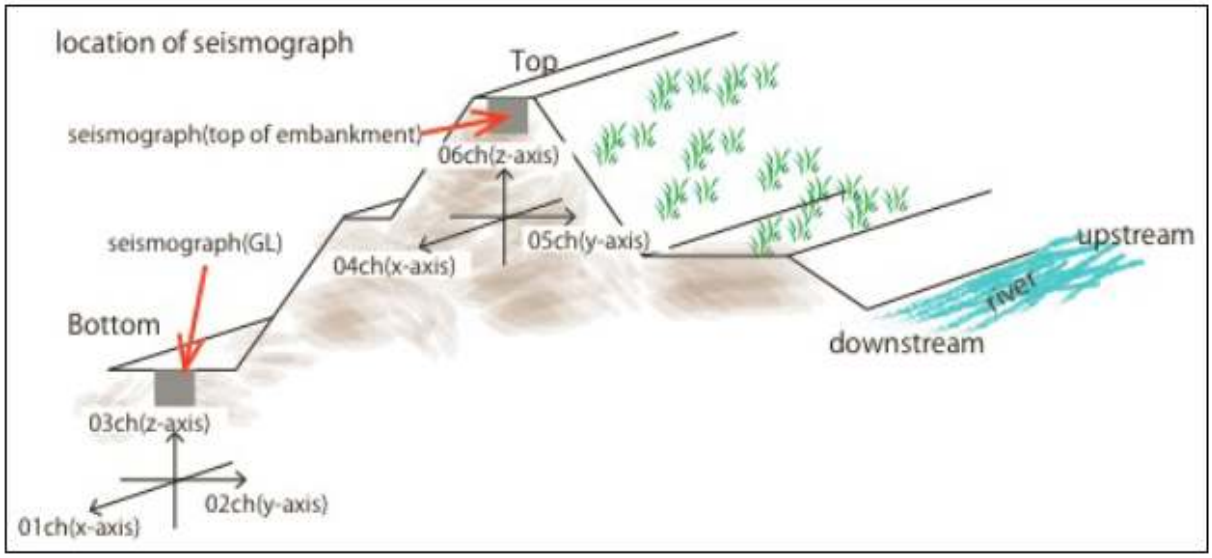

Figure 4.1 Sensor position and orientation at each ODCD strong motion station with respect to the levee. (Personal communication T. Sato).

Table 4.1 Recording stations near levees during 2003 Tokachi-Oki earthquake

Station Name	Station Code	Owner/ Network	Location		V_{S30} (m/s)	PGA (g)		Liquefaction evidence[c]
			Lon (deg)	Lat (deg)		Toe	Crest	
Toitokki	TTK	ODCD	143.6043	42.7281	117.2[a]	0.648	0.481	Yes
Rabirai	RB	ODCD	143.5642	42.7556	150.5[a]	0.431	0.416	Yes
Horooka	HK	ODCD	143.5489	42.7841	102.2[a]	0.350	0.602	No
Reisakubetsu	RSB	ODCD	143.4744	42.8359	181.4[a]	0.668	0.706	No
Gyushubetsu	GSB	ODCD	143.4622	42.7921	130.8[a]	0.307	0.498	Yes
Higashiinaho	HNH	ODCD	143.6063	42.7876	211.5[b]	0.656	0.541	No
-	TKCH07	NIED	143.5203	42.8114	140.1[b]	0.371	NA	No
-	51563	JMA	143.5060	42.8014	302.2[b]	0.550	NA	No

[a]From Vs profile inverted from SASW testing, extrapolated to 30 m where necessary

[b]Estimated from geomorphology and slope proxy based on Wakamatsu and Matsuoka (2013)

[c]Reported from the reconnaissance survey

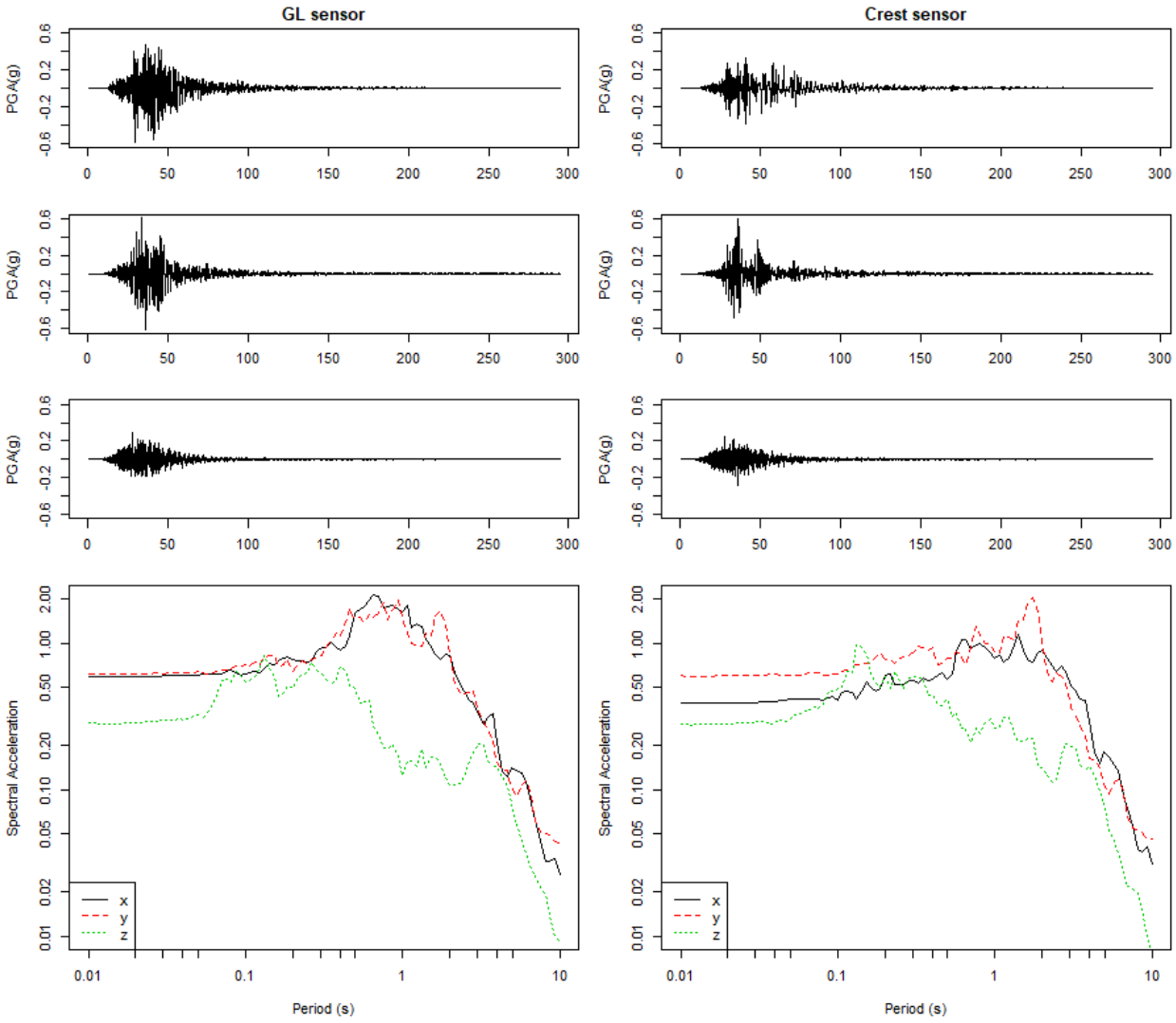

Figure 4.2 Time histories and response spectra at Toitokki station (TTK).

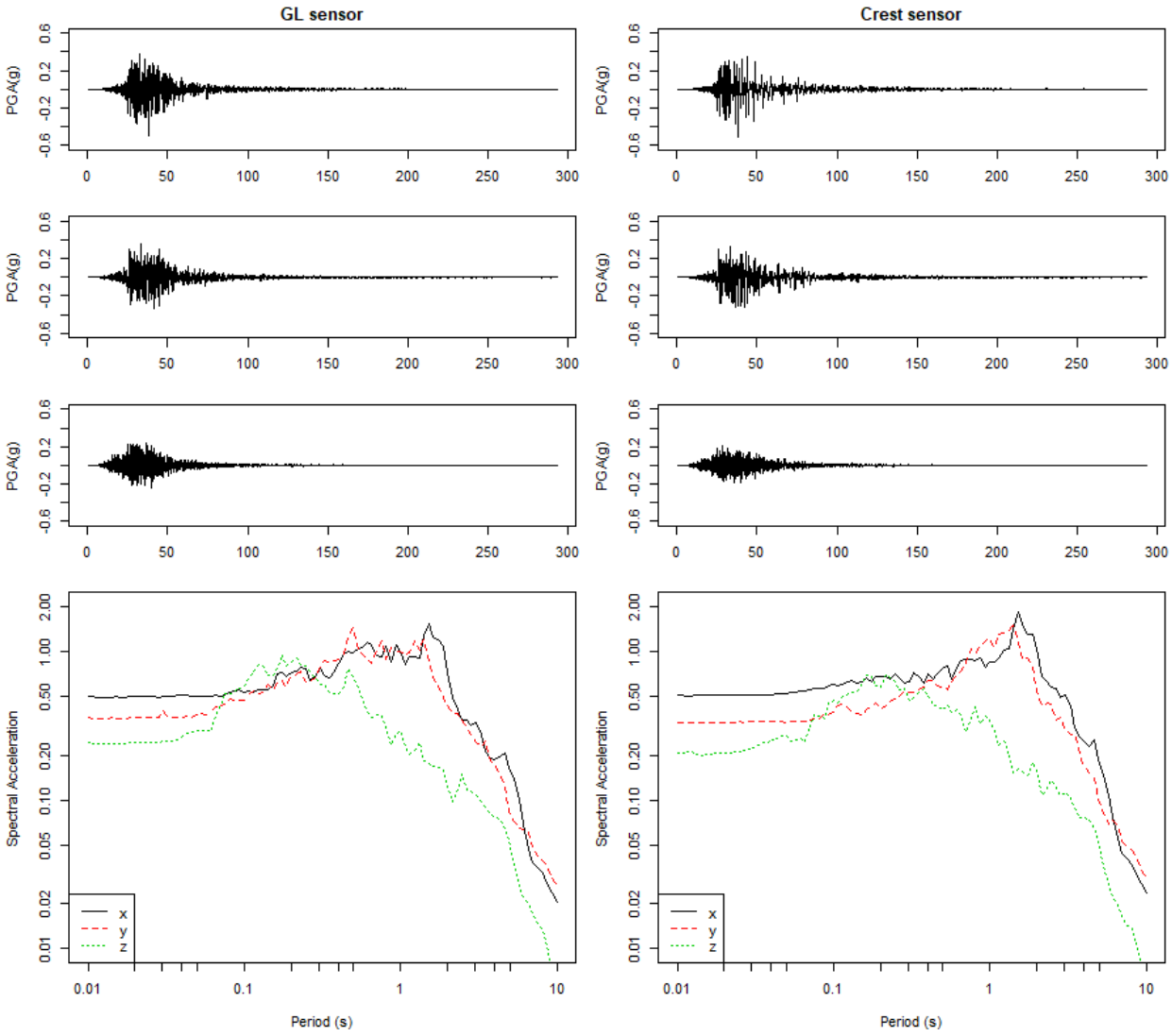

Figure 4.3 Time histories and response spectra at Rabirai station (RB).

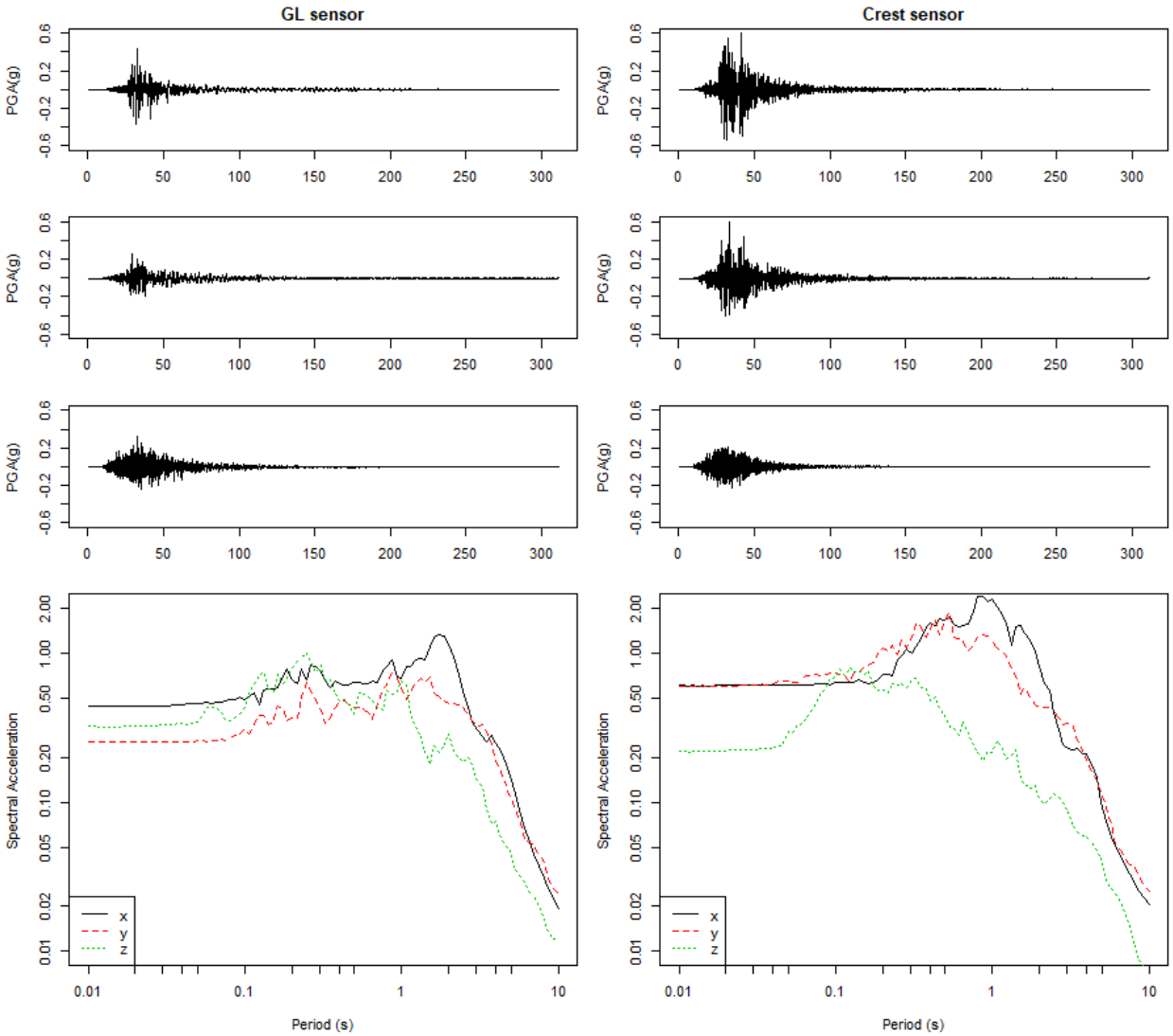

Figure 4.4 Time histories and response spectra at Horooka station (HK).

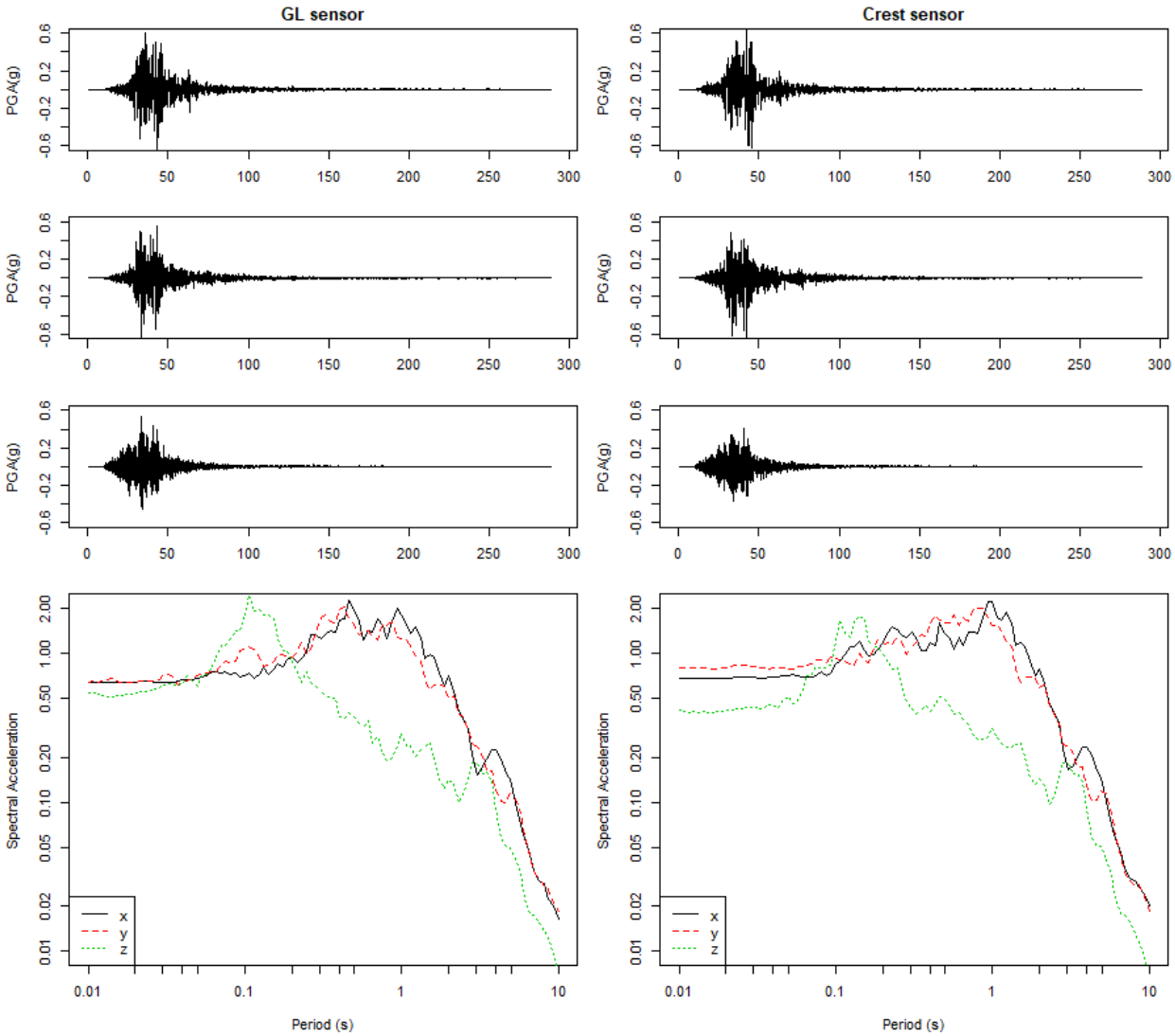

Figure 4.5 Time histories and response spectra at Reisakubetsu station (RSB).

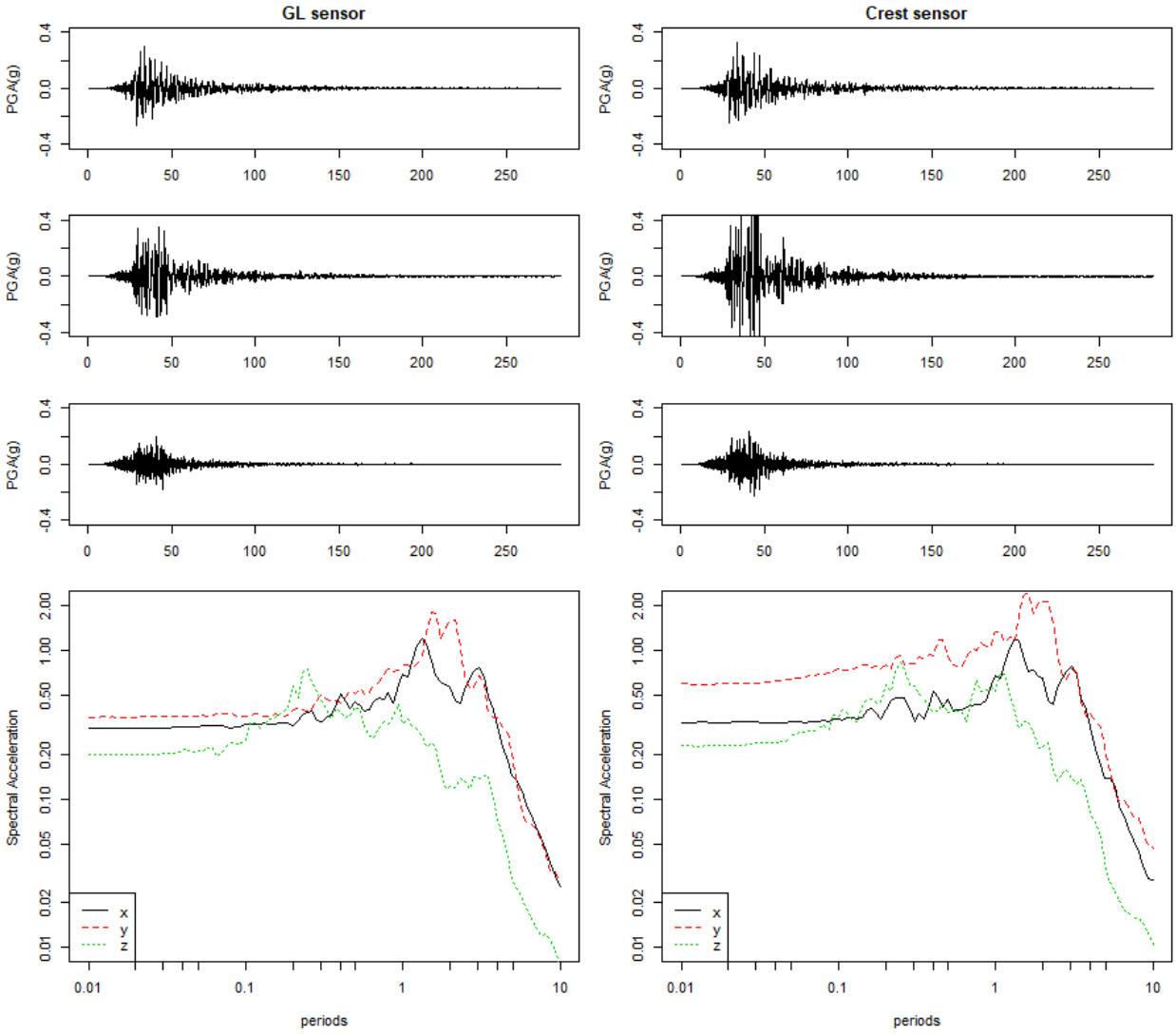

Figure 4.6 Time histories and response spectra at Gyushubetsu station (GSB).

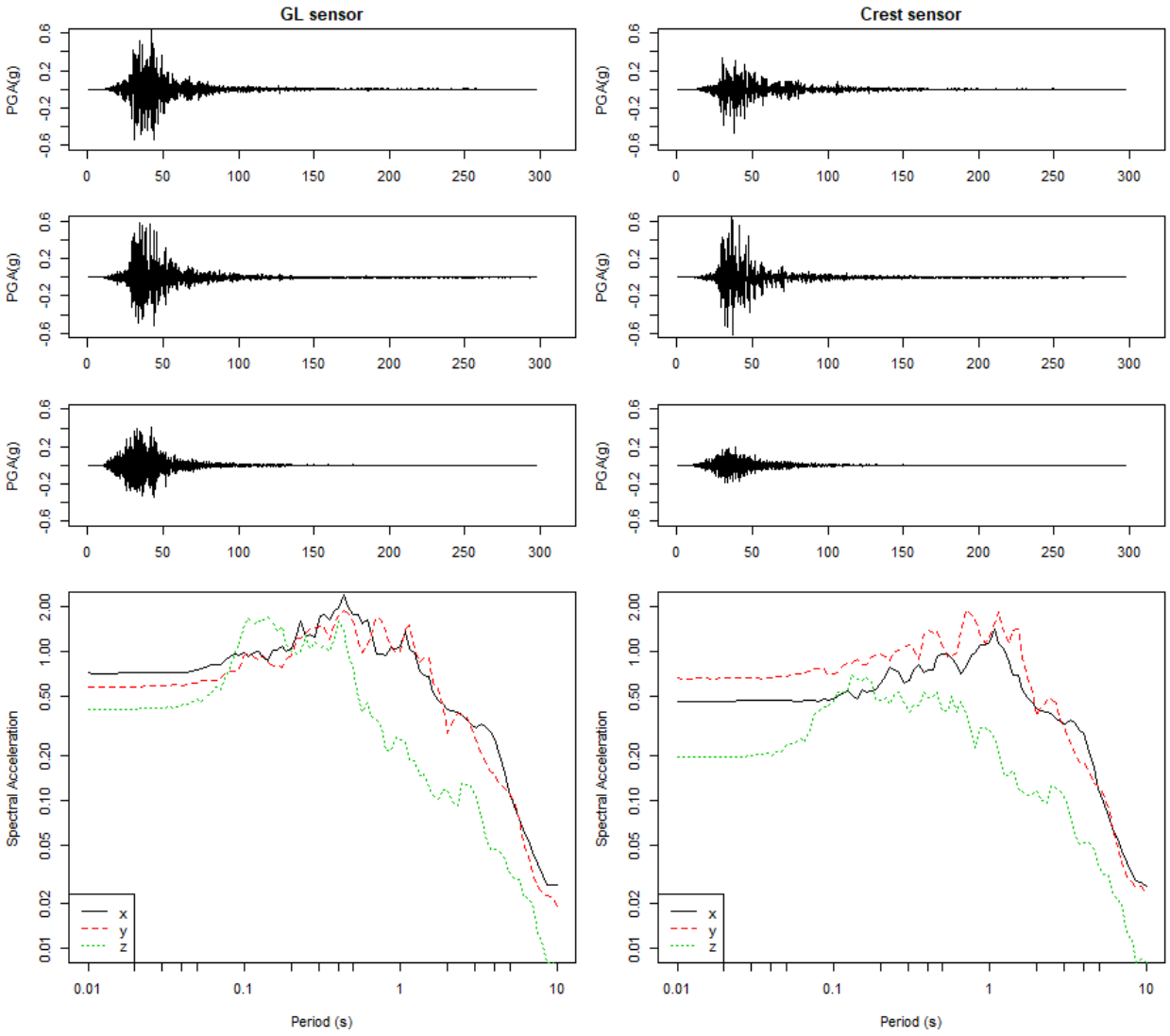

Figure 4.7 Time histories and response spectra at Higashiinaho station (HNH).

4.3 SUBSURFACE CONDITIONS AND OBSERVATIONS

Immediately after the 2003 Tokachi-oki earthquake, engineers from local management agencies visually inspected all levee systems along the major rivers in the region. Visible damage was reported and accompanied by measurements of subsidence, differential settlement and cracks and evidence of liquefaction (e.g., sand boils) where encountered (Hokkaido River Disaster Prevention Research Center, 2004). The engineers did not explicitly report undamaged levees. However, since all of the levees were inspected, a lack of reported damage is interpreted as evidence of a lack of damage. Besides the initial inspection, additional detailed investigations were conducted at 22 locations in the months following the earthquake, as shown in Figure 4.8, concentrating on the downstream region. The investigations included Standard Penetration Tests (SPTs), Cone Penetration Tests (CPTs), open excavations and laboratory testing to study the failure mechanisms and evaluate the performance of the existing structure, and to inform subsequent repair efforts.

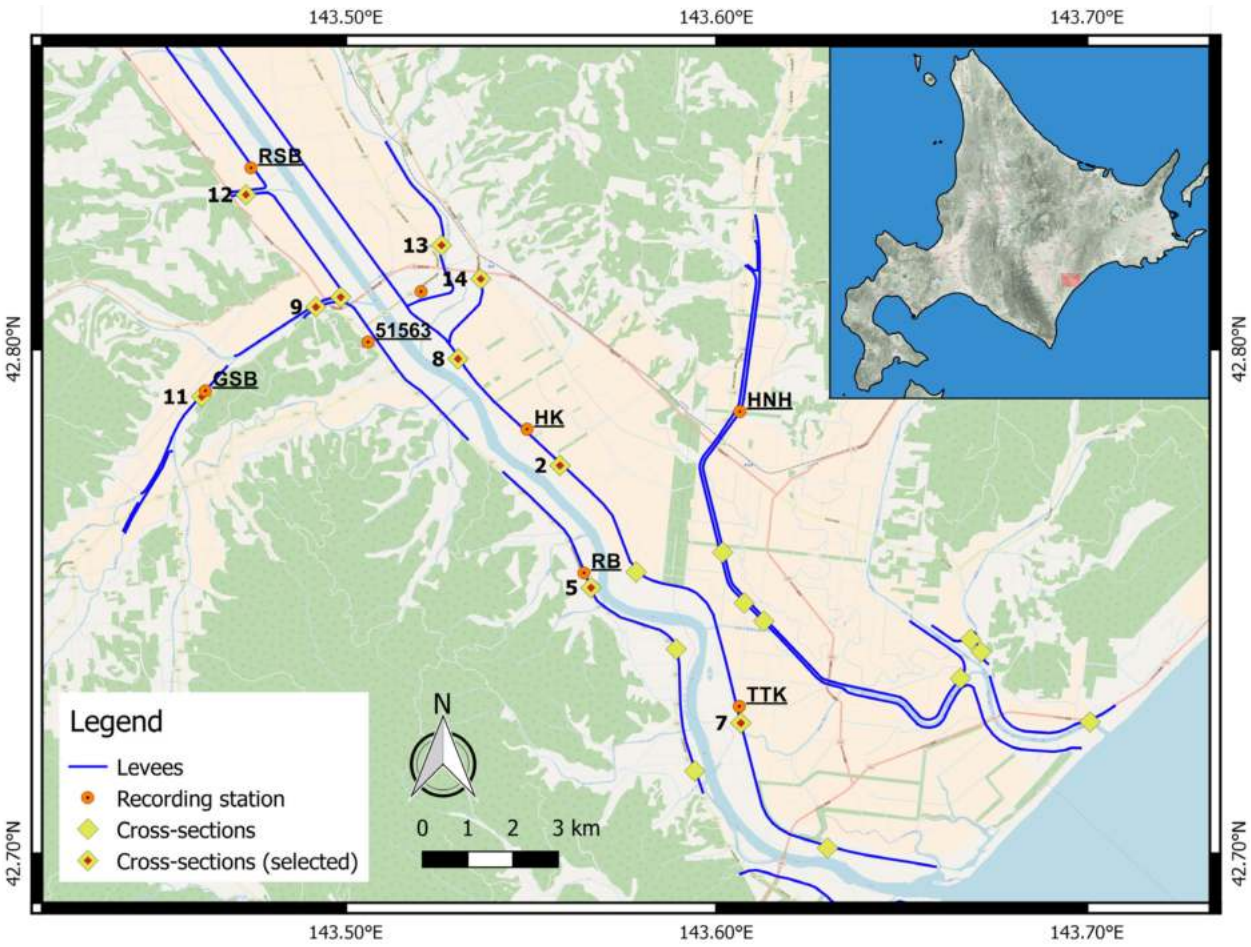

Figure 4.8 Downstream region of Tokachi River with strong motion recording stations and post-earthquake investigations performed after the 2003 Tokachi-oki earthquake.

We selected 10 sites that were near the ODCD recording stations for detailed analysis. These sites exhibited varying levels of damage, and numbering of the sections here follows the numbering from the reconnaissance investigation for consistency. Sites 2, 5, 7, 8 are along the main Tokachi River, and levees rest atop a thick peat layer. The levees along the Tokachi River are broad and gently sloped, with side slopes of around 1:4 to 1:6. They were expanded in the late 1990s to reduce problems associated with subsidence on the soft peat soils and provide a larger cross-section to prevent loss of water retention capabilities should failure occur. Sites 9 -14 are along the tributary streams, with thinner peat soils beneath the levees and the steeper side slopes around 1:2.5 to 1:3. The location and performance at each site is summarized in Table 4.2.

Table 4.2 Location and performance of selected levee sections

Section	Location		Nearest station	Crack dimension		Subsidence (cm)	Damage Level	Liquefaction evidence
	Lon (deg)	Lat (deg)		Width (cm)	Depth (cm)			
2	143.558	42.777	HK	120-140	75-120	30-70	4	Yes
5	143.566	42.753	RB	285	80	-	3	Yes
7	143.607	42.726	TTK	120	30	-	2	None
8	143.531	42.798	TKCH07	120-195	25-50	40	3	Yes
9	143.492	42.808	51563	130	80	-	3	Yes
10	143.498	42.810	51563	200	270	Large (~50)	4	Yes
11	143.461	42.791	GSB	105	74	220	4	Yes
12	143.473	42.831	RSB	~50	~100	50-70	3	Yes
13	143.526	42.820	TKCH07	0	0	0	0	None
14	143.537	42.814	TKCH07	110	~60	-	3	None

4.3.1 Section 2 - Tokachi River left bank

Section 2 is located around 16 km upstream of the river mouth and 300 m from the active channel. The closest station is HK, located on the levee around 1000 m upstream from Section 2 (Figure 4.9). The levee was constructed in stages, with the core placed in the 1950s and composed mainly of clean sands with small amounts of gravels and silts. The levee section was broadened in the late 1990s on the land-side, using fill with a higher fines content classifying as silty sands to silts. Groundwater was encountered within the levee fill during site investigations after the earthquake.

The levee is underlain by a laterally continuous peat layer about 3 to 4 m thick. The blow count ranges from 1-5 and is highest below the levee crest. The peat transitions into a thin clay layer (Ac) of around 1 m thick. Below that, the sand content increases with depth, and is mainly clean sands (As) at 10 m below the free-field ground surface. The resistance also picks up rapidly in this layer.

The segment was severely damaged with extensive longitudinal cracks on the crest. Crack depths and widths up to 140 cm and 120 cm were observed, with sand boils visible in and around the cracks on the access road on the levee crest (Figure 4.10). Subsidence of 30-70 cm and settlement were observed on the land-side portion of the levee.

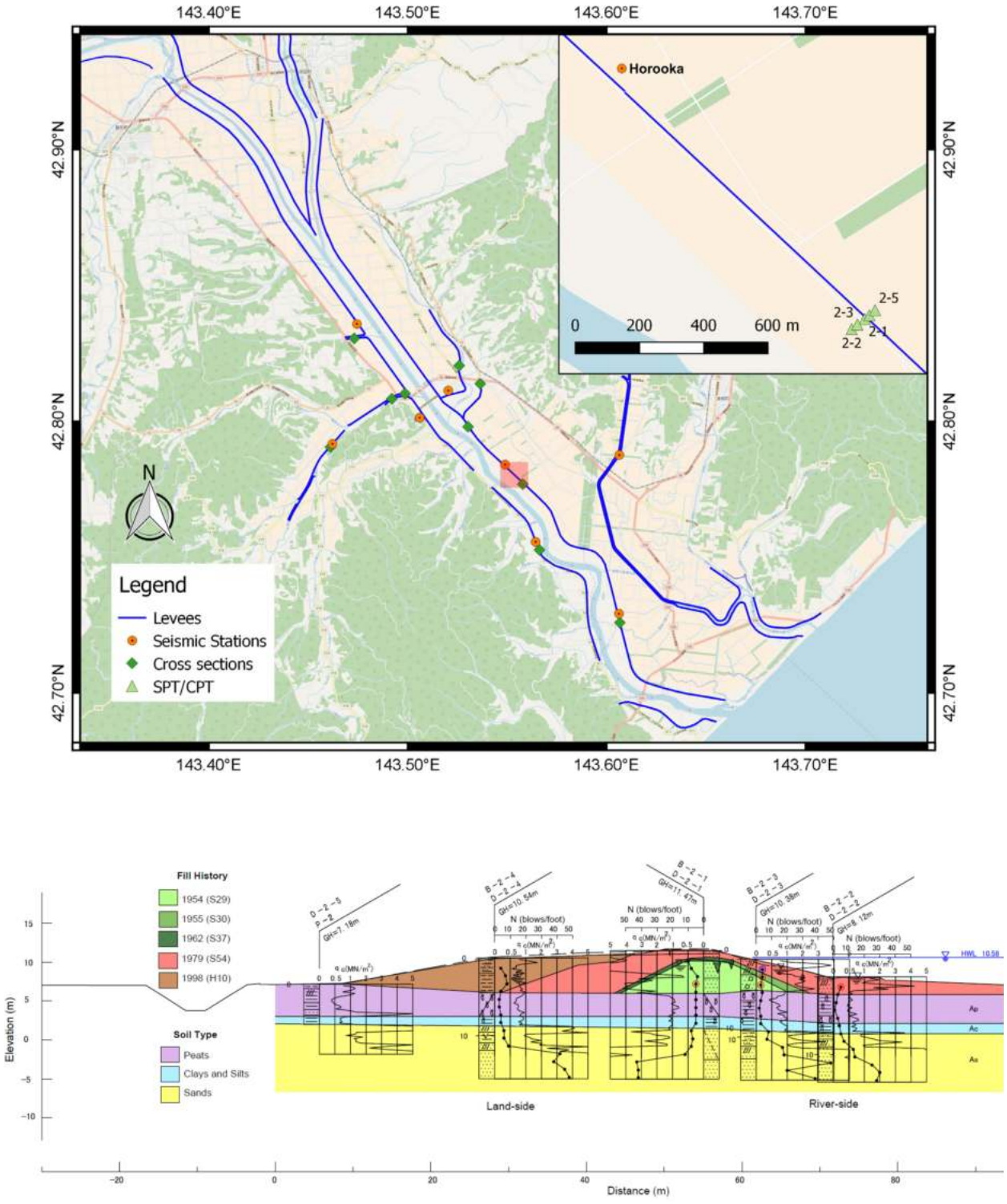

Figure 4.9 Vicinity map and subsurface investigation for Section 2.

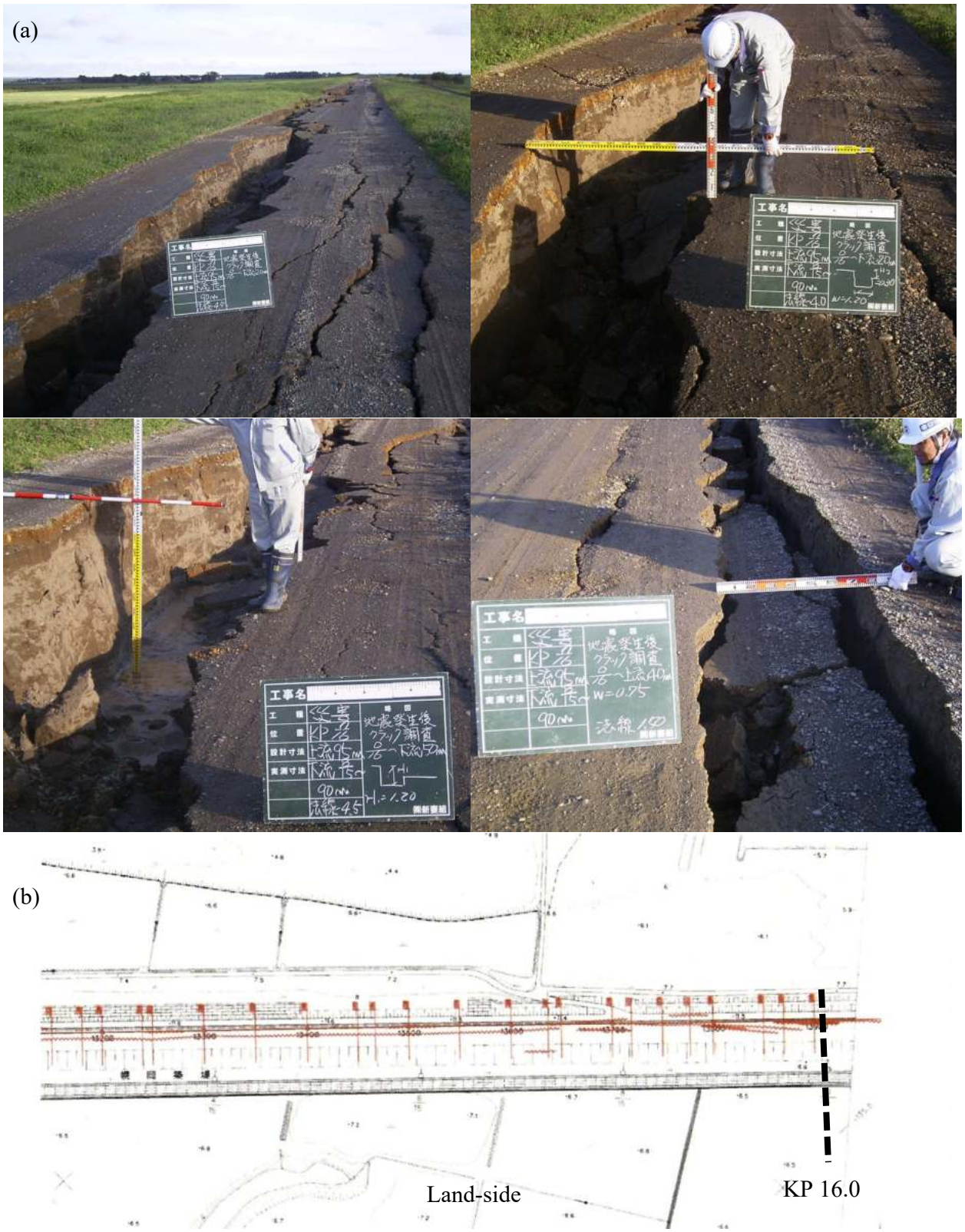

Figure 4.10 (a) Extensive cracking on access road and sand boils visible in some of the cracks at Section 2. (b) Plan view showing distribution of longitudinal cracks on levee crest.

4.3.2 Section 5 - Tokachi River right bank

Section 5 is located on the outer bend around 100 m from the river channel and around 13.2 km from the river mouth. The RB station is located on the levee on the same side of the river, around 400 m upstream. The original levee was constructed in 1965-1966 with clean sands containing small amounts of gravels. The levee was subsequently expanded towards the river in 1989 using sandy fill containing low to moderate amounts of silt. The water level is elevated in the levee body, likely from several precipitation events earlier in the month.

A continuous layer of peat and organic clays underlies the levee, around 5 m thick on the land-side and thinning to around 2 m on the river-side. The material transitions to sand below the organic layer, with a clayey seam on the land-side tapering out under the levee crest. The blow count ranges between 10-20 in the sandy layer and is lower in zones with higher fines content.

A short segment of the levee was severely damaged, with longitudinal cracks, settlement and slumping on the land-side slope only (Figure 4.12). Displacement was not observed in the free-field peat away from the levee, suggesting that the failure is contained within the body of the levee.

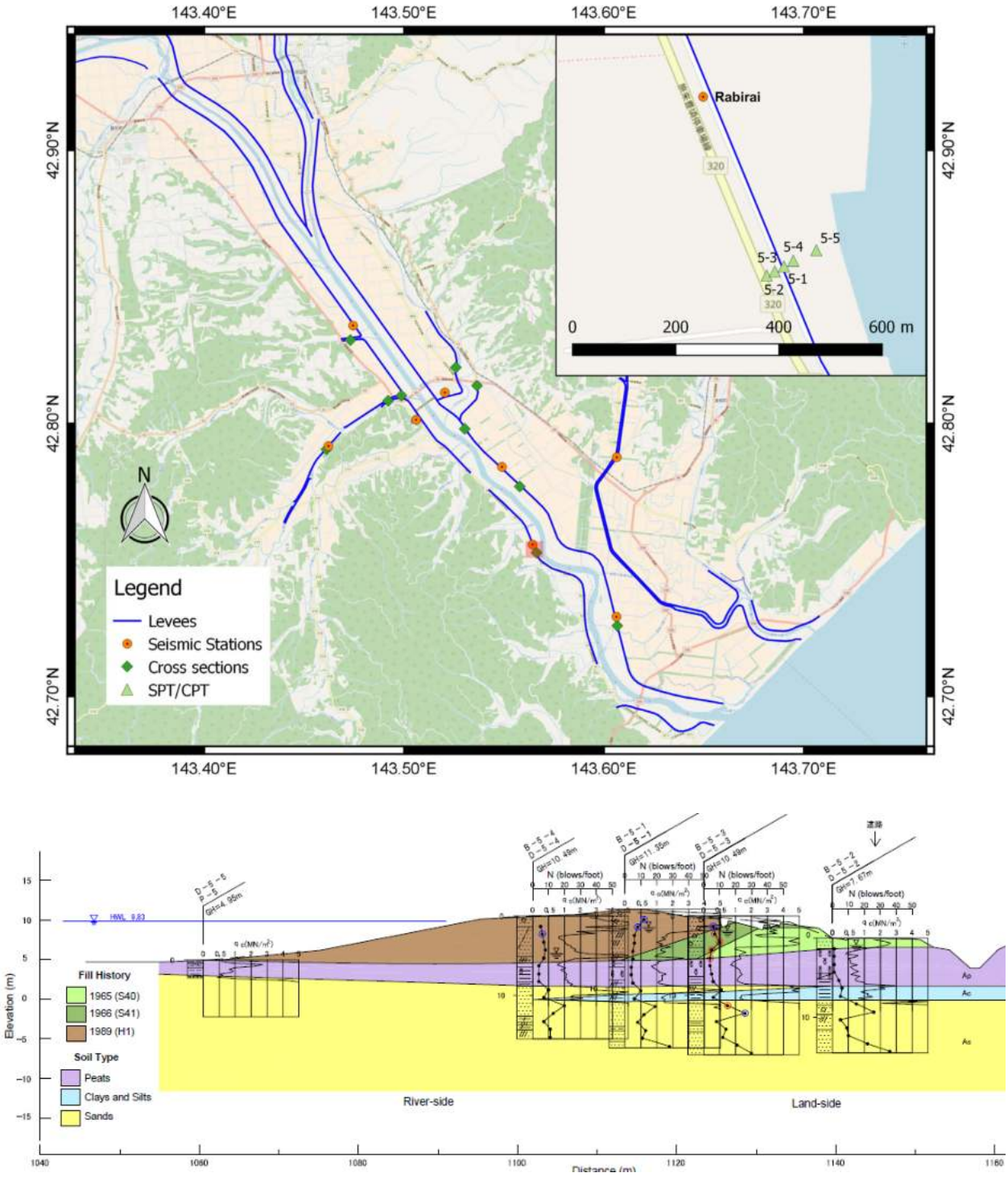

Figure 4.11 Vicinity map and subsurface investigation for Section 5.

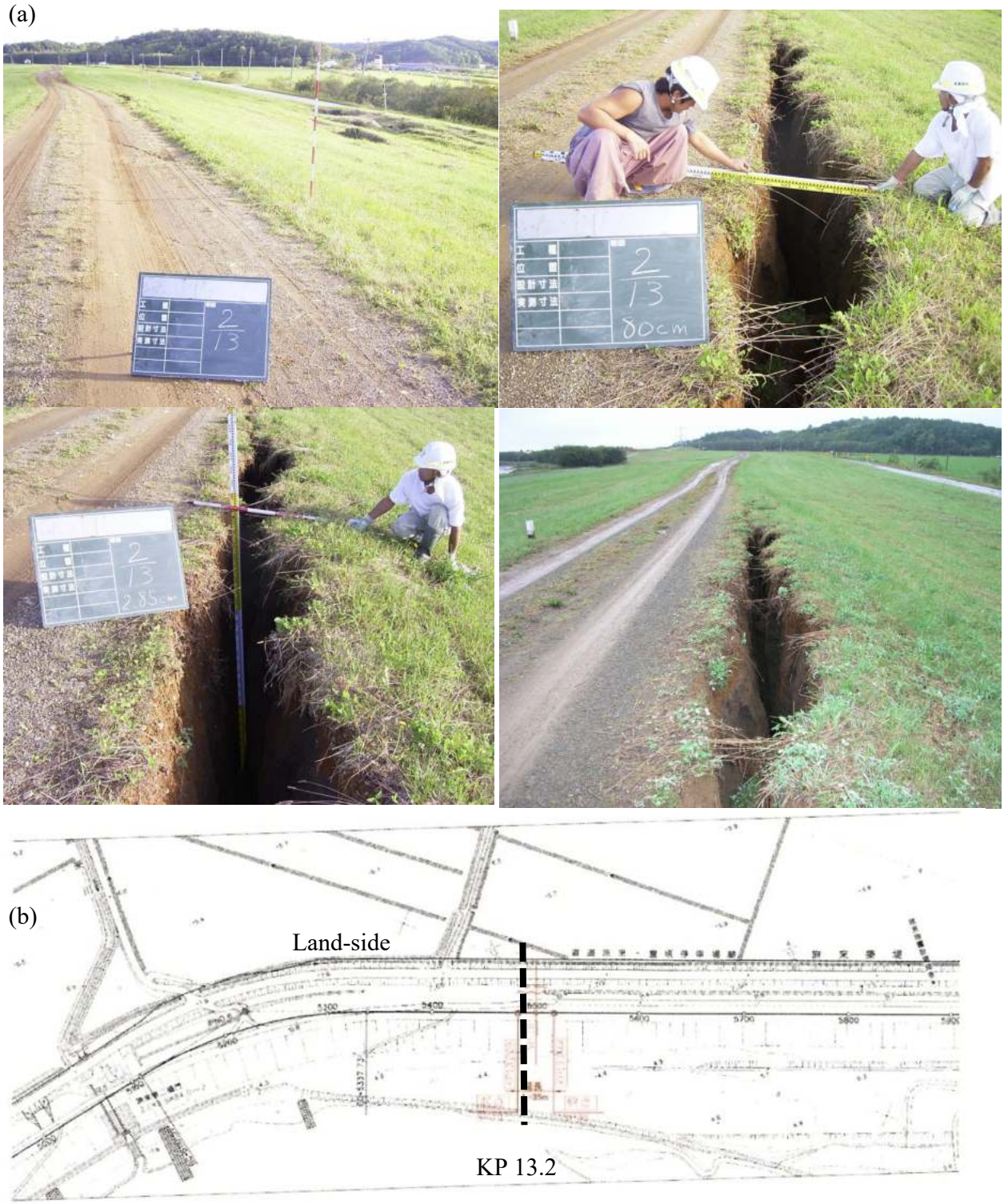

Figure 4.12 (a) Severe localized damage at Section 5 on the land-side slope, with deep cracks at the land-side edge of the access road on the levee crest. (b) Plan view of longitudinal cracks observed.

4.3.3 Section 7 - Tokachi River left bank

Section 7 is around 700 m inland from the river channel and 8.6 km from the river mouth. TTK is the closest station around 400 m upstream and on the same side of the river (Figure 4.13). The land-side portion of the levee is mainly sand with minor amounts of gravels. The silt content is higher on the upper and riverside portion of the levee. The construction history of the levee here is unknown, but expected to be similar to neighboring sections where the initial sandy core is expanded in phases. The ground water is elevated within the levee body.

A continuous peat layer (Ap) around 4 m thick underlies the levee and extends out into the free-field, with blow counts of 1-3. Under the peat is a thin silty sand layer (As1), followed by a silty layer (Ac), which finally transitions into stiffer, relatively clean sands at around 10 m below the free-field surface.

The section suffered moderate damage from displacement of the land-side slope, concentrated mostly within a 50 m stretch of the levee. Cracks up to 120 cm deep and 30 cm wide are observed on the crest access road (Figure 4.14). Evidence of liquefaction was not observed at this location.

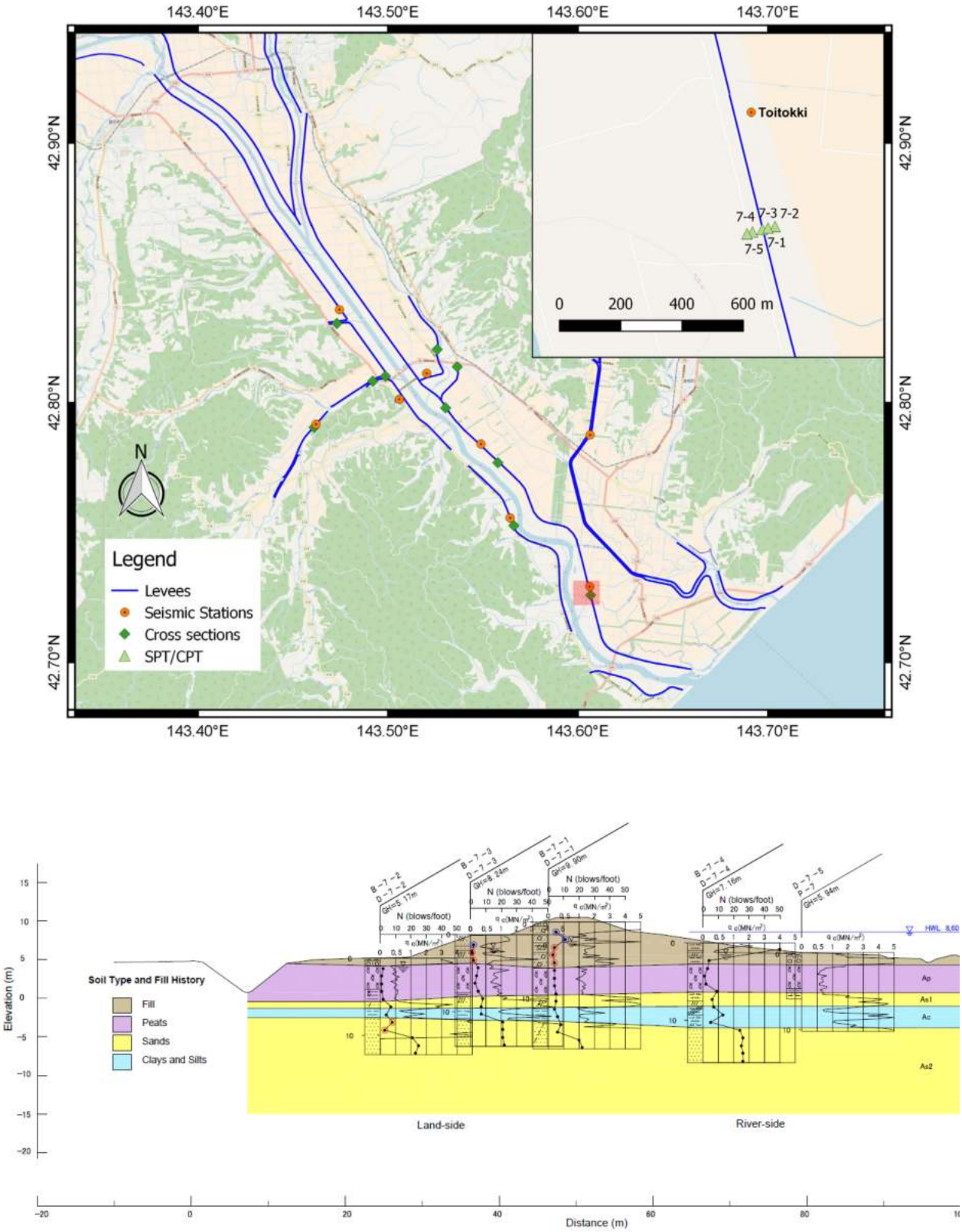

Figure 4.13 Vicinity map and subsurface investigation for Section 7.

Figure 4.14 Cracks and differential settlement on the crest access road at Section 7.

4.3.4 Section 8 - Tokachi River left bank

Section 8 is located near the intersection of the Tokachi River and Satsubunnai River, around 19.2 km upstream from the river mouth. The nearby stations are TKCH07 and 51563, both located upstream and off the levee in the free-field (Figure 4.15). The core of the current levee was placed in 1952 and expanded on both slopes in two phases to create gentler slopes while maintaining the original crest. The original fill was predominantly sand with minor amounts of silt. The 1978 fill has higher fines content, and prior testing shows some plasticity. The fill placed in 1996 has high fines content and significant plasticity in the upper zones, transitioning to lower fines in the lower portion. The ground water is elevated within the levee.

Directly underneath the fill is an interbedded layer of peat and clay (Ap), with visible peat fibers, around 5-6 m thick. The material is very soft, with blow counts around 2-3 in the free-field and increasing to around 5 under the levee. The organic content decreases with depth and transitions to a 1-2 m thick layer of clayey silts (Ac1), followed by a sandy layer with low to moderate fines content (As1), which tapers from about 4 m on the riverside, to around 0.5 m on the land-side.

Subsidence up to 40 cm was present over a broad region of the levee, and cracks around 120-195 cm deep and 25-50 cm wide were reported. Sand boils were observed on the access road on the levee crest. Cracking and settlement are concentrated near the crest, likely resulting from liquefaction and settlement of the older fill material.

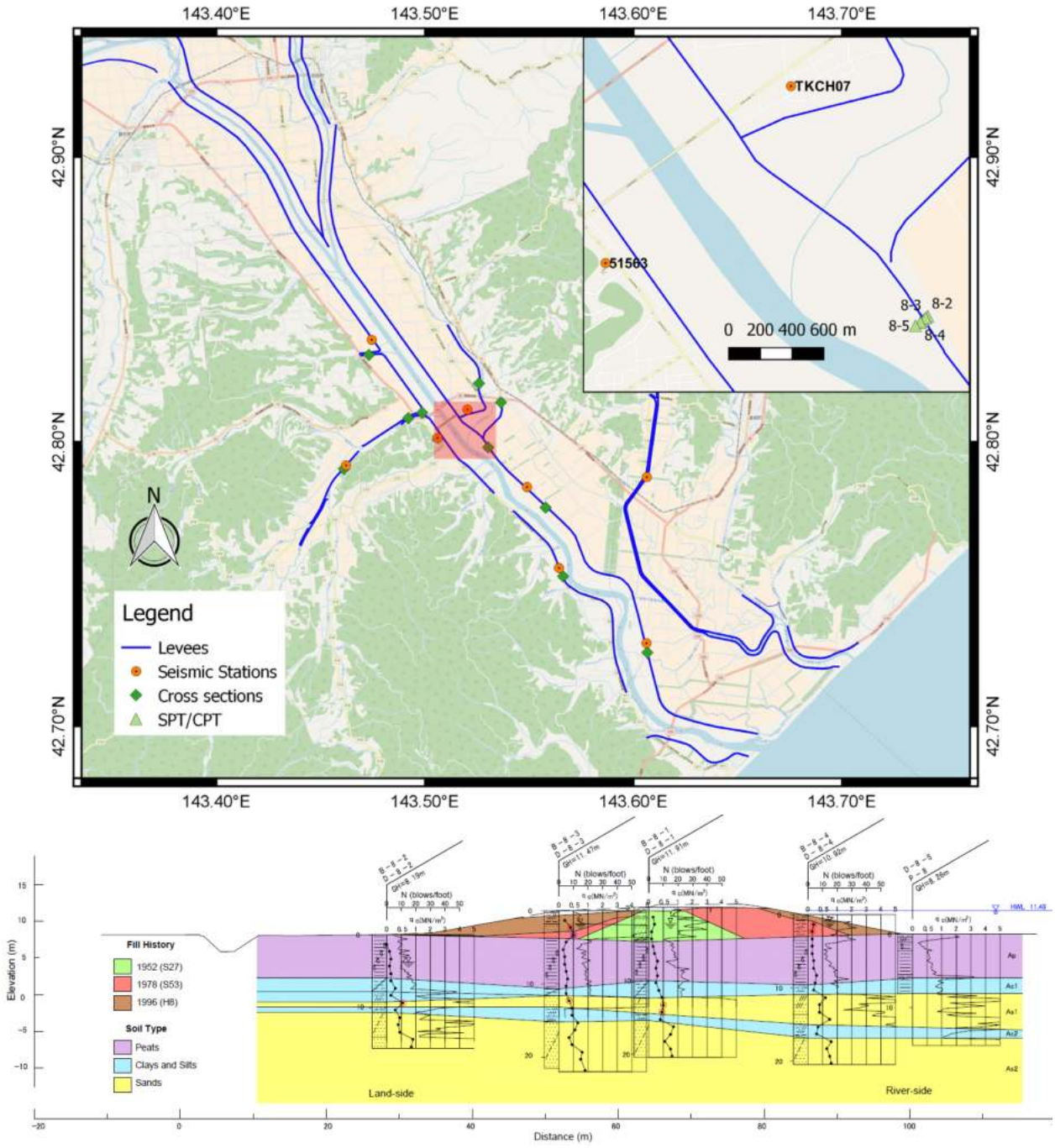

Figure 4.15 Vicinity map and subsurface investigation for Section 8.

Figure 4.16 Cracking on the crest (top) and land-side slope (bottom left) at Section 8. Sand boils on crest access road downstream (bottom right).

4.3.5 Section 9 and 10 - Gyushubetsu River

The Gyushubetsu River joins the Tokachi River on the right bank around 21 km upstream from the river mouth. Sections 9 and 10 are located close to the intersection, on the right and left bank respectively. The nearest station is 51563 located downstream along the Tokachi River (Figure 4.17).

The original date of construction is unknown for both locations. Section 9 was enlarged in 1972 to have a higher crest elevation. The fill is composed of sand and gravelly sand, and the ground water is elevated within the levee. The levee has settled around 1 m into the underlying peat layer (Ap), which is about 2 m thick directly beneath the crest and 3-5 m thick in the free-field. A 2 m continuous clay layer (Ac) lies immediately below the peat layer, and transitions into sands (As) with fines content decreasing with depth (Figure 4.18).

The section is moderately damaged, with cracks up to 130 cm deep and 80 cm wide on the access road on the levee, and settlement of the levee crest and the land-side slope (Figure 4.19).

Section 10 underwent 2 major expansion in 1961 and 1980 on the land-side slope (Figure 4.20). The earlier fill was predominantly sand with minor amounts of silt. The fill placed in 1980 contained moderate amount of silts with small amounts of gravels. A layer of peat and organic clay (Ap, Ac1) lies directly below the levee, with the organic content highest near the surface. Below the material alternates from silty sands (As1) to sandy silts (Ac2), and back to silty sands (As2) with fines content decreasing with depth. Layers with higher sand content are reflected by increased cone tip resistance.

The section was severely damaged; cracks up to 200 cm deep and 270 cm wide were observed on the roadway on the levee crest. The slope slid and budged outwards, and was accompanied by subsidence of the levee crest. (Figure 4.21).

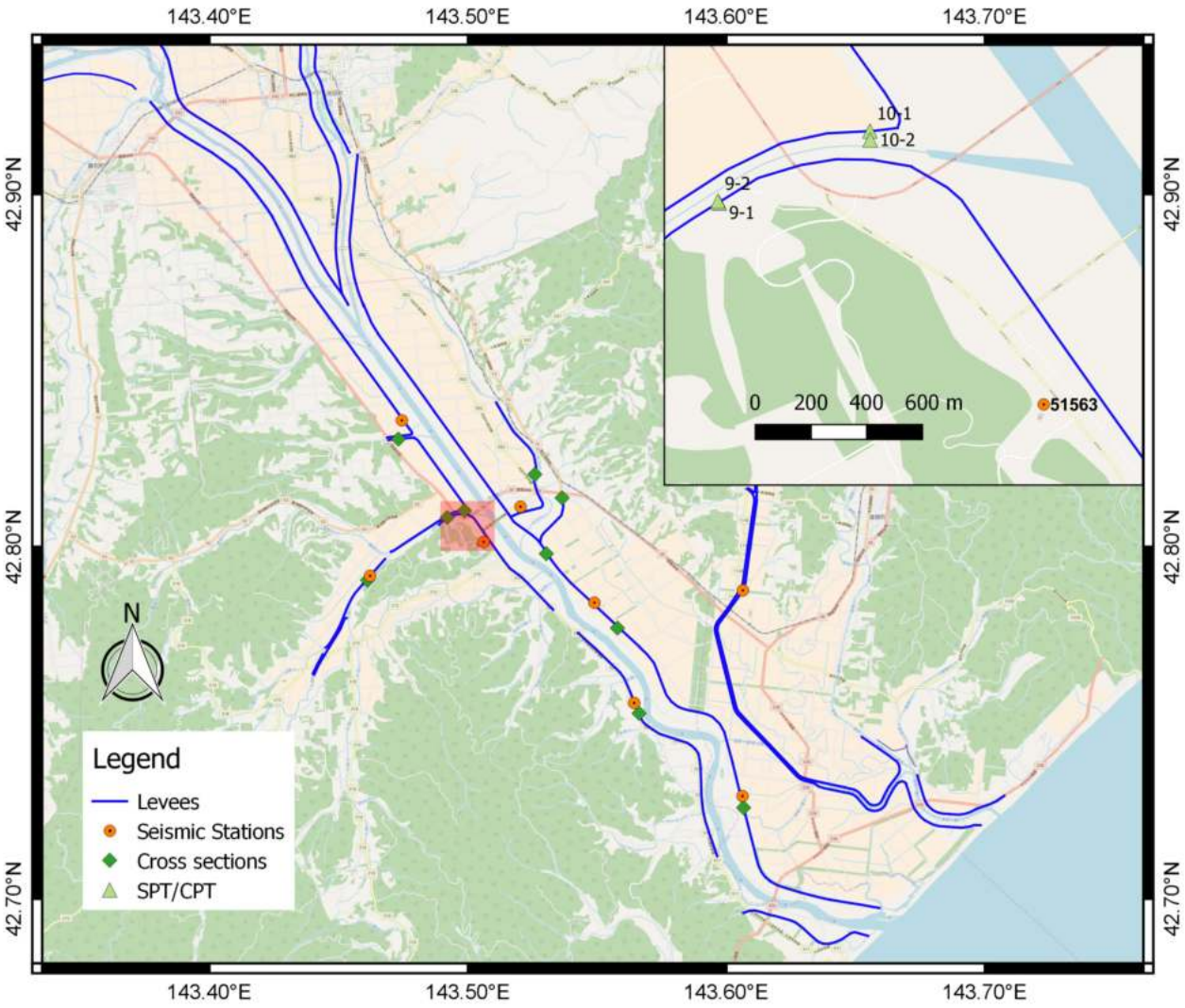

Figure 4.17 Vicinity map for Sections 9 and 10.

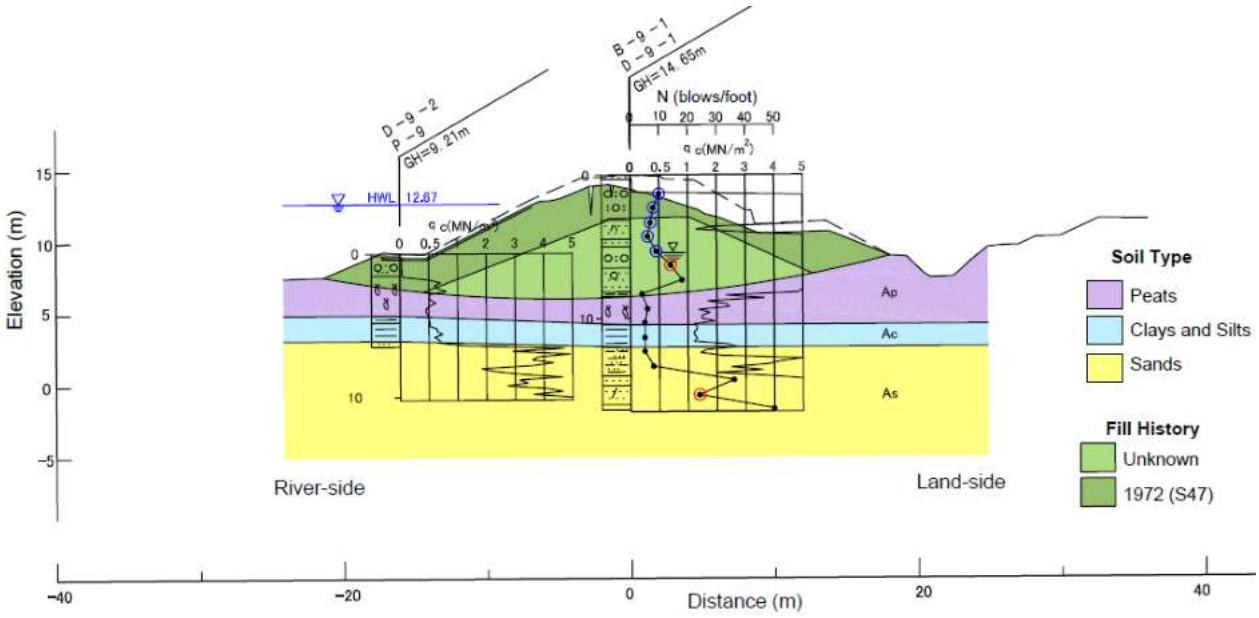

Figure 4.18 Subsurface investigation for Section 9.

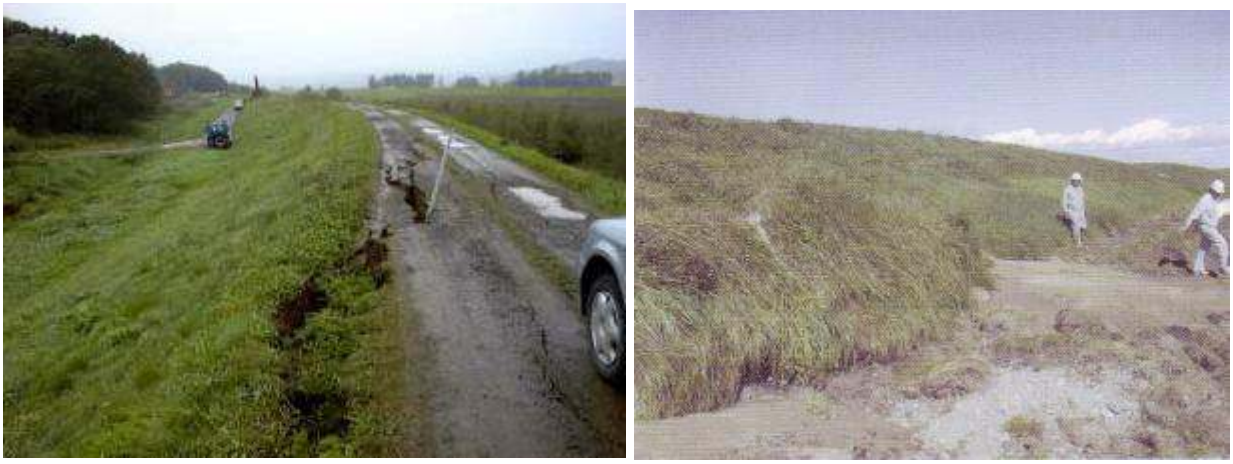

Figure 4.19 Cracking on the access road on the levee crest at Section 9 with slip and settlement on the land-side slope.

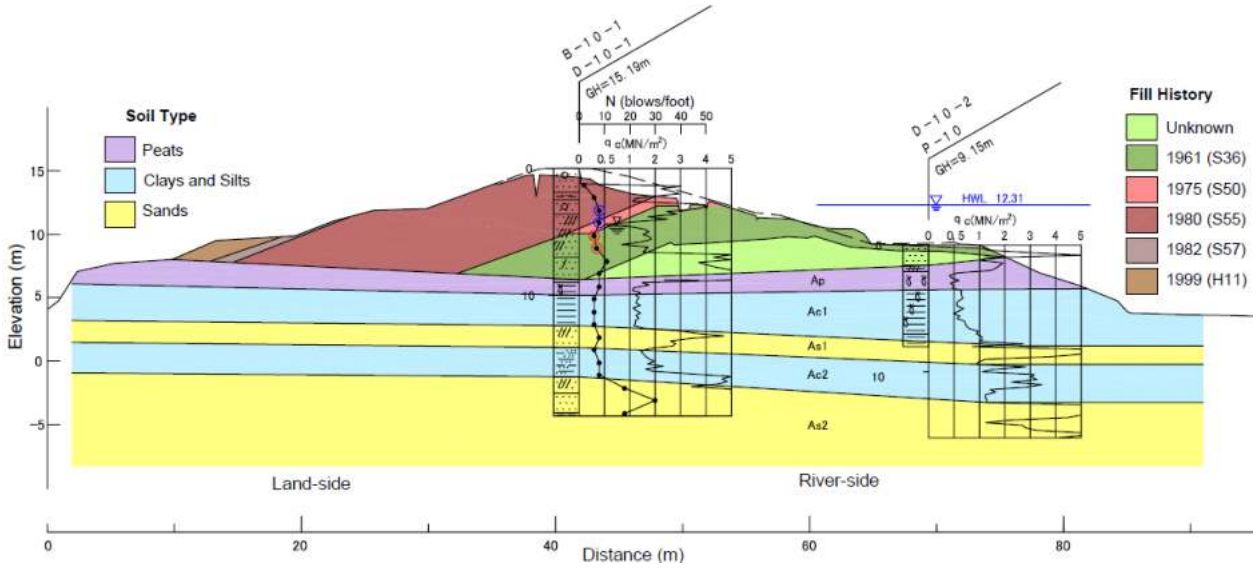

Figure 4.20 Subsurface investigation for Section 10.

Figure 4.21 Cracking of the roadway on the levee crest accompanied by slip on the slope at Section 10.

4.3.6 Section 11 - Gyushubetsu River left bank

The Gyushubetsu River joins the Tokachi River on the right bank around 21 km upstream of the river mouth. The cross section is located around 4.0 km from the intersection, and the closest station is GSB on the levee around 100 m downstream (Figure 4.22). The oldest portion of the levee is predominantly peat, with layers of fine sand. The construction date is unknown and is likely unengineered fill. The fill placed in 1956 is tested and found to consist of fine to medium sand with 20% gravels of 5-10 mm and some silts. The subsequent expansion of the levee involved sandy soil with minor amounts of gravels. Ground water level is elevated within the levee fill.

The levee rests directly on peaty soils (Ap) around 5 m thick in the free-field, with the levee fill settling around 2 m into the peat. A thick clay layer (Ac) underlies the peat, before transitioning into coarser material (As) at 20 m

The section suffered extensive damage, with crack widths of 60-270 cm and crack depth up to 200 cm. The levee subsided up to 3 m at the crest and essentially collapsed. (Figure 4.23). Complete replacement was necessary, and the location of the site investigation was opportunely excavated and mapped during the restoration process (Figure 4.24). Sand boils and ejecta could not be identified definitively due to the severe damage. The deformation pattern of the fill layers suggests loss of bearing capacity in the submerged portion, leading to instability and collapse of the levee. Laboratory tests on retrieved samples identified the fill placed in 1956 (S31) to be primary composed of coarse sands, with minor gravels and minimal fines, to be susceptible to liquefaction. The drainage ditch on the land-side toe of the levee was intact, and the failure through the peat layer is unlikely.

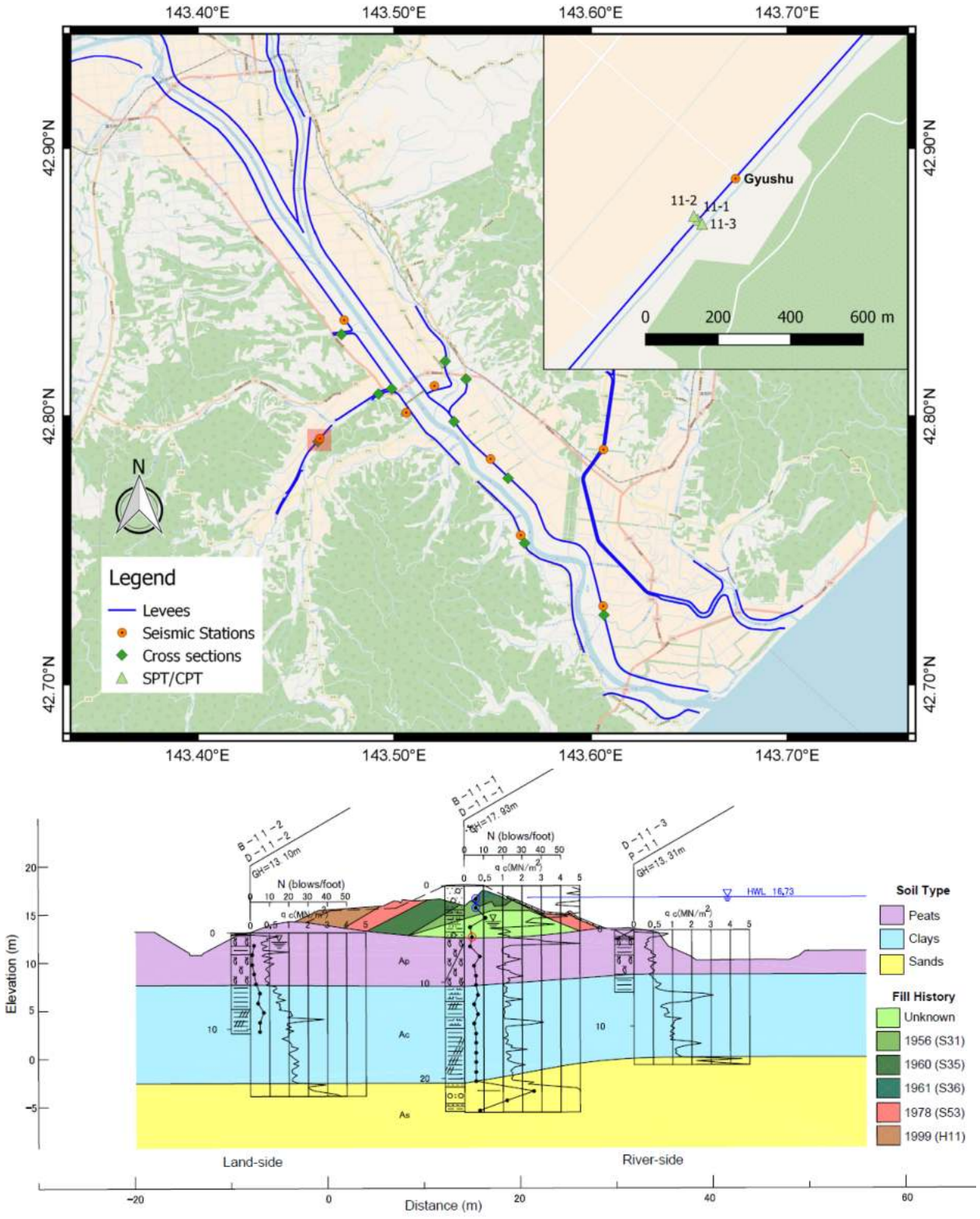

Figure 4.22 Vicinity map and subsurface investigation at section 11.

Figure 4.23 Extensive subsidence and collapse of the levee at Section 11.

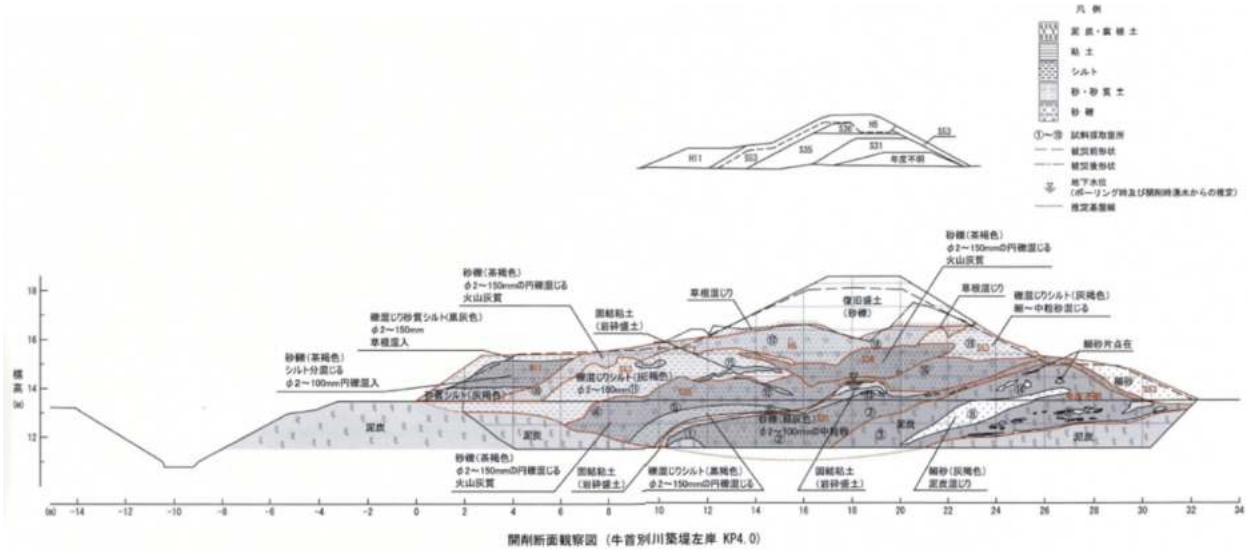

Figure 4.24 Mapped surface of excavation at Section 11, showing fill placement history and failure geometry. The fill placed in 1956 (S31) likely liquefied during the earthquake.

4.3.7 Section 12 - Satsusakubetsu River right bank

The Satsuakubetsu River joins the Tokachi River on the right bank around 24.6 km upstream of the river mouth. The cross section is around 500 m from the intersection and the closest station is RSK, located around 500 m upstream on the levees on the right bank of Tokachi River (Figure 4.25). The levee was initially constructed in the 1959 and 1960, and subsequently expanded in 1975. The levee fill consists mainly of sandy gravels, with average blow count of about 5. The CPT at the crest terminated near the base of the levee, which is likely early due to contact with gravel. Ground water was encountered at the base of the levee at the top of the peat layer, which is unusually low compared to other locations.

The levee rests on top of a peat layer (Ap) around 4 m thick, with seams of sand and silts (As1) in the free-field away from the levee. A sandy layer (As2) of variable thickness underlies the peat layer, and is followed by a sandy silt layer (Ac) that decreases in fines to be predominately sands deeper into the profile (As3). The sandy layers are observed to have higher cone tip resistance that is not readily reflected in the blow counts.

The levees were heavily damaged, crest subsidence was estimated to be around 50-70 cm and accompanied by cracks up to 100 cm wide and 50 cm deep with cracks with width and depth up to 80 cm and 100 cm and crest subsidence around 50 cm (Figure 4.26). The. Sand boils and additional cracks around 5 cm wide and 50 cm deep were observed on the slope.

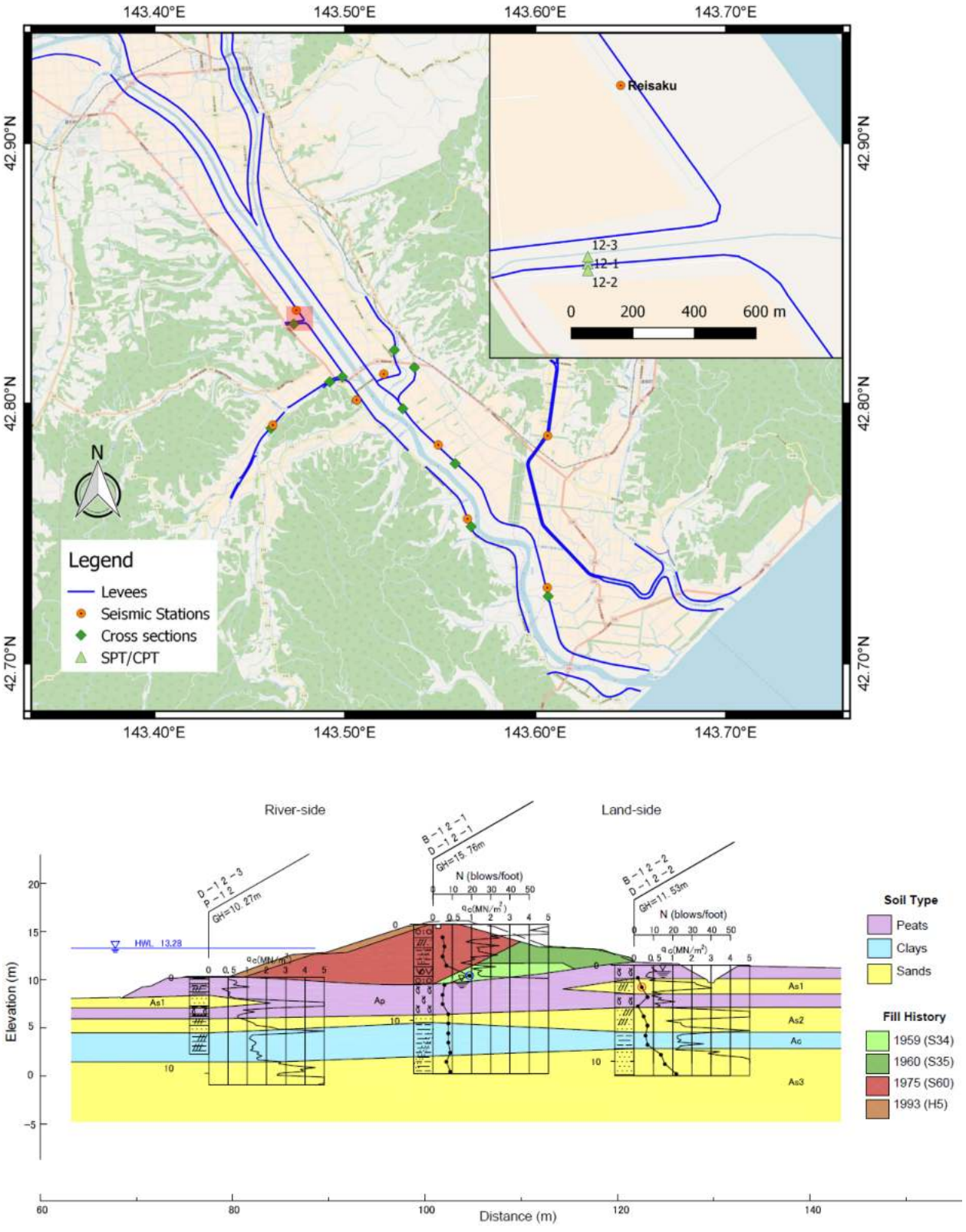

Figure 4.25 Vicinity map and subsurface investigation at Section 12.

Figure 4.26 Damage at Section 12, cracks on the roadway on the levee crest (top left). Slip and displacement of the land-side slope towards the levee toe (top right, bottom).

During the restoration process, the section where the SPTs and CPTs were advanced was excavated and mapped (Figure 4.27). Laboratory tests identified the fill placed in 1959 (S34) and 1960 (S35) to be primarily composed of coarse sands, with gravels mixed in and minimal fines, to be susceptible to liquefaction. Ground water was encountered around 2 m from the base of the levee fill. Deformation in the foundation was not observed and slip through the peat layer was deemed unlikely.

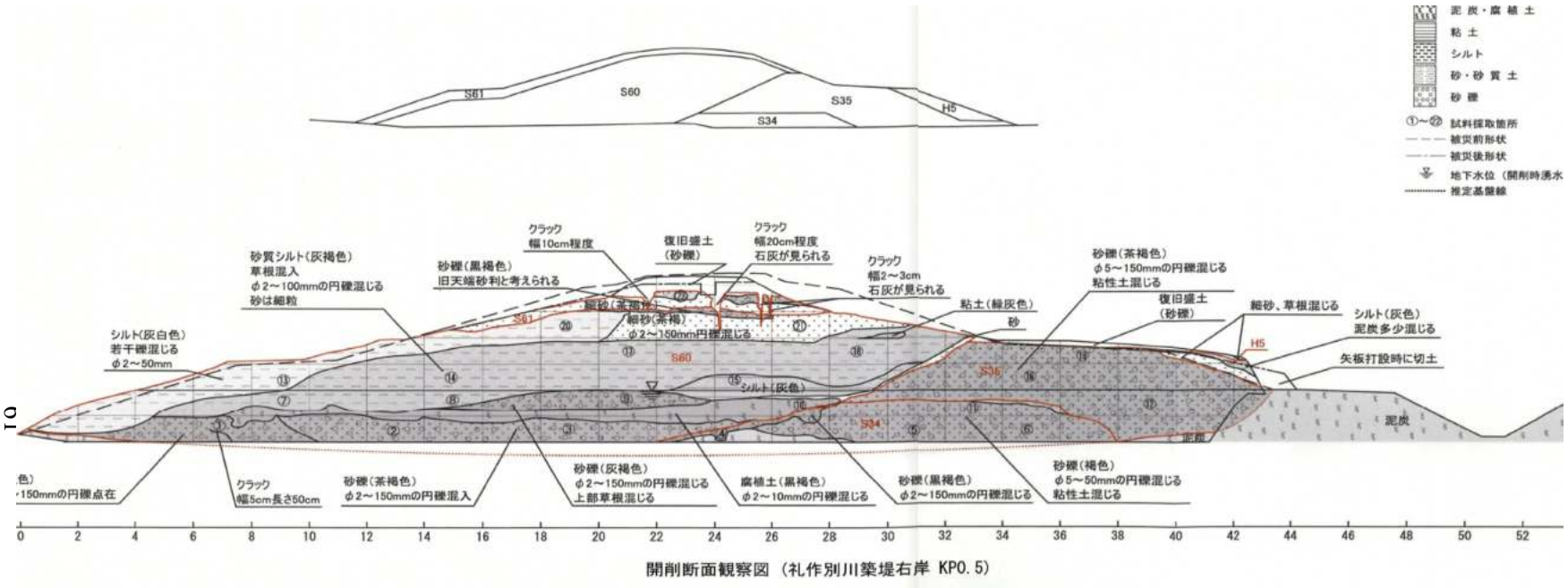

Figure 4.27 Mapped surface of the excavation at section 12 showing fill placement history and failure geometry. Fill placed in 1959 (S34) and 1960 (S35) composed of coarse sands with gravels is deemed to be susceptible to liquefaction.

4.3.8 Sections 13 and 14 - Satsubunnai River

The Satsubunnai River is a subsidiary stream and joins the Tokachi River around 20 km upstream from the river mouth. Section 13 is on the right bank around 1.7 km upstream of the intersection and is close to the river channel. Section 14 is on the left bank around 0.9 km upstream from the intersection, with a setback of around 400 m from the river channel. The closest station is TKCH07, located further upstream and inland off the right bank, shown in Figure 4.28 together with the two sections.

At section 13, both the fill and the foundation contain mainly sands; peats and clays are absent at this location (Figure 4.29). The upper layer of sand (As1) contains minor amounts of silt beneath the levee, increasing in fines content towards the land-side toe. Directly beneath that is around 5 m of clean sands, interbedded with silts at larger depth (As2). Ground water was encountered around 1 m below the free-field surface and the levee fill is unsaturated. No damage was observed at this section, though severe cracking and settlement at the crest was observed around 100 m downstream

At section 14, the levee is underlain by around 2 m of peat (Ap) followed by around 1 m of clay (Ac1) (Figure 4.30). A highly interbedded sandy layer (As1) is sandwiched between the upper and lower clayey layers (Ac2). The lower sand layer (As2) is much stiffer, as reflected by the rapid increase in blow counts and cone tip resistance. The ground water table is within the peat layer, around 1 m below the free-field surface, and the levee fill is unsaturated.

The section experienced extensive cracking and warping of the paved roadway on the crest, with settlement and slip on the land-side slope. Cracks around 110 cm deep and 60 cm wide, and differential settlement over 30 cm of the levee slope from the edge of the asphalt roadway (Figure 4.31).

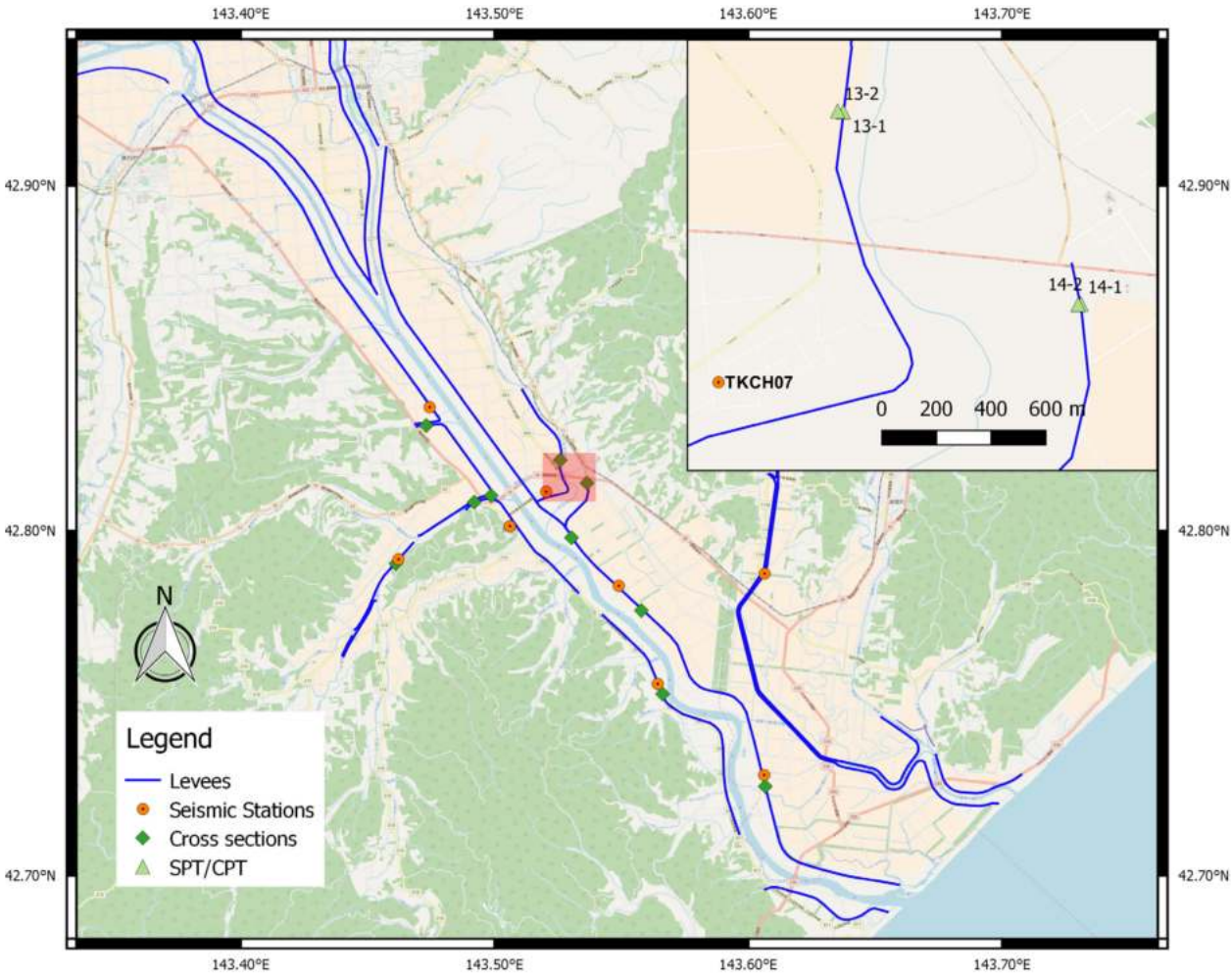

Figure 4.28 Vicinity map for Sections 13 and 14 on the subsidiary Satsubunnai River.

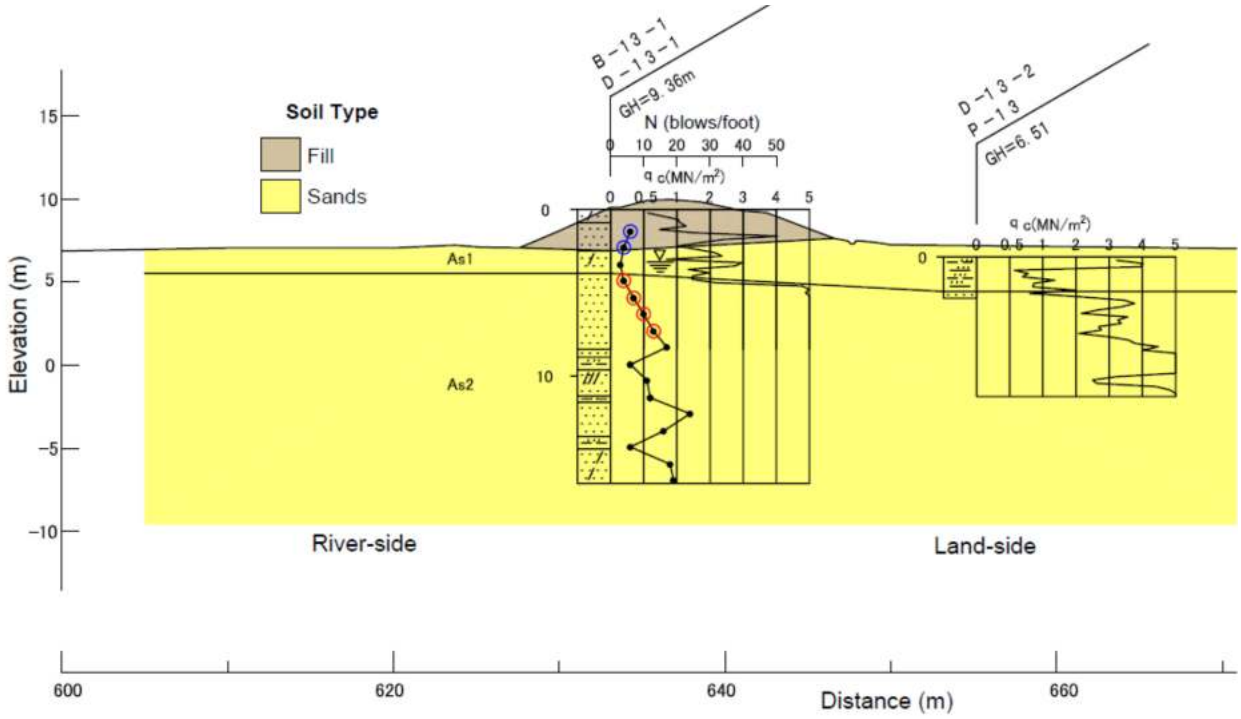

Figure 4.29 Subsurface investigation for Section 13.

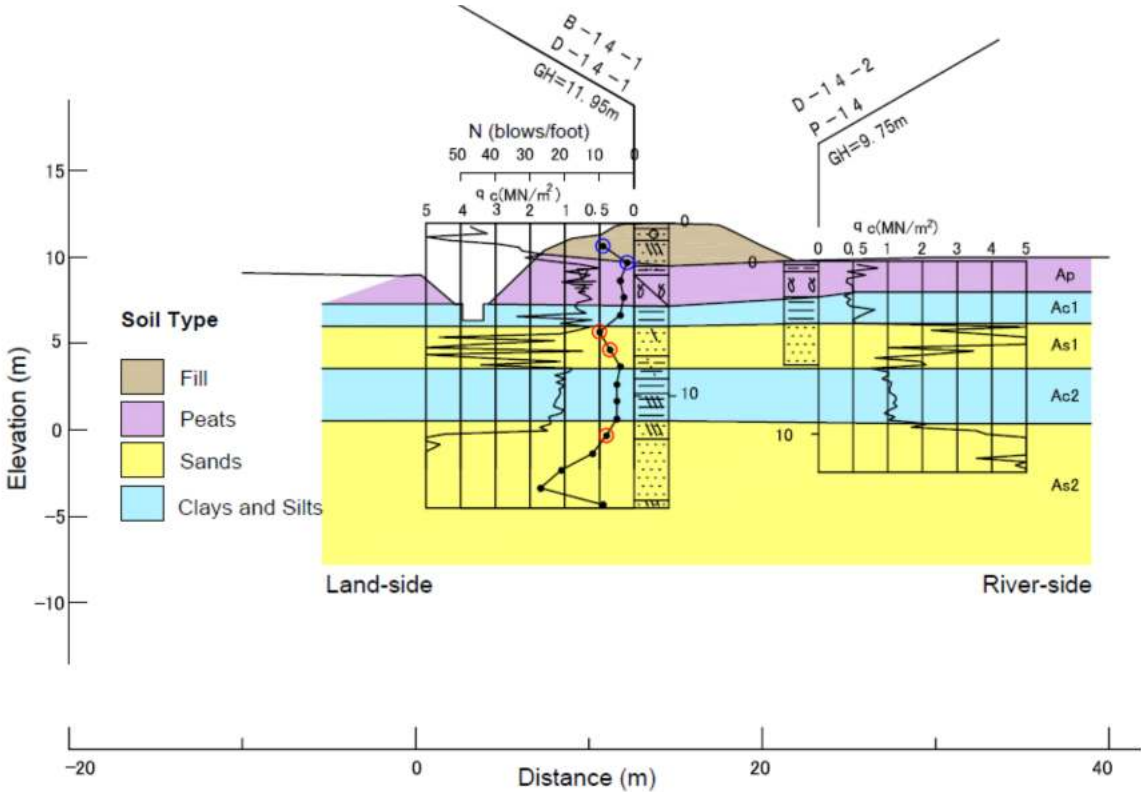

Figure 4.30 Subsurface investigation for Section 14.

Figure 4.31 Cracks on the roadway on the levee crest at Section 14 from slip on land-side slope.

4.4 ANALYSIS OF LEVEE CROSS SECTIONS

Damage to the levees presented above was caused by liquefaction, bearing capacity failure in the soft underlying peat, or a combination of both. This section presents an analysis procedure for predicting these effects. The analysis procedure utilizes liquefaction severity indices with slope stability and Newmark displacements. Liquefaction severity indices integrate liquefaction potential in some manner over depth, and are therefore more severe for thick liquefiable layers. They have been shown to correlate reasonably well with liquefaction damage observations. However, they are performed for a single boring, and do not inherently capture lateral variability. Slope stability simulations combined with Newmark sliding block analyses provide a better assessment of lateral continuity of weak zones, but this approach is relatively insensitive to the thickness of liquefiable or weak layers. The two approaches are therefore viewed as complementary, and the aggregate damage potential is defined as a function of both analyses.

The analysis procedure is outlined below:

1) Determine liquefaction susceptibility of material present and evaluate the cyclic resistance;
2) For the given seismic loading, determine factor of safety against liquefaction or cyclic softening. If strength loss is likely, apply the appropriate procedures to evaluate residual strengths;
3) Compute liquefaction severity indices for each SPT and CPT profile;
4) Compute FS, yield accelerations and Newmark displacements for each cross section;
5) Combine the results from Steps 3 and 4 to assign an aggregate damage level.

The aggregate damage levels from Step 5 above are then compared with observed levee damage.

4.4.1 Strength loss mechanisms

Assessing liquefaction susceptibility is the critical step to the process of characterizing soil behavior under cyclic loading. Liquefaction triggering procedures should be used to assess soils determined to be susceptible to liquefaction, whereas cyclic softening procedures should be applied to fine-grained soils deemed too clay-rich to liquefy. The estimated resistance is then compared with the anticipated seismic demands the soil to determine if significant loss of strength and/or large strains are expected. In current geotechnical engineering practice, susceptibility is typically evaluated through the soil's index properties, such as gradation, liquid limit (LL) and plasticity index (PI), that characterize the composition and properties of the soil mixture. Bray and Sancio (2006) consider both PI and LL, with material with PI < 12 and LL > 0.85 as susceptible, PI > 18 as not liquefiable, but can have large strength loss and strains, and intermediate PI with LL > 0.8 to be moderately susceptible. Boulanger and Idriss (2006) focused on differentiating between sand-like and clay-like behavior to select the appropriate procedure for characterize the behavior of fine-grained soils, and recommend soils with PI ≥ 7 are clay-like, and with PI < 7 are sand-like.

The classification from the boring logs is used to estimate liquefaction susceptibility. The Japanese soil classification adopts a three letter code based the following scheme (JHPC, 2005):

1) The first letter represents soil type of the major fraction, which > 50% of the dry soil is composed of by weight;
2) The second letter represents the minor fraction, which 15-50% of the dry soil is composed of by weight;
3) The third letter represents a minority fraction, which 5-15% of the dry soil is composed of by weight. It is preceded by a dash to distinguish it from the letter for the minor fraction. (e.g., S-M)

The letters for each soil type is similar to the Unified Soil Classification System (USCS), with G for gravels, S for sands, M for silts, C for clays. Less common materials present here are peat (P) and traces of volcanic ash (V). Under this system, a material classified as "SM-G" would be a silty sand with traces of gravel, with the silt and gravel content not exceeding 50% and 15% respectively. Alternatively, "S" would indicate relatively clean sands, with no other soil type comprising more than 5% (if present). In addition, index tests on samples from the two excavated sections showed levee fill with major fraction of silt to have high PI (≥ 7). Based on the classification scheme, the strength loss mechanisms employed in subsequent analysis is given in Table 4.3 based on the soil classification.

Table 4.3 Susceptibility based on soil classification

Group	Soil Classification	Description	Cyclic Strength Loss Mechanism
1	S, SM, SM-G, S-G, S-M, SV	Clean sands, sand with minor mixtures, silty sands, gravelly sands,	Liquefaction
2	M, MC, MS, M-C, M-G, M-S C, CM, C-M, C-S P, PC, PM, P-C, P-G	Silts, clays and peats	Cyclic softening
3	G, GS, V	Gravels and volcanic soils	None

4.4.2 Liquefaction Severity Indices

Surface manifestation of liquefaction depends on both loading intensity and site conditions (e.g., depth of liquefiable layers, thickness of non-liquefiable crust, lateral continuity), requires liquefaction to be triggered in a stratum that is sufficiently thick and shallow, such that the excess pore pressure will exit at the ground surface. Liquefaction severity indices combine liquefaction triggering with site characteristics to assess the occurrence and severity of surficial manifestation, which is linked to the

potential for liquefaction induced damage. Four indices are considered for estimating cross-section performance, as summarized below. For consistency across different indices, FS_{liq} and D_R are computed using either the blow counts or cone tip resistance following the procedures in Boulanger and Idriss (2012 and 2016).

The Liquefaction Potential Index (LPI) proposed by Iwasaki et al. (1978) integrates the factor of safety against liquefaction triggering (FS_{liq}) after applying a weighting function that decreases with depth. All else being equal, liquefaction of a shallower layer yields a higher LPI, reflecting that the shallowest layers in a profile most strongly influence surface manifestation and damage. Based on the 55 case histories from Japan examined, severe liquefaction is expected for LPI >15, and not expected for LPI <5.

$$LPI = \int_0^{20\,m} F \times w(z)\, dz \tag{4.1}$$

$$F = \begin{cases} 1 - FS, & if\ FS \leq 1 \\ 0, & if\ FS > 1 \end{cases} \tag{4.2}$$

$$w(z) = 10 - 0.5z \tag{4.3}$$

Maurer et al. (2015) extended the LPI framework to incorporate the suppressive effects of non-liquefiable crusts presented by Ishihara (1985), and incorporated case histories from a global dataset (e.g., the 1989 Loma Prieta (USA), 1994 Northridge (USA), 1999 Kocaeli (Turkey), 1999 Chi-Chi (Taiwan), 2010 Darfield (New Zealand), and 2011 Christchurch (New Zealand) earthquakes). The updated Ishihara-inspired index, LPI_{ISH}, employs a power law depth weighting function.

$$LPI_{ISH} = \int_0^{20\,m} F_1 \times \frac{25.56}{z}\,dz \tag{4.4}$$

where

$$F_1 = \begin{cases} 1 - FS, & if\ FS \le 1 \cap H_1 \times m(FS) \le 3 \\ 0, & if\ FS > 1 \end{cases} \tag{4.5}$$

$$m(FS) = \exp\left(\frac{5}{25.56(1 - FS)}\right) - 1$$

H_1 is the thickness of the non-liquefiable crust and is estimated as the surface to the top of the first susceptible layer. The authors recommend a minimum of 0.4 m for shallow ground water cases. As shown in Figure 4.32, the upper 3 m of the profile is weighted more than in LPI's linear depth weighting function. LPI_{ISH} shares the same performance thresholds as LPI.

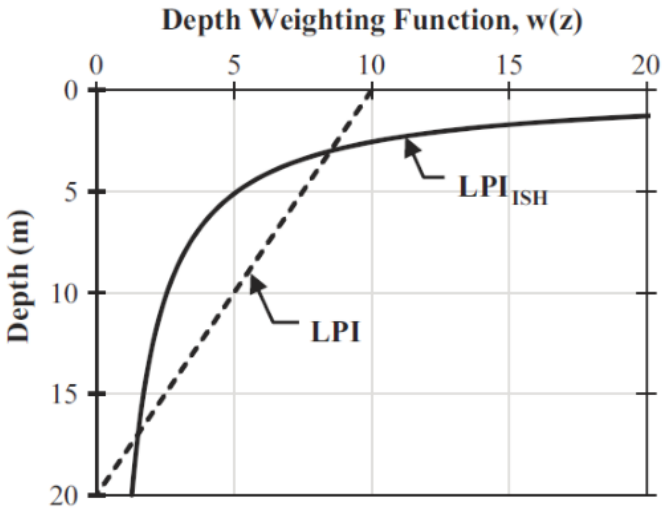

Figure 4.32 Shallow layers are weighted more in the LPI_{ISH} than LPI procedure (Maurer et al., 2015).

Van Ballegooy et al. (2014) examined over 11,500 CPT profiles and liquefaction manifestation during the Canterbury earthquake sequence in New Zealand. The Liquefaction Severity Number (LSN) estimates the potential ground surface settlement by integrating one-dimensional reconsolidation strains over the upper 20 m of the profile,

$$LSN = 10 \int_{0}^{20\,m} \frac{\epsilon_v}{z}\, dz \tag{4.6}$$

where z is the depth below the ground surface in meters and ϵ_v is the post-liquefaction volumetric strains (%), which can be correlated to relative density (D_R) and FS_{liq} (e.g., Yoshimine et al., 2006). Severe liquefaction is expected where LSN > 40, and minimal to no manifestation is expected where LSN < 20, with moderate to severe manifestation where 20 ≤ LSN ≤ 40.

The Lateral Displacement Index (LDI) by Zhang et al., (2004) presents a potential maximum lateral displacement at the ground surface by considering the cyclic shear strains mobilized over the profile,

$$LDI = \int_{0}^{z_{max}} \gamma_{max}\, dz \tag{4.7}$$

where z_{max} is the depth below all potentially liquefiable material with FS < 2. The limiting shear strain, γ_{lim}, is based on Idriss and Boulanger (2008) and restricted to 0.5% to avoid a single loose measurement dominating the estimated strains. The mobilized shear strains in each liquefiable layer is based on correlations with FS_{liq} and shear strains observed in lab tests by Ishihara and Yoshimine (1992).

$$\gamma_{max} = \begin{cases} 0, & FS \geq 2 \\ \gamma_{lim}, & FS \leq F_\alpha \\ \min\left(\gamma_{lim}, 0.035 \times (1 - F_\alpha)\left(\dfrac{2 - FS}{FS - FS_\alpha}\right)\right) & otherwise \end{cases} \tag{4.8}$$

$$F_\alpha = 0.032 + 4.7\mathrm{D_R} - 6.1\,(D_R)^2 \tag{4.9}$$

$$\gamma_{lim} = 1.859(1.1 - D_R)^3 \leq 0.5 \tag{4.10}$$

4.4.3 Initial material strengths

Material below the ground water table is assumed to be saturated and the undrained strength is used for seismic analysis of fine-grained soils and coarse-grained soils deemed susceptible to liquefaction. Coarse-grained material above the water table is assumed to be unsaturated and drained strength parameters are used. Fine-grained material above the water table is assumed to be saturated due to capillary rise, and undrained strength is used. Coarse-grained material below the water table (e.g., gravels without a low-permeability capping layer) are assigned drained strength parameters. Soil properties such as relative density, peak friction angle, and undrained shear strength are estimated for a given unit.

For sandy soils, shear strength is defined with the friction angle, ϕ', correlated with penetration resistance from SPT or CPT (e.g., Hatanaka and Uchida (1996)), or as a sum of the critical state friction angle and the difference between peak and critical state friction angle ($\phi' - \phi_c$) (Bolton 1986). The difference can be related to the relative dilatancy index, which is a function of the relative density and mean effective stresses for the material.

$$\phi' = \phi'_c + 3I_R \tag{4.11}$$

$$I_R = D_R(10 - \log \sigma'_m) - 1 \tag{4.12}$$

$$Mean\ effective\ stress, \sigma'_m = \frac{1 + 2K_0}{3} \times \sigma'_v \tag{4.13}$$

$$K_0 = 1 - sin\phi' \tag{4.14}$$

where ϕ'_c is a function of minerology and ranges between 32-40°, and is typically taken to be 32° or quartz sands. Relative densities are correlated from SPT or CPT based on Idriss and Boulanger (2008):

$$D_R = \sqrt{\frac{(N_1)_{60,cs}}{46}} \tag{4.15}$$

$$D_R = 0.478\, {q_{c1Ncs}}^{0.264} - 1.063 \tag{4.16}$$

$$21 \leq q_{c1Ncs} \leq 254 \tag{4.17}$$

For cohesive soils, the undrained shear strength (S_u) is correlated to in-situ measurements from the cone tip resistance, q_c and an empirical cone factor (N_k) as:

$$S_u = \frac{q_c - \sigma_{vo}}{N_k} \tag{4.18}$$

N_k of 15 and 12 are selected for clays and silts (Lunne et al, 1985). For peat, N_k is estimated to range from 20 - 25 from CPTs and direct simple shear tests on peat samples from Sherman Island, California (Shafiee 2016), and 21 for peats in Hokkaido (Hayashi and Hayashi 1991). The latter is adopted since the testing program involved samples from multiple river systems in Hokkaido having similar depositional environment, and are more representative of peat along the Tokachi River. For typical monotonic undrained shear strength tests, Stewart et al. (2014) suggests a 20-40% increase to account for rate effects as loading during from earthquake is much faster. The strain rates for the CPTs pushed are unknown and strength adjustments are not applied.

4.4.4 Residual strengths

Considering the effects of strength loss, liquefied strengths for susceptible layers with FS_{liq} <1 are estimated using relationships proposed by Olson and Stark (2002), Idriss and Boulanger (2007) and Kramer and Wang (2015). Both SPT and CPT based approaches are utilized measurements for susceptible material with FS_{liq} <1 during the 2003 earthquake. Estimated residual strength is capped at $\sigma_v' \tan \phi'$ at shallow depths, such that the drained shear strength of the material is not exceeded.

Olson and Stark (2002) and Idriss and Boulanger (2007) proposes relationships for normalized residual strength estimated using both SPT and CPT data. Olson and Stark (2002) back analyzed thirty liquefaction flow failures to estimate residual shear strengths,

$$\frac{S_u(liq)}{\sigma'_{v0}} = 0.03 + 0.0075(N_1)_{60} \qquad N_1 \leq 12 \quad (4.19)$$

$$\frac{S_u(liq)}{\sigma'_{v0}} = 0.03 + 0.0143(q_{c1}) \qquad q_{c1} \leq 6.5MPa \quad (4.20)$$

$$q_{c1} = q_c \left(\frac{1.8}{0.8 + \frac{\sigma'_{v0}}{p_a}} \right) \quad (4.21)$$

The ratios ranges from 0.24 to 0.30. For both CPT and SPT correlations, the standard deviation is 0.025, with ±0.030 for the upper and lower bounds.

Idriss and Boulanger (2007) adopts a fines correction factor based on Seed (1987), summarized in Table 4.4, which is distinct from the fines correction in liquefaction triggering analysis. Effects of void redistribution are considered where the formation of a water film may further reduce the shear strength. For the sites considered here, a low permeability capping layer is absent from the levee fill and the foundation, so void redistribution effects are ignored. Additionally, the blow counts are within the liquefiable layers are generally below 10, and the recommended curves for the two cases are mostly overlapping. Given the above, void redistribution effects are not expected to be significant and the residual strength ratio is estimated as follows,

$$\frac{S_r}{\sigma'_{v0}} = \exp\left(\frac{(N_1)_{60-Sr}}{16} + \left(\frac{(N_1)_{60-Sr} - 16}{21.2} \right)^3 - 3.0 \right) \times \left(1 + \exp\left(\frac{(N_1)_{60-Sr}}{2.4} - 6.6 \right) \right) \quad (4.21)$$

$$\frac{S_r}{\sigma'_{v0}} = \exp\left(\frac{q_{c1N-Sr}}{24.5} - \left(\frac{q_{c1N-Sr}}{61.7}\right)^2 + \left(\frac{q_{c1N-Sr}}{106}\right)^3 - 4.42\right) \times \left(1 + \exp\left(\frac{q_{c1N-Sr}}{11.1} - 9.82\right)\right) \quad (4.22)$$

Table 4.4 Fines correction recommended for estimating residual strengths

Fines Content	$\Delta(N_1)_{60-Sr}$	Δq_{c1N-Sr}
10	1	10
25	2	25
50	4	45
75	5	55

Lastly, Kramer and Wang (2015) directly relates residual strength to penetration resistance and effective stresses instead of a normalized strength ratio,

$$\ln(S_r) = -8.444 + 0.109(N_1)_{60} + 5.379(\sigma'_{v0})^{0.1} \qquad (atm) \qquad (4.23)$$

Cyclic failure of clay-like soils are assessed with a framework similar to liquefaction in sands. The cyclic resistance of the soil is compared to the estimated cyclic stress imposed by the earthquake, and where the factor of safety $\left(FS = \frac{CRR}{CSR}\right)$ is below 1, cyclic failure where large deformation develop are likely (exceeding 3% strain). To account for effect of number of cycles on resistance, scaling related to earthquake magnitude is developed, the MSF for clays is much flatter for clays than sands, and is close to unity for the M_w 8.2 Tokachi-oki earthquake considered.

$$MSF = 1.12\exp\left(-\frac{M_w}{4}\right) + 0.828 = 0.957 \quad (4.24)$$

The cyclic strength of clay-like soils can be obtained either directly from cyclic laboratory testing, or correlated to monotonic undrained shear strength (s_u) with empirical factors to account for rate and direction effects (Boulanger & Idriss 2007). The undrained shear strength may be measured in the field (e.g., vane shear, CPT), from laboratory testing, or estimated based on normalization with stress history.

Boulanger and Idriss (2007) recommended taking cyclic strength ratio $\left(\frac{\tau_{cyc}}{s_u}\right)$ = 0.83 for natural deposits of clay-like fine grained soils (PI > 7) for any OCR, and the cyclic resistance ratio (CRR) for normally consolidated soils to be $\frac{\tau_{cyc}}{\sigma'_{vc}} = 0.18$ for two dimensional cyclic loading with 30 equivalent cycles. Later works suggest that the ratio may be dependent on PI, and suggest a transition of cyclic strength ratio from 0.611 at PI = 10 to 0.8 at PI >18 (Eslami 2017).

$$CRR_{M=7.5} = \frac{\tau_{cyc}}{\sigma'_{vc}} = \left(\frac{\tau_{cyc}}{s_u}\right)\left(\frac{s_u}{\sigma'_{vc}}\right) \tag{4.25}$$

Cyclic loading in cohesive soils tend reduce the undrained shear strength and stiffness, especially in sensitive soils. Normally consolidated clays that are cyclically sheared sufficiently to achieve cyclic softening have been observed to have pore pressure ratios within the range 0.30 to 0.80, which develop for shear strain amplitudes varying from 1 to 9.5% (Boulanger and Idriss 2006; Dahl et al. 2014). Excess pore pressure ratio is lower than sands even at large strains, and drastic reduction of strength at the level experienced during liquefaction of granular material is unlikely. The extent of strength loss in claylike soils from cyclic softening depends on the magnitude of seismically-induced shear strains, OCR and sensitivity of the soil.

Testing performed by Yasuhara (1994) on Akita peat showed post-cyclic undrained shear strength to be a function of the excess pore pressure at the end of cyclic loading (Figure 4.33). Shafiee (2016) performed undrained monotonic tests after cyclic strain controlled loading on Sherman Island peat, and observed an average 25% reduction in the undrained shear strengths from 15 cycles of loading and reaching shear strains around 10% and pore pressure ratios around 0.37. The strength reduction is larger for Sherman Island peat than Akita peat with a similar the pore pressure ratio.

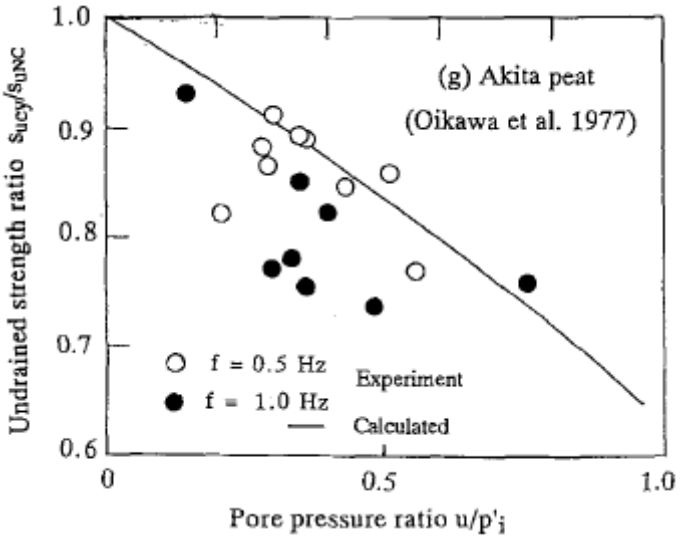

Figure 4.33 Undrained strength ratio decreasing with pore pressure ratio for Akita peat (Yasuhara, 1994).

An alternative metric to consider is the shear strain developed during cyclic loading. The ultimate undrained shear strength of a saturated soil is governed by the void ratio and soil fabric, therefore if the cyclic loading has not altered the void ratio or the soil structure, the undrained strength at large strains will remain the same. As the cyclic strain amplitude approaches the strain level of failure for monotonic loading, the soil structure is being altered and the monotonic strength decreases. Using the FS as an indicator of potential levels of strains for the applied cyclic load, minor strains are expected for high FS (i.e., FS $\geq$ 1.5) and cyclic softening is not expected. For small strains (1.0 < FS < 1.5) and moderate strains, the monotonic undrained shear strength is reduced by 10% and 20% respectively to account for cyclic softening.

4.4.5 Slope stability and Newmark displacements

The model geometry is defined using the pre-earthquake dimensions from the cross-sections; the material properties and layering are based on the penetration resistance and soil classification from the boring logs. If multiple estimates of material strengths are available within the same material unit, the 33rd percentile value was assigned as an equivalent uniform property, which produces displacements

in reasonable agreement with dynamic simulations using stochastic models that consider spatially-correlated variable subsurface properties (Montgomery & Boulanger 2017). In addition, a unit may be subdivided to reflect lateral and vertical transitions in material strengths. This is most prevailing in the peat layers, where the resistance under the levee crest is significantly higher than in the free-field from consolidation under the additional stresses from the levee fill, as well as the higher confining stresses. For cohesive materials, tension cracks are accounted for and the depth of cracking is given by $z_{cr} = \frac{2c'}{\gamma\sqrt{K_a}}$ for c- ϕ material, and as $z_{cr} = \frac{2S_u}{\gamma}$ for undrained conditions (Duncan et al., 2014). Cohesion is assumed to be low in predominantly sandy material in the levee fill, though from the deep cracks observed in the reconnaissance, the fines content is likely sufficient to develop some cohesion. Without further testing, higher cohesion is not adopted since the deeper tension cracks is balanced by a higher strength within the material. The sensitivity of the analysis to cohesion assumed and the corresponding crack depth will be considered in a future study.

Stability analyses were performed in *SLIDE* considering failure of both slope faces with initial material strengths and subsequently with reduced strength where liquefaction or cyclic softening is predicted. For the non-circular failure surfaces considered, Spencer and Morgenstern-Price methods of slices are utilized because both methods satisfy force and moment equilibrium. The resulting factor of safety (FS), yield accelerations (a_y) and displacements are largely similar for a given section, and Spencer's method is used in subsequent analyses. All levees are stable under static conditions and generally FS $\geq$ 1.5 for the initial material properties estimated in Section 4.4.3. The minimum horizontal pseudo-static seismic load that will destabilize the slope (FS $\leq$ 1.0) is computed for both orientations and taken as the yield acceleration. The analysis is repeated with strength reductions to include the effects of liquefaction and cyclic softening. Flow failure are expected where FS < 1.0, indicating the levee is unstable and large displacements are expected. For sections where FS > 1.0, rigid sliding block

analyses are used to predict seismic displacement potential of slopes (Newmark 1965), by assuming accumulation of displacement whenever the yield acceleration is exceeded by the earthquake acceleration. The levee perpendicular component of the recording from the nearest station (Table 4.2) is used for each cross section.

4.4.6 Example LPI calculations and model construction

The analysis is demonstrated with section 11, which had extensive damage during the earthquake (Section 4.3.6). The bottom of the levee fill is predominantly sand, with trace amounts of gravel and susceptible to liquefaction. CPT and SPT measurements through the levee crest is shown in Figure 4.34, with measurements in susceptible layers highlighted. Appendix B contains the plots for each profile. The shallower susceptible layer corresponds to the saturated fill. The thick layer of peat and clay directly under the levee fill is not liquefiable, followed by a thick layer of dense sand that is susceptible but has high penetration resistance. The cyclic resistance ratio is estimated from the normalized and fines corrected tip resistance and blow counts, which is compared to the cyclic stress ratio estimated from the PGA measured at the ground level sensor at the GSB station. The FS against liquefaction is significantly lower than 1.0, and triggering of liquefaction is expected. The dense sand layer is beyond the 20 m considered, and only the saturated portion of the levee fill contributes to the indices. The process is repeated for profiles on either side of the levee toe.

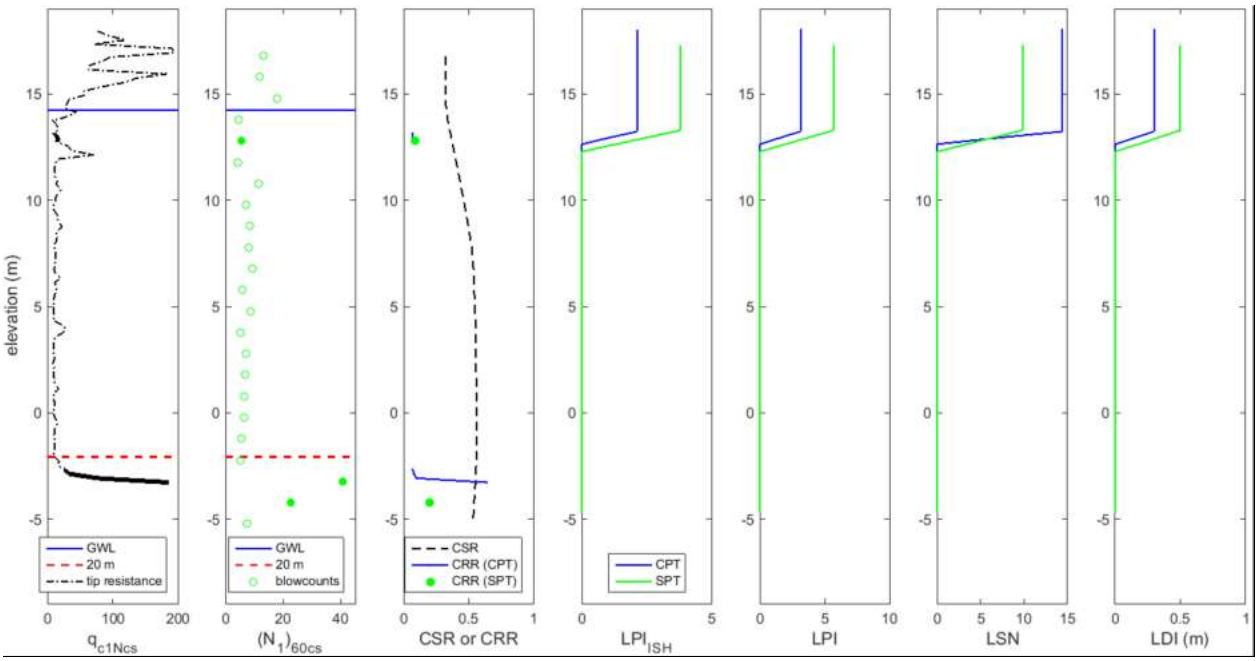

Figure 4.34 Liquefaction indices calculated from SPT and CPT through the crest at section 11. Susceptibility is based on material classification and ground water level from boring log.

For the 2-D slope stability model, the shear strength of levee fill and the dense sand are defined with the Mohr-Coulomb model using friction angles estimated from blow counts. For the peat and clay layers, the undrained shear strengths for the peat and clay layers are correlated from the cone tip resistance. The tip resistance is typically higher under the crest than in the free-field within the same strata, and reflects the higher stresses and consolidation from the placement of the levee fill. The resistance may also differ between the land-side and river-side, and is typical for the broad levees (spanning 60-80m at the base) along the main Tokachi River. For section 11, shear strength is similar between the two sides and an averaged value is assigned, as shown Figure 4.36 by the symmetric color coded material assignment. Materials with comparable classification are given similar colors, with lighter shades corresponding to lower strengths.

With the initial material properties, the static factor of safety is 1.81 and 1.72, with yield acceleration of 0.23 g and 0.22 g for the riverside and land-side respectively. Moderate displacements of 25 cm and 35 cm are estimated.

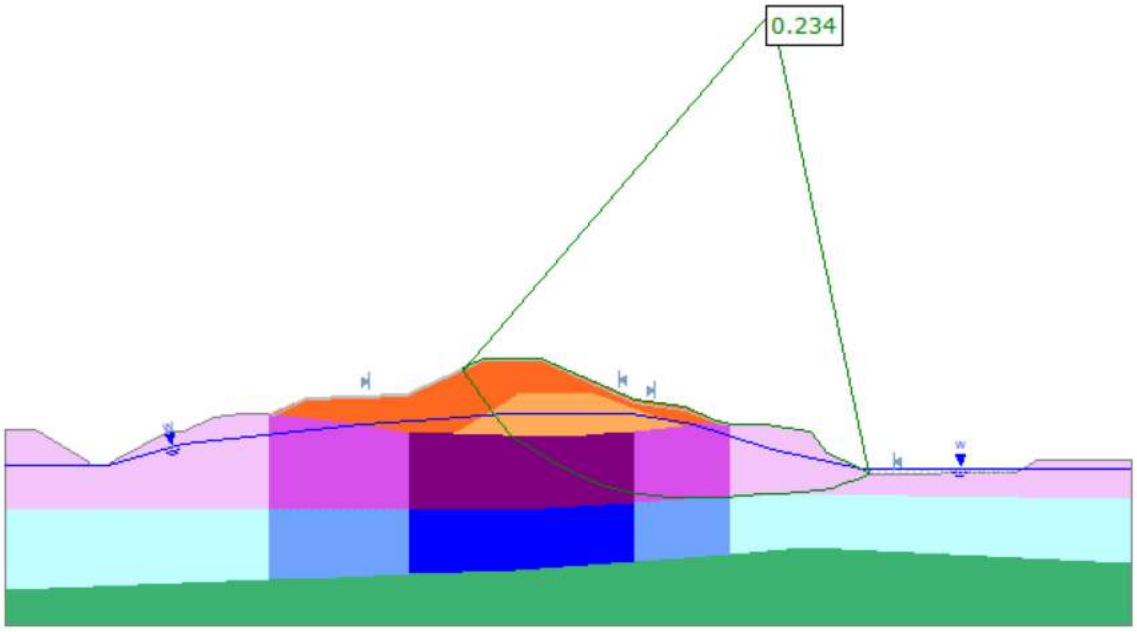

Figure 4.35 2-D model of section 11 showing yield acceleration for slope failure towards the river-side with pre-earthquake material properties.

The next step is to consider the influence of cyclic loading on material strengths. The potential for cyclic softening is assessed for the peat and clay layers. The FS exceeds 1.5 in the peat underneath the levee and the clay layers, and the initial strength is retained. For the free-field peat, FS is between 1.0 and 1.5 for the free-field peat and the undrained strength is reduced by 10%. Liquefaction is expected in the saturated levee fill in the levee. Judging by the construction history and samples taken during the open excavation, this corresponds to fill placed in 1956 and liquefied strength is assigned. With the strength reductions, FS falls to 1.01 and 1.60 for the river-side and land-side slopes. The river-side slope shown in Figure 4.36 is essentially on the verge of a flow failure and very low yield acceleration of 0.002 g is obtained. The calculated Newmark displacements is around 20 m, which indicating large

movements are expected, but is not physically meaningful since the rigid block assumption would be violated prior to achieving movement of that magnitude.

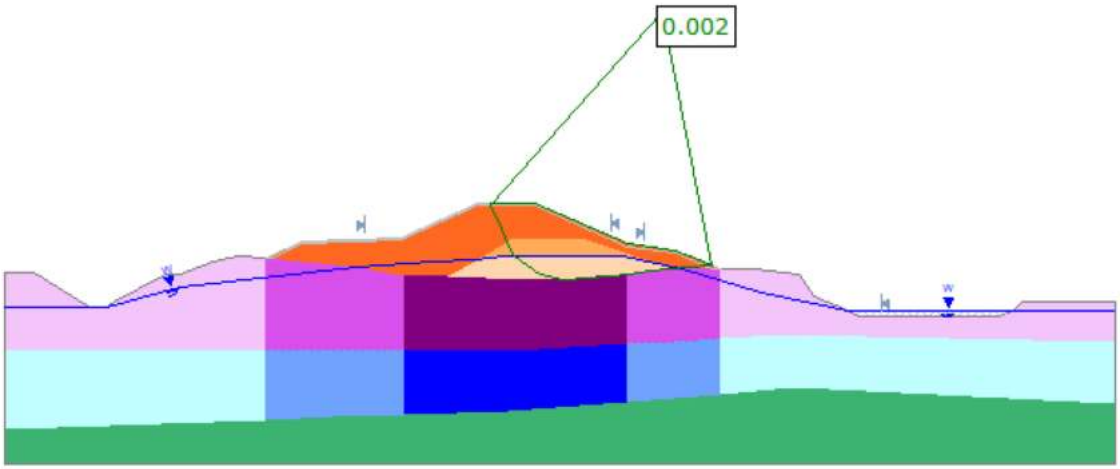

Figure 4.36 2-D model of section 11 showing slope failure towards the river-side with liquefied strength in saturated fill with softened strength in clay and peat.

Appendix B contains plots of the calculations for the liquefaction indices for each profile, as well as the *SLIDE* models showing the critical failure surfaces and the relevant material properties for each section.

4.5 COMBINED DAMAGE ASSESSMENT

The following section describes the framework for incorporating both liquefaction indices and Newmark displacements into damage level prediction for levee cross sections. Representative values for both metrics and thresholds for damage level are first determined individually, and combined to capture the potential effects from different failure mechanisms.

Multiple SPT or CPT are present at different locations on the levee and the resulting indices represents the local condition which generally vary across the levee. Figure 4.38 shows values from profiles at each cross section together with the original thresholds for minor, moderate and severe liquefaction

manifestation (Ishihara, 1985; Maurer et al., 2015; Van Ballegooy et al., 2014). The results for the sections are offset in the x-axis for visualization (i.e., DL 4 was observed for sections 2, 10 and 11). From the post-earthquake geometry and deformation patterns observed, it appear the shallower layers within or directly below the levees have more contribution than the deeper liquefiable layers to damage. As LPI weighs the contribution of the liquefiable strata linearly with depth, and LDI does not explicitly account for depth of the liquefiable layer, both tend to overestimate severity, with the majority of the values lying above the severe manifestation boundary. The power-law weighting used in LPI_{ISH} and LSN capture the observed performance better. These two indices are strongly correlated, and utilizing both is therefore unnecessary. LPI_{ISH} is adopted in subsequent analysis because it incorporates a broader dataset and includes the mitigating influence of a non-liquefiable crust.

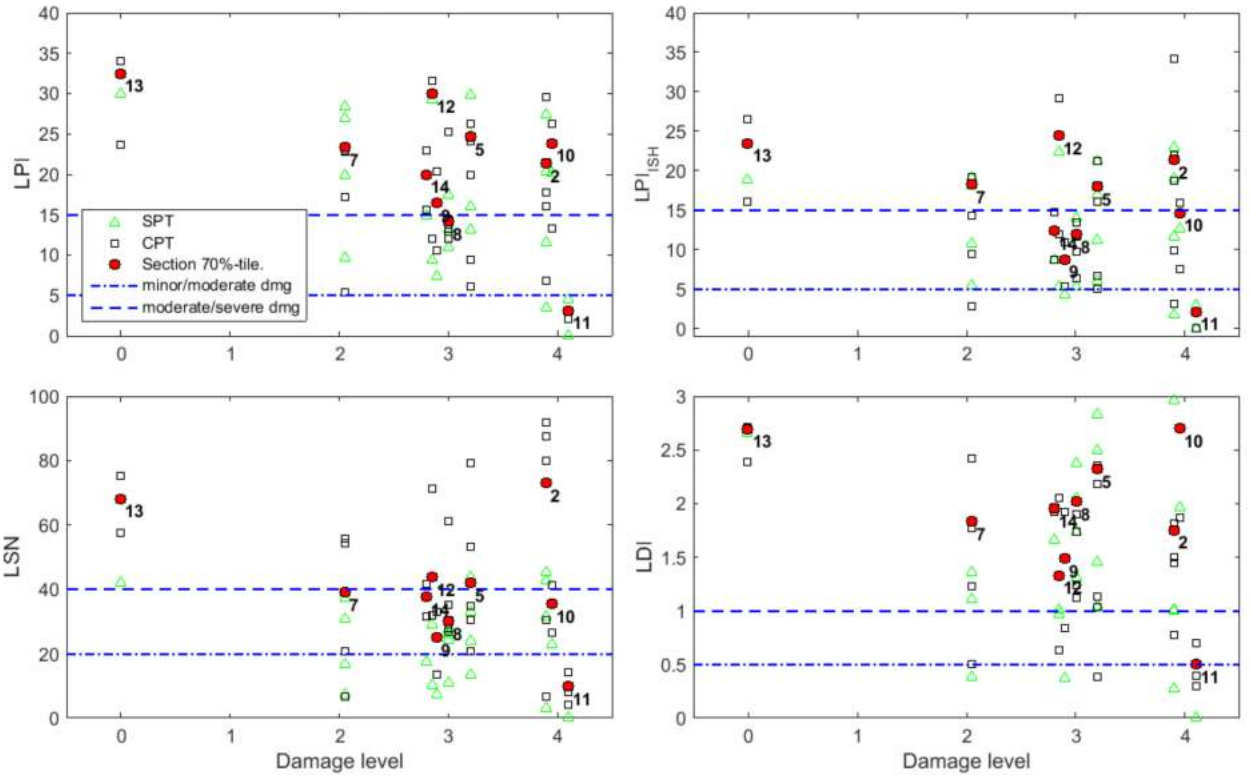

Figure 4.37 Liquefaction severity indices at each cross section based on all SPTs and CPTs shows a range of values. Cross sections with the same damage level are offset in the x-axis for visualization.

The liquefaction indices are computed along a vertical boring log or CPT profile, and therefore do not inherently capture the effects of lateral variability. When multiple liquefaction indices are computed for a levee cross-section, a decision must be made regarding how to combine them into an aggregate liquefaction index for assessing levee damage. In this case, the 70^{th} percentile LPI_{ISH} value is selected as representative of the levee, which emphasize the effects of loose regions in the fill or foundation on the overall performance at a levee section. Additionally, based on the deformation patterns observed in the photographs and open excavation of damaged levee segments, liquefaction within the fill is likely more damaging than within the foundation due to the static driving shear stresses present within the levee. For composite failures with liquefaction predicted in both the fill and foundation, indices from the profiles through the levee are assigned double weight when computing the 70^{th} percentile. The process to select a representative LPI_{ISH} value for the different scenarios is summarized in Figure 4.38.

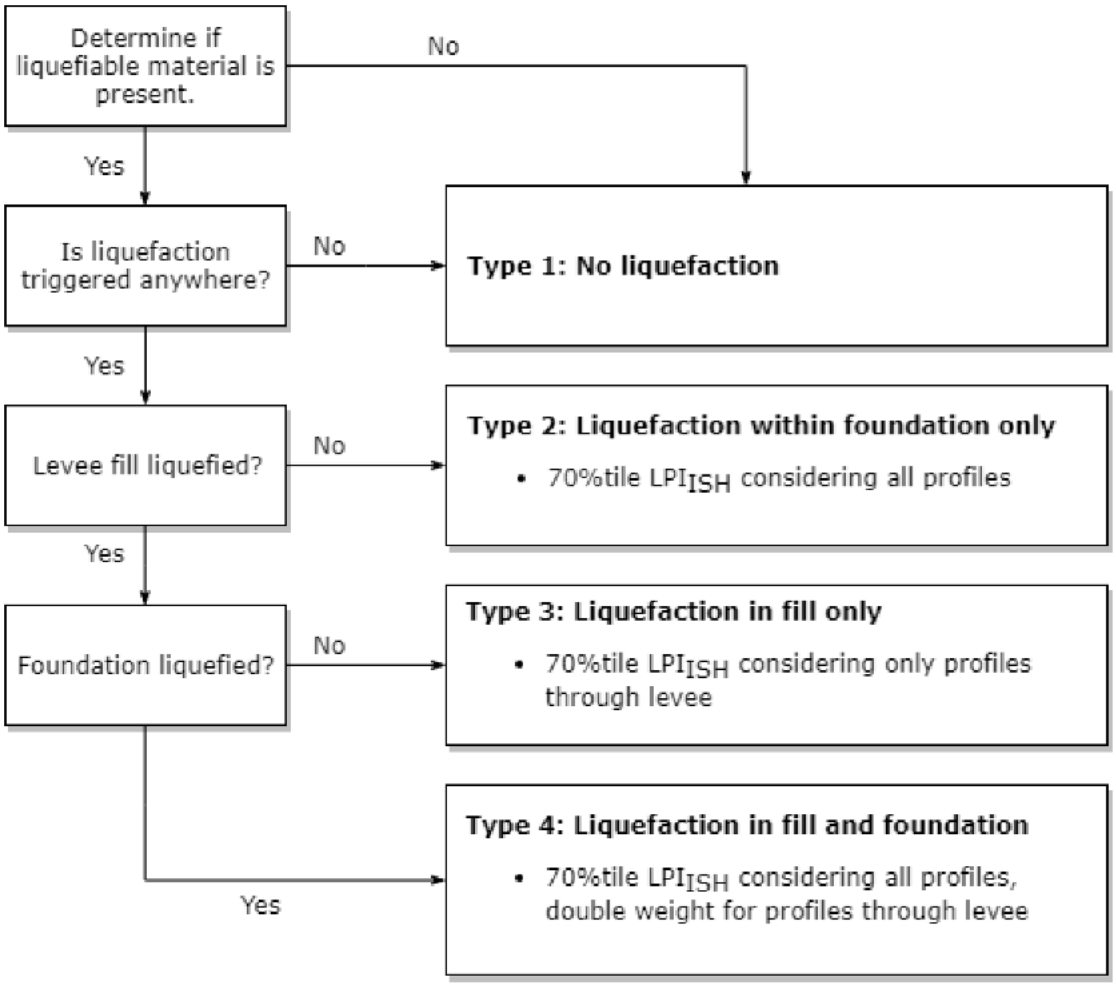

Figure 4.38 Flowchart for selecting representative value of liquefaction severity index from multiple borings at a cross section.

For slope stability, the displacements computed with fully liquefied strengths represent an upper bound estimate, since several loading cycles may be necessary to induce liquefaction. Both shear strains and volumetric strains are diminishes greatly FS exceeds 1.0, and are approximately zero with FS ≥ 2.0 (Figure 4.39).

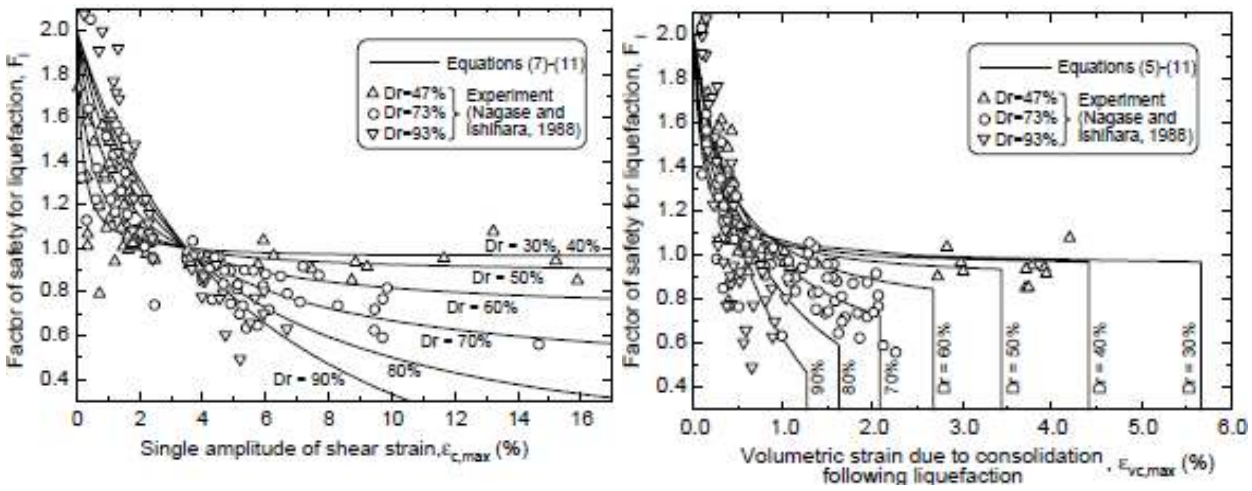

Figure 4.39 Relationships between maximum shear strain during cyclic loading (left) and volumetric strain following liquefaction (right) with factor of safety. Both tend towards zero as factor of safety exceeds 2.0 (Yoshimine et al., 2006)

The computed Newmark displacements from the initial and residual strengths are interpolated linearly based on Eq. (4.26), using the average FS within the liquefied strata that the critical failure surface passes through. In the limiting case where the material liquefied at the start of shaking (FS = 0), the full deformation assuming with the liquefied strengths would be expected.

$$\Delta_{interpolated} = \begin{cases} \Delta_{pre-EQ} + \dfrac{2 - FS_{critical}}{2}\left(\Delta_{\text{post EQ}} - \Delta_{pre-EQ}\right), & FS \le 2.0 \\ \Delta_{pre-EQ}, & FS > 2.0 \end{cases} \quad (4.26)$$

The damaged levels are predicted separately for the representative LPI_{ISH} and interpolated Newmark displacements. The LPI_{ISH} thresholds for surface manifestation severity recommended by Maurer et al. (2015b) performs well and is applied with a minor modification of subdividing the "severe liquefaction" category into damage levels 3 and 4. The thresholds for Newmark displacements are initially selected to be consistent with the subsidence criteria used to define the damage levels, then subsequently revised to reflect the overall higher range of displacements obtained from the analysis. The difference may arise from the rigid body assumption being violated as the levee deforms at large

displacement to a configuration with lower driving shear stresses and higher yield acceleration. The thresholds are summarized in Table 4.5.

Table 4.5 Damage level thresholds for LPI_{ISH} and Newmark displacements

Damage Level	LPI_{ISH}	Newmark Displacements
0	<1	<10
1	1-5	10-30
2	5-13	30-100
3	13-20	100-200
4	>20	>200

Having established a selection protocol for representative values, the resulting damage level predicted are compared with observations based on a single index and shown in Figure 4.40. Using only LPI_{ish}, predicted damage level shows fair amount of scatter and is significantly under predicting for section 11. Considering only Newmark, damage level is under predicted for sections 9 and 10, and over predicted for section 13.

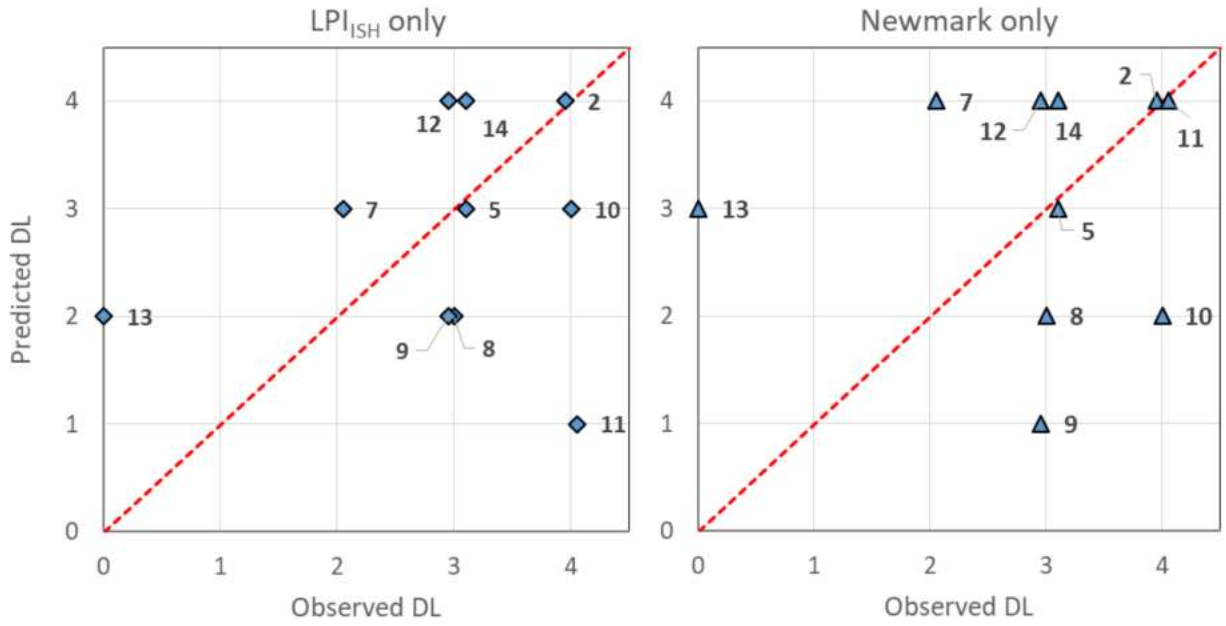

Figure 4.40 Damage levels predicted with only LPI_{ISH} or Newmark displacements tend to underestimate at high damage levels.

With the view that the two metrics are complementary and account for different causes of levee damage, a combined damage level is assigned as the more severe predicted damage level from the two methods, and is assigned to the cross section and shown in Figure 4.41. With the exception of sections 7 and 13, the damage level predicted with the combined index is within one level's difference from the observed performance. In particular, underestimation previously observed for sections 9, 10 and 11 are remedied by considering both metrics together. The combined damage assessment is therefore superior to either the liquefaction displacement index method or the Newmark sliding block method on its own.

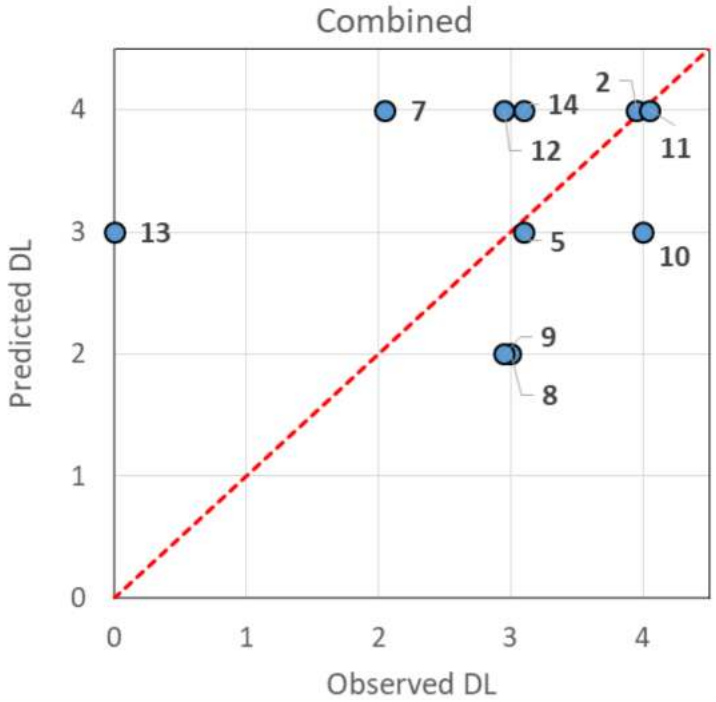

Figure 4.41 Predicted damage levels based on both Newmark displacements and LPI_{ish} minimizes under prediction for high damage levels and are generally within one damage level of the observed performance.

While the combined index improves the prediction at higher damage levels, over prediction for the lower damage levels is observed. In the following, example cases are discussed for a section where the combined index worked well, and for sections where damage was over-predicted.

4.5.1 Cross section 7

Damage level 2 was observed at cross section 7, whereas LPI_{ISH} predicts damage level 3 and Newmark sliding block predicts damage level 4 due to a flow failure. This section explores possible reasons for the over-predictions.

Unlike other sections, the detailed construction history was unavailable at this location. Judging from the distinctive benched geometry and the cross sections of nearby segments, the levee likely started as a smaller structure and was subsequently expanded out towards the river. The oldest fill typically has low fines content and is susceptible to liquefaction. This zone is defined to be under the landside bench based on soil classification from the boring logs. The critical failure surface with FS <1.0 is shown in Figure 4.42 and passes through the liquefied levee fill.

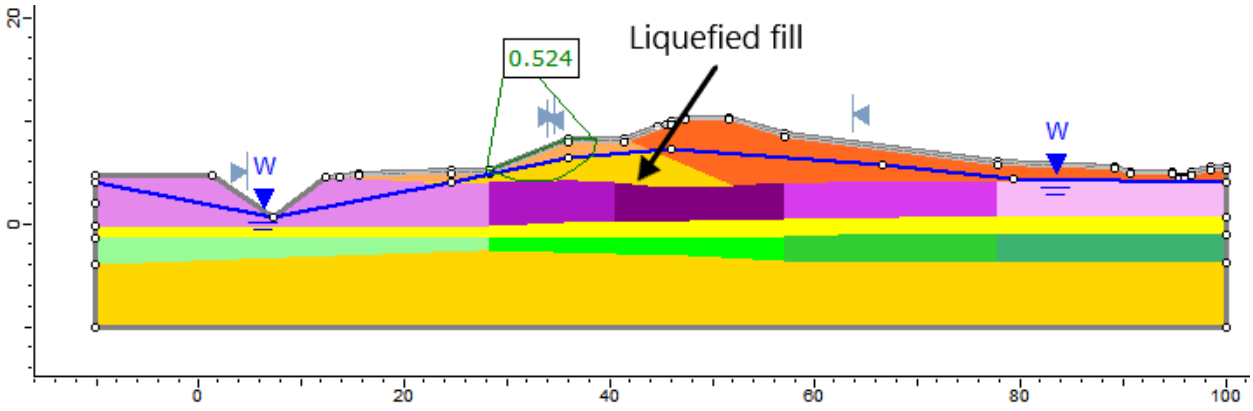

Figure 4.42 Flow failure predicted on land-side slope through liquefied levee fill (FS<1.0). The uncertainty in the extent of the liquefiable fill greatly influence the damage level predicted.

However, there is some uncertainty regarding the spatial extent of materials susceptible to liquefaction. The upper layers in the liquefiable zone contains moderate amount of silt, but the plasticity characteristics of the silt are not known. The silt may render the sand non-susceptible to liquefaction. In addition, the position of the groundwater table within the levee is known only at certain positions in the cross section at the time the boring logs were performed. It is possible that the groundwater table

was deeper within the predicted failure region. Both of these factors could contribute to an over-prediction of the spatial extent of liquefied soils, and therefore an over-prediction of damage.

4.5.2 Cross section 11

The levee section suffered extensive subsidence and deformation and required complete replacement after the earthquake. Newmark sliding block predicts damage level 4 and is in agreement with the observations, while LPI_{ISH} predicts damage level 1 and drastically underestimates the damage. This section explains the reasons for the significant difference in predictions, and highlights the benefits of accounting for complex damage mechanisms through applying multiple indices.

A thick non-liquefiable crust of peat and clay is present at this location. The sandy, saturated zone near the base of the levee and the silty sand layer below the clay is susceptible to liquefaction. The deeper sand layer expected to have minor influence given its greater depth and higher plasticity.

The liquefiable fill material is encountered in the SPT and CPT through the crest, but not in the investigations near the levee toe. LPI_{ISH} for the individual profiles ranges from 2-3 and unanimously predicts minor surficial manifestation. However the liquefied zone corresponds to the oldest levee fill and extends over most of the base on the river side. The reduced shear strength within this zone destabilizes the levee, and the critical surface now passes through the liquefied fill as shown in Figure 4.43. The FS for river side slope is barely above 1.0 which indicates the levee is on the verge of flow failure. Yield acceleration is similarly greatly reduced, and the Newmark displacements predicts several meters of movement.

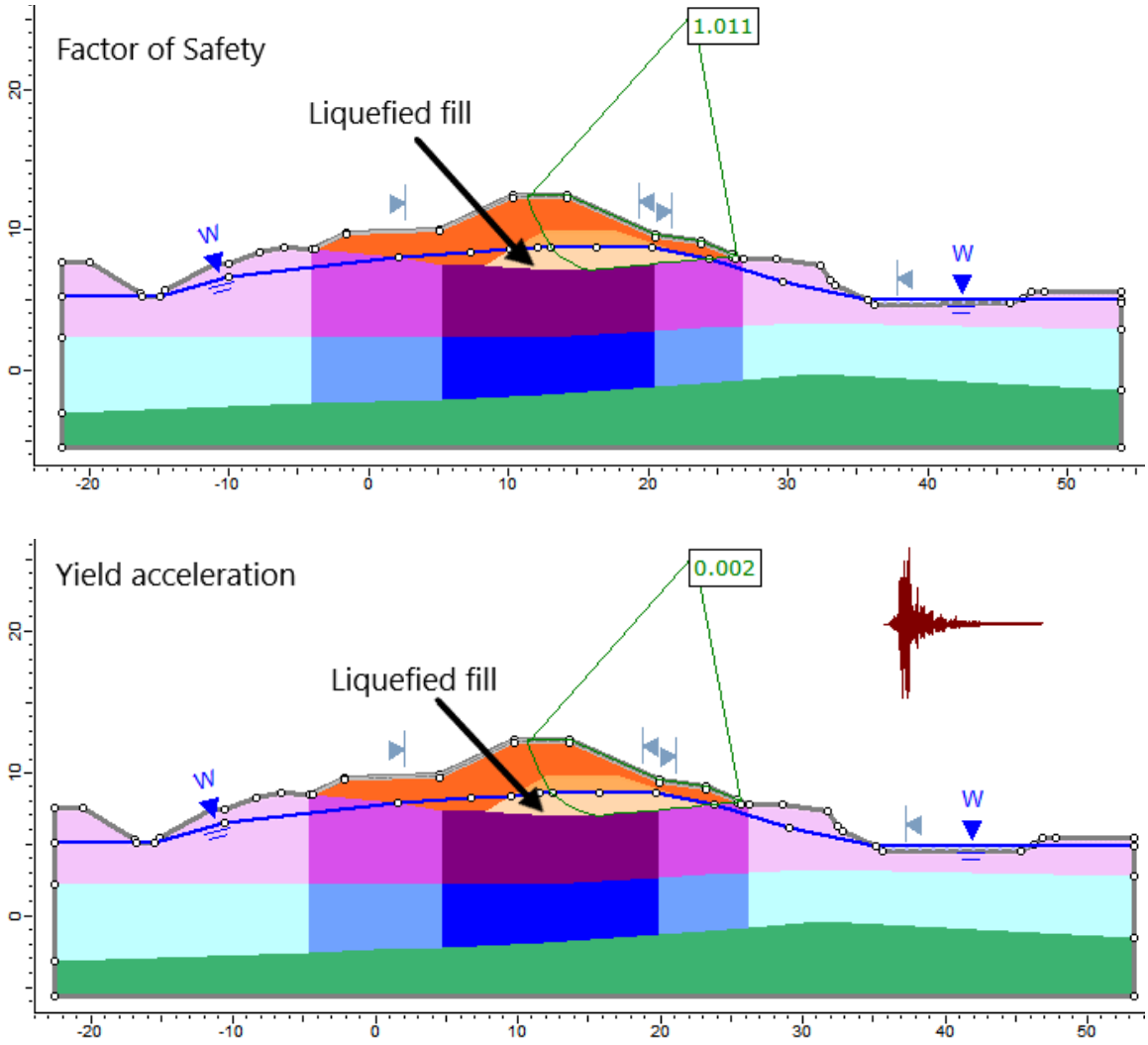

Figure 4.43 Reduced strength in the liquefiable zone at the base of the levee destabilized the levee. The factor of safety (top) and yield acceleration (bottom) are greatly lowered, with Newmark sliding block predicting large displacements.

Liquefaction indices considers a 1D soil column and cannot directly account for 2D effects such as lateral continuity and instability from existing shear stresses. For cross section 11, the damage due to a thin but laterally extensive liquefiable layer is greatly underestimated. Complementing the damage assessment with a 2D limit equilibrium slope stability analysis allows the potential instability to be identified from the location of the critical surface, low FS and high Newmark displacements.

4.5.3 Cross section 13

No visible damage was observed at cross section 7 despite LPI_{ISH} and Newmark sliding block predicting damage levels 2 and 3 (moderate to severe damage). This section discuss possible reasons for the over-prediction by both indices.

The subsurface conditions is relatively simple, with the levee resting directly on a thick layer of sand. The ground water is below the levee fill, but sufficiently shallow that surface manifestation through the unsaturated crust is expected if the underlying sand layer liquefies. The upper 0.5-1.0 m contains minor to moderate amounts of silt, below which the material transitions to clean sands. Liquefaction is predicted to be triggered in the saturated sand layer and lowers both the FS and yield acceleration. The slope is stable, but large displacements up to 2.4 m is predicted by the Newmark sliding block.

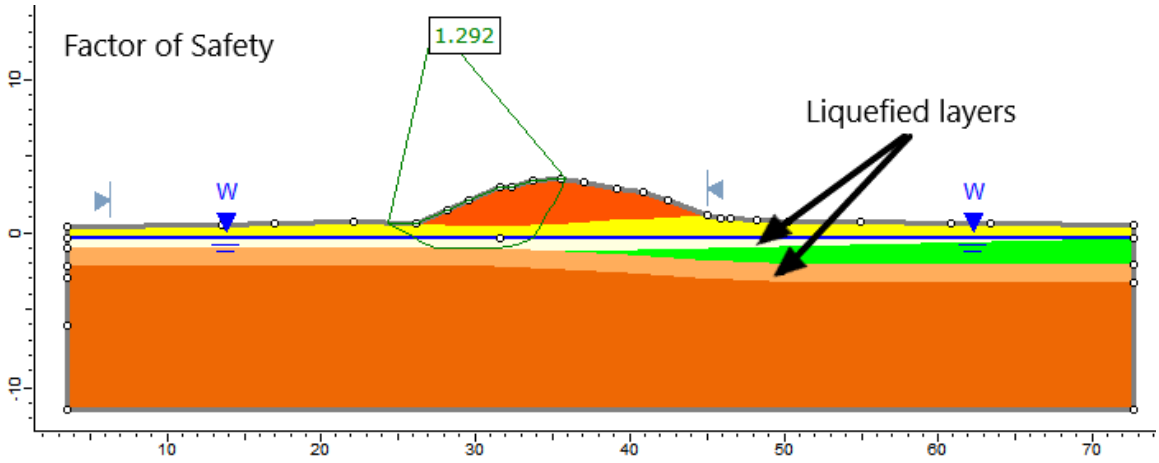

Figure 4.44 Liquefaction triggering is predicted in the saturated sand layer directly below the levee but leads to over-estimation of damage. Possible explanation is partial saturation in the upper layers during the earthquake.

Considering the lack of visible damage, liquefaction was likely not triggered in the surficial sand layers during the earthquake. Given the presence of the thick layer of clean sand with low blow counts which is clearly susceptible, incomplete saturation is the most plausible explanation for the absence of liquefaction. The ground water level is only measured at the crest for this location, therefore the depth

in the free field carries significant uncertainty. In addition, fluctuations in the ground water level may result in the shallower layers not being fully saturated. This case shows that the damage assessment is highly sensitive to the assessment of the liquefaction susceptibility and triggering.

4.6 SUMMARY

Geotechnical engineering assessments are performed for 10 levee cross sections to predict damage severity and compared to the performance observed following the 2003 Tokachi-oki earthquake. Ground motion intensities and acceleration time histories are obtained from recording stations sited on the levees, which greatly reduce the uncertainty associated with estimating the seismic demand. Liquefaction severity indices, 2D slope stability and Newmark displacements are considered in combination to produce an overall damage level. The selection of a representative value for liquefaction severity indices associated with multiple investigations at a cross section is presented based on position of the liquefiable region to approximately account for effects of lateral continuity and static shear stress within the levee that is not directly captured by the 1-D analysis. The combined assessment accounts for different failure mechanisms and reduces under prediction seen with application of a single index, especially for higher damage levels.

The actual failure of the levee is highly complex and only partially represented in the simplified assessment. The deviation between predicted and observed damage severity may arise from a combination of factors, significant ones being (1) errors in determining liquefaction susceptibility solely based on soil classification available; (2) differences in ground water level present during the earthquake and measured during the site investigation, (3) differences in PGA between recording station and levee section; and (4) other contributing mechanisms, such as secondary consolidation of the underlying peat, that are not considered. Analysis of additional cross sections with lower damage

levels would be beneficial to ascertain if the suggested approach tend to over predict and make any necessary adjustments.

5 REGIONAL LINEAR SITE AMPLIFICATION MODEL FOR SOFT PEAT SITES

5.1 INTRODUCTION

The application of ergodic site terms in ground motion models (GMMs) to regions having very soft, peaty organic soils carries large epistemic uncertainty. One substantial driver of this uncertainty is the low time-averaged shear wave velocities in the upper 30 m (V_{S30}) at these sites. Figure 5.1 shows the distribution of V_{S30} for stations in the NGA-West2 and NGA-Subduction databases. The peat sites in the downstream regions have V_{S30} around 100-200 m/s, and are on the lower limit of the dataset used to derive the ergodic models.

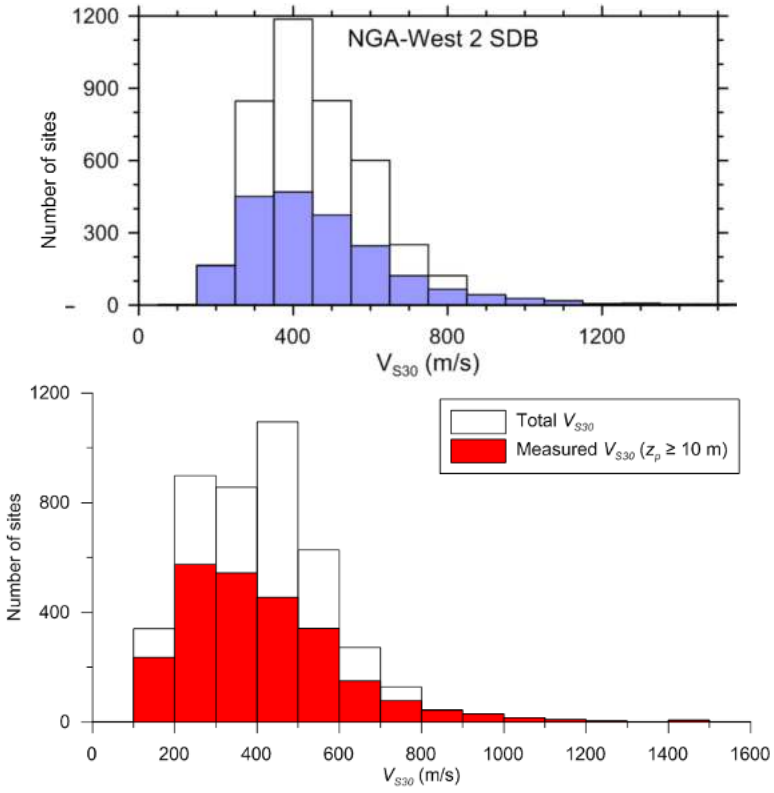

Figure 5.1 Histograms of V_{S30} for sites in NGA-West2 database (top, Seyhan and Stewart, 2014) and NGA-Subduction database (bottom, Ahdi et al. 2017).

In addition, as soft peats usually overlie relatively firm, inorganic soils at depth, the steep velocity gradients within the site profile that can give rise to more pronounced impedance and resonance effects than would be typical at non-peat sites. Such effects produce site response transfer functions with strong peaks at one or more site frequencies. These features of site response cannot be captured by V_{S30}-based models as used in typical GMMs, although they could potentially be captured by a model that combines V_{S30}-scaling terms with site resonance terms that take the peak frequency (f_{peak}) as a site parameter (e.g., Kwak et al., 2017; Hassani and Atkinson, 2018a and 2018b).

As a result, the ergodic site terms in current GMMs for subduction earthquakes in Japan, whether based on V_{S30} (Abrahamson et al. 2016, 2018) or site class (Zhao et al. 2016a and 2016b), are expected to have bias and large uncertainty when applied to peaty organic soil sites in Hokkaido. The objective in this study is to improve ground motion estimates by developing region-specific ergodic site amplification models derived from non-ergodic site responses at recordings sites. In other words, we seek to gain insights into the features of local site response from non-ergodic analyses, including impedance and resonance effects, and then to build a more generic (local but ergodic) model from those results.

The approach taken in this chapter is to develop a linear site amplification model using recordings with relatively low amplitudes, where significant nonlinear effects are not expected. We subsequently examine nonlinear effects through residuals analysis using data from one event that produced relatively strong shaking. Nonlinear effects are further investigated using ground response analysis in Chapter 6.

5.2 DATA SOURCES

The region-specific analysis performed in this study applies to the portion of the Tokachi River in Hokkaido, Japan passing through peaty organic soil layers that extend roughly from the river mouth to 50 km upstream of the river mouth, as shown in Figure 5.2. This region contains seven instruments owned and operated by the Obihiro Development and Construction Department (ODCD), for which we have processed recordings from nine earthquakes in the NGA-Sub database. This section discusses the data compiled for analysis of non-ergodic site responses at these seven stations.

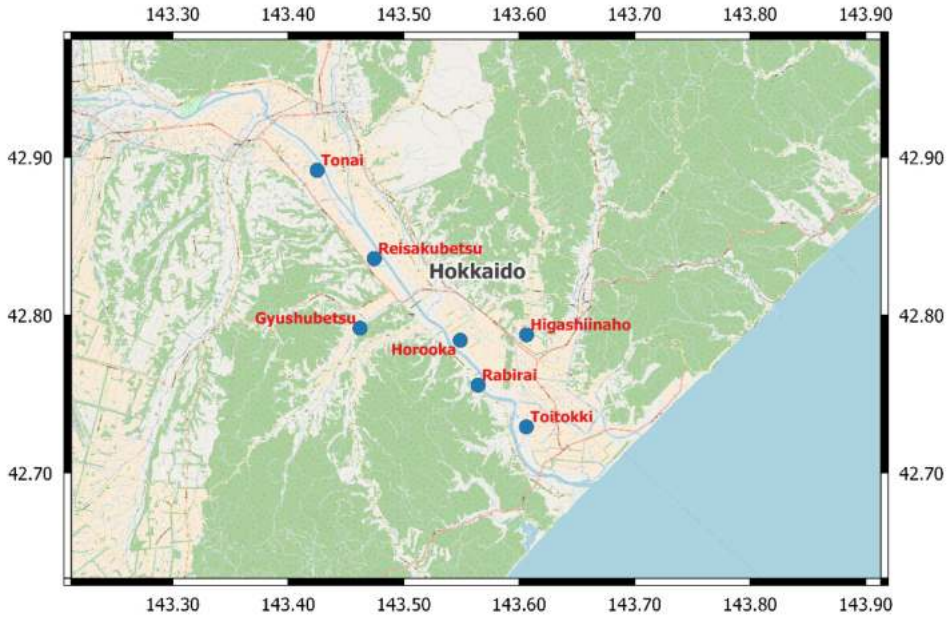

Figure 5.2 Recording stations on levees in the downstream region of Tokachi.

5.2.1 Ground Motions and Related Metadata

Table 5.1 provides the metadata for the seven stations in the study region. The station locations were provided by ODCD and the basis for the site information (V_{S30} and classification) is provided in Section 5.2.2. As shown in Figure 5.2, the stations are distributed evenly with good spatial coverage across the study region.

Table 5.1 Metadata of ODCD stations

Station Name	Longitude	Latitude	V_{S30} (m/s)	f_{peak} (Hz)	Site Class
Gyushubestu	143.4622	42.7921	130.8	1.14	IV
Higashiinaho	143.6063	42.7876	211.5	1.6	III
Horooka	143.5589	42.7841	102.2	1.42	IV
Reisakubetsu	143.4744	42.8359	181.4	1.62	IV
Rabirai	143.5642	42.7556	150.5	1.14	IV
Toitokki	143.6043	42.7 281	117.2	0.88	IV
Gyushubestu	143.4622	42.7921	130.8	1.14	IV
Tonai	143.4250	42.8917	181.4	1.50	IV

The stations have recorded 25 earthquakes from 1994 to 2013, of which nine are included in the NGA-Subduction database (Kishida et al. 2017). The event metadata and the number of processed recordings available are summarized in Table 5.2, and the hypocenter locations are shown in Figure 5.3.

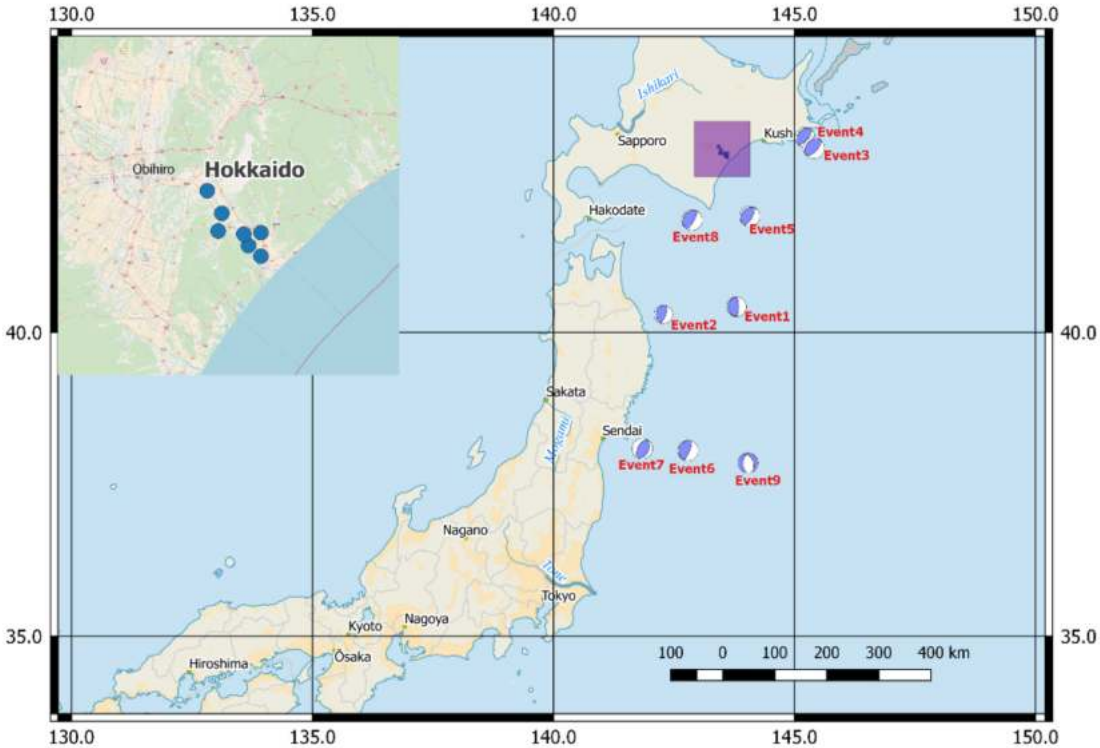

Figure 5.3 Focal mechanisms of events in NGA-subduction databases that have produced recordings at the ODCD stations.

Table 5.2 Metadata for the nine considered earthquakes

Event	Date	M_W	Event Type	Longitude Latitude	Hypocenter Depth (km)	NGA-SUB recordings		ODCD Stations
						Total	Used	
1	1994/12/28	7.7	Interface	143.75, 40.43	10	31	10	3
2	1995/01/06	7	Interface	142.31, 40.22	47.8	13	0	3
3	2004/11/28	7	Interface	145.28, 42.95	48.17	378	84	7
4	2004/12/06	6.7	Interface	145.34, 42.85	45.84	204	57	7
5	2008/09/11	6.8	Interface	144.15, 41.78	30.86	407	64	6
6	2011/03/11	9.1	Interface	142.86, 38.10	23.74	1293	698	7
7	2011/04/07	7.1	Slab	141.92, 38.20	65.9	799	445	7
8	2011/11/24	6.2	Interface	142.89, 41.75	43.21	177	57	6
9	2012/12/07	7.3	Slab	144.12, 37.84	52	866	359	7
10	2003/09/25	8.29	Interface	144.09, 41.78	25	302	173	6

Note: All events are subduction earthquakes with reverse faulting

For each event, a subset of the NGA-Sub recordings is used, as illustrated in Figure 5.4 for Event 6 (the 2011 Tohuku earthquake). Stations beyond the maximum limiting distance criteria provided in the NGA-Sub flatfile are shown in pink and stations in the backarc (northwest of the volcanic arc) are in blue, both are excluded and only stations in green are used in the subsequent analysis. Limiting distance criteria is intended to avoid potential bias from recordings with weaker amplitudes failing to trigger the instruments. Stations beyond a maximum distance R_{max} are excluded. The cutoff distance depends on instrument properties and varies between the networks. In cases where the rupture distances of Obihiro stations are modestly larger than R_{max}, we extend the NGA-Subduction values of R_{max} (by no

more than 40%) to include the stations at these distance ranges. Backarc stations are not used because the Obihiro sites of interest in are in the forearc, and our principle interest is source-site wave paths within the forearc. Event 2 is excluded due to deficiency in useable recordings - of the 13 recordings in the NGA-Sub database, nine are removed based on the R_{max} criteria, and the remaining four have rupture distances much less than those for ODCD stations (113 vs 300 km).

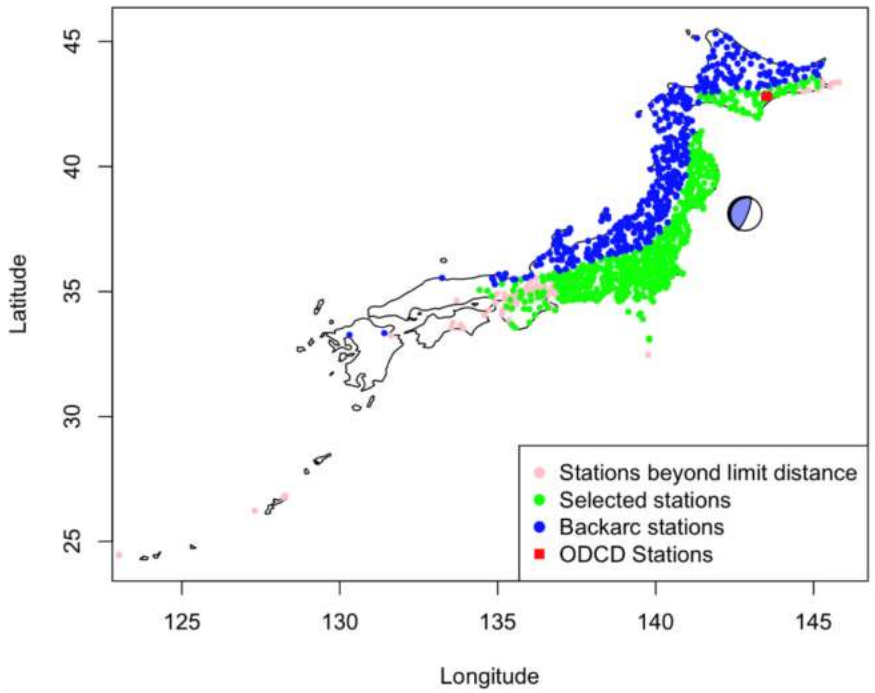

Figure 5.4 Recordings for Event 6 (2011 Tohoku earthquake), showing stations used in this study (green), stations not considered on basis of distance cutoff criteria developed in the NGA-Subduction project (pink), stations not considered due to their location in the backarc region of Japan (blue), and ODCD stations (red).

The recordings at the ODCD stations are not part of the NGA-Subduction database and the raw digital recordings were provided by S. Takashi (personal communication, last update November 10th, 2017). The data was processed following PEER procedures (Ancheta et al. 2014), and included instrument correction, application of both high and low pass acausal filters at operator-determined corner frequencies and baseline correction. The median-component intensity measures RotD50 (Boore, 2010)

for peak acceleration, peak velocity, and 5% damped pseudo-spectral accelerations (PSA) are computed from the post-processed recordings with the R package by Wang et al. (2017).

As shown in Figure 5.5, Events 1-9 produced relatively weak motion recordings at the ODCD stations, which are useful for developing the linear component of a regional site amplification model. In contrast, Event 10 (2003 Tokachi-Oki Earthquake) produces appreciably stronger shaking. Accordingly, our approach to model development is to develop a linear model using data from Events 1-9, and then to perform residuals analysis using data from Event 10 to investigate potential nonlinearity effects.

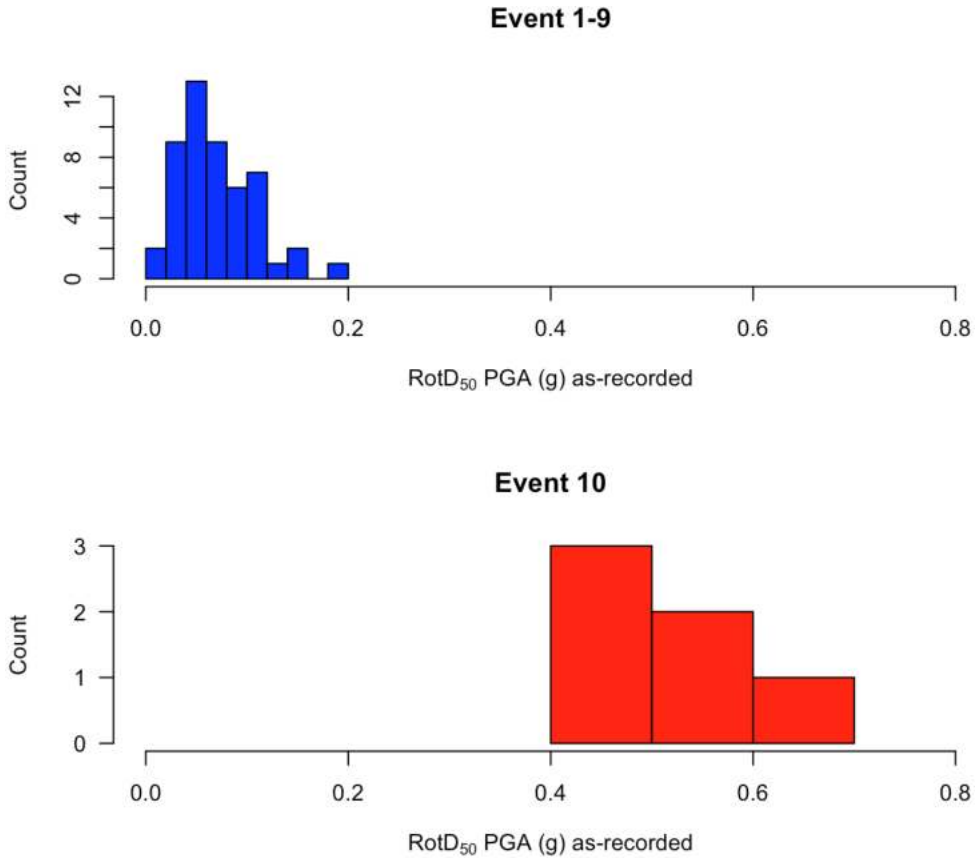

Figure 5.5 Histograms of median-component peak accelerations at ODCD stations for Events 1-9 and Event 10, with the latter having significantly higher intensity.

Development of the linear component of the site amplification function requires recordings of weak motions such that nonlinearity is not expected to have significant influence. The median rock PGA

predicted by the GMM at the stations for each earthquake is used to screen out stronger motions, which is taken as PGA_{rock} exceeding 0.1 g. Event 1-9 are below this threshold and used to develop the linear component of the site response, while event 10 is set aside to examine the effect of nonlinearity.

5.3 GROUND MOTION DATA ANALYSIS

This section presents our analyses of ground motion recordings to support model development, which is presented in Section 5.4. Sections 5.3.1 describes analyses that provide region-adjusted, within event residuals for event i and recording j, δW_{ij}^{reg}, at the seven ODCD sites. Non-ergodic site responses are evaluated for each site in Section 5.3.2. Section 5.3.3 describes the analysis of H/V spectral ratios from ground motion recordings at the ODCD instruments; such information supplements the geophysical site exploration presented in Section 5.2.2.

5.3.1 Event terms and region terms

Our approach to data analysis operates on residuals, which are the difference between the natural log of an observation and its prediction from a GMM. Models developed from recordings of subduction earthquakes in Japan by Zhao et al. (2016a and 2016b) (Zea16 herein) is selected. We investigate sensitivity to the GMM by also examining residuals of the data relative to the Abrahamson et al (2018) (Aea18 herein) GMM applied with Japan regionalized path terms (Section 5.5).

Total residuals are computed using the reference GMM as:

$$R_{ij} = ln(Y_{ij}) - (\mu_{lnY})_{ij} \quad (5.1)$$

where Y_{ij} is the observed RotD50 intensity measure for recording j from event i, and $(\mu_{lnY})_{ij}$ is the natural log mean prediction from a GMM for the given magnitude, site-source distance, site condition,

and other parameters used in the model. Non-zero residuals indicate deviation from the observed ground motion from the prediction, and have several potential causes. The ground motions from a given earthquake may be systematically low or high relative to the median prediction from the GMM. Likewise, a particular source-to-site path may have attenuation that is higher or lower than the average rate. As the ultimate goal is to quantify the site response from the residuals, systematic (repeatable) effects related to source or path are removed from the total residuals computed using Eq. (5.1). The remainder of this section addresses the adjustment to the total residuals based on the available data.

Figure 5.6 to 5.9 show total residuals versus rupture distance. Bias in the GMM path term appear as positive or negative trend with distance. Residuals from events 3, 4, and 7 show slopes at short periods, trending up for Hokkaido stations beyond 200 km (Event 3 and 4, periods 0.005 s and 0.08 s) and divergent slopes for Hokkaido stations and Honshu stations beyond about 300 km. We considered adjusting the path term to model these regional differences, but eventually elected to limit the distances to 200 km for Events 3 and 4, and 300 km for Event 7 where the residuals are nearly flat. Trends with distance are not observed for the remaining events.

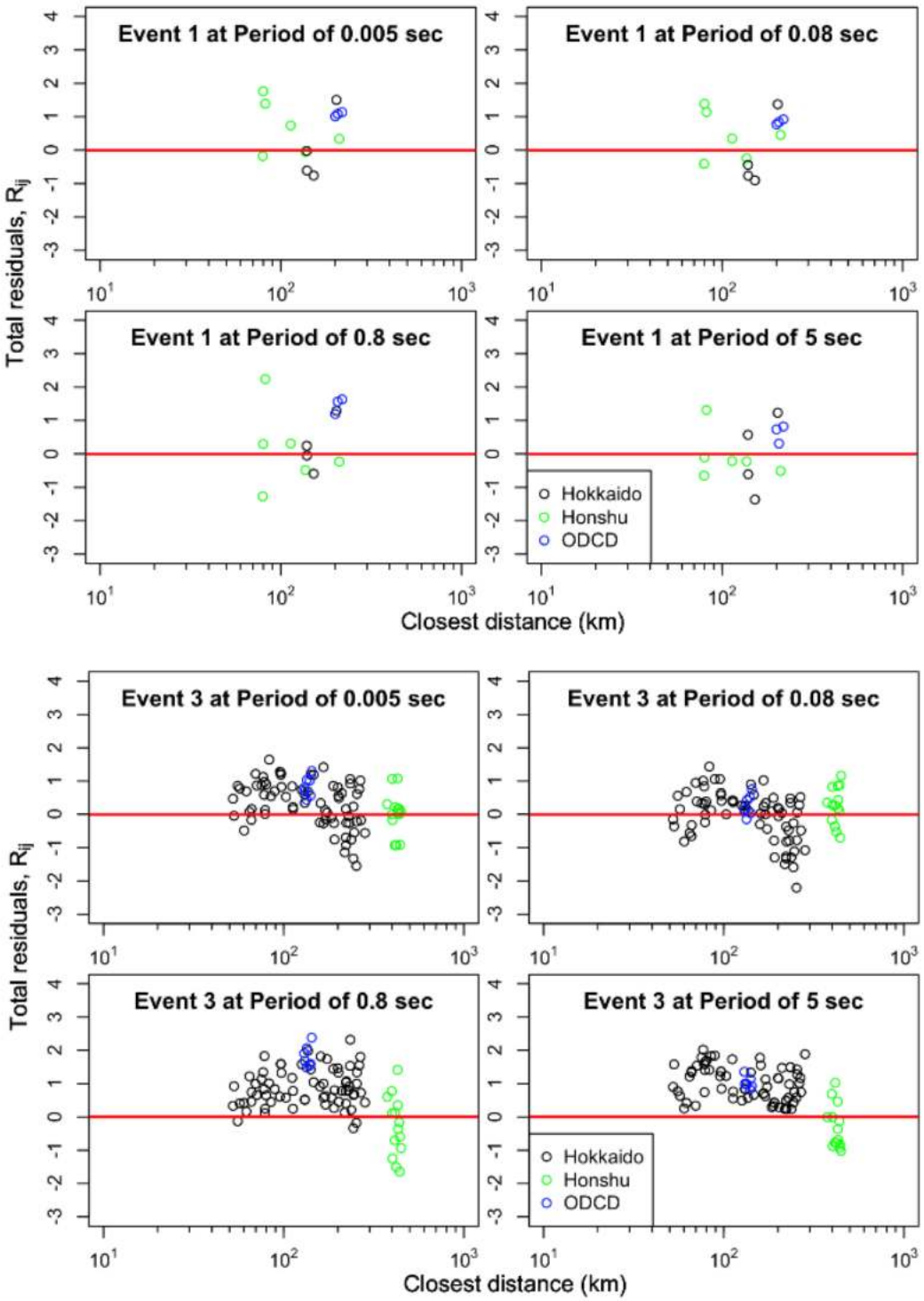

Figure 5.6 Variation of total residuals with distance for Events 1 and 3. Event 3 shows a negative trend with distance at short periods.

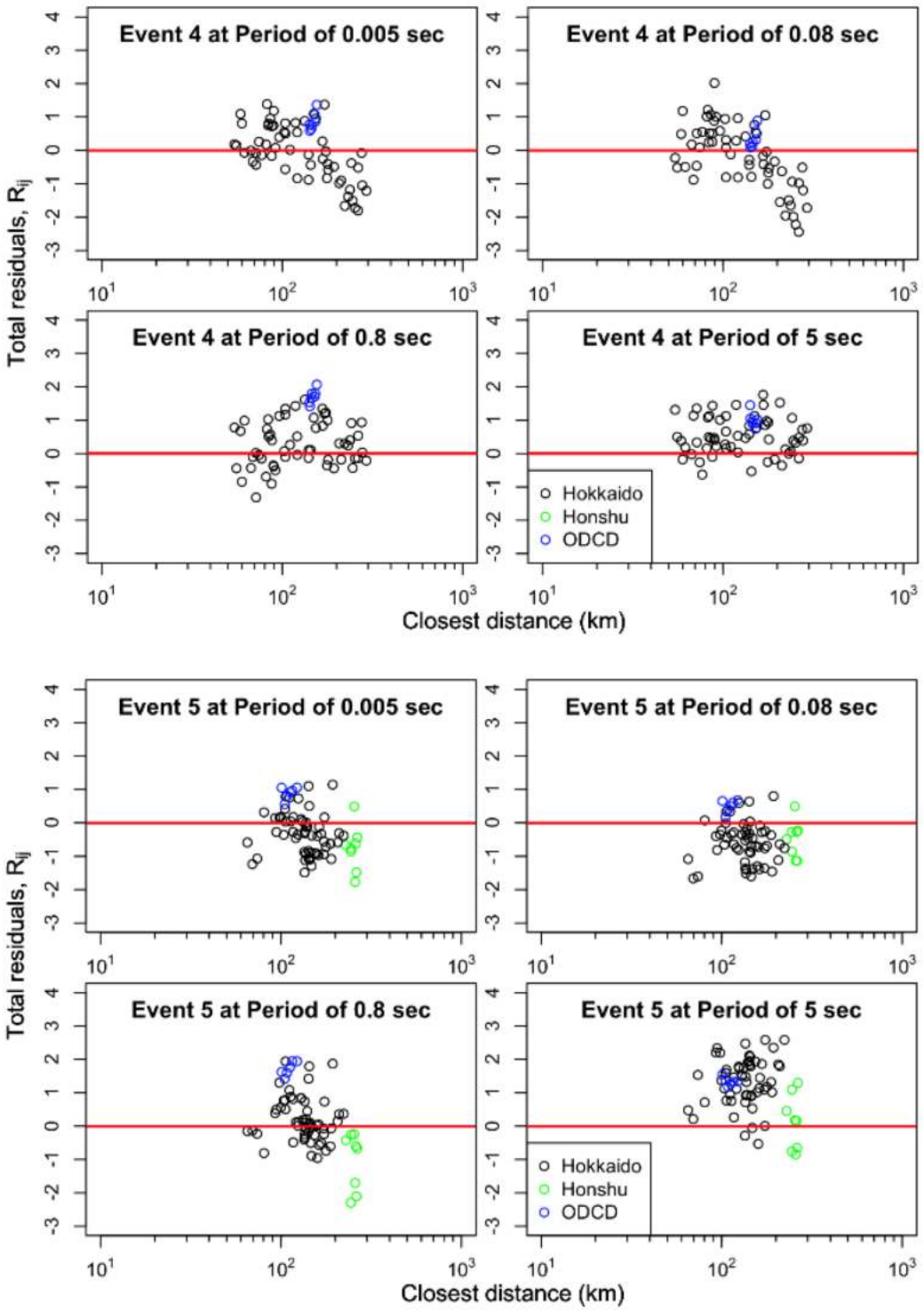

Figure 5.7 Variation of total residuals with distance for Events 4 and 5. Event 4 shows a negative trend with distance at short periods.

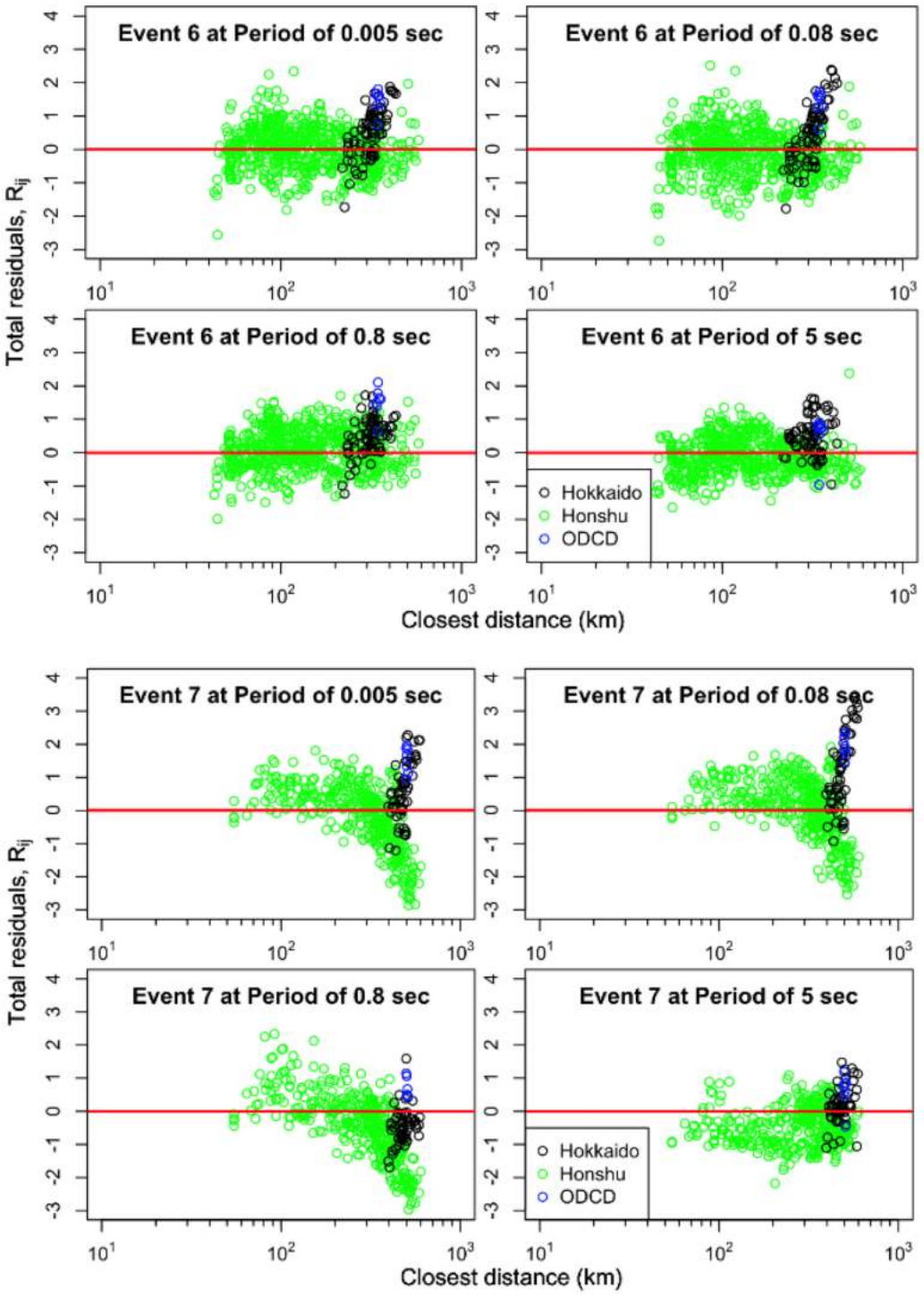

Figure 5.8 Variation of total residuals with distance for Event 6 and 7. Event 7 shows a strong negative trend with distance for Honshu stations (green) and a positive trend for Hokkaido stations (black) at short periods.

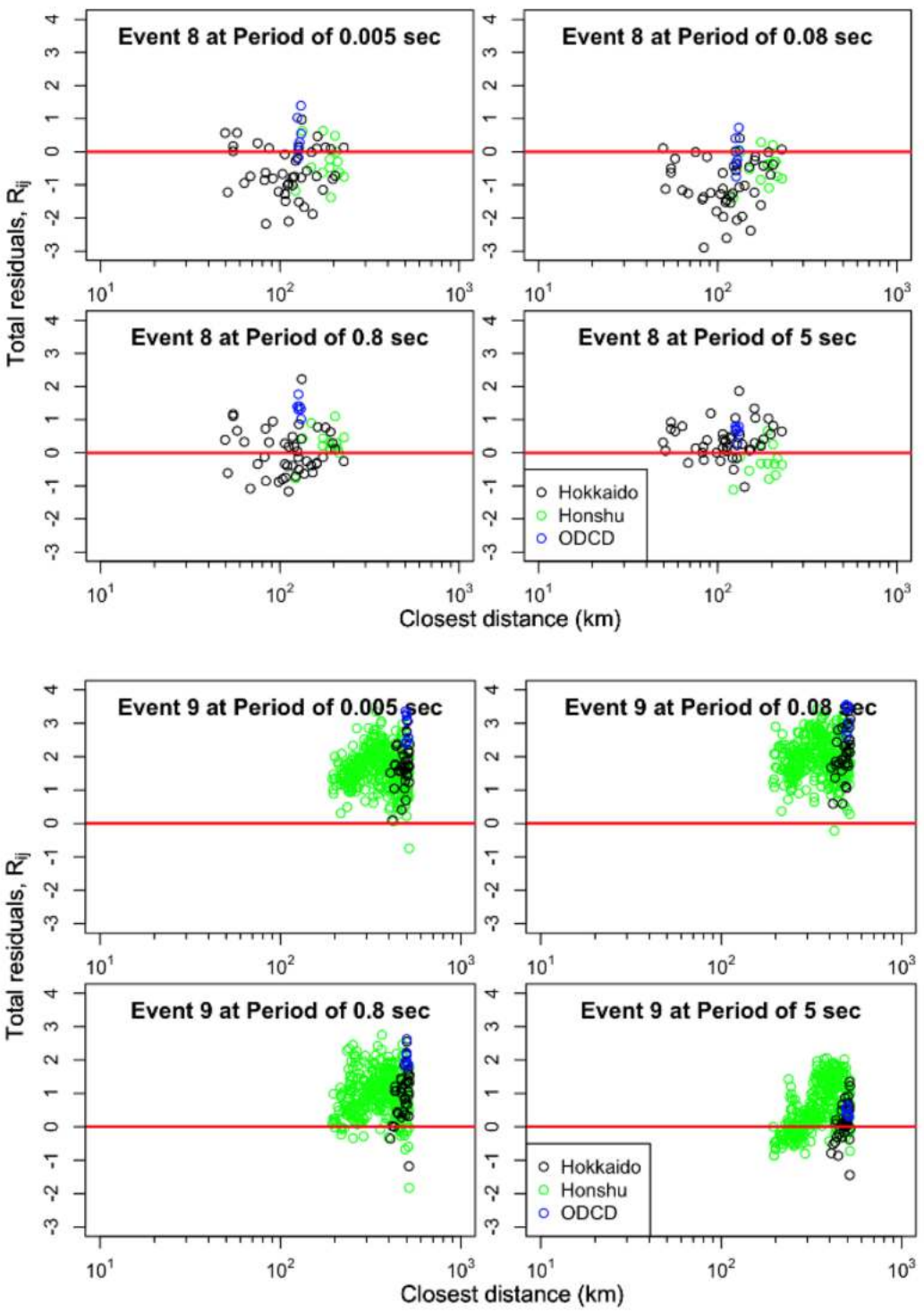

Figure 5.9 Variation of total residuals with distance for Events 8 and 9.

For a given event *i*, the event term is taken as the average of the residuals:

$$\eta_{E,i} = \frac{1}{n_i}\sum_{j=1}^{n_i} R_{ij} \tag{5.2}$$

where n_i is the number of recordings from stations within the range of applicability of the selected GMM for event *i*. Eq. (5.2) represents a use of Frequentist statistics, with the other option being a random effects model (Bayesian statistics). We adopt the Frequentist approach so as to provide unbiased estimators for the event terms (Stewart et al. 2017). As described in Section 5.2.1, stations in the backarc and with site-to-source distances beyond maximum limiting distance of NGA-Subduction data are excluded. Data are also excluded beyond the aforementioned limiting distances for Events 3, 4, and 7. The use of Eq. (5.2) implies the GMM is unbiased overall, otherwise a constant term accounting for the model bias (usually denoted as c_c) should be added for all events. A model may be biased when applied to data from a different region, since Zea16

Event terms obtained from Eq. (5.2) are shown in Figure 5.9. Most of the event terms are positive, indicating under-prediction by Zea16. The exception is Event 9 with a large positive event term, around 1.5-2.0 for periods less than 0.3 sec.

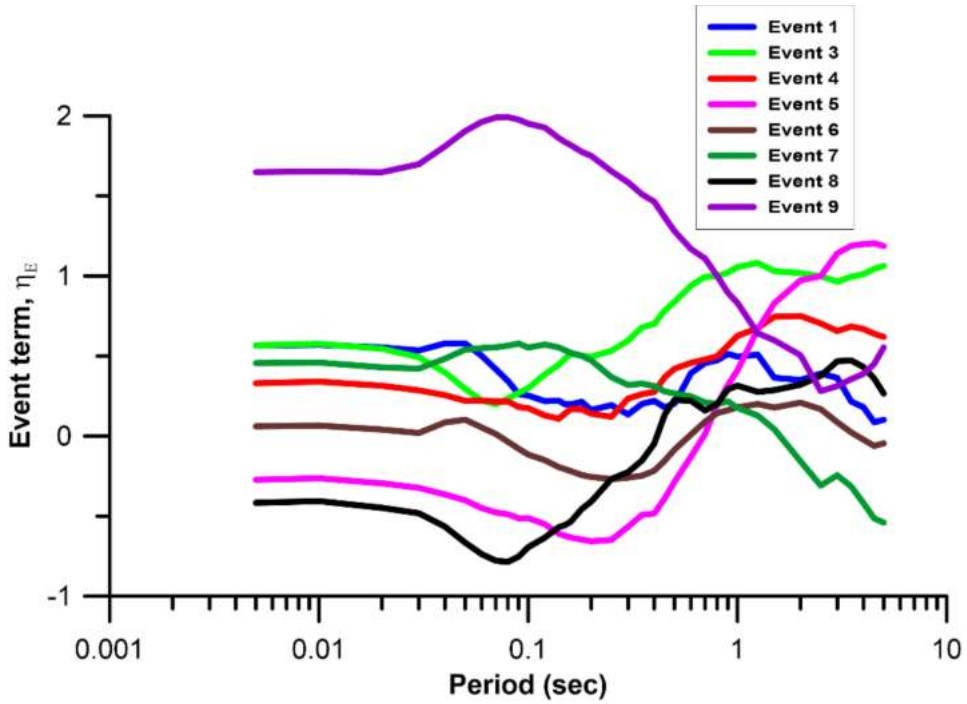

Figure 5.10 Event terms across periods for the eight events recorded by the ODCD stations

Japan is known to have strong regional variations in anelastic attenuation (e.g., Ghofrani and Atkinson, 2011) which can introduce systematic differences in residuals between the forearc and backarc sites. The effects of paths crossing the volcanic front was addressed by excluding backarc stations. Additional regional complexities in the forearc, observed for Events 3, 4 and 7, were addressed with implementing distance cutoffs. The remaining issue considered here is potential effects of travel paths passing between Honshu and Hokkaido (i.e., the rupture near Hokkaido is recorded by a station on Honshu). To investigate this, we first compute the within-event residual as,

$$\delta W_{ij} = R_{ij} - \eta_{Ei} \tag{5.3}$$

which is plotted against distance in Figure 5.10. Honshu stations show a negative trend with distance, while Hokkaido stations shows a positive trend with distance starting around 300 km, and is most apparent for short periods. Since these divergences are a path phenomenon, they should be removed prior to the site term analysis. Accordingly, we separate sources and sites into North (latitude > 39

degrees) and South (latitude < 39 degrees) regions to examine if region terms are necessary when a subset of recordings are in a different region than the earthquake occurs in one region. The North group includes Hokkaido sites and Events 1, 3, 4, 5, and 8. The South group includes Honshu sites and Events 6, 7, and 9.

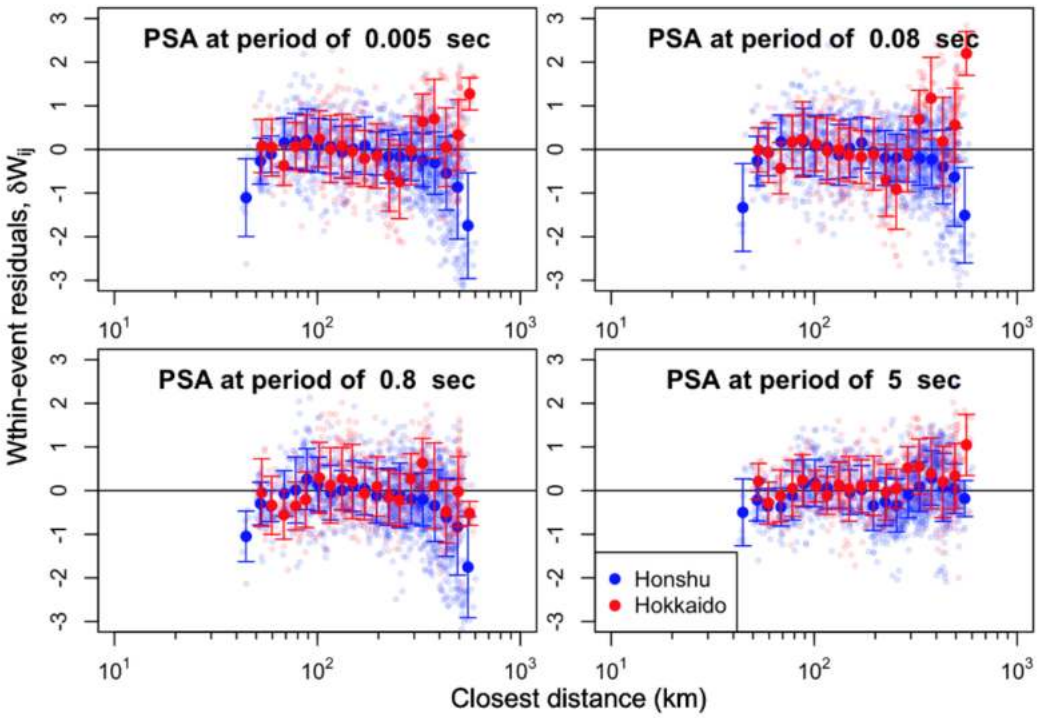

Figure 5.11 Within-event residuals for all eight events. Trends with distance differ between Honshu and Hokkaido stations and is most apparent at short periods.

Region terms for each combination of event and station regions are computed as the average of the within-event residuals,

$$\eta_{reg,l,k} = \frac{1}{n_{l,k}} \sum_{\forall i \in l,\ \forall j \in k} \delta W_{ij} \tag{5.4}$$

where i is the event index and j the recording index respectively, the $\forall$ symbol in combination with $\in$ (e.g., $\forall i \in l$) indicates 'for any value of i among the set specified by array l', which sorts the data into source-path groups. We take $l \in \{0, 1\}$ (i.e., l can be 0 or 1) to segregate event regions (0 refers to

South Events and 1 refers to North Events) and $k \in \{0, 1\}$ to segregate station regions (0 refers to Honshu and 1 refers to Hokkaido). Figure 5.11 plots the region terms over the period range 0.08 sec to 5 sec with their 95% confidence intervals for each source-station regional combination. For cases with source and station in the same region (e.g., Honshu stations recording South region events, index $l = 0$ and $k = 0$), region terms are relatively small without distinct trend with period. However large biases are present when the indices differ. The highly positive region terms at short periods (< 2 sec) for South events and Hokkaido stations is consistent with the upward (positive) trend in the residuals in Figure 5.10. There is also a large negative bias at long periods for North events recorded by Honshu stations.

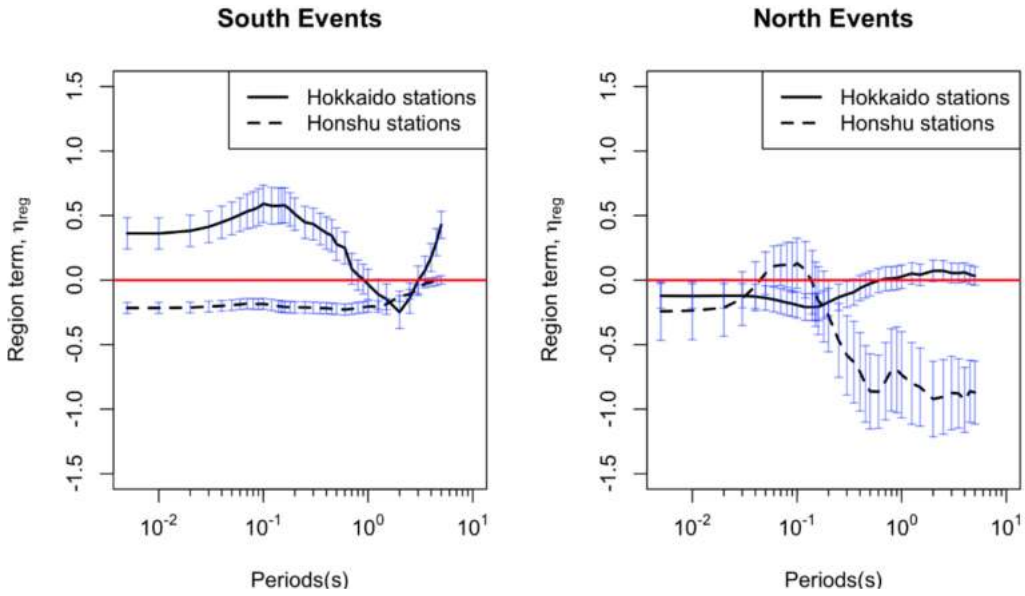

Figure 5.12 Region terms for Hokkaido and Honshu stations for events from South or North region.

The between-island effect is a novel observation, therefore prior to including these regional effects in subsequent analyses, the statistical significance of the distinguishing between the data groups is judged with statistical F test (Cook and Weiberg, 1999). The F test examines whether a data set is better described by a combined single model or a set of sub-models; the combined model would not consider the regional terms, whereas the sub-models would include the four regional combinations. The F statistic is given by,

$$F = \frac{(RSS_f - \sum_{l=0}^{1}\sum_{k=0}^{1} RSS_{l,k})/(\sum_{l=0}^{1}\sum_{k=0}^{1} p_{l,k} - p_f)}{\hat{\sigma}^2} \tag{5.5}$$

where $RSS_{l,k}$ represents the residuals sum of squares (RSS) of the submodel for the l event region and k station region, and p refers to the number of fitted parameters in the full model and submodels. Since the 'models' are simply the means, $p = 1$ in each case (for combined model and each individual sub-model). The denominator is given by,

$$\hat{\sigma}^2 = \frac{\sum_{l=0}^{1}\sum_{k=0}^{1} RSS_{l,k}}{\sum_{l=0}^{1}\sum_{k=0}^{1}(N_{l,k} - p_{l,k})} = \frac{\sum_{l=0}^{1}\sum_{k=0}^{1} RSS_{l,k}}{\sum_{l=0}^{1}\sum_{k=0}^{1} df_{l,k}} \tag{5.6}$$

where $N_{l,k}$ is the number of recordings for the data belonging to source group l and station group k, $p_{l,k}$ is the number of fitted parameters for that sub-model, and $df_{l,k} = N_{l,k} - p_{l,k}$ is the degree of freedom for that sub-model. The degree of freedom of the full (combined) model is $df_f = N - p_f = \sum_{l=0}^{1}\sum_{k=0}^{1} N_{l,k} - p_f$. In this case, the summation in Eq. (5.5) and (5.6) unrelated to *RSS* are $\left(\sum_{l=0}^{1}\sum_{k=0}^{1} p_{l,k} - p_f\right) = df_f - \sum_{l=0}^{1}\sum_{k=0}^{1} df_{l,k} = 3$, and $\sum_{l=0}^{1}\sum_{k=0}^{1} df_{l,k} = 1820$.

The F statistic is compared to the F distribution to evaluate a significance level (p) for the test, where values exceeding a select threshold (i.e., $p > 0.05$) imply the sub-models are not distinct. The results from F-test for four selected periods are shown in Table 5.3 for the case of one overall combined model in comparison to four sub-models. The F statistic, the minimum value of the F statistic for $p = 0.05$, and the significance level are provided. In each case, the testing indicates that the sub-models are distinct and justifies the use of regional terms.

Table 5.3 F-test for significance of region effects for both sources and sites

Period (s)		Full model f	Submodels $l = \{0, 1\}$ $k = \{0, 1\}$	F-statistic	F-critical$_{(3, 1827)}$ value at significance level p=0.05	p-value
0.005	*RSS*	1174.09	1081.39	52.00	2.61	0
	df	1823	1820			
0.08	*RSS*	1211.89	1102.70	60.07		0
	df	1823	1820			
0.80	*RSS*	1184.04	1102.36	44.95		0
	df	1823	1820			
5.00	*RSS*	724.74	659.52	60.00		0
	df	1823	1820			

We also consider two additional F tests to examine the difference between Honshu and Hokkaido recordings, considering only data from source region (i.e., only South event data in one set of tests, and only North event data in a second set of tests). In this case, the F-statistic is computed as:

$$F_l = \frac{(RSS_l - \sum_{k=0}^{1} RSS_{l,k})/(\sum_{k=0}^{1} p_{l,k} - p_l)}{\hat{\sigma}_l^2} \tag{5.7}$$

where l is either 0 or 1, and the denominator is,

$$\hat{\sigma}_l^2 = \frac{\sum_{k=0}^{1} RSS_{l,k}}{\sum_{k=0}^{1}(N_{l,k} - p_{l,k})} = \frac{\sum_{k=0}^{1} RSS_{l,k}}{\sum_{k=0}^{1} df_{l,k}} \tag{5.8}$$

The combined model for these tests groups Honshu and Hokkaido recordings for a given event group $l = 0$ or 1, and RSS_l represents the *RSS* for that combined model. The results of two F-tests for $l = 0$ (South Event) and $l = 1$ (North Event) are given in Table 5.4 and 5.5. For most cases, the testing confirms that the separation of regions for each event group is justified. These exceptions occur at periods where the regional terms in Figure 5.11 are nearly zero (e.g., T=0.08s for North events, where the p-value is 0.35).

Table 5.4 F-test for significance of region effects for both sources and sites

Period (s)		South Event model $l = 0$	Submodels $l = 0$ $k = \{0, 1\}$	F-statistics	F-critical$_{(1, 1521)}$ at significance level p=0.05	p-value
0.005	*RSS*	963.59	909.49	90.46	3.85	0
	df	1522	1521			
0.08	*RSS*	1014.85	928.29	141.83		0
	df	1522	1521			
0.80	*RSS*	931.52	921.12	17.19		0
	df	1522	1521			
5.00	*RSS*	578.81	549.33	81.64		0
	df	1522	1521			

Table 5.5 F-test for significance of region effects for both sources and sites

Period (s)		North Event model $l = 1$	Submodels $l = 1$ $k = \{0, 1\}$	F-statistics	F-critical$_{(1, 299)}$ at significance level p=0.05	p-value
0.005	*RSS*	172.41	171.90	0.88	3.87	0.35
	df	300	299			
0.08	*RSS*	177.46	174.41	5.22		0.02
	df	300	299			
0.80	*RSS*	199.03	181.23	29.36		0
	df	300	299			
5.00	*RSS*	139.12	110.19	78.51		0
	df	300	299			

Based on the results seen in Figure 5.11 and the statistical testing, we consider the between-island regional terms significant and incorporated regional terms into the residuals analysis. The region terms to the within-event residuals from Eq. (5.4) as follows:

$$\delta W_{ij}^{reg} = \delta W_{ij} - \eta_{reg,l,k} \tag{5.9}$$

where δW_{ij}^{reg} is the region-adjusted within-event residual.

Figure 5.12 shows the variation with distance of δW_{ij}^{reg} for (a) all data, (b) North events only and (c) South events only. The results in Figure 5.12(a) can be compared to those in Figure 5.10 to see the effect of the regional terms on residuals trends – those trends are slightly reduced but not eliminated. While the residual trends for North events are generally flat, the gradients remain for the much better recorded South events. The vertical lines in Figure 5.12(b) and (c) indicate the distance range of ODCD stations across all events in the respective groups (around 100-200 km for North events, 320-500 km for South events). The residuals trends within these distance ranges are reasonably flat, indicating acceptable performance of the path model with the regional corrections applied. This feature of the data holds even for Hokkaido recordings of South events (Fig. 1.12c). As a result of these findings, our conclusion is that no further adjustments to the path models in Zea16 are needed for the analysis of site terms.

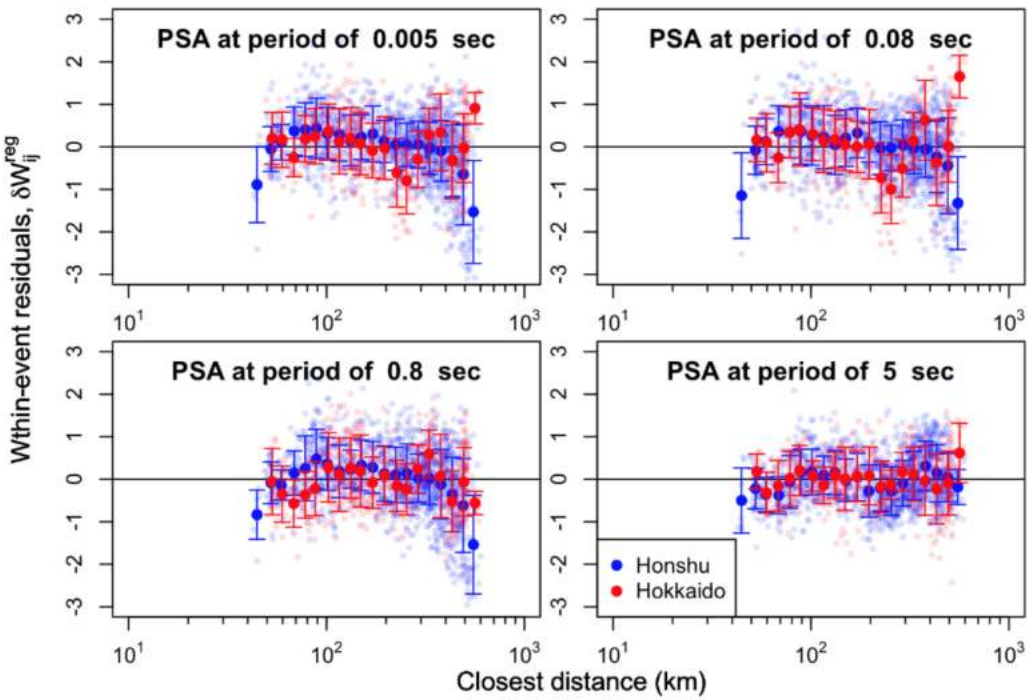

Figure 5.13(a) Trend of region-corrected within-event residuals with closest distance for all data. Distance range for ODCD stations are marked out.

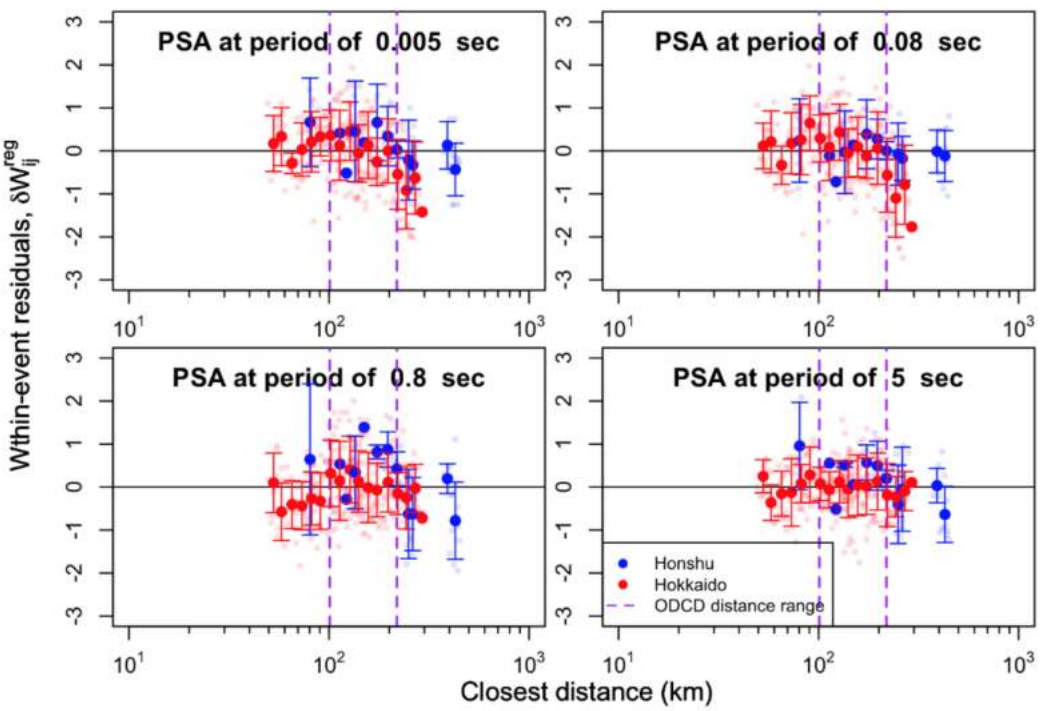

Figure 5.14(b) Trend of region-corrected within-event residuals with closest distance for North events only. Distance range for ODCD stations are marked out.

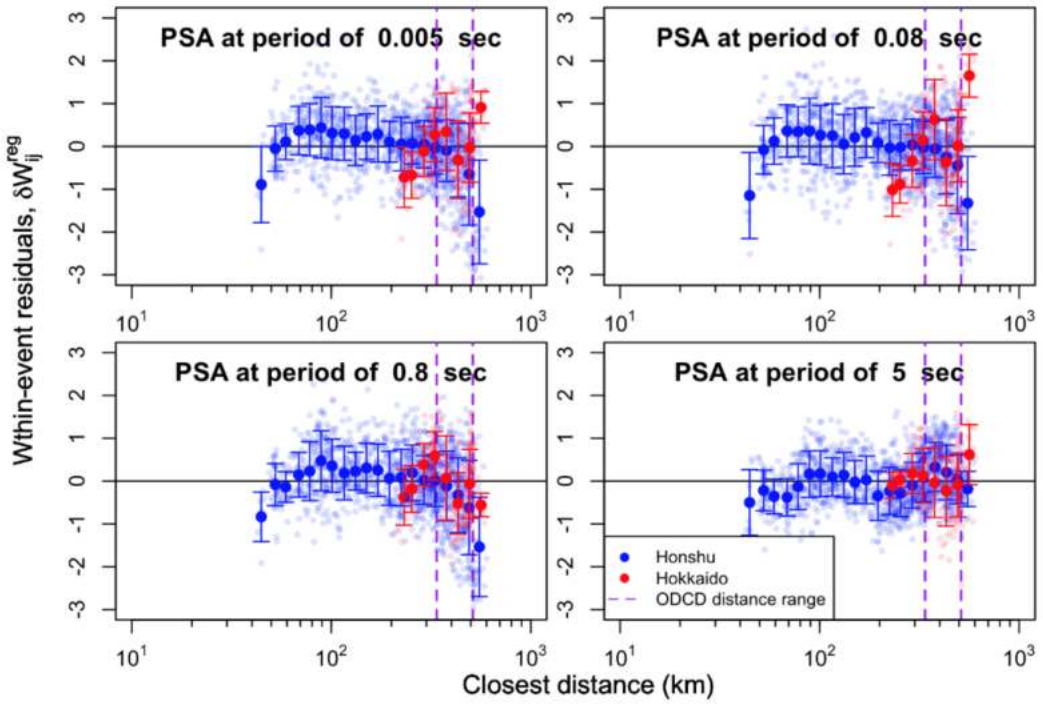

Figure 5.15(c) Trend of region-corrected within-event residuals with closest distance for South events only. Distance ranges for ODCD stations are marked.

5.3.2 Site terms

By adjusting residuals for event biases, $\eta_{E,i}$ and regional biases, $\eta_{reg,l,k}$, the remaining region-adjusted within-event residual, δW_{ij}^{reg}, represents errors in the prediction of observed intensity measures from the GMM that can be attributed to the combination of systematic site effects at each station and relative random, event-to-event path errors. If the path errors are indeed random, they would average to zero when summed over many observations. With this in mind, we estimate the effect of site, also called the site term, $\eta_{S,j}$, at site j as follows,

$$\eta_{S,j} = \frac{1}{n_j}\sum_{i=1}^{n_j} \delta W_{ij}^{reg} \tag{5.10}$$

where n_j is the number of recordings for station j. As with the event term computation, this represents a frequentist interpretation of the problem statistics.

The site response model assumed to apply for a given intensity measure at a given site is taken as (Stewart et al. 2017):

$$F_S = f_1 + f_2 \ln\left(\frac{x_{IMref} + f_3}{f_3}\right) \tag{5.11}$$

where x_{IMref} represents the amplitude of shaking for a reference site condition (generally rock) for a particular earthquake at a particular site (expressed as an intensity measure, which is often PGA), f_1 is the coefficient representing linear site response, f_2 represents the slope (generally negative) in amplification-x_{IMref} space for $x_{IMref} \gg f_3$, and f_3 represents a transitional value of the reference site intensity measure below which the site response is nearly linear, and above which the trend of amplification with x_{IMref} is nearly linear in log-log space.

The site term in Eq. (5.10) represents the misfit between the observed site response and the site response predicted by the ergodic model in the GMM. Assuming the ground motions are sufficiently weak that nonlinear response is marginal, f_1 from Eq. (5.11) can be evaluated as,

$$(f_1)_j = \eta_{S,j} + F_{S,j} \tag{5.12}$$

where $F_{S,j}$ is the ergodic site response as evaluated from the selected model (for the case of the Zhao's GMM, this is a constant value for a given intensity measure for class IV sites).

Figure 5.13 shows for each of the seven sites, the region-adjusted within-event residuals δW_{ij}^{reg} (top) and the total site response (bottom) computed as in Eq. (5.12). Each of the sites exhibits a peaked site response at an apparent site period. For example, at the Toitokki site (dark blue), the first peak site response occurs at a period of about 0.5 sec, and the amplification at that period is approximately $e^{2.8} \approx 16.4$. This very high site amplification is likely associated with resonance and impedance effects from the soft upper peat layers relative to deeper, stiffer sediments.

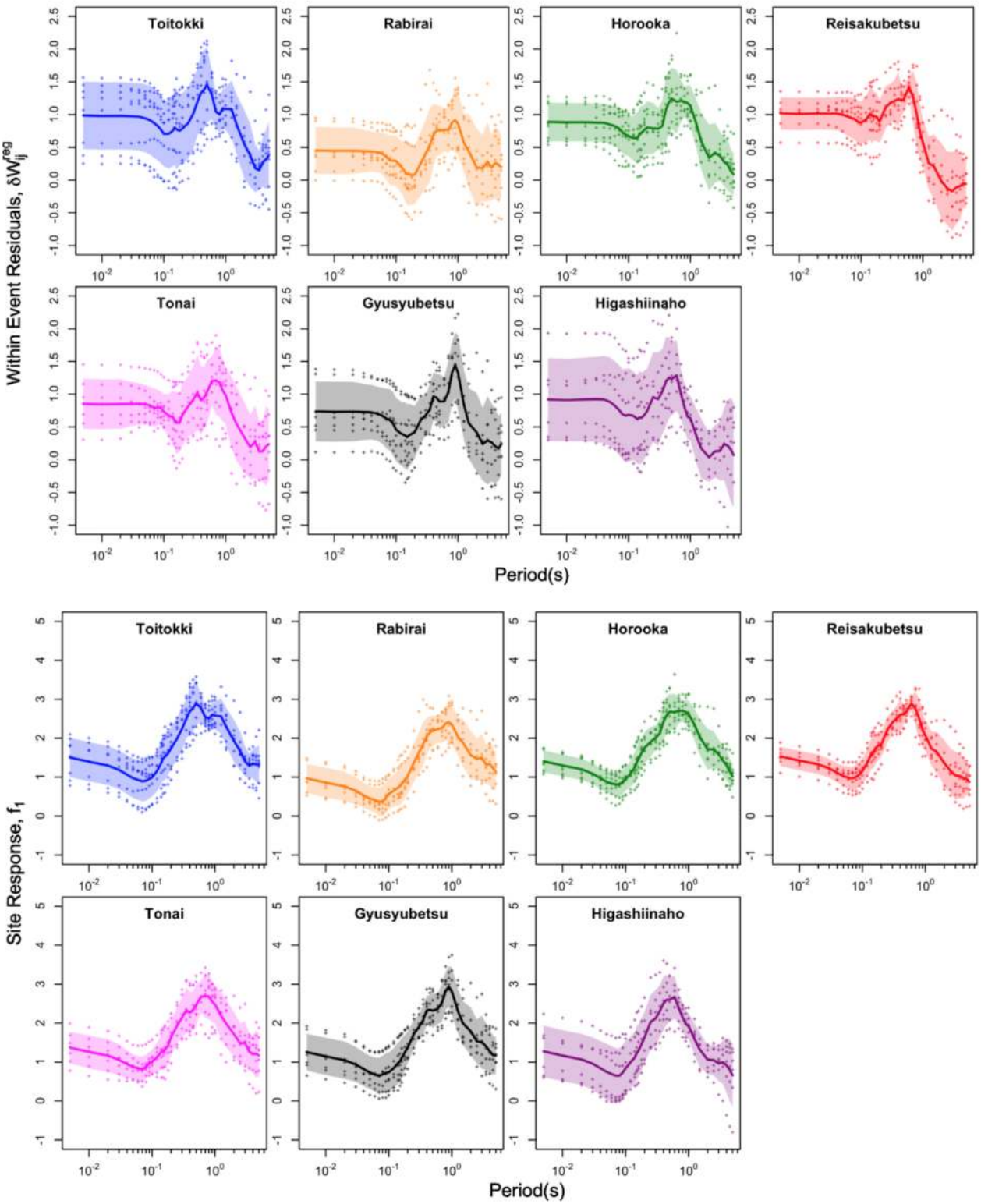

Figure 5.16 Region-adjusted within event residuals (top) and estimated site response (bottom) for the seven Obihiro stations

5.3.3 H/V spectral ratios from pre-event noise and application to site amplification

As the sites within the study region exhibit site amplification patterns pointing towards resonance at the site frequency, we sought to use H/V spectral ratios to estimate the frequency of the peak response (f_{peak}). The concept is to use f_{peak} as a site parameter to be used in the regional ergodic model. Ambient noise measurements (microtremors) is used to estimate of f_{peak} independently from the ground motions. Before proceeding, a point of clarification on notation – frequency f_0 is taken as the frequency of the peak site response as obtained from non-ergodic analysis (Section 5.3.2), which is not an independent variable (it is derived from ground motions, hence it is not independent of those motions), while frequency f_{peak} is measured from H/V spectral ratios and hence is an independent site parameter if measured from noise signals. Some prior research has shown that f_{peak} is consistent with f_0 for many soil sites (Lermo and Chávez-García. 1993, Lachet et al. 1996, Theodulidis et al. 1996, Bonilla et al. 2002, Kawase et al. 2011, Cadet et al. 2012, and Ghofrani et al. 2013).

Geophysical testing was performed in the vicinity of the Toitokki, Horooka, Rabirai, Reisakubtsu, and Gyushubetsu stations and provided Rayleigh wave dispersion curves and horizontal-to-vertical spectral ratios (HVSR). The V_{S30} and f_{peak} values obtained from these measurements are summarized in Table 5.1. Tests were not performed near Tonai and Higashiinaho stations and here we investigate the use of ground motion signals from the sites to develop H/V spectral ratios, which is the only source of this site attribute for the two sites without measurements. To ensure the selected pre-event signals are mainly noise, we first estimate the p-wave arrival time, and then take preceding portions of the signals for use in analysis. Fourier amplitude spectra (FAS) are computed for both horizontal, as-recorded components and the vertical component. The horizontal FAS is taken as the geometric mean of the two components. The horizontal and vertical FAS are smoothed using the Konno-Ohmachi window

smoothing technique (Konno and Ohmachi, 1998) with parameter $b = 20$. Finally, H/V spectra are computed as the ratio of smoothed horizontal FAS to smoothed vertical FAS.

Figure 5.14 shows the resulting H/V spectral ratios in gray (from microtremors where available, for pre-event noise otherwise) for the seven Obihiro stations, with fitted Gaussian pulses in blue (Ghofrani and Atkinson. 2014, Kwak et al. 2017). The f_{peak} values are established through the pulse fitting procedure and marked with a vertical line. Also shown in Figure 5.17 are the estimated site responses (Eq. 5.12) in red. Sites Toitokki and Rabirai have two H/V peaks, which raises the question of selecting f_{peak}. This following approach is adopted: (1) if the peaks are of comparable amplitude but distinct in frequency (ratio of the peak frequencies is greater than about 3-5), the lower frequency peak is adopted as f_{peak}; (2) if the peaks are of significantly different amplitude (more than a factor of two), the peak with the large amplitude is adopted (this is usually the lower frequency peak); and (3) if the peaks are of comparable amplitude and the frequencies are similar (ratio of the peak frequencies is less than about 3-5), re-fit the Gaussian function to encompass both peaks together. Case 1 applies to the Rabiri site and Case 3 applies to the Toitokki site. Note that adopting this approach provides values of f_{peak} that are in reasonable accord with f_o.

Values of f_0 at the peaks of the observed responses are in good agreement with f_{peak} values, as shown in Figure 1.15. The approach described above for selecting f_{peak} for sites with two peaks was applied for Toitokki and Rabirai. While the linear regression between the two frequencies does not fall on the 45 degree line, the 95% confidence intervals around the fit include the 45$^{\mathrm{o}}$ line. As a result, f_{peak} can be taken as a suitable estimate of f_0 for the Obihiro sites.

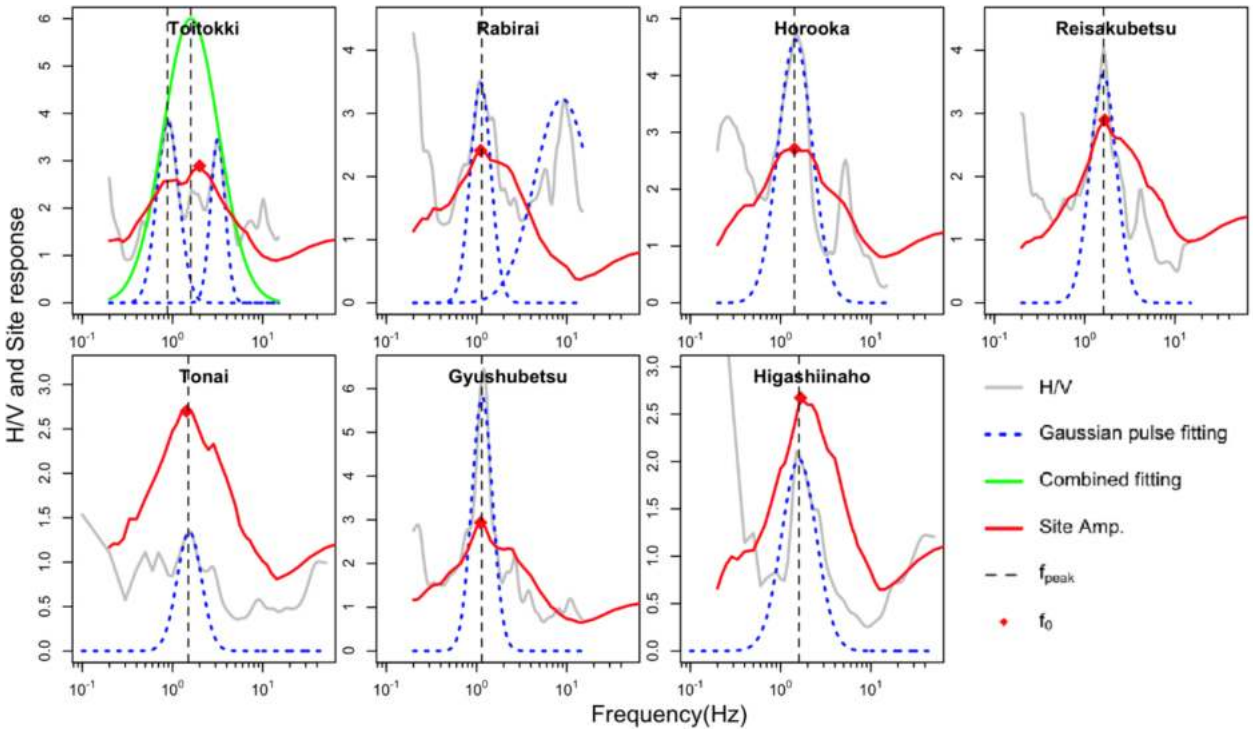

Figure 5.17 Comparison of H/V spectral ratios (data and fit) with observed total site response.

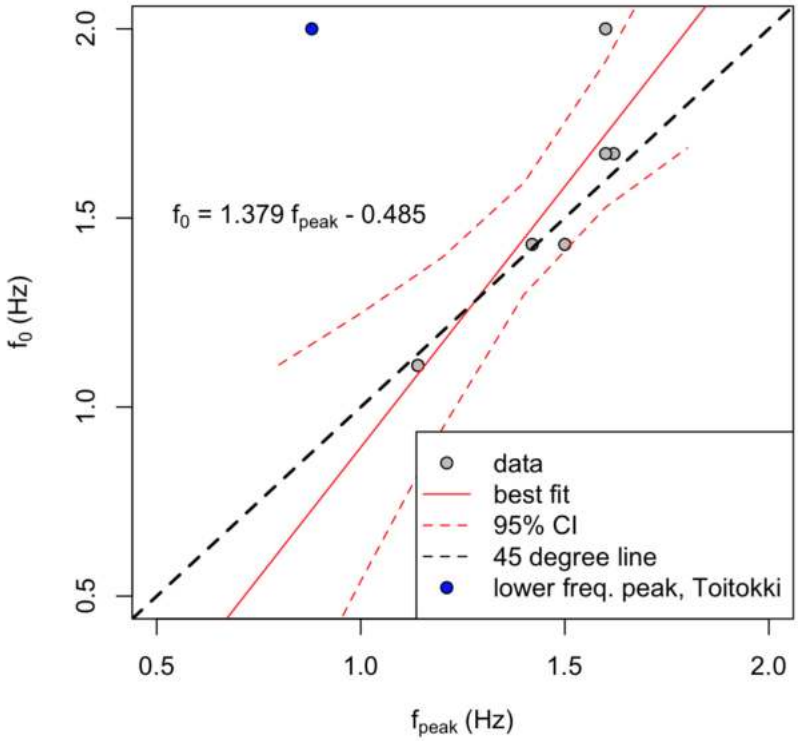

Figure 5.18 Relationship between peak in H/V spectra (f_{peak}) and peak in PSA site amplification (f_0). Linear regression provides $f_0 = 1.379 f_{peak} - 0.485$ (frequencies in Hz).

5.4 MODEL DEVELOPMENT

In this section, we develop a site amplification function that takes f_{peak} as input to capture the observed site amplification in an average sense across the seven sites and which presumably would have general applicability across the study region shown in Figure 5.2. We also develop an alternative model in which the only site information is that it is located on peat in the general study region, but f_{peak} is unknown.

5.4.1 Mean amplification

In order to capture the peaked shape of site amplification observed at the Obihiro sites, we selected a Mexican hat wavelet function (Ryan, 1994). This function is intended to capture site resonance effects that dominate amplification shapes at short to intermediate periods ($T < 2$ sec). A linear decay function is used at longer periods ($T > 2$ sec).

The recommended site amplification function for linear conditions is as follows,

$$f_1(T, t_0) = \begin{cases} c_0 + \dfrac{2c_1}{\sqrt{3c_2}\pi^{1/4}}\left(1 - \left(\dfrac{\ln(Tf_{\text{p}})}{c_2}\right)^2\right) e^{-\frac{1}{2}\left[\frac{\ln(Tf_{\text{p}})}{c_2}\right]^2} & \text{for } T \le T_{tr} \\ c_3 \ln\left(\dfrac{T}{T_{\text{tr}}}\right) + f_1(T_{\text{tr}}, f_{\text{p}}) & \text{for } T > T_{tr} \end{cases} \tag{5.13}$$

where c_0 controls the overall level of site amplification, c_1 scales the amplitude of the hat function, c_2 describes the width of the PSA peak in natural log period space, $T_{\text{tr}} = 2$ sec is the transition period between the Mexican hat and linear functions, and c_3 describes the linear decay of amplification with log period beyond T_{tr}. Frequency f_{p} is the frequency of the peak in the Mexican hat fitting function. Eq. 5.13 fitted to the observed amplification at each site by minimizing the sum square of errors, with the model coefficients are summarized Table 5.6. The fitted functions are plotted in Figure 5.16. For

sites with multi-mode responses, such as the two peaks observed for Toitokki, only the first mode (lower frequency) is captured. Higher modes are not Due to the unpredictability of higher modes, we have not attempted to capture such modes in the amplification model.

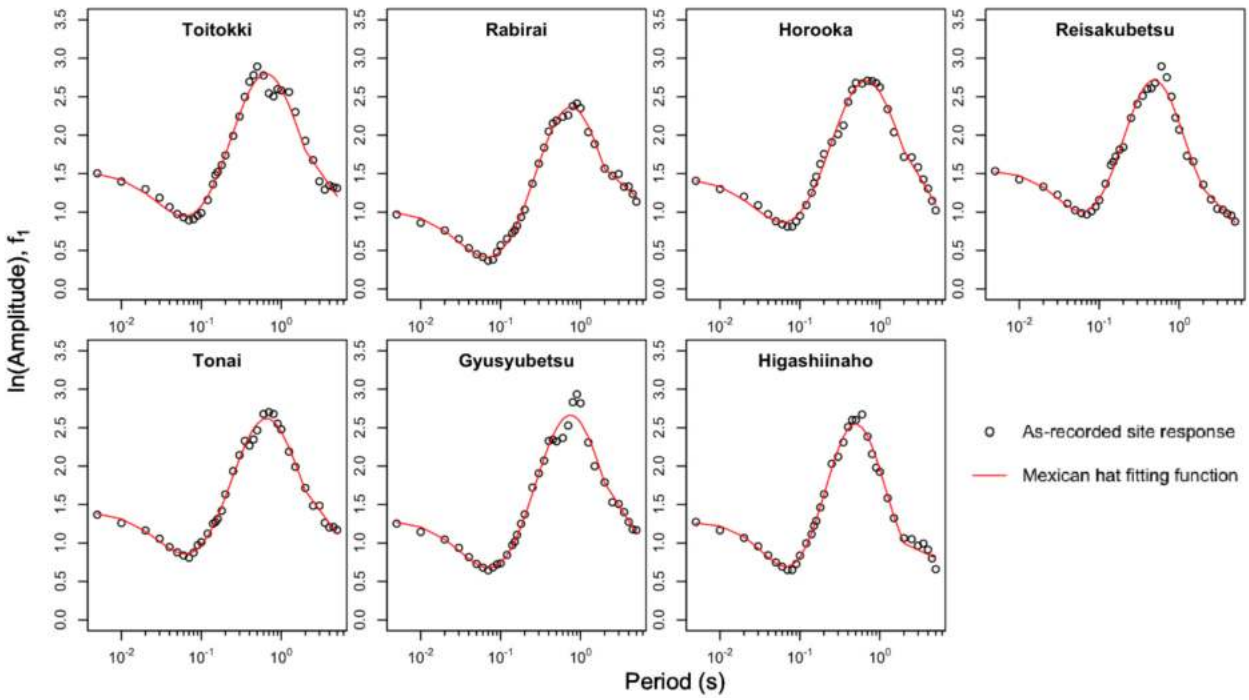

Figure 5.19 Fit of model to observed amplification with model coefficients from site-specific optimization

Table 5.6 Model coefficients obtained by fitting Eq. (5.13)

	Toitokki	**Rabirai**	**Horooka**	**Reisakubetsu**	**Tonai**	**Gyushubetsu**	**Higashiinaho**
c_0	1.518	1.015	1.434	1.534	1.403	1.288	1.267
c_1	1.724	1.839	1.729	1.496	1.635	1.846	1.597
c_2	1.362	1.398	1.387	1.202	1.355	1.358	1.162
c_3	-0.647	-0.401	-0.757	-0.475	-0.614	-0.717	-0.210
f_p (Hz)	1.549	1.319	1.480	2.062	1.529	1.343	2.008

To develop the model for sites other than the seven stations in the study region, we examined the relationship between f_p and f_{peak} as shown in Figure 5.15. The best fit line is parallel to the 45º line and encompasses it within the 95% confidence interval. The best linear regression relation is $f_p =$

$1.125f_{\text{peak}} + 0.002$. As a result, we take f_{peak} values as unbiased estimators of f_{p} for use in the Mexican hat function. All other coefficients are taken as constant across all sites. The other coefficients were obtained by minimizing the sum of square of errors after specifying f_{p} as above, with the resulting values obtained as $c_0 = 1.341$, $c_1 = 1.703$, $c_2 = 1.413$, and $c_3 = -0.849$. In summary, for the case where f_{peak} is known at a site from an H/V spectrum, the regional ergodic site amplification is computed with the above coefficients. The predictions from the general model are compared to data for the seven Obihiro sites in Figure 5.21. The results are generally good with some loss of fidelity relative to the site specific (non-ergodic) fits shown in Figure 5.19.

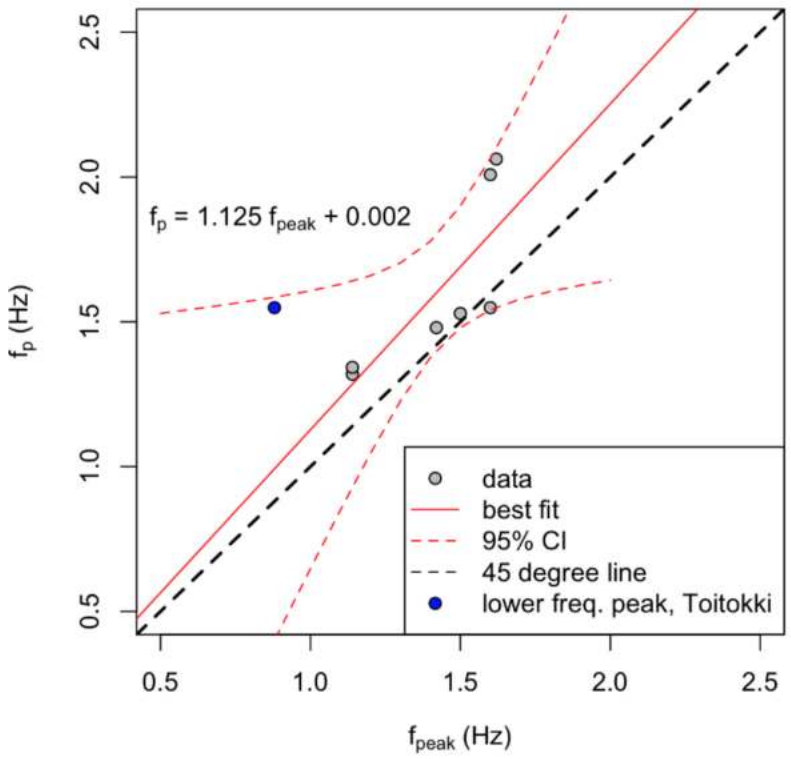

Figure 5.20 Relationship between peak in H/V spectra (f_{peak}) and peak in Mexican hat fitting function of site response (f_{p}).

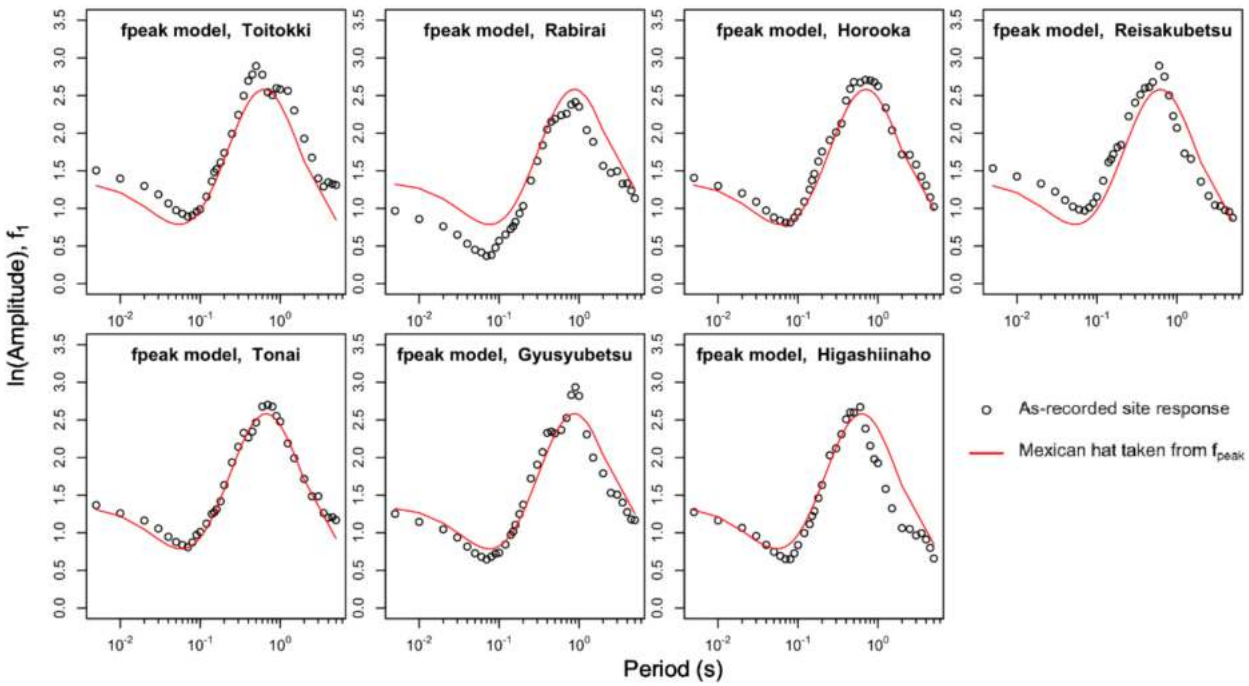

Figure 5.21 Fit of model to observed amplification when model coefficients are taken from regional average model

For the case where f_{peak} is unknown, we regressed Eq. (5.13) to the combined data set for all sites to obtain a new set of coefficients as follows: $c_0 = 1.346$, $c_1 = 1.668$, $c_2 = 1.326$, $c_3 = -0.526$, and $f_{\text{p}} = 1.594$ Hz. Note that the f_{p} obtained here is a regional average site frequency. By combining all sites, the pulse width and linear decay rate at long periods are both slightly increased. The regional average curve is plotted relative to the observed amplification levels at all Obihiro sites in Figure 5.22.

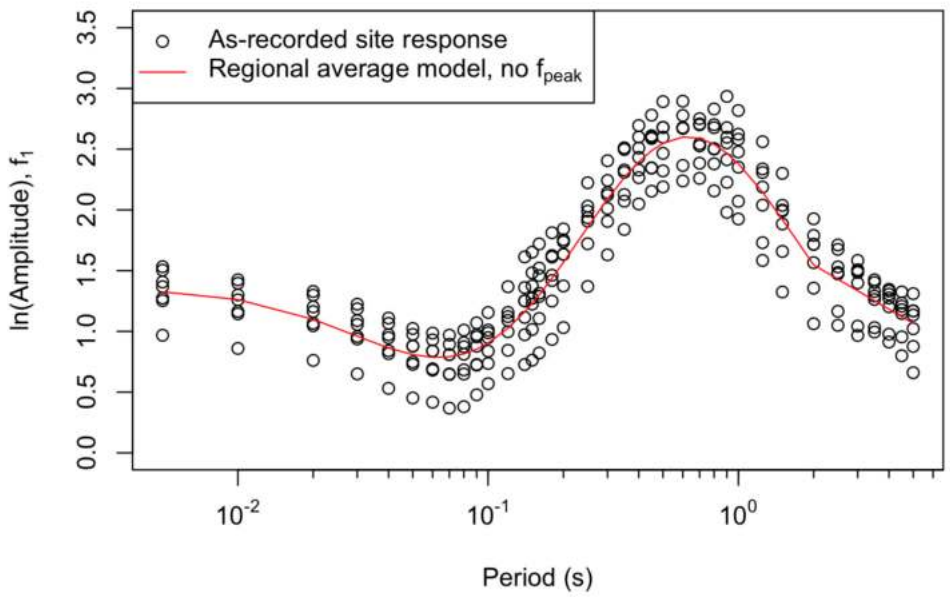

Figure 5.22 Relationship between peak in H/V spectra (f_{peak}) and peak in Mexican hat fitting function of site response (f_{p}).

To compare the fitting performance between f_{peak} model and regional average model, their sums of square error are computed. They are 13.0 for the regional average model and 11.0 for the model that incorporates site-specific f_{peak} values. Not surprisingly, given the additional site-specific information (f_{peak}), the latter model fits the data better.

5.4.2 Aleatory variability model and Model bias

The standard deviation terms to use with the proposed site amplification model are τ for between-event variability and ϕ for within-event variability. The τ model is assumed to be unaffected by the site amplification model described here, and can be taken from GMMs. The ϕ model can be taken from the standard deviation of the within-event residuals obtained through the use of the Zhao's GMM (Zhao et al, 2016a and 2016b) in combination with the proposed site amplification models. To develop this within-event standard deviation model, we compute residuals as in Eq. (5.2), but now using the region-specific site amplification model in lieu of the Zhao's GMM (Zhao et al, 2016a and 2016b) site term.

After subtracting event terms (Eq. (5.3)) and regional terms (Eq. (5.9)), we then partition the within event residual as:

$$\delta W_{ij}^{reg} = c + \eta_{S,j} + \varepsilon_{ij} \tag{5.14}$$

where c is the model bias, η_S is the site term, and ε_{ij} is the remaining residual. The model bias indicates the overall model misfit relative to the data (equivalent to the average of all δW_{ij}^{reg}). The standard deviation of η_S is denoted the site-to-site dispersion (ϕ_{S2S}) while the standard deviation of ε_{ij} is the single-station within-event dispersion (ϕ_{SS}).

These standard deviations are shown in Figure 5.23 and 5.24 for the model employing regional average parameters and in Figure 5.25 and 5.26 for the model employing site-specific f_{peak} values. Arguably, the regional average model could be considered as ergodic because site-specific information is not incorporated, whereas the model incorporating site-specific f_{peak} values is effectively non-ergodic.

Figure 5.23 shows that the site-to-site dispersion (ϕ_{S2S}) is approximately 0.2, which is significantly below the average for the entire Japan (from Al Atik, 2015). This is expected given the relatively similar geotechnical conditions within the study region.

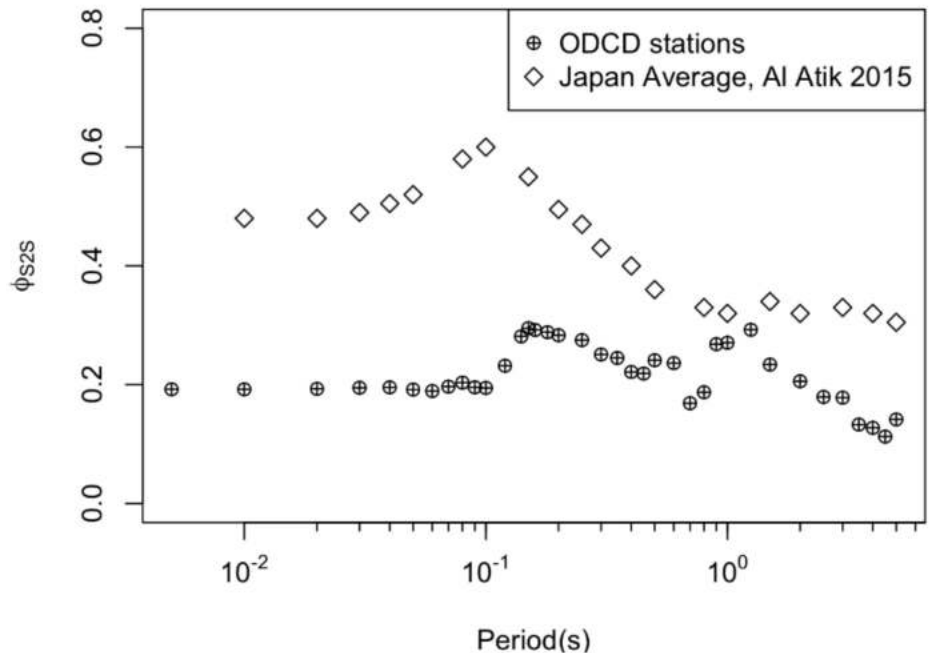

Figure 5.23 Comparison of site-to-site standard deviations from Obihiro stations (this study) and Japan average from Al Atik (2015).

Figure 5.24 shows single-station standard deviations (ϕ_{ss}), which are remarkably consistent with the Japan average values obtained previously by Rodriguez-Marek et al. (2011). Figure 5.25 compares these two standard deviation terms for the regional average and site specific models. The respective dispersions for the two alternate models are very similar.

Figure 5.26 compares the model bias for the regional average and site specific models, both of which are effectively zero. Also shown for comparative purposes is the bias obtained using the site term in the Zhao's GMM (Zhao et al, 2016a and 2016b), which is very large (indicating under-prediction). The substantial bias of the GMM for the Obihiro sites demonstrates the need for site-specific site factors for these peaty organic soils.

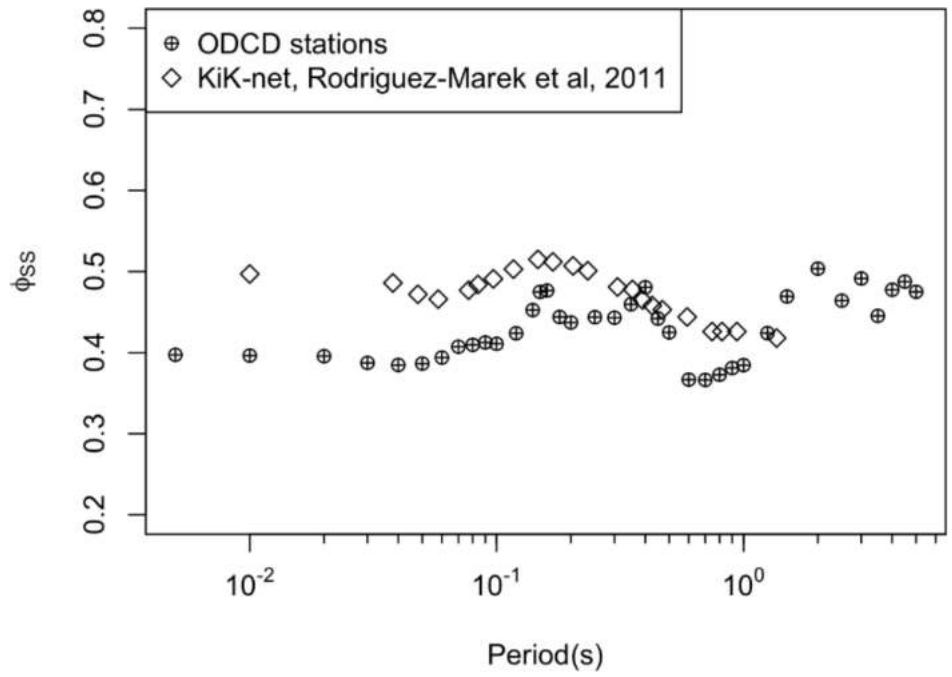

Figure 5.24 Comparison of single station standard deviations from Obihiro stations (this study) and KiK-net database from Rodriguez-Marek et al (2011).

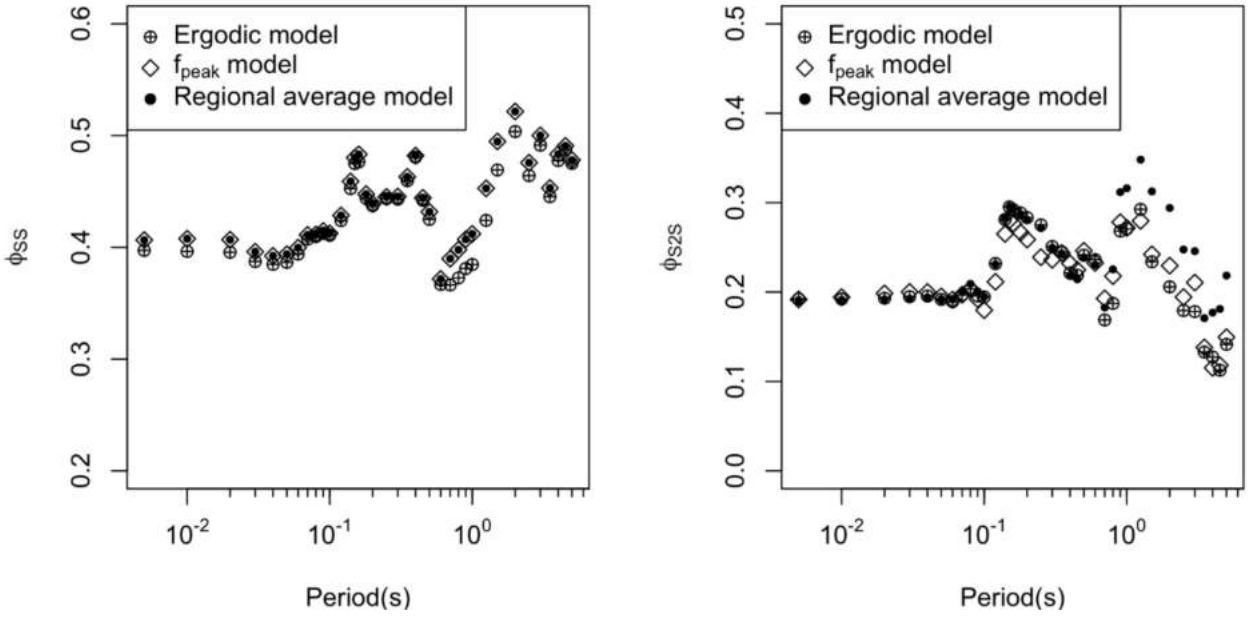

Figure 5.25 Comparison of single station and site-to-site standard deviation terms for the two forms of the proposed site amplification model.

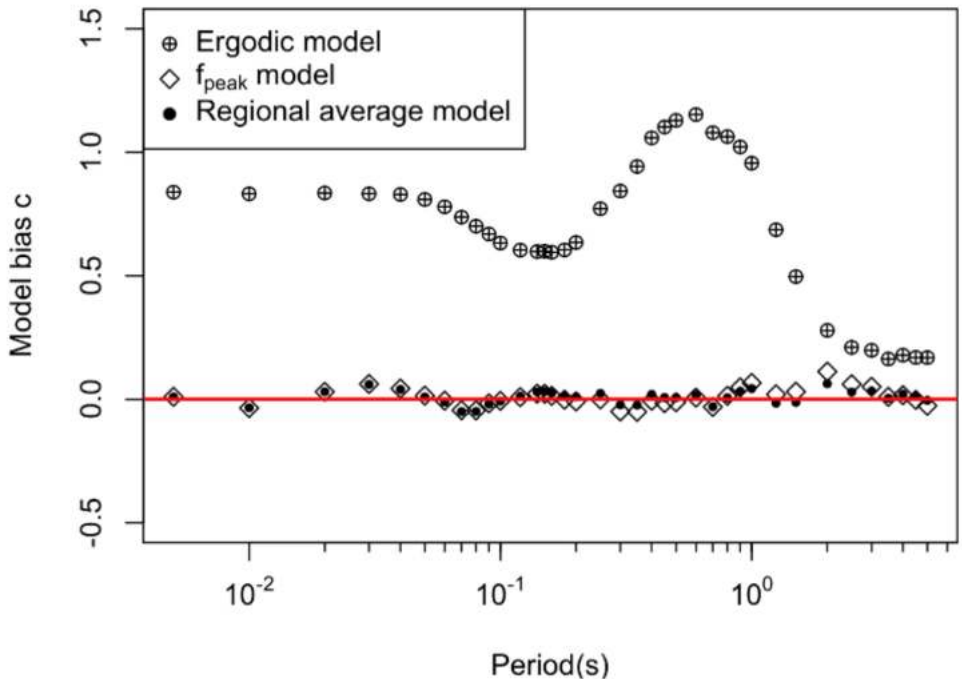

Figure 5.26 Comparison of model bias for the ergodic model of Zhao et al. (2016a, 2016b) and the Zhao et al. model combined with the two proposed region-specific site amplification models.

5.4.3 Nonlinearity

The models for mean site response provided in Section 5.4.1 were developed based on relatively weak ground motions from 8 events for linear site amplification. To investigate the potential effects of nonlinearity, we examine model misfits relative to the data from Event 10 (the 2003 Tokachi-Oki Earthquake), which produces significantly stronger ground motions than the other considered events at the ODCD stations (Figure 5.5).

The ratio of PGV to shear wave velocity is often taken as an indicator of nonlinearity (refs), and is considered here to differentiate shaking demands for Event 10 vs the other events considered in model development. Idriss (2016) and Kim et al (2016) adapted this concept to propose a shear strain index (I_γ) as follows:

$$I_\gamma = \frac{PGV^r}{V_{S30}} \tag{5.15}$$

This parameter was used by Kim et al. (2016) to identify conditions where equivalent linear and nonlinear ground response analysis results are comparable ($I_\gamma < 0.03\%$) vs those where nonlinear analyses are required (larger I_γ). We could not apply Eq. (5.15) because the reference rock level PGV is unknown. Instead we use the soil surface PGV as follows

$$I_\gamma^s = \frac{PGV}{V_{S30}} \tag{5.16}$$

This parameter is used here to differentiate approximate strain demands for the different events. The indices computed here cannot be directly compared to the thresholds recommended by Kim et al (2016). Figure 1.24 compares soil surface strain index from Eq. (5.16) from Events 1-9 to those from Event 10 in the form of box plots. Clearly Event 10 induced much larger strains and nonlinear site response is more likely to be observed.

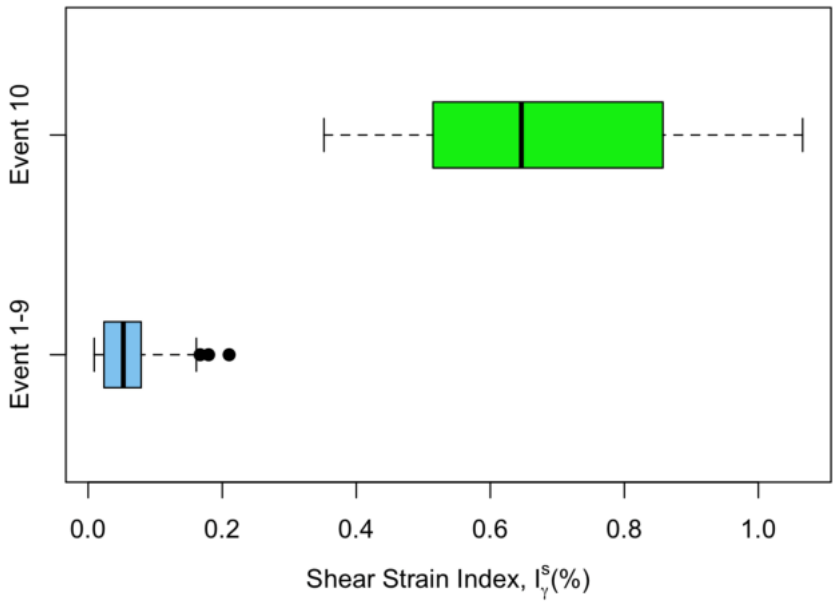

Figure 5.27 Boxplots of soil surface shear strain index I_γ^S for Event 1-9 and Event 10. Strains from Event 10 is significantly higher and nonlinear behavior is anticipated.

The analysis of Event 10 follows the process used for other events. Eq. (5.1) is used to compute total residuals, and Eq. (5.2) is used to compute the event terms ($\eta_{E,10}$). Figure 5.28 compares the event terms for Event 10 to the other events considered. In the case of ODCD stations, the GMM used for residuals calculation is modified from the published version,

$$(\mu_{lnY})_{ij} = \mu_{lnY}^{r} + f_1 \tag{5.16}$$

is where μ_{lnY}^{r} is the mean ground motion prediction for reference rock (i.e., Site Class 1) from Zhao et al. (2016) and f_1 is from Eq. (5.13).

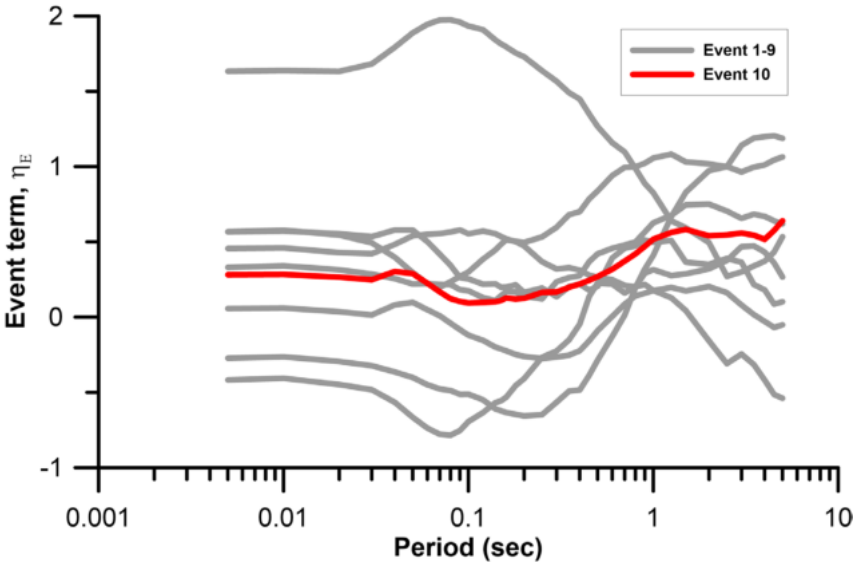

Figure 5.28 Event term for Event 10 compared to Event 1-9.

Region-adjusted within event residuals are computed using Eq. (5.9). Figure 5.29 plots δW_{ij}^{reg} for Event 10 along with those for the other events, using ODCD stations only. The residuals are plotted as a function of PGA^r, which is the median peak acceleration for the reference site condition from the Zhao GMM for Site Class 2. If the site response from the various events recorded at the ODCD sites is effectively linear, then no trend in δW_{ij}^{reg} would be expected with PGA^r. This is effectively the case for the Event 1-9 data for each of the intensity measures for which results are shown in Figure 5.29,

with the possible exception of a small upward trend for 5.0 sec PSA. The Event 10 data, however, indicate PGA^r dependencies that are downward at short periods and upward at 5.0 sec.

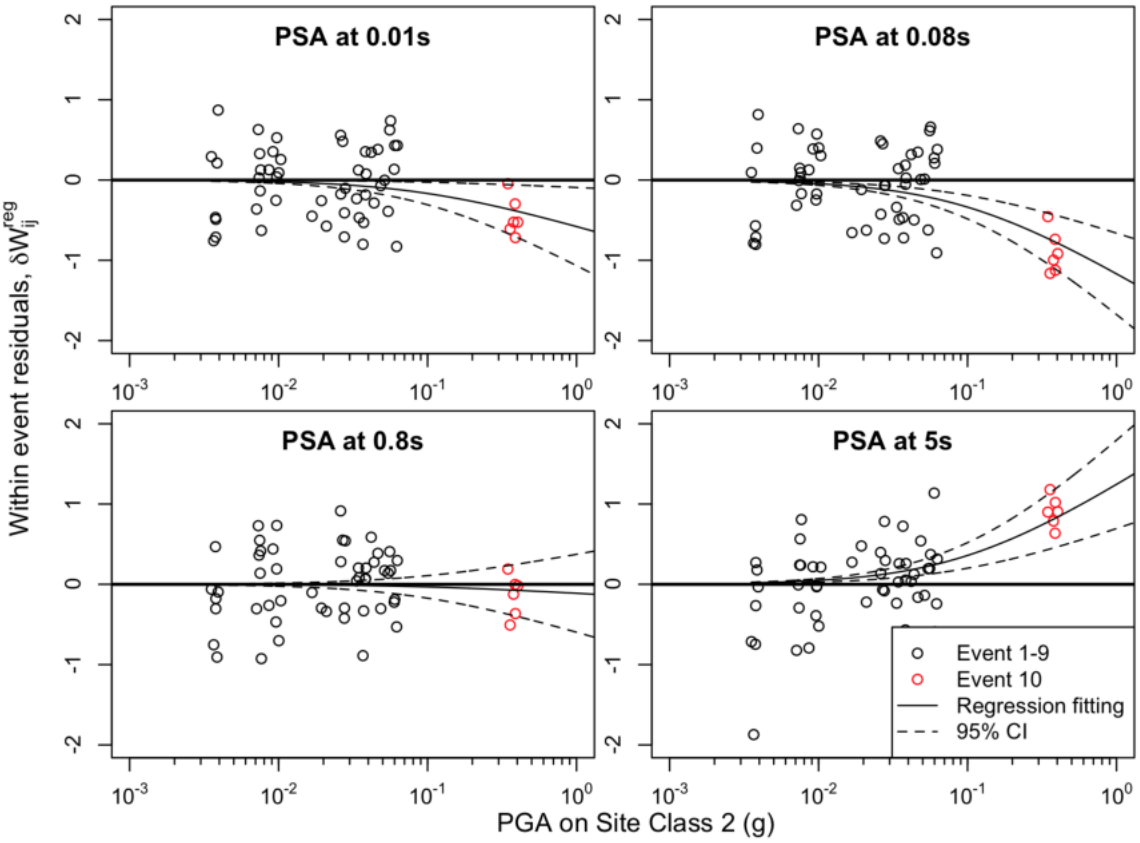

Figure 5.29 Region adjusted within event residuals for data recorded at ODCD stations versus reference site PGA^r (Site Class 2).

The trends of the results in Figure 5.29 are fitted by regression using the relation in Eq. (5.11) with $f_1 = 0$ (the setting of f_1 to zero is because of its inclusion in the model used for residuals analysis; Eq. 16) and $f_3 = 0.1$g (a typical value). As a result, only parameter f_2 is set by regression. Nonlinearity is evident from curvature in the fit line, and is quantified by $f_2 \neq 0$. The downward curvature at short periods is expected, and results from increased damping in sediments as strains increase. The upward trend at long periods is also fairly common. This typically occurs because nonlinearity softens the soil, increasing its fundamental period. Because the elastic (small strain) period is in the range of 1-2 sec,

this softening will bring the soil deposits to resonance at longer periods, which would be reflected by increased long period PSA as indicated by the trend line.

Nonlinear site response for the peaty organic soils encountered along the Kushiro and Tokachi Rivers in Hokkaido is investigated further in Chapter 6 using ground response simulations. The model used to represent nonlinearity in fragility modeling is described there.

5.5 MODEL COMPARISON

The model development described previously in this chapter was based on the Zhao (2016) model as the conditioning GMM. The residuals in Eq. (5.1) were computed relative to this model, the event terms in Eq. (5.2), path corrections in Eq. (5.4), and non-ergodic site terms (Eq. 5.10) are relative to this model, and the ergodic component of the regional site response utilizes the site term in this model (Eq. 5.12). Given the pervasive influence of GMM throughout the process, a natural question to ask is whether the site response results would be appreciably different had a different model been selected?

The manner in which the site response effects from Obihiro ground motions are expressed in the development of the regional model is through within-event residuals, δW. Accordingly, the most direct means by which to answer the question of GMM influence is to compare these residuals as computed for multiple models. The Abrahamson et al. (2018) model (hereafter Aea18) was selected for this purpose. To enable comparisons of within-event residuals, event terms were developed for Events 1-9 relative to the Aea18 GMM.

As was described in Section 5.3.1, there are some complicating issues related to path effects when the path from source-to-site travels between islands (Honshu to Hokkaido or vice-versa, which affect δW). In order to minimize the effects of such complications for this comparison, we compute within-event

residuals for common source – station combinations. Figure 5.30(a) shows for Event 5 (located near Honshu) the correlation of within-event residuals for Honshu stations as computed from both GMMs. The correlation is strong (r = 0.86). Figure 5.30(b) shows a similar comparison, but in this case it is for Event 7 (near Hokkaido) and the residuals are for Hokkaido stations. In this case r = 0.90. The correlations are strong in both cases, and similarly strong correlations were encountered for other events. As a result, we do not expect that the choice of GMM significantly influences the regional site response model developed here.

Figure 5.30(b) shows with green symbols δW for the ODCD stations. The offset from the 1:1 line is due to a reference site incompatibility issue (between the Aea18 GMM and site term), described below.

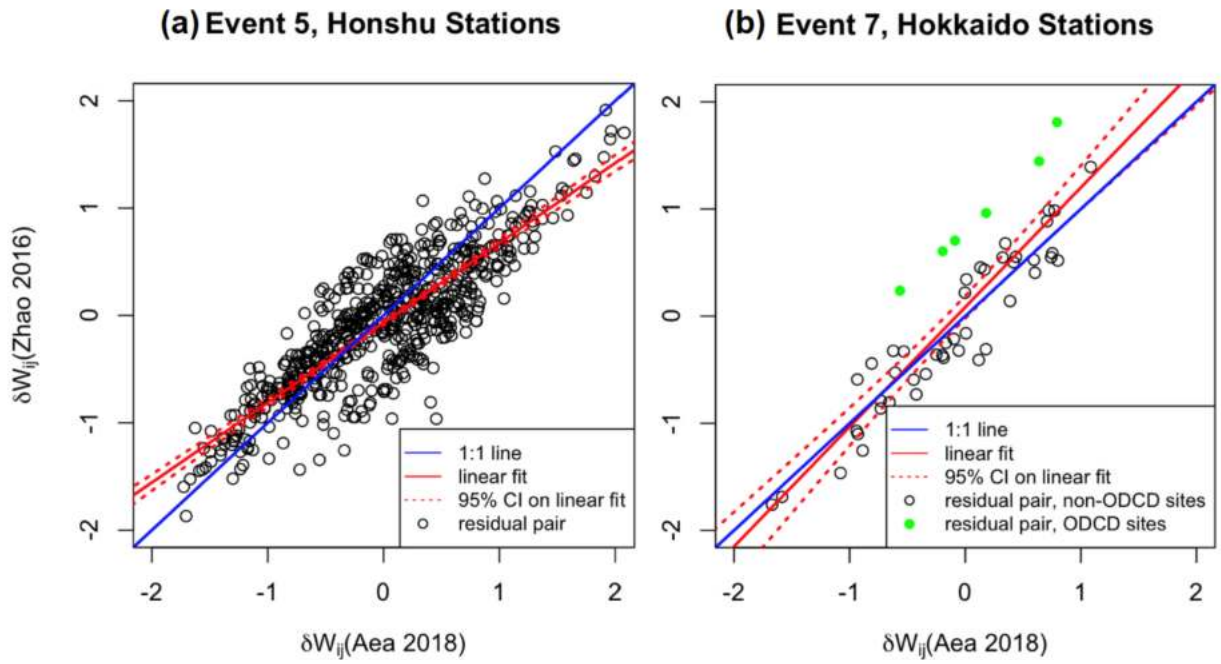

Figure 5.30 Within event residuals (event terms corrected) of OCDC stations by Abrahamson's model.

Next, we investigate the applicability of the regional site amplification model with the Aea18 GMM by specifically examining residuals for ODCD stations. For these sites, total residuals (Eq. 5.1) are computed by combining the Aea18 GMM with site response models (per Eq. 5.16), and then

subsequently correcting total residuals to within-event residuals by removing event terms. In Eq. (5.16), μ_{lnY}^{r} is taken as the Aea18 mean ground motion prediction for an assumed reference site condition of V_{S30} = 1.0 km/s. Two representations of f_1 are used. First, it is taken as the ergodic model in Aea18, with the results in Figure 5.31. Next, f_1 is taken from Eq. (5.13) (regional model), with the result shown in Figure 5.32. No regional path corrections were applied in the use of the Aea18 model, although the Japan-specific anelastic attenuation model was applied.

The results shown in Figure 5.31 with the ergodic site response model indicate substantial underprediction bias (positive residuals), which demonstrates the need for a regional site response model for the Obihiro sites. When the regional model is applied (Figure 5.32), there is clear improvement, with mean residuals being much closer to zero. Some misfit remains, which is a consequence of the assumed reference site condition for the Aea18 model (V_{S30} = 1.0 km/s) being incompatible with the reference condition in the regional model. This is a common issue when combining a site response model with a GMM, and is corrected in forward application through adjustment of the GMM constant term.

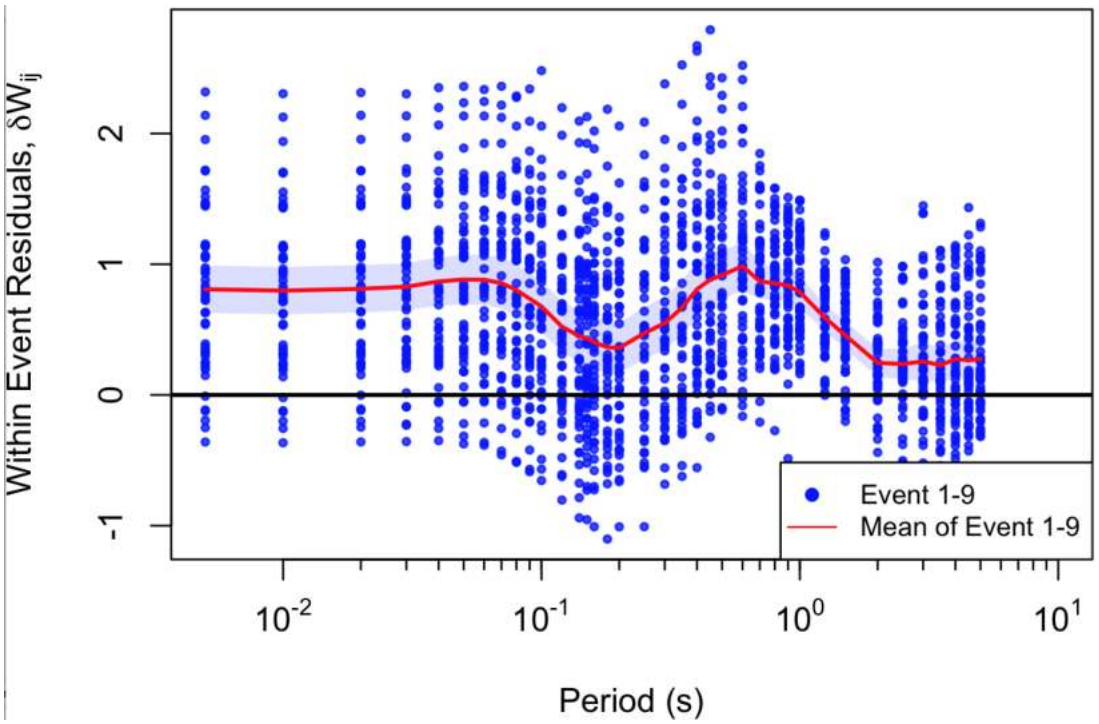

Figure 5.31 Within event residuals for OCDC stations using recordings from Events 1-9 and Aea18 model with its ergodic site term.

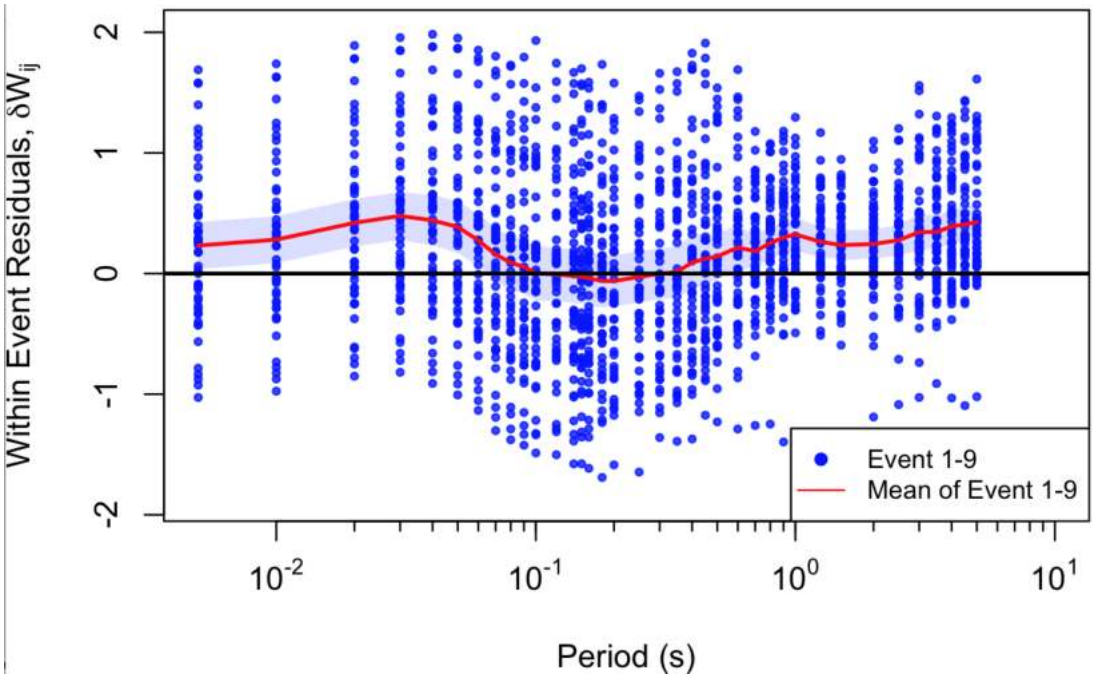

Figure 5.32 Within event residuals for OCDC stations by using recordings from Events 1-9 and Aea18 model with the regional site term developed in this chapter.

5.6 LIMITATIONS

The models for mean site response and within-event standard deviation provided in Section 5.4 apply for the Obihiro area along the Tokachi River, Japan, as shown in Figure 5.2. The model is based on data from seven sites, and could be in error for sites in the study region if they contain peat deposits of significantly different character or thickness. In the absence of validation, it cannot be considered as applicable to peat sites in regions other than Obihiro.

6 NONLINEAR RESPONSE OF SOFT ORGANIC SOIL SITES

For a site amplification model to be applicable over a wide range of input parameters (i.e., weak to strong shaking, soft to stiff site conditions), it is often necessary to supplement components of the model constrained by recorded ground motions with additional components constrained at least in part by the results of simulations. In the case of the Obihiro sites, the data limitation is not necessarily related to poorly represented site conditions, but rather to a relative lack of recordings with strong shaking intensities. As a result, the nonlinear behavior is not likely to be adequately constrained by the available data (e.g., the dataset from the Obihiro stations contains only a single high intensity event). This limitation is addressed in this chapter by performing, and interpreting the results of, one-dimensional (1-D) nonlinear ground response analysis (GRA) to propagate motions through a soil column representing the subsurface conditions at the site or region of interest. These simulations are used, along with the available data, to develop the nonlinear component of the Obihiro site amplification model (the linear portion was presented in Chapter 5). The development of the soil profiles and analysis using *DEEPSOIL* v7.0 (Hashash et al. 2016) are presented subsequently. The results are then interpreted to derive nonlinear site amplification coefficients for modeling purposes.

6.1 SITE CHARACTERIZATION

The subsurface conditions in the downstream region along Kushiro River and Tokachi River were evaluated by reviewing geotechnical investigations performed by the Kushiro Development and Construction Office and Obihiro Development and Construction Office. Data available from these investigations includes boring logs with Standard Penetration Test (SPT) blow counts, Cone Penetration Tests (CPTs), seismic velocities from suspension logging, laboratory testing of soil samples. The format and quantity of data available differs between the two regions and is presented in

Chapter 2. Shear wave velocities for the surficial layers are supplemented by additional geophysical site characterization performed as part of this study using SASW. The subset of information pertinent to developing the soil profiles are presented here.

6.1.1 Soil classification and index properties

A wealth of subsurface information in the form of boring logs with SPT blow counts and laboratory test data is available for the Kushiro area, and includes unit weight, water content, gradation (coefficient of uniformity, mean grain size), density, and organic content. In addition, Atterberg limits, consolidation and unconfined compression tests were performed on cohesive soils and peat. Results from site investigation between KP7.0-11.0 on the left bank is summarized in Table 6.1. The OCR of the silts and clays in Kushiro is estimated to range from 1.2-2.5 based on consolidation tests. Figure 6.1 shows borings and Vs measurements in the downstream region of Kushiro River.

Table 6.1 Laboratory tests along left bank of Kushiro River

Unit	Material	Specific Gravity (Gs)	Natural Water Content (%)	Composition (%)			Liquid Limit	Plastic Limit	Density (g/cm3)	Organic Content (%)
				Gravels	Sand	Fines				
Ap	Peat	1.39-1.73	510-830						1.02-1.05	72-85
As	Silty Sand (fine to medium)	2.59-2.67	23-45	0-2	68-86	12-31				
As	Gravelly Sand	2.51	26	26	73	1				
Ac	Silt (sand seams)	2.63	53	0	21	79	47	12	1.64	
Ac	Sandy Silt	2.57-2.61	35-45	0-4	32-45	51-68	42	9	1.72	
Dg	Silty Sand (fine to medium)	2.62-2.63	22	1-3	72-74	23-27				
Dg	Gravelly Sand	3.65-2.72	14	20-29	63-69	5-12				

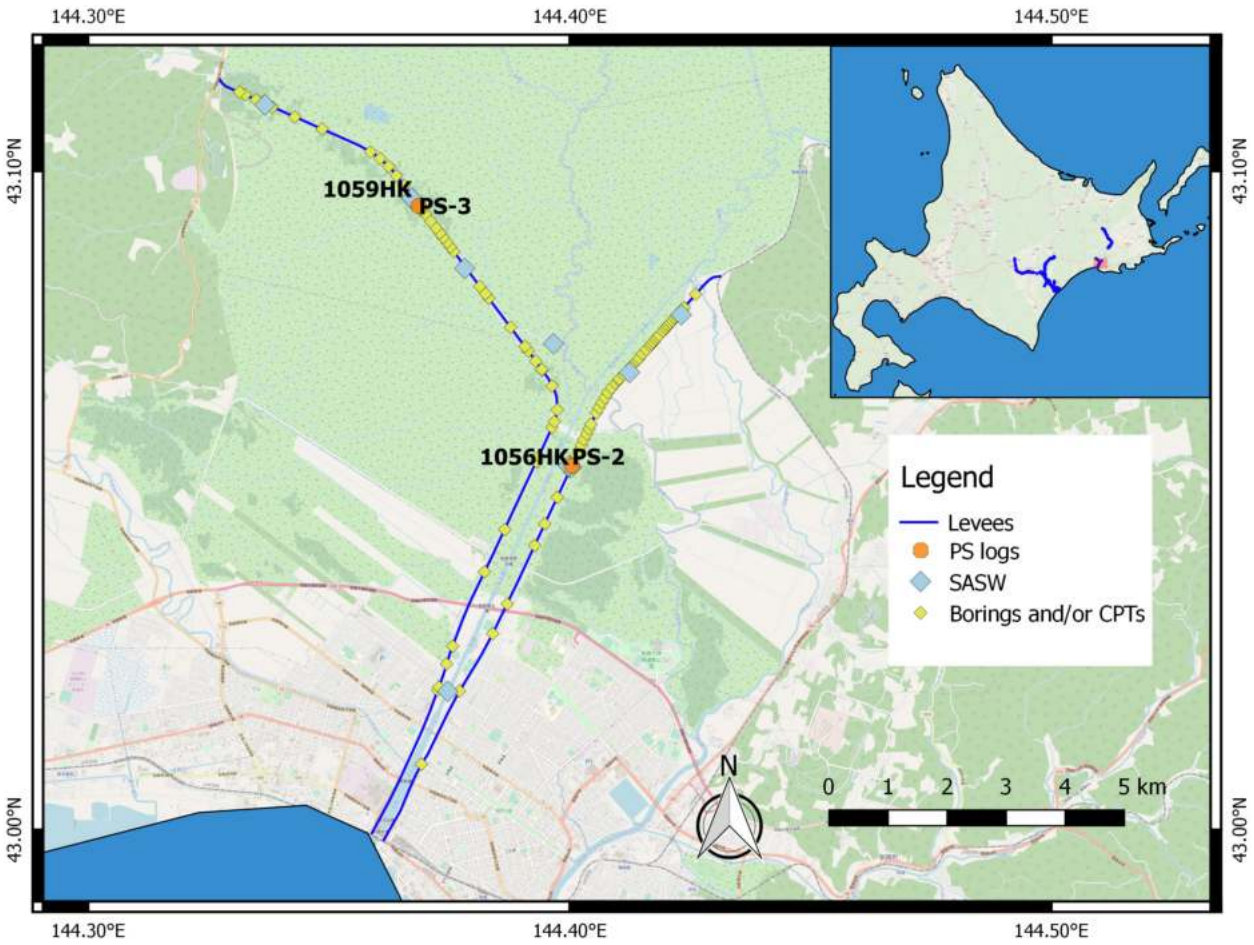

Figure 6.1 Large number of borings are available along the Kushiro levees in downstream marshland and are used to assignment of material properties and MRD relationships. The pair of collocated suspension log (PS-2) and SASW test (1056HK) is used to develop shear wave velocity profiles for the GRA in *DEEPSOIL*.

For the Tokachi region, laboratory tests are limited and the material properties are mostly correlated from soil classification and descriptions from boring logs. Figure 6.2 shows available borings, which are used to estimate the thickness of the soft peat and plastic soils, as well as the depth to firmer material. Plasticity is measured for samples taken from two open excavations performed after the 2003 Tokachi-oki earthquake (section 4.1.6 and 4.1.7); plasticity is assumed to be similar for fill materials sharing the same soil classification and placed during the same time period. The SASW tests are not collocated with the suspension logs as the data was obtained after the geophysical field investigation (Chapter 3) was completed.

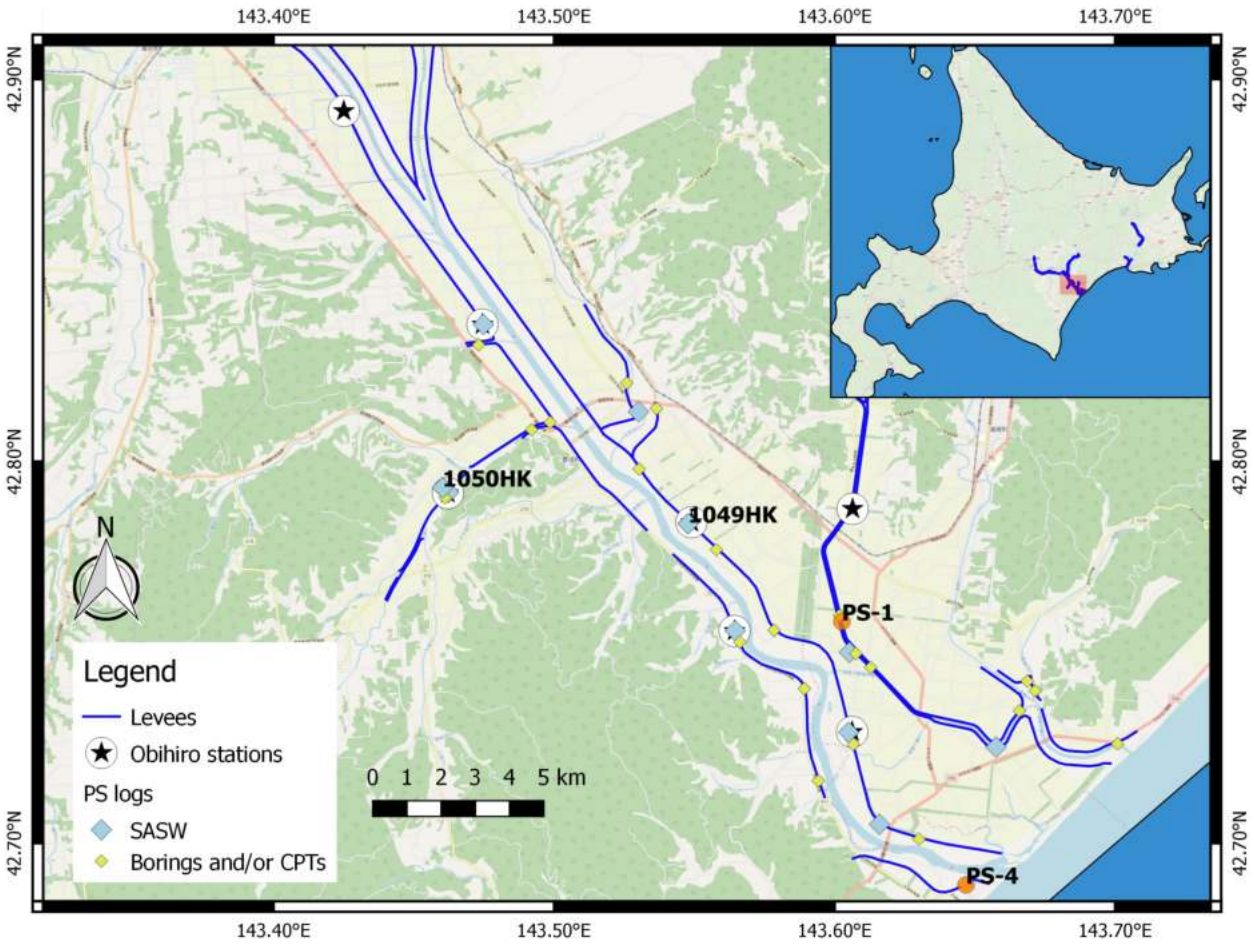

Figure 6.2 Suspension logs and SASW investigations in the downstream region Tokachi River used to develop shear wave velocity profiles. Stratigraphy from nearby borings and CPTs provides soil type for assignment of material properties and MRD relationships.

6.1.2 Shear strength

For cohesive soils, the undrained shear strength is applied below the ground water table. In Tokachi, CPTs were co-located or close to SASW test sites. For these sites, the undrained shear strength is evaluated from the cone tip resistance and an empirical cone factor (Section 4.2.3). Based on test data provided in Sheahan et al. (1996), Stewart et al. (2014) suggests 20-40% increase of shear strength to account for rate effects, due to the faster rate of shearing in earthquake loading than in typical laboratory testing. The lower bound value of 20% is adopted. In Kushiro, where CPTs were not

advanced near the SASW test sites, the undrained shear strength ratio was estimated based on strength normalization (Ladd 1991),

$$\frac{s_u}{\sigma'_{v0}} = S \times OCR^m \tag{6.1}$$

Where typical values of m and S are 0.8 and 0.2-0.25 respectively. The OCR used in Eq. (6.1) is based on consolidation test results.

For cohesionless material, the peak friction angle was estimated from SPT blow counts in a manner consistent with critical state soil mechanics, with a critical state friction angle of 32° assumed for quartz sand (Negussey et al., 1988). Dilation is also assumed to contribute to friction angle (Section 4.2.3), and the friction angle used for analysis range from $\phi' = 38 - 41$ deg. The shear strength is estimated as $\tau_{ff} = \sigma'_v \tan\phi'$, where σ'_v is the vertical effective stress at the middle of the layer, and ϕ' is the average friction angle for the stratigraphic unit.

6.1.3 Shear wave velocity profiles

Downhole suspension logging was performed in Kushiro and Tokachi by the local River Management Offices. In Kushiro, the logs extend to a depth of 75 m for PS-2 on the left bank, and to 60 m on the right bank for PS-1 (Figure 6.3). Both reached relatively firm material with V_S exceeding 300m/s at the base of the borehole. Two suspension logs were performed in Tokachi, to depth of 50 m for PS-1 and to 55 m for PS-2; in both cases Vs exceeds 390 m/s at the base of the boreholes. Each suspension log is accompanied by SPT blow counts and a stratigraphic column. The raw measurements are not provided and the available profiles averaged V_S over depth intervals corresponding roughly to soil type. Due to the post processing, the resolution of the suspension logs is low. For example, both logs indicate $V_S \approx 110$ m/s in the upper 9-11 m, which unexpectedly high for peat. It is likely that the profiles contain

softer units near the surface that are not represented due to averaging and smoothing. With the expectation that the soft surficial layers of peat and organic soils will strongly influence the site response, the suspension logs are supplemented with SASW-based profiles.

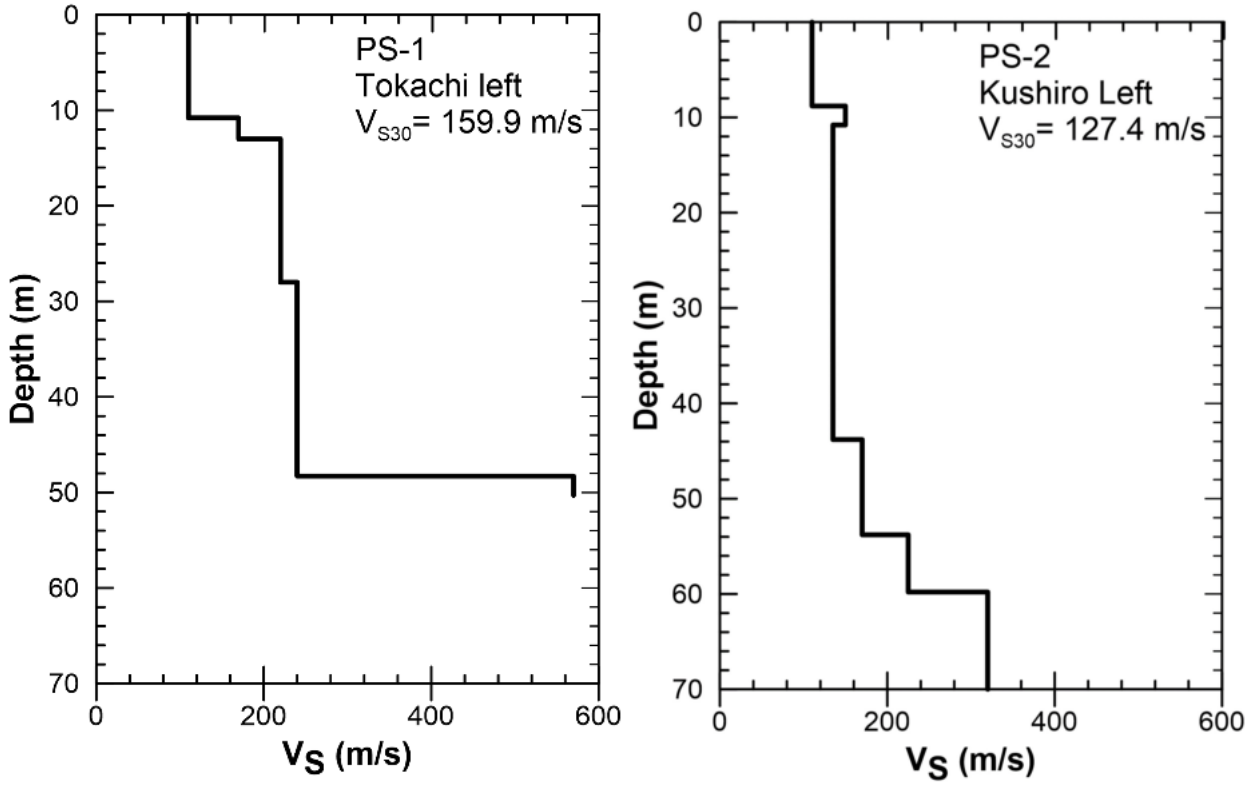

Figure 6.3 Processed shear wave velocity profiles from downhole suspension logging in Tokachi and Kushiro. The logs were presented in this smoothed form by the Hokkaido River Disaster Prevention Research Center and the Kushiro Development and Construction Office.

Two profiles were developed for analysis in the Kushiro and Tokachi regions. For Kushiro, the profiles represent a combination of surface wave data near the ground surface and suspension logging data at greater depth. For Tokachi, the profiles are again based on surface wave data near the surface, but as the SASW was not collocated with a suspension log (the data was made available after the field investigation), the velocities at depth are estimated based on stratigraphy at the SASW site, and velocity gradients in the same material unit based on the suspension logs. Both profiles are extended to sufficient depth such that shear wave velocities of about 300 to 400 m/s are encountered. This reference

condition corresponds to site class II in the Zhao et al. (2016) Ground Motion Models used to develop the empirical site term in Chapter 5. Significant extrapolation would be necessary to extend the profiles to a stiffer reference condition, and would be highly uncertain without any measurements or soil type information at that depth within the study region. Therefore the choice was made to retain a shorter profile. The underlying elastic half-space used for modeling below the seismic velocity profiles has a V_S compatible with the reference site condition.

The objective in developing these profiles was not the capture the full range of conditions present in the respective study regions, which would be needed for a simulation-based estimate of site response as a whole. Rather, the goal is to define the nonlinear component of site response, which are based on the composite profiles shown in Figure 6.4. Both locations are seen to be inversely dispersive from the SASW.

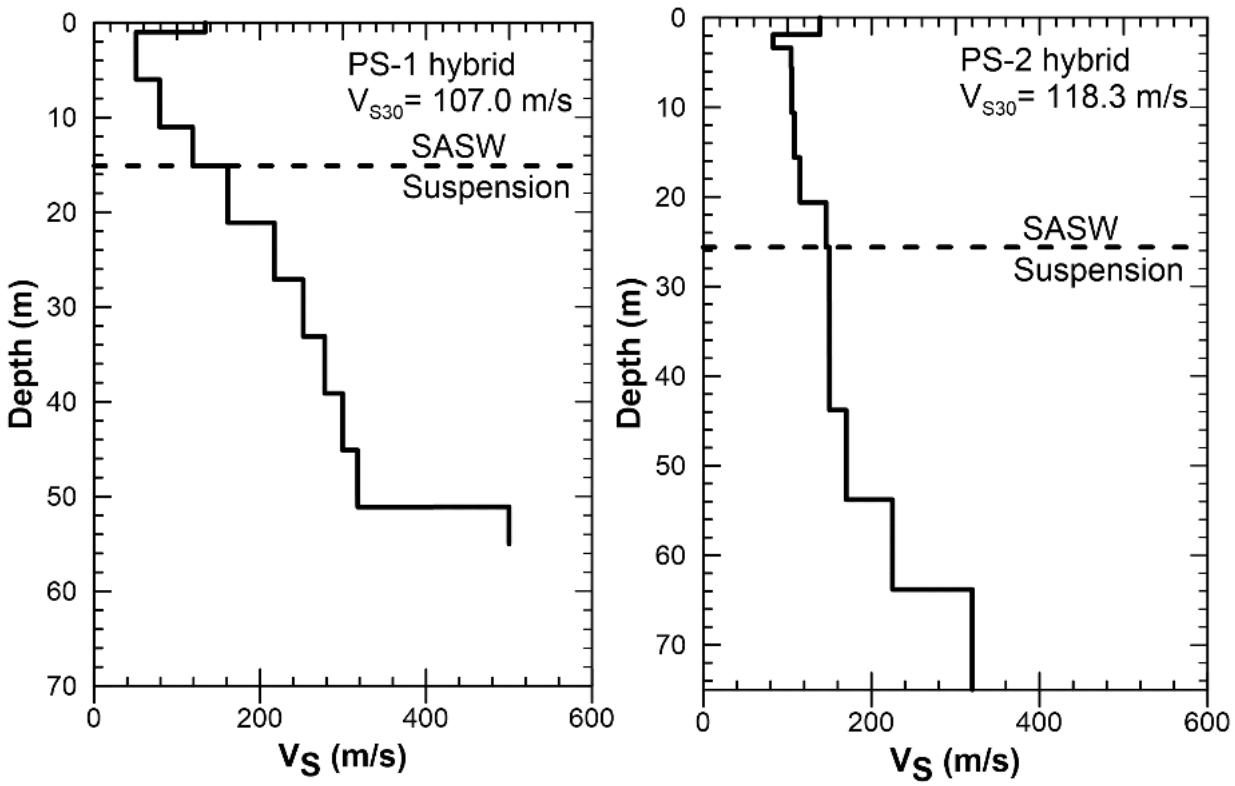

Figure 6.4 Representative shear wave velocity profiles with combining surface wave measurements and suspension logs.

6.1.4 Modulus reduction and damping curves

(a) Available information from literature

The strain-dependence of shear modulus and material damping ratio are characterized by modulus reduction and damping versus shear strain (MRD) curves. The shear stress-shear strain curve (also known as a backbone curve) is often represented with a hyperbolic function. Upon some rearrangement of this function, the modulus reduction curve can be expressed as,

$$\frac{G(\gamma)}{G_{max}} = \frac{1}{1 + \left(\frac{\gamma}{\gamma_r}\right)^{\alpha}} \tag{6.2}$$

where the maximum shear modulus is calculated from the shear wave velocity and mass density,

$$G_{max} = \rho V_s^2 \tag{6.3}$$

Empirical modulus reduction curves are derived by regressing laboratory data to obtain γ_r, the pseudo-reference shear strain where the modulus is reduced to half of G_{max} and α, which is the curvature coefficient that controls the steepness of the curve near γ_r. Both parameters are dependent on the soil properties (e.g., PI and uniformity coefficient) and mean effective stress. Higher γ_r indicates linear behavior over a larger range of shear strains.

Modulus reduction curves (G/G_{max} -γ) were developed using empirical models by Darendeli (2001) for both plastic and non-plastic fine-grained soils (clays and silts). The model by Menq (2003) was applied for granular soils. The input parameters are plasticity index (*PI*), overconsolidation ratio (*OCR*), and mean effective stress (σ'_m) for Darendeli (2001), and the mean grain size (D_{50}), coefficient of uniformity (C_u), and mean effective stress for Menq (2003). Mean effective stress is related to vertical effective stress (σ'_v) through,

$$\sigma'_m = \sigma'_v \left(\frac{1 + 2K_0}{3}\right) \tag{6.4}$$

where K_0 is the coefficient of earth pressure at rest, which is estimated as (Jaky, 1948; Mayne and Kulhawy, 1982),

$$K_0 = (1 - \sin\phi) \times OCR^{\sin\phi} \tag{6.5}$$

The properties are taken from testing performed on samples nearby for Kushiro, and estimated from soil classification and descriptions from the boring logs for Tokachi, where detailed information from lab tests is unavailable.

Empirical models for MRD curves in peat are less well established than for more common soil types (clays, silts, sands). However, various investigators have found the dynamic behavior of peat to differ from that of inorganic soils. Tokimatsu and Sekiguchi (2006) examined recordings of the 2004 **M** 6.6 Niigata-ken Chuetsu earthquake from three nearby stations in Ojiya. Two of the stations are sited on soft surficial soils over stiffer gravel deposits. At the third site, peat is present at depths around 1.5-3.0 m under the K-NET Ojiya station. This peat has V_S of around 50 m/s, as measured from suspension logging. The ignition loss (*LI*) is around 62% for the tested peat sample (*LI* is related to Organic content; ASTM D 2974-00). Cyclic torsional shear tests were conducted on undisturbed hollow specimens to characterize the nonlinear dynamic properties of the surficial soils. The MRD curves presented in Figure 6.5 show this peat material to have high small strain damping (e.g., $D_{min} \approx$ 3-4%) and significantly lower nonlinearity (i.e., larger γ_r) as compared to sands and clays.

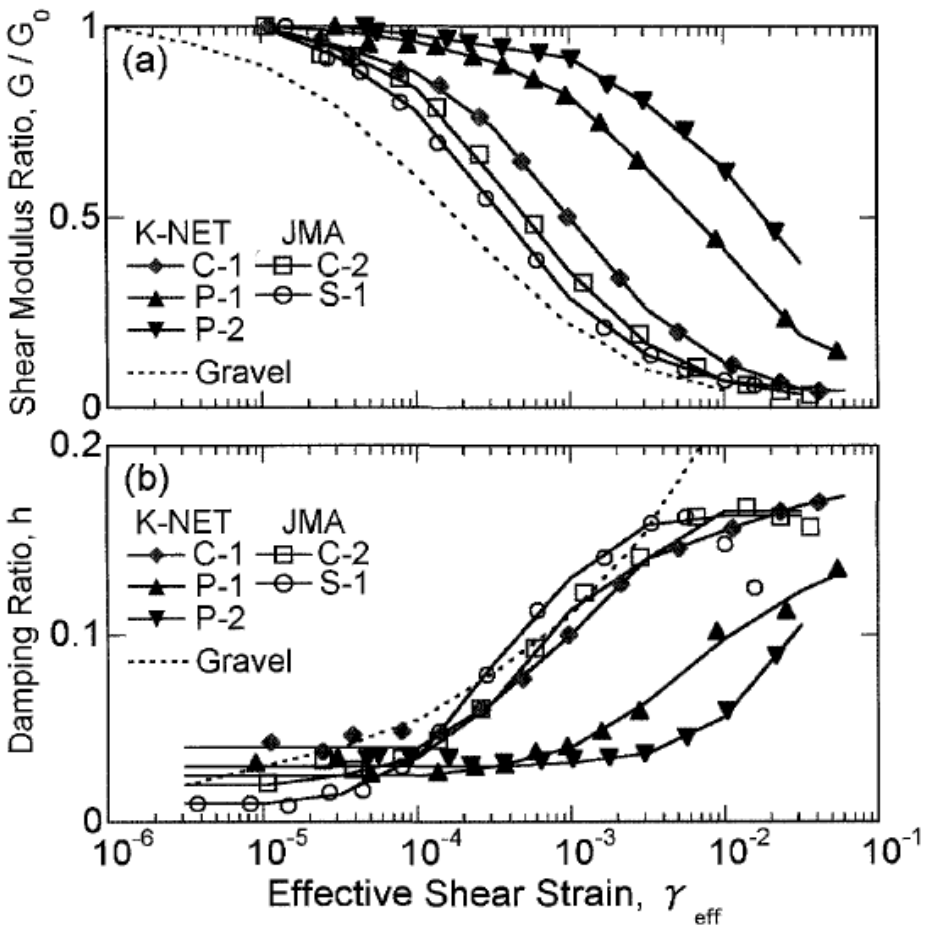

Figure 6.5 Modulus reduction and damping curves from cyclic torsional shear tests on samples of sandy silt (S-1), silty clay (C-1, C-2) and peat (P-1, P-2). Modulus reduction in peats is more gradual with higher damping at small strains (Tokimatsu and Sekiguchi, 2006).

Kishida et al. (2009) developed regression models for the dynamic properties of highly organic soils from a collection of cyclic triaxial and resonant-column/torsional-shear tests. The secant shear modulus (G) and damping ratio are dependent on the shear strain amplitude (γ_c), vertical effective consolidation stresses (σ'_{vc}) and organic content (OC). Increasing OC and σ'_{vc} increase γ_r, making the soil effectively more linear. The OC-dependence of the behavior is similar to PI-dependence classically observed for clays (Vucetic and Dobry 1991). For highly organic soils, the Kishida et al. (2009) model shows that increasing σ'_{vc} has less effect on the modulus reduction behavior. This feature of the model contrasts

with a strong σ'_{vc} effect that has been observed for some of the same peat materials used to develop the model (Wehling et al. 2003).

Hayashi et al. (2018) performed cyclic torsional tests on undisturbed samples collected from seven sites in Hokkaido. The eight samples of peat and two samples of organic clays encompass a range of physical properties, with ignition loss between 18-95%, and natural water content between 143 and 970%. Relationships for maximum shear modulus, reference strain and maximum damping with ignition loss and confining stresses are derived from test data. The Hardin-Drnevich model is applied to the results, but does not match the observed damping well at small strains.

Figure 6.6 compares MRD curves from the peat from Shinotsu in Ebetsu City tested by Hayashi et al. (2018), two peat speciments near Niigata by Tokimatsu and Sekiguchi (2006), and the general model for organic soil by Kishida et al. (2009) (applied with the OC = 67% and σ'_v = 45kPa). D_{min} is high and relatively consistent at around 3% for all the materials. Even among the organic peats tested, P-2 shows very linear behavior over a large range of strains. The test data compiled by Hayashi et al. (2018) is used to represent the peat behavior in both Kushiro and Tokachi, since the samples are from Hokkaido, and therefore may be derived from soil units with a similar geologic history to the peats in the study region.

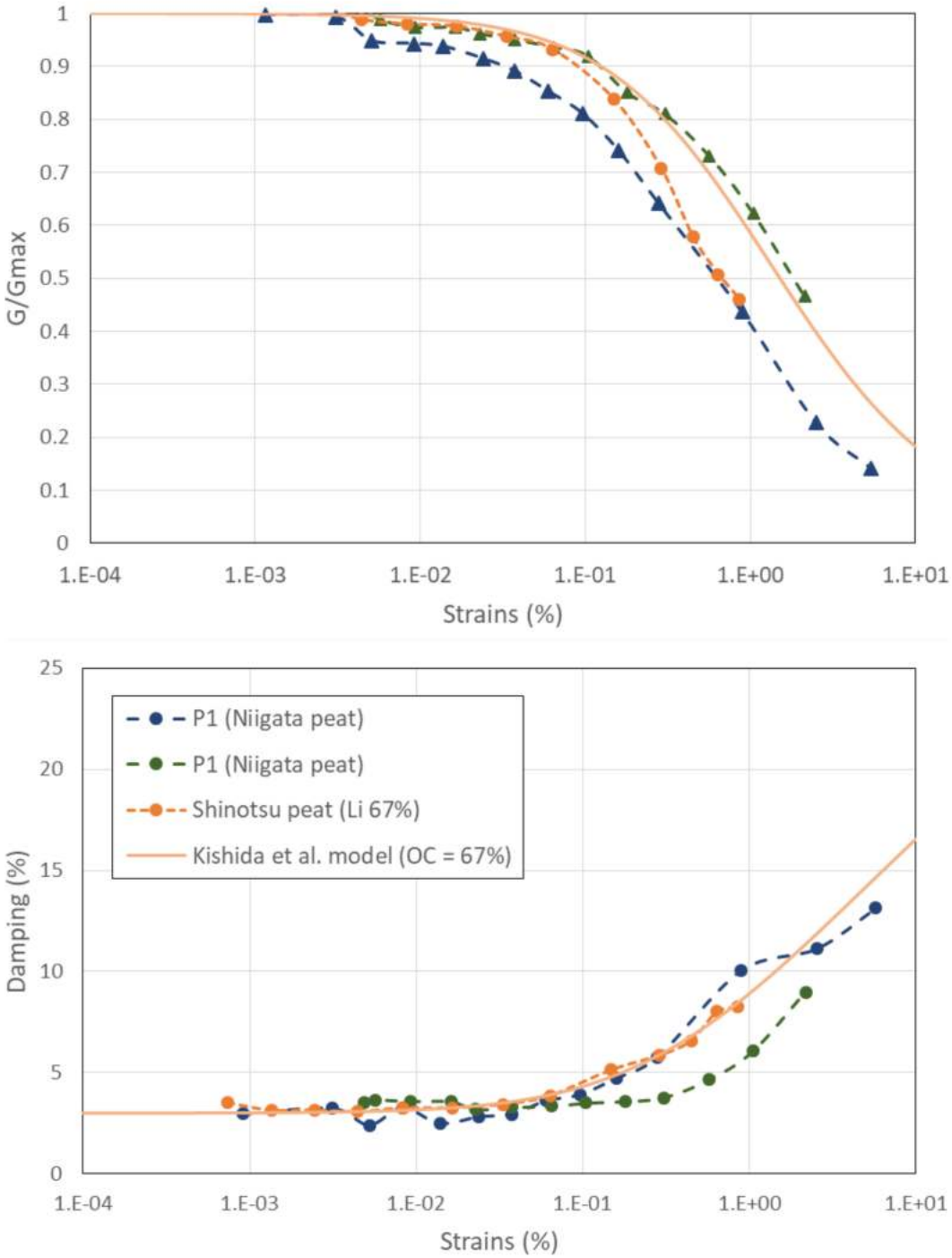

Figure 6.6 MRD curves for Shinotsu peat from Hokkaido (Hayashi et al. 2018), peat from the Niigata region (Tokimatsu and Sekiguchi 2006), and a mean model prediction for organic soils by Kishida et al. (2009).

Figure 6.7 compares MRD curves for organic clays from Hokkaido tested by Hayashi et al. (2018), and the Darendeli (2001) model as applied for clays of variable plasticity. The Hokkaido organic clays lie beyond PI = 100 curves from Darendeli (2001). The Hokkaido materials have very low damping at large strains, but larger D_{min}. The following section describes the MRD curves selected for analysis.

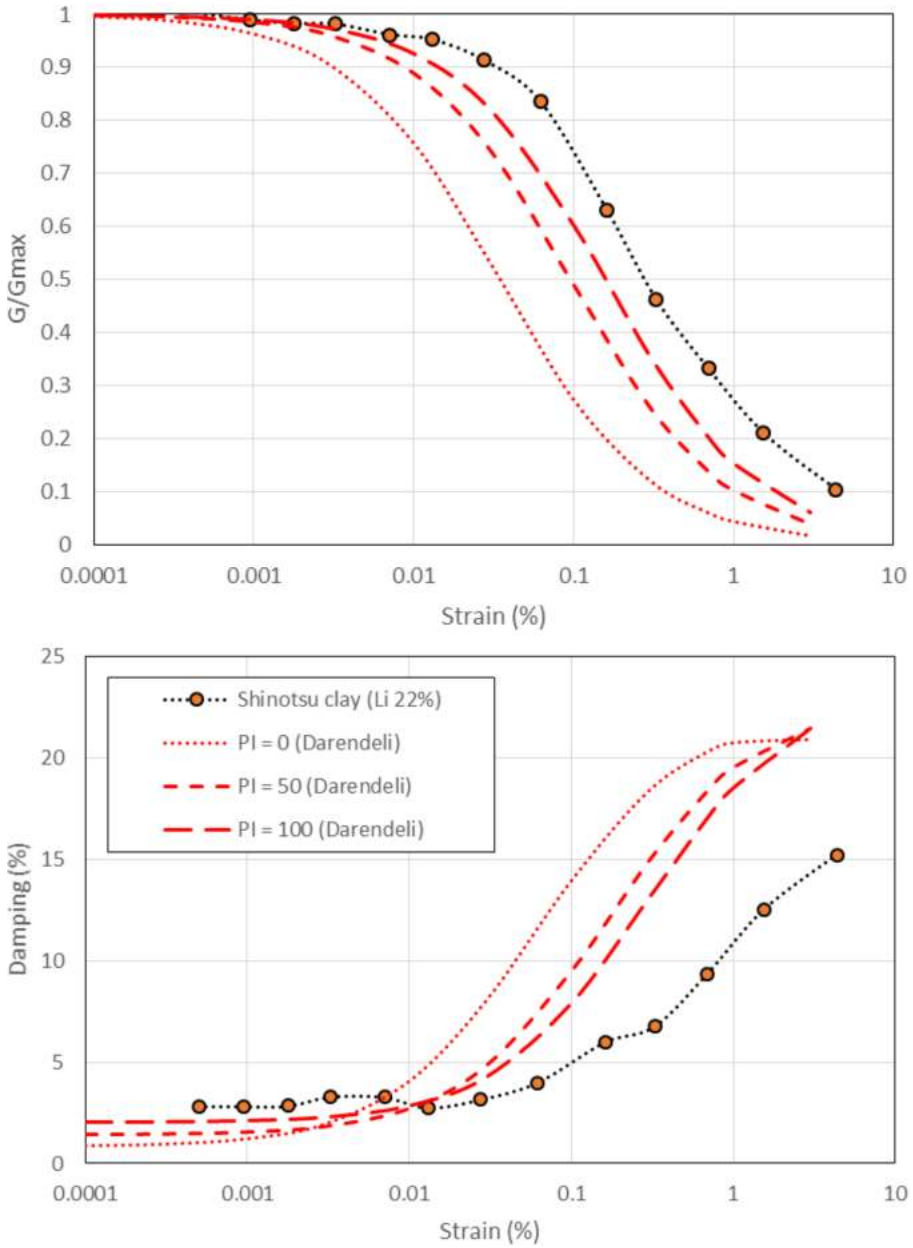

Figure 6.7 Comparison of the Darendeli (2001) modulus reduction and damping curves for clays of variability plasticity to tests on highly organic clays for the Hokkaido region (Hayashi et al., 2018)

(b) MRD relations considered in analysis

Two sets of MRD curves were initially selected for analysis. One set consists of the Darendeli (2001) curves, which are used for clay materials with an assumed PI of 50. In this first set of curves, the peat layers are modeled using test data from Hayashi et al. (2018). The second set of MRD curves again uses the Hayashi et al. (2018) data for the peat layers. However, the Hokkaido organic clay curves were used for clays and silts. This has the joint effect of increasing the small strain damping (approximately from around 1% to 4%) and reducing the nonlinearity.

Additional MRD curves are being considered in ongoing analyses to reduce the level of nonlinearity from what is provided by the two sets of curves that were initially considered. This will be considered in future work.

6.2 INPUT MOTIONS

Strong motion recordings from stations at the surface are specified as outcropping motions at the base of the soil profile in DEEPSOIL. Recordings of subduction events at stations having similar site conditions as those at the base of the modeled soil column are therefore preferred. Two stations, HKD094 (K-NET) and TKCH11 (KiK-net), located in the forearc region of Hokkaido (west of the volcanic front) are selected. The V_S profiles of those sites, as taken from the NIED web site are shown Figure 6.8 (NIED, 2018). The V_{S30} values for these sites are indicated in the figure (326-459 m/s). In the case of the HKD094 site, V_{S30} is established using the extrapolation procedure of Midorikawa and Nogi (2015) as the profile is under 30 m in depth. The recordings from eight subduction events are filtered and processed following PEER procedures (Ancheta et al. 2014), and scaled arithmetically to cover a range of shaking intensities. Table 6.2 lists the selected records and the levels of scaling that were applied.

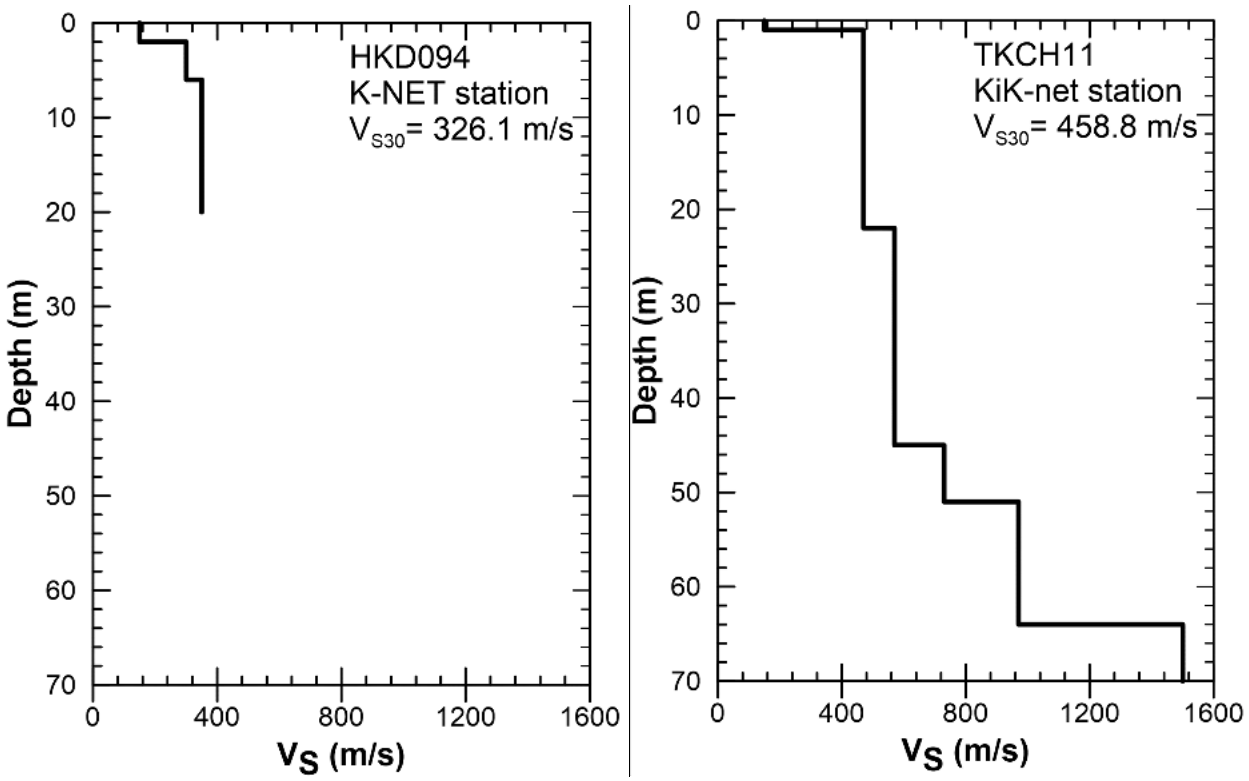

Figure 6.8 V_S profiles for strong motion recording station HKD094 (left) and TKCH11 (right) with to be compatible with the base of the modeled soil column.

Table 6.2 PGA and scaling for input ground motion used for analysis

Station ID	Event	Depth (km)	Magnitude	PGA (g)		Scaling
				NS	EW	
HKD094	10/8/2003	28	5.7	0.0022	0.0022	0.5, 2.0, 3.0, 4.0
HKD094	6/15/1997	99	4.9	0.012	0.013	0.3, 0.5, 3.0
HKD094	8/14/2015	80	5.1	0.02	0.025	0.3, 3.0
HKD094	5/13/1999	104	6.4	0.048	0.05	2.0, 3.0
HKD094	9/26/2003	42	8.0	0.1	0.14	0.3, 0.5, 2.0, 3.0
TKCH11	10/7/2003	28	4.7	0.00065	0.00066	2.0, 3.0, 4.0
TKCH11	9/26/2003	42	5.7	0.23	0.26	0.3, 0.5, 2.0, 3.0
TKCH11	2/2/2013	102	4.9	0.22	0.27	0.3, 0.5, 2.0, 3.0

6.3 GROUND RESPONSE ANALYSIS

Nonlinear ground response analyses were performed using DEEPSOIL v7.0 (Hashash et al 2016), with the soil properties and input motions described in Sections 6.1 and 6.2, respectively. Specific information regarding implementation of the target soil properties from Section 6.1 is summarized here:

- Shear strains in the profiles are expected to be large. As a result, the MRD curves need to apply over a wider strain range than is provided by the curves presented in Section 6.1.4. The General Quadratic Hyperbolic (GQ/H) model (Groholski et al. 2016) was used with the MRD curves from Section 6.1.4 at small strains (up to approximately 0.1-0.5%) and the large strain behavior constrained based on the shear strengths estimated in Section 6.1.2.
- Non-Masing rules were used to ensure that the hysteretic damping provided by unload-reload relationships reasonably match the target damping (Phillips and Hashash, 2009).
- As the maximum frequency a layer can propagate is $f_{max} = V_s/4H$, the initial layer thicknesses are further subdivided to ensure the maximum frequency that can propagate exceeds 35 Hz. This is particularly important for the soft surficial sediments (e.g., peat), which otherwise could produce artificially low PSA at short periods as a result of numerical filtering of high frequency waves (Kwok et al. 2007; Hashash et al., 2011).

In addition to the nonlinear analysis, linear (visco-elastic) analysis was performed in which modulus reduction does not occur and damping remains at D_{min} regardless of strain level. This provides an estimate of the linear amplification. Pore pressure generation was not considered in any of the analyses since the majority of the profile contains peat and clays.

6.3.1 Initial results and damping adjustments

Linear and non-linear analysis are performed for each input ground motion and each of the profiles. Site amplification at a given spectral period is taken as the ratio between the spectral acceleration at the surface and the input motion, given by,

$$Y = \frac{PSA_{surface}}{PSA_{input}} \tag{6.6}$$

Site amplifications computed in this manner for spectral periods of 0.01, 0.05, 0.1, 0.5, 1.0 and 5.0 s are plotted as a function of the input peak acceleration (PGA_r) in Figure 6.9. Results of the linear analyses are plotted along the y-axis (PGA_r = 0.001 g). The simulation results in Figure 6.9 are fitted using the following expression for nonlinear site response (Stewart et al. 2017)

$$f_{site} = f_1 + f_2 \left(\frac{f_3 + PGA_r}{f_3}\right) \tag{6.7}$$

Coefficients for the nonlinear amplification function are obtained by fixing f_3 at 0.1g and then regressing coefficients f_1 and f_2. The amplification is systematically higher with the Tokachi profile for periods between 0.5-1.0 s. The natural periods of the Tokachi and Kushiro profiles are around 1.5 s and 1.9 s respectively. Hence, the divergence for PSA at 0.5-1.0 s is not likely related to fundamental mode responses. The current interpretation is that the Tokachi profile has a stronger second mode response within this period range. Beyond the site period, GRA are unable to reliably predict site response and it is recommended to estimate the site terms from semi-empirical models (Stewart et al. 2014).

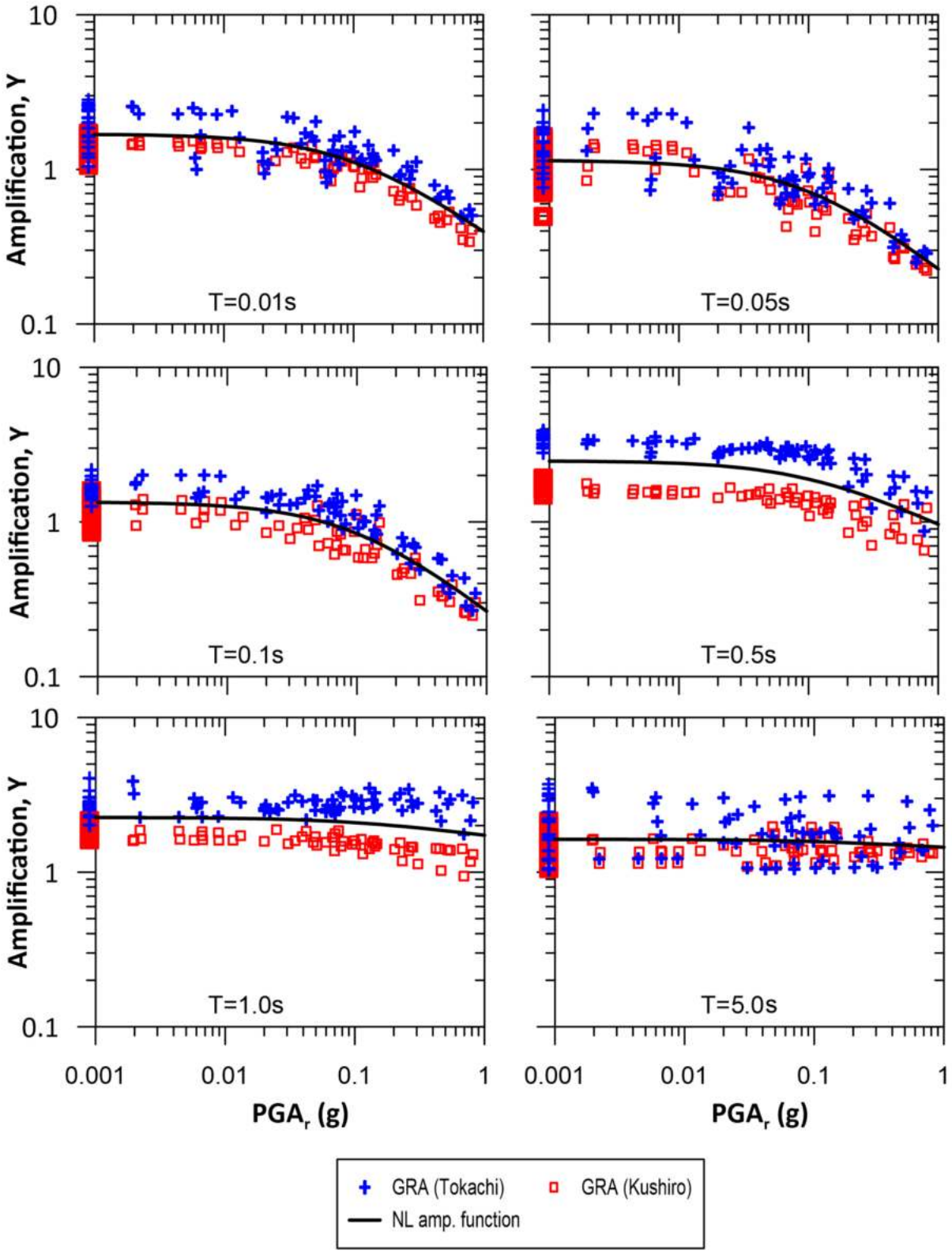

Figure 6.9 GRA results and fitted nonlinear amplification model. Amplification for Tokachi profile is systematically higher for Kushiro, particularly at periods between 0.5-1.0 s.

Since the motivation for performing ground response analyses is to constrain the nonlinear component of the site amplification model (i.e., f_1 is set separately as given in Chapter 5), the between-motion and between-profile variations among nonlinear amplification results can be largely removed by normalizing nonlinear amplification values (Y_{NL}) by their linear amplification counterpart for the same input motion and V_s profile Y_{lin}),

$$Y_{normalized} = \frac{Y_{NL}}{Y_{lin}} \tag{6.8}$$

Figure 6.10Figure 7.7 shows the normalized amplification values, which have significantly reduced scatter. This data can be fit with a modified form of Eq. 6.8 as follows:

$$f_{NL} = f_2 \left(\frac{f_3 + PGA_r}{f_3} \right) \tag{6.9}$$

This approach avoids the fitted function passing between the two clusters of data points from the different profiles, and leads to more statistically stable estimates of nonlinear parameters f_2 as seen in Figure 6.10.

The analysis is performed for both sets of MRD curves given in Section 6.1.4, which produces different estimates of f_2. The Hayashi et al. (2018) MRD curves produce less nonlinearity than the Darendeli (2001) curves. Figure 6.11 shows the resulting f_{NL} functions with empirical data from Section 5.4. The data contain a single event with sufficient shaking intensity to produce nonlinearity, and the empirical fit is shown together with its 95% confidence interval. The functions fitted to the simulated data are lower than the empirical curves, particularly at short periods where they are below the 95% confidence interval.

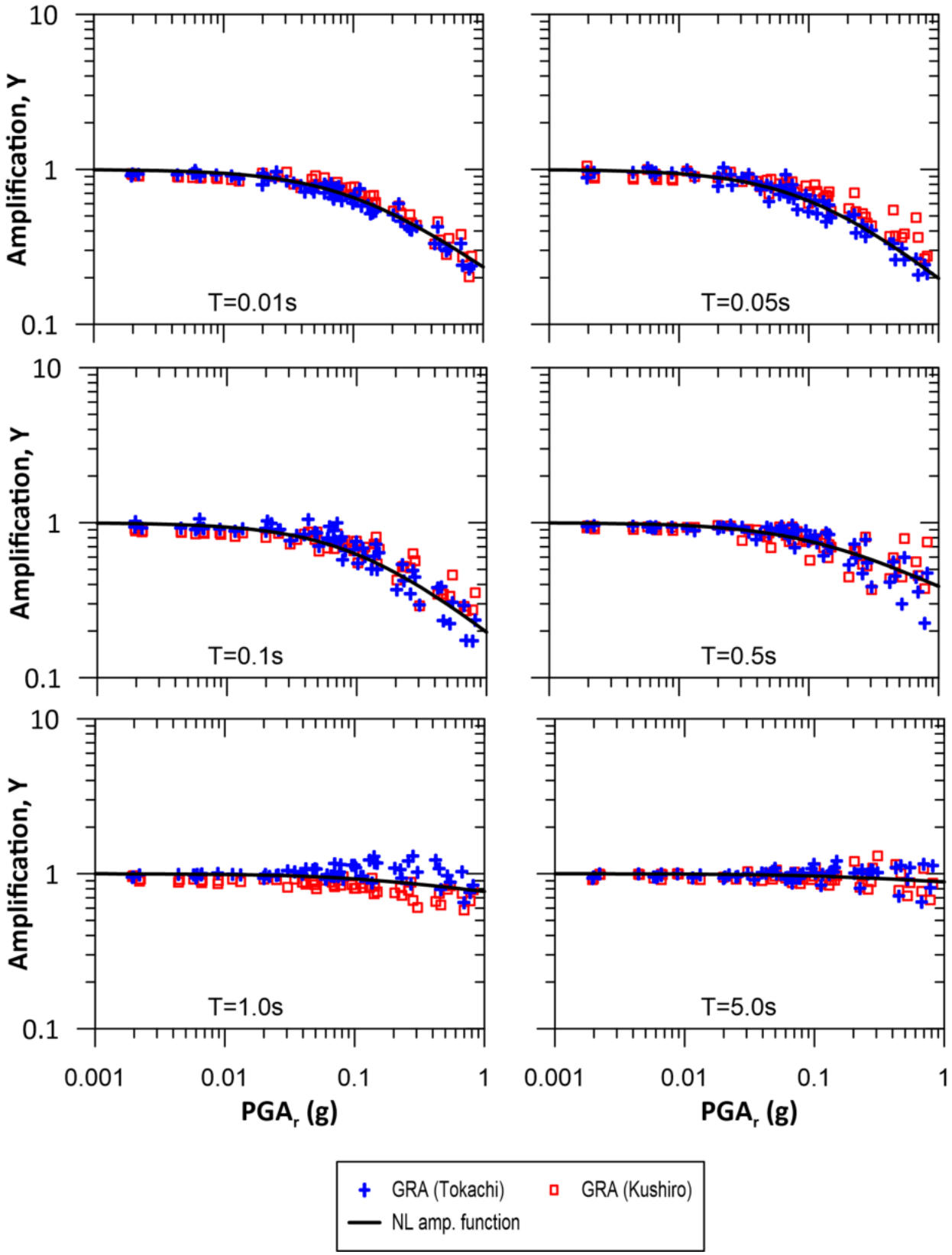

Figure 6.10 Normalized amplification highlighting the effects of nonlinearity.

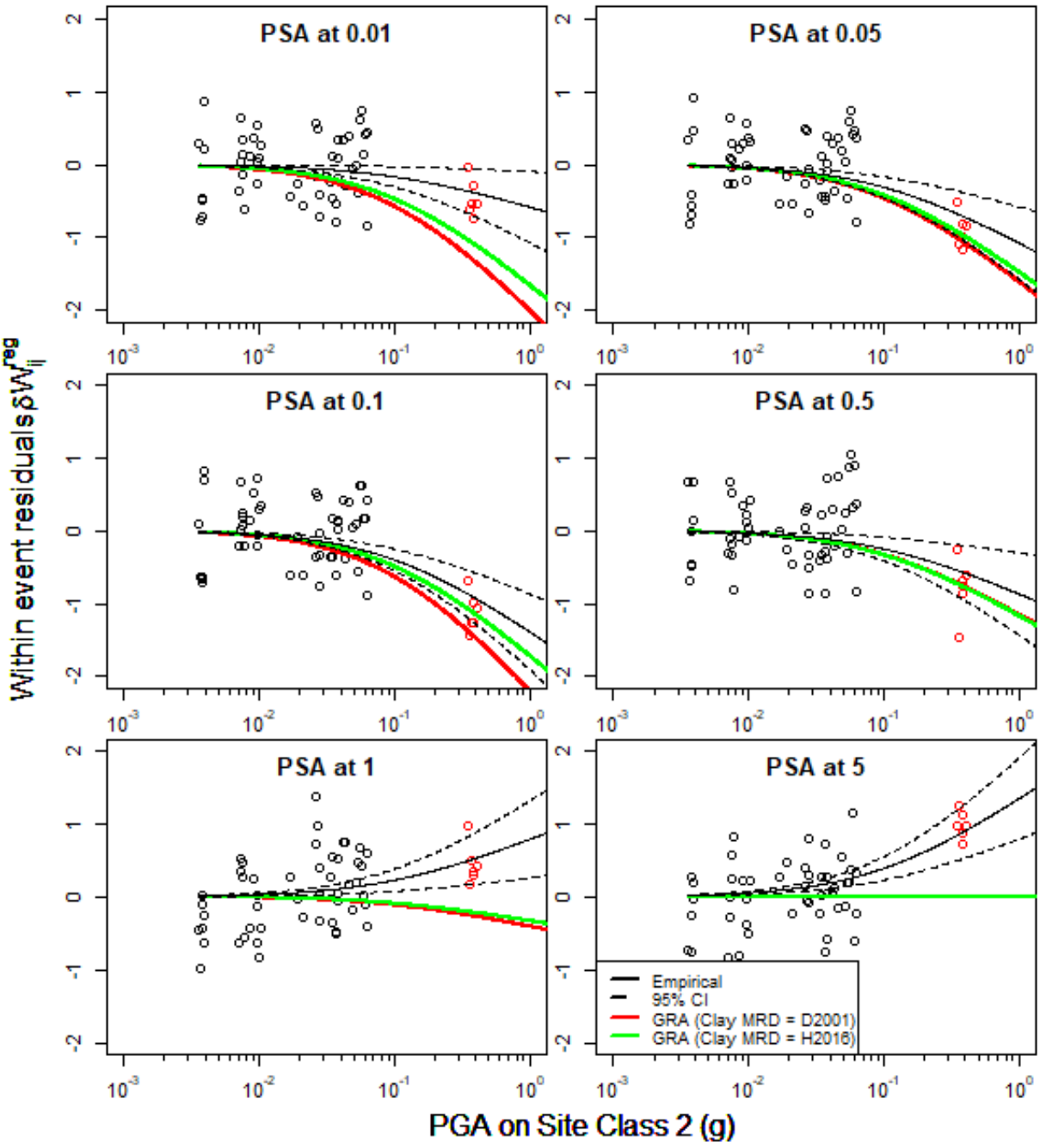

Figure 6.11 Comparison of nonlinear amplification functions based on data and ground response analysis. At short periods, the simulation results fall outside the 95% confidence interval from data.

The nonlinear parameters from all three analyses smoothed across the spectra periods are plotted in Figure 6.12, and values of f_2 are given in Table 6.3 for select periods. More negative f_2 values imply more nonlinearity and stronger deamplification as shaking intensity increases. As noted previously, the empirical data implies lower nonlinearity than the simulations.

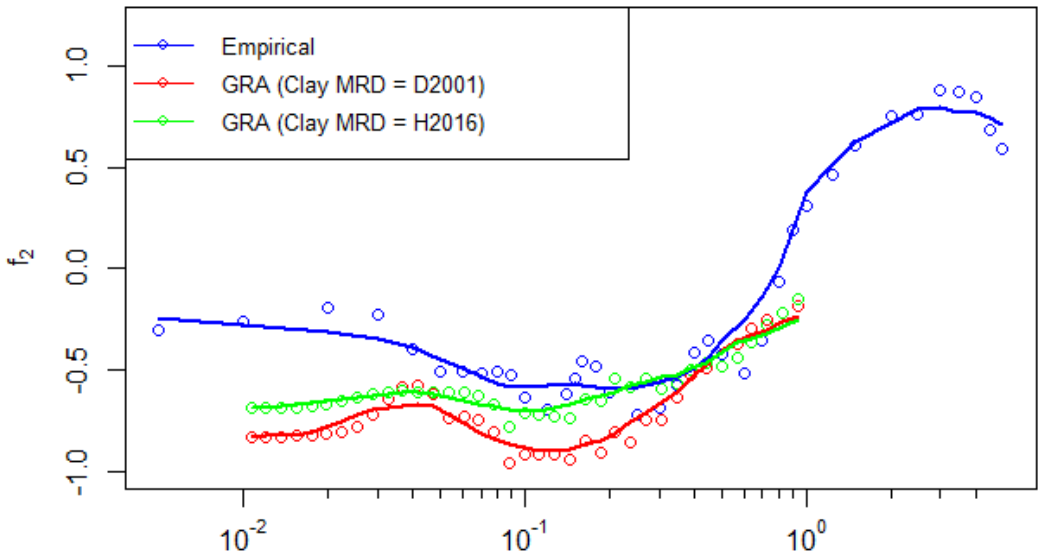

Figure 6.12 f_2 derived from data and GRA smoothed across periods. The GRA are performed with MRD curves for clays based on Hayashi et al. (2018) and Darendeli (2001), with the latter showing more nonlinearity.

Table 6.3 Values of f_2 regressed from empirical data and GRA with different MRD relationship.

Period (s)	Nonlinear term f_2		
	Empirical	GRA (D01)	GRA (Hea16)
0.01	-0.279	-0.831	-0.687
0.02	-0.317	-0.78	-0.656
0.05	-0.446	-0.701	-0.631
0.1	-0.589	-0.889	-0.71
0.2	-0.591	-0.837	-0.628
0.5	-0.355	-0.42	-0.42
0.9	0.192	-0.239	-0.254
0.01	-0.279	-0.831	-0.687

The amplification functions derived above can be compared to results from two other studies involving sites and profiles with highly organic peat soils. Kishida et al. (2009b) (Kea09) developed a site response model (conceptually similar to Eq. 6.7, but with a different function) for the Sacramento-San Joaquin Delta using 1-D equivalent linear GRA for eighteen soil profiles, all of which contains highly organic soils ranging from 1 to 9 m thick. The dynamic soil properties are defined based on Kishida et al. (2009a). Monte Carlo simulations are used to introduce randomness to the dynamic soil properties. The reference condition is taken as the NERHP site class D based on the V_S of the dense sand layer below the organic soils. The results are regressed against combinations of parameters, which included PGA on reference site condition, M_W, S_1 and V_{S10}. S_1 is defined as the ratio of Sa(1.0) and Sa(0.2), and is selected to represent spectral shape of the ground motion. Model 3 depends on PGA and M_W only, and is adopted for comparison.

Terronez (2017) examined two profiles in the Kushiro basin and developed amplification functions using ground response analyses in *DEEPSOIL*. Differences between the analyses performed by Terronez (2017) (T17) and those performed in this study include: 1) the T17 V_S profiles are correlated from blow counts using Kwak et al. (2015) and are not measured, 2) T17 used MRD curves for fine grained soils from Darendeli (2001) and for peat from on Kishida et al. (2009a), and 3) ground motions from crustal strike-slip earthquakes compiled by (Baker et al., 2011) were used. The reference conditions are taken as 450 m/s and 600 m/s for the profiles on the west and east side of the Kushiro basin respectively.

The amplification functions from this study are compared to those recommended by Kea09 (Model 3) and T17 in Figure 6.13 with and without the linear term. The results shown for comparison purposes from this study include the empirical amplification (Chapter 5) and the GRA-based model as derived using Hayashi et al. (2018) MRD curves. While linear terms cannot be directly compared since each

study considered different reference conditions, the empirical linear terms significantly exceed those based on simulations. The data likely contain site effects (e.g., basin effects) that 1-D GRA is unable to capture. Considering only the nonlinear portion of the site response, Kea09 and the empirical model are similar. The GRA-based model for the Hokkaido sites in this study are similar to those from T17, both of which show more nonlinearity than the empirical or Kea09 models.

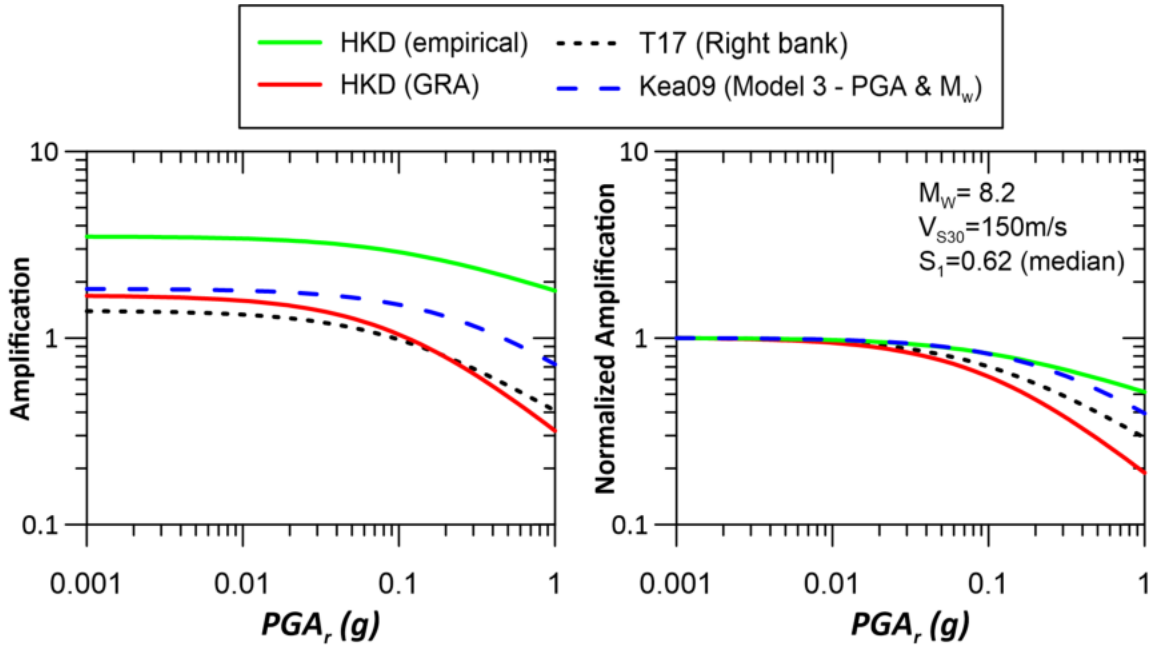

Figure 6.13 Amplification functions for peat sites from this study compared with GRA by Terronez (2017) and Kishida et al. (2009). Empirically derived site amplification function shows more linear amplification and lower nonlinearity than the simulations.

6.4 SUMMARY

A site amplification model is developed for the Tokachi and Kushiro regions based on 1-D linear and nonlinear ground response analyses (GRA) with two profiles and a range of input motions. Two sets of MRD relationships are considered for the thick layer of fine grained soils underlying the surficial peat, and the selection of the dynamic properties significantly affects the GRA results. At short periods, the nonlinear term derived from 1-D GRA is more negative and suggests more nonlinearity than is

evident from the data. At longer periods, the nonlinear factor lies within the 95% confidence interval of the values regressed from the data. The GRA would benefit from additional profiles to consider the sensitivity of the results to V_S and material properties. The empirical site amplification function is adopted for ground motion estimated subsequently. This selection is reinforced by the similarity of the nonlinear model to a previously published model for peaty sites (Kishida et al. 2009b).

7 DEVELOPMENT OF FRAGILITY FUNCTIONS

7.1 INTRODUCTION

The Pacific Earthquake Engineering Research (PEER) center developed the performance-based earthquake engineering (PBEE) methodology to estimate losses associated with future earthquakes. The average annual rate of exceeding a particular level of the decision variable is obtained through the triple integral (Moehle and Deierlein, 2004),

$$\lambda(\mathrm{DV}) = \int_{dm}\int_{edp}\int_{im} \mathrm{G}(\mathrm{DV}|\mathrm{DM})\ \mathrm{dG}(\mathrm{DM}|\mathrm{EDP})\ \mathrm{dG}(\mathrm{EDP}|\mathrm{IM})\ \mathrm{d}\lambda(\mathrm{IM}) \tag{7.1}$$

The decision variable can be quantities such as repair cost, casualty and downtime which are of interest to stakeholders. The remaining variables in the framework consists of DM, EDP and IM. DM represents a damage measure, such as freeboard loss for a dam or levee, or cracking of a reinforced concrete member. EDP is an engineering demand parameter, such as slope displacement or settlement of a soil structure, or inter-story drift ratio of a building. IM is an intensity measure used to characterize the ground shaking intensity, such as PGA, PGV, or spectral acceleration. $G(x|y) = P(X > x|Y = y)$ represents the probability of exceeding a given value of X conditioned on Y = y, and $dG(EDP|IM)$ represents the slope of $G(x|y)$ with respect to y. A fragility function links the structure performance to loading intensity by providing the probability of exceeding a damage measure as a function of an intensity measure (IM) or engineering design parameter (EDP).

The Delta Risk Management Strategy (DRMS) estimated the risks of levee failure in the California Bay-Delta region using the PBEE methodology. Their seismic levee fragility functions are obtained from Monte Carlo simulations by considering the horizontal levee deformation as a function of the earthquake magnitude and peak ground accelerations, which is combined with a judgment-based

probability of levee breaching conditioned on loss of freeboard. Vorogushyn et al. (2009) developed fragility curves for levees considering other failure mechanisms, such as overtopping, piping, and seepage conditioned on height of water in the channel impounded by the levee and duration of flooding using Monte Carlo simulations. Kwak et al. (2016) considered flood control levees along the Shinano River and developed fragility functions based on field performance during the 2004 **M** 6.6 Niigata-ken Chuetsu and 2007 **M** 6.6 Niigata-ken Chuetsu-oki earthquakes. The levees are founded predominantly on sands and gravels with low fines content, and peat is rarely encountered.

For this study, fragility functions are derived empirically from field performance of levees along the Kushiro and Tokachi Rivers. Downstream regions are considered, where peaty organic soils are present in the levee foundations, as well as upstream regions without organic soils in the levee foundations.

7.2 DAMAGE DATA

The damage data comprises information on levee performance, which is observed in post-event reconnaissance, and the imposed loading, which is represented here by a ground motion intensity measure. Table 7.1 summarizes six analysis methods presented by Porter et al. (2007) for synthesizing fragility functions depending on the damage data available. In Table 7.1, IM can be substituted for EDP as the conditioning variable.

For the levee systems and earthquakes considered, the performance of the levee segments are known, and the maximum shaking intensities are estimated, falling under Method B in the above framework. Section 2.4 summarizes available observations along the levees from both earthquakes considered, and the assignment of damage levels based on crack dimensions and subsidence. The maximum demand experienced by the levee segments are characterized by the PGA, and the procedure to estimate PGA along the levees are presented subsequently.

Table 7.1 Analysis methods and data employed (Porter et al., 2007)

Method	Data used
A. Actual failure EDP	All specimens failed at observed values of EDP
B. Bounding EDP	Some specimens failed; maximum EDP for each is known
C. Capable EDP	No specimens failed; maximum EDP for each is known
D. Derived fragility	Fragility functions produced analytically
E. Expert opinion	Expert judgment is used
U. Updating	Enhance existing fragility functions with new method-B data

7.3 GROUND MOTION DISTRIBUTION

Shaking intensity is used as the primary demand parameter for levee damage. Ideally ground motion is recorded at the location of interest, however recording stations are sparse relative to the spatial extent of the levees. Spatial interpolation of ground motions from available recording stations is necessary to estimate ground motion at the levee segments. Kriging is a linear interpolation method for estimating a spatially continuous variable from observations at limited locations. Values at locations without observations are solved for by minimizing the mean squared error of prediction based on available observations together with a correlation function. The correlation between two points are described by the semi-variogram, which expresses the semi-variances of the data as a function of separation distance. This reflects the physical phenomenon that two closely located points will have similar ground motions since travel path and site conditions are comparable. Kriging is thus useful for interpolating observed recordings to estimate motions at the locations of interest.

A key assumption inherent to the simple Kriging method is that the variable is generated by a stationary process (variables have a constant mean in space and/or time). Levees are typically founded on alluvial deposits that are softer than the soils outside of the floodplain, where recording stations are usually sited. Figure 7.1 shows the distribution of V_{S30} at the recording stations and from measurements along

the levees in the downstream region of both river systems. The latter is a combination of existing shear wave velocity profiles from KDCO and ODCO, and the geophysical site investigation presented in Chapter 3. The V_{S30} at the levees is mostly between 100 - 200 m/s, while it generally exceeds 200 m/s at the stations. Seismic site effects are different at soft and relatively stiff soil sites, thus the systematic differences between site conditions at the recording stations and the levees would be expected to bias interpolated ground motion if Kriging were performed on the ground motions directly. These differences could be especially acute for the present application because of the unusually soft peaty organic soils underlying the levees, which would be expected to produce strong differences from non-peat conditions as encountered at many of the recording stations. Therefore direct interpolations from the stations without accounting for the difference in site response are likely to be inaccurate.

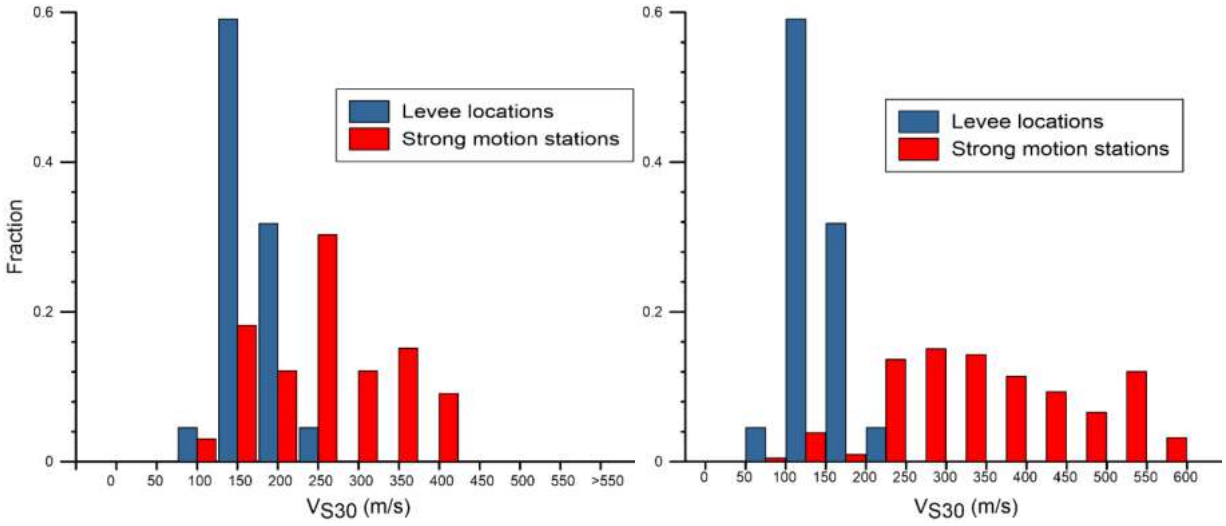

Figure 7.1 Distribution of V_{S30} at strong motion stations that recorded the 1993 (left) and 2003 (right) events compared to distribution of V_{S30} measured at the levees. Site conditions at levees are generally softer than at the recording stations and at the lower limit of empirical site amplification models.

Accordingly, spatial interpolation is not performed directly on the measured intensity measures from the stations, but rather on the within-event residuals of a suitable ground motion model (GMM) based on the methodology presented by Kwak et al., (2016). The Kriging method is applied to the within-

event residuals (Eq. 5.4), a spatial map of the deviation from the GMM event-specific median prediction. This approach accounts for the effects of different site conditions across the study region, to the extent that the GMM is able to capture them. The methodology is as follows:

1. Estimate V_{S30} at recording stations and levees from measured shear wave velocity profiles. If measurements are unavailable, use geomorphic proxies (e.g., Wakamatsu & Matsuoka, 2013) or interpolate from nearby measurements.
2. For earthquake *i*, the total residual is the difference between intensity measures from recording *j* and the median from the selected GMM for the magnitude, distance, and site conditions at site *j* during event *i*. The within-event residual subtracts the event term from the total residual, and is computed as:

$$\delta W_{i,j} = \ln\left(IM_{i,j}^{rec}\right) - \left(\mu_{i,j} + \eta_{E,i}\right) \tag{7.2}$$

Where $IM_{i,j}^{rec}$ = intensity measure from recording *j*

$\mu_{i,j}$ = GMM median in natural log units

$\eta_{E,i}$ = event term for earthquake *i*

3. Apply the Kriging method to obtain a map of the within-event residuals.
4. Compute an estimate of IM at site as:

$$\ln\left(IM_{i,k}\right) = \delta W_{i,k}^{K} + \mu_{i,k} + \eta_{E,i} \tag{7.3}$$

Where $\mu_{i,k}$ = GMM median in natural log units for conditions at site *k*

$\delta W_{i,k}^{K}$ = residual at site *k* estimated from Kriging

In this approach, the selection of a suitable GMM is critical. GMMs by Abrahamson et al. (2018) and Zhao et al. (2016b, 2016c) are chosen as they are developed from datasets of subduction events with

large proportions of Japanese recordings, and perform well against existing data from Japan as a whole in capturing observed trends such as magnitude saturation and magnitude dependent distance scaling (although local variations in path effects are encountered in Hokkaido that these models do not capture; Section 5.3.1). Both include a V_{S30}-dependent nonlinear site term, which is critical for the combination of strong shaking and soft sites in the downstream regions during both the 1993 and 2003 earthquakes, where large strains and nonlinearity are anticipated.

Semi-variograms are fitted to describe the spatial correlation of empirical data at short separation distances. These models are used in Kriging to characterize the relative influence of different observations on an interpolated value at a point of interest, with closer stations having stronger correlation and more influence on the resulting estimate (Jayaram and Baker, 2009). The Kriging process only considered stations in the forearc region of Hokkaido Island, as both levee systems are within the forearc. This avoids potential bias from inaccurate modeling of distance attenuation in the backarc and for travel paths between Hokkaido and Honshu (Section 5.3.1). The distribution of interpolated residuals for the 2003 earthquake is shown in Figure 7.2 for the forearc region. The number of recording stations and the coverage is drastically lower for the 1993 event, and the variograms developed from the 2003 event are applied here.

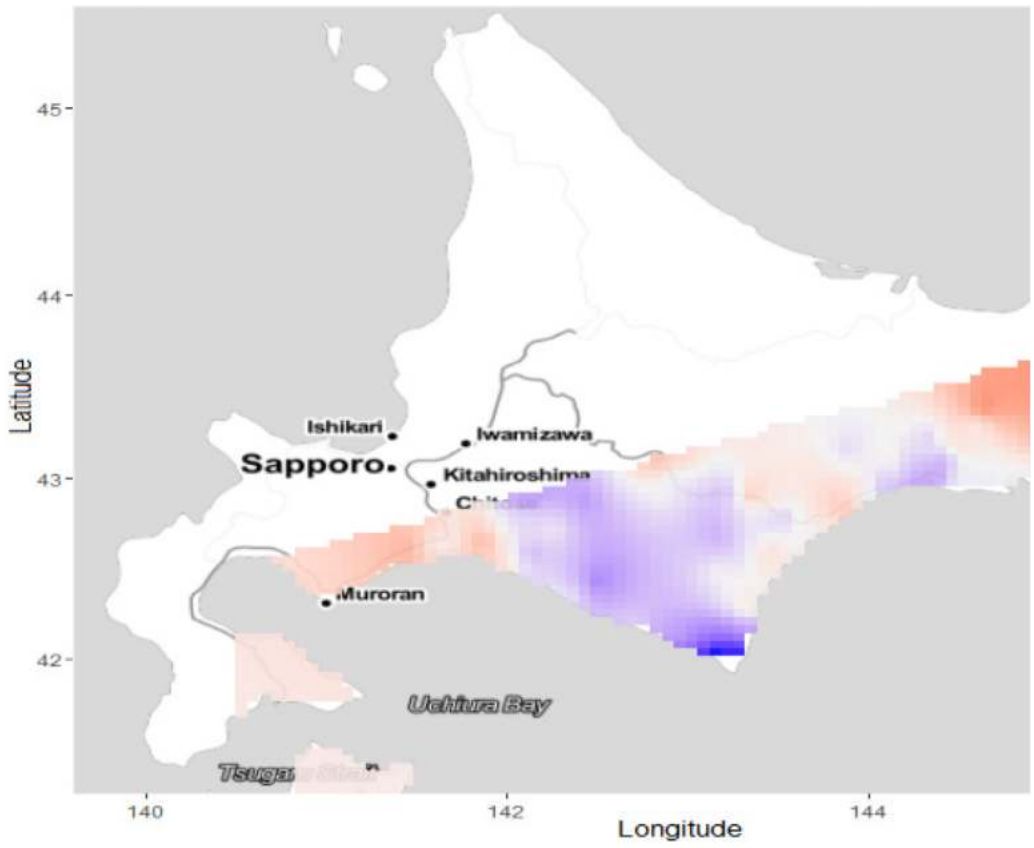

Figure 7.2 Within-event residuals with respect to Zea16 GMM in the forearc region for 2003 earthquake.

The region-specific site amplification models developed from the recordings along the Tokachi River (Chapters 5 and 6) are applied in place of the site terms from the GMMs in the shaded regions shown in Figure 7.3. The Tokachi and Kushiro regions have similar subsurface conditions, which are assumed to be compatible with the site conditions at the Obihiro stations considered in the development of the region-specific model. The organic deposits underlain by thick soft sediments at those sites are not well represented by ergodic site terms in the GMMs. The predictions using the region-specific site terms are assumed to transition linearly to the ergodic prediction over a 5 km zone beyond the edge of the shaded region in Figure 7.3 in order to avoid introducing unrealistic jumps at the edges of the shaded regions.

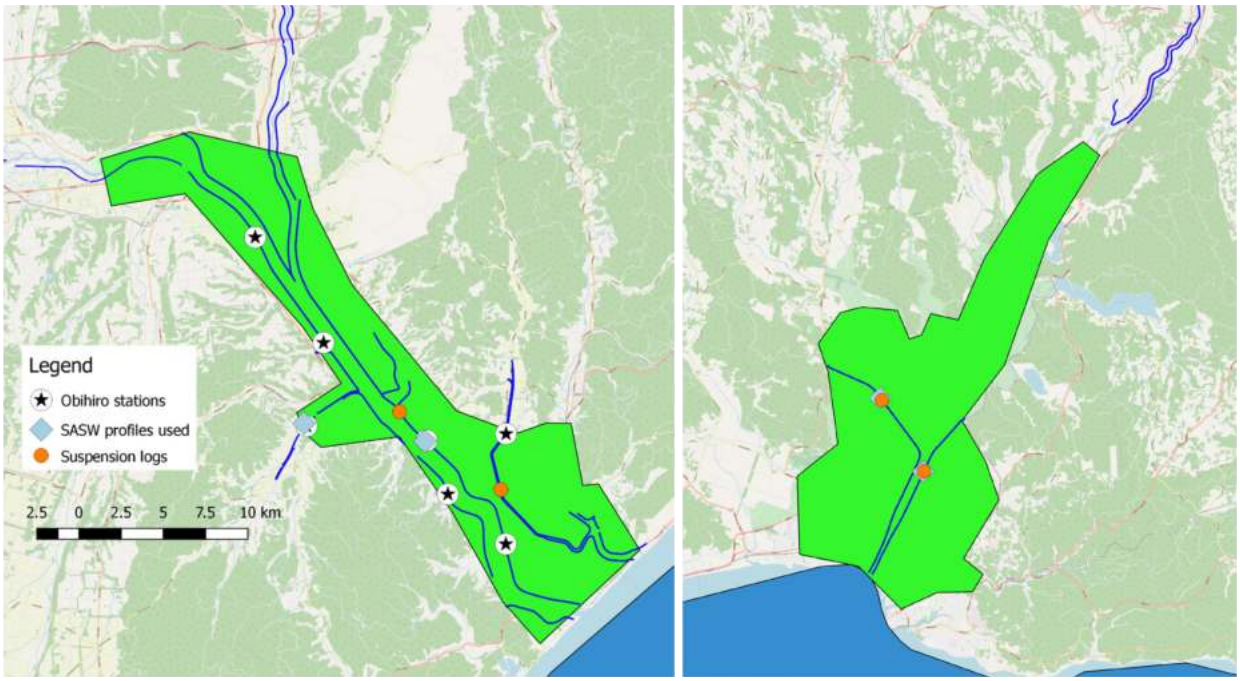

Figure 7.3 Region-specific amplification models are applied in the highlighted areas along the Tokachi (left) and Kushiro (right) Rivers. These areas have thick soft sediments and site response that differs from the ergodic model.

7.4 FRAGILITY FUNCTION

The site conditions of the foundation soil beneath the upstream and downstream portions of the levee systems are distinct - the downstream regions have relatively soft soils, including peat, within the foundation materials. In addition, the groundwater level is typically at or above the interface between the peat layer and the levee fill. The saturated sandy soils within the levees are susceptible to liquefaction in many cases, and can result in significant damage, as seen in the section analysis in Chapter 4. The foundation material in the upstream areas consists mainly of granular materials (no peat) with deep groundwater. Based on the difference in hydrological and foundation conditions, levee segments with and without peat in the foundations are separated for the development of fragility data points.

The extent of peat within the foundation was defined from the dense boring logs along the Kushiro levees and from the longitudinal cross section (Figure 2.2). Along the Tokachi levees, borings are limited to the downstream region and the longitudinal cross section only covers the first 20 km from the river mouth of the main Tokachi River (Figure 2.3). The backmarsh category indicated on the engineering geomorphologic classification maps corresponds well with peat occurrence within Kushiro (NIED, 2018). Assuming this correlation also exists at Tokachi, the extent of peat in the upstream portion of the Tokachi levee system and along the tributary branches are assigned according to the surface geomorphology on the engineering geomorphologic classification maps. Each 50 m levee segment is sorted based on their location within the two river systems, with 3,370 of the total 9,768 segments characterized as having peat present in the foundation.

The statistical analysis of fragility is based on grouping observations into bins having consistent estimates of shaking intensity. Porter et al. (2007) recommended selecting the number of bins based on the size of the dataset, taking the total number of bins as the square root of the total number of specimens. This approach is adopted with a modification suggested by Kwak et al. (2016) of the denominator from one to four.

$$m_{bin} = \frac{\sqrt{N_{total}}}{4} \tag{7.4}$$

This reduces the number of required bins, which in turn increase the number of observations per bin, to a level that provides for stable estimates of fragility (probability of damage).The probability of damage for bin i is computed as the number of failed segments n_i, divided by the total number of segments N_i, conditioned on pga_i, the median PGA for the bin.

$$P_i(DL > dl|PGA = pga_i) = \frac{n_i}{N_i} \tag{7.5}$$

The levees on peat have 21 bins with 320-321 segments each, and levees on inorganic soils have 29 bins with around 436-437 segments each. The slight difference in number of segments is necessary to distribute the segments among the bins required by Eq. (7.4), and has minor effects on the fragility associated with each bin. The damage measure used for the levees is the damage level (DL) determined from the field observations (Section 2.4). Each combination of probability of damage and PGA is taken as a 'fragility data point' for the analysis that follows.

A fitting approach with an appropriate functional form is required to produce a fragility function from the empirical fragility data points. The lognormal cumulative distribution function (CDF) is commonly adopted for structural applications (Porter et al., 2007) and has also been applied successfully for fitting levee fragility data (Kwak et al. 2016). The CDF operates between probabilities of zero for demands approaching zero and one for demands approaching infinity, which are realistic bounds. The probability of exceeding a given damage level is given by:

$$P(DL > dl|IM = im) = \Phi\left(\frac{\ln im - \mu_{ln}}{\beta}\right) \tag{7.6}$$

The function is fully defined by the mean (μ_{ln}) and standard deviation (β) of the distribution, both with clear physical meaning. μ_{ln} and β are estimated from the empirical fragility data points using the maximum likelihood estimation (MLE) presented in Baker (2015). The approach seeks to maximize the likelihood function such that the fitted fragility function has the highest probability of producing the observed data.

The probability of n out of the N segments in bin i exceeding a given damage level is given by the binomial distribution,

$$P(n_i \; of \; N_i \; segments \; with \; DL > dl) = \binom{N_i}{n_i} p_i^{n_i} (1 - p_j)^{N_i - n_j} \tag{7.7}$$

where p_j is the probability of an individual segment will experience a higher damage level when subjected to the shaking intensity (median of the bin), and is represented by lognormal CDF in Eq. (7.6). For all the fragility data points across all the bins, the likelihood of observing the data is given by,

$$L = \prod_{i=1}^{M} \binom{N_i}{n_j} p_j^{m_j} (1 - p_j)^{Mj - m_j} \tag{7.8}$$

Fragility functions obtained with the MLE for segments experiencing any level of damage (DL > 0) are shown in Figure 7.4. Estimated PGAs at segments with organic foundation soils range from 0.18-0.62 g for modified Zea16, and 0.22-0.74 g for modified Aea18 (the 'modification' being to the site term, Section 7.3). These differences in PGAs are reflected by higher values of μ_{ln} for Aea18 than for Zea16. The probability of any damage occurring reaches around 0.4 at the highest PGA constrained by the data.

The levee segments on inorganic foundations generally experienced lower levels of shaking. The majority of these segments are located in upstream areas, which have longer distances to the fault rupture. At high PGAs (where appreciable damage was observed for levee segments on peaty foundations), the probability of damage is significantly lower. For example, fragilities based on modified Zea16 at PGA = 0.6 g are 0.40 and 0.18, respectively, for levee segments with and without peat in the foundations.

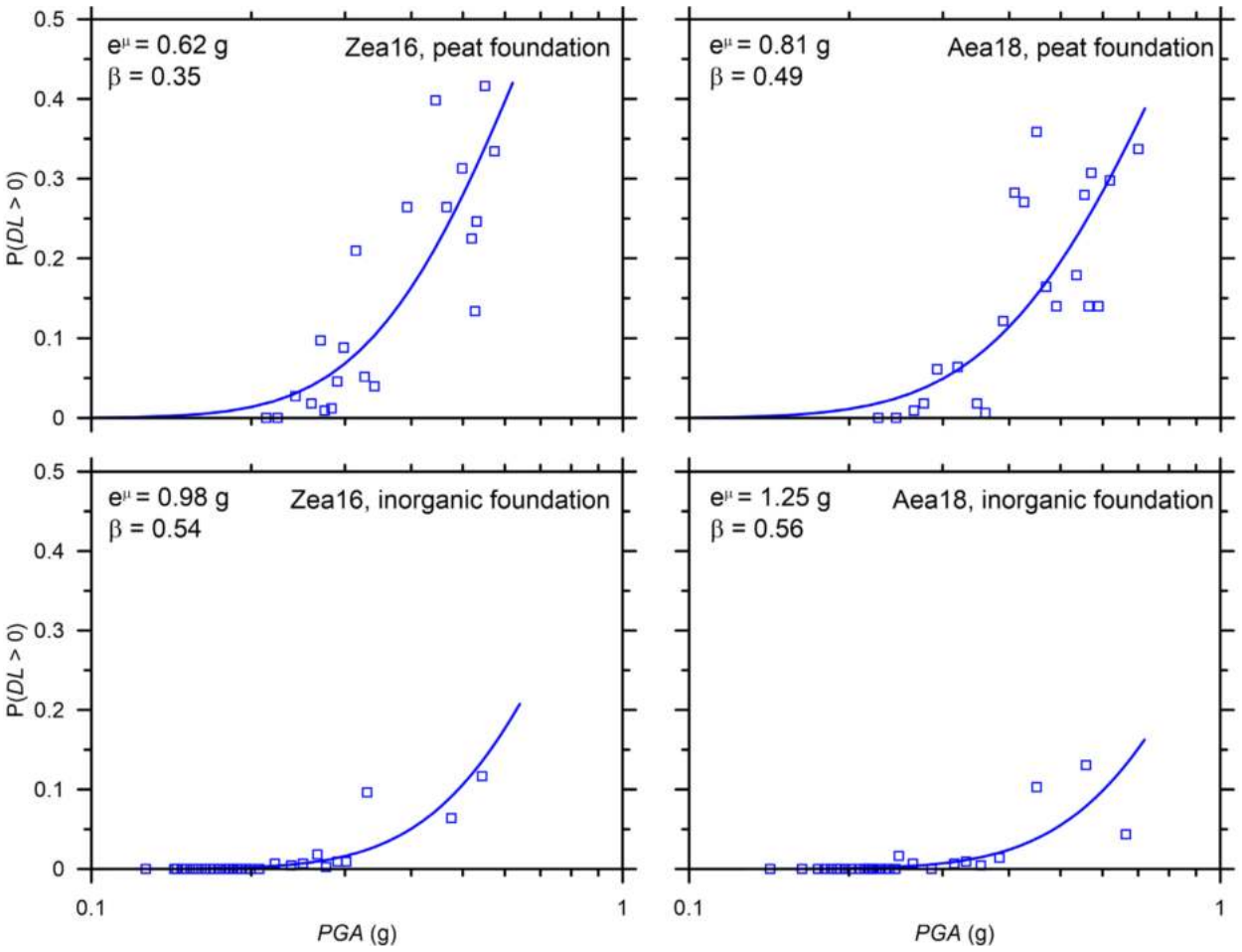

Figure 7.4 Fragility functions for occurrence of any damage conditioned on PGA. Segments on peat has higher probability of damage than segments on inorganics when subjected to the same PGA.

To evaluate fragility functions for higher damage levels, the numerator in Eq. (7.5) is adjusted to consider only segments exceeding the damage level of interest. The fitting is initially performed with both μ_{ln} and β as variable parameters, and the resulting fragility functions are shown in Figure 7.5. For fragility data based on PGA estimated with the modified Zea16 GMM, this produced fragility functions that cross at low PGA, implying a higher probability of incurring more severe damage, which is physically unrealistic. Fragility functions for segments on inorganic materials do not have this issue. Kwak et al. (2016) encountered similar difficulties with Shinano river levee data.

To avoid this problem, an alternative approach is applied whereby the data fitting uses a constant β across damage levels. The β used in the fitting is that set from for $DL > 0$ data. With this constraint applied, the lower probabilities associated with higher damage levels are reflected by an increase in μ_{ln}. This ensures that fragility functions for increasing damage levels do not cross. Table 7.2 summarizes the μ_{ln} and β parameters fitted with both approaches, and the corresponding log values of the MLE (larger values of likelihood indicate better fits). Fits with and without constraint of β generally produce visually similar fragility curves with comparable likelihood values, and the curves with constrained β are adopted subsequently.

Table 7.2 Mean and standard deviation of lognormal CDFs for PGA-based fragility curves

GMM	Damage Level	Variable β			Fixed β		
		e^{μ}	β	LL	e^{μ}	β	LL
Zea16	DL>0	0.69	0.56	-216.1	0.69	0.56	-216.1
	DL>1	0.82	0.65	-213.2	0.75	0.56	-218.9
	DL>2	0.99	0.54	-192.6	1.03	0.56	-192.9
	DL>3	2.08	0.75	-94.9	1.44	0.56	-97.9
Aea16	DL>0	0.86	0.64	-235.5	0.86	0.64	-235.5
	DL>1	0.98	0.67	-211.3	0.87	0.64	-218.3
	DL>2	1.88	0.87	-174.9	1.17	0.64	-193.0
	DL>3	3.15	0.88	-92.3	1.65	0.64	-99.2

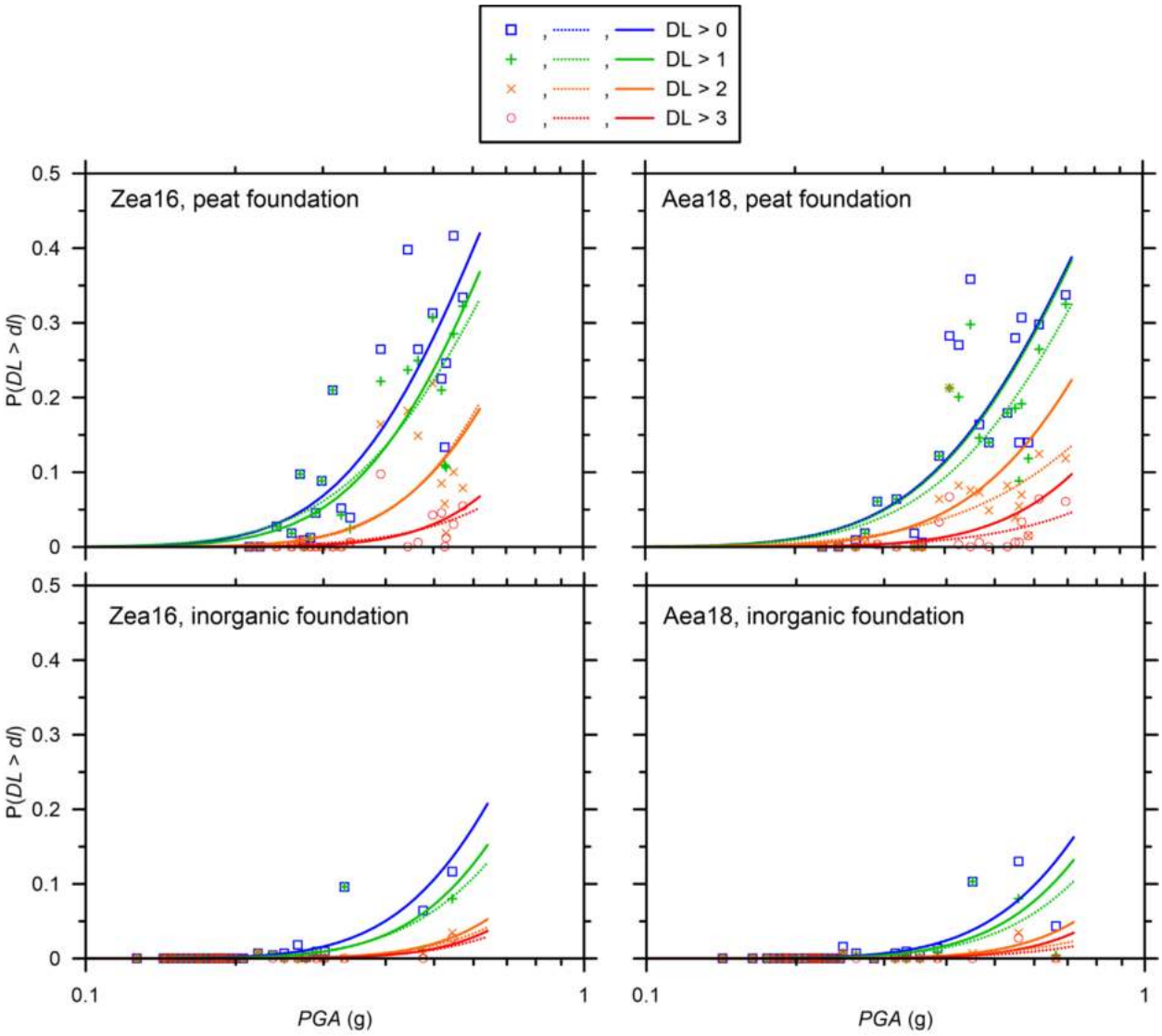

Figure 7.5 Empirical fragility data points and fitted fragility functions for varying damage levels. Fitting performed with β variable (dashed lines) and fixed (solid lines).

Figure 7.6 compares the difference between fragility functions derived using PGA estimated by the modified Zea16 and Aea18 GMMs. These differences reflect epistemic uncertainty associated with the ground motion estimates. The steepness of the fitted functions are governed by β and reflect aleatory variabilities inherent to the data set, which include variable geotechnical conditions along the levee systems and aleatory uncertainties in the ground motion estimates. Lower β indicates reduced dispersion and higher predictive power. The β may be reduced by improving estimates of PGA or by

using an alternative intensity measure that better describes demand (e.g., PGV). Reductions in β could, in principle, be achieved by incorporating levee response into the conditioning parameter by replacing intensity measures with EDPs such as LI and Newmark displacement (which was examined in section analyses, Chapter 4). The latter would require knowledge of the geometry and geotechnical properties of many cross sections along the length of the levees. Since this information is not available at the required levels of resolution, it was not considered in the present work.

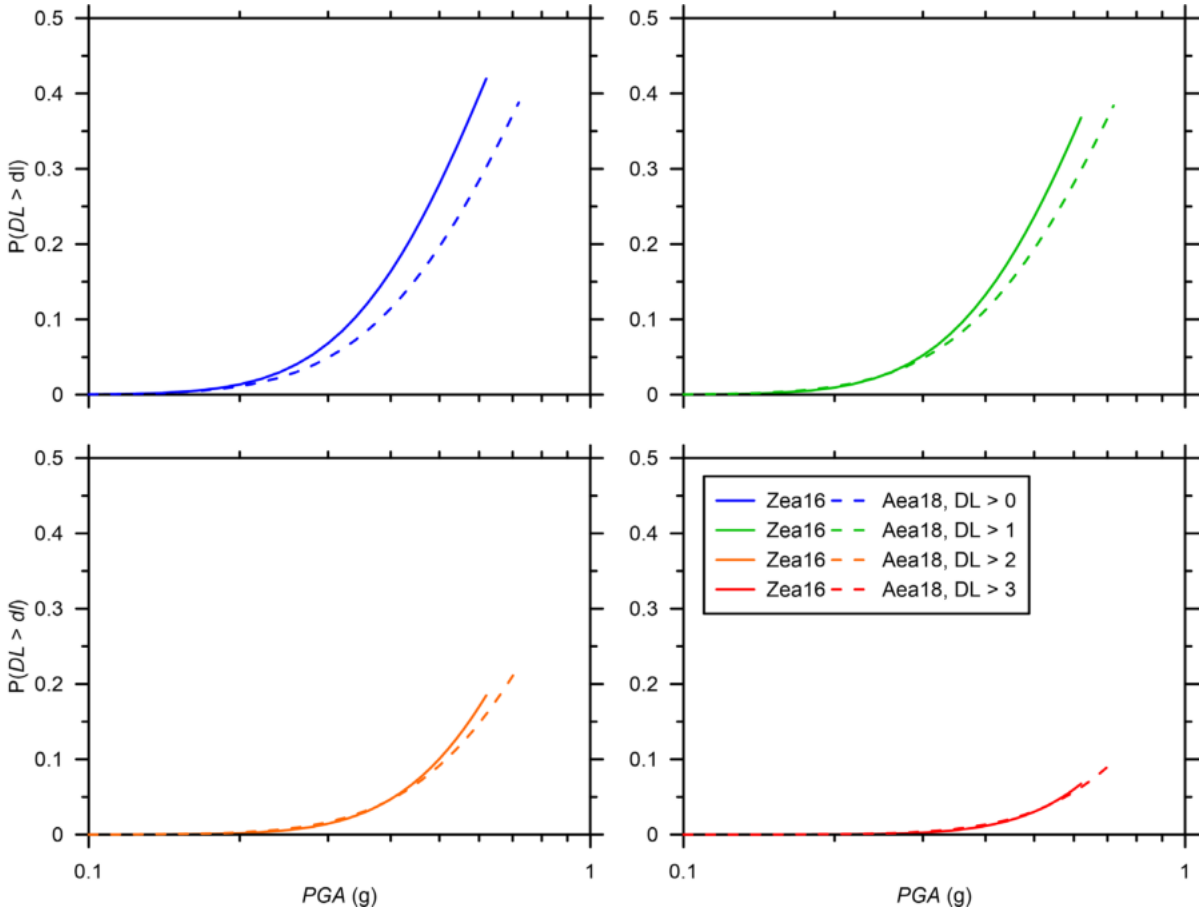

Figure 7.6 Fragility functions for levee segments founded on peaty foundation materials as derived using ground motion estimates from the modified Aea18 and Zea16 GMMs.

Fragility functions derived for the levees in this study (labeled HKD) are compared with those developed for levees along the Shinano River (Kwak et al., 2016) in Figure 7.7. At PGA below 0.27 g,

the probability of damage for the levees on peat is slightly lower. However the probability of damage increases drastically as PGA exceeds 0.30 g.

For levees on inorganic foundations, the Hokkaido levees are less fragile across the range of PGA supported by the data. Possible factors responsible for the observed differences may include differences in the age, minerology and depositional environments between the two regions, as well as hydrological differences. Along the Kushiro and Tokachi Rivers, the majority of the levees on inorganic foundations are in upstream areas, where the ground water level is below the levee foundation level. Moreover, these upstream areas along the Kushiro and Tokachi Rivers have relatively high gradients in the stream channels, which tends to produce stiffer and stronger sediments than in low-gradient regions. In contrast, the levees along the Shinano River system includes sections through flood plains, where the ground water level is higher and the gradients are lower. In addition, the type of motion the two systems are subjected to differs, given the Shinano River was shaken by lower magnitude, crustal earthquakes, which are shorter in duration and likely richer in higher frequencies than the subduction events examined for the Hokkaido levees.

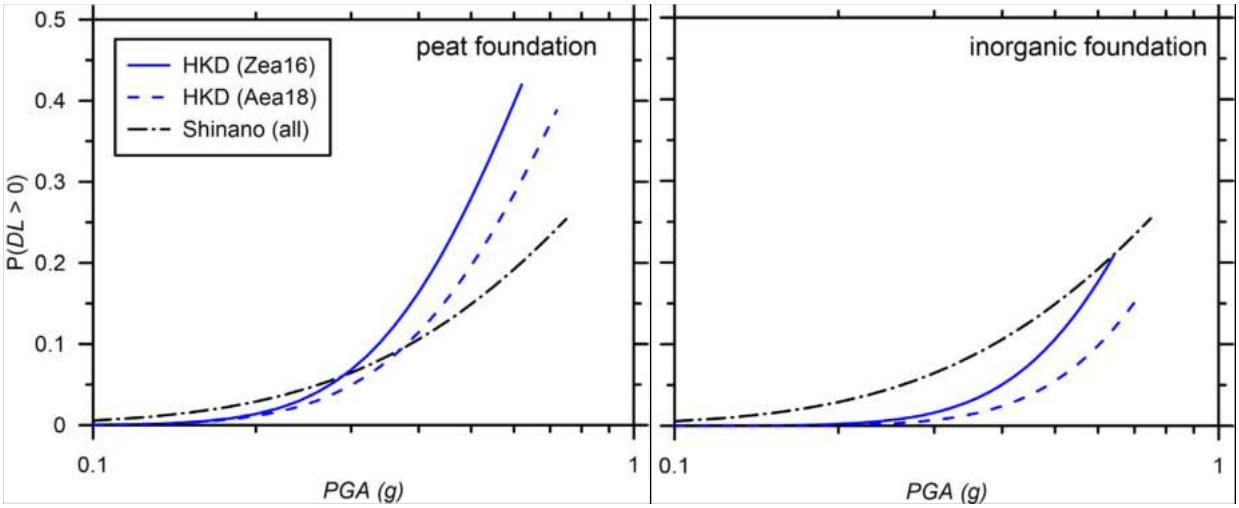

Figure 7.7 Comparison of fragility curves for probability of any damage level (DL>0) as evaluated for Hokkaido levees (this study) and Shinano River levees (Kwak et al. 2016).

7.5 SUMMARY AND DISCUSSION

Field performance of levees along the Kushiro River and Tokachi River are combined with estimates of ground motion intensity to provide empirical fragility functions for varying damage levels. For levee segments with peat in the foundation, the fragility is observed to be higher than segments without peat in the foundation within the same river systems in Hokkaido. Compared with fragility functions derived for levees along the Shinano River with inorganic foundation soils, the Hokkaido levees with peat in the foundation have appreciably higher fragility above a threshold PGA of about 0.25 g, as well as a lower β reflected by a steeper curve.

Empirically derived fragility functions reflect ground truth for the complex mechanisms underlying levee damage during an earthquake. Application of the models should be cognizant of the differences and similarities in the conditions of the Hokkaido levees and other levee systems. For instance, levees in the San Francisco Bay-Delta region are constantly impounding water, and would be anticipated to be more susceptible to earthquake damage as a result of the lateral loading and seepage forces from the impounded water as well as a greater degree of saturation of the levee fills, making the soils more susceptible to liquefaction. Given the conditions in the Delta, the fragilities based on the Hokkaido levees would likely present a lower bound of the expected fragility of Delta levees.

Sources of uncertainty associated with the fragility models stem from (1) variations in geotechnical conditions in the levee and foundation materials and (2) aleatory uncertainties in the estimated demand. The damage provided in the reconnaissance reports is relatively objective, and is not considered to be a significant source of uncertainty. Aleatory uncertainties in demand are estimated as part of the Kriging process, and increase with the spacing of ground motion stations. These uncertainties are relatively large for the 1993 Kushiro-oki earthquake (sparse recordings) and smaller for the 2003 Tokachi-oki earthquake.

8 CONCLUSION AND RECOMMENDATIONS

8.1 CONCLUSIONS

Case histories of the performance of levee systems founded on peat along the Kushiro and Tokachi Rivers during two large magnitude subduction earthquakes are collected and analyzed. Geotechnical analyses are performed at ten location along Tokachi River where the subsurface was characterized and ground motions can be reasonably estimated from nearby recording stations.

Four liquefaction severity indices, as well as slope stability and Newmark-type displacements, are performed to estimate the severity of liquefaction induced damage and levels of permanent slope deformations. Liquefaction susceptibility is based on field classification and testing of samples of materials recovered from trenching across two of the sections. The Newmark displacement analyses are performed using yield accelerations derived from 2-D limit-equilibrium models of the levee cross sections in the computer program SLIDE. The predicted performance is compared with field observations from post-earthquake reconnaissance. The effectiveness of indices that place more weight on shallow layers, such as LPI_{ISH} and LSN, are found to perform better. Taking the 70^{th} percentile value is recommended when multiple borings and/or CPT profiles are present across a cross section. The rationale for use of a greater than median percentile is that damage is expected to be governed by looser than average pockets of susceptible material within the levee fill or in the foundation. Damage assessment considering both liquefaction indices and Newmark displacements shows improved prediction ability with respect to observed performance.

Fragility functions express the probability of exceeding a damage level (DL) conditioned on an intensity measure. Fragility functions for damage occurrence (DL>0) conditioned on PGA are derived by fitting a lognormal cumulative distribution function (CDF) to damage probabilities estimated

empirically from post-event reconnaissance for the levees along Kushiro and Tokachi Rivers for the two subduction earthquakes considered. The fragility functions for occurrence of any damage, P(DL>0) are developed for levees with and without peat in the foundations. Levees on peat foundations are significantly more fragile than levees on inorganic soils within the same system.

As part of the process of improving estimates of ground motion intensity at the levees, particularly within the downstream region with soft soils, a region-specific site amplification function is derived. The model is based on non-ergodic site responses at recording stations developed from analysis of recordings on levees within the basin. The empirical analyses are supplemented with results of 1D ground response analysis (GRA) using *DEEPSOIL v7.0.* The empirical linear amplification is high, and may indicate basin effects that are not captured by the 1D analysis. Nonlinearity is stronger in the amplification function derived from the 1D GRA, especially at short periods.

8.2 RECOMMENDATIONS FOR FUTURE RESEARCH

This dissertation research included substantial effort to collect a comprehensive dataset of levee performance during strong shaking and related site characterization to develop empirical fragility functions. Future research recommendations are divided into forward application of the fragility functions, and areas that can be further explored by leveraging the available data.

1) Risk assessment for the Delta previously used fragility functions based on simulations and expert opinions. While there are differences in the site conditions between the Hokkaido and Delta levees, most notably in the thickness of the peat and the impoundment of water by the latter, an initial reassessment of the seismic hazard using the updated fragility function would be an interesting comparison.

2) Probability of failure for the levee as a connected system depends on the spatial correlation of both capacity and demand. Spatial correlation of demand may be estimated using autocorrelation from the segment performance, and compared between the two levee systems and earthquakes.
3) The 1D ground response analysis suggests higher nonlinearity than is evident from the empirical data, especially at shorter spectral periods. The differences are not satisfactorily explained with the limited analysis conducted. Additional soil profiles can be developed from the shear wave velocity profiles from the geophysical investigation for both systems, and recordings from the Obihiro stations, especially at higher shaking intensities, could be considered to constrain the empirical nonlinear term.
4) PGV has been shown to be a better predictor of levee performance by Kwak et al. (2016). Following the release of additional GMMs from the NGA-SUB project, PGV may replace PGA as the predictor for damage in fragility functions.

APPENDIX A: HVSR, SASW ARRAY SETUP AND DISPERSION CURVES

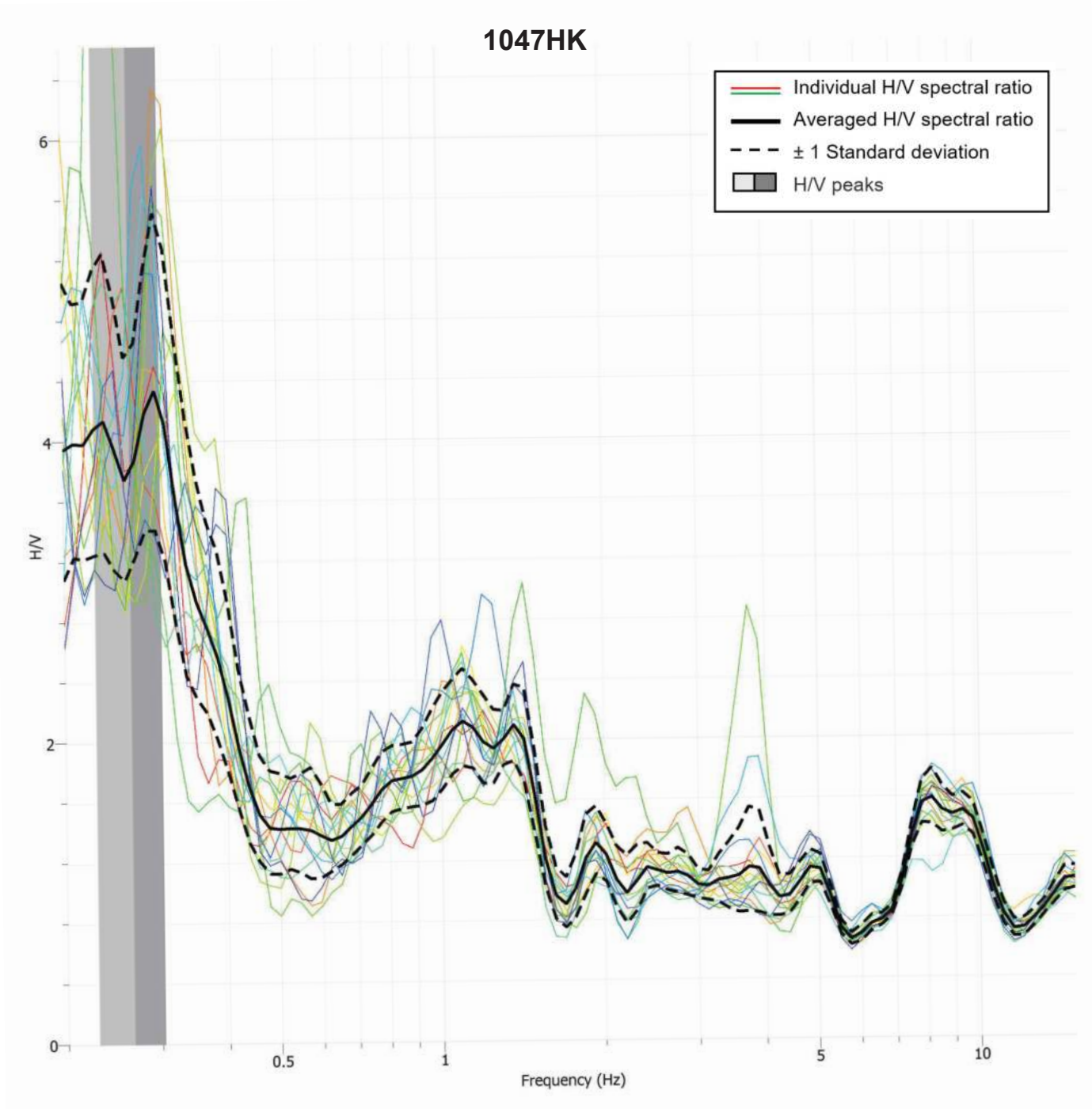
1047HK
Individual H/V spectral ratio
Averaged H/V spectral ratio
± 1 Standard deviation
H/V peaks
H/V
Frequency (Hz)
0
2
4
6
0.5
1
5
10

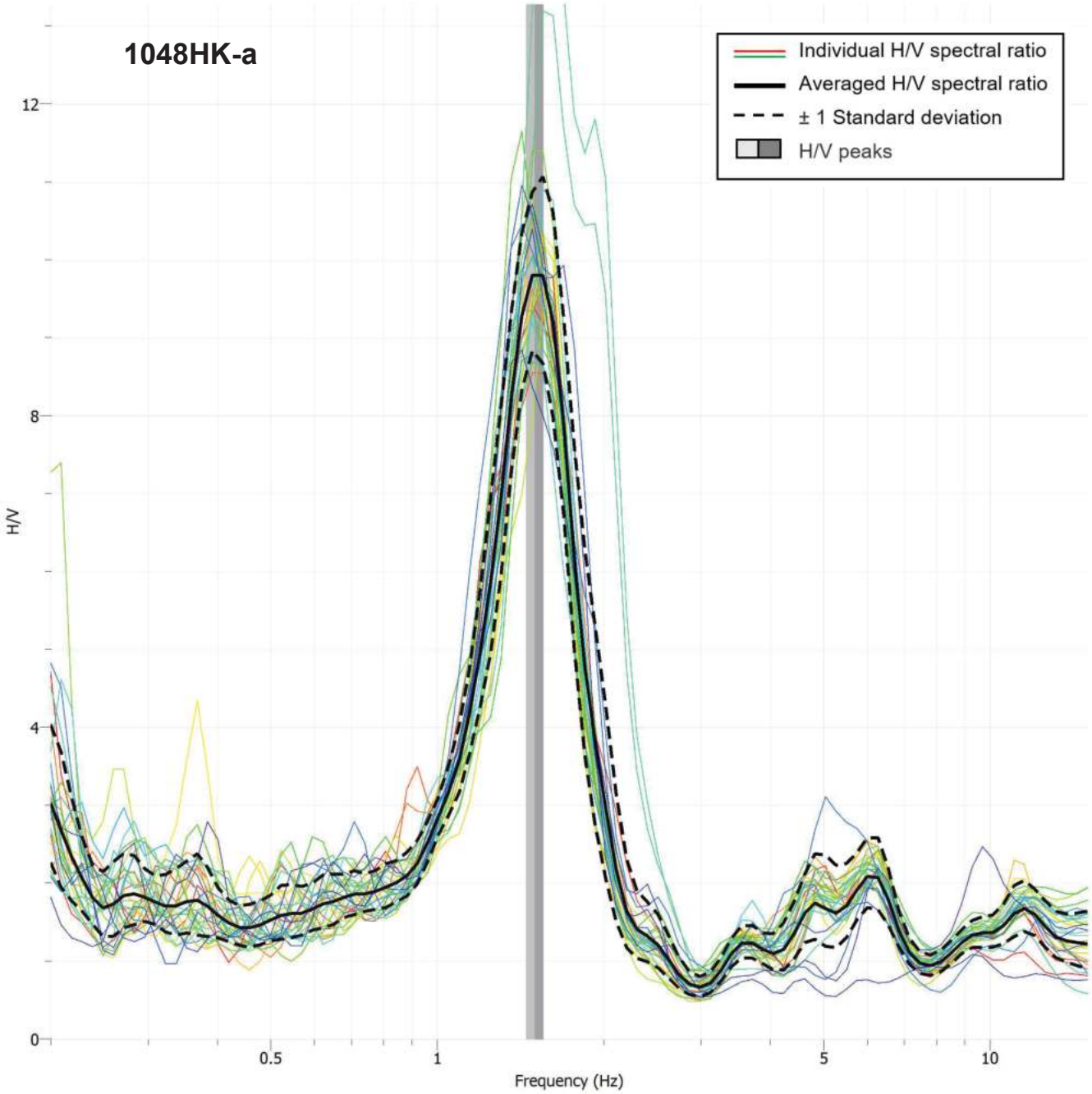
1048HK-a
Individual H/V spectral ratio
Averaged H/V spectral ratio
± 1 Standard deviation
H/V peaks
H/V
Frequency (Hz)
0
4
8
12
0.5
1
5
10

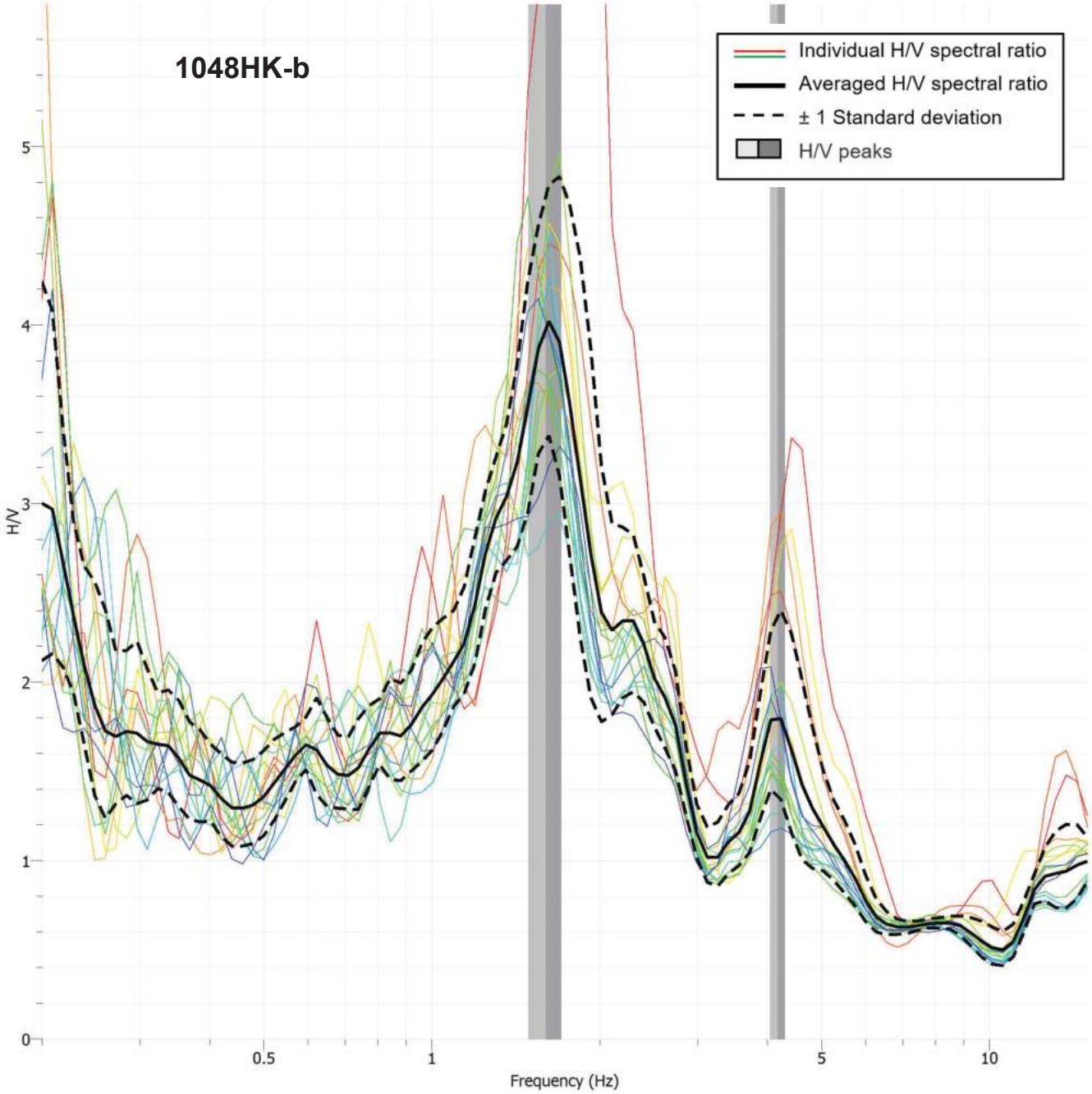
1048HK-b
Individual H/V spectral ratio
Averaged H/V spectral ratio
± 1 Standard deviation
H/V peaks
H/V
Frequency (Hz)
0
1
2
3
4
5
0.5
1
5
10

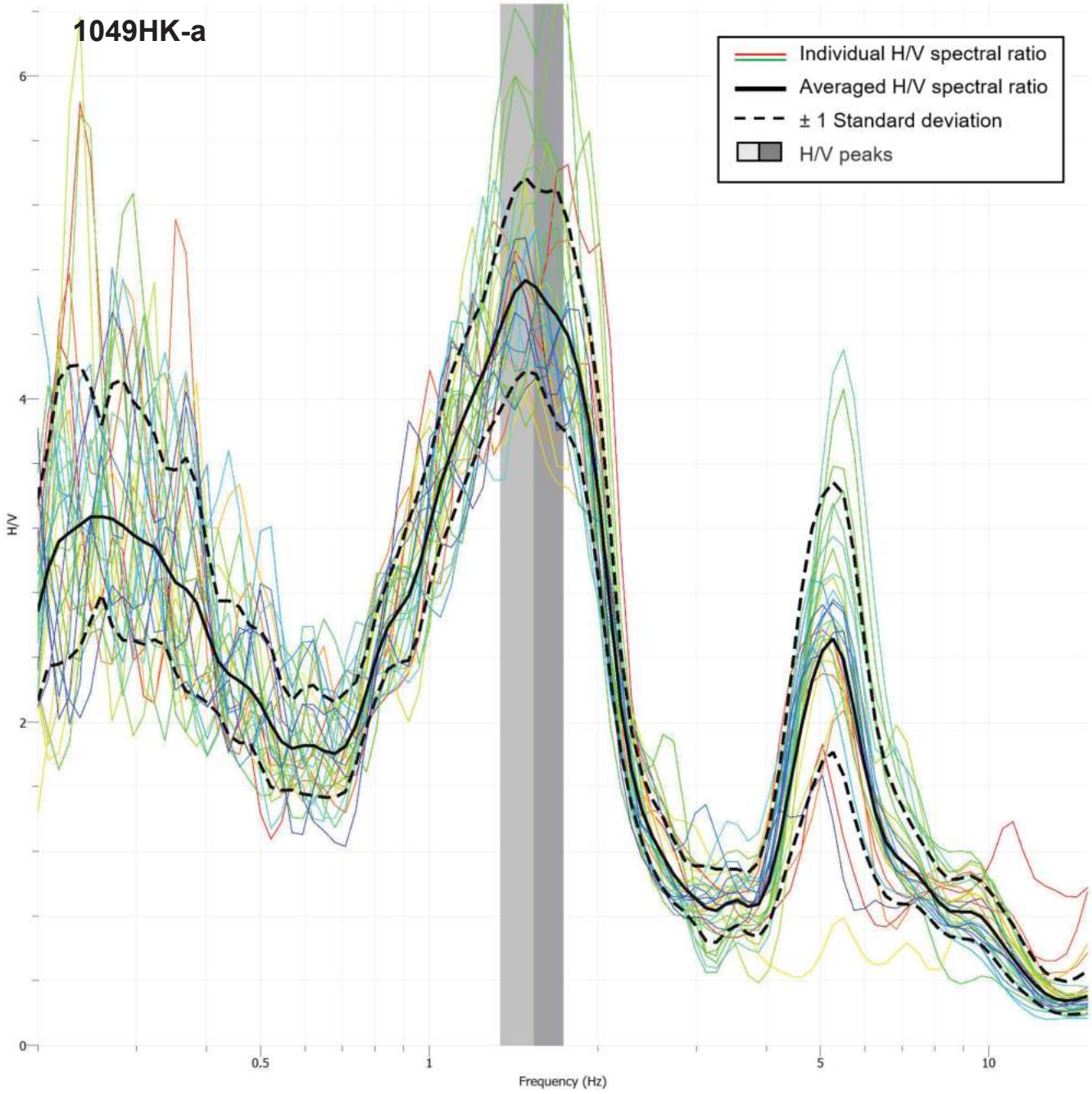
1049HK-a
Individual H/V spectral ratio
Averaged H/V spectral ratio
± 1 Standard deviation
H/V peaks
H/V
Frequency (Hz)
0
2
4
6
0.5
1
5
10

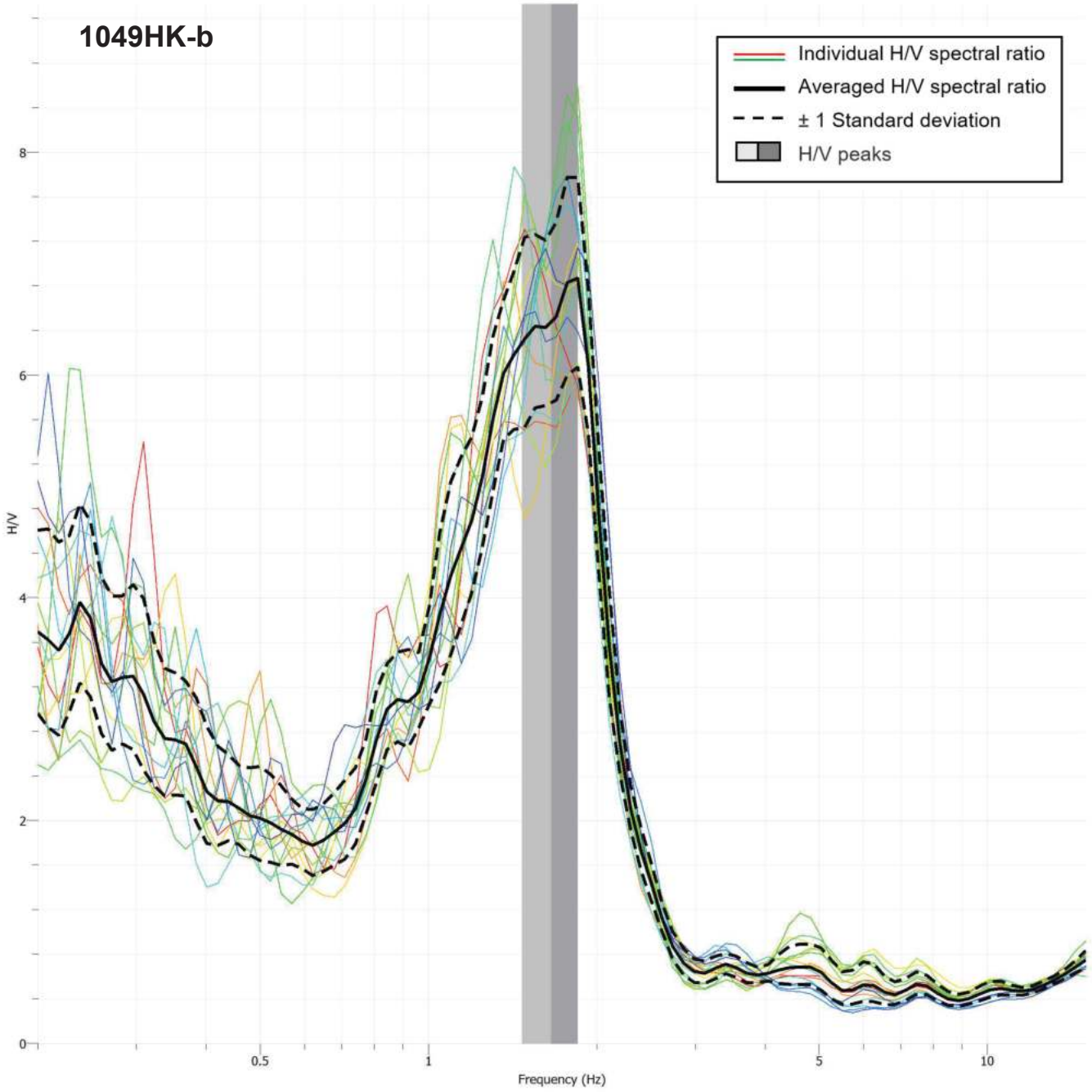
1049HK-b
Individual H/V spectral ratio
Averaged H/V spectral ratio
± 1 Standard deviation
H/V peaks
H/V
Frequency (Hz)
0
2
4
6
8
0.5
1
5
10

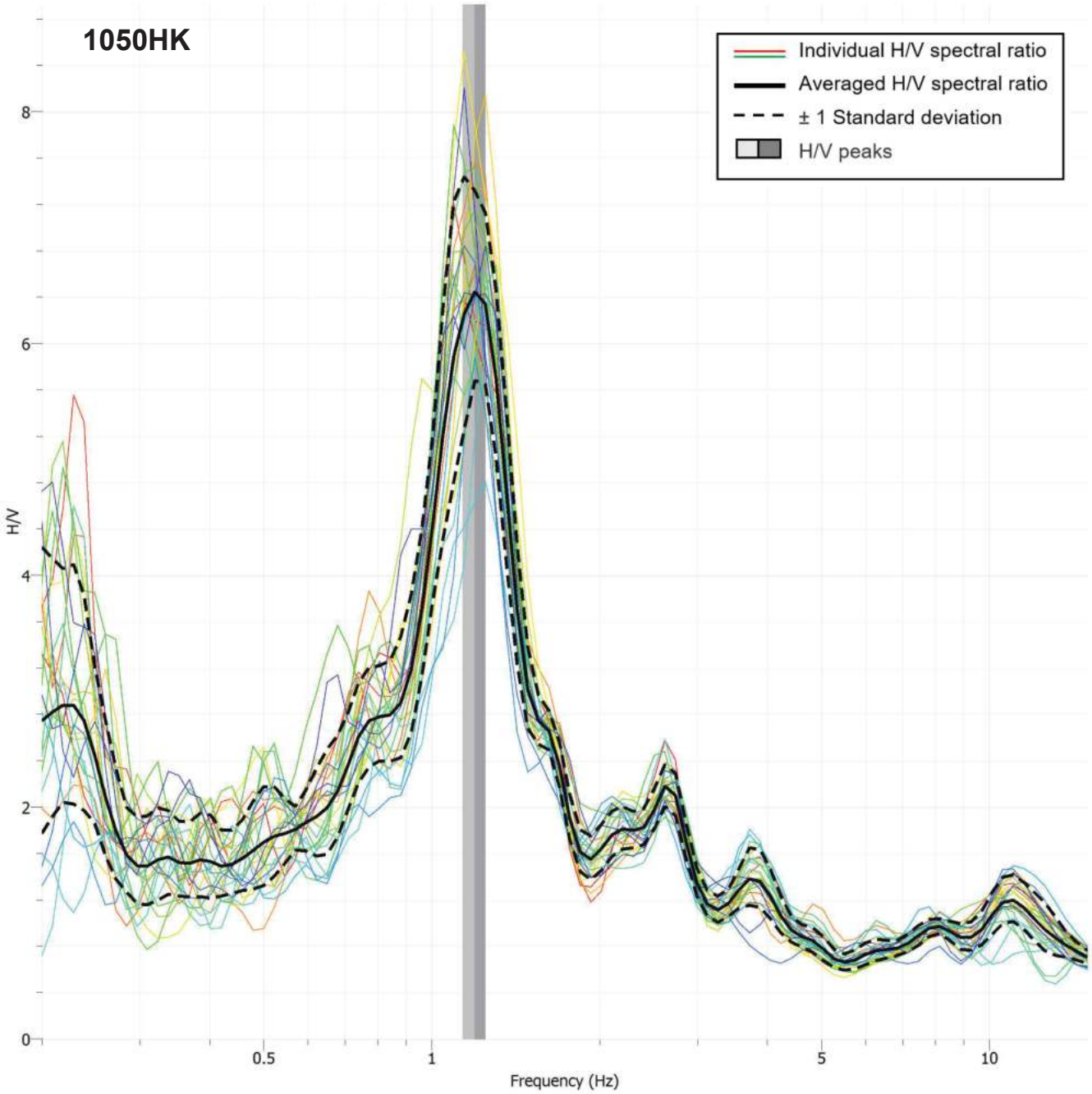
1050HK
Individual H/V spectral ratio
Averaged H/V spectral ratio
± 1 Standard deviation
H/V peaks
H/V
0
2
4
6
8
0.5
1
5
10
Frequency (Hz)

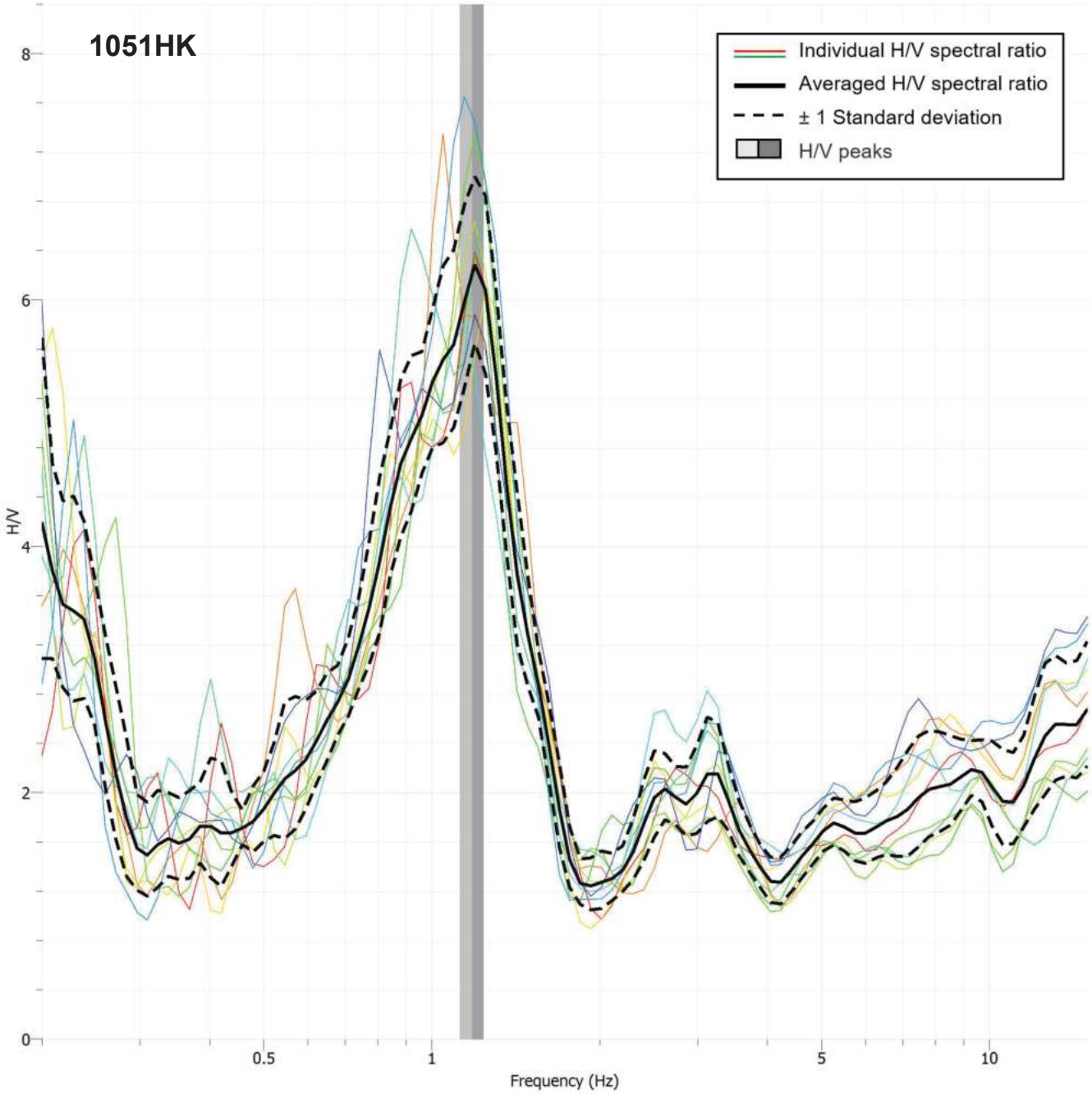
1051HK
Individual H/V spectral ratio
Averaged H/V spectral ratio
± 1 Standard deviation
H/V peaks
H/V
Frequency (Hz)
0
2
4
6
8
0.5
1
5
10

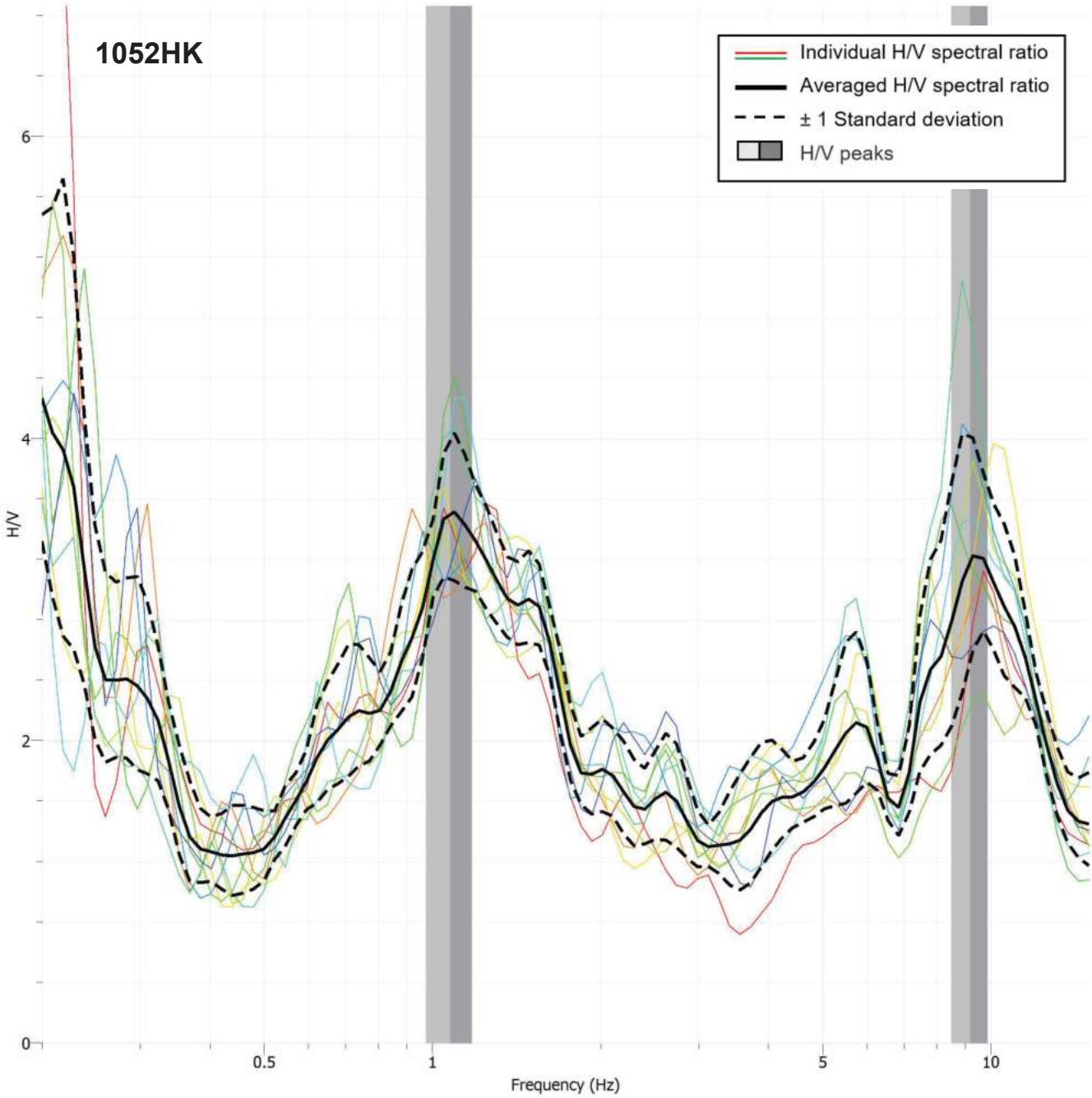
1052HK
Individual H/V spectral ratio
Averaged H/V spectral ratio
± 1 Standard deviation
H/V peaks
H/V
0
2
4
6
0.5
1
5
10
Frequency (Hz)

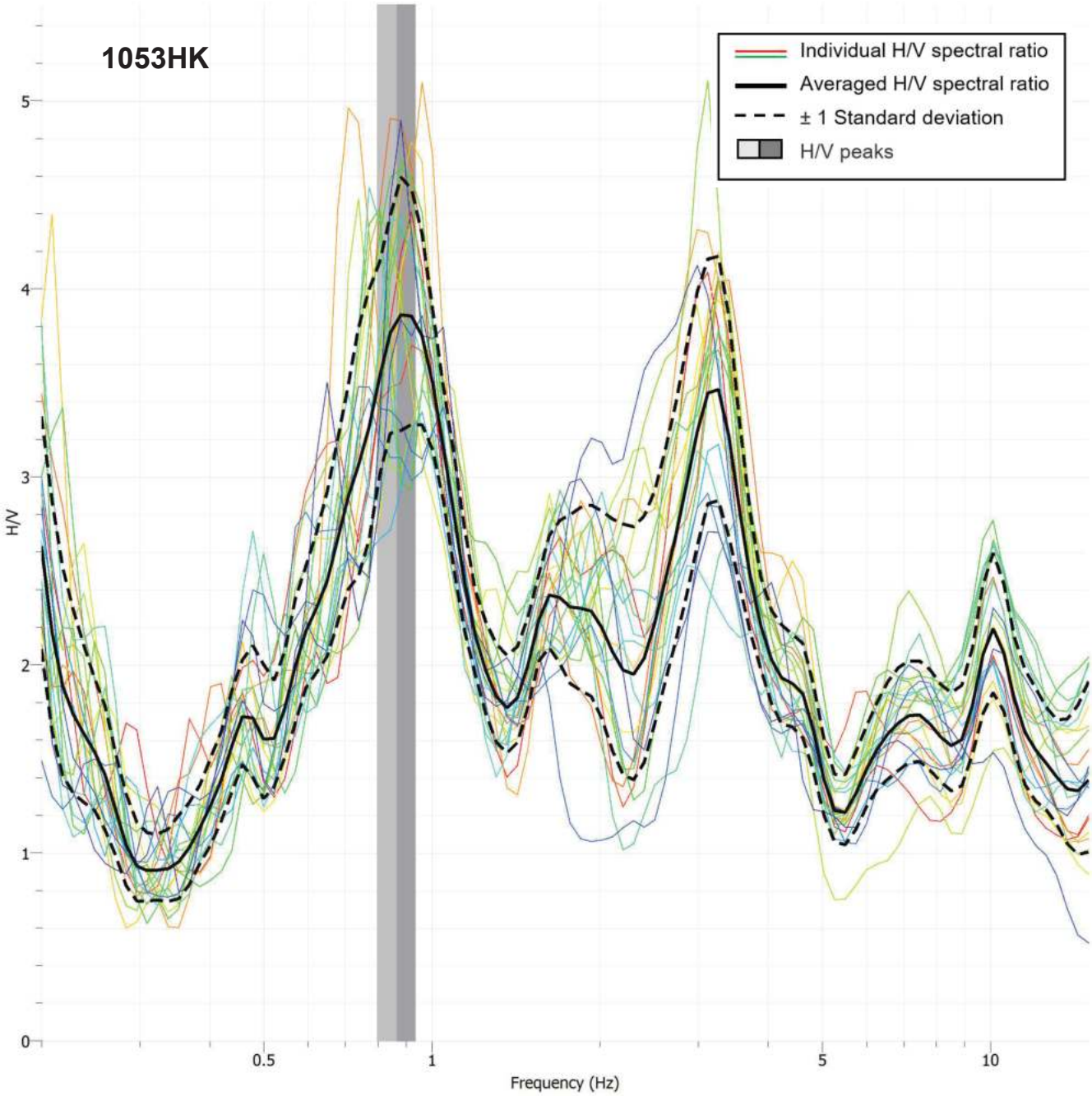
1053HK
Individual H/V spectral ratio
Averaged H/V spectral ratio
± 1 Standard deviation
H/V peaks
H/V
Frequency (Hz)
0
1
2
3
4
5
0.5
1
5
10

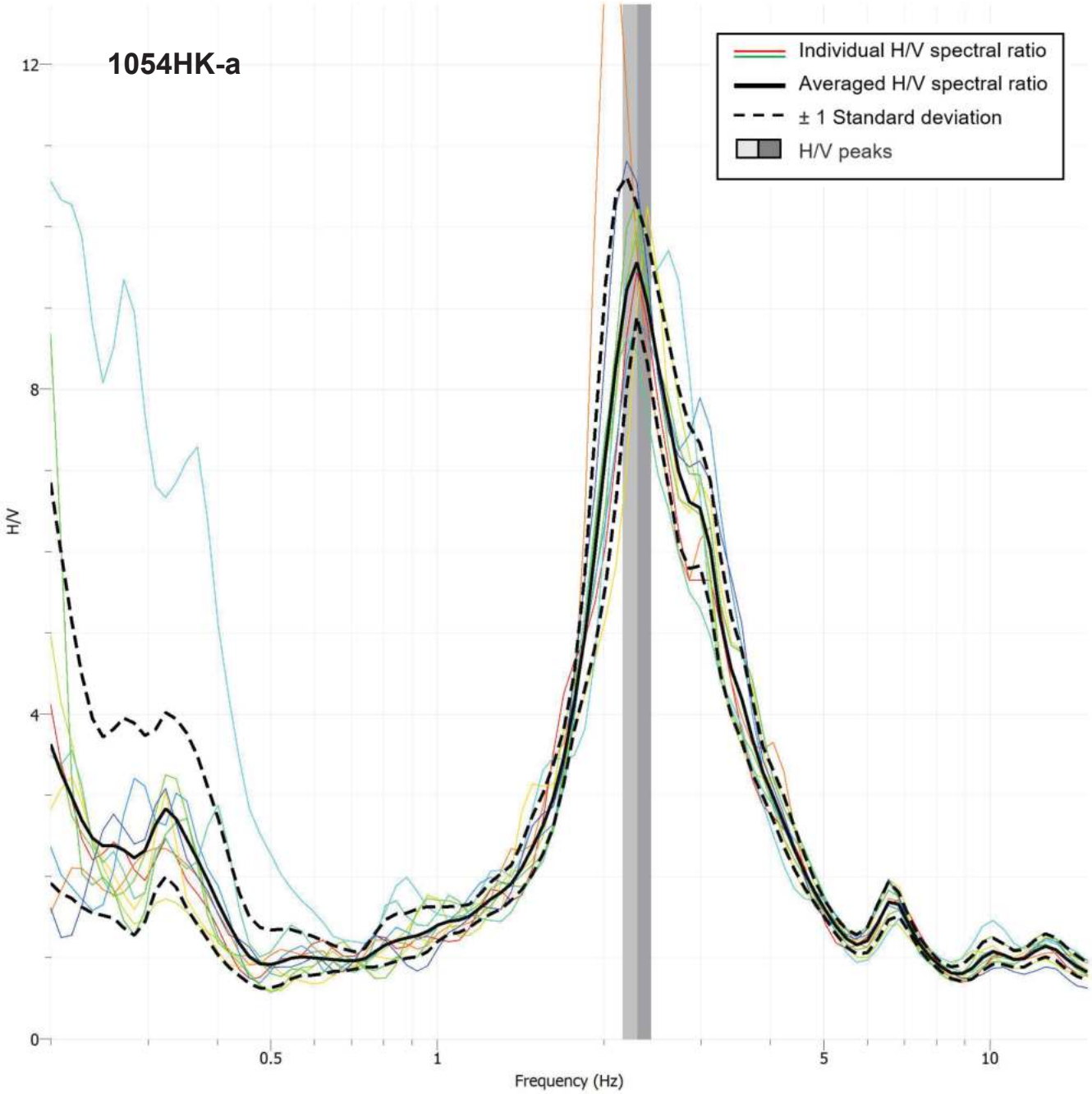
1054HK-a
Individual H/V spectral ratio
Averaged H/V spectral ratio
± 1 Standard deviation
H/V peaks
H/V
Frequency (Hz)
0
4
8
12
0.5
1
5
10

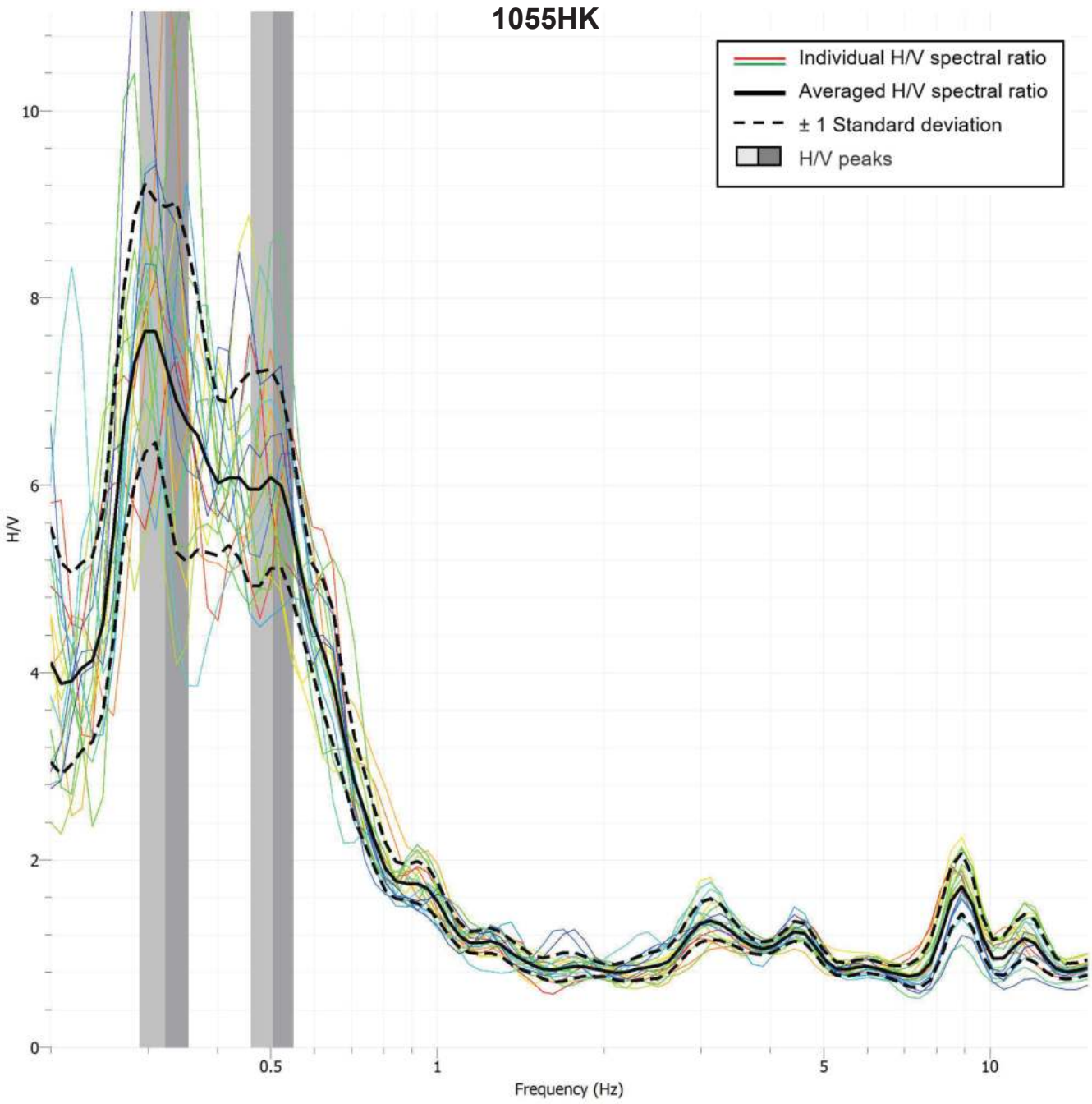
1055HK
Individual H/V spectral ratio
Averaged H/V spectral ratio
± 1 Standard deviation
H/V peaks
H/V
Frequency (Hz)
0
2
4
6
8
10
0.5
1
5
10

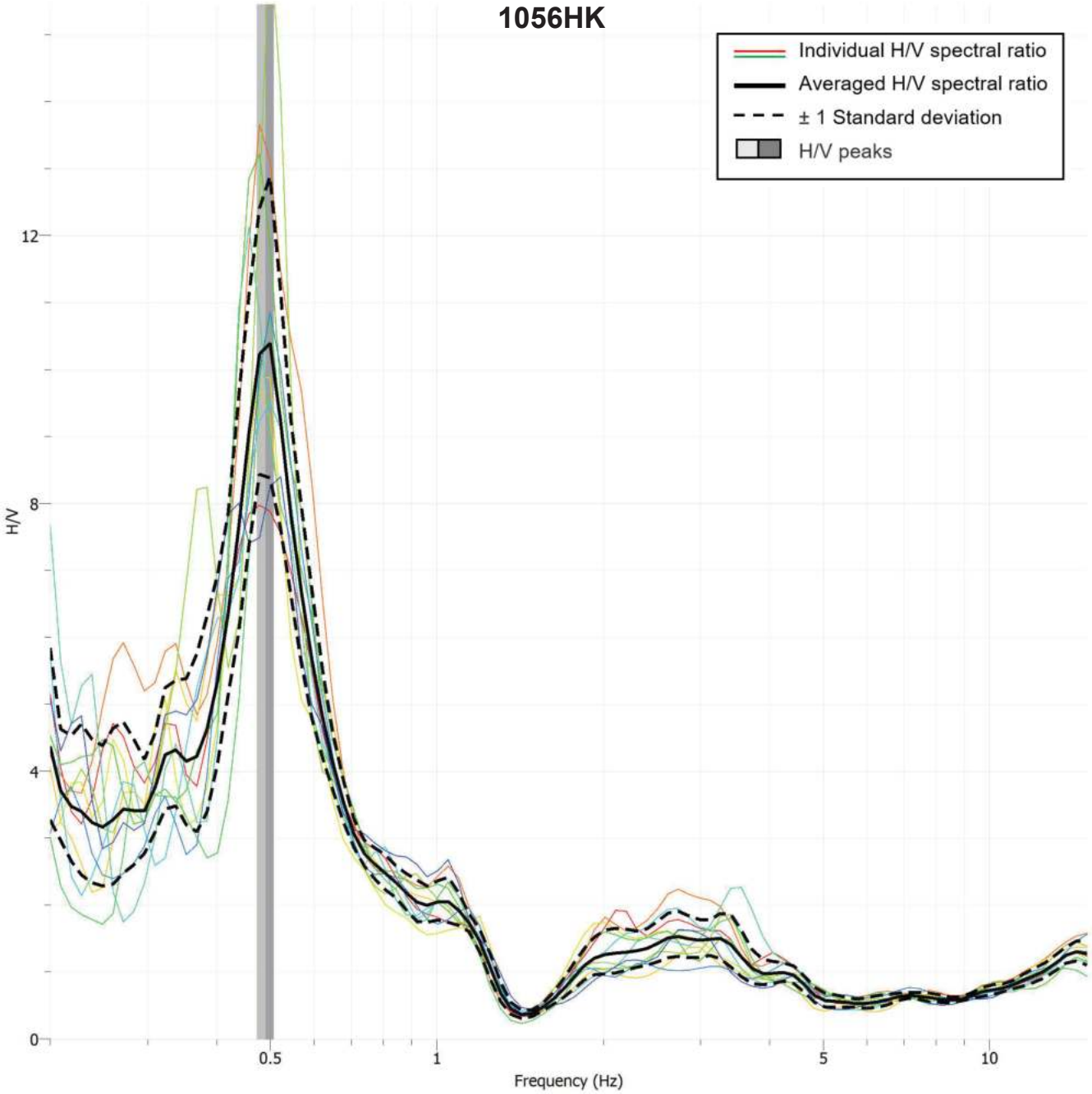
1056HK
Individual H/V spectral ratio
Averaged H/V spectral ratio
± 1 Standard deviation
H/V peaks
H/V
0
4
8
12
0.5
1
5
10
Frequency (Hz)

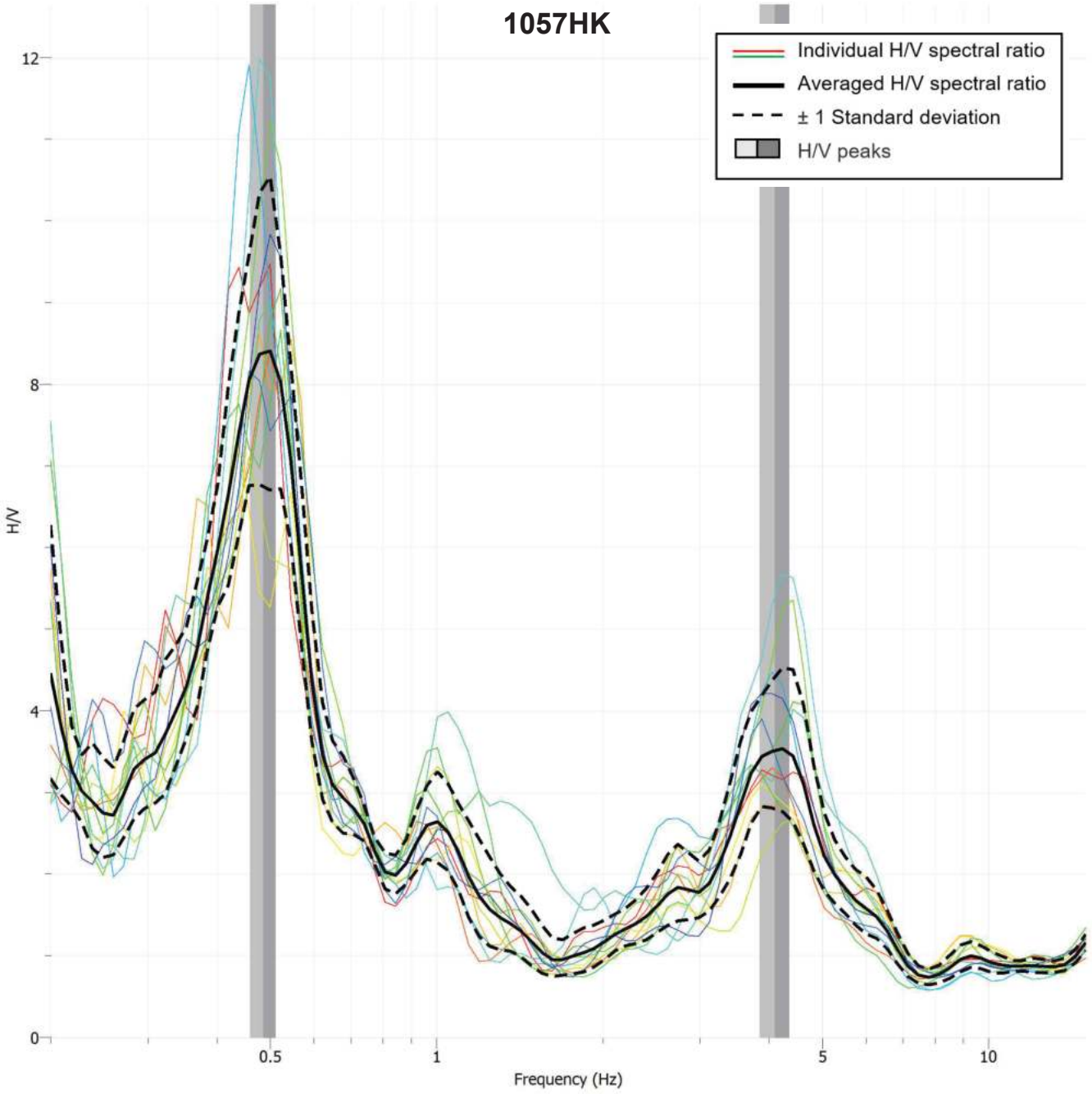
1057HK
Individual H/V spectral ratio
Averaged H/V spectral ratio
± 1 Standard deviation
H/V peaks
H/V
Frequency (Hz)
0
4
8
12
0.5
1
5
10

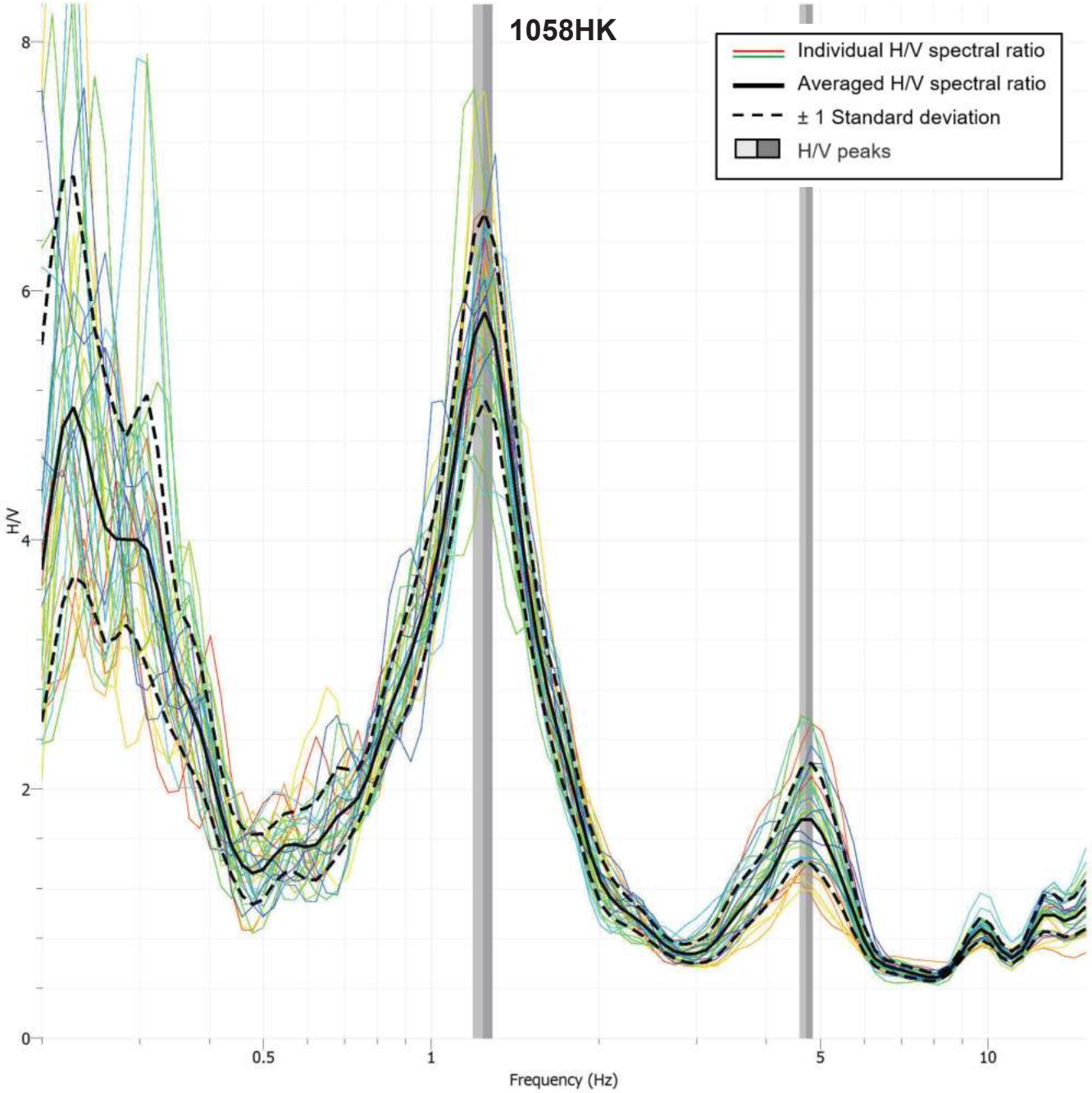
1058HK
Individual H/V spectral ratio
Averaged H/V spectral ratio
± 1 Standard deviation
H/V peaks
H/V
Frequency (Hz)
0
2
4
6
8
0.5
1
5
10

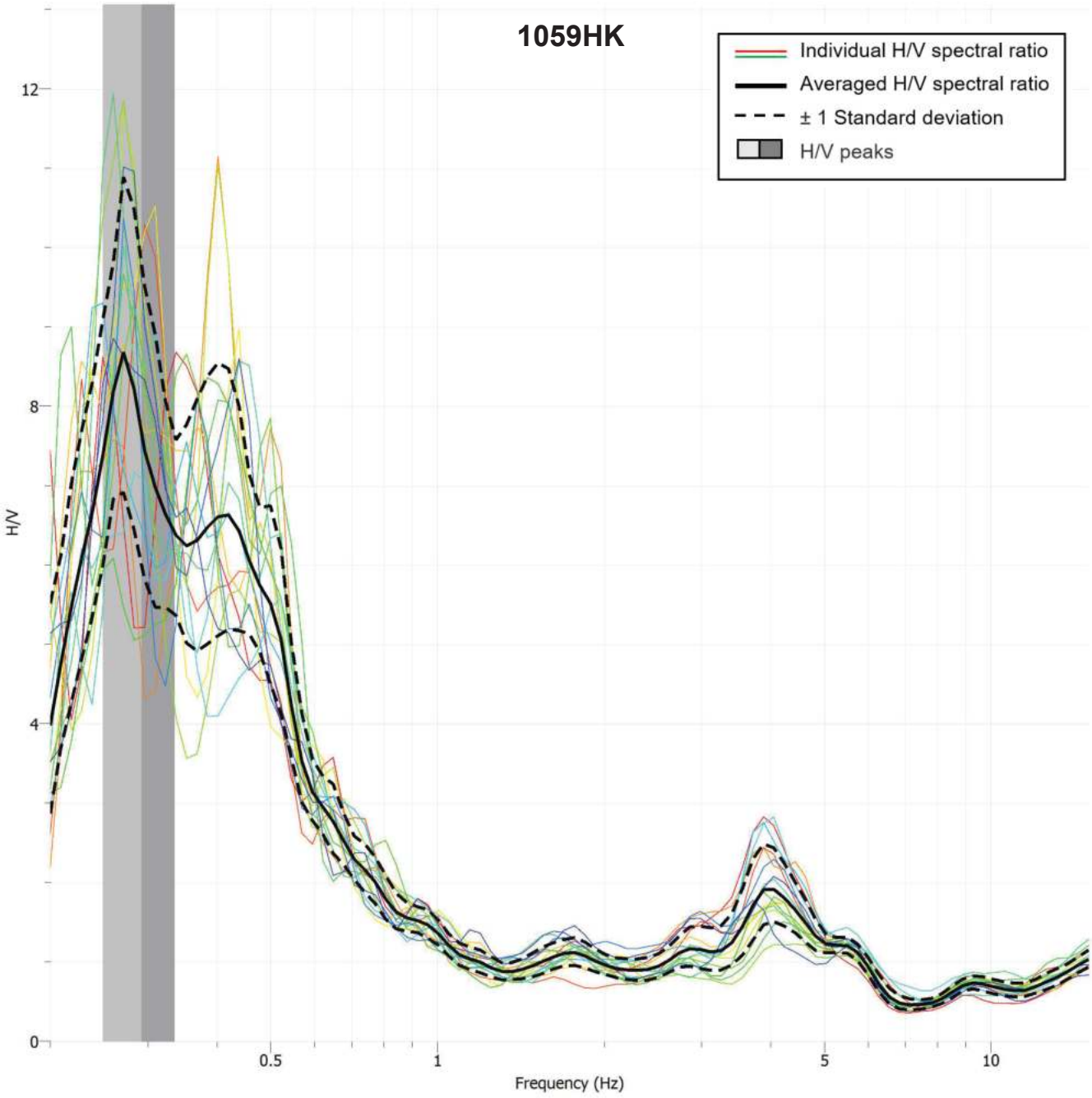
1059HK
Individual H/V spectral ratio
Averaged H/V spectral ratio
± 1 Standard deviation
H/V peaks
H/V
Frequency (Hz)
0
4
8
12
0.5
1
5
10

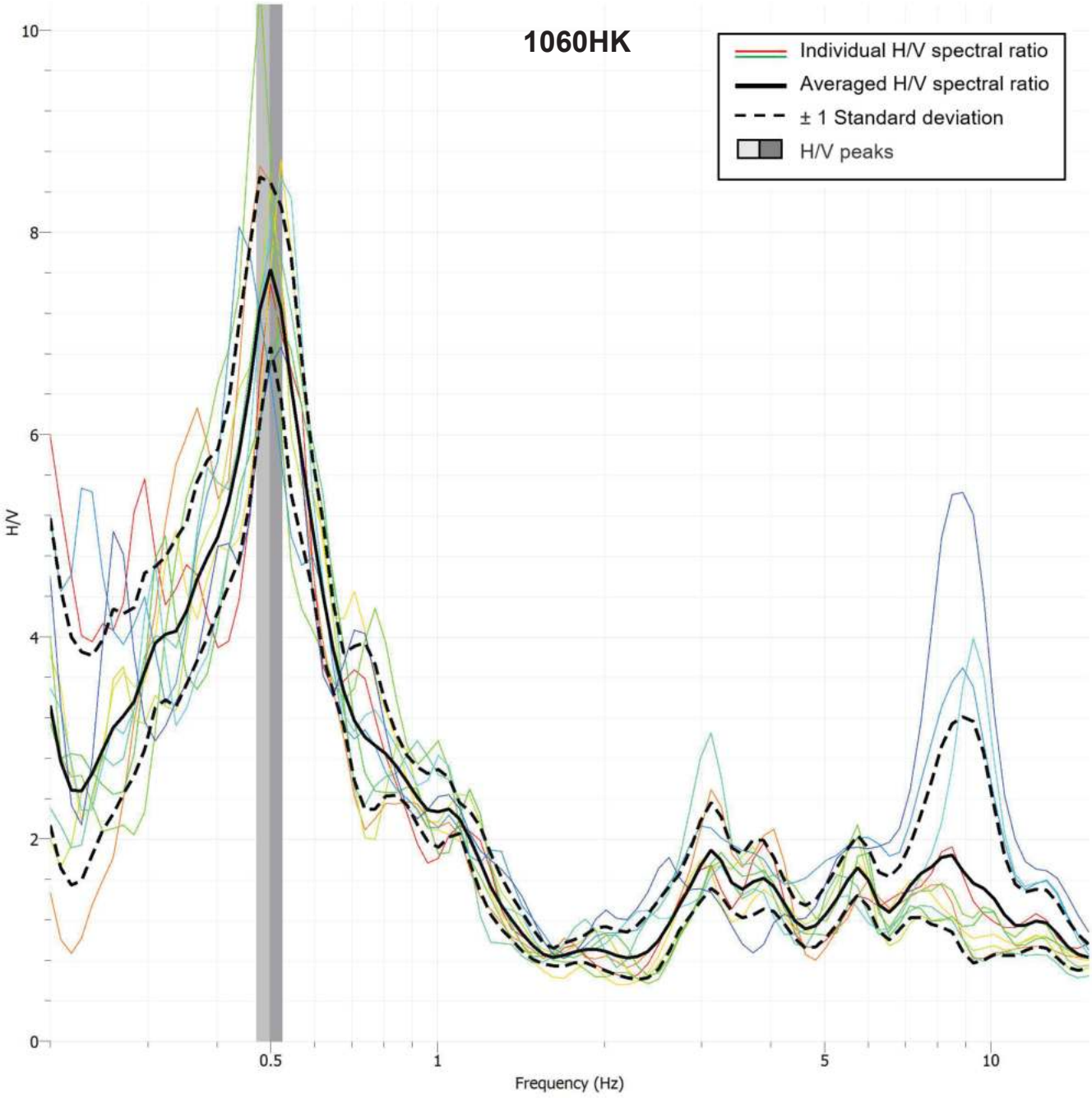
1060HK
Individual H/V spectral ratio
Averaged H/V spectral ratio
± 1 Standard deviation
H/V peaks
H/V
Frequency (Hz)
0
2
4
6
8
10
0.5
1
5
10

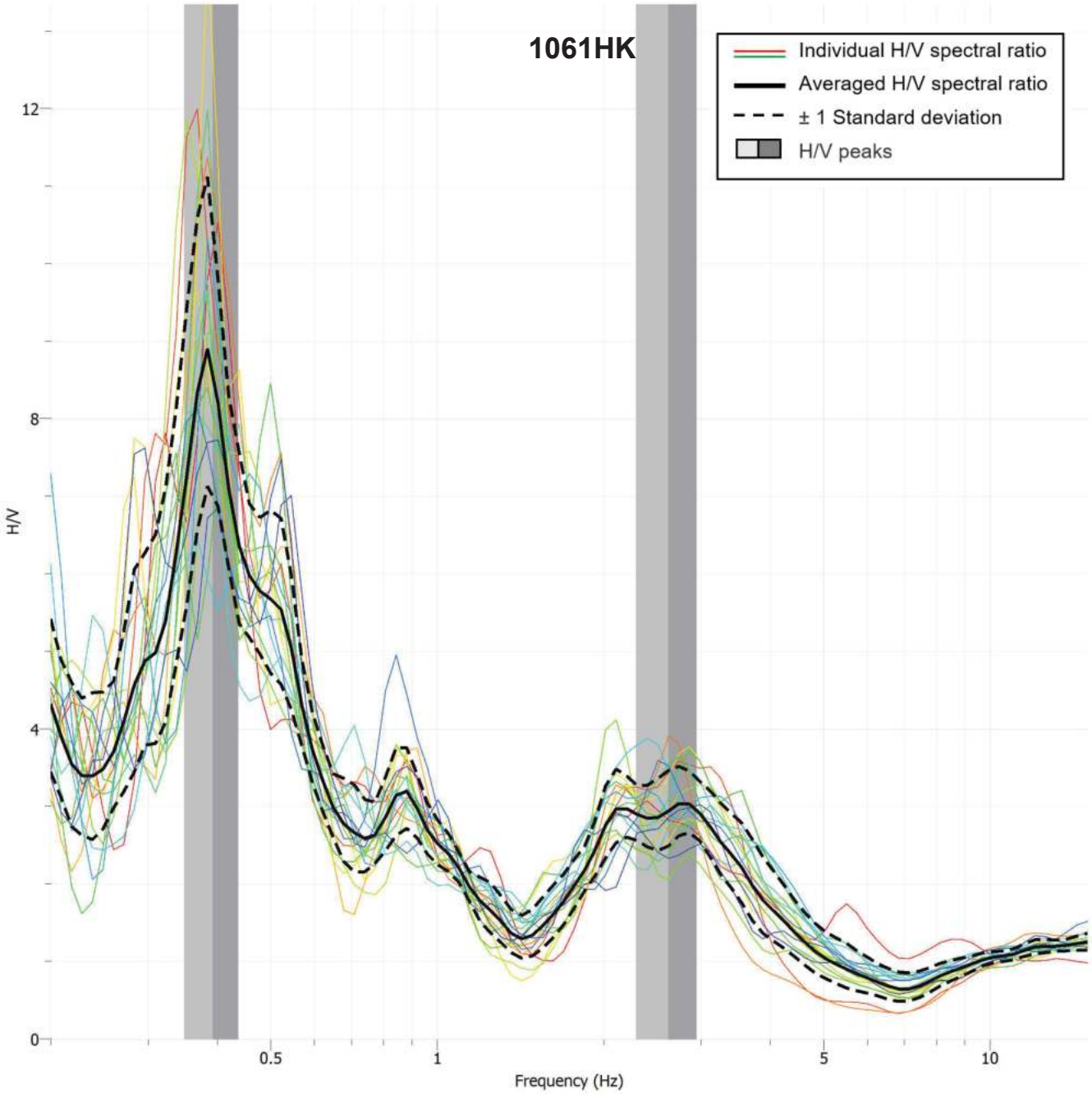
1061HK
Individual H/V spectral ratio
Averaged H/V spectral ratio
± 1 Standard deviation
H/V peaks
H/V
12
8
4
0
0.5
1
5
10
Frequency (Hz)

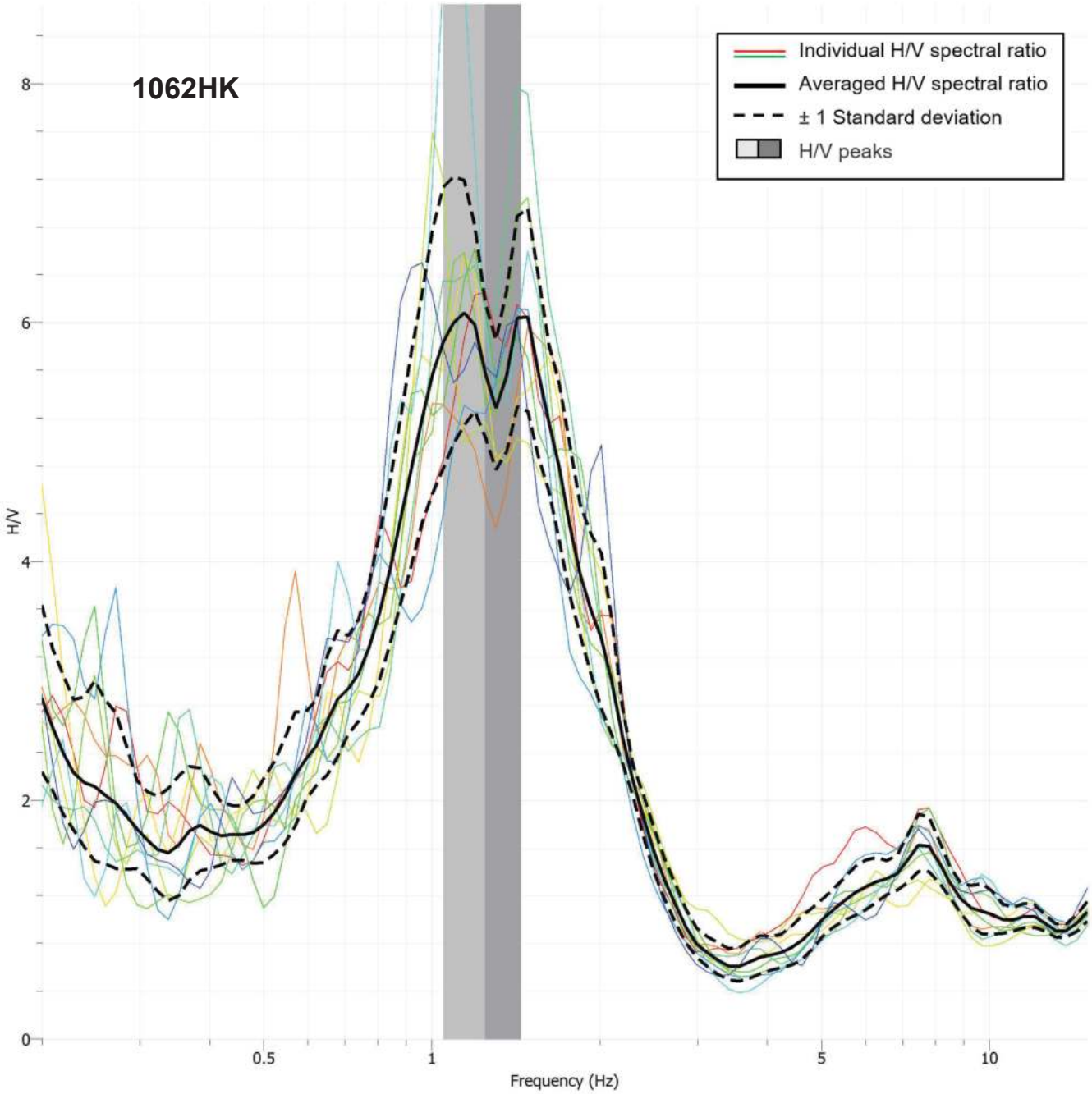
1062HK
Individual H/V spectral ratio
Averaged H/V spectral ratio
± 1 Standard deviation
H/V peaks
H/V
Frequency (Hz)
0
2
4
6
8
0.5
1
5
10

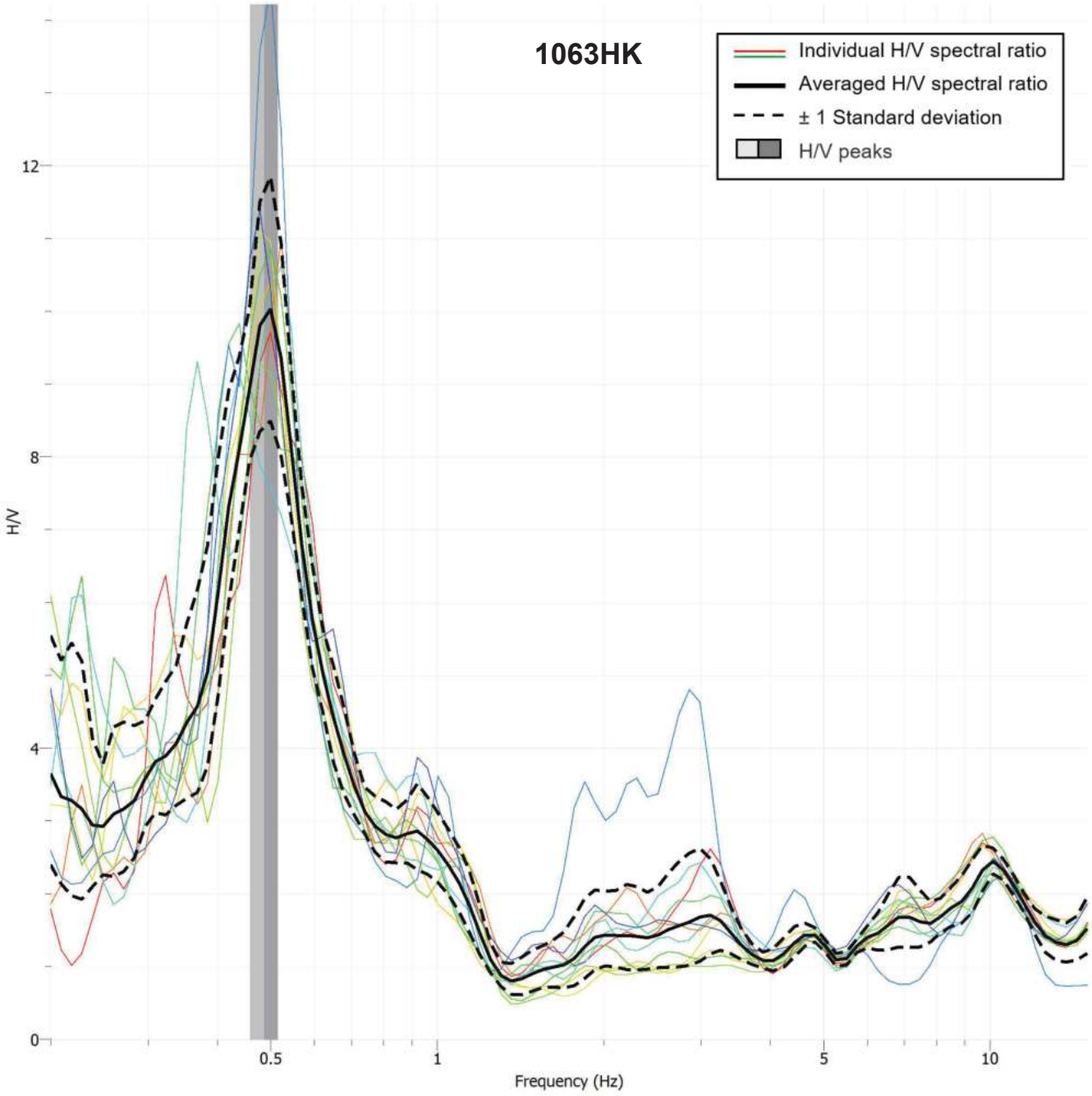
1063HK
Individual H/V spectral ratio
Averaged H/V spectral ratio
± 1 Standard deviation
H/V peaks
H/V
12
8
4
0
0.5
1
5
10
Frequency (Hz)

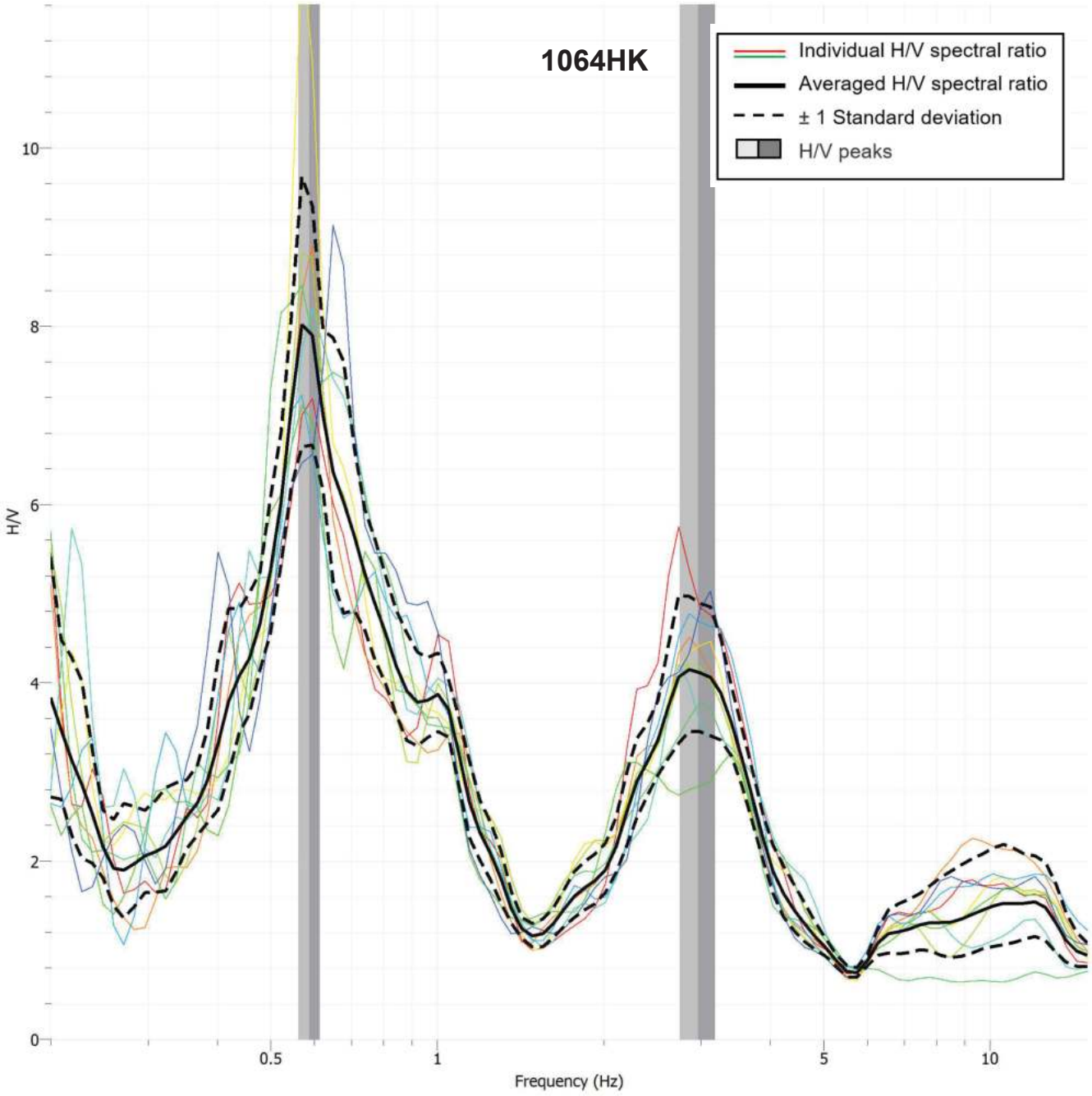
1064HK
Individual H/V spectral ratio
Averaged H/V spectral ratio
± 1 Standard deviation
H/V peaks
H/V
Frequency (Hz)
0
2
4
6
8
10
0.5
1
5
10

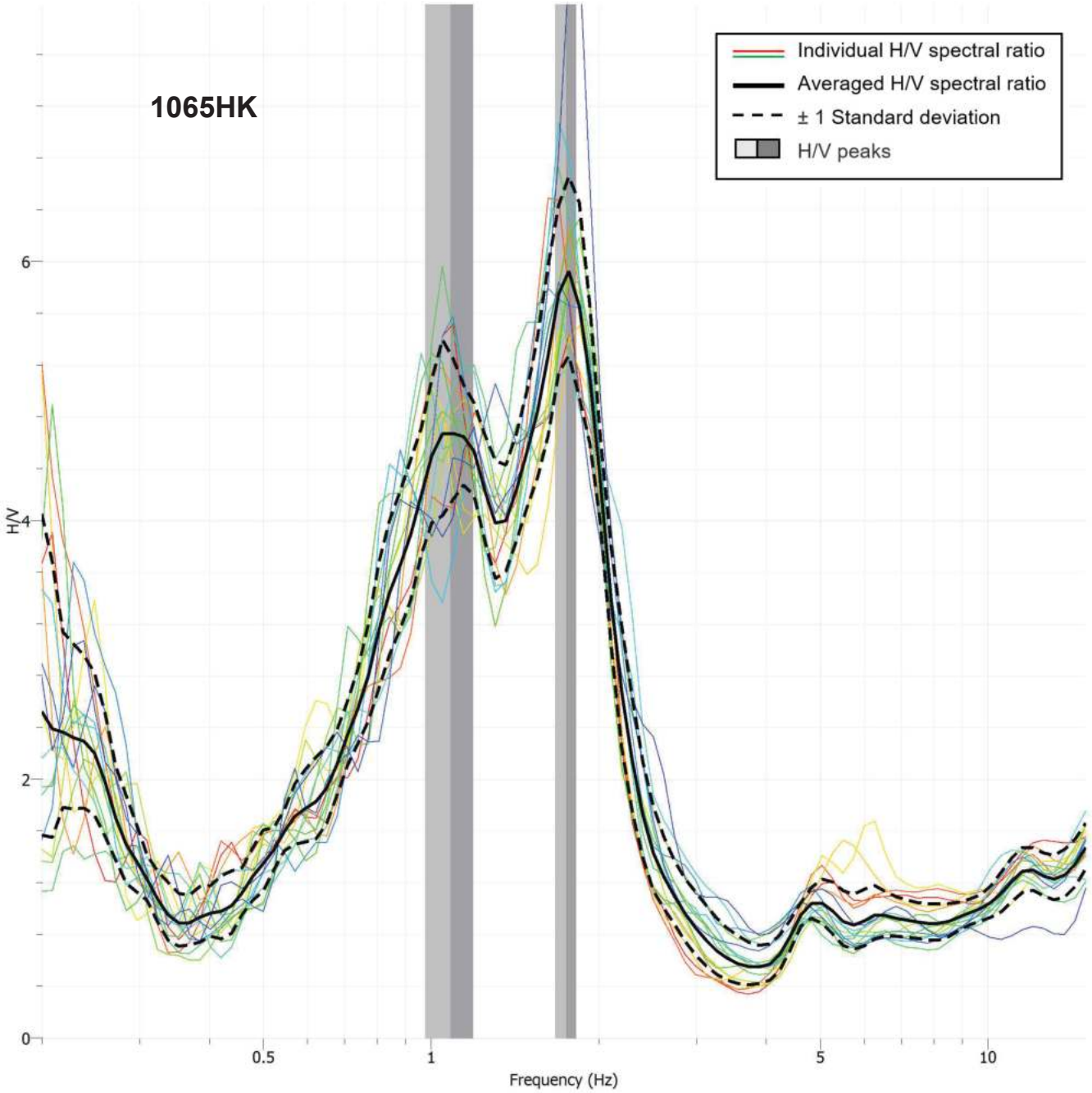
1065HK
Individual H/V spectral ratio
Averaged H/V spectral ratio
± 1 Standard deviation
H/V peaks
H/V
0
2
4
6
0.5
1
5
10
Frequency (Hz)

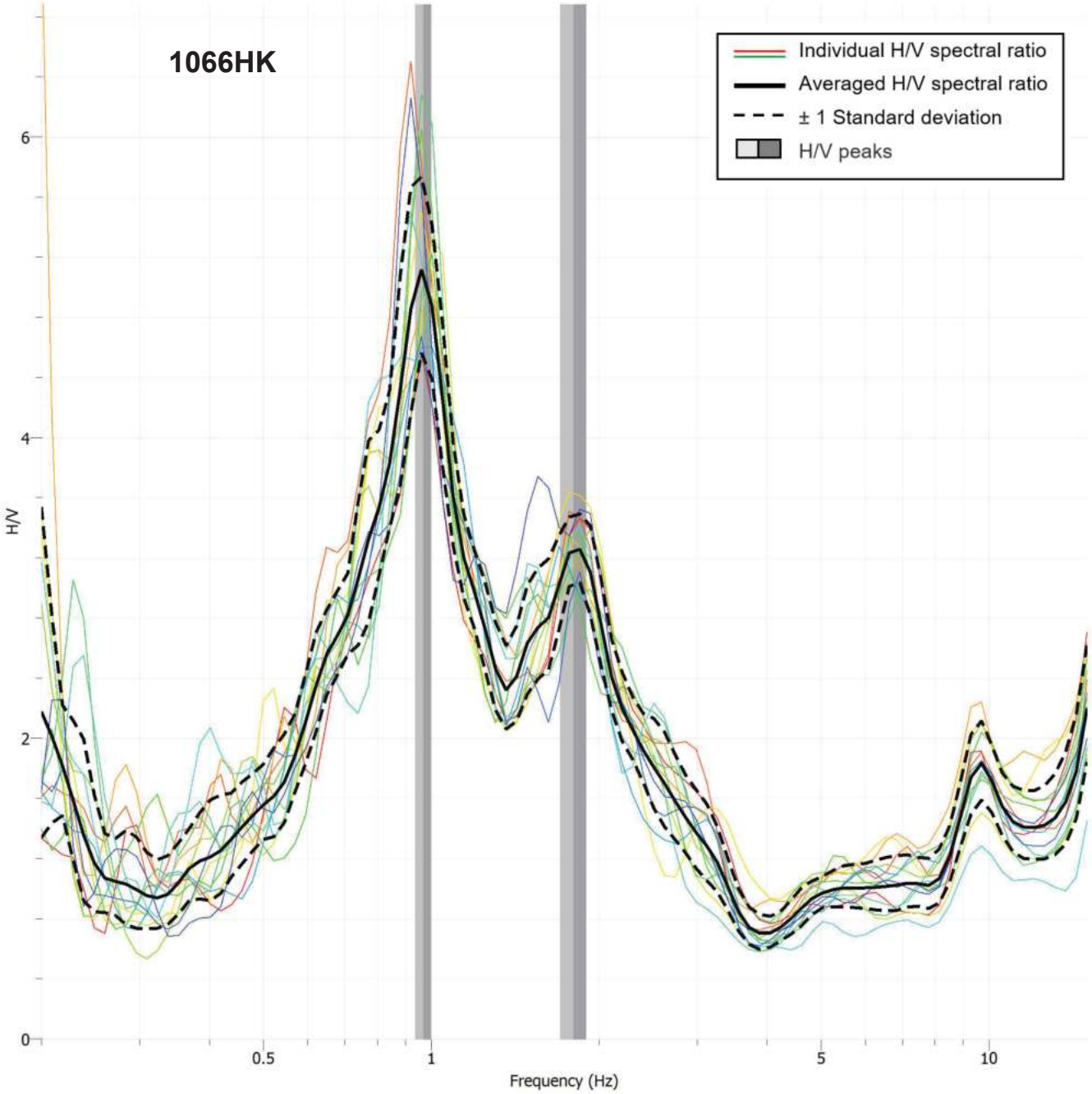
1066HK
Individual H/V spectral ratio
Averaged H/V spectral ratio
± 1 Standard deviation
H/V peaks
H/V
0
2
4
6
0.5
1
5
10
Frequency (Hz)

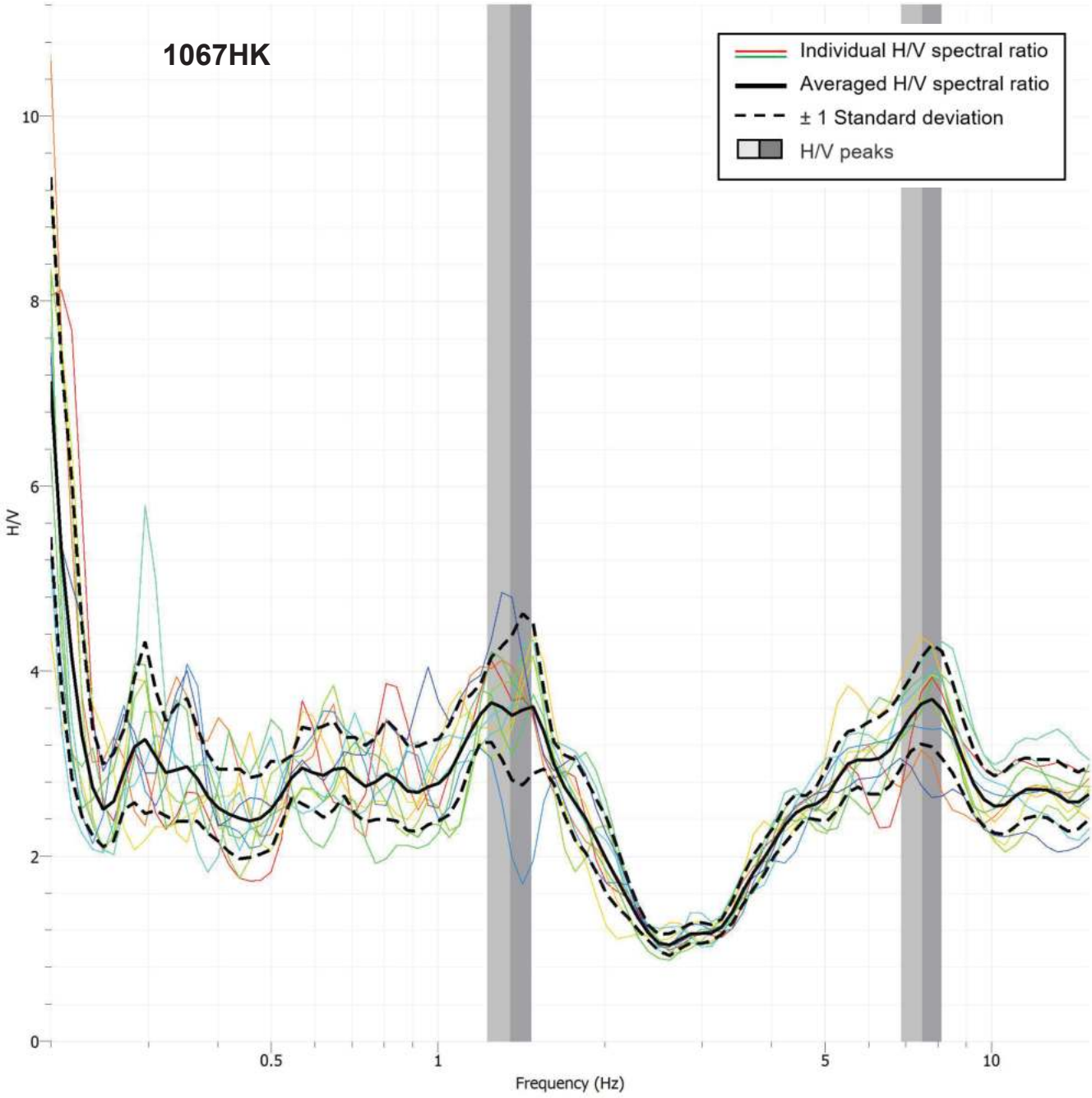
1067HK
Individual H/V spectral ratio
Averaged H/V spectral ratio
± 1 Standard deviation
H/V peaks
H/V
Frequency (Hz)
0
2
4
6
8
10
0.5
1
5
10

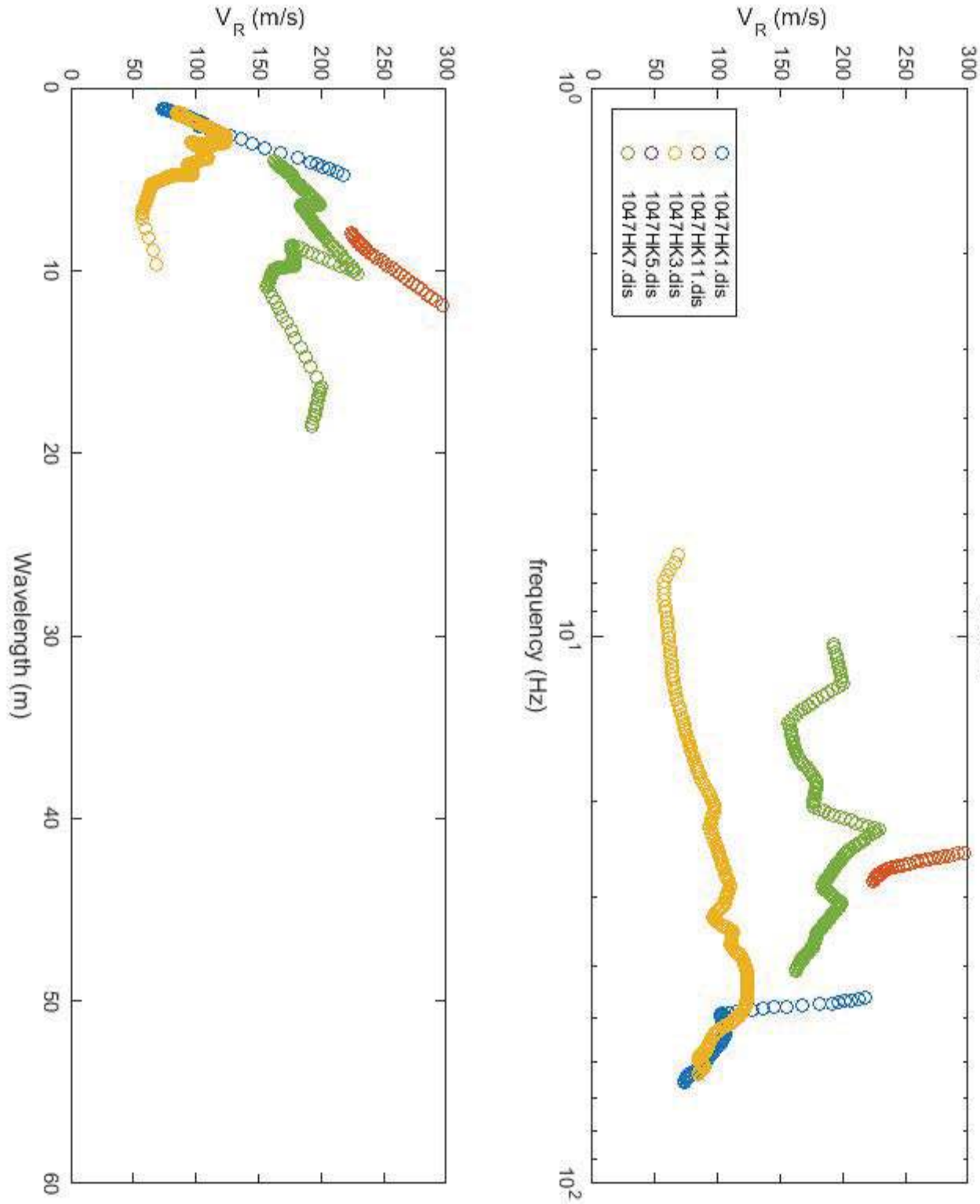
1047HK
V_R (m/s)
frequency (Hz)
1047HK1.dis
1047HK11.dis
1047HK3.dis
1047HK5.dis
1047HK7.dis
V_R (m/s)
Wavelength (m)

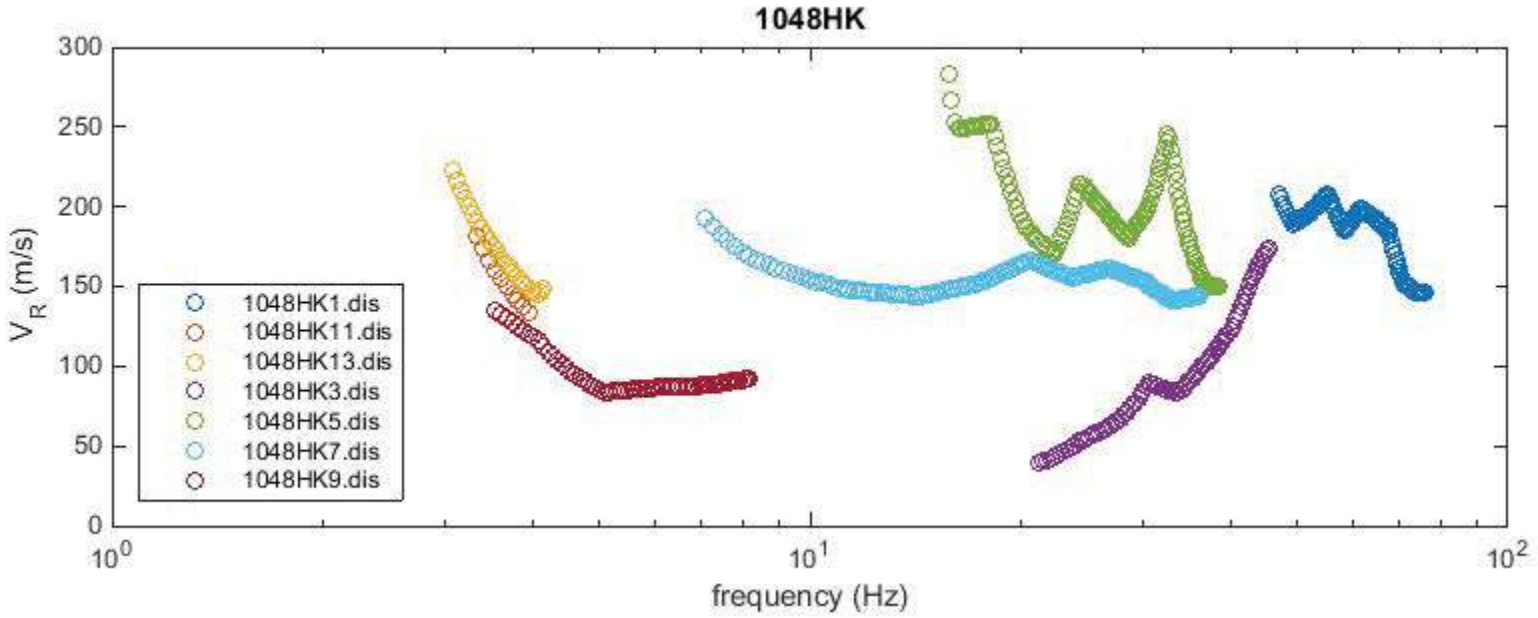
1048HK
300
250
200
150
100
50
0
V_R (m/s)
1048HK1.dis
1048HK11.dis
1048HK13.dis
1048HK3.dis
1048HK5.dis
1048HK7.dis
1048HK9.dis
10^0
10^1
10^2
frequency (Hz)

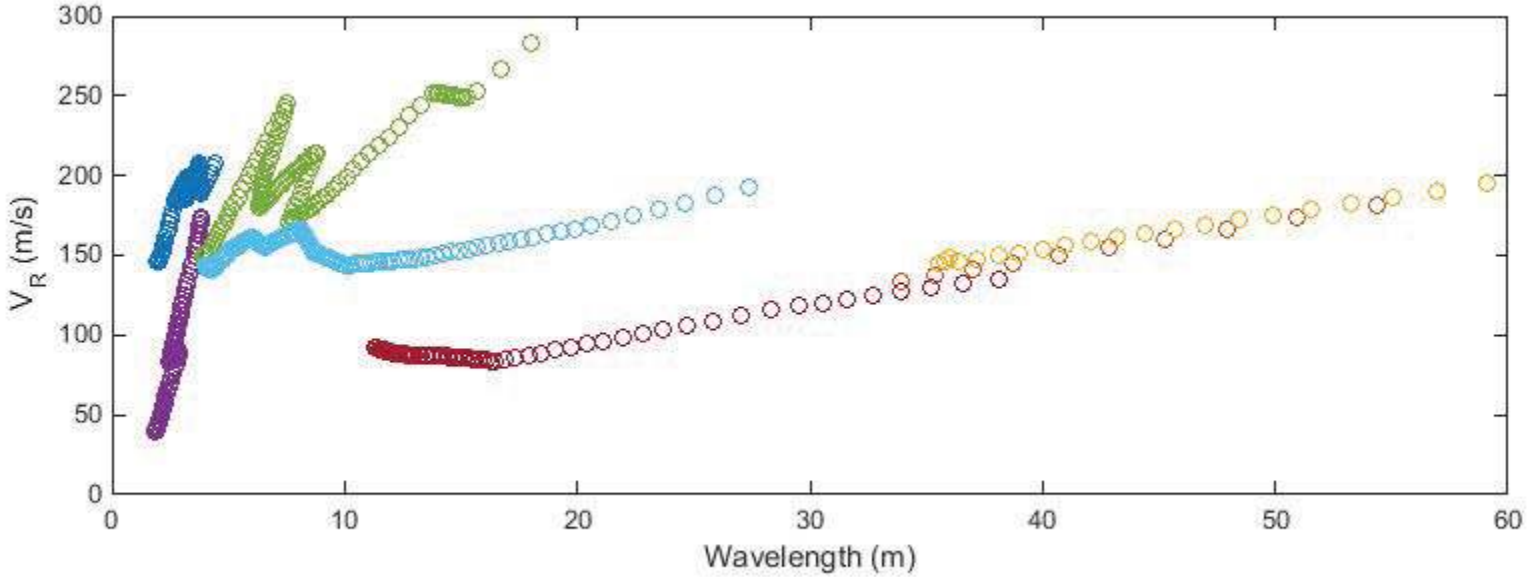
300
250
200
150
100
50
0
V_R (m/s)
0
10
20
30
40
50
60
Wavelength (m)

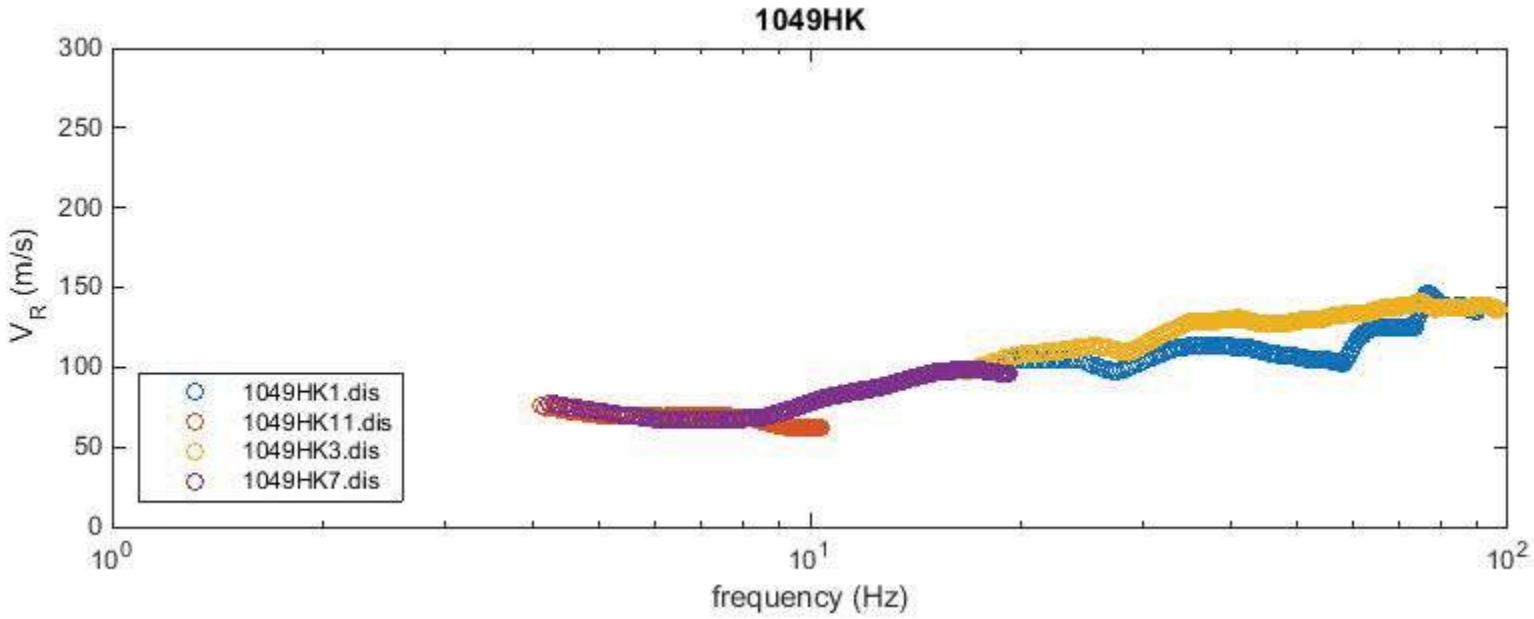
1049HK
300
250
200
150
100
50
0
V_R (m/s)
1049HK1.dis
1049HK11.dis
1049HK3.dis
1049HK7.dis
10^0
10^1
10^2
frequency (Hz)

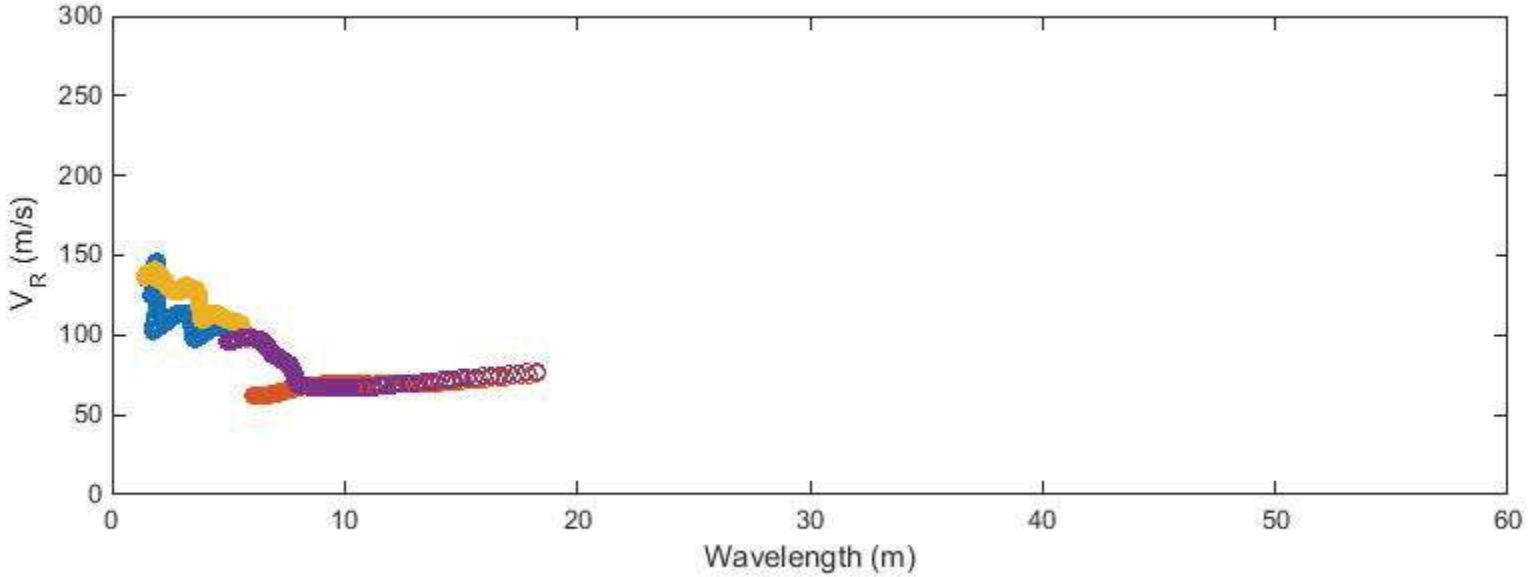
300
250
200
150
100
50
0
V_R (m/s)
0
10
20
30
40
50
60
Wavelength (m)

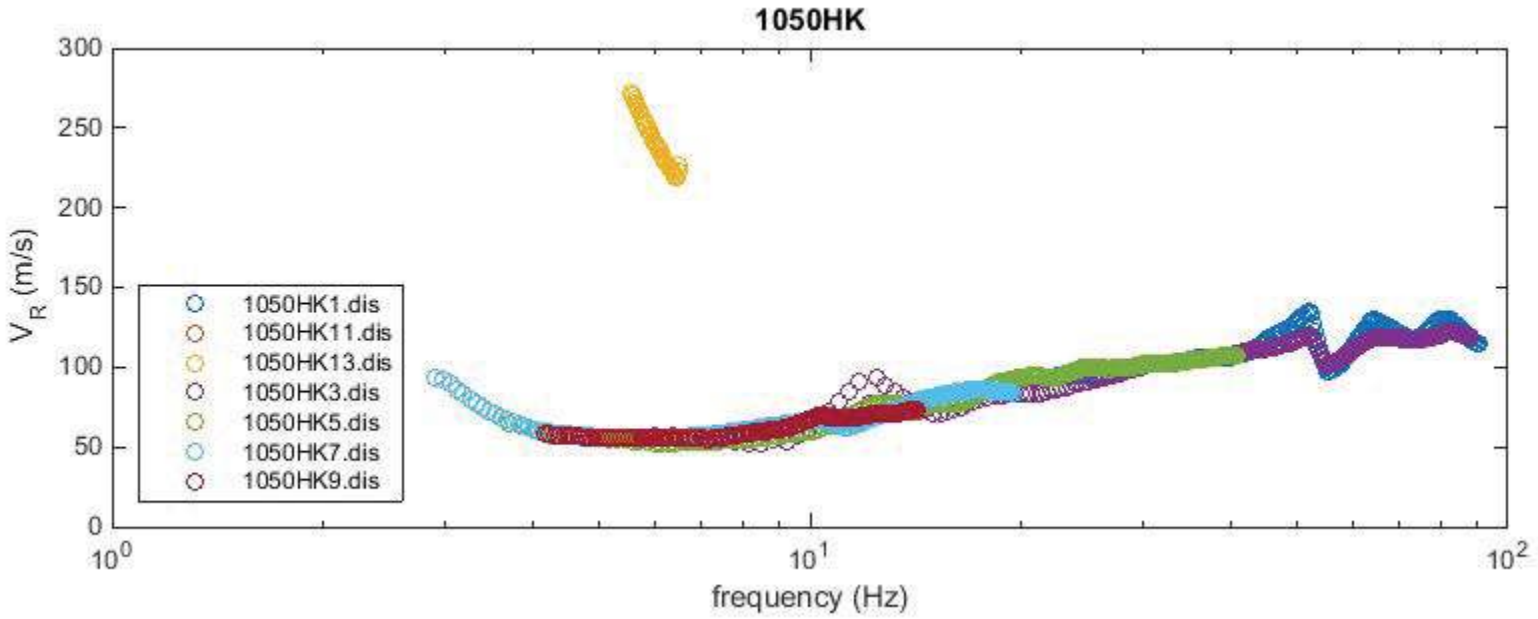
1050HK
300
250
200
150
100
50
0
V_R (m/s)
1050HK1.dis
1050HK11.dis
1050HK13.dis
1050HK3.dis
1050HK5.dis
1050HK7.dis
1050HK9.dis
10^0
10^1
10^2
frequency (Hz)

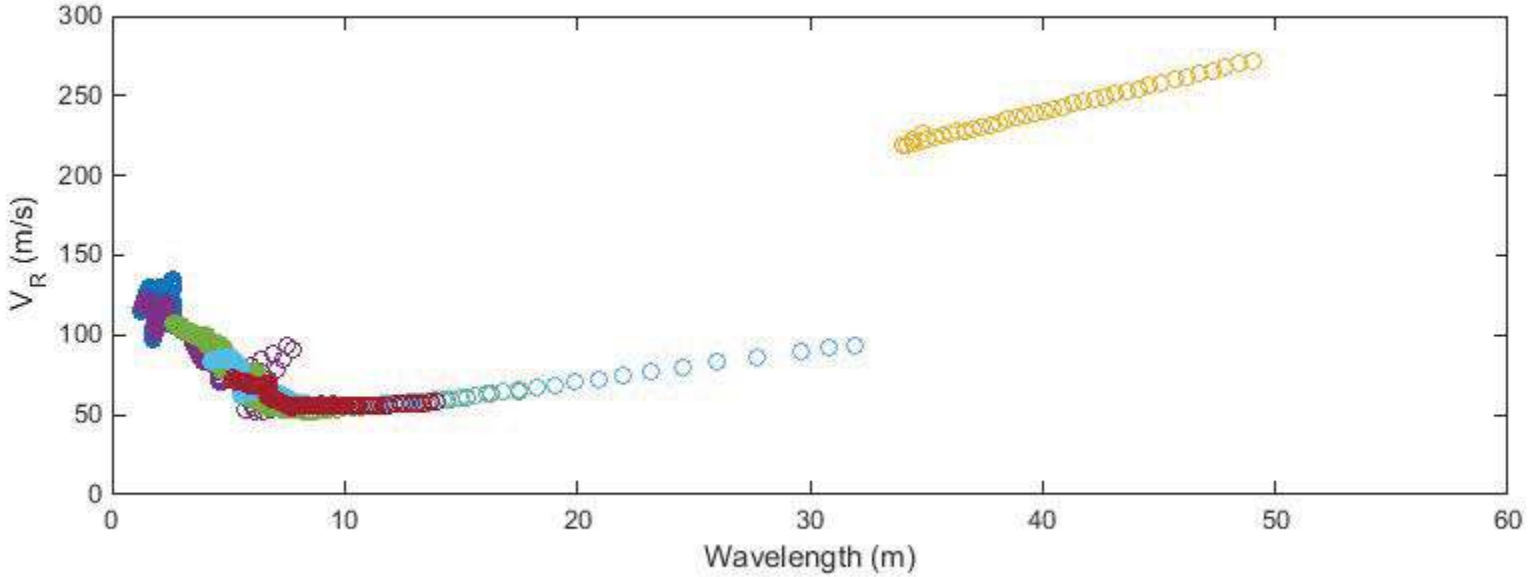
300
250
200
150
100
50
0
V_R (m/s)
0
10
20
30
40
50
60
Wavelength (m)

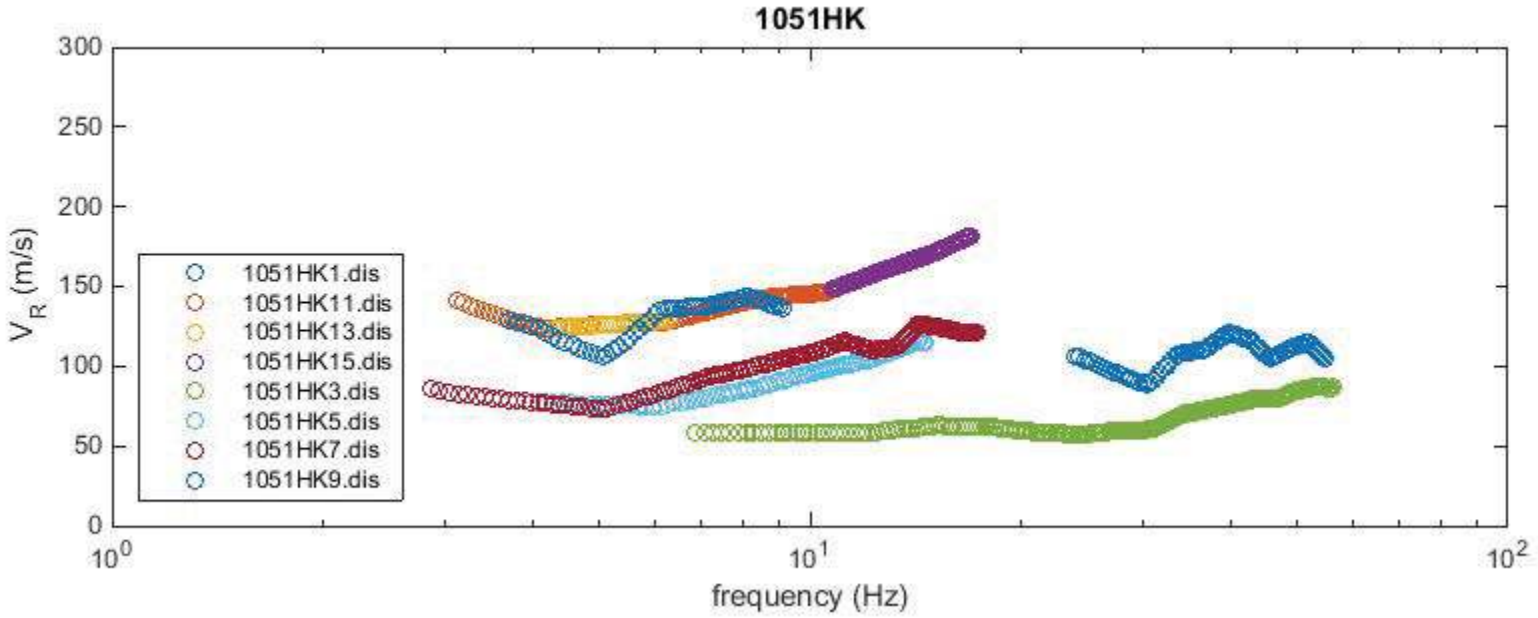
1051HK
300
250
200
150
100
50
0
V_R (m/s)
1051HK1.dis
1051HK11.dis
1051HK13.dis
1051HK15.dis
1051HK3.dis
1051HK5.dis
1051HK7.dis
1051HK9.dis
10^0
10^1
10^2
frequency (Hz)

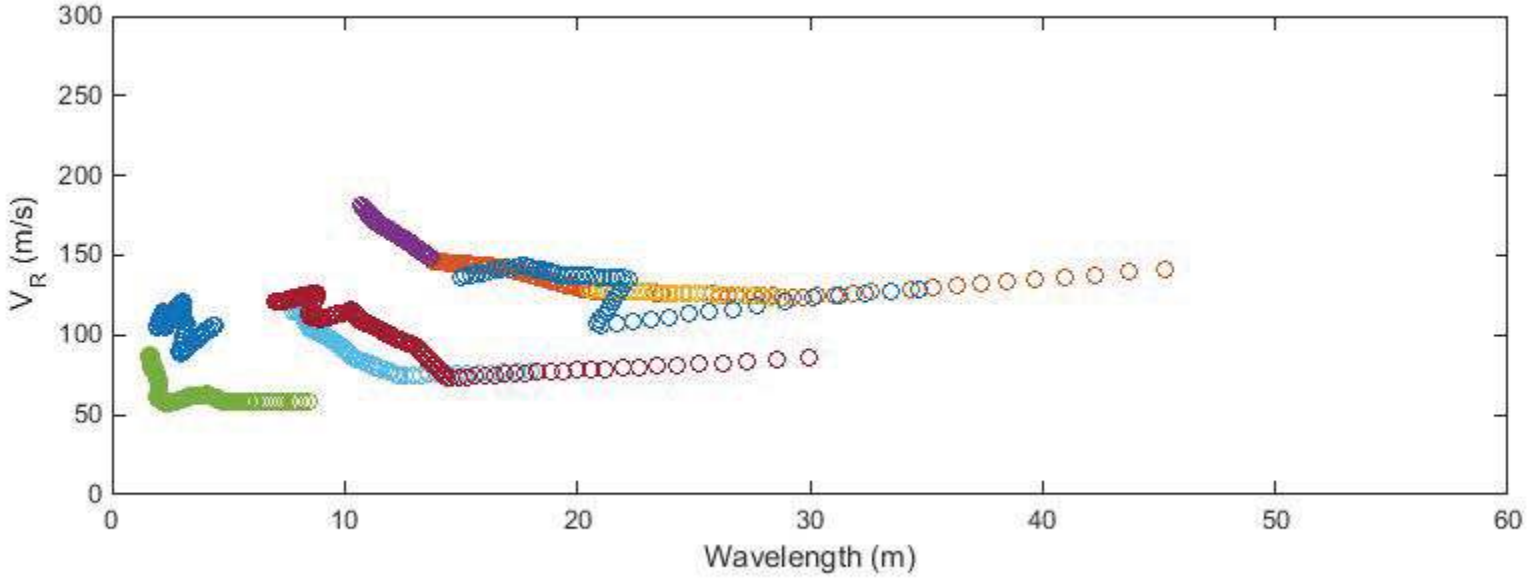
300
250
200
150
100
50
0
V_R (m/s)
0
10
20
30
40
50
60
Wavelength (m)

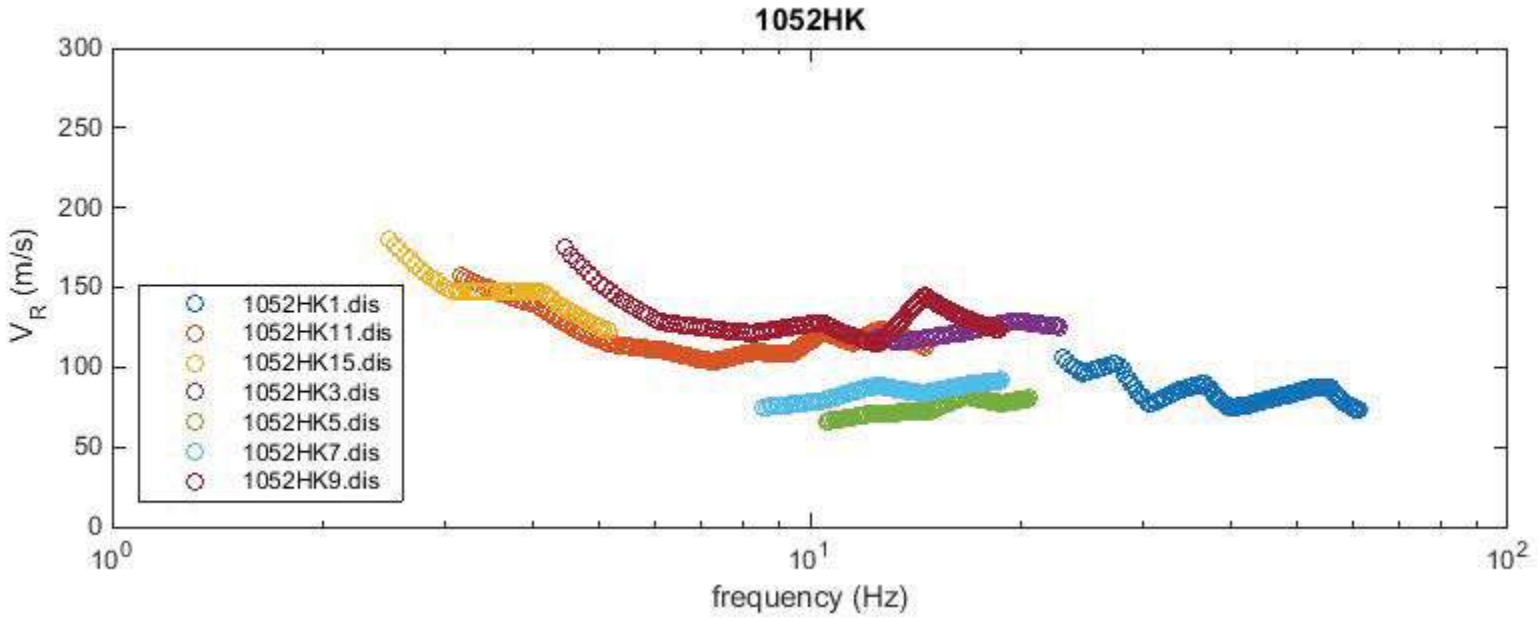
1052HK
300
250
200
150
100
50
0
V_R (m/s)
1052HK1.dis
1052HK11.dis
1052HK15.dis
1052HK3.dis
1052HK5.dis
1052HK7.dis
1052HK9.dis
10^0
10^1
10^2
frequency (Hz)

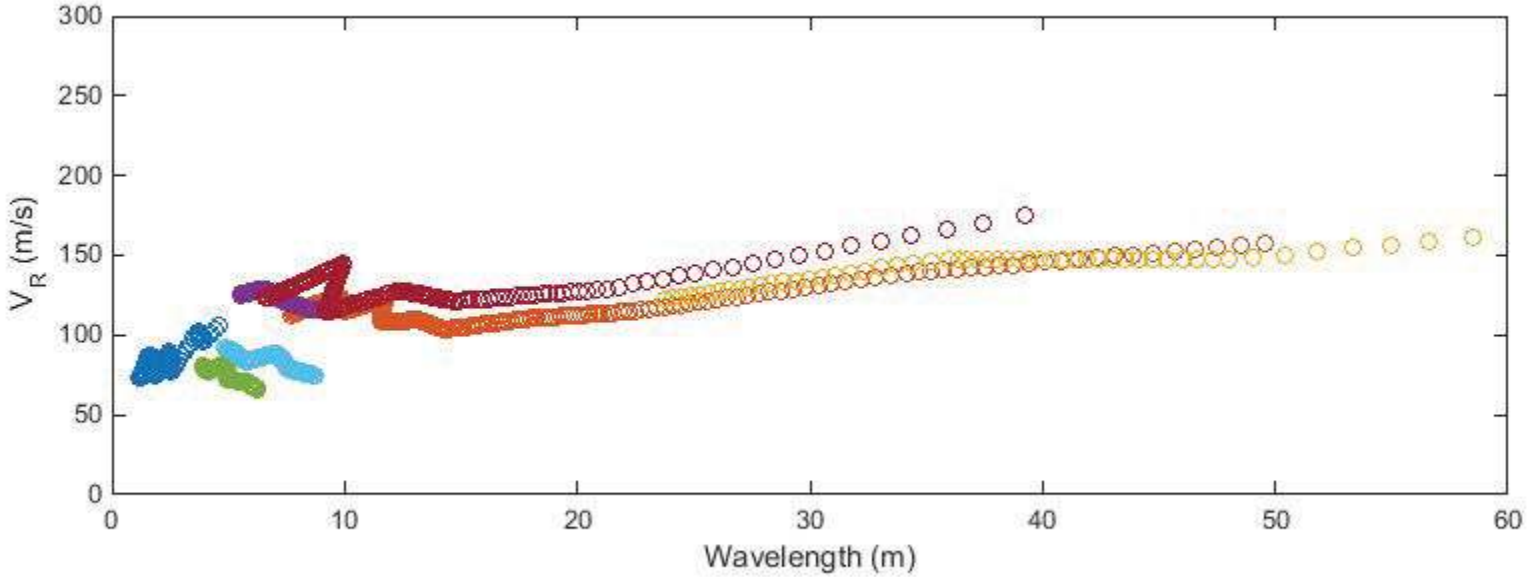
300
250
200
150
100
50
0
V_R (m/s)
0
10
20
30
40
50
60
Wavelength (m)

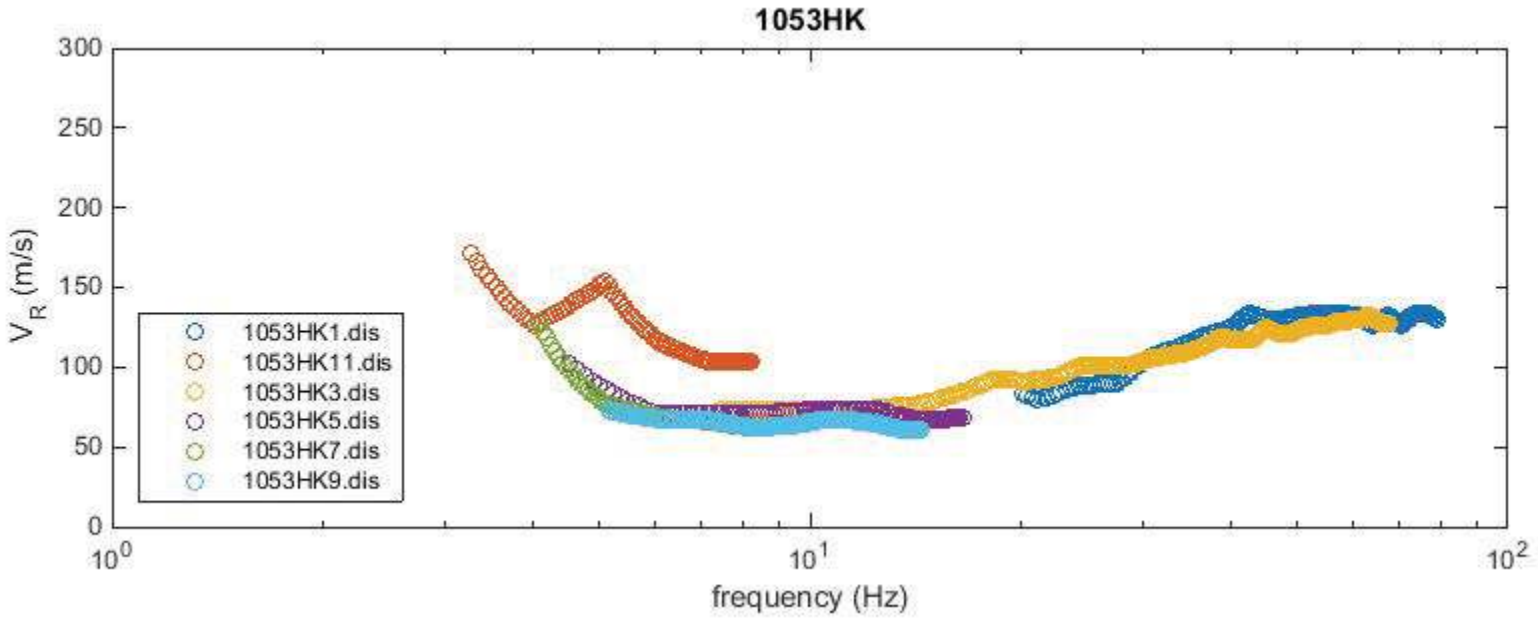
1053HK
300
250
200
150
100
50
0
V_R (m/s)
1053HK1.dis
1053HK11.dis
1053HK3.dis
1053HK5.dis
1053HK7.dis
1053HK9.dis
10^0
10^1
10^2
frequency (Hz)

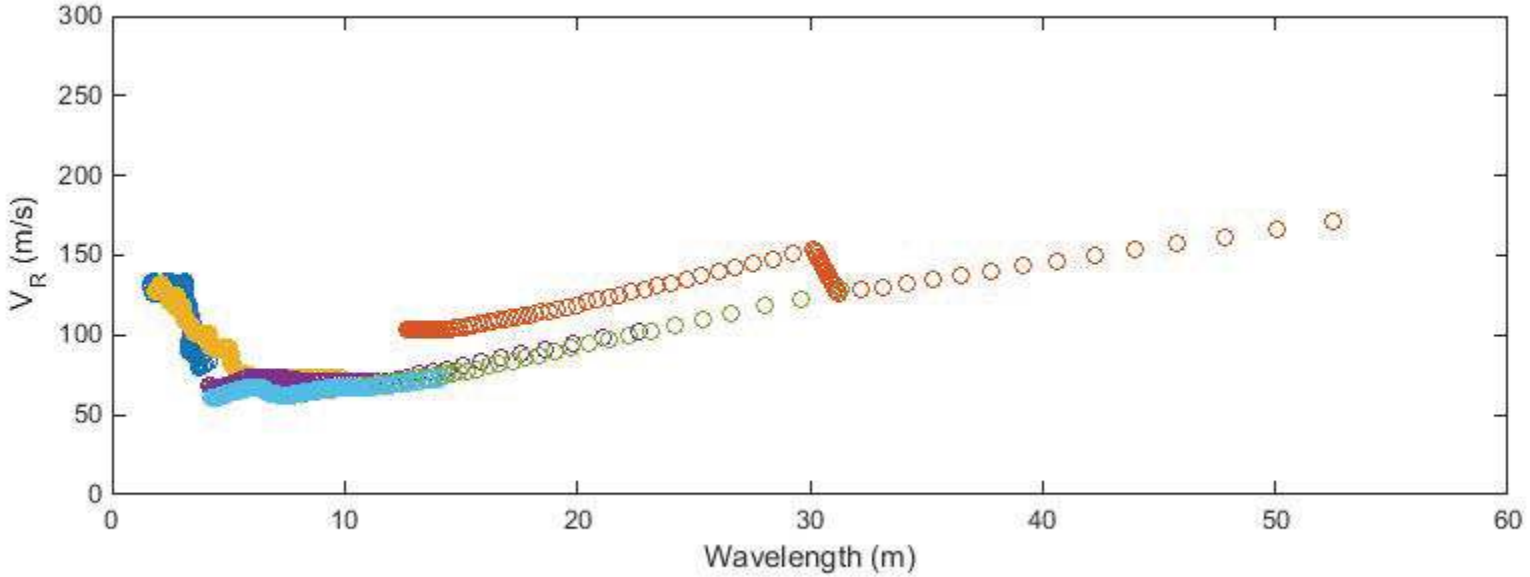
300
250
200
150
100
50
0
V_R (m/s)
0
10
20
30
40
50
60
Wavelength (m)

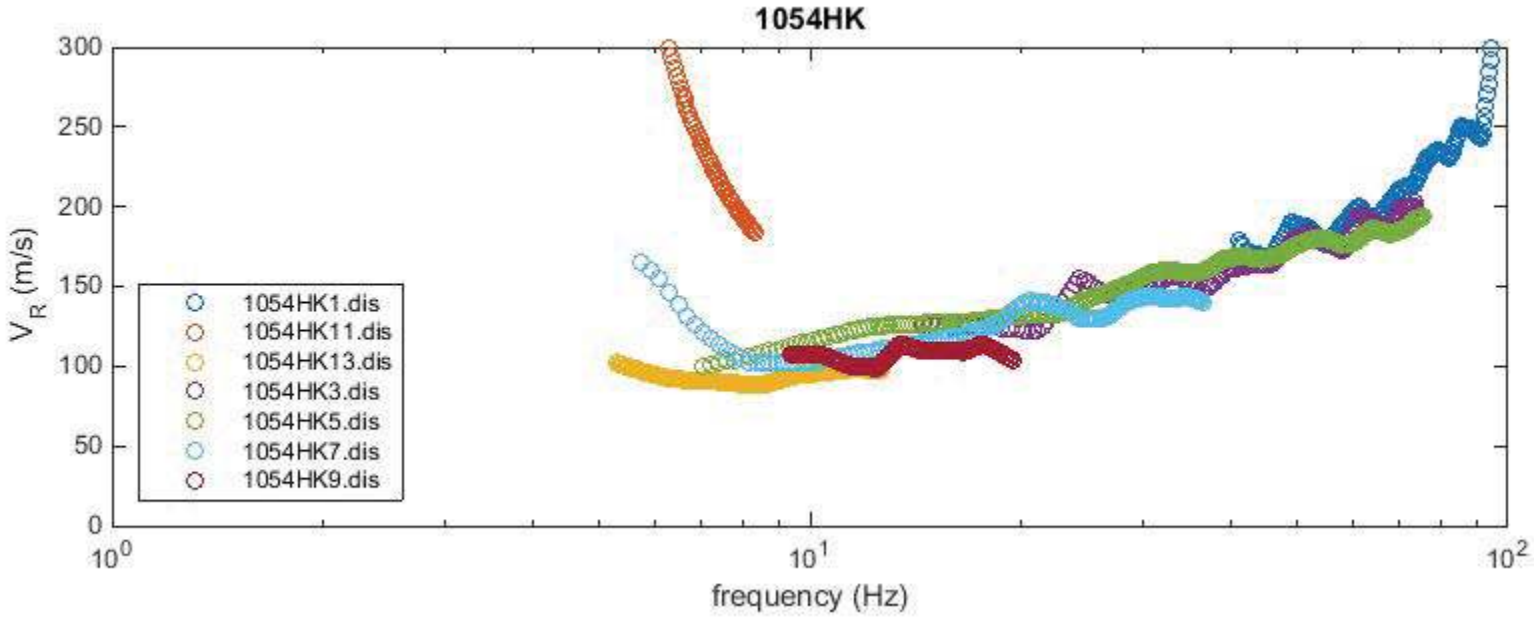
1054HK
300
250
200
150
100
50
0
V_R (m/s)
1054HK1.dis
1054HK11.dis
1054HK13.dis
1054HK3.dis
1054HK5.dis
1054HK7.dis
1054HK9.dis
10^0
10^1
10^2
frequency (Hz)

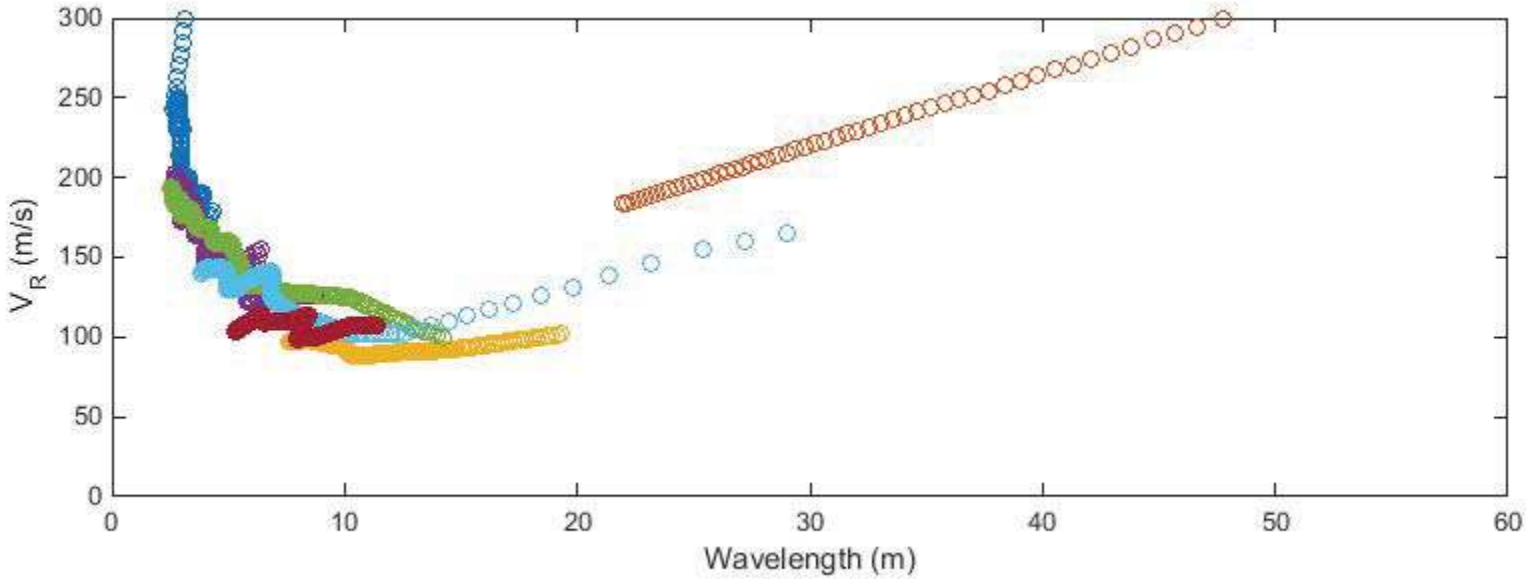
300
250
200
150
100
50
0
V_R (m/s)
0
10
20
30
40
50
60
Wavelength (m)

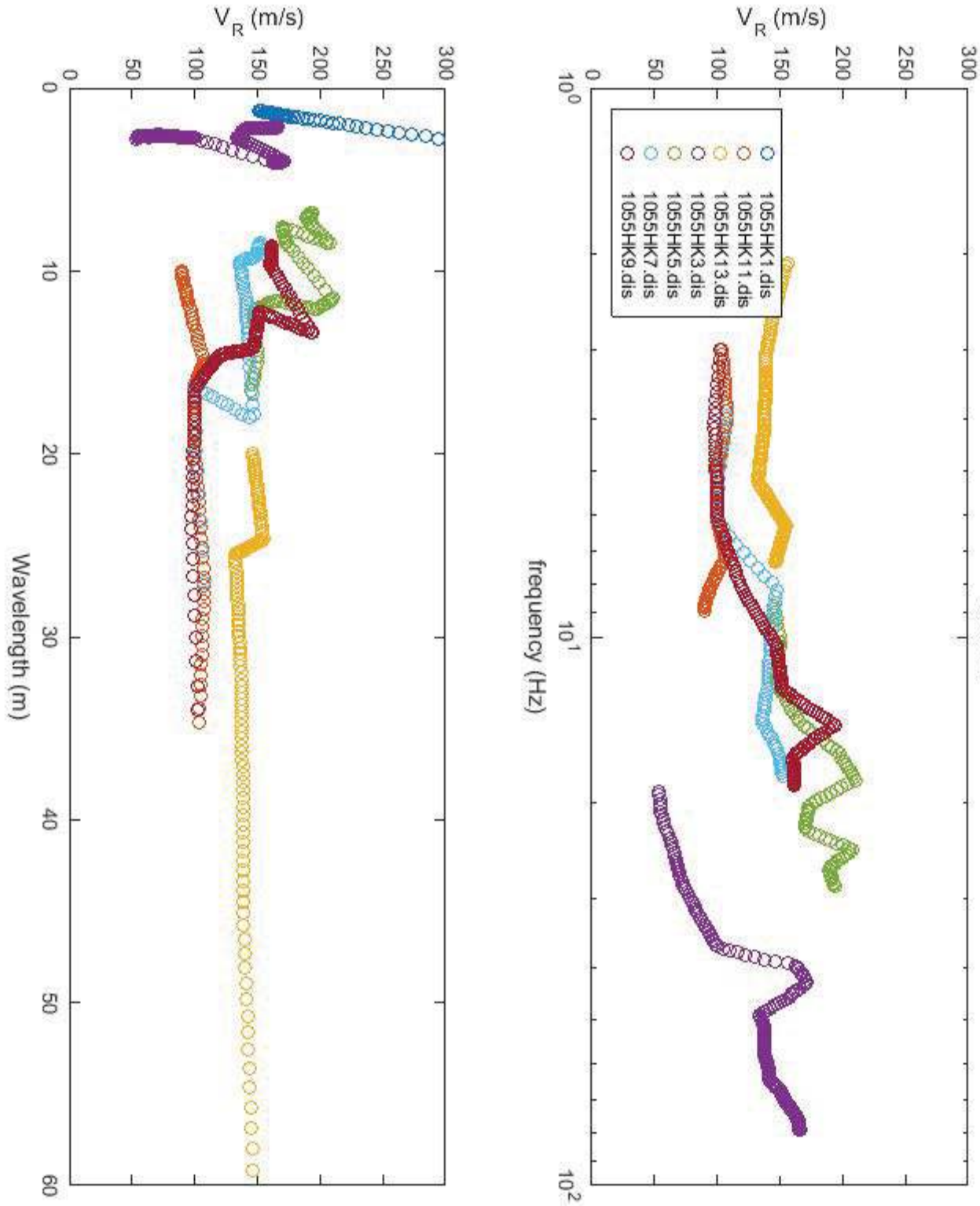
1055HK
V_R (m/s)
frequency (Hz)
1055HK1.dis
1055HK11.dis
1055HK13.dis
1055HK3.dis
1055HK5.dis
1055HK7.dis
1055HK9.dis
V_R (m/s)
Wavelength (m)

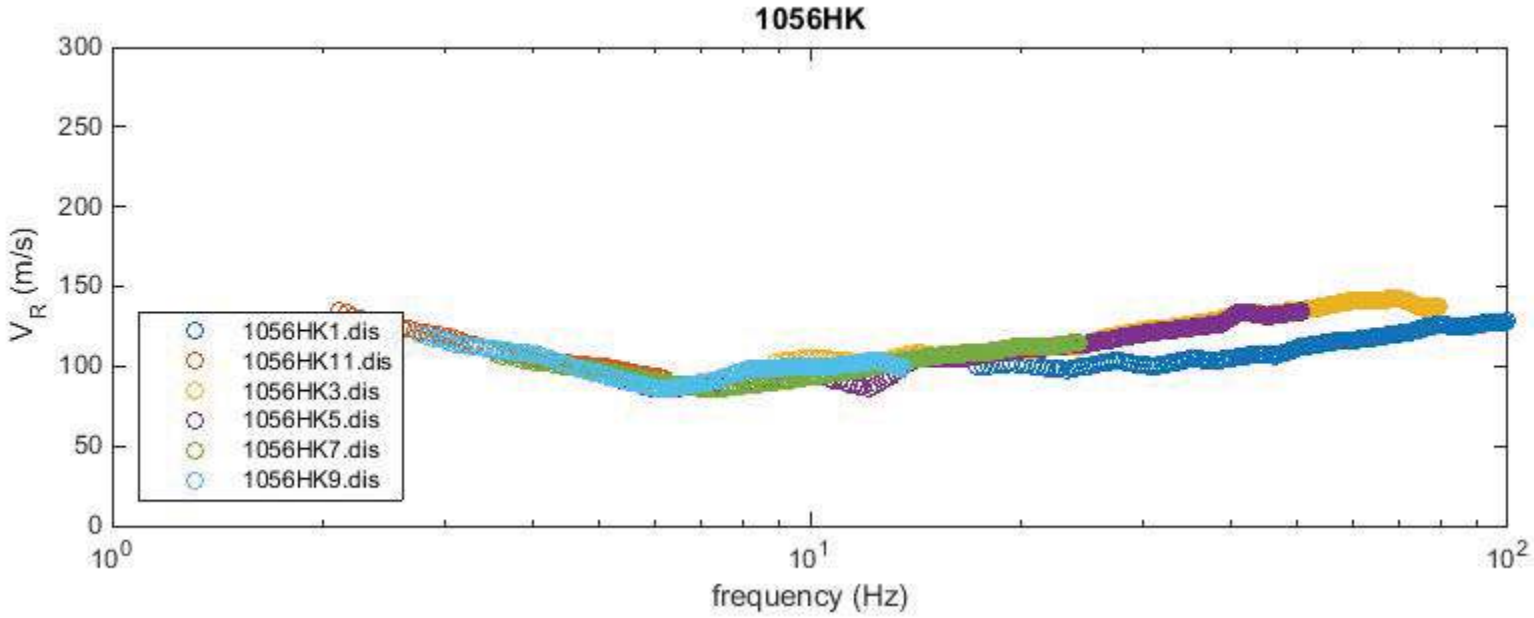
1056HK
300
250
200
150
100
50
0
V_R (m/s)
1056HK1.dis
1056HK11.dis
1056HK3.dis
1056HK5.dis
1056HK7.dis
1056HK9.dis
10^0
10^1
10^2
frequency (Hz)

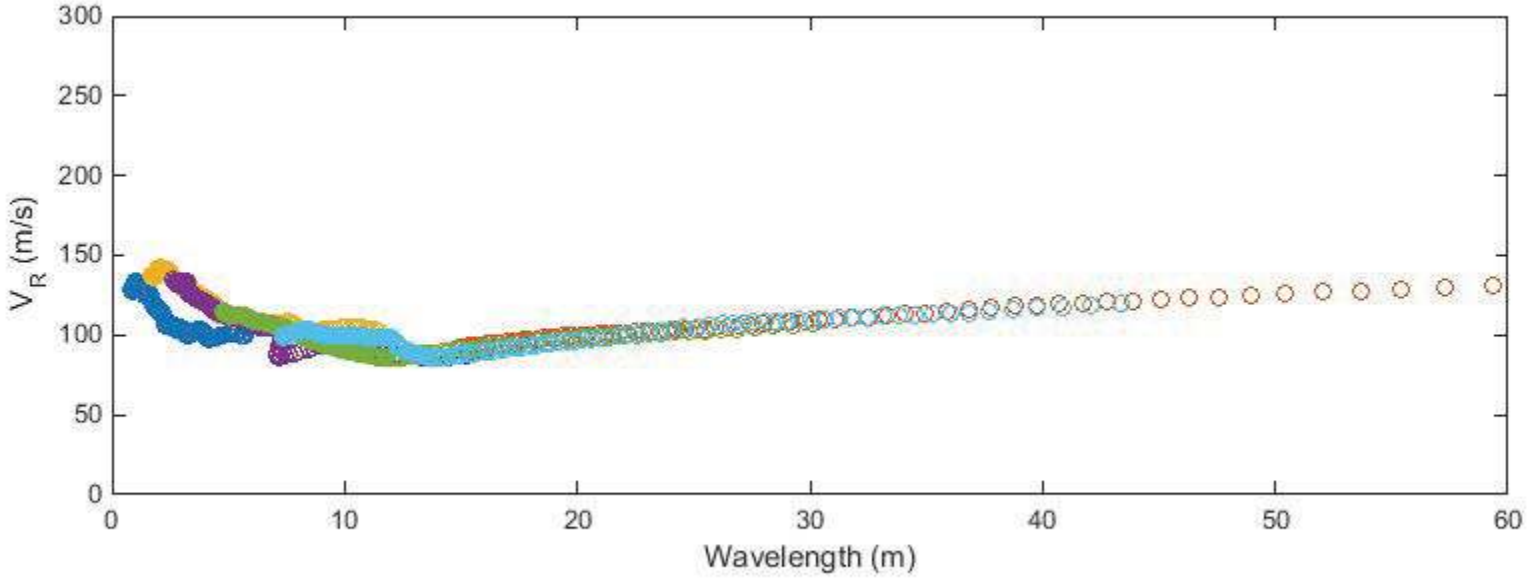
300
250
200
150
100
50
0
V_R (m/s)
0
10
20
30
40
50
60
Wavelength (m)

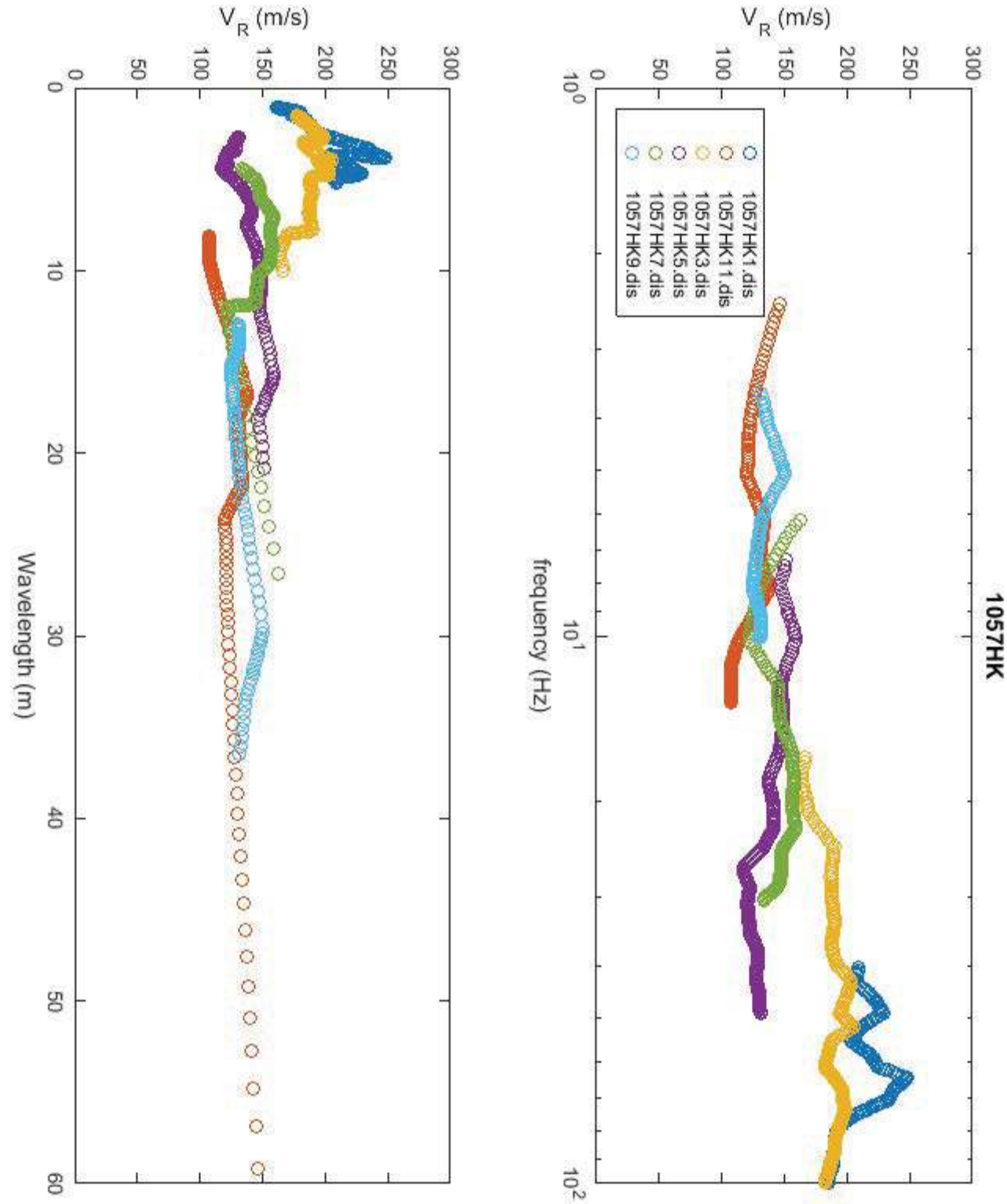
1057HK
V_R (m/s)
frequency (Hz)
1057HK1.dis
1057HK11.dis
1057HK3.dis
1057HK5.dis
1057HK7.dis
1057HK9.dis
V_R (m/s)
Wavelength (m)

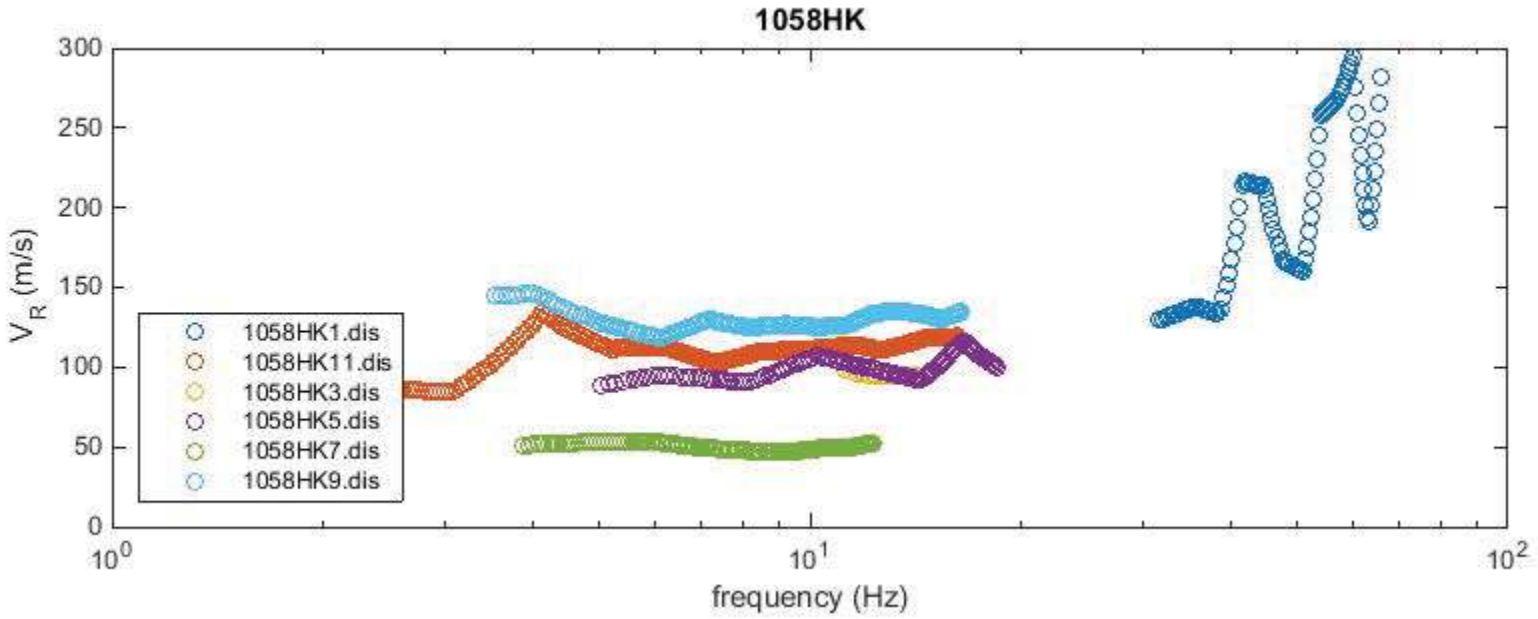
1058HK
300
250
200
150
100
50
0
V_R (m/s)
1058HK1.dis
1058HK11.dis
1058HK3.dis
1058HK5.dis
1058HK7.dis
1058HK9.dis
10^0
10^1
10^2
frequency (Hz)

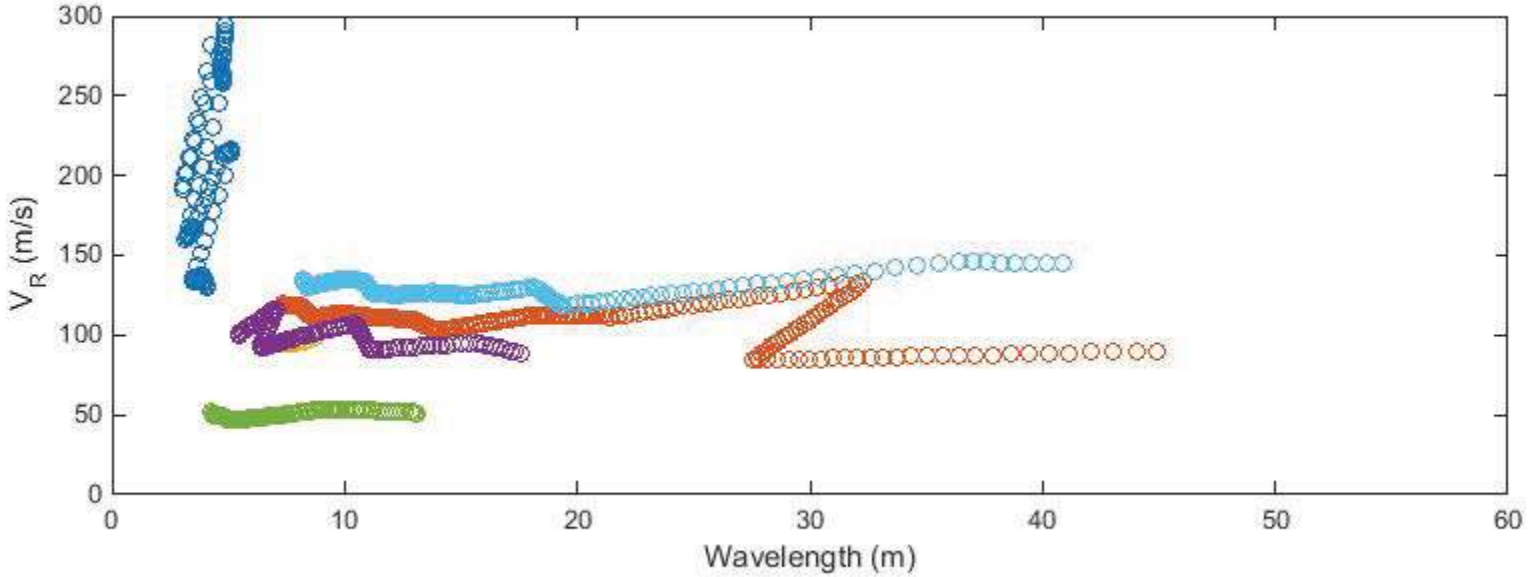
300
250
200
150
100
50
0
V_R (m/s)
0
10
20
30
40
50
60
Wavelength (m)

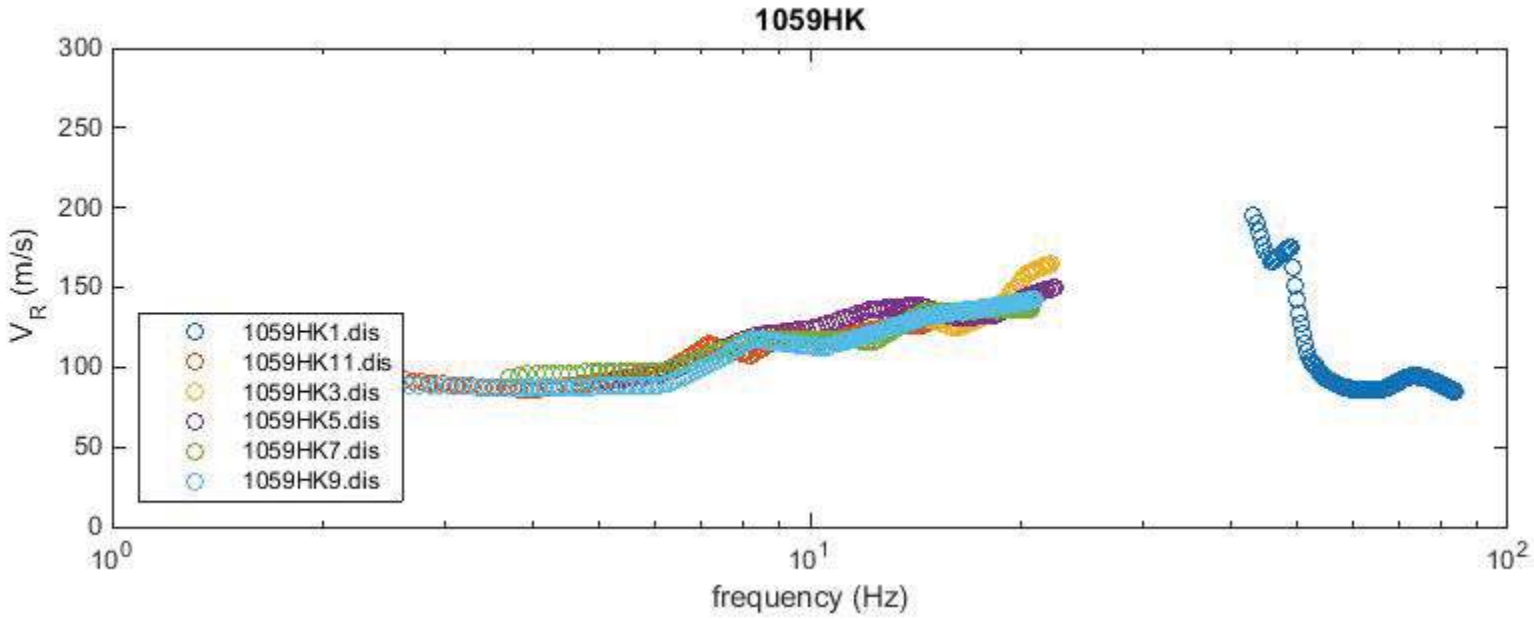
1059HK
300
250
200
150
100
50
0
V_R (m/s)
1059HK1.dis
1059HK11.dis
1059HK3.dis
1059HK5.dis
1059HK7.dis
1059HK9.dis
10^0
10^1
10^2
frequency (Hz)

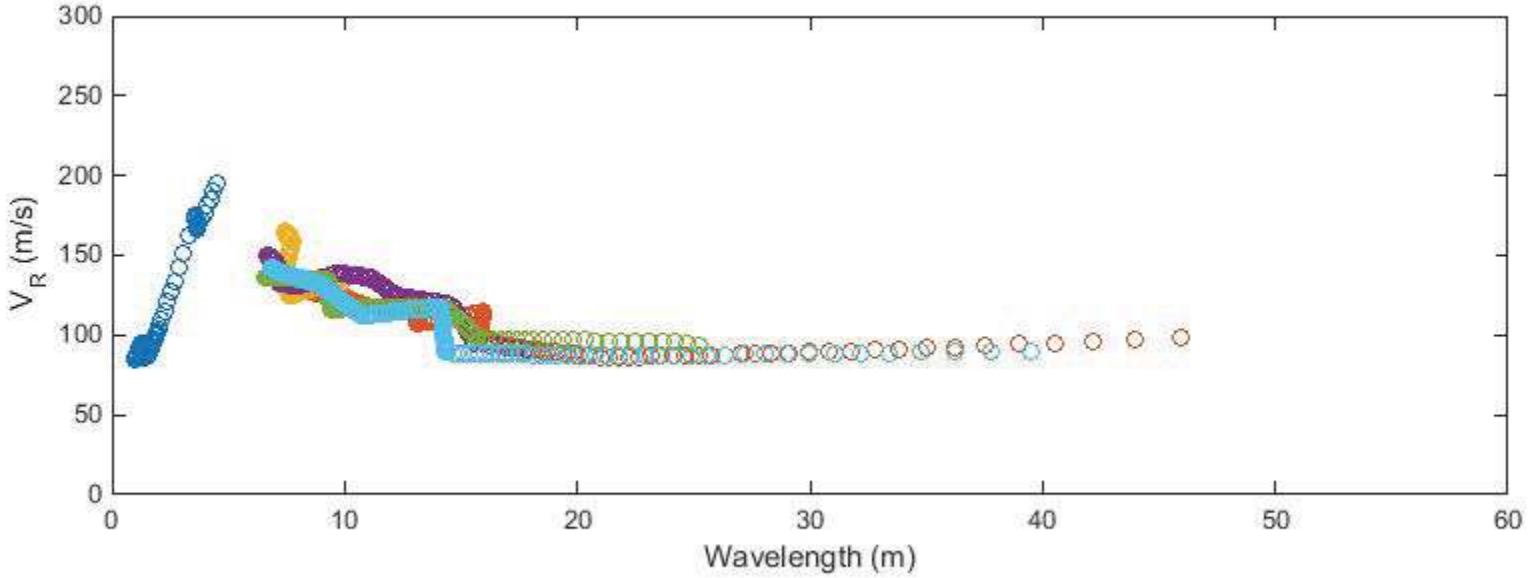
300
250
200
150
100
50
0
V_R (m/s)
0
10
20
30
40
50
60
Wavelength (m)

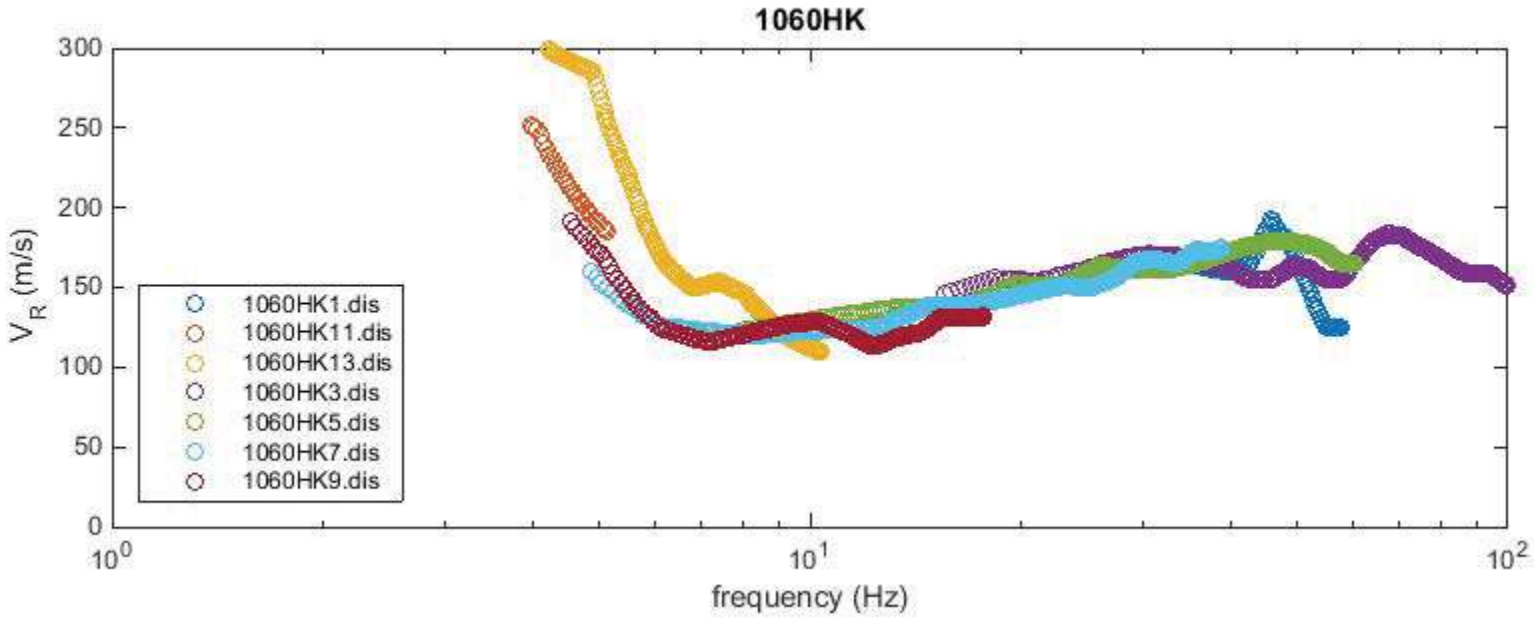
1060HK
300
250
200
150
100
50
0
V_R (m/s)
1060HK1.dis
1060HK11.dis
1060HK13.dis
1060HK3.dis
1060HK5.dis
1060HK7.dis
1060HK9.dis
10^0
10^1
10^2
frequency (Hz)

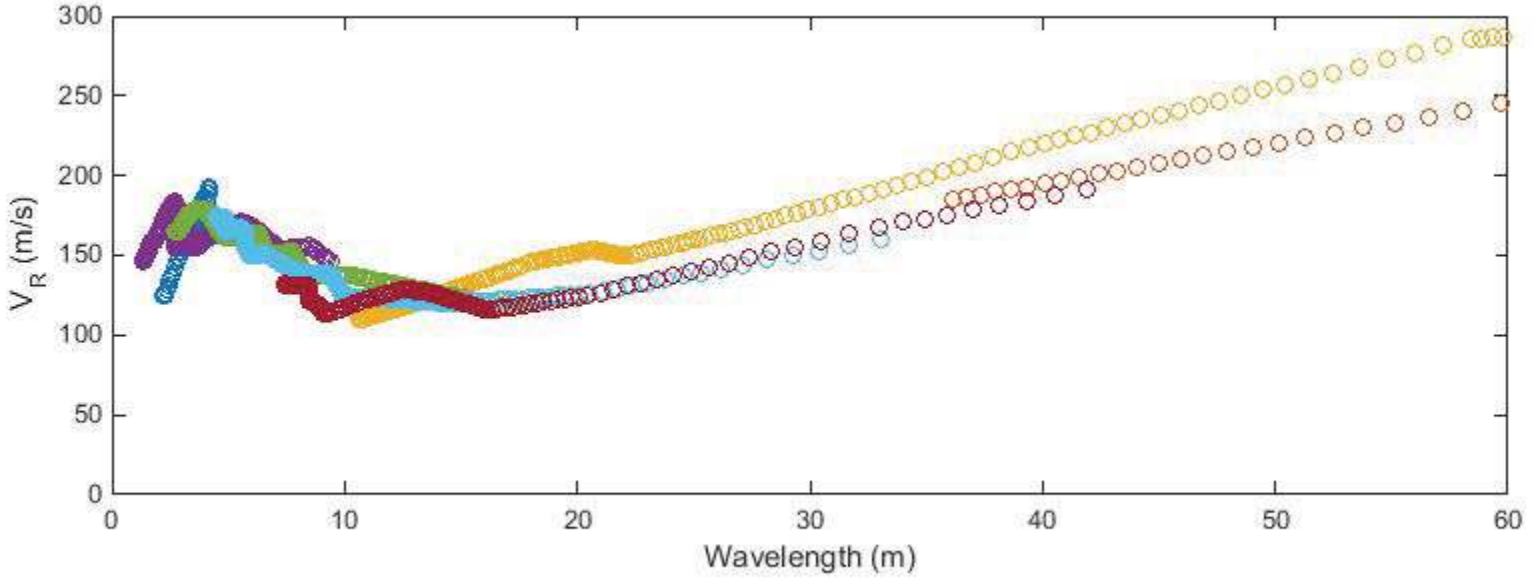
300
250
200
150
100
50
0
V_R (m/s)
0
10
20
30
40
50
60
Wavelength (m)

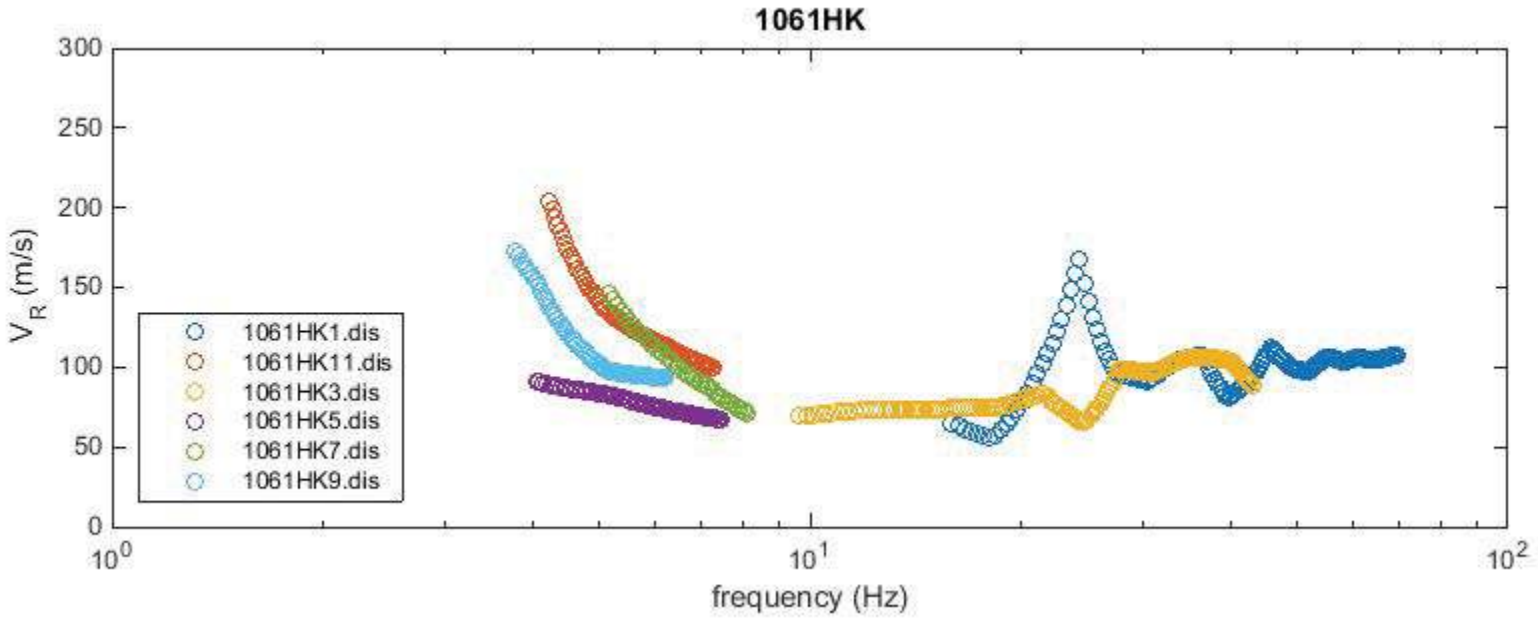
1061HK
300
250
200
150
100
50
0
V_R (m/s)
1061HK1.dis
1061HK11.dis
1061HK3.dis
1061HK5.dis
1061HK7.dis
1061HK9.dis
10^0
10^1
10^2
frequency (Hz)

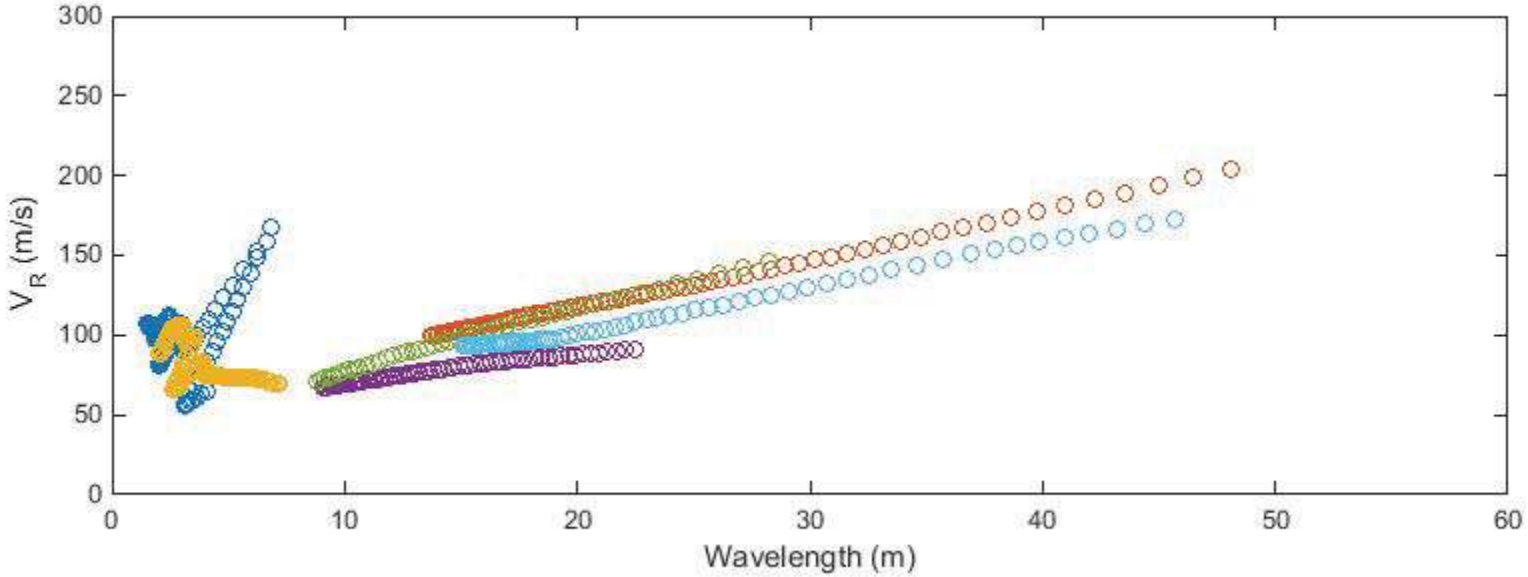
300
250
200
150
100
50
0
V_R (m/s)
0
10
20
30
40
50
60
Wavelength (m)

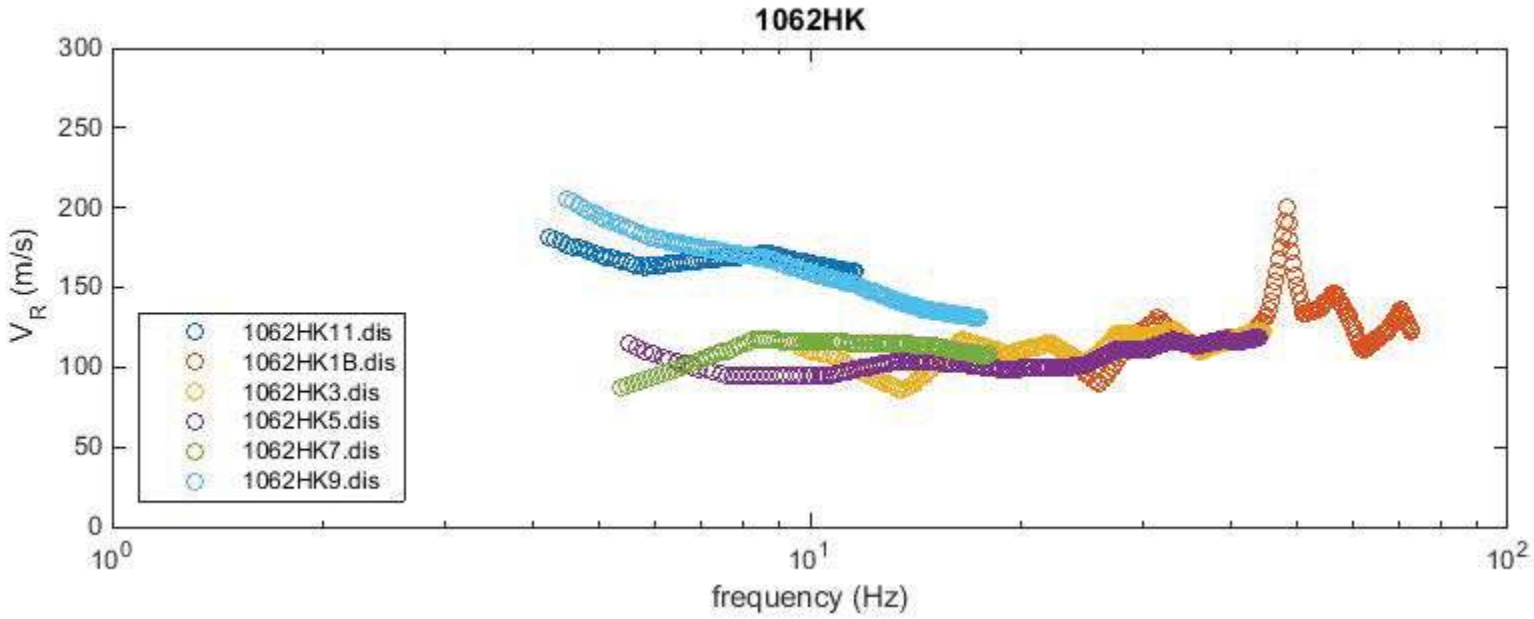
1062HK
300
250
200
150
100
50
0
V_R (m/s)
1062HK11.dis
1062HK1B.dis
1062HK3.dis
1062HK5.dis
1062HK7.dis
1062HK9.dis
10^0
10^1
10^2
frequency (Hz)

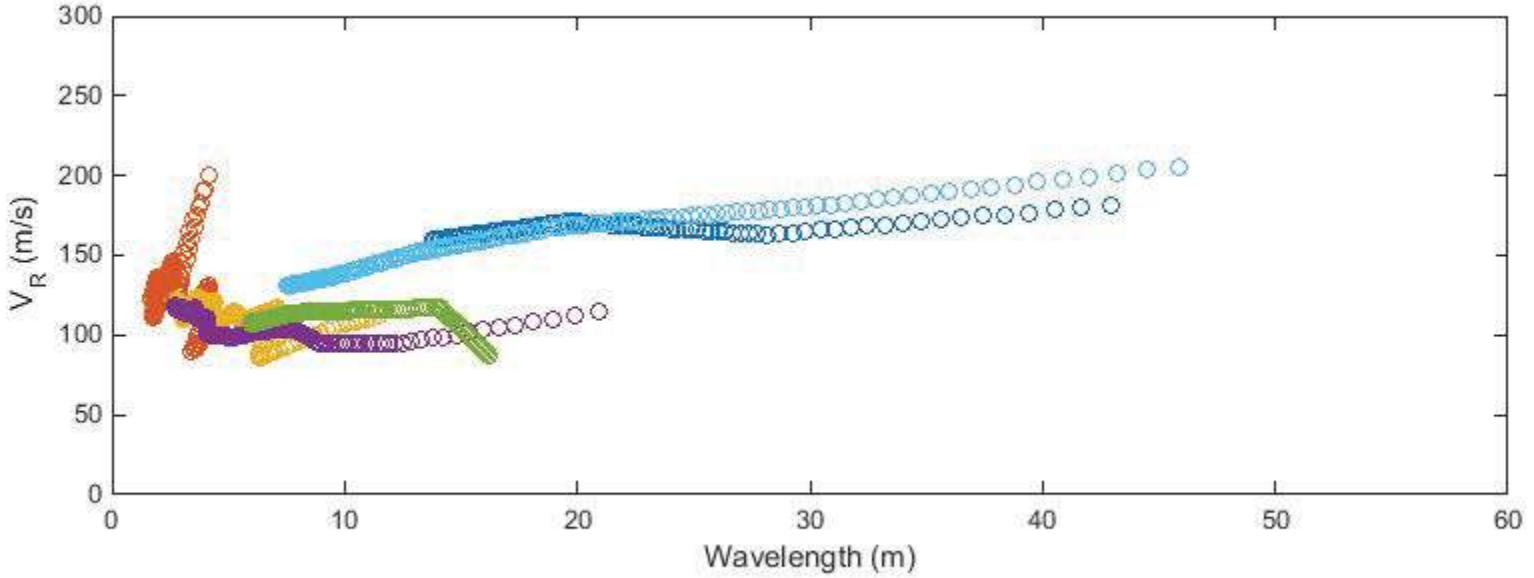
300
250
200
150
100
50
0
V_R (m/s)
0
10
20
30
40
50
60
Wavelength (m)

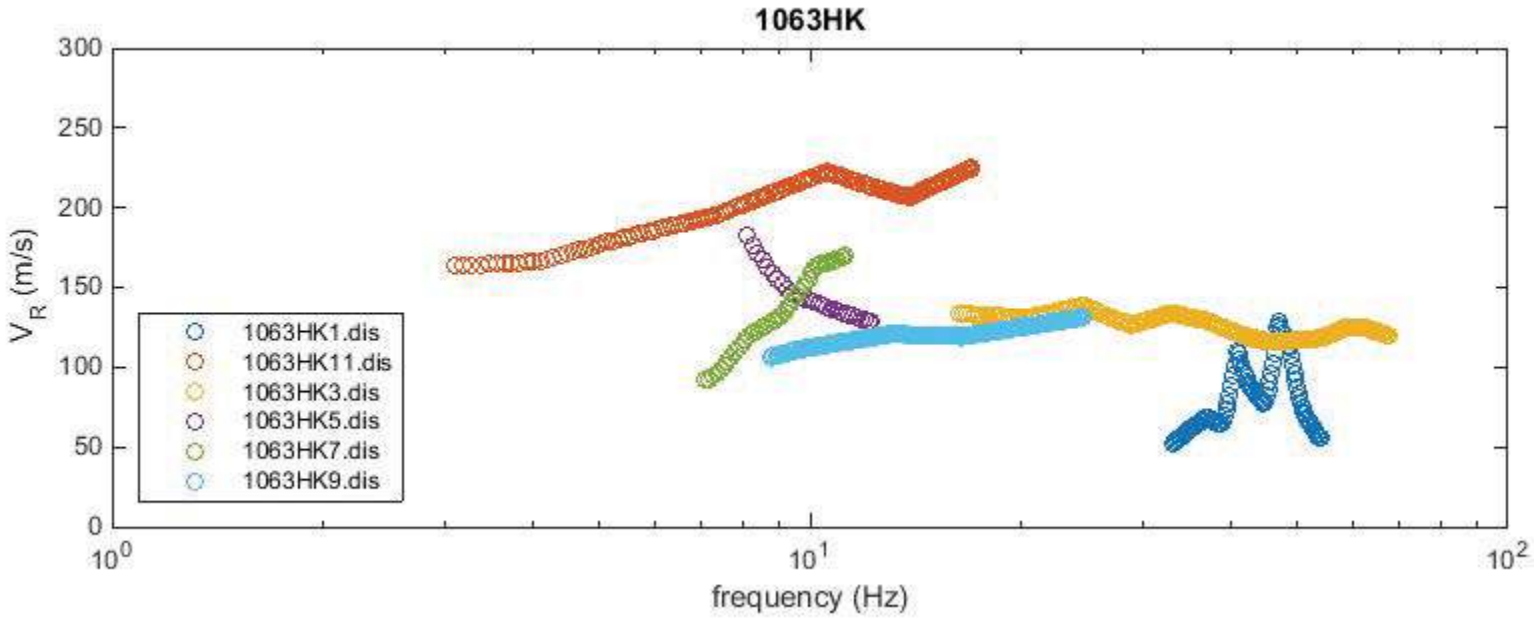
1063HK
300
250
200
150
100
50
0
V_R (m/s)
1063HK1.dis
1063HK11.dis
1063HK3.dis
1063HK5.dis
1063HK7.dis
1063HK9.dis
10^0
10^1
10^2
frequency (Hz)

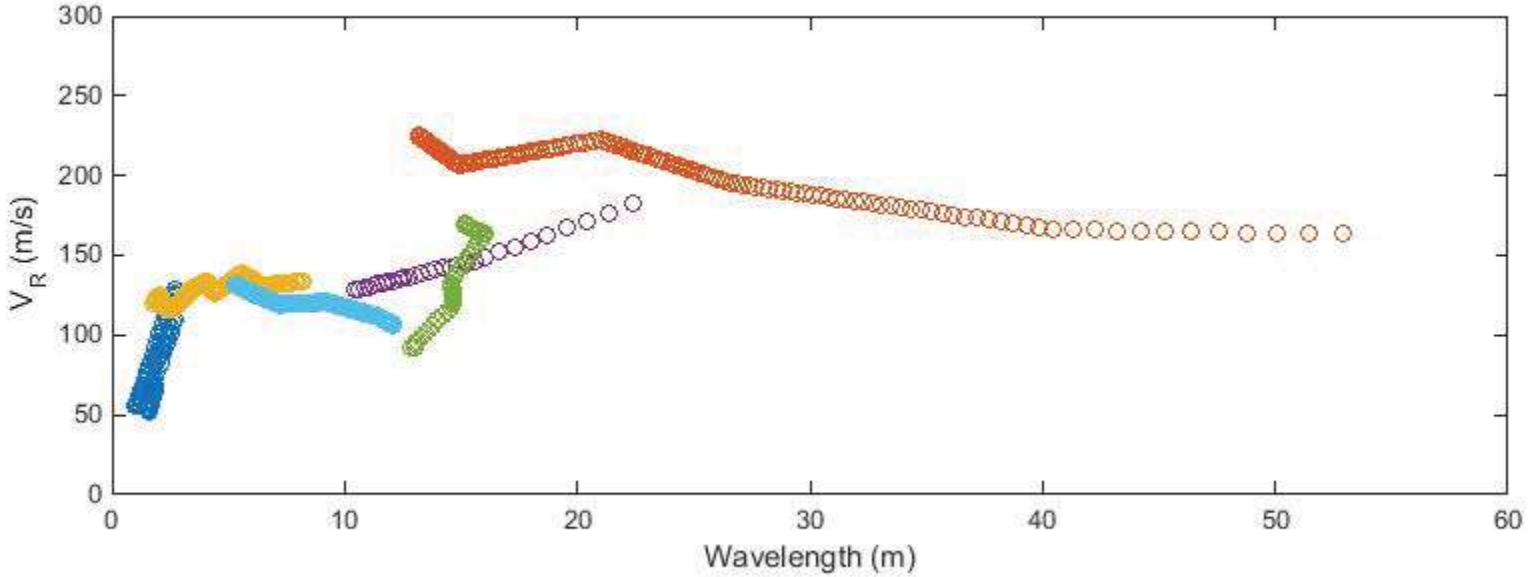
300
250
200
150
100
50
0
V_R (m/s)
0
10
20
30
40
50
60
Wavelength (m)

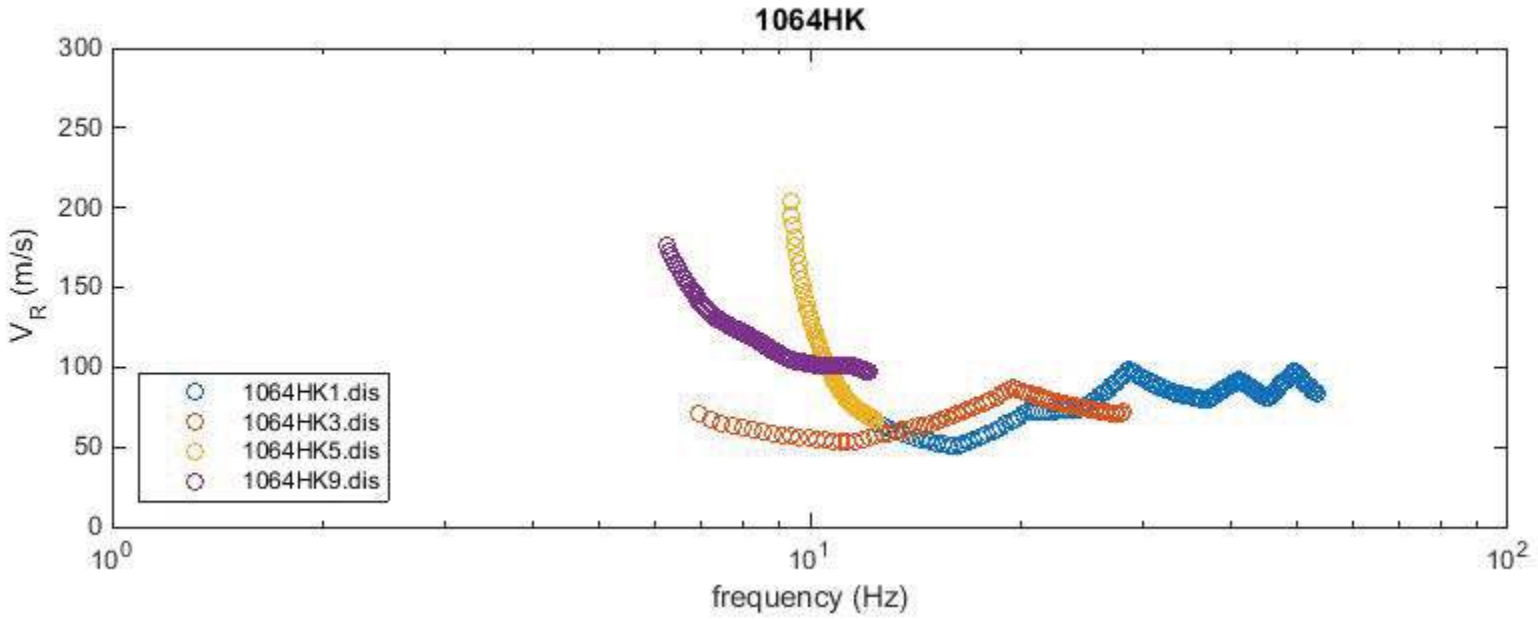
1064HK
300
250
200
150
100
50
0
V_R (m/s)
1064HK1.dis
1064HK3.dis
1064HK5.dis
1064HK9.dis
10^0
10^1
10^2
frequency (Hz)

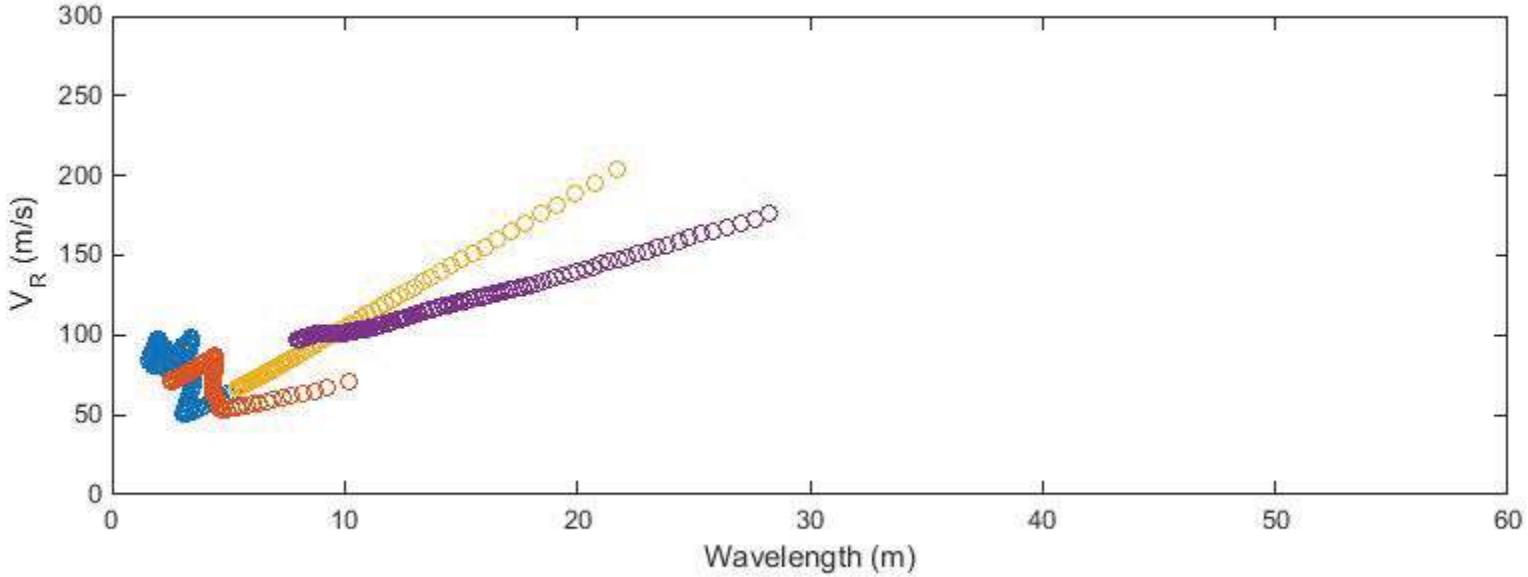
300
250
200
150
100
50
0
V_R (m/s)
0
10
20
30
40
50
60
Wavelength (m)

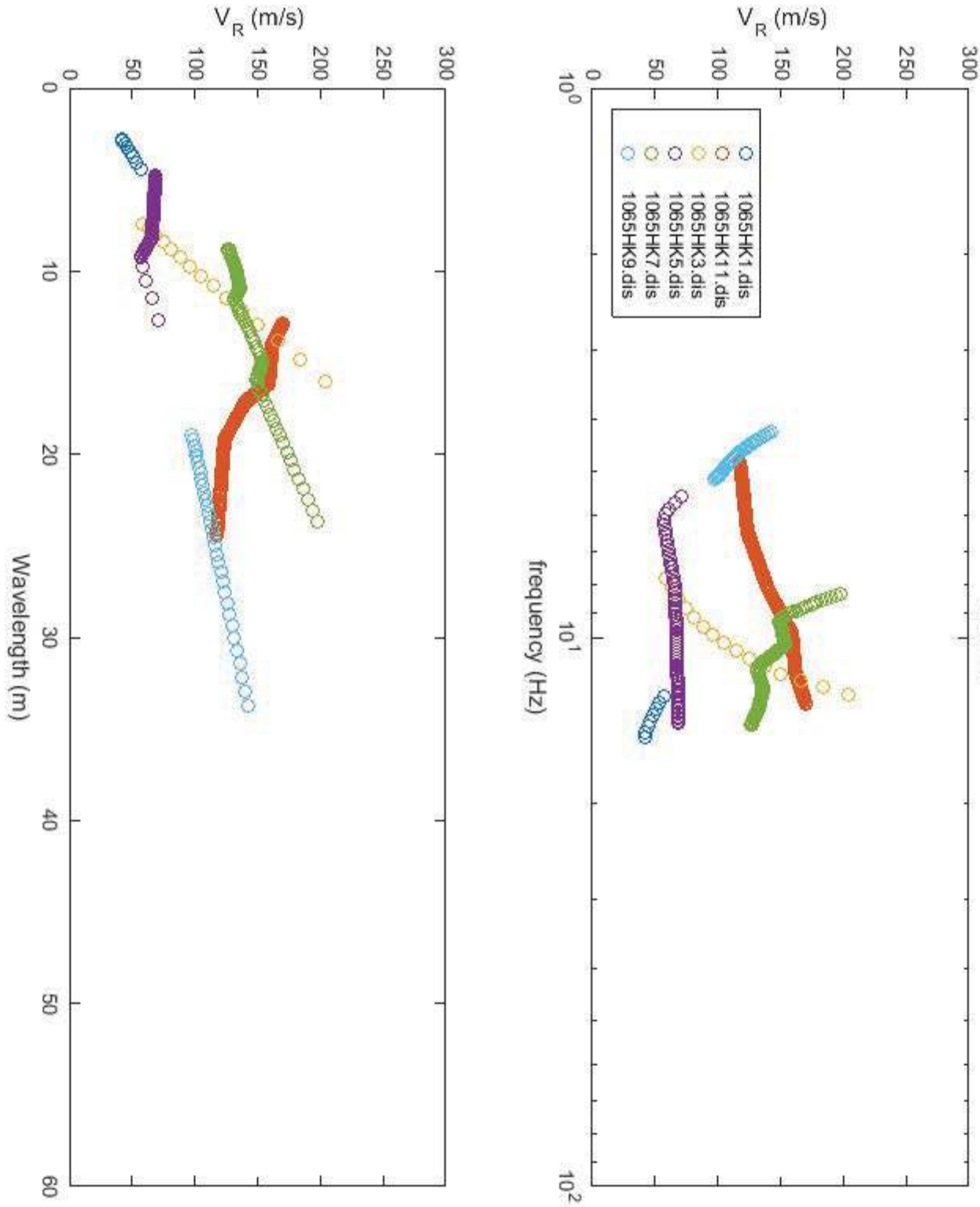
1065HK
V_R (m/s)
frequency (Hz)
1065HK1.dis
1065HK11.dis
1065HK3.dis
1065HK5.dis
1065HK7.dis
1065HK9.dis
V_R (m/s)
Wavelength (m)

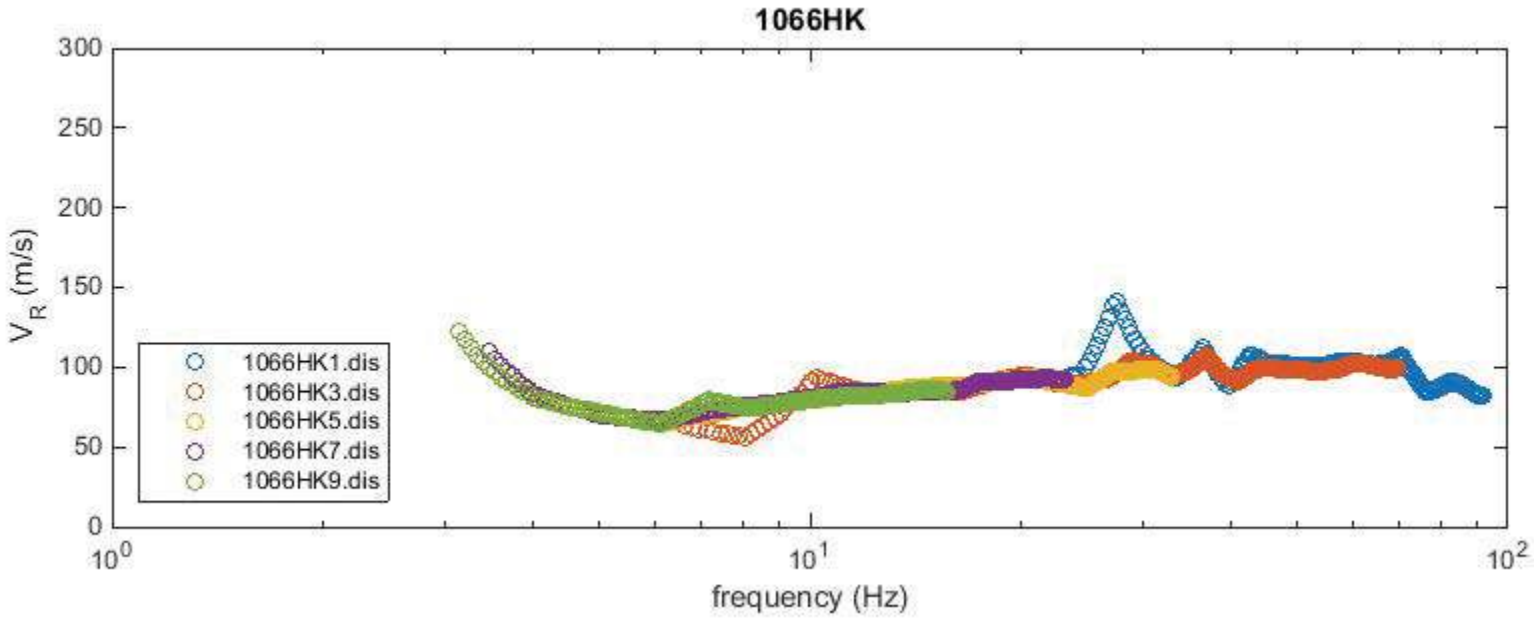
1066HK
300
250
200
150
100
50
0
V_R (m/s)
1066HK1.dis
1066HK3.dis
1066HK5.dis
1066HK7.dis
1066HK9.dis
10^0
10^1
10^2
frequency (Hz)

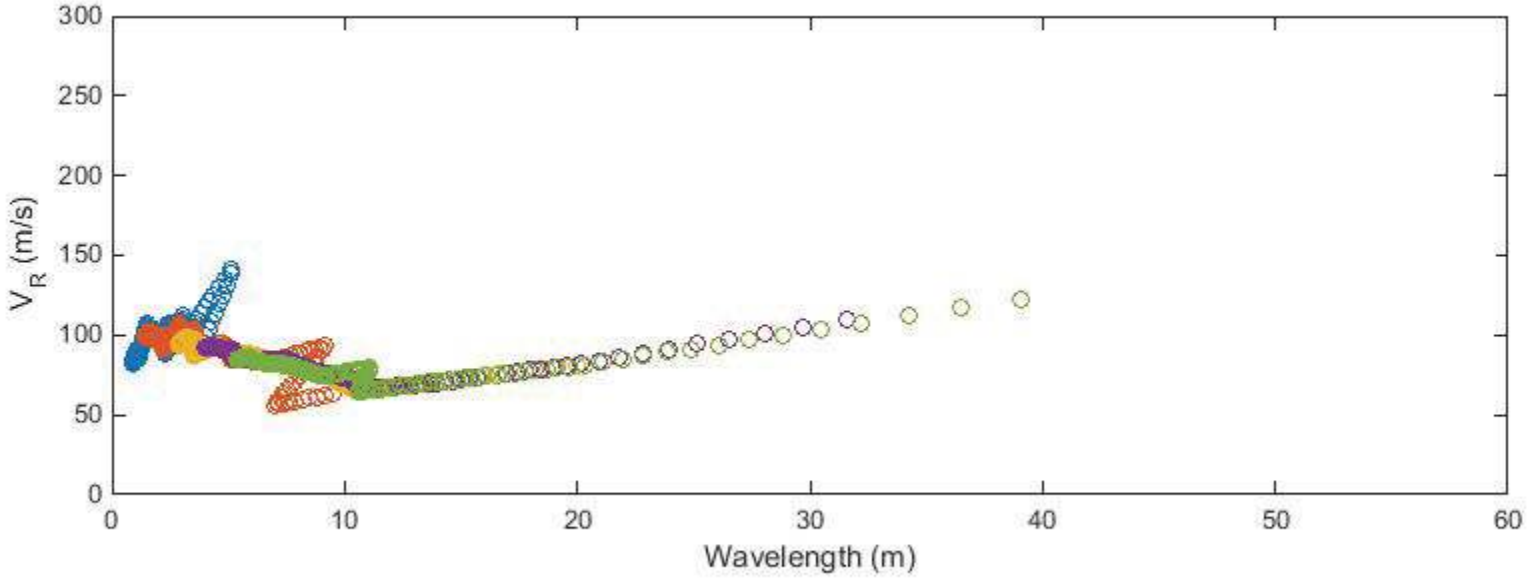
300
250
200
150
100
50
0
V_R (m/s)
0
10
20
30
40
50
60
Wavelength (m)

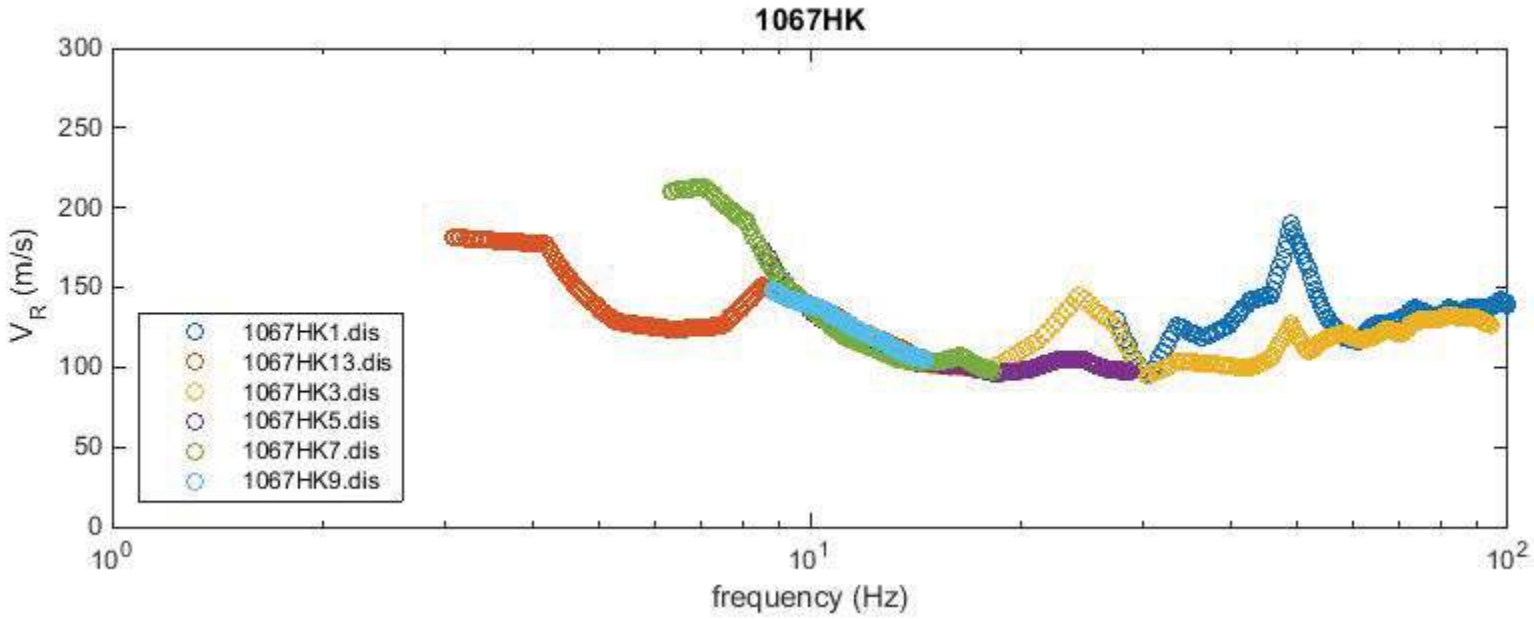
1067HK
300
250
200
150
100
50
0
V_R (m/s)
1067HK1.dis
1067HK13.dis
1067HK3.dis
1067HK5.dis
1067HK7.dis
1067HK9.dis
10^0
10^1
10^2
frequency (Hz)

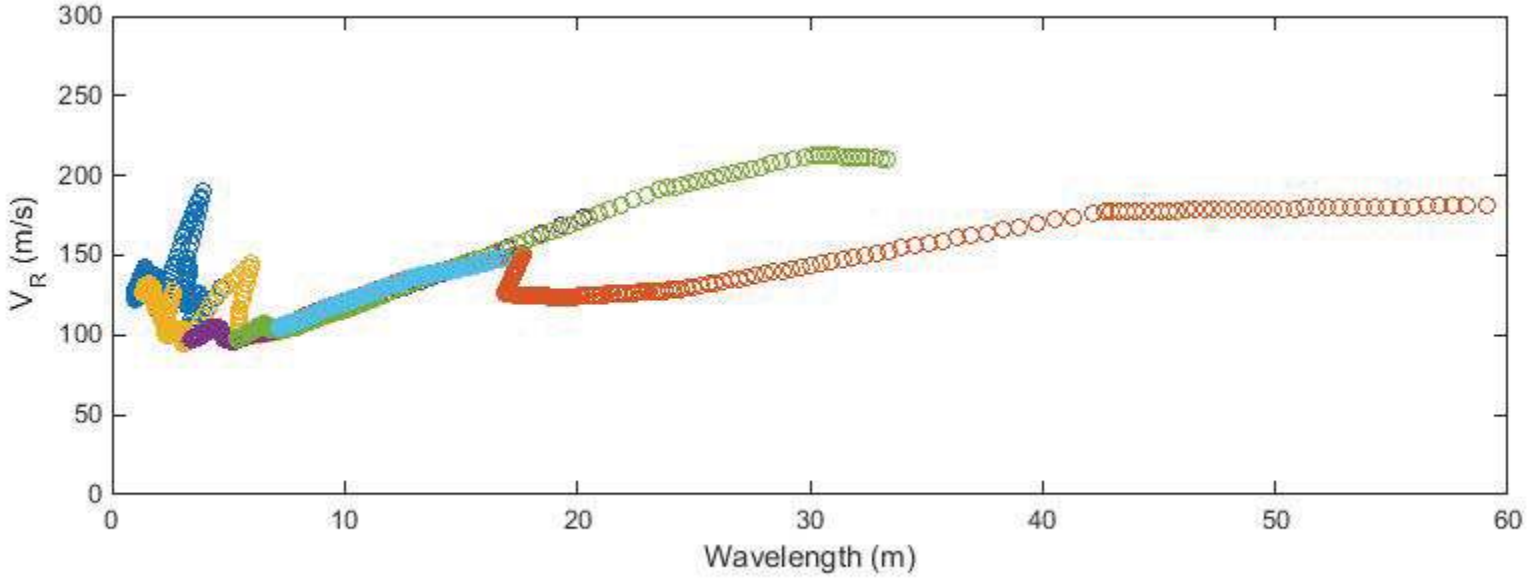
300
250
200
150
100
50
0
V_R (m/s)
0
10
20
30
40
50
60
Wavelength (m)

Surface wave test site 1047HK located on the SW bank of the Tokachi River16 km east of Obihiro, Hokkaido, Japan (lat 42.92140, long143.3858). A) view northwest from the shaker; B) view southeast toward the seismometer array; C) site information; D) view to the northeast from the test site; E) satellite view of the local site, yellow bar is seismometer array; F) site location near Obihiro, Hokkaido, Japan.

Surface wave test site 1048HK located on the right bank Tokachi River dike 22 km SE of Obihiro, Hokkaido, Japan (lat 42.8359, long143.47497). A) view southeast to seismometer array on dike crest; B) view northwest on the dike from near the shaker; C) another view northwest; D) site information; E) satellite view of the local site, yellow bar is seismometer array; F) site location near Obihiro, Hokkaido, Japan.

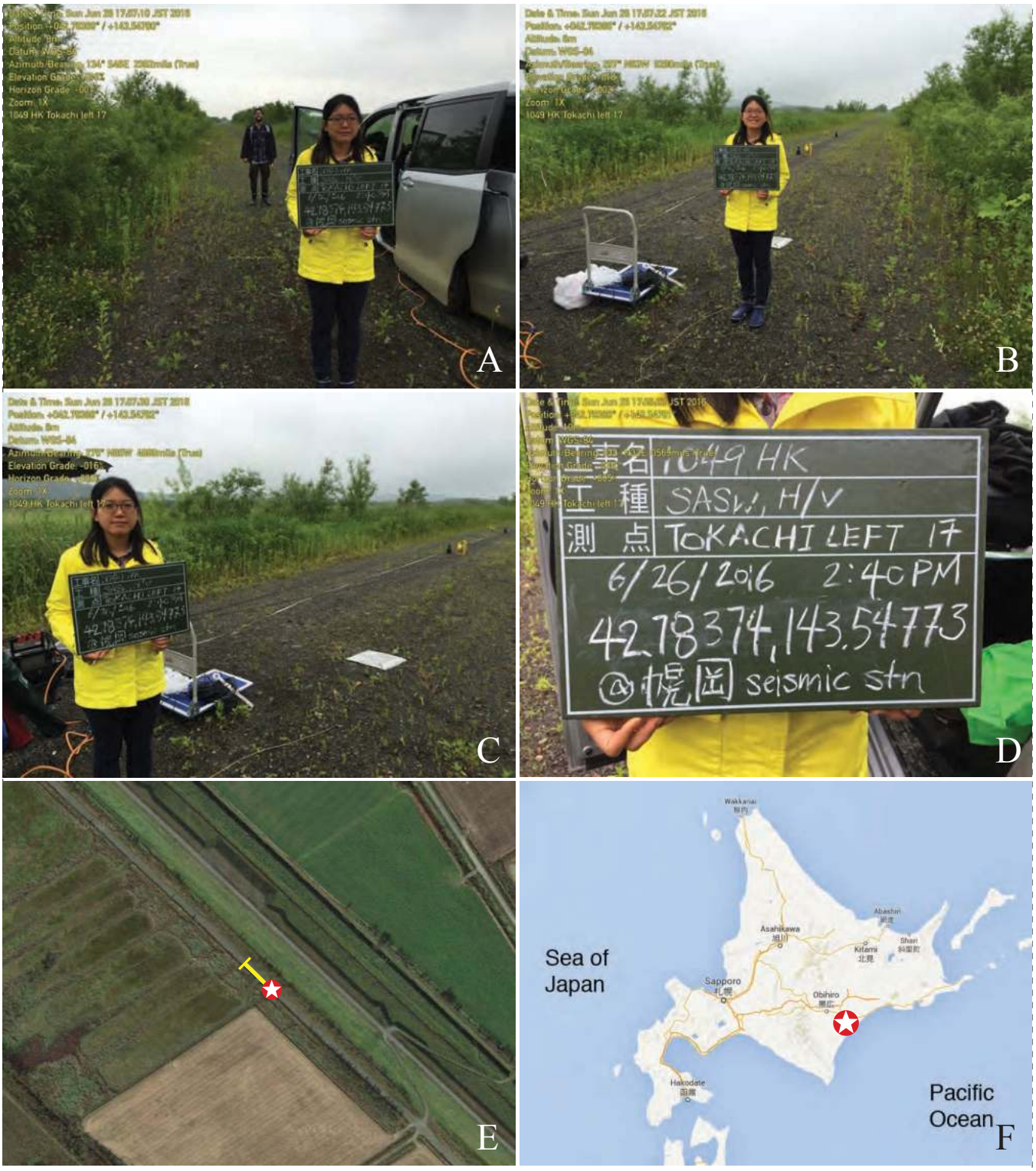

Surface wave test site 1049HK located on the inside of the left bank dike of the Tokachi River, location L17, 30 km SW of Obihiro, Hokkaido, Japan (lat 42.78367, long143.54781). A) view southeast from near the shaker to seismometer array; B) view northwestward from the shaker; C) view westward from the shaker; D) site information; E) satellite view of the local site, yellow bar is seismometer array; F) site location near Obihiro, Hokkaido, Japan.

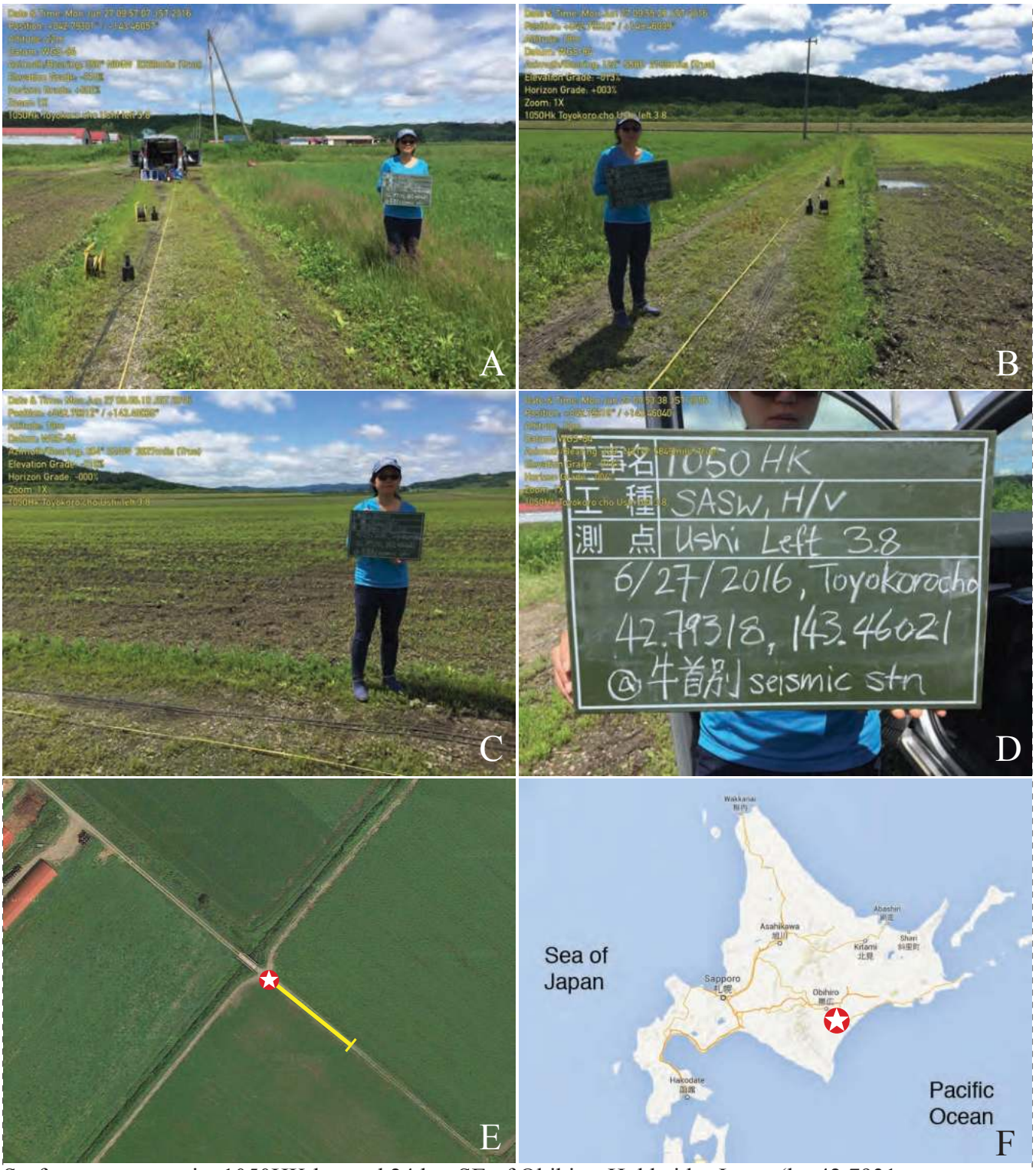

Surface wave test site 1050HK located 24 km SE of Obihiro, Hokkaido, Japan (lat 42.7931, long143.46039). A) view northwest along the seismometer array toward the shaker; B) view southeast along the seismometer array; C) view southwestward along the seismometer array; D) site information; E) satellite view of the local site, yellow bar is seismometer array; F) site location near Obihiro, Hokkaido, Hokkaido, Japan.

Surface wave test site 1051HK located 23 km SE of Obihiro, Hokkaido, Japan (lat 42.79196, long 143.462348). A) view northeast from the shaker to the seismometer array; B) view southwest toward the shaker; C) view to the west from the test site; D) site information; E) satellite view of the local site, yellow bar is seismometer array; F) site location near Obihiro, Hokkaido, Japan.

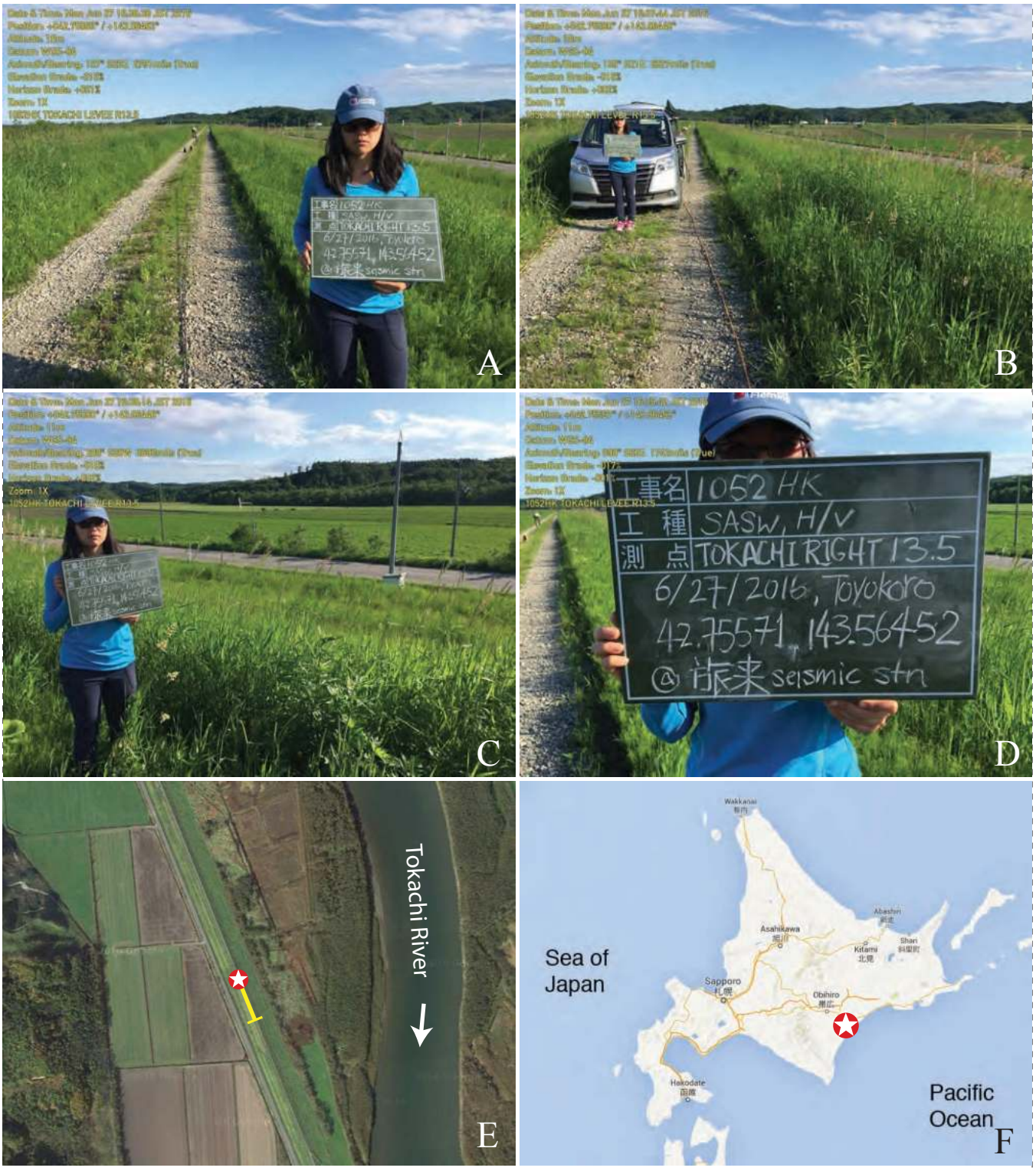

Surface wave test site 1052HK located on the Tokachi River right bank levee, location 13.5, 33 km SE of Obihiro, Hokkaido, Japan (lat 42.75571, long143.56452). A) view southeast from the shaker to the seismometer array; B) another view southeast toward the shaker; C) view southwest from the test site; D) site information; E) satellite view of the local site, yellow bar is seismometer array; F) site location near Obihiro, Hokkaido, Japan.

Surface wave test site 1053HK located inside the Tokachi River left bank levee, location L8.8, 37 km SE of Obihiro, Hokkaido, Japan (lat 42.72905, long143.60495). A) view southward from the shaker to the seismometer array; B) view northward toward the shaker; C) view to the north from the shaker; D) site information; E) satellite view of the local site, yellow bar is seismometer array; F) site location near Obihiro, Hokkaido, Japan.

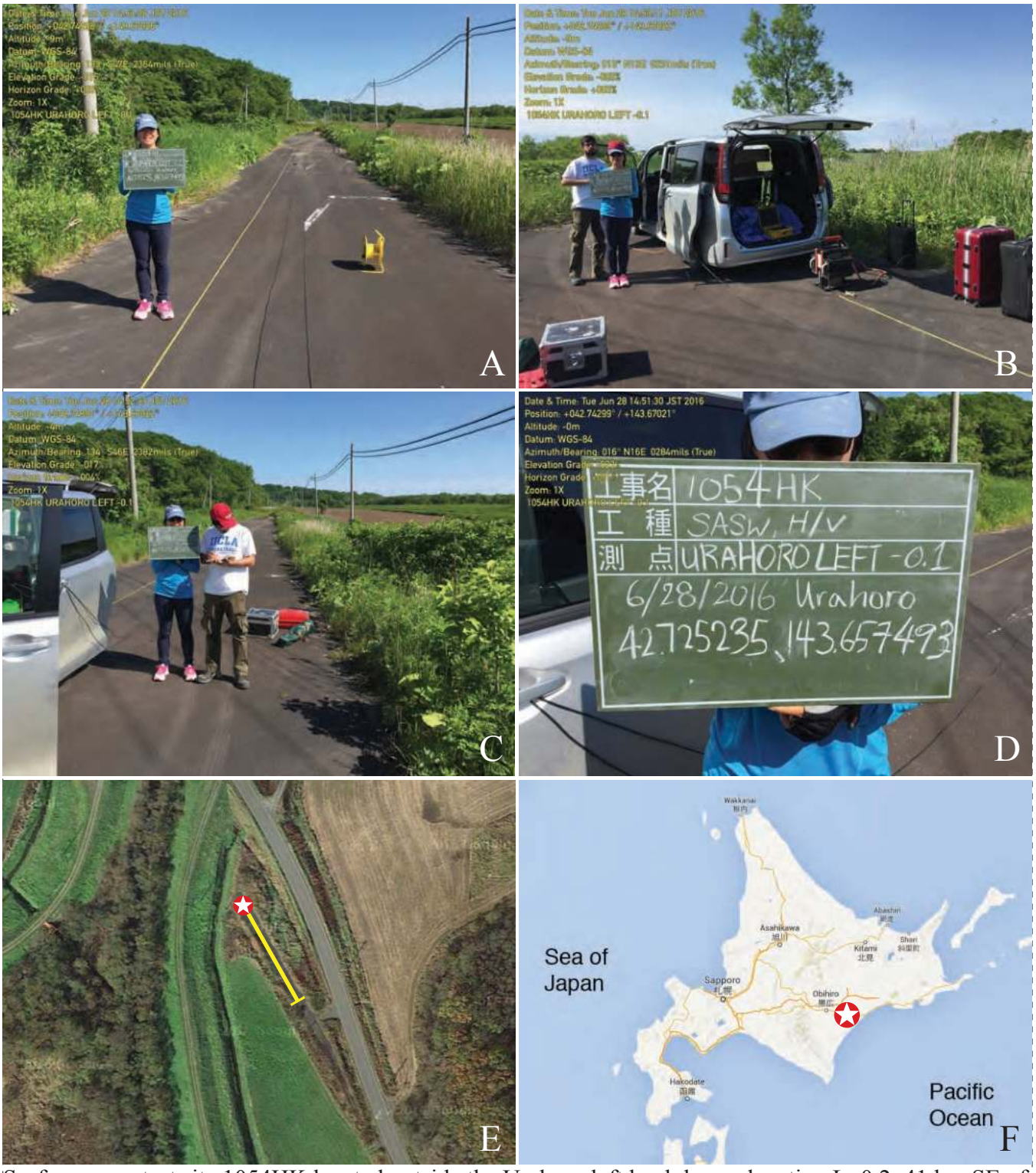

Surface wave test site 1054HK located outside the Urahoro left bank levee, location L -0.2, 41 km SE of (lat 42.743, long143.67023). A) view southeast from the shaker to the seismometer array; B) view north at the shaker location; C) another view southeast from the shaker; D) site information; E) satellite view of the local site, yellow bar is seismometer array; F) site location near Obihiro, Hokkaido, Japan.

Surface wave test site 1055HK located 7 km north of Kushiro, Hokkaido, Japan (lat 43.08519, long144.3782). A) view southeast from the shaker to the seismometer array; B) view northwest from the shaker location; C) another view northwest from the shaker; D) site information; E) satellite view of the local site, yellow bar is seismometer array; F) site location near Kushiro, Hokkaido, Japan.

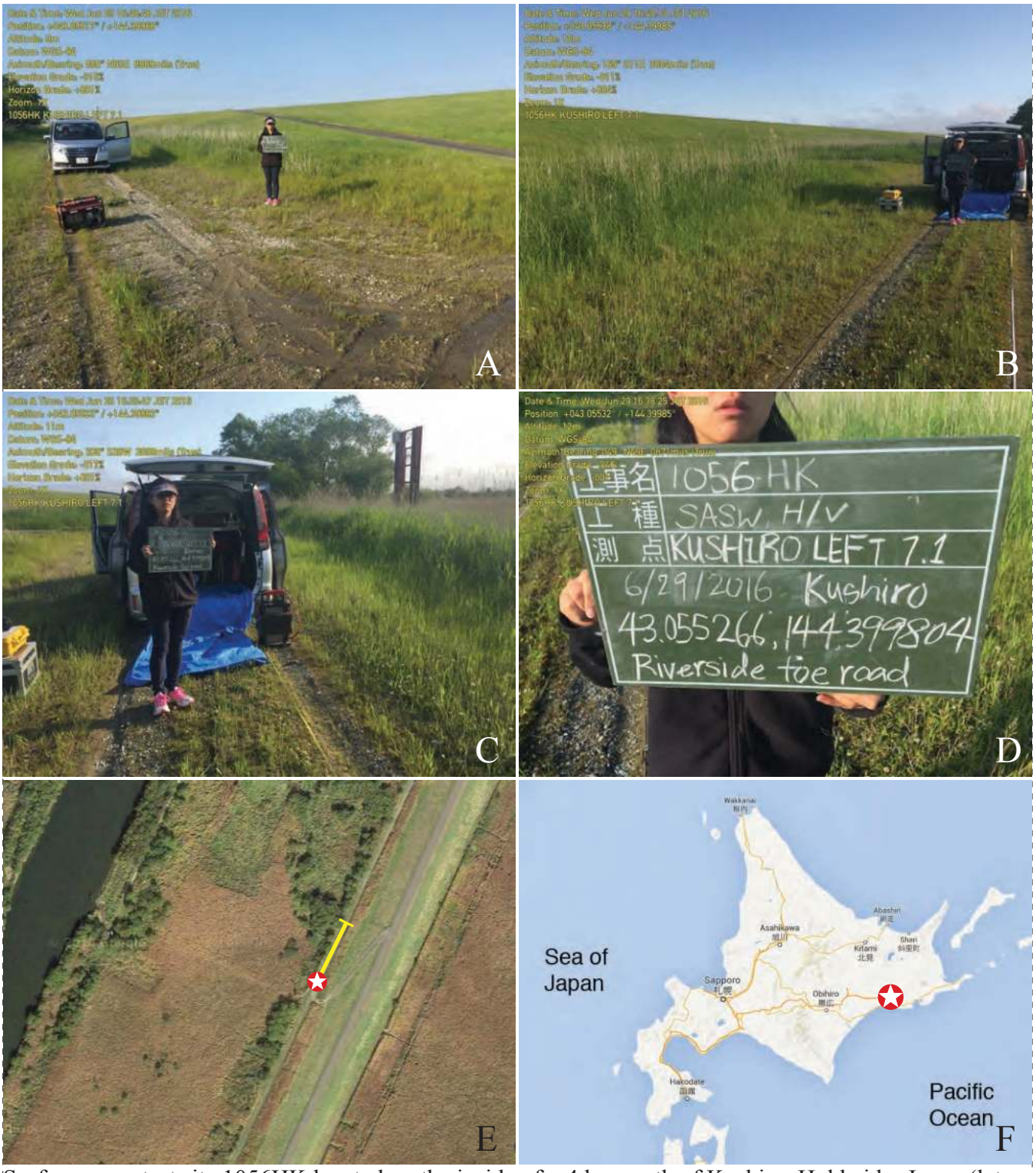

Surface wave test site 1056HK located on the inside of 4 km north of Kushiro, Hokkaido, Japan (lat 43.05526, long144.39984). A) view northeast to the test site; B) view southwest toward the shaker location; C) another view southwest from the shaker; D) site information; E) satellite view of the local site, yellow bar is seismometer array; F) site location near Kushiro, Hokkaido, Japan.

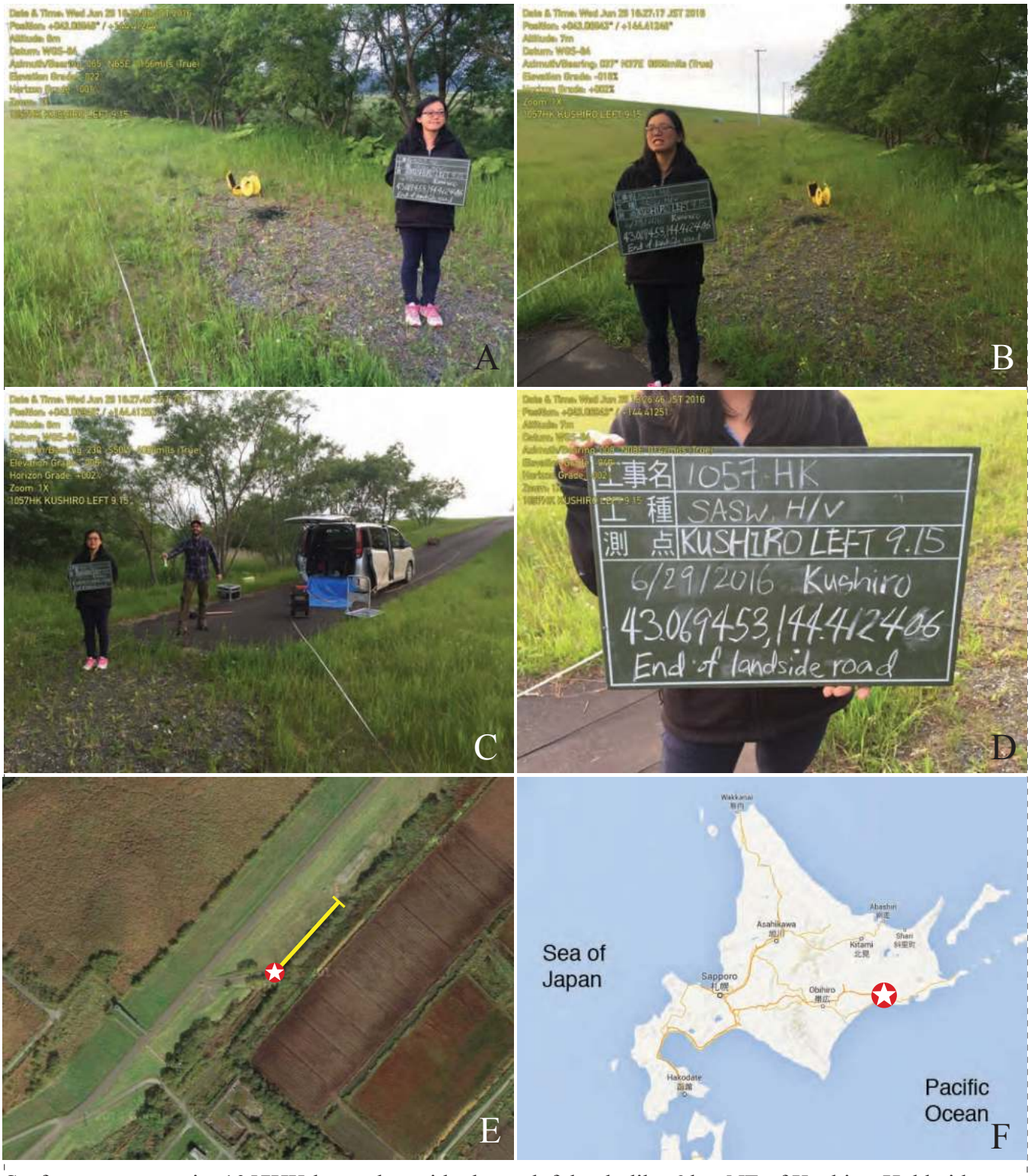

Surface wave test site 1057HK located outside the xx left bank dike 6 km NE of Kushiro, Hokkaido, Japan (lat 43.069453, long144.412406). A) view northeast from the shaker to seismometer array; B) view north to the seismometer array; C) view southwest to the shaker location; D) site information; E) satellite view of the local site, yellow bar is seismometer array; F) site location near Kushiro, Hokkaido, Japan.

Surface wave test site 1058HK located 10 km north of Kushiro, Hokkaido, Japan (lat 43.11004, long144.33671). A) view northwest to the shakerlocation; B) view southeast from near the shaker; C) view southward across the test site; D) site information; E) satellite view of the local site, yellow bar is seismometer array; F) site location near Kushiro, Hokkaido, Japan.

Surface wave test site 1059HK located 8 km north of Kushiro, Hokkaido, Japan (lat 43.09583, long144.36730). A) view southeast from the shaker; B) view northwest toward the seismometer array; C) view west across the test site; D) site information; E) satellite view of the local site, yellow bar is seismometer array; F) site location near Kushiro, Hokkaido, Japan.

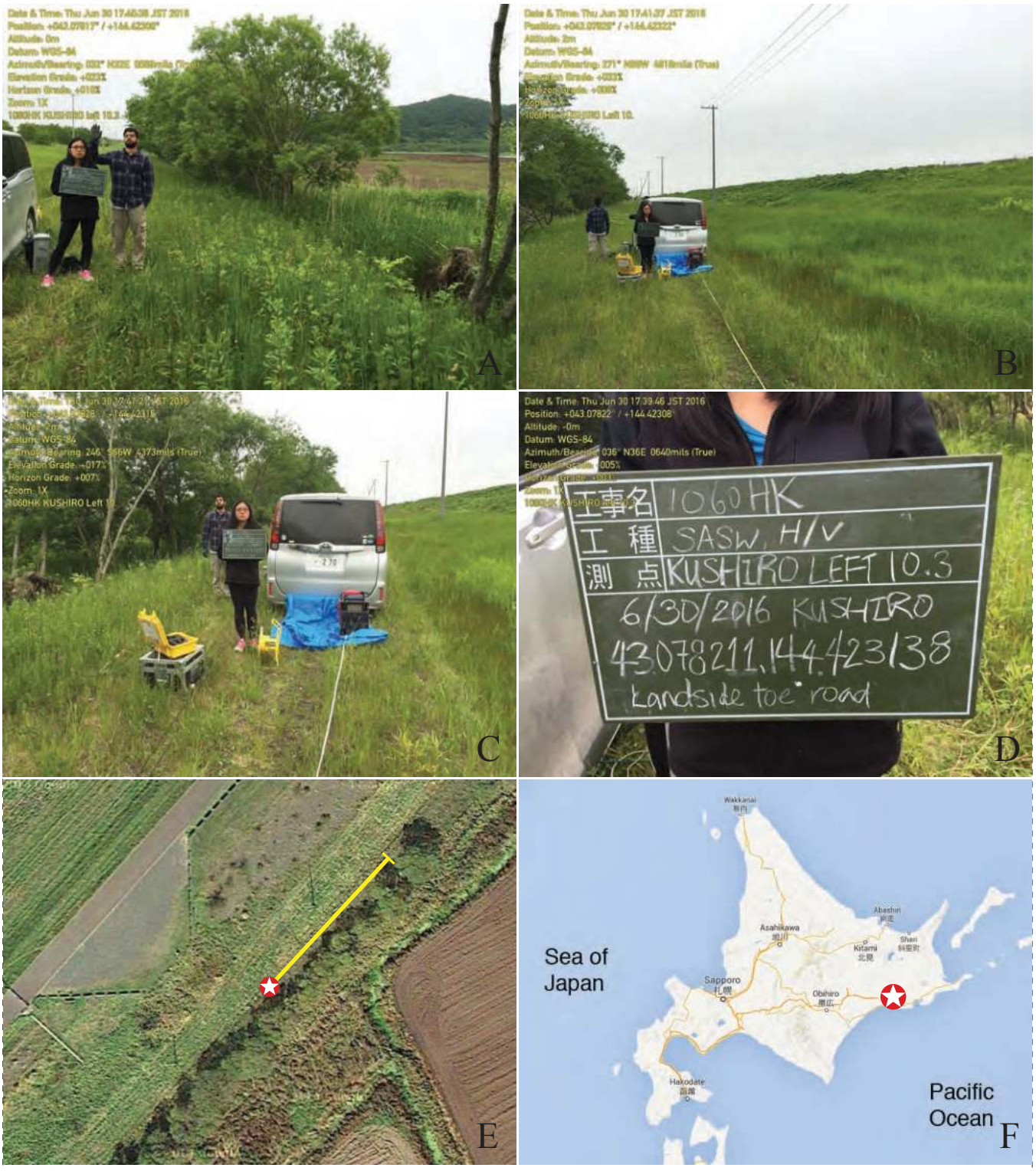

Surface wave test site 1060HK located about 6 km north of Kushiro, Hokkaido, Japan (lat 42.07822, long144.4231). A) view northeast from the shaker; B) view southwestward toward the shaker; C) another view southwest toward the shaker; D) site information; E) satellite view of the local site, yellow bar is seismometer array; F) site location near Kushiro, Hokkaido, Japan.

Surface wave test site 1061HK located 5 km north of Kushiro, Hokkaido, Japan (lat 43.073835, long144.396618). A) view northwest from the shaker toward the seismometer array; B) view eastward from near the shaker; C) another view northwestward to the test site; D) site information; E) satellite view of the local site, yellow bar is seismometer array; F) site location near Kushiro, Hokkaido, Japan.

Surface wave test site 1062HK located 28 km NE of Kushiro, Hokkaido, Japan (lat 43.24672, long144.55061). A) view northwest toward the shaker; B) view southeast from near the shaker; C) another view northwest at the test site; D) site information; E) satellite view of the local site, yellow bar is seismometer array; F) site location near Kushiro, Hokkaido, Japan.

Surface wave test site 1063HK located 3 km north of Kushiro, Hokkaido, Japan (lat 43.05511, long144.40033). A) viewsouthwest toward the shaker; B) view northeast from the the shaker; C) view northward from the test site; D) site information; E) satellite view of the local site, yellow bar is seismometer array; F) site location near Kushiro, Hokkaido, Japan.

Surface wave test site 1064HK located at northern Kurshiro, Hokkaido, Japan (lat 43.025103, long144.374643). A) view north to the shaker; B) view south toward the seismometer array; C) view southwest to the test site; D) site information; E) satellite view of the local site, yellow bar is seismometer array; F) site location in Kushiro, Hokkaido, Japan.

Surface wave test site 1065HK located 7 km SW of Urahoro, Hokkaido, Japan (lat 42.75003, long143.60518). A) view south toward the shaker; B) view north toward the seismometer array; C) another view north from the shaker location; D) site information; E) satellite view of the local site, yellow bar is seismometer array; F) site location near Urahoro, Hokkaido, Japan.

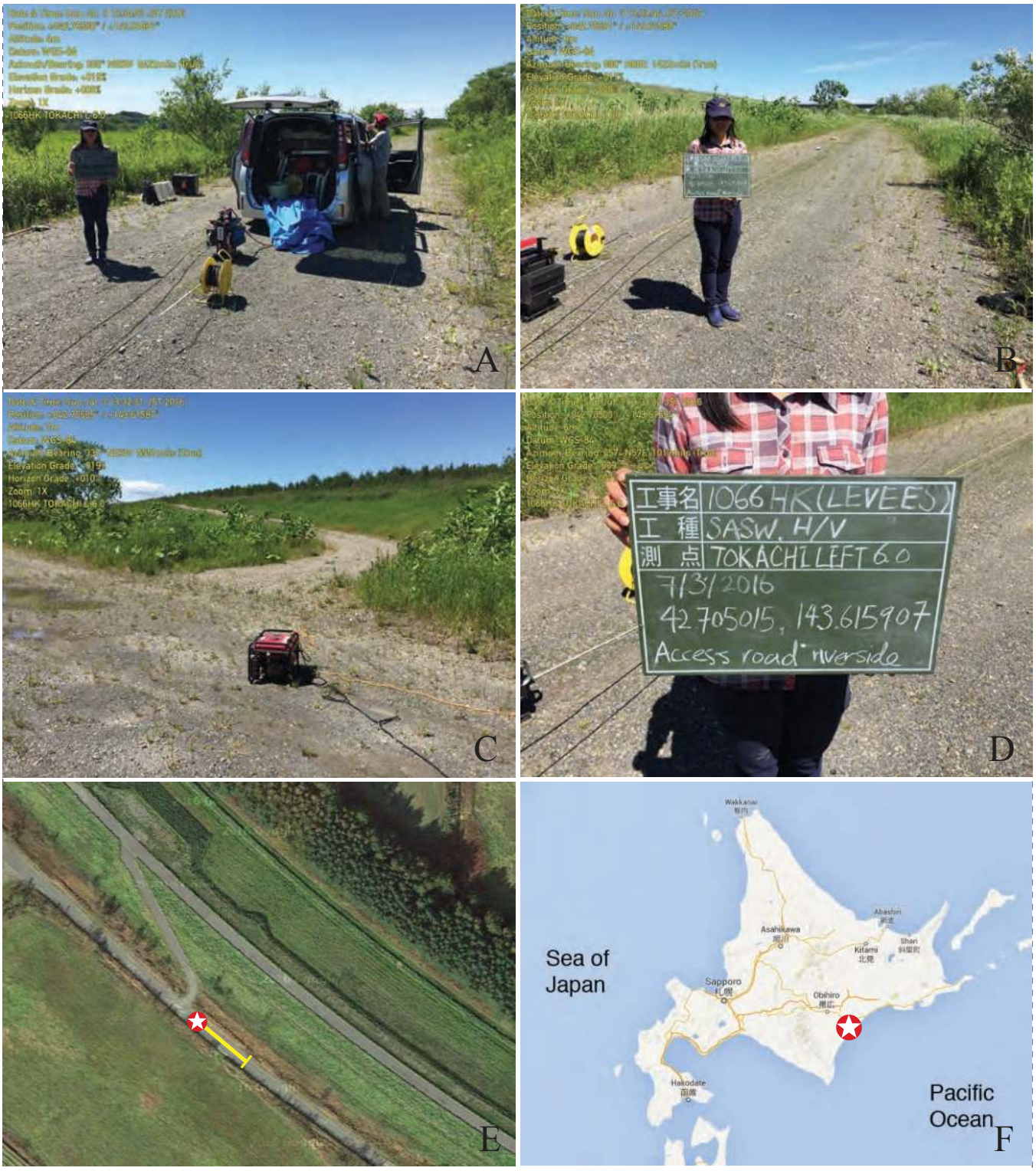

Surface wave test site 1066HK located inside the left bank levee of the Tokachi River near its mouth 11 km SW of Urahoro, Hokkaido, Japan (lat 42.70503, long143.61595). A) view northwest from the shaker; B) view southeast toward the seismometer array; C) view north from the test site; D) site information; E) satellite view of the local site, yellow bar is seismometer array; F) site location near Urahoro, Hokkaido, Japan.

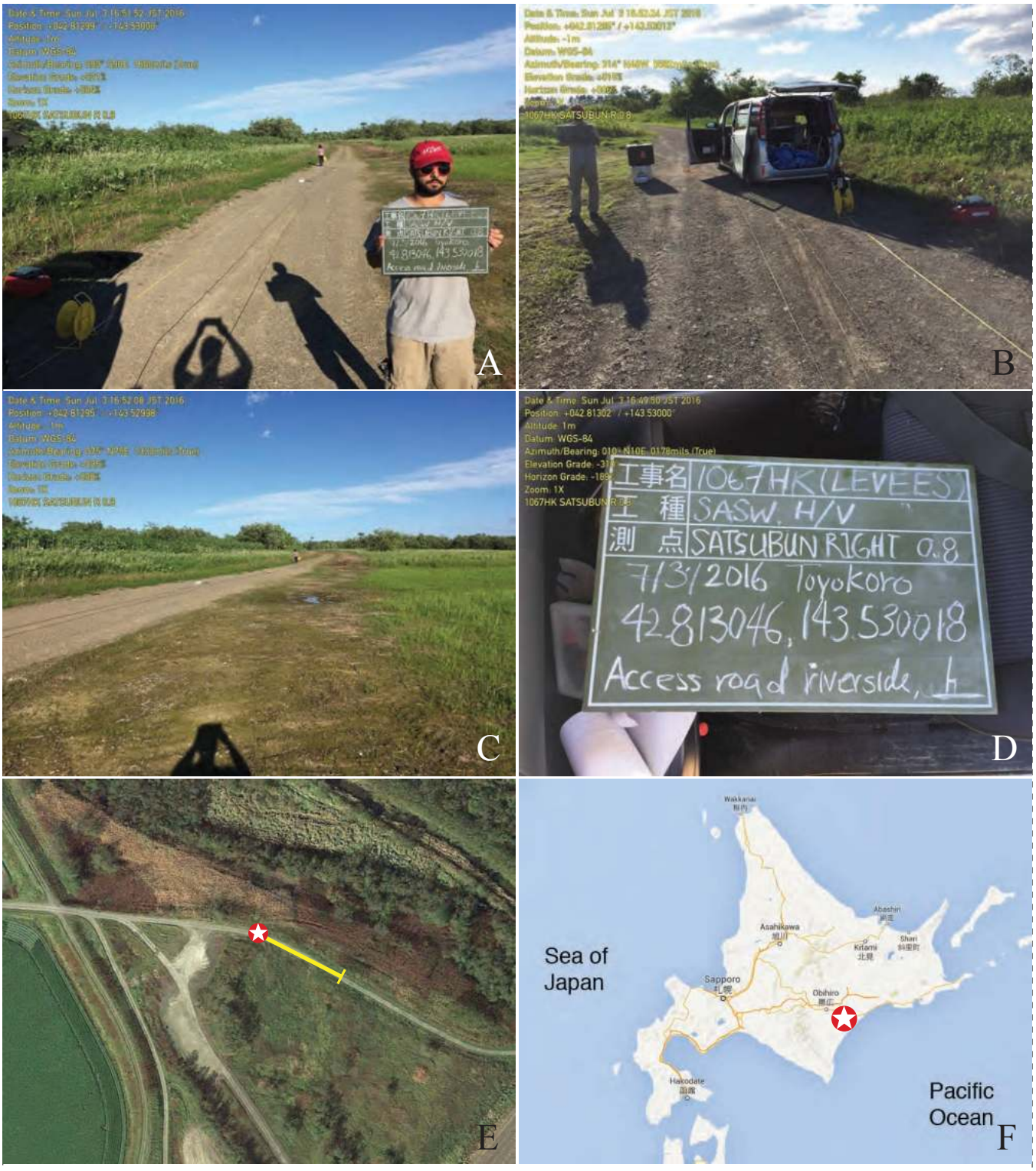

Surface wave test site 1067HK located 10 km west of Urahoro, Hokkaido, Japan (lat 42.81302, long143.52979). A) view southeast from the shaker to the seismometer array; B) view northwest toward the shaker; C) another view southeast across the test site; D) site information; E) satellite view of the local site, yellow bar is seismometer array; F) site location near Urahoro, Hokkaido, Japan.

APPENDIX B: LIQUEFACTION SEVERITY INDICES AND 2-D MODELS

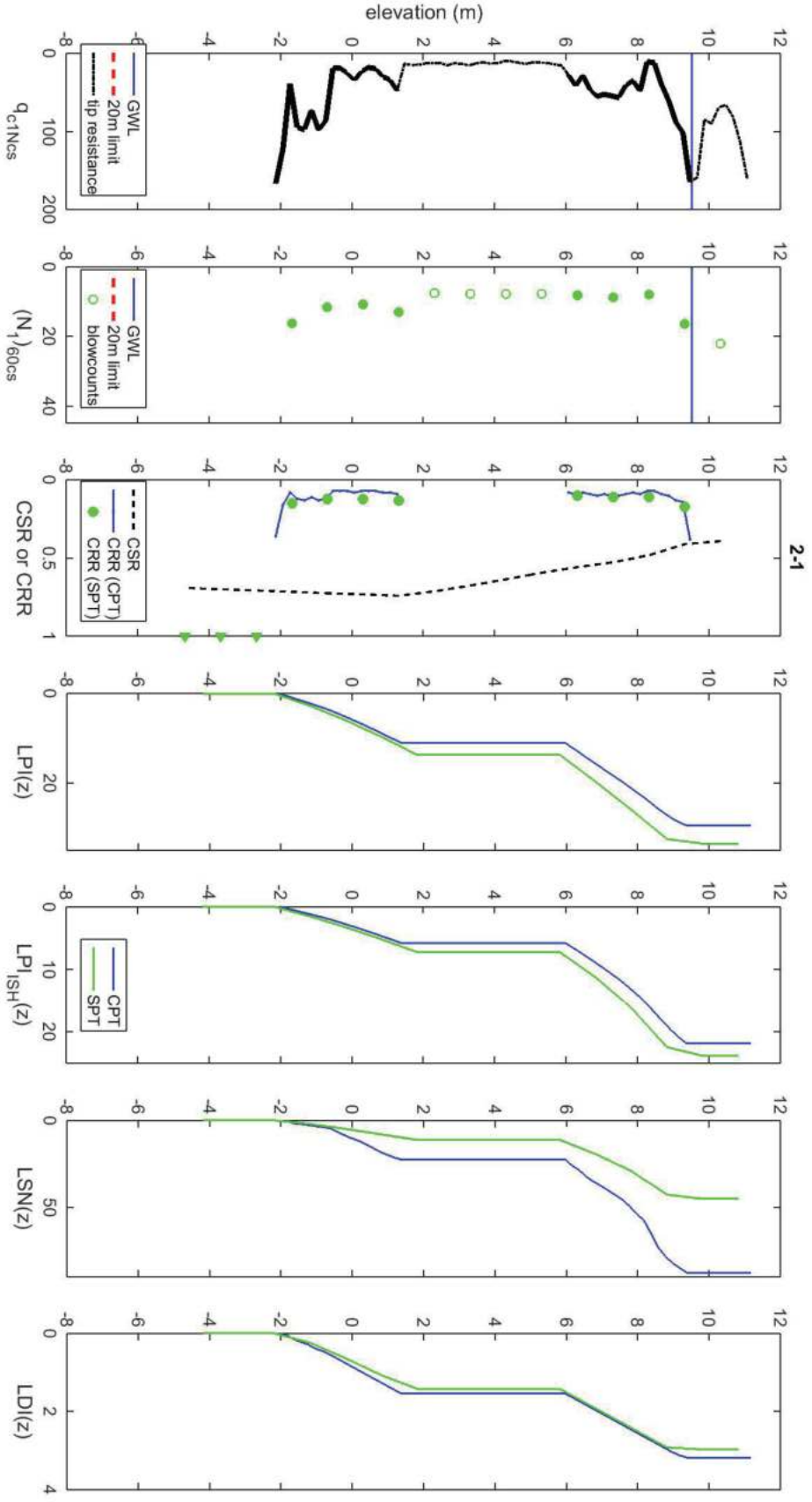
elevation (m)
q_{c1Ncs}
GWL
20m limit
tip resistance
$(N_1)_{60cs}$
blowcounts
CSR or CRR
CSR
CRR (CPT)
CRR (SPT)
2-1
LPI(z)
$LPI_{ISH}(z)$
CPT
SPT
LSN(z)
LDI(z)

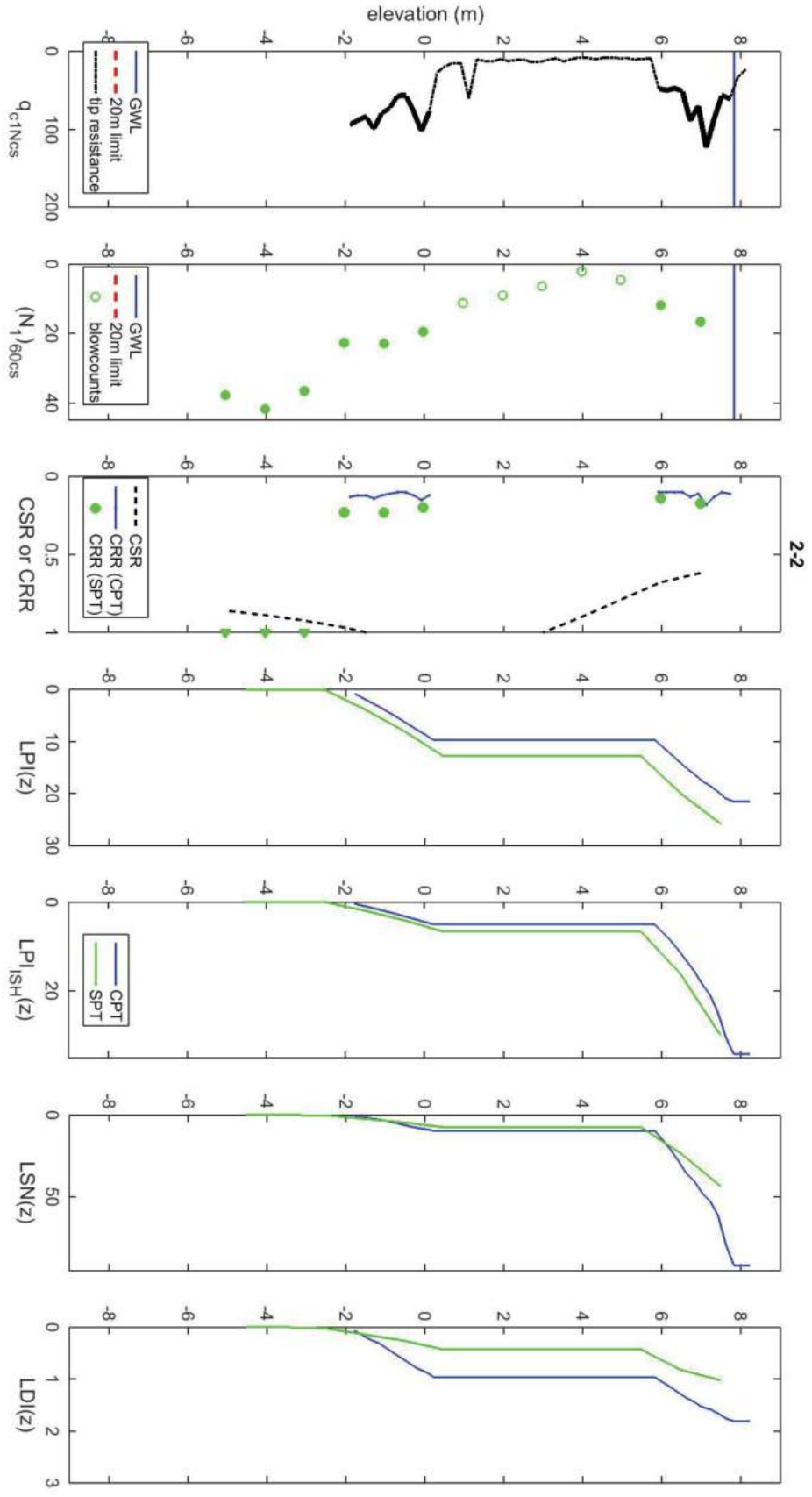
elevation (m)
q_{c1Ncs}
GWL
20m limit
tip resistance
$(N_1)_{60cs}$
blowcounts
CSR or CRR
CSR
CRR (CPT)
CRR (SPT)
2-2
LPI(z)
$LPI_{ISH}(z)$
CPT
SPT
LSN(z)
LDI(z)

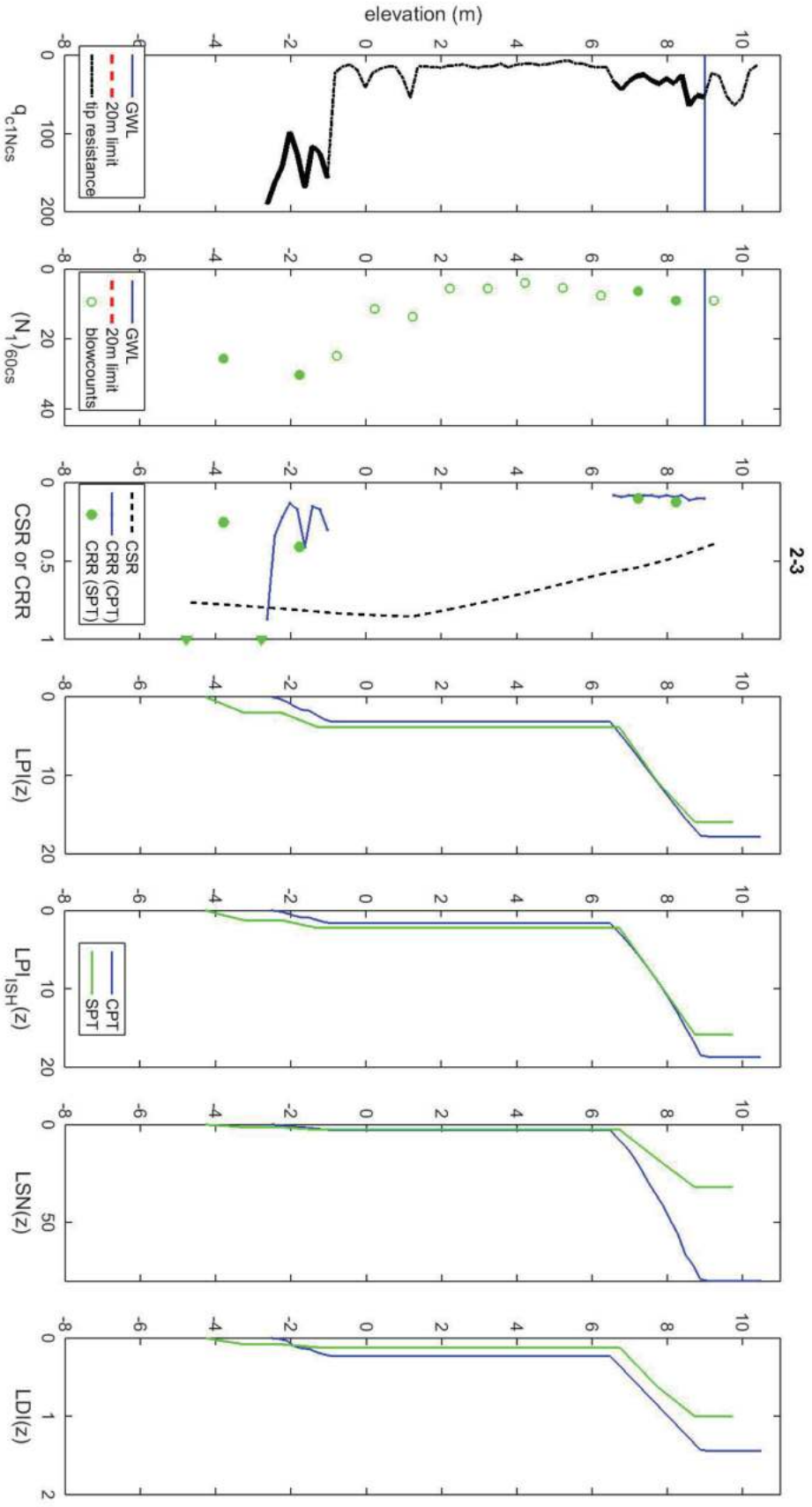
elevation (m)
q_{c1Ncs}
GWL
20m limit
tip resistance
$(N_1)_{60cs}$
blowcounts
CSR or CRR
CSR
CRR (CPT)
CRR (SPT)
2-3
LPI(z)
$LPI_{ISH}(z)$
CPT
SPT
LSN(z)
LDI(z)

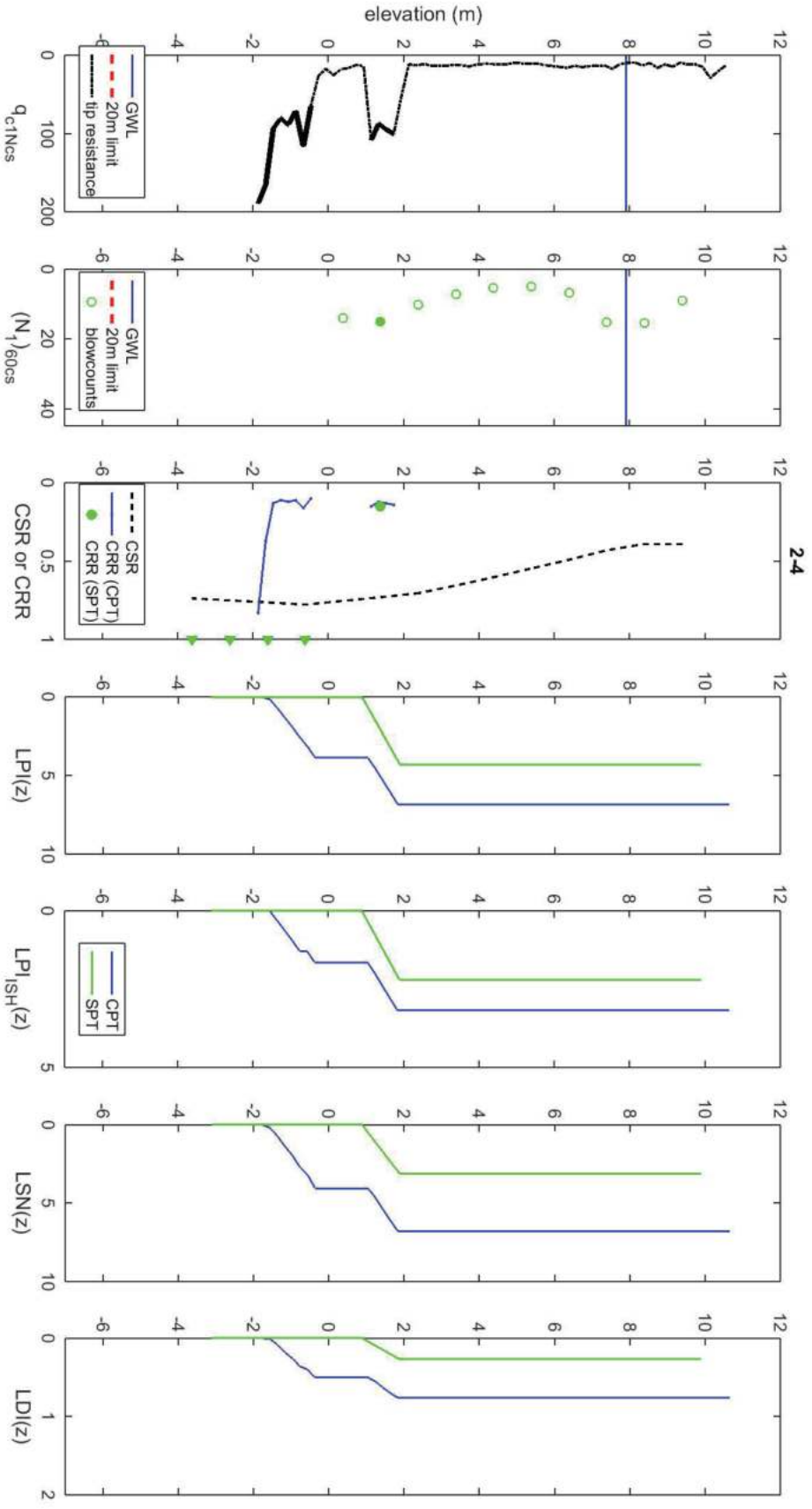
elevation (m)
GWL
20m limit
tip resistance
q_{c1Ncs}
GWL
20m limit
blowcounts
$(N_1)_{60cs}$
CSR
CRR (CPT)
CRR (SPT)
CSR or CRR
2-4
LPI(z)
CPT
SPT
$LPI_{ISH}(z)$
LSN(z)
LDI(z)

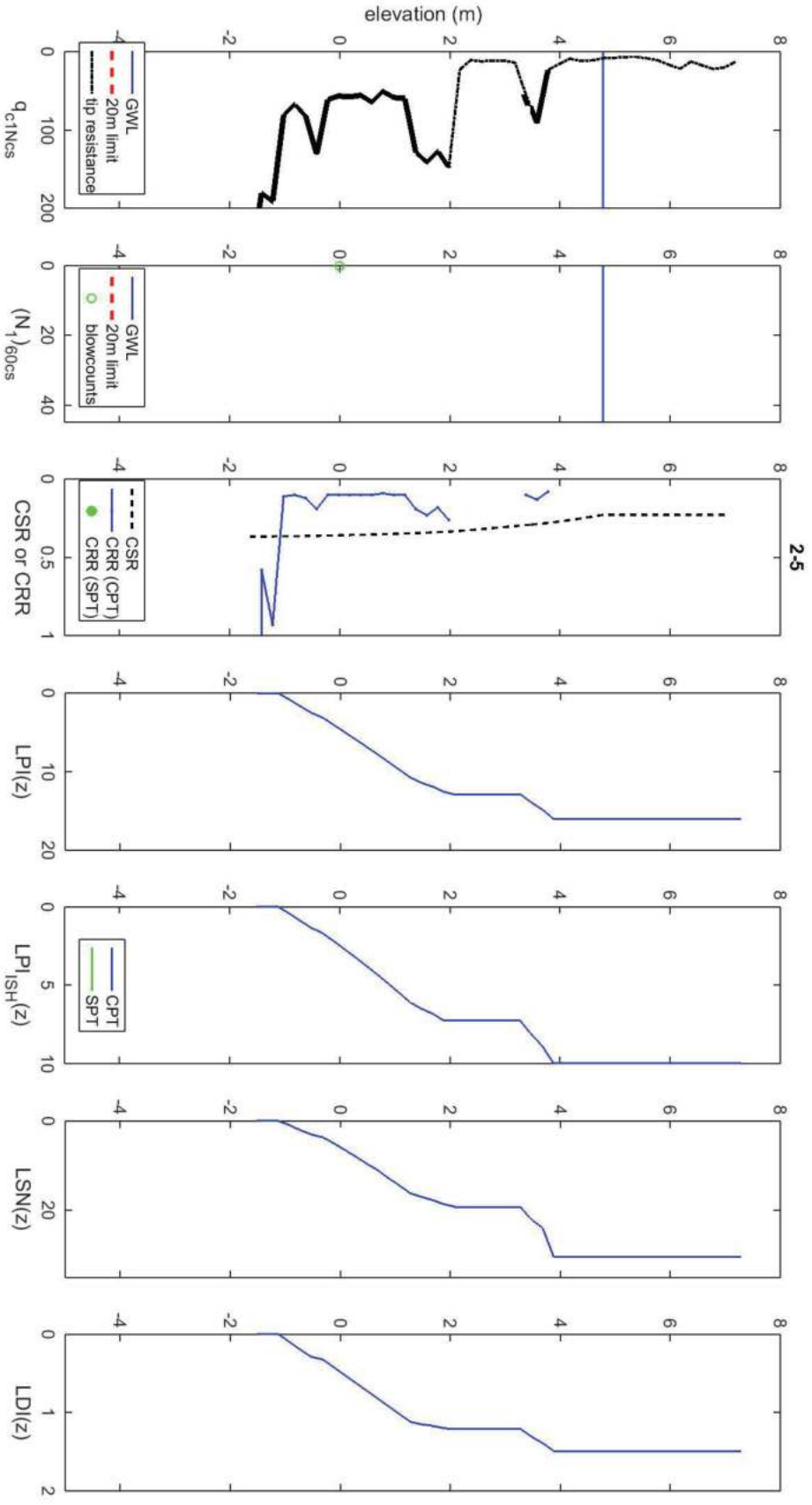
elevation (m)
q_{c1Ncs}
GWL
20m limit
tip resistance
$(N_1)_{60cs}$
blowcounts
CSR or CRR
CSR
CRR (CPT)
CRR (SPT)
2-5
LPI(z)
$LPI_{ISH}(z)$
CPT
SPT
LSN(z)
LDI(z)

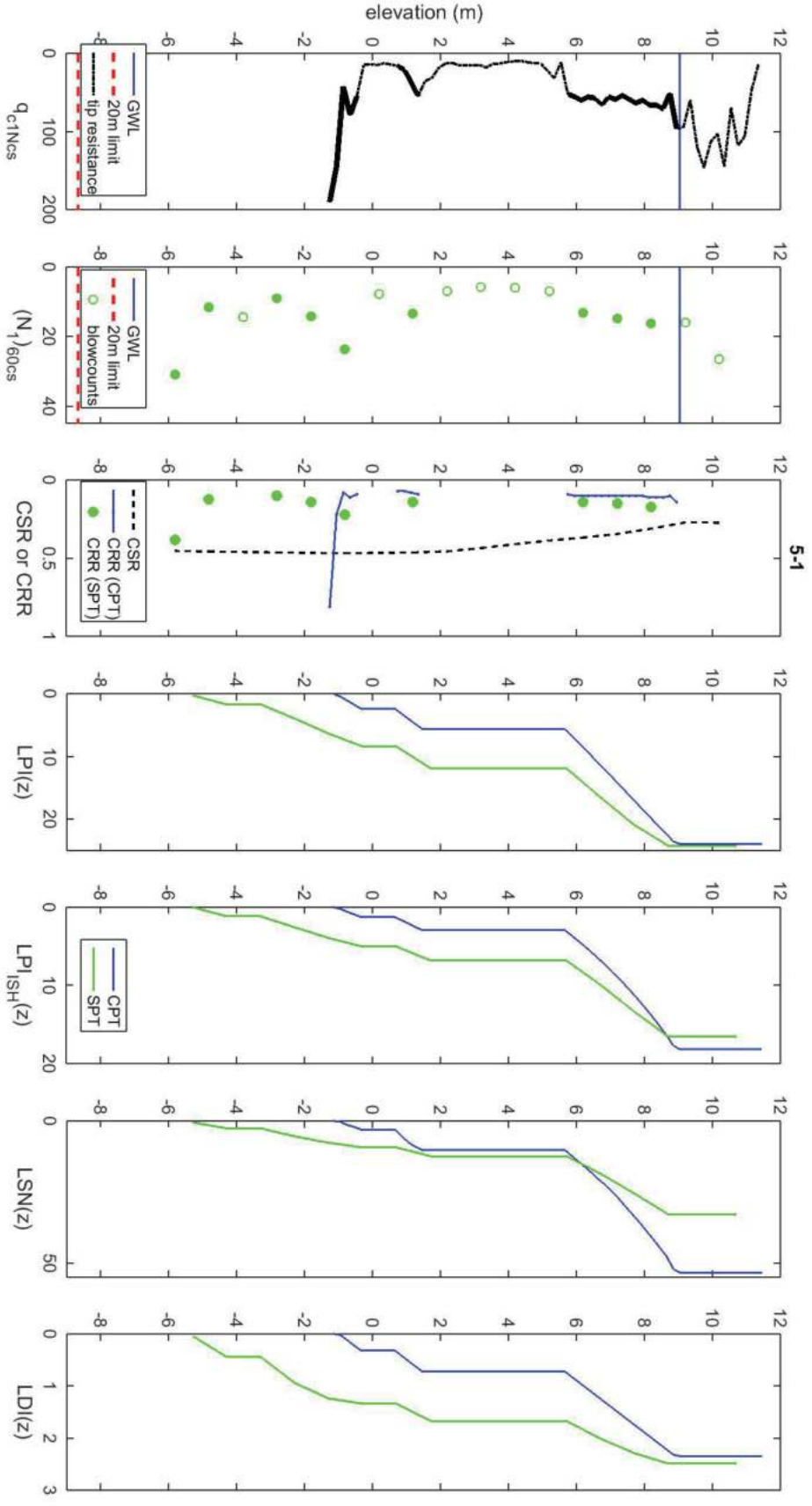
elevation (m)
GWL
20m limit
tip resistance
q_{c1Ncs}
GWL
20m limit
blowcounts
$(N_1)_{60cs}$
CSR
CRR (CPT)
CRR (SPT)
CSR or CRR
5-1
LPI(z)
CPT
SPT
$LPI_{ISH}(z)$
LSN(z)
LDI(z)

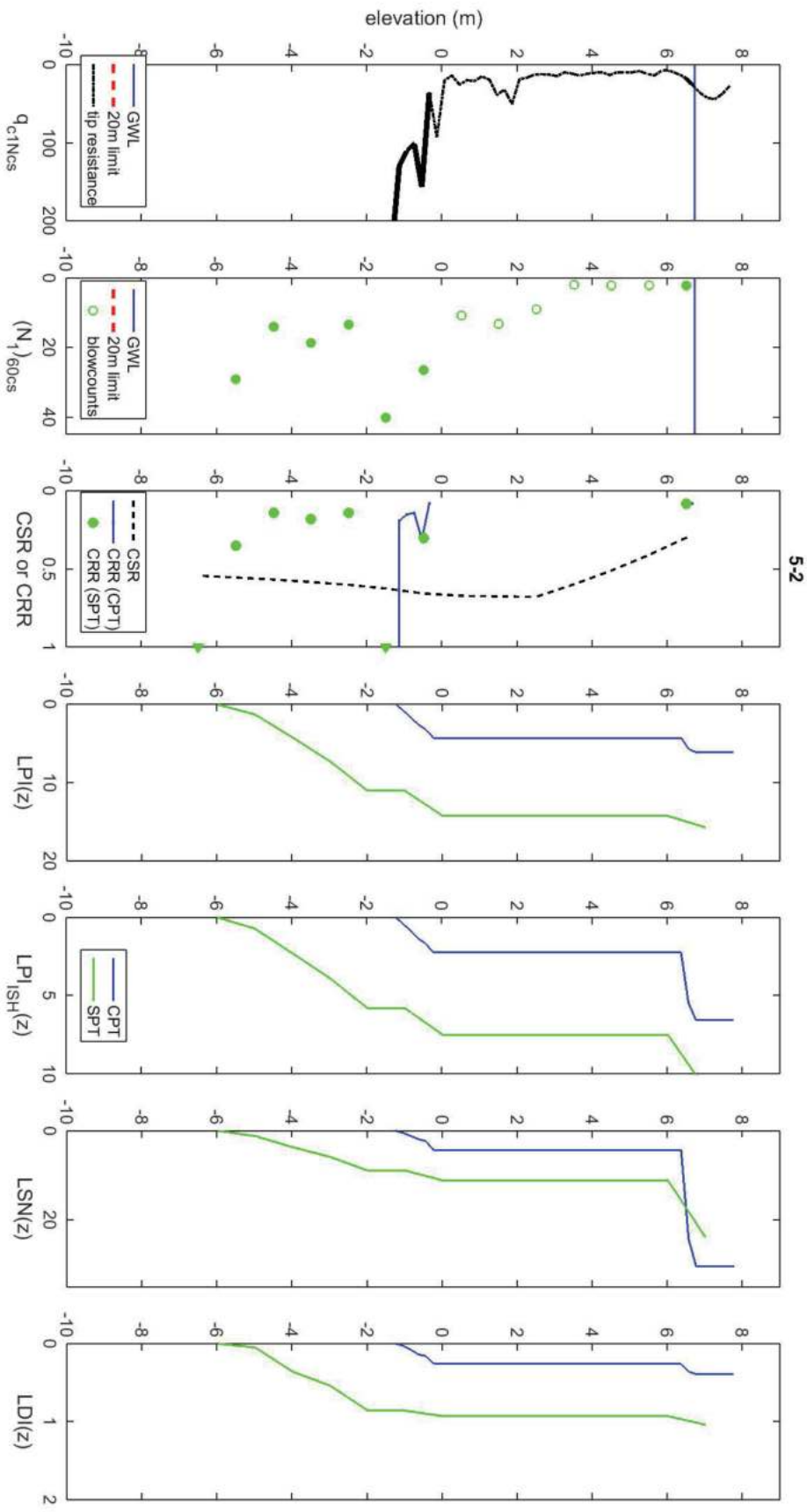
elevation (m)
GWL
20m limit
tip resistance
q_{c1Ncs}
blowcounts
$(N_1)_{60cs}$
CSR
CRR (CPT)
CRR (SPT)
CSR or CRR
LPI(z)
CPT
SPT
$LPI_{ISH}(z)$
LSN(z)
LDI(z)
5-2

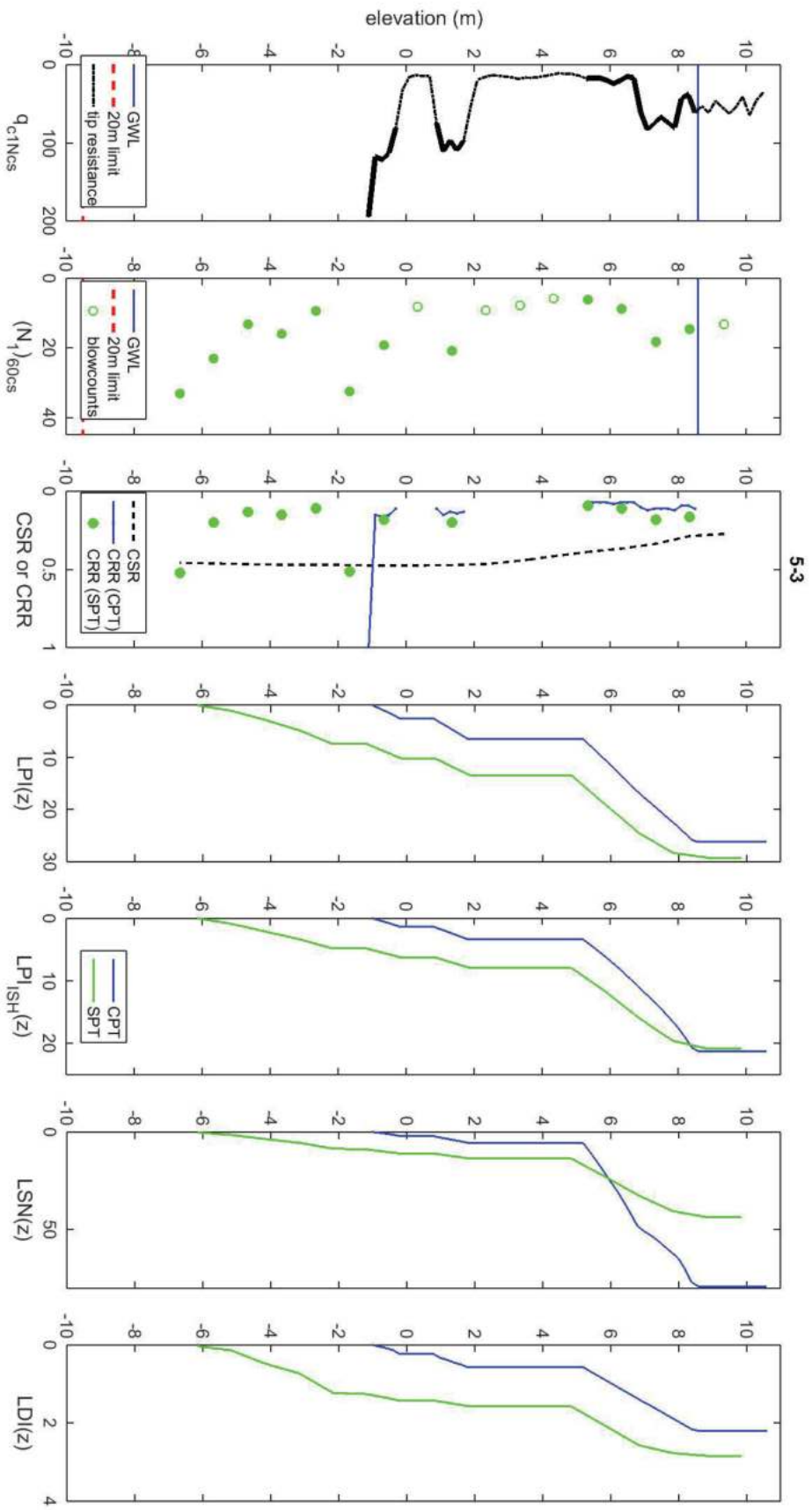
elevation (m)
q_{c1Ncs}
GWL
20m limit
tip resistance
$(N_1)_{60cs}$
blowcounts
CSR or CRR
CSR
CRR (CPT)
CRR (SPT)
LPI(z)
$LPI_{ISH}(z)$
CPT
SPT
LSN(z)
LDI(z)
5-3

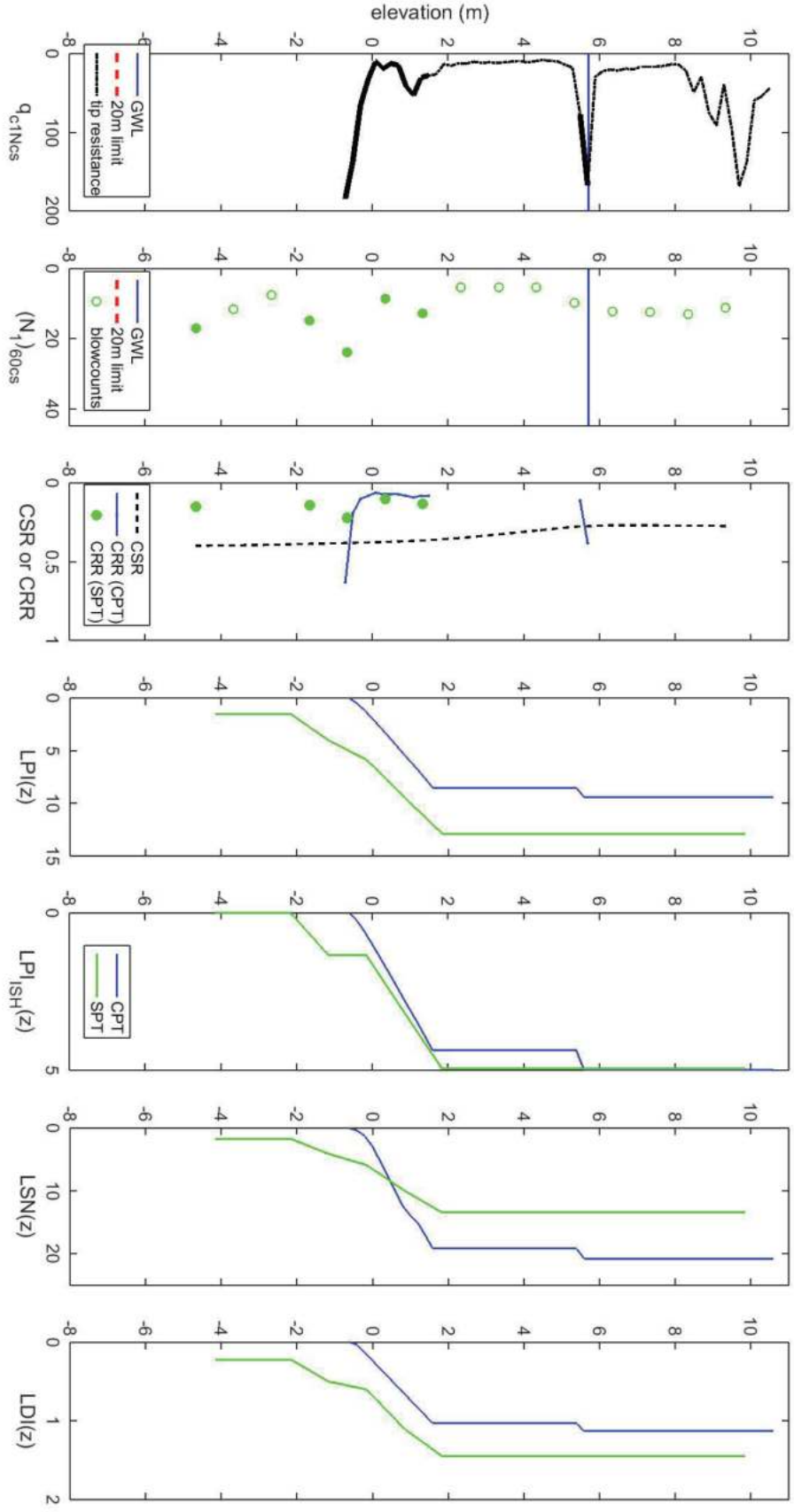
elevation (m)
q_{c1Ncs}
GWL
20m limit
tip resistance
$(N_1)_{60cs}$
blowcounts
CSR or CRR
CSR
CRR (CPT)
CRR (SPT)
LPI(z)
$LPI_{ISH}(z)$
CPT
SPT
LSN(z)
LDI(z)

5-4

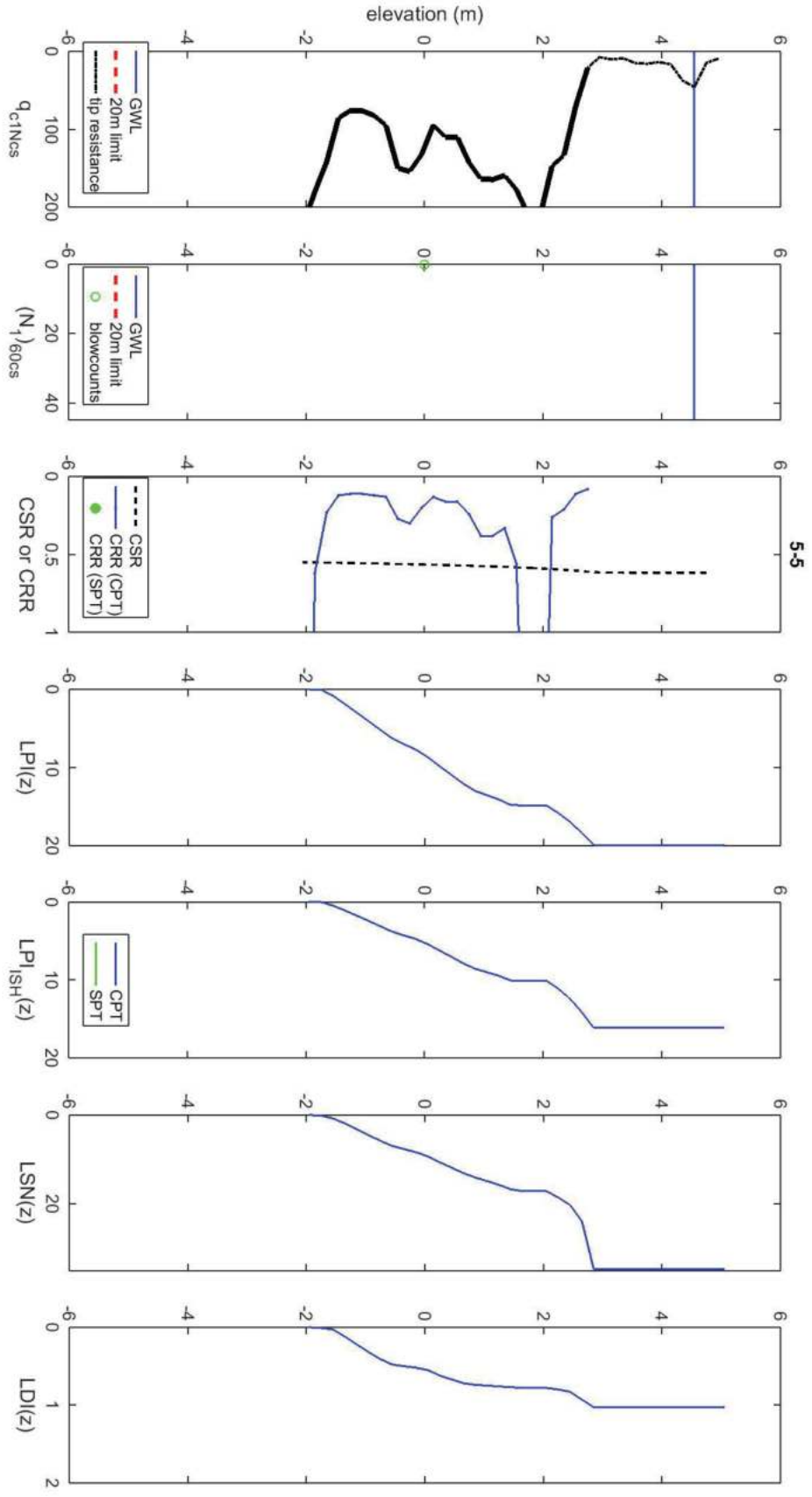
elevation (m)
GWL
20m limit
tip resistance
q_{c1Ncs}
GWL
20m limit
blowcounts
$(N_1)_{60cs}$
CSR
CRR (CPT)
CRR (SPT)
CSR or CRR
5-5
LPI(z)
CPT
SPT
$LPI_{ISH}(z)$
LSN(z)
LDI(z)

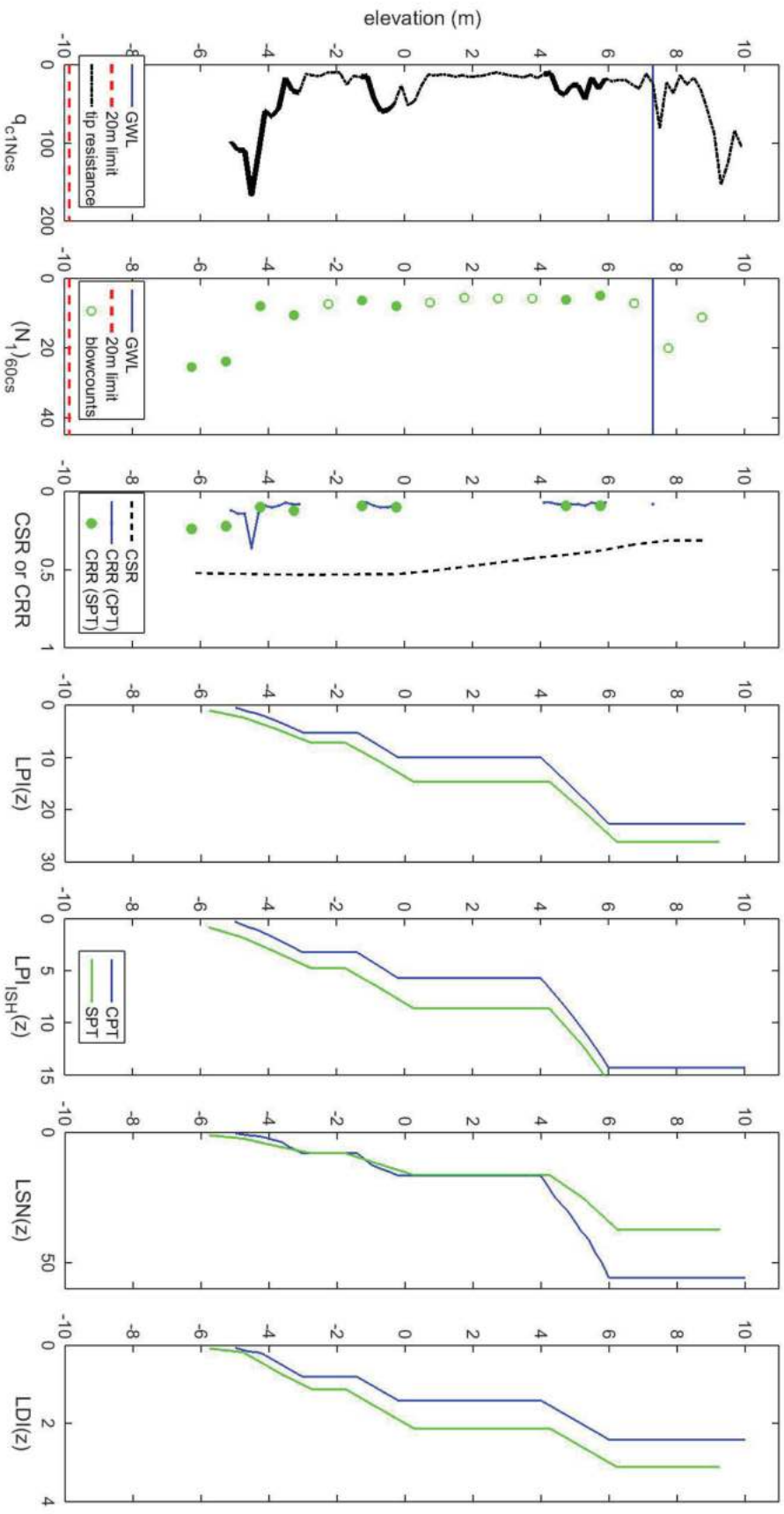
elevation (m)
q_{c1Ncs}
GWL
20m limit
tip resistance
$(N_1)_{60cs}$
blowcounts
CSR or CRR
CSR
CRR (CPT)
CRR (SPT)
LPI(z)
$LPI_{ISH}(z)$
CPT
SPT
LSN(z)
LDI(z)
7-1

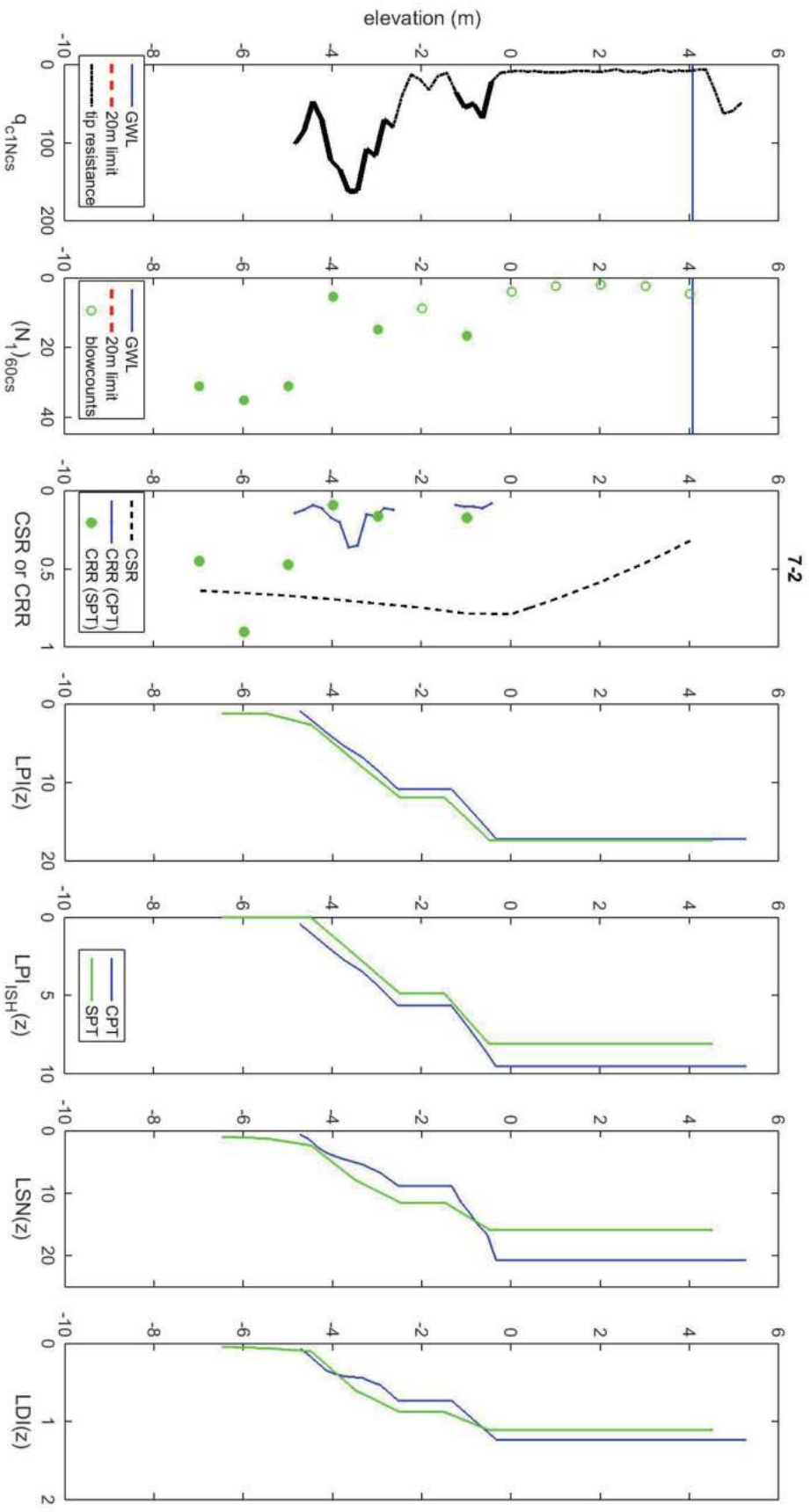
elevation (m)
GWL
20m limit
tip resistance
q_{c1Ncs}
blowcounts
$(N_1)_{60cs}$
CSR
CRR (CPT)
CRR (SPT)
CSR or CRR
7-2
LPI(z)
CPT
SPT
$LPI_{ISH}(z)$
LSN(z)
LDI(z)

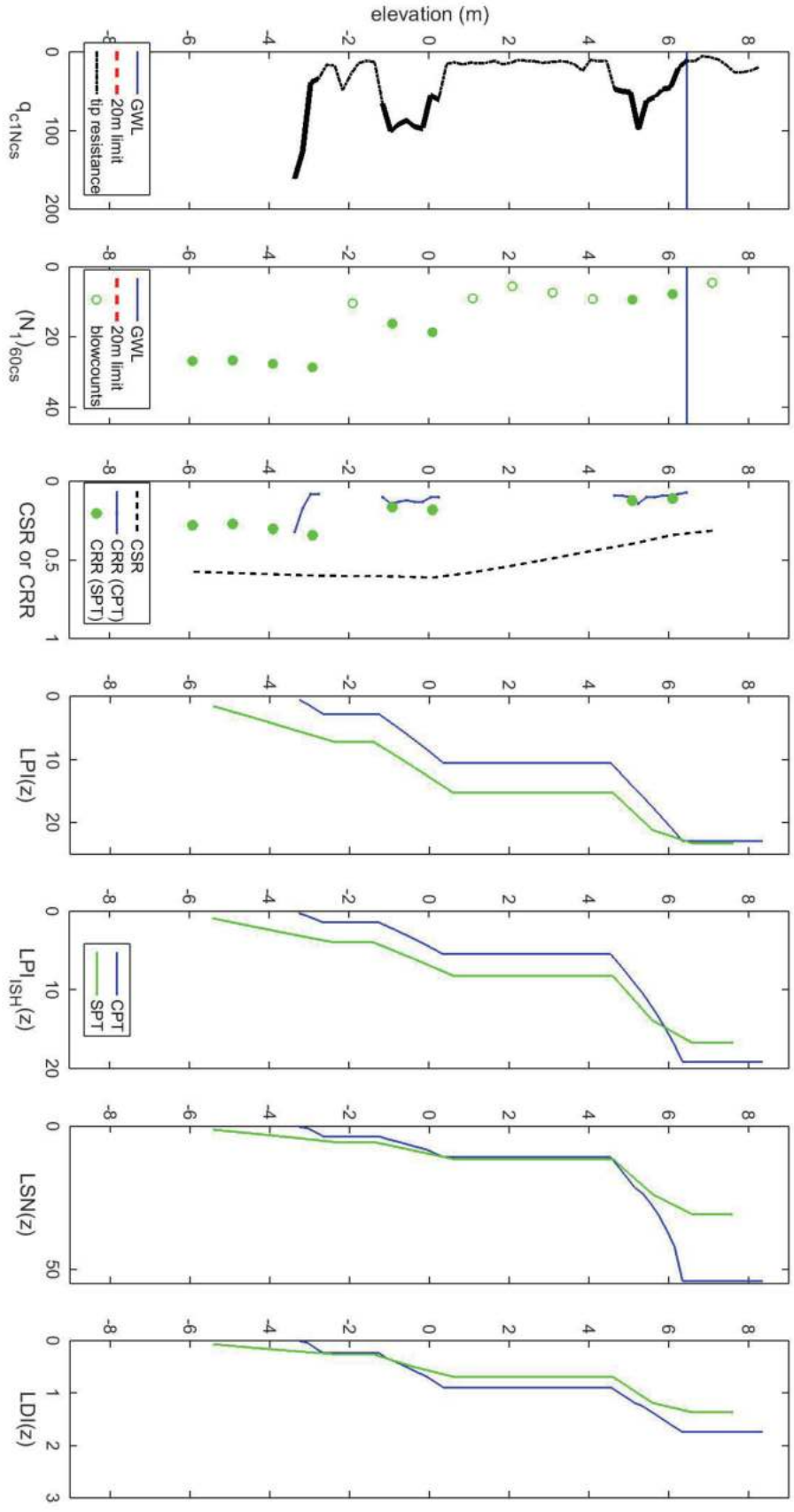
elevation (m)
q_{c1Ncs}
GWL
20m limit
tip resistance
$(N_1)_{60cs}$
blowcounts
CSR or CRR
CSR
CRR (CPT)
CRR (SPT)
LPI(z)
$LPI_{ISH}(z)$
CPT
SPT
LSN(z)
LDI(z)
7-3

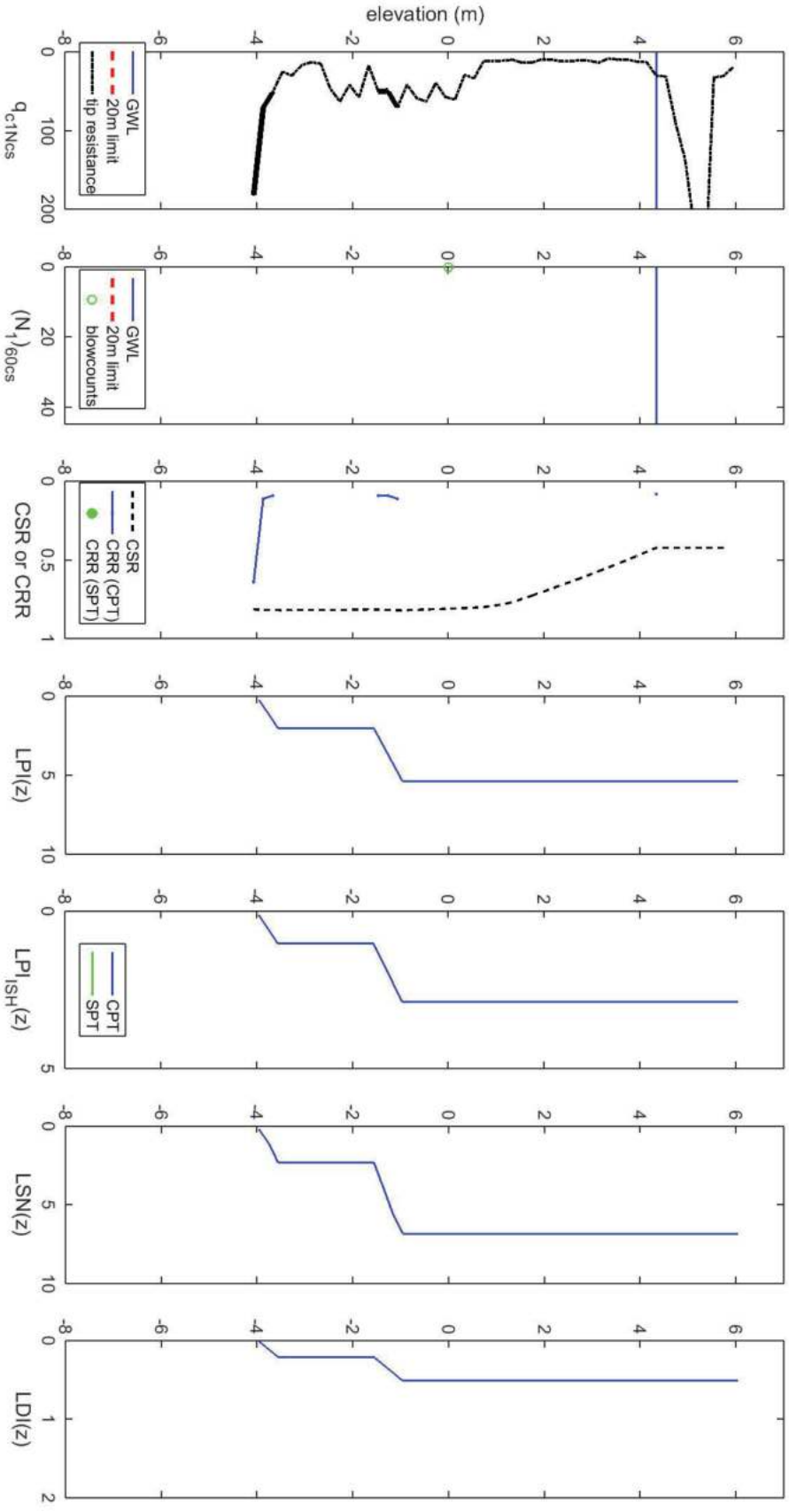
elevation (m)
7-5
q_{c1Ncs}
GWL
20m limit
tip resistance
$(N_1)_{60cs}$
blowcounts
CSR or CRR
CSR
CRR (CPT)
CRR (SPT)
LPI(z)
$LPI_{ISH}(z)$
CPT
SPT
LSN(z)
LDI(z)

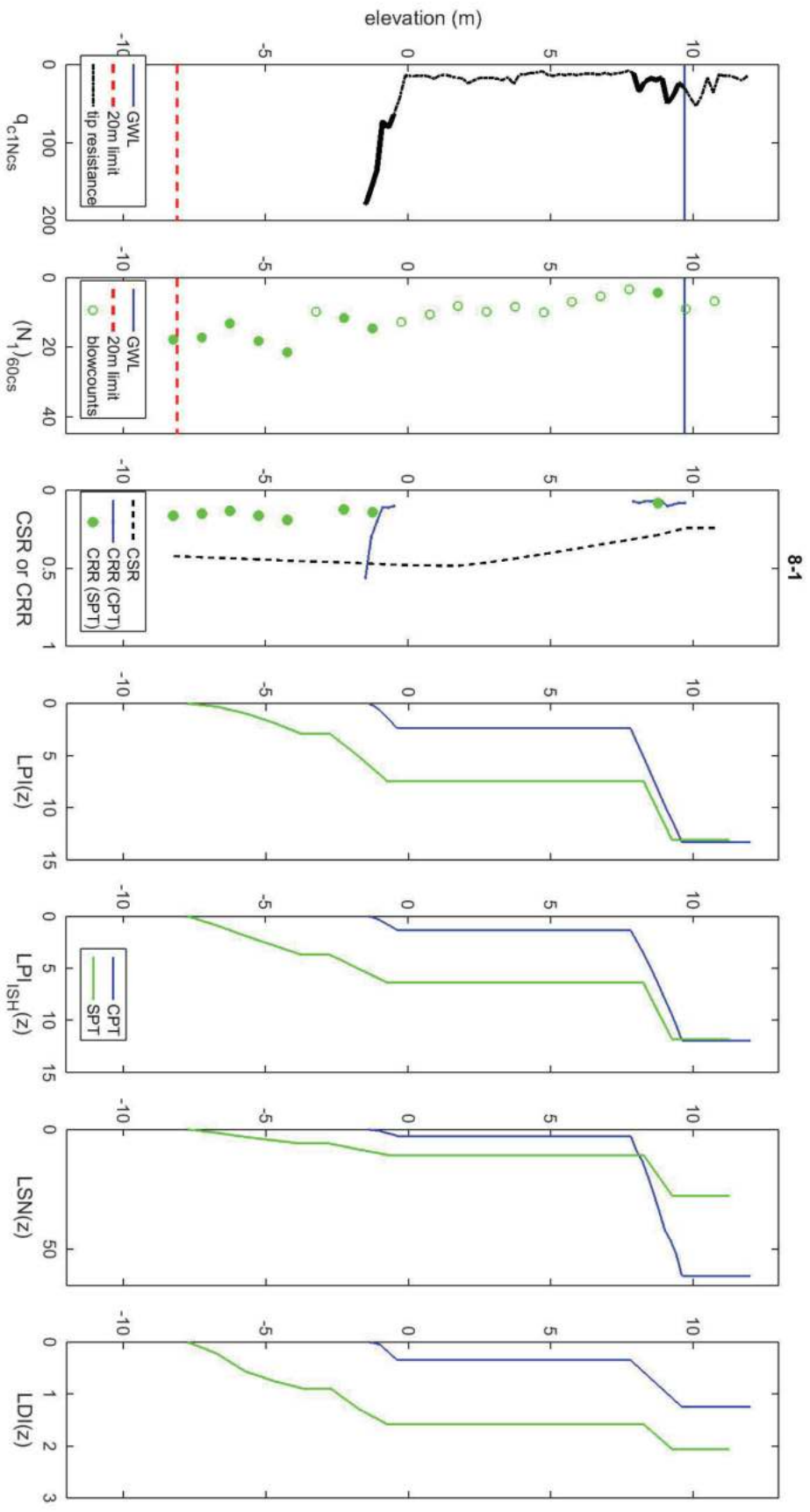
elevation (m)
q_{c1Ncs}
GWL
20m limit
tip resistance
$(N_1)_{60cs}$
blowcounts
CSR or CRR
CSR
CRR (CPT)
CRR (SPT)
LPI(z)
$LPI_{ISH}(z)$
CPT
SPT
LSN(z)
LDI(z)
8-1

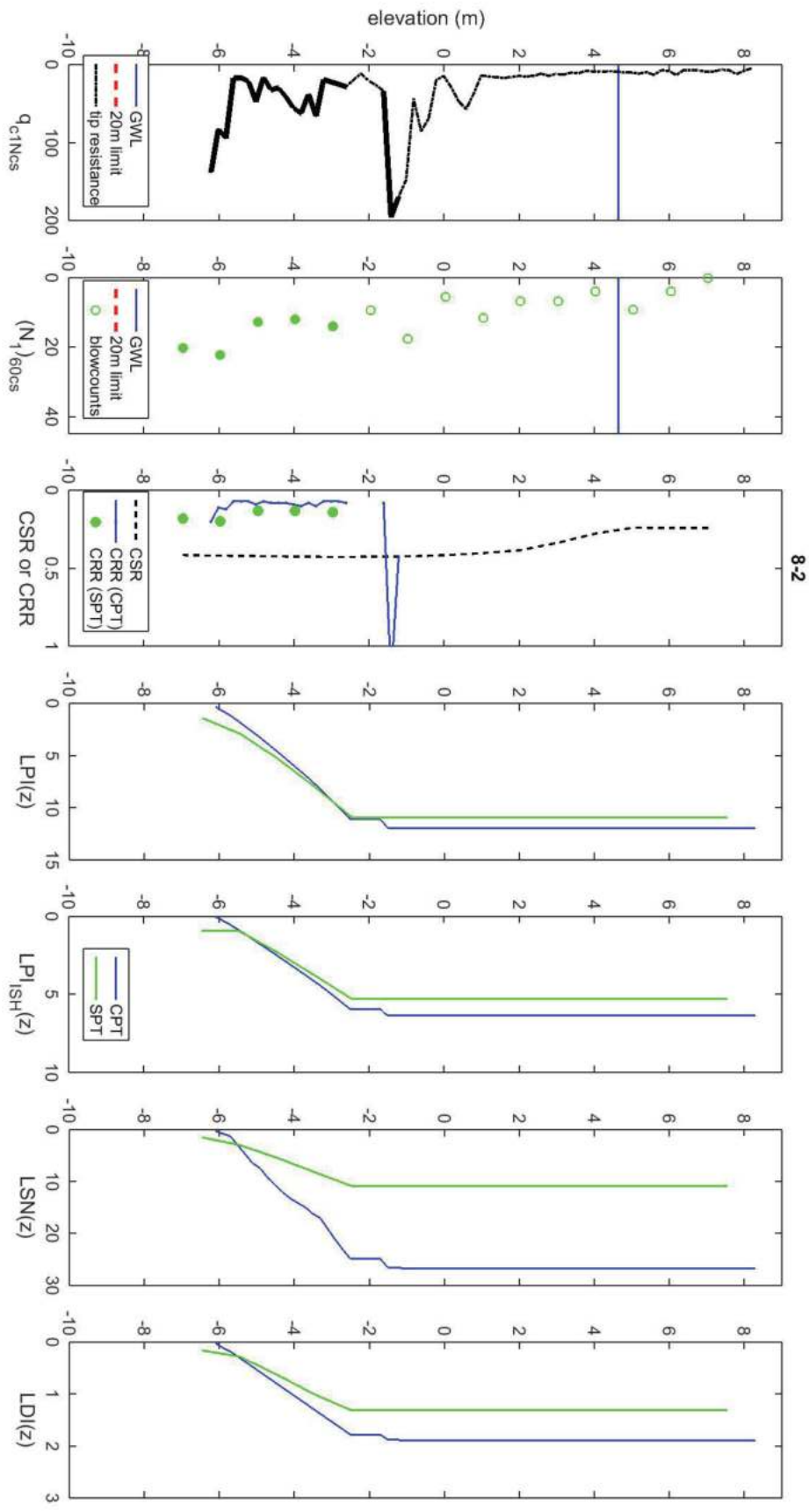
elevation (m)
q_{c1Ncs}
GWL
20m limit
tip resistance
$(N_1)_{60cs}$
blowcounts
CSR or CRR
CSR
CRR (CPT)
CRR (SPT)
8-2
LPI(z)
$LPI_{ISH}(z)$
CPT
SPT
LSN(z)
LDI(z)

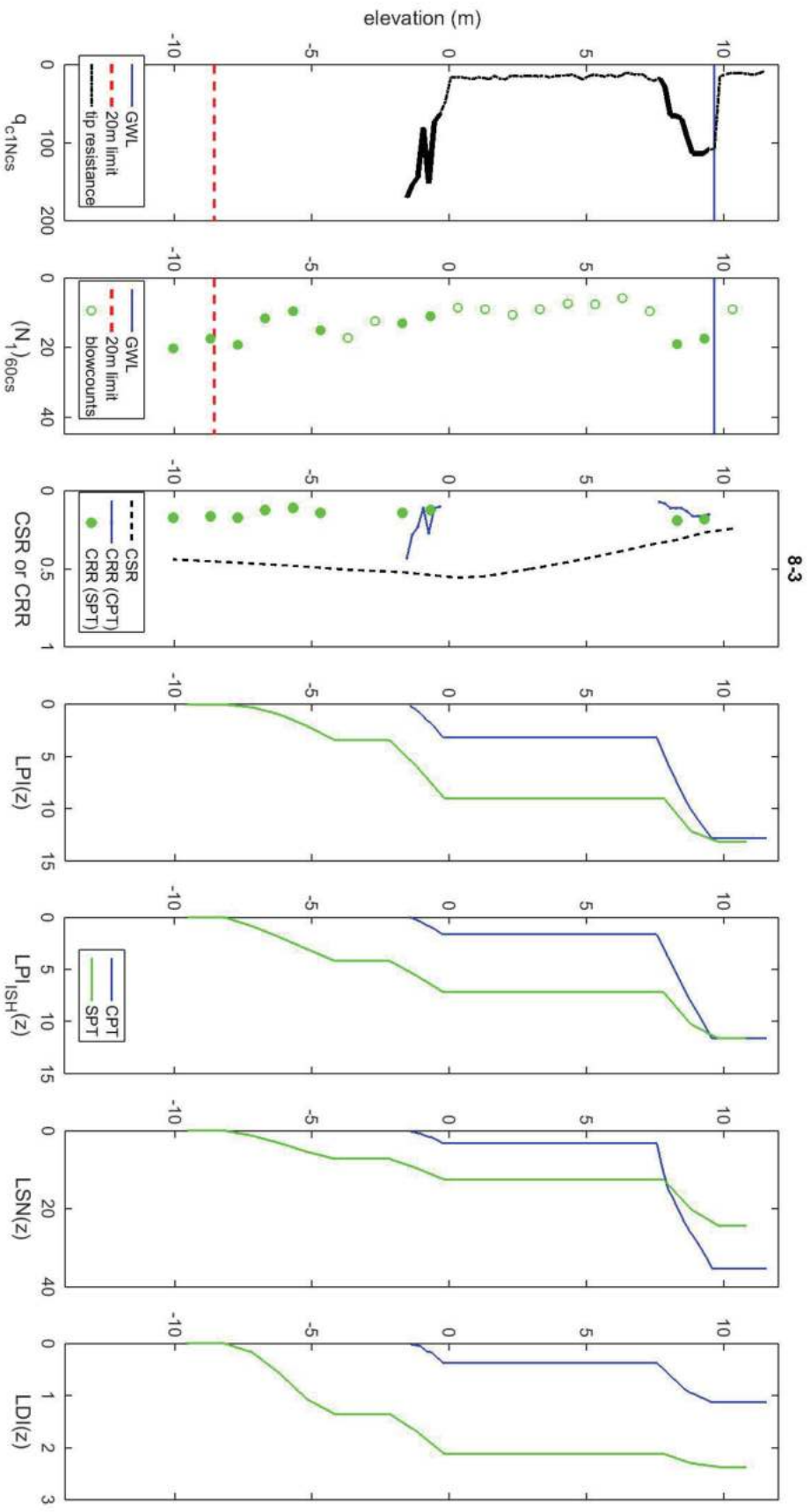
elevation (m)
GWL
20m limit
tip resistance
q_{c1Ncs}
blowcounts
$(N_1)_{60cs}$
CSR
CRR (CPT)
CRR (SPT)
CSR or CRR
LPI(z)
CPT
SPT
$LPI_{ISH}(z)$
LSN(z)
LDI(z)
8-3

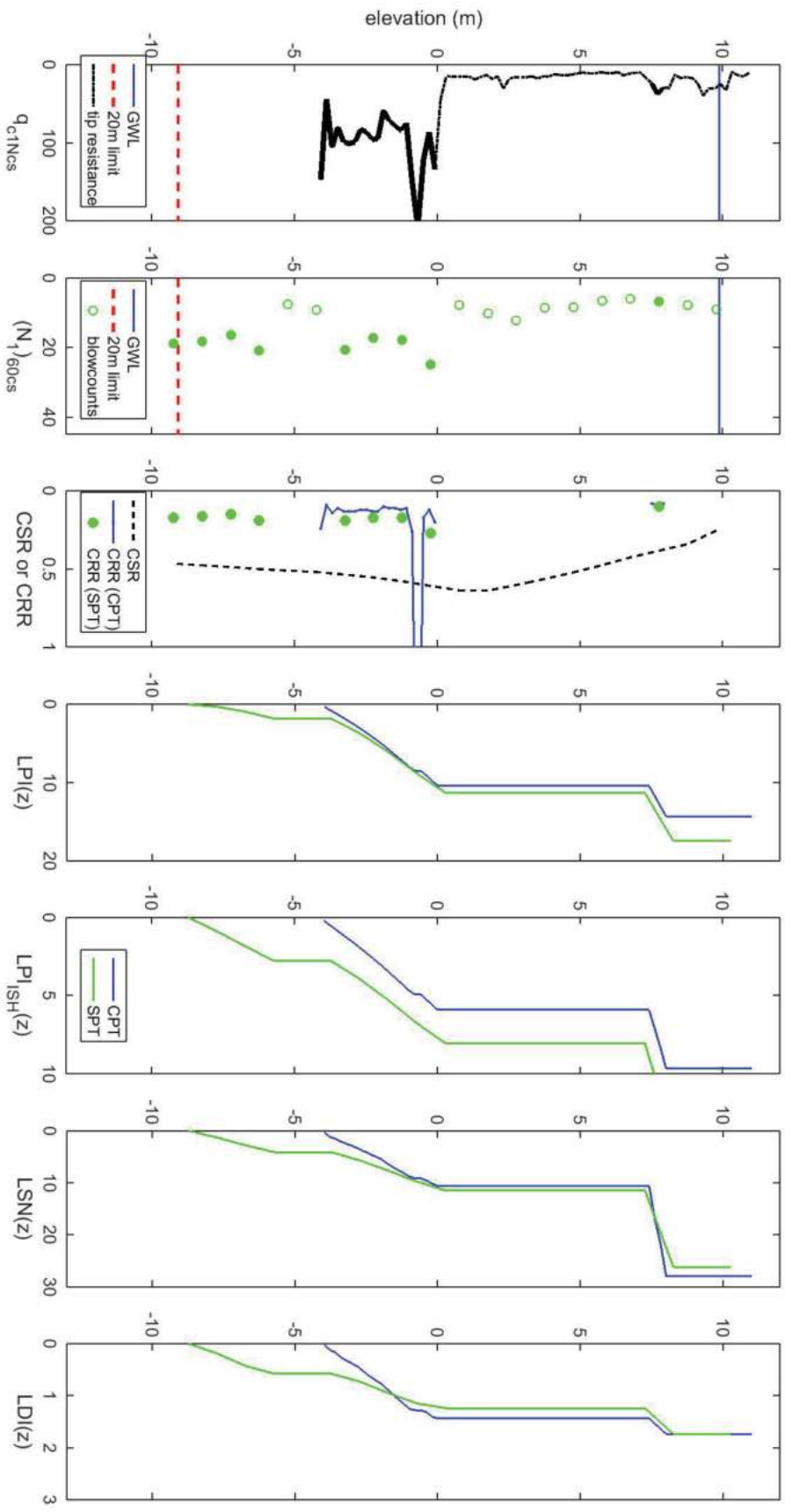
elevation (m)
q_{c1Ncs}
GWL
20m limit
tip resistance
$(N_1)_{60cs}$
blowcounts
CSR or CRR
CSR
CRR (CPT)
CRR (SPT)
LPI(z)
$LPI_{ISH}(z)$
CPT
SPT
LSN(z)
LDI(z)

8-4

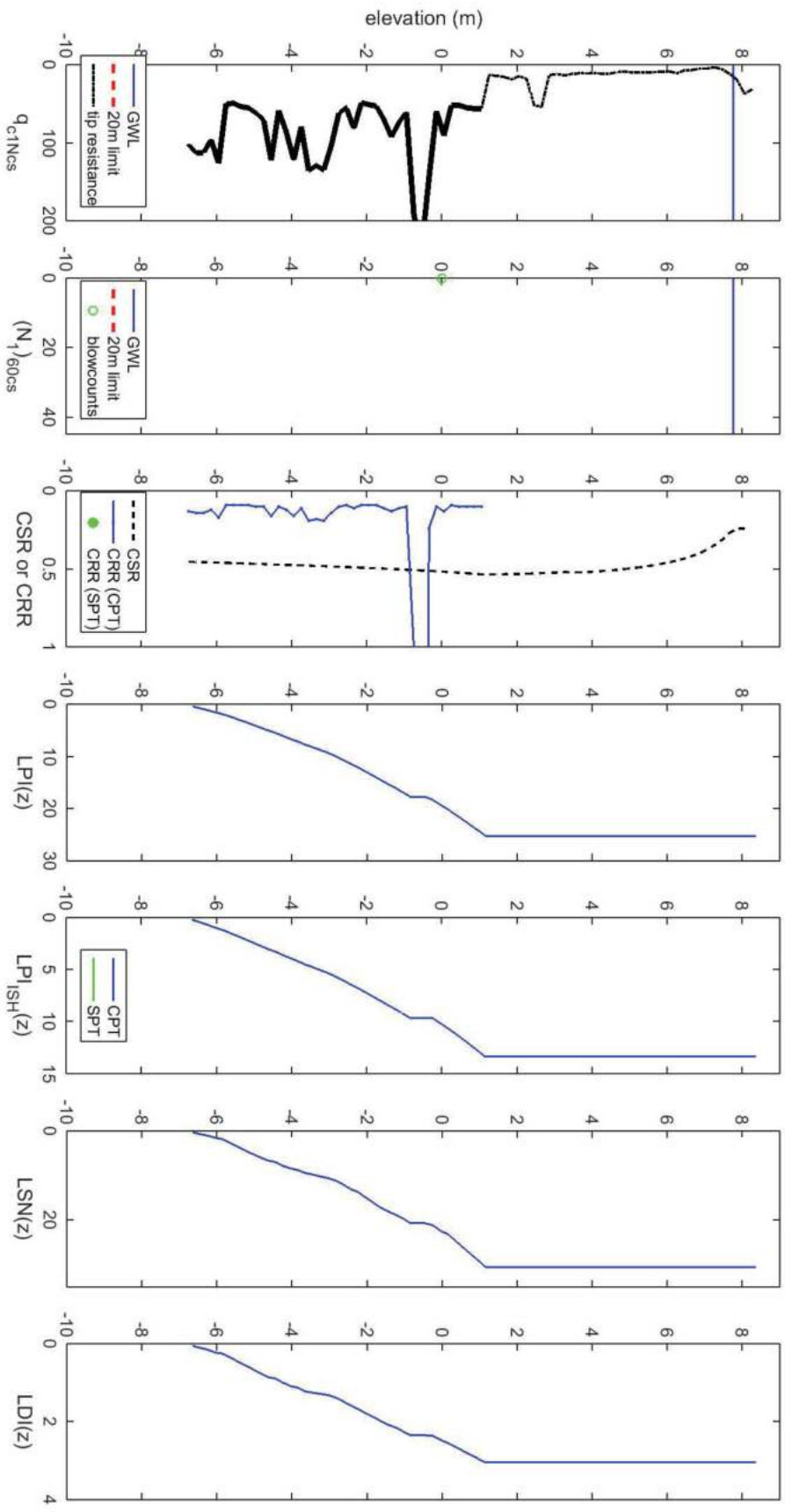
elevation (m)
q_{c1Ncs}
GWL
20m limit
tip resistance
$(N_1)_{60cs}$
GWL
20m limit
blowcounts
CSR or CRR
CSR
CRR (CPT)
CRR (SPT)
LPI(z)
$LPI_{ISH}(z)$
CPT
SPT
LSN(z)
LDI(z)
8-5

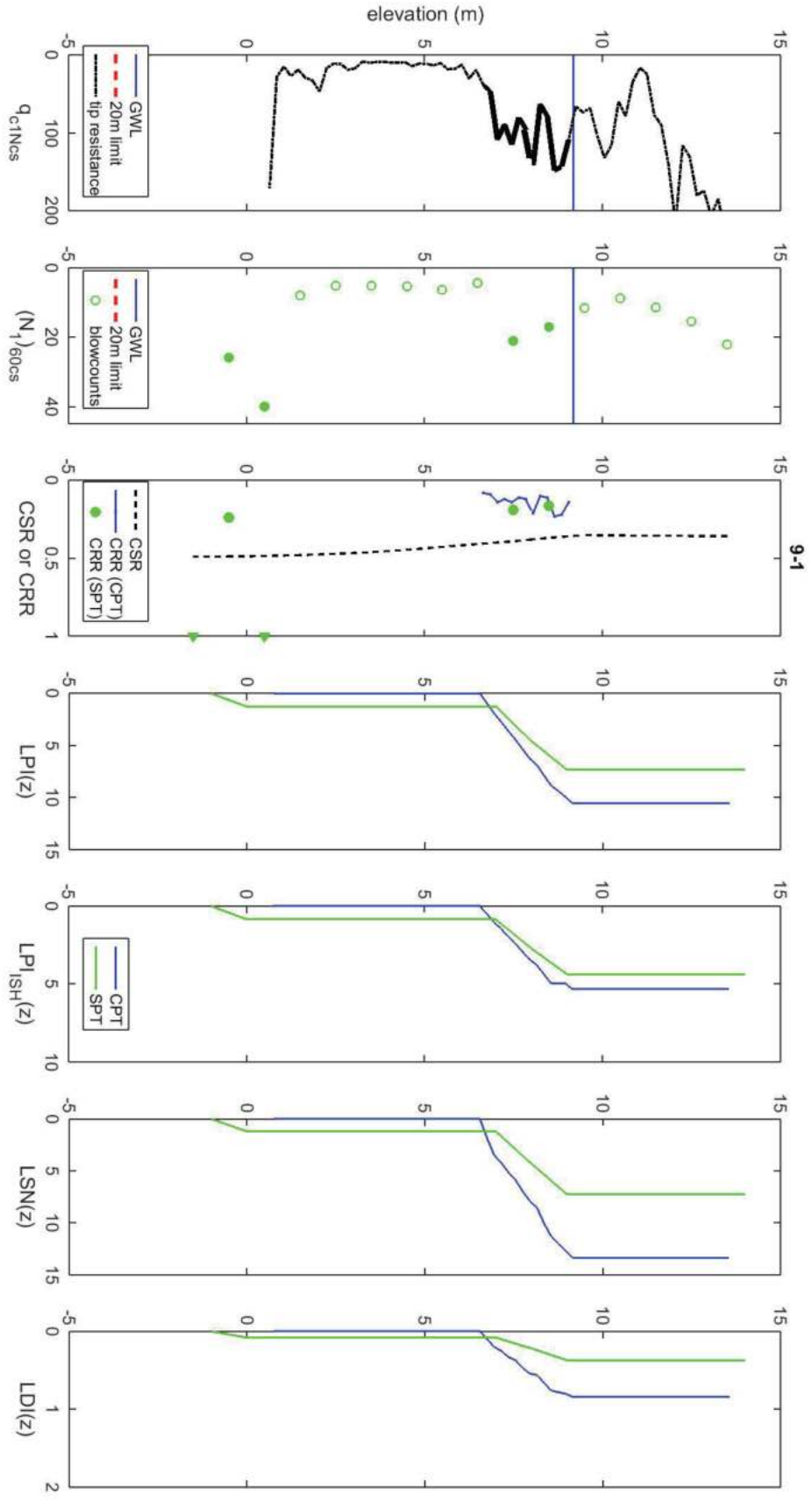
elevation (m)
GWL
20m limit
tip resistance
q_{c1Ncs}
GWL
20m limit
blowcounts
$(N_1)_{60cs}$
CSR
CRR (CPT)
CRR (SPT)
CSR or CRR
9-1
LPI(z)
CPT
SPT
$LPI_{ISH}(z)$
LSN(z)
LDI(z)

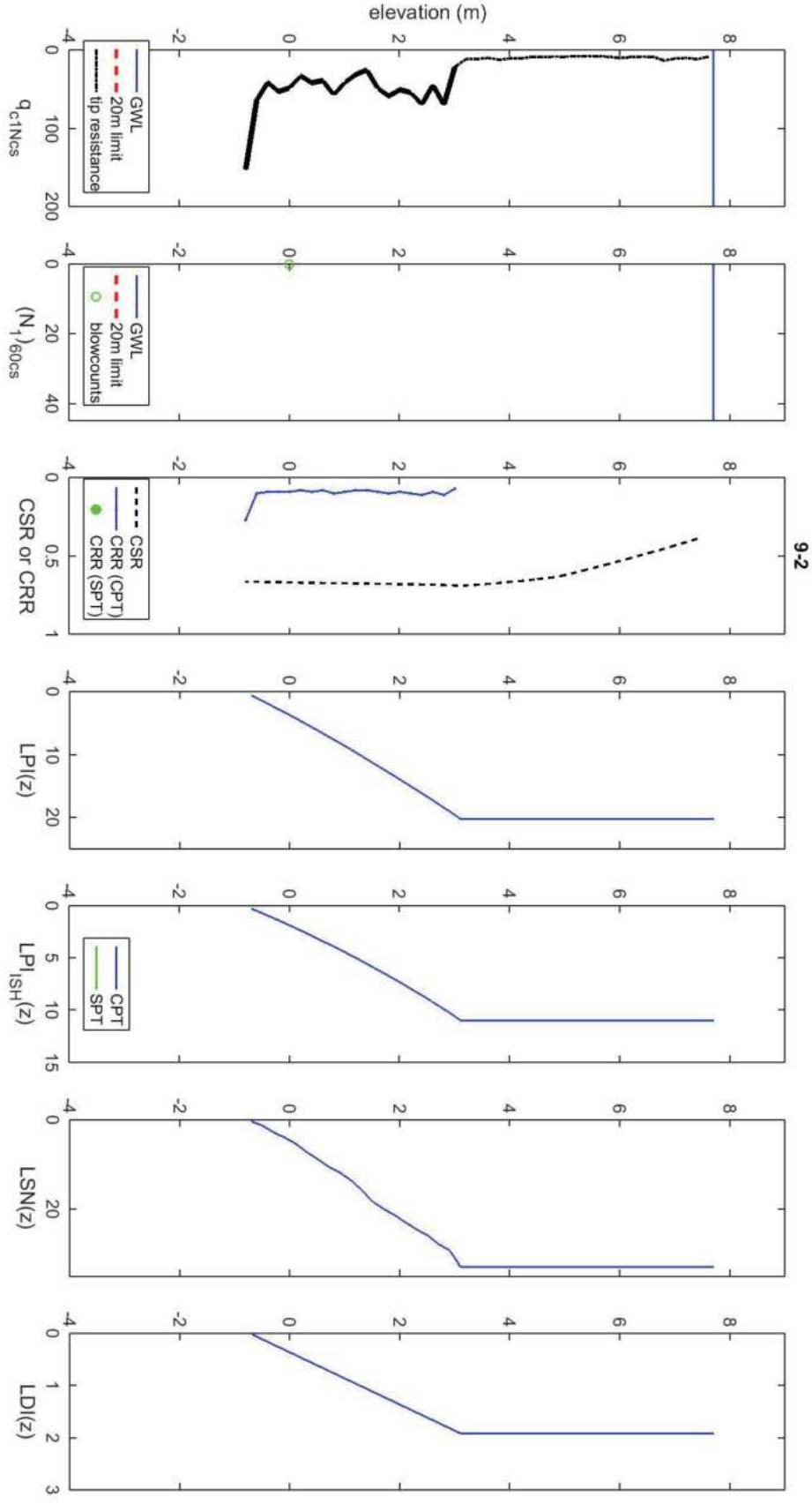
elevation (m)
q_{c1Ncs}
GWL
20m limit
tip resistance
$(N_1)_{60cs}$
GWL
20m limit
blowcounts
CSR or CRR
CSR
CRR (CPT)
CRR (SPT)
LPI(z)
$LPI_{ISH}(z)$
CPT
SPT
LSN(z)
LDI(z)
9-2

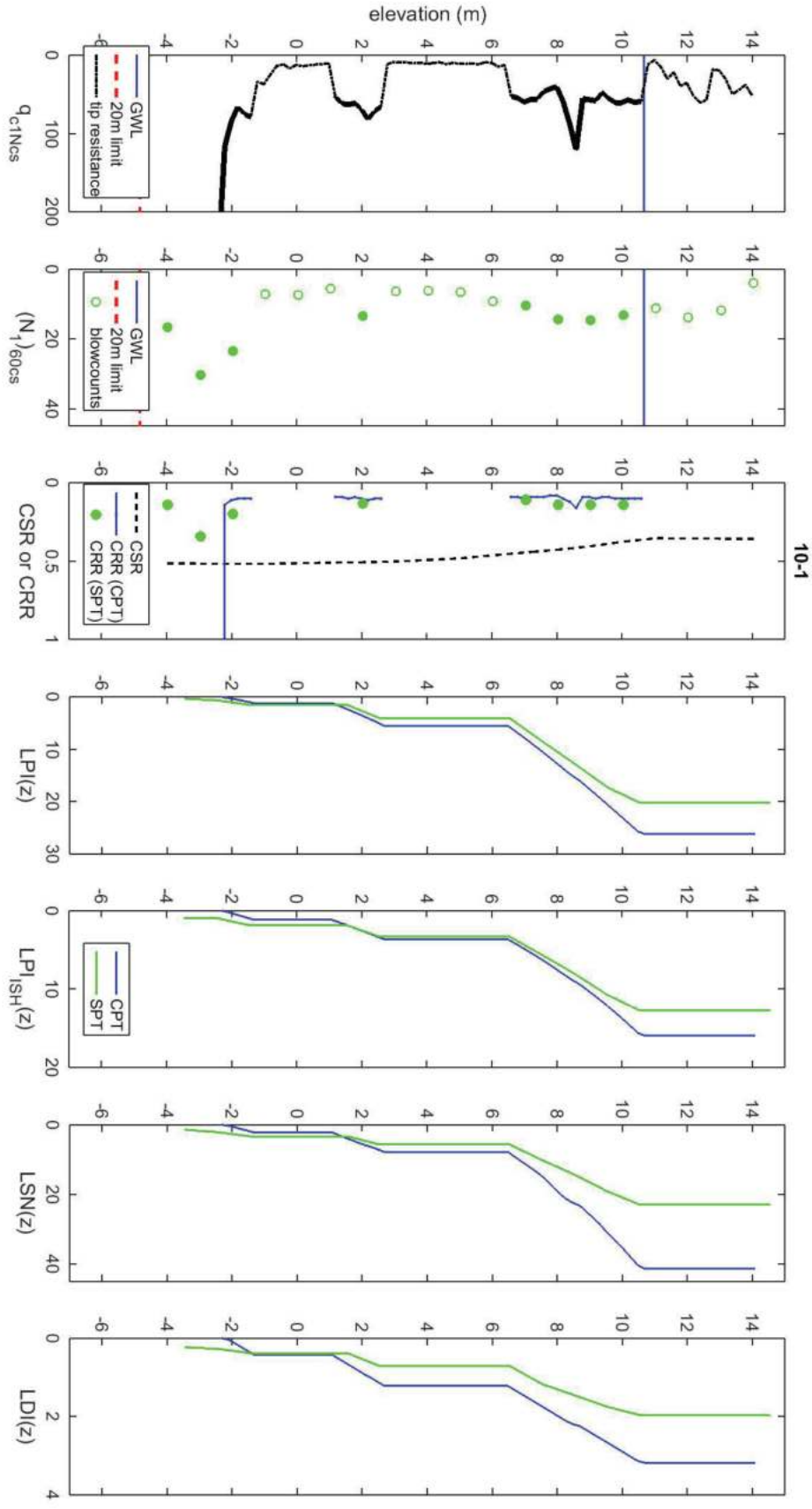
elevation (m)
q_{c1Ncs}
GWL
20m limit
tip resistance
$(N_1)_{60cs}$
blowcounts
CSR or CRR
CSR
CRR (CPT)
CRR (SPT)
10-1
LPI(z)
$LPI_{ISH}(z)$
CPT
SPT
LSN(z)
LDI(z)

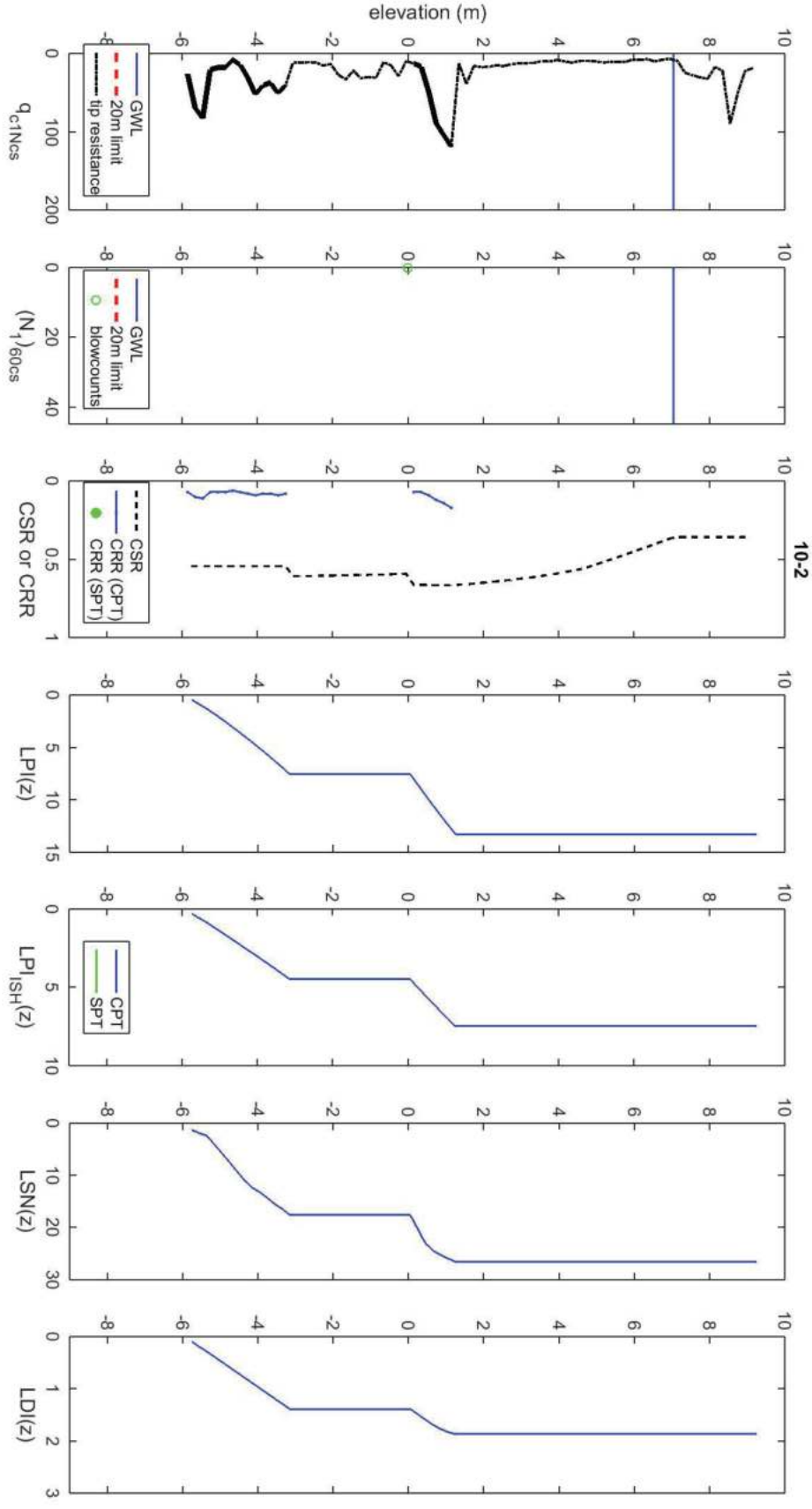
elevation (m)
GWL
20m limit
tip resistance
q_{c1Ncs}
blowcounts
$(N_1)_{60cs}$
CSR
CRR (CPT)
CRR (SPT)
CSR or CRR
10-2
LPI(z)
CPT
SPT
$LPI_{ISH}(z)$
LSN(z)
LDI(z)

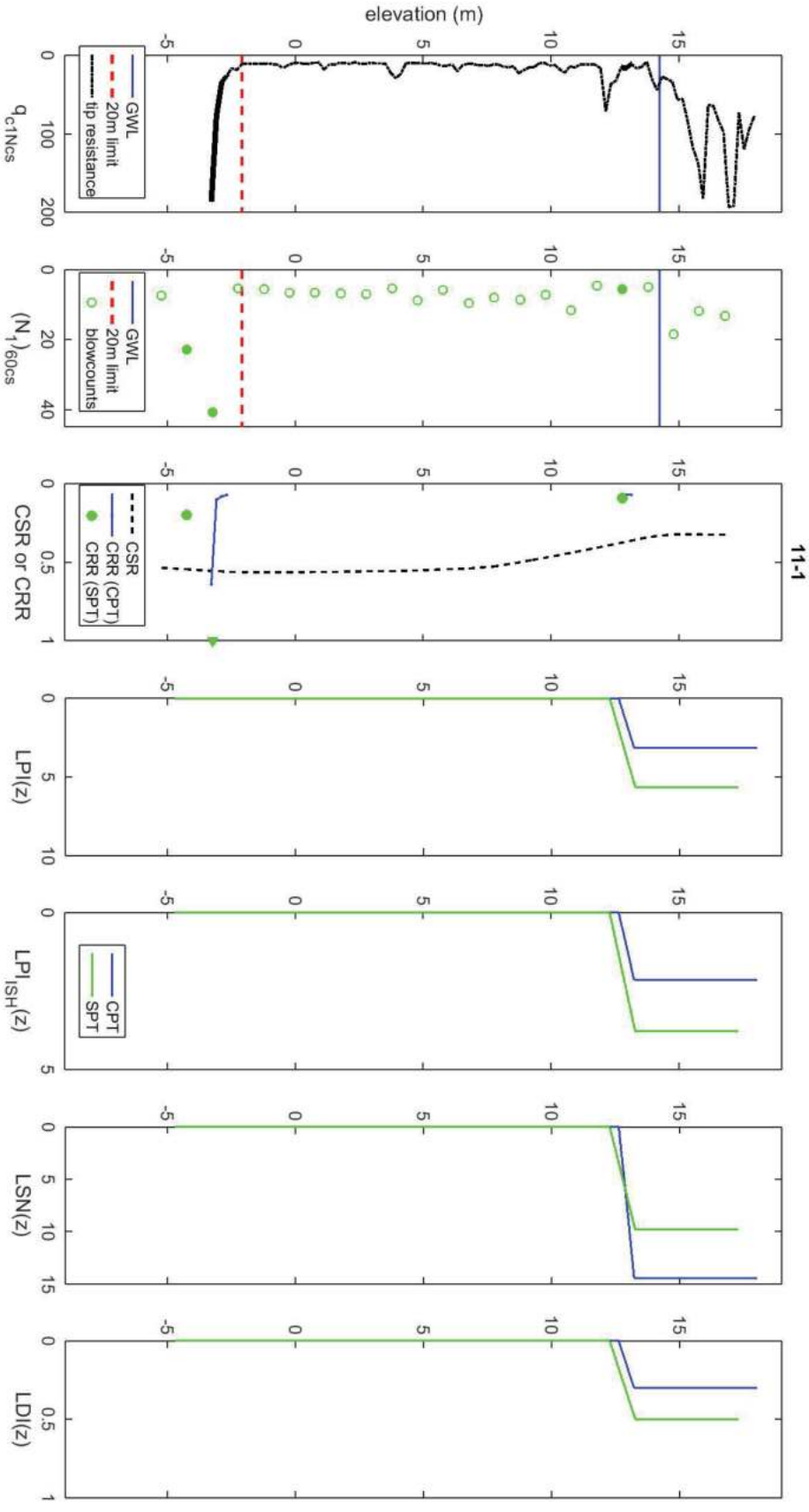
elevation (m)
q_{c1Ncs}
GWL
20m limit
tip resistance
$(N_1)_{60cs}$
blowcounts
CSR or CRR
CSR
CRR (CPT)
CRR (SPT)
11-1
LPI(z)
$LPI_{ISH}(z)$
CPT
SPT
LSN(z)
LDI(z)

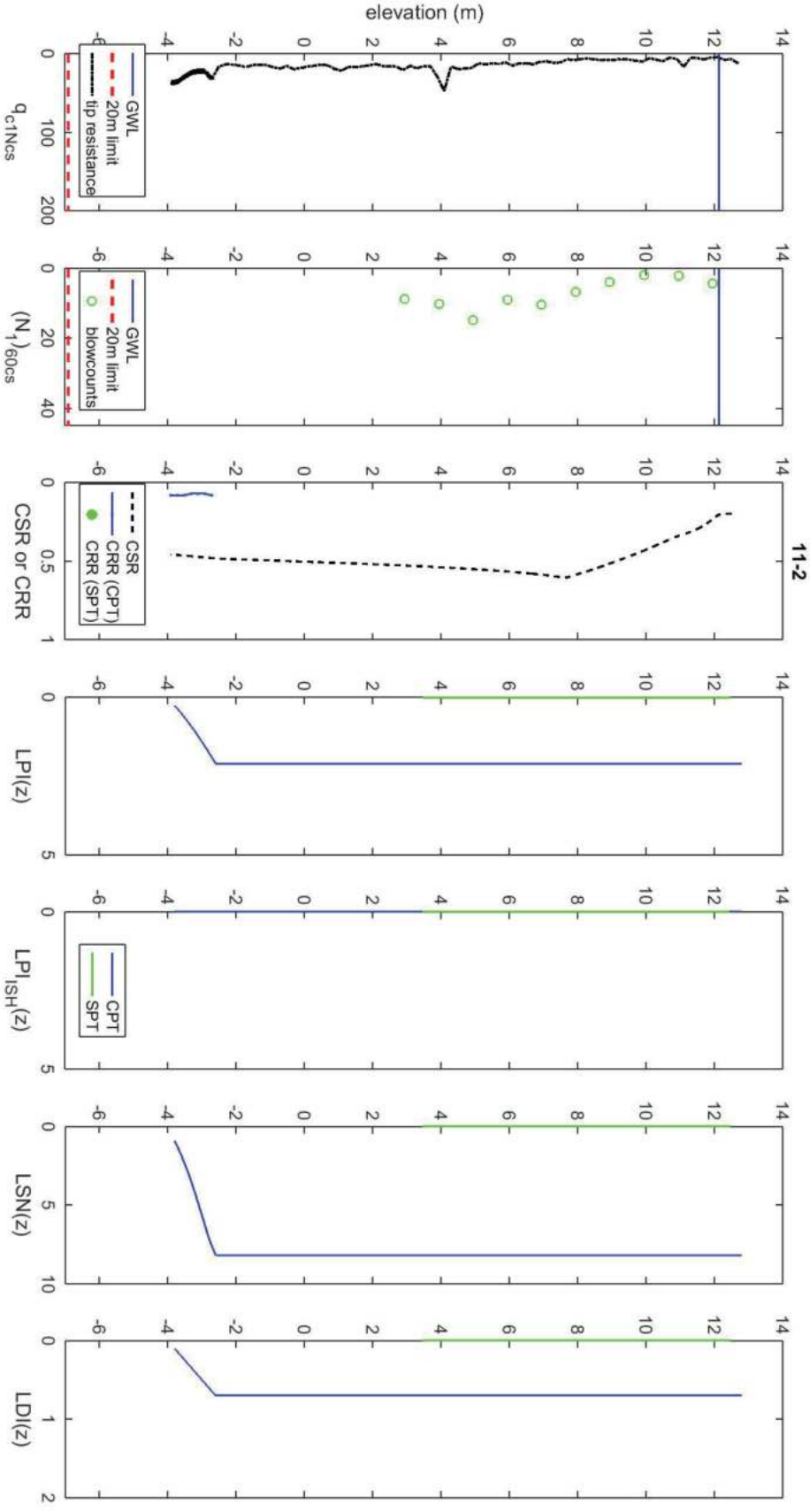
elevation (m)
GWL
20m limit
tip resistance
q_{c1Ncs}
blowcounts
$(N_1)_{60cs}$
CSR
CRR (CPT)
CRR (SPT)
CSR or CRR
11-2
LPI(z)
CPT
SPT
$LPI_{ISH}(z)$
LSN(z)
LDI(z)

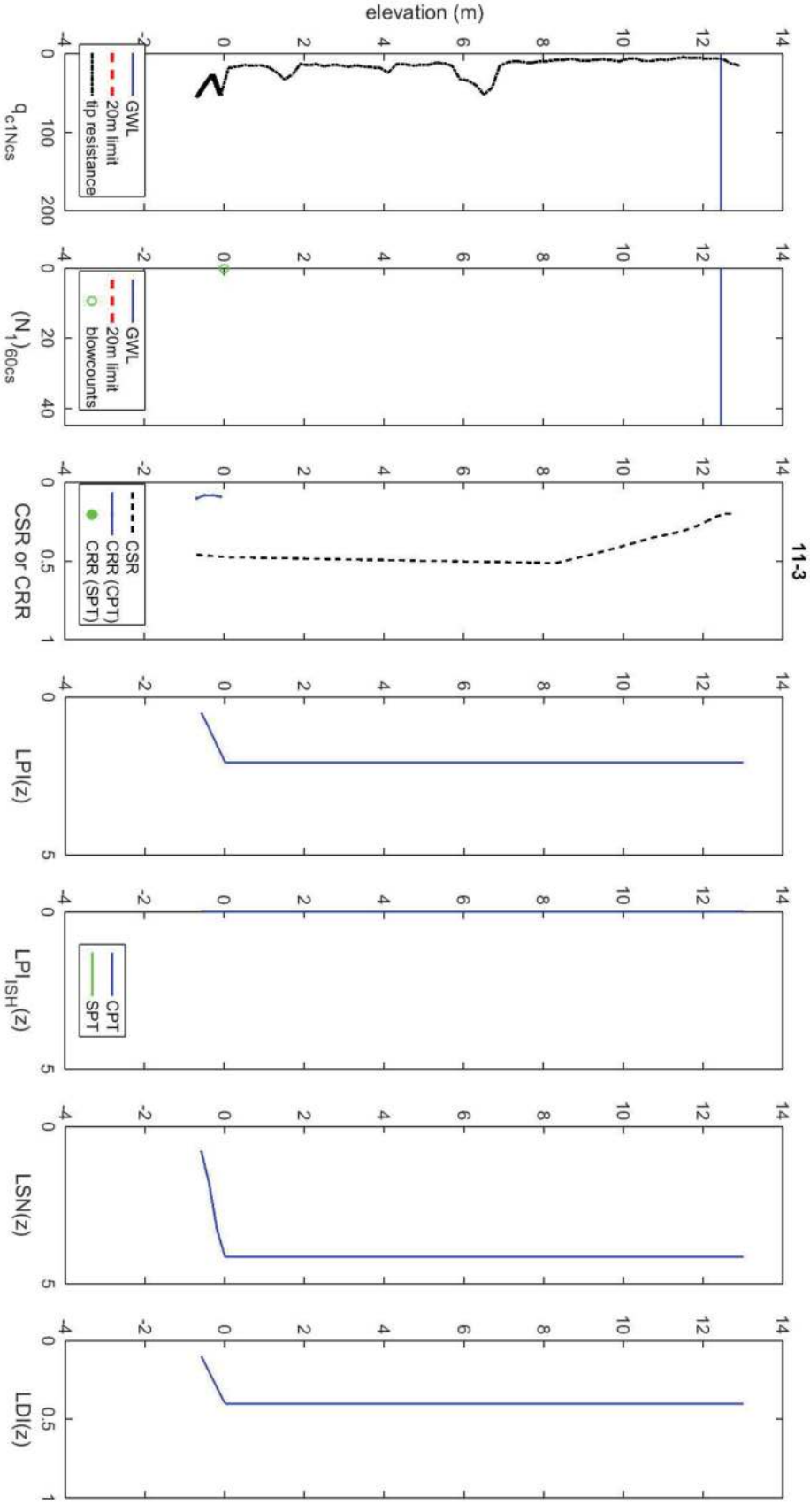
elevation (m)
q_{c1Ncs}
GWL
20m limit
tip resistance
$(N_1)_{60cs}$
blowcounts
CSR or CRR
CSR
CRR (CPT)
CRR (SPT)
11-3
LPI(z)
$LPI_{ISH}(z)$
CPT
SPT
LSN(z)
LDI(z)

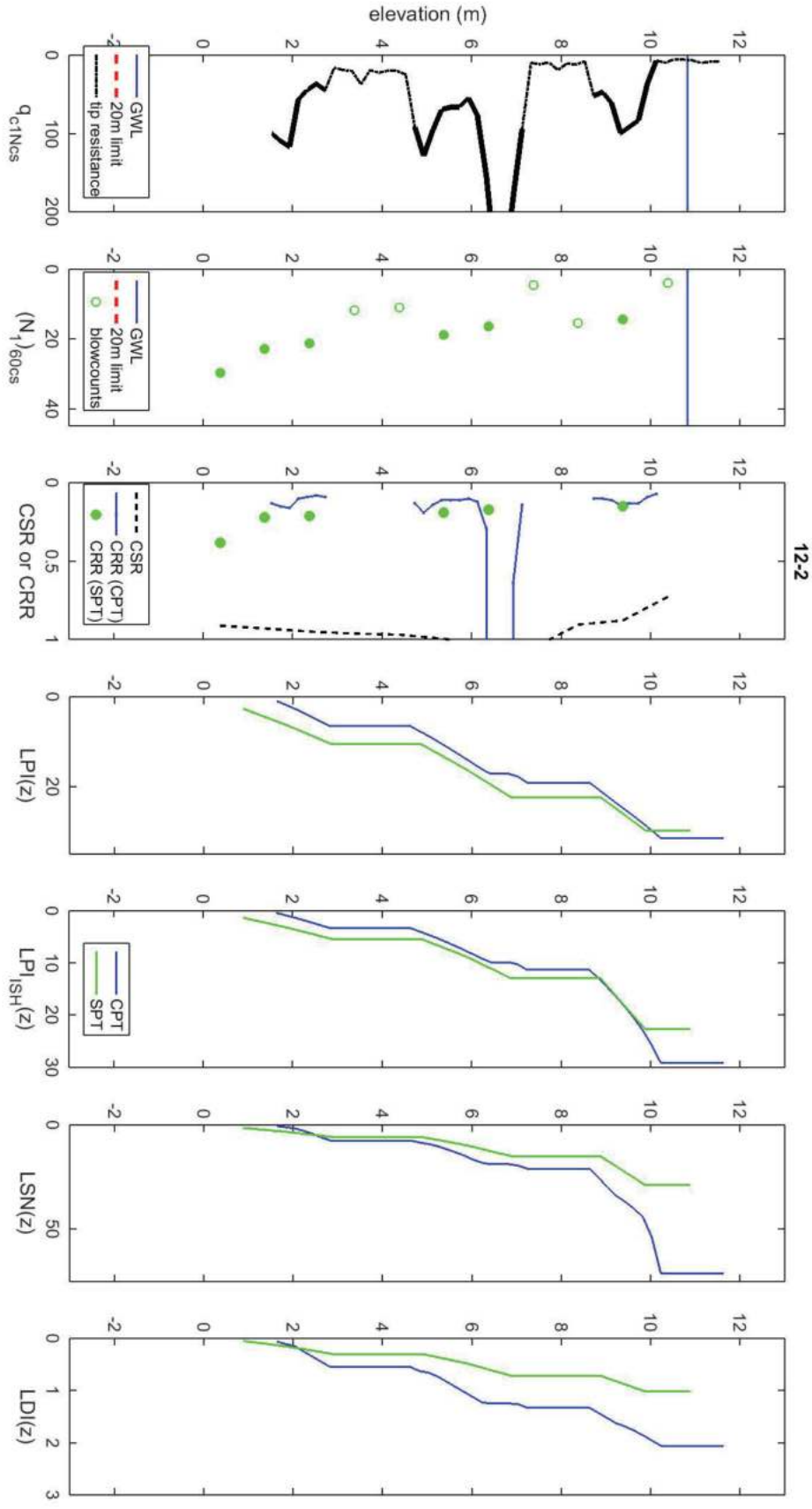
elevation (m)
GWL
20m limit
tip resistance
q_{c1Ncs}
GWL
20m limit
blowcounts
$(N_1)_{60cs}$
CSR
CRR (CPT)
CRR (SPT)
CSR or CRR
12-2
LPI(z)
CPT
SPT
$LPI_{ISH}(z)$
LSN(z)
LDI(z)

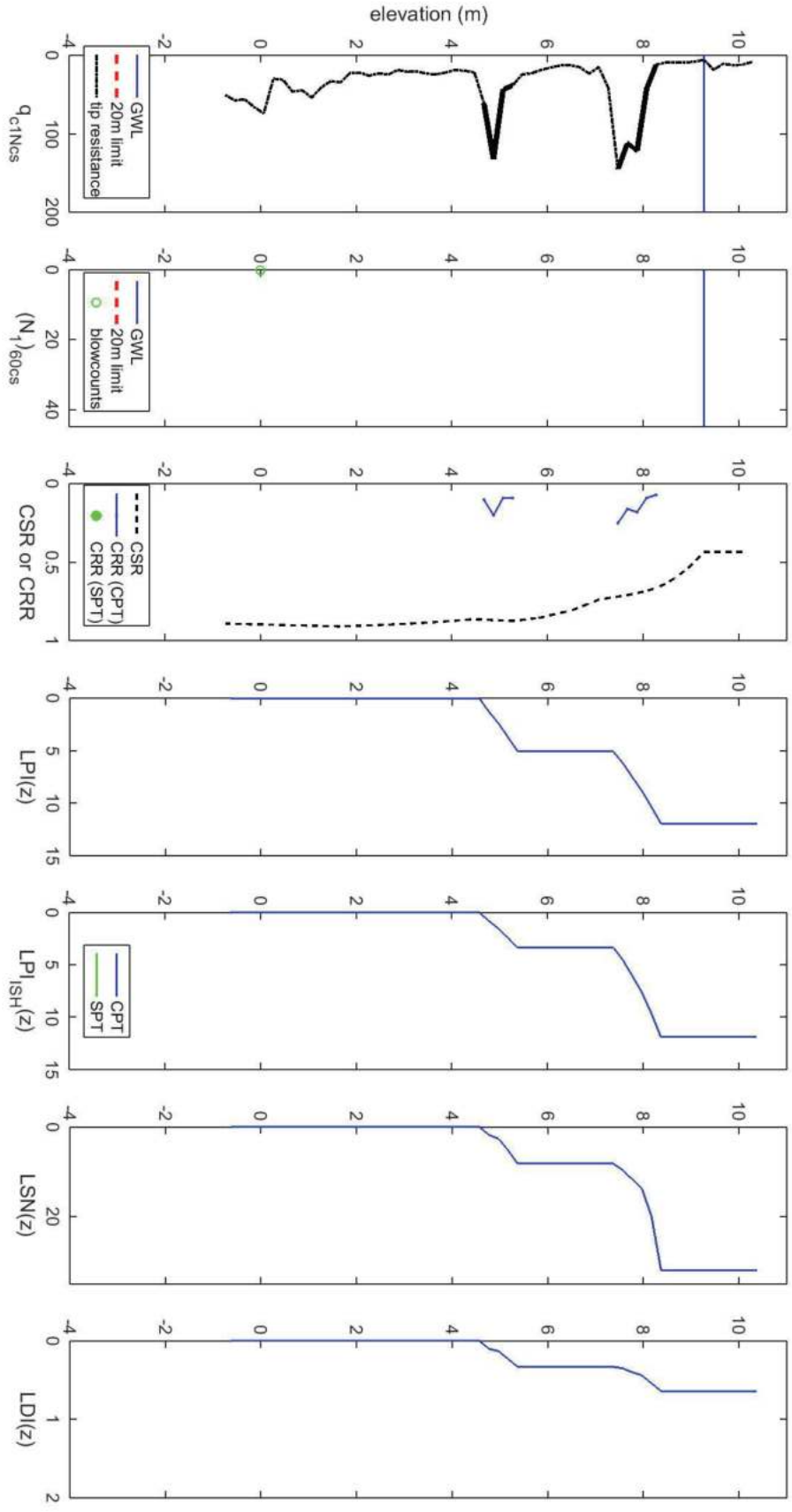
elevation (m)
12-3
q_{c1Ncs}
GWL
20m limit
tip resistance
$(N_1)_{60cs}$
blowcounts
CSR or CRR
CSR
CRR (CPT)
CRR (SPT)
LPI(z)
$LPI_{ISH}(z)$
CPT
SPT
LSN(z)
LDI(z)

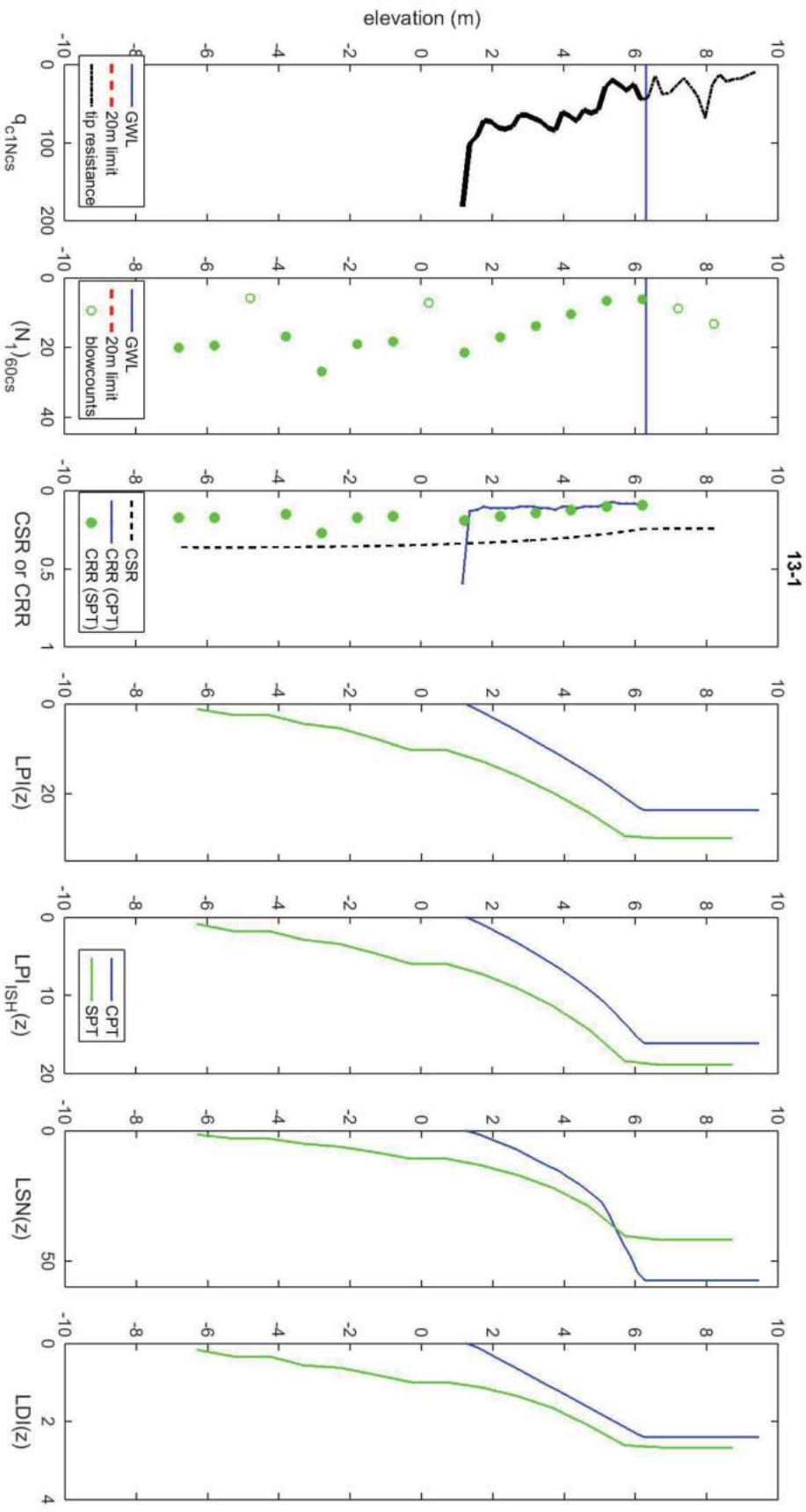
elevation (m)
13-1
q_{c1Ncs}
GWL
20m limit
tip resistance
$(N_1)_{60cs}$
blowcounts
CSR or CRR
CSR
CRR (CPT)
CRR (SPT)
LPI(z)
$LPI_{ISH}(z)$
CPT
SPT
LSN(z)
LDI(z)

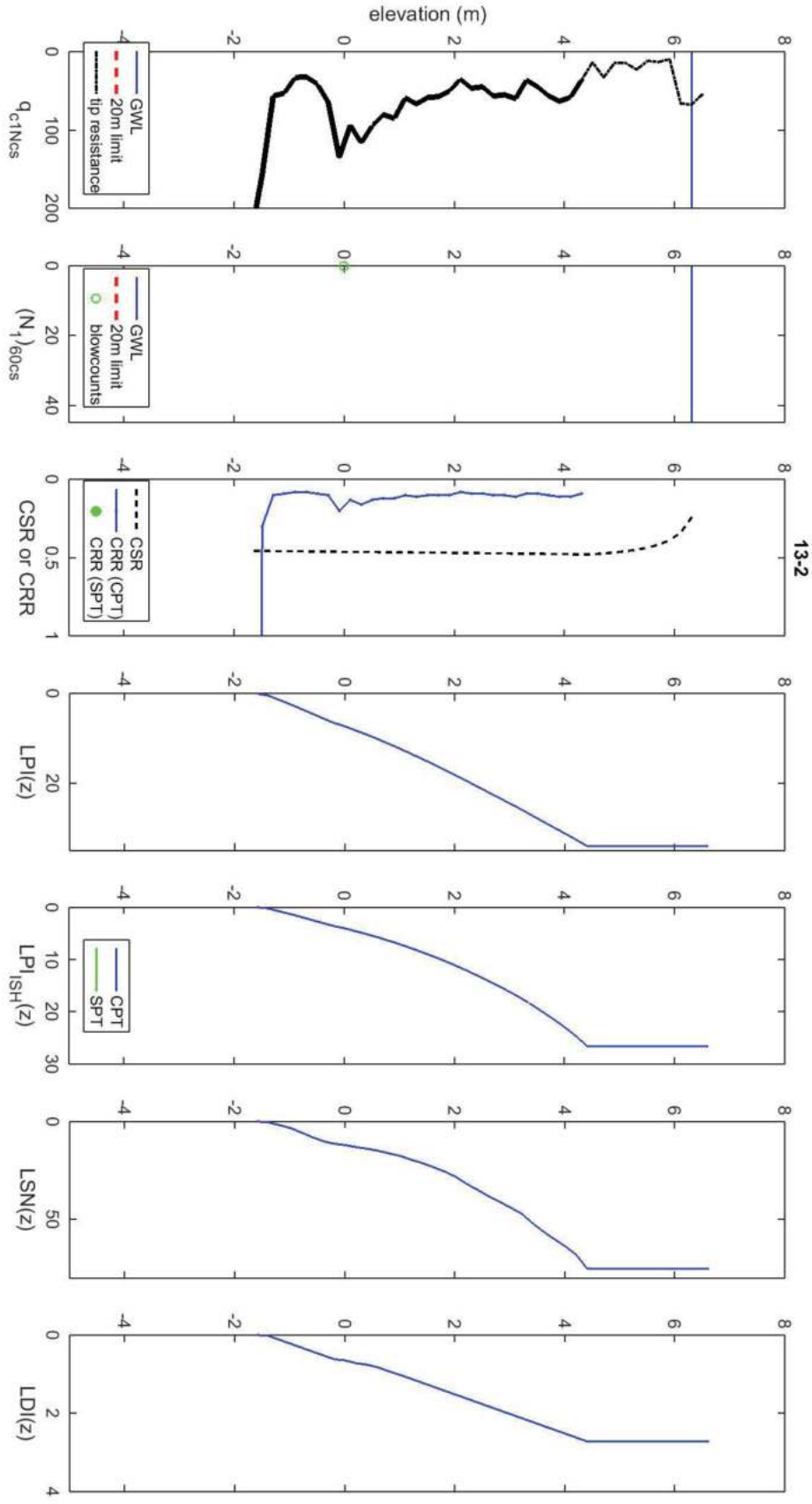
elevation (m)
13-2
q_{c1Ncs}
GWL
20m limit
tip resistance
$(N_1)_{60cs}$
blowcounts
CSR or CRR
CSR
CRR (CPT)
CRR (SPT)
LPI(z)
$LPI_{ISH}(z)$
CPT
SPT
LSN(z)
LDI(z)

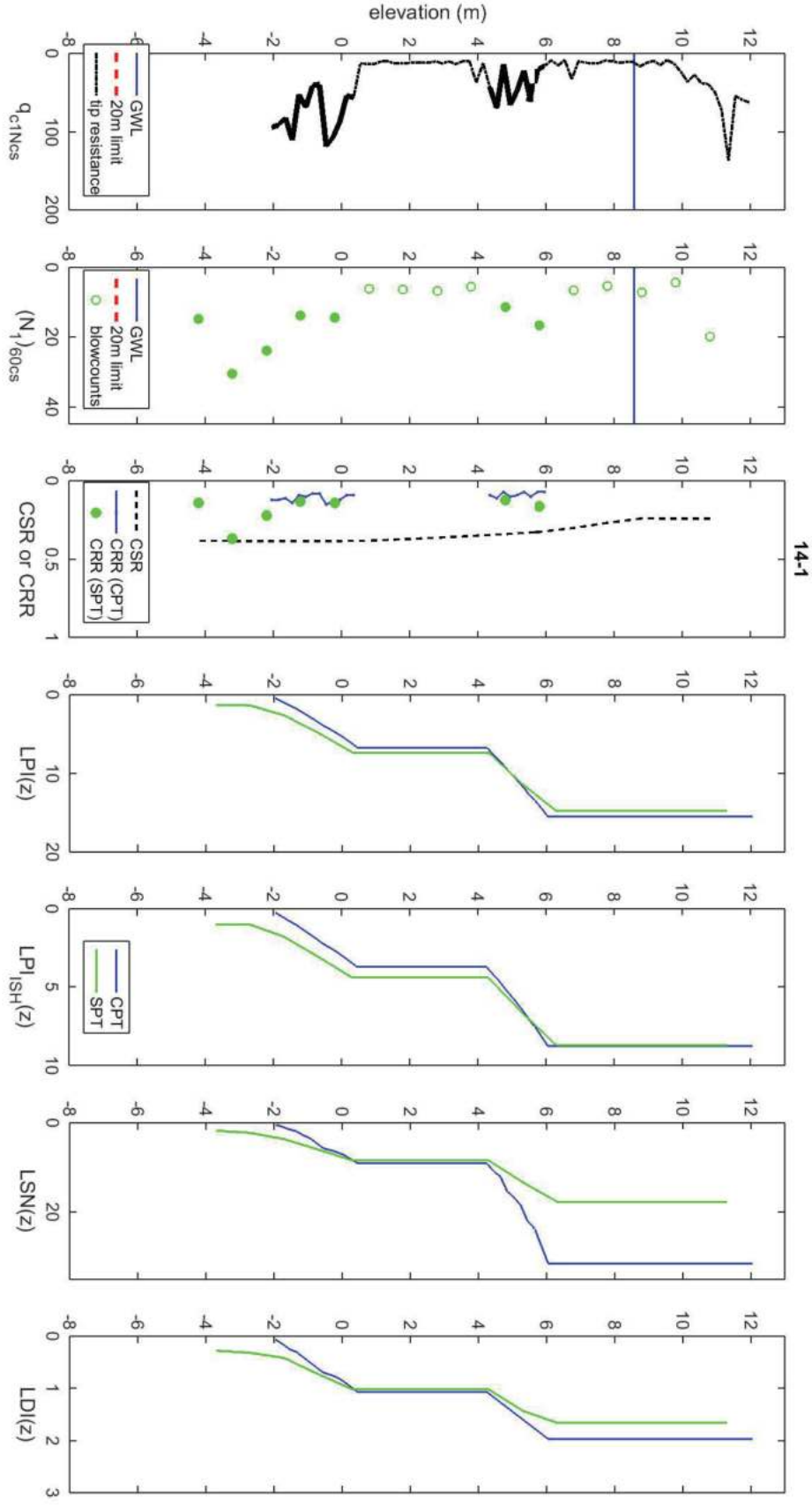
elevation (m)
q_{c1Ncs}
GWL
20m limit
tip resistance
$(N_1)_{60cs}$
blowcounts
CSR or CRR
CSR
CRR (CPT)
CRR (SPT)
14-1
LPI(z)
$LPI_{ISH}(z)$
CPT
SPT
LSN(z)
LDI(z)

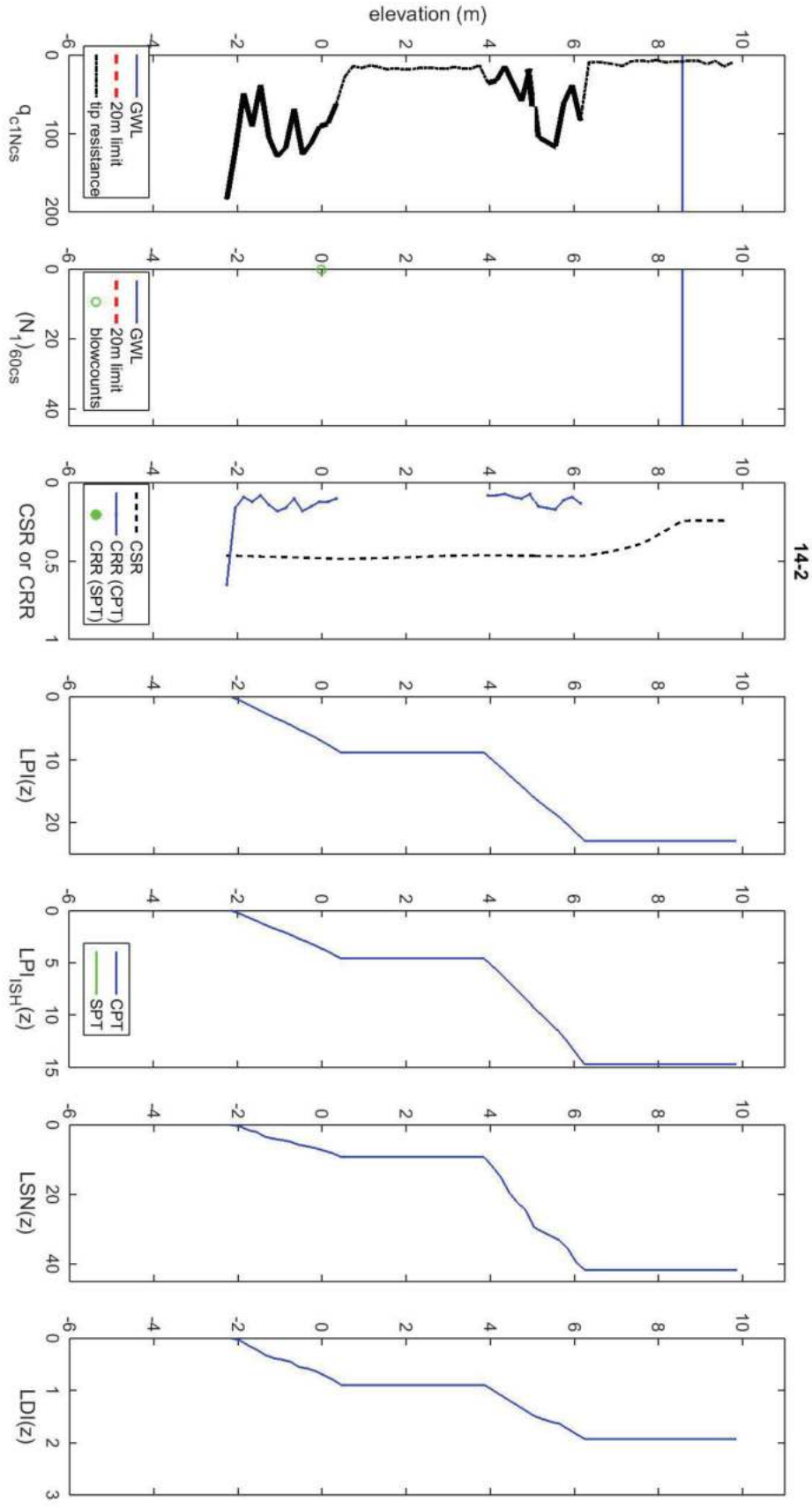
elevation (m)
14-2
q_{c1Ncs}
GWL
20m limit
tip resistance
$(N_1)_{60cs}$
blowcounts
CSR or CRR
CSR
CRR (CPT)
CRR (SPT)
LPI(z)
$LPI_{ISH}(z)$
CPT
SPT
LSN(z)
LDI(z)

Section 2 – Pre-earthquake

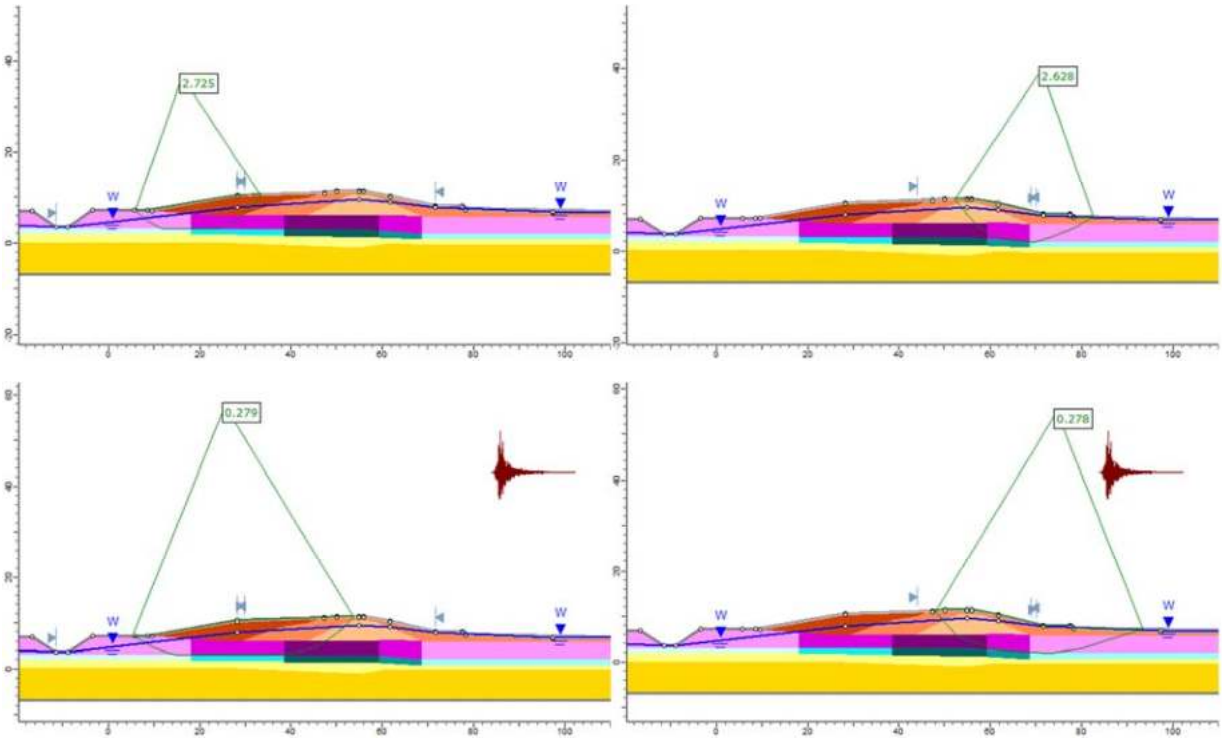

Material Name	Color	Unit Weight (kN/m3)	Sat. Unit Weight (kN/m3)	Strength Type	Cohesion (kPa)	Phi (deg)	Cohesion Type	Water Surface	Hu Type	Hu
Fill 1		19	20	Mohr-Coulomb	1	44		Water Surface	Custom	1
Fill 2		19	20	Mohr-Coulomb	1	44		Water Surface	Custom	1
Fill 3		19	20	Mohr-Coulomb	1	38		Water Surface	Custom	1
Peat 1		10	11	Undrained	42.1		Constant	Water Surface	Custom	1
Peat 2		10	11	Undrained	31.4		Constant	Water Surface	Custom	1
Peat 3		10	11	Undrained	23.6		Constant	Water Surface	Custom	1
Clay 1		14	16	Undrained	59		Constant	Water Surface	Custom	1
Clay 2A		14	16	Undrained	55.6		Constant	Water Surface	Custom	1
Clay 2B		14	16	Undrained	49.3		Constant	Water Surface	Custom	1
Clay 3A		14	16	Undrained	58.2		Constant	Water Surface	Custom	1
Clay 3B		14	16	Undrained	42		Constant	Water Surface	Custom	1
Sand 1		19	20	Mohr-Coulomb	1	41		Water Surface	Custom	1
Sand 2		19	20	Mohr-Coulomb	1	48		Water Surface	Custom	1

Section 2 – Post-earthquake

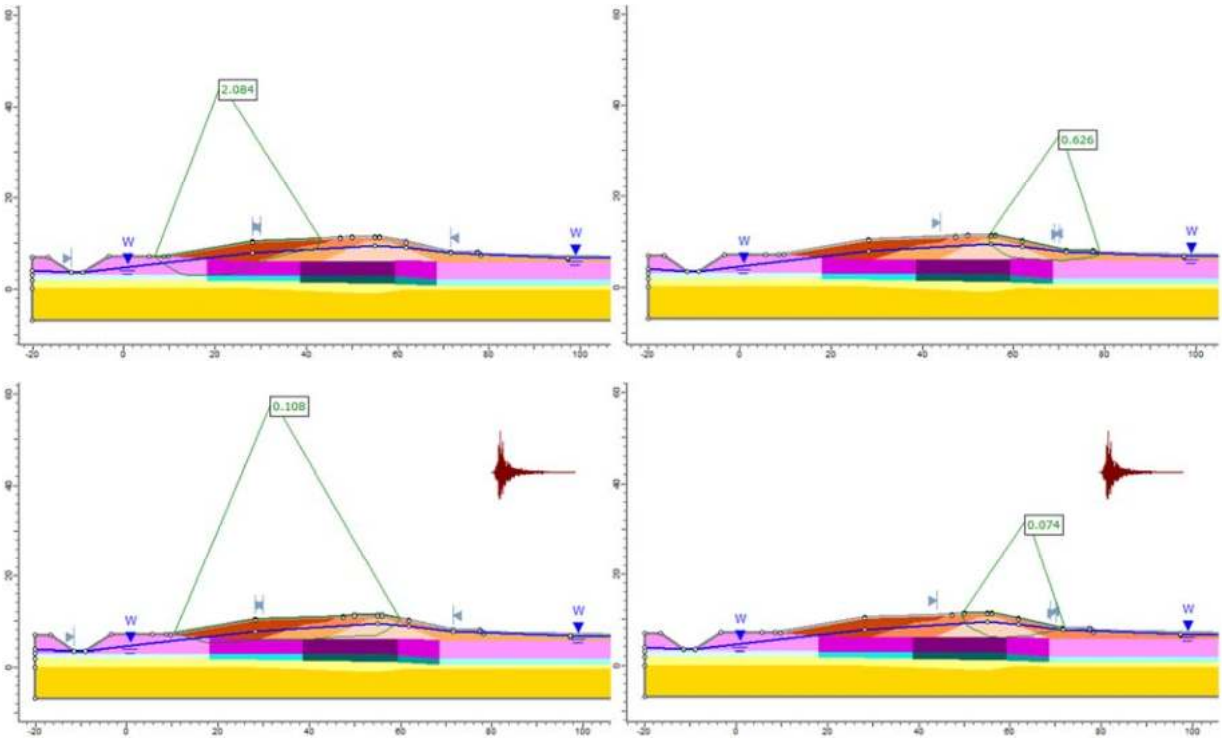

Material Name	Color	Unit Weight (kN/m3)	Sat. Unit Weight (kN/m3)	Strength Type	Cohesion (kPa)	Phi (deg)	Cohesion Type	Water Surface	Hu Type	Hu
Fill 1		19	20	Mohr-Coulomb	1	44		Water Surface	Custom	1
Fill 2		19	20	Mohr-Coulomb	1	44		Water Surface	Custom	1
Fill 3		19	20	Mohr-Coulomb	1	38		Water Surface	Custom	1
Peat 1 (soften)		10	11	Undrained	37.9		Constant	Water Surface	Custom	1
Peat 2 (soften)		10	11	Undrained	28.3		Constant	Water Surface	Custom	1
Peat 3		10	11	Undrained	23.6		Constant	Water Surface	Custom	1
Clay 1		14	16	Undrained	59		Constant	Water Surface	Custom	1
Clay 2A		14	16	Undrained	55.6		Constant	Water Surface	Custom	1
Clay 2B		14	16	Undrained	49.3		Constant	Water Surface	Custom	1
Clay 3A		14	16	Undrained	58.2		Constant	Water Surface	Custom	1
Clay 3B		14	16	Undrained	42		Constant	Water Surface	Custom	1
Sand 1		19	20	Mohr-Coulomb	1	41		Water Surface	Custom	1
Sand 2		19	20	Mohr-Coulomb	1	48		Water Surface	Custom	1
S29-37 (liq)		19	20	Undrained	5.4		Constant	Water Surface	Custom	1

Section 5 – Pre-earthquake

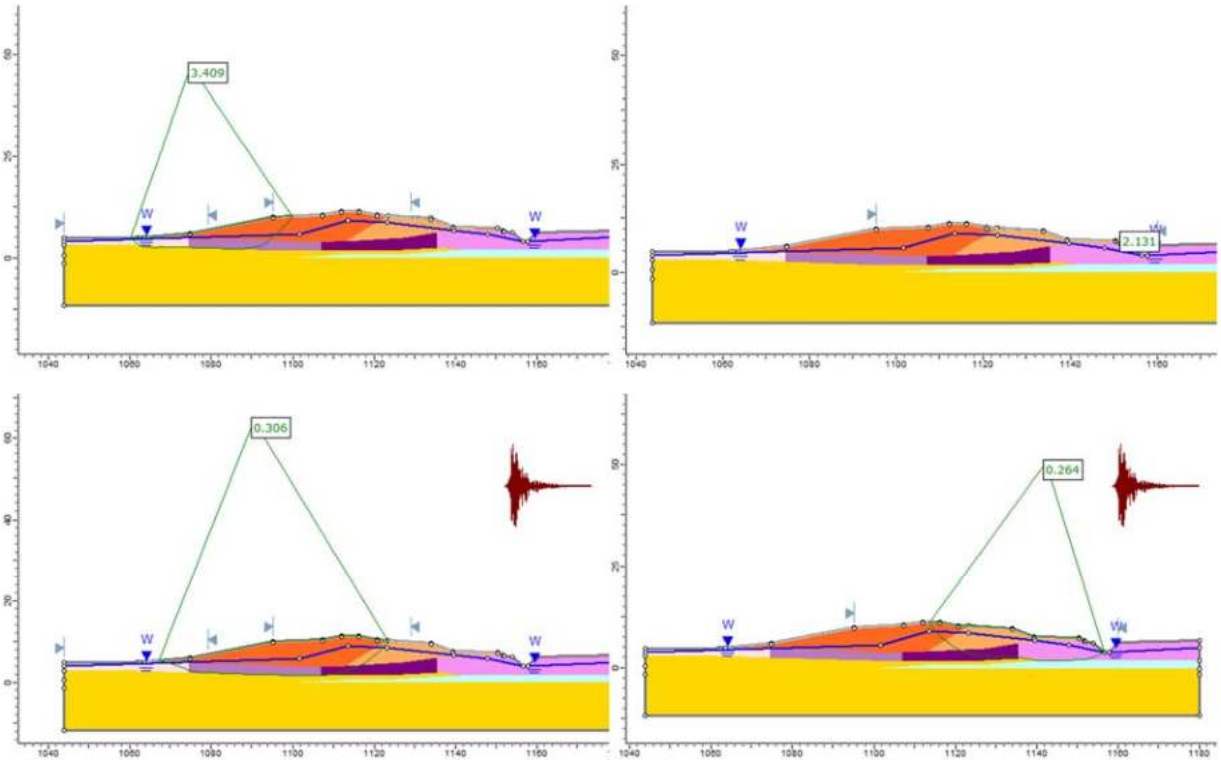

Material Name	Color	Unit Weight (kN/m3)	Sat. Unit Weight (kN/m3)	Strength Type	Cohesion (kPa)	Phi (deg)	Cohesion Type	Water Surface	Hu Type	Hu
Fill 1		19	20	Mohr-Coulomb	1	42		Water Surface	Custom	1
Fill 2		19	20	Mohr-Coulomb	1	37		Water Surface	Custom	1
Peat 1		10	11	Undrained	43.9		Constant	Water Surface	Custom	1
Peat 2		10	11	Undrained	41.3		Constant	Water Surface	Custom	1
Peat 3R		10	11	Undrained	25.3		Constant	Water Surface	Custom	1
Peat 3L		10	11	Undrained	31.3		Constant	Water Surface	Custom	1
Clay 3		14	16	Undrained	69		Constant	Water Surface	Custom	1
Sand 1		19	20	Mohr-Coulomb	1	41		Water Surface	Custom	1

Section 5 – Post-earthquake

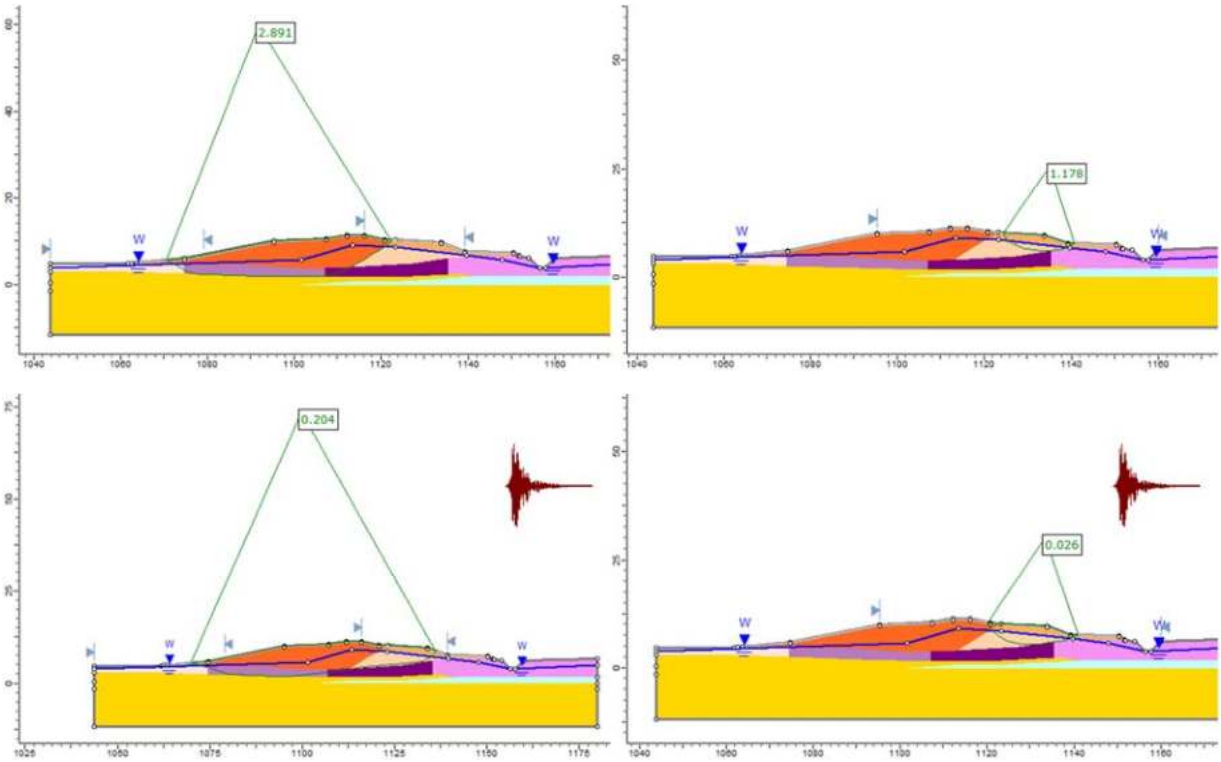

Material Name	Color	Unit Weight (kN/m3)	Sat. Unit Weight (kN/m3)	Strength Type	Cohesion (kPa)	Phi (deg)	Cohesion Type	Water Surface	Hu Type	Hu
Fill 1		19	20	Mohr-Coulomb	1	42		Water Surface	Custom	1
Fill 2		19	20	Mohr-Coulomb	1	37		Water Surface	Custom	1
Peat 1 (soften)		10	11	Undrained	39.5		Constant	Water Surface	Custom	1
Peat 2 (soften)		10	11	Undrained	37.2		Constant	Water Surface	Custom	1
Peat 3R(soften)		10	11	Undrained	22.8		Constant	Water Surface	Custom	1
Peat 3L(soften)		10	11	Undrained	31.3		Constant	Water Surface	Custom	1
Clay 3		14	16	Undrained	69		Constant	Water Surface	Custom	1
Sand 1		19	20	Mohr-Coulomb	1	41		Water Surface	Custom	1
Fill 2 (liquefied)		19	20	Undrained	6.1		Constant	Water Surface	Custom	1

Section 7 – Pre-earthquake

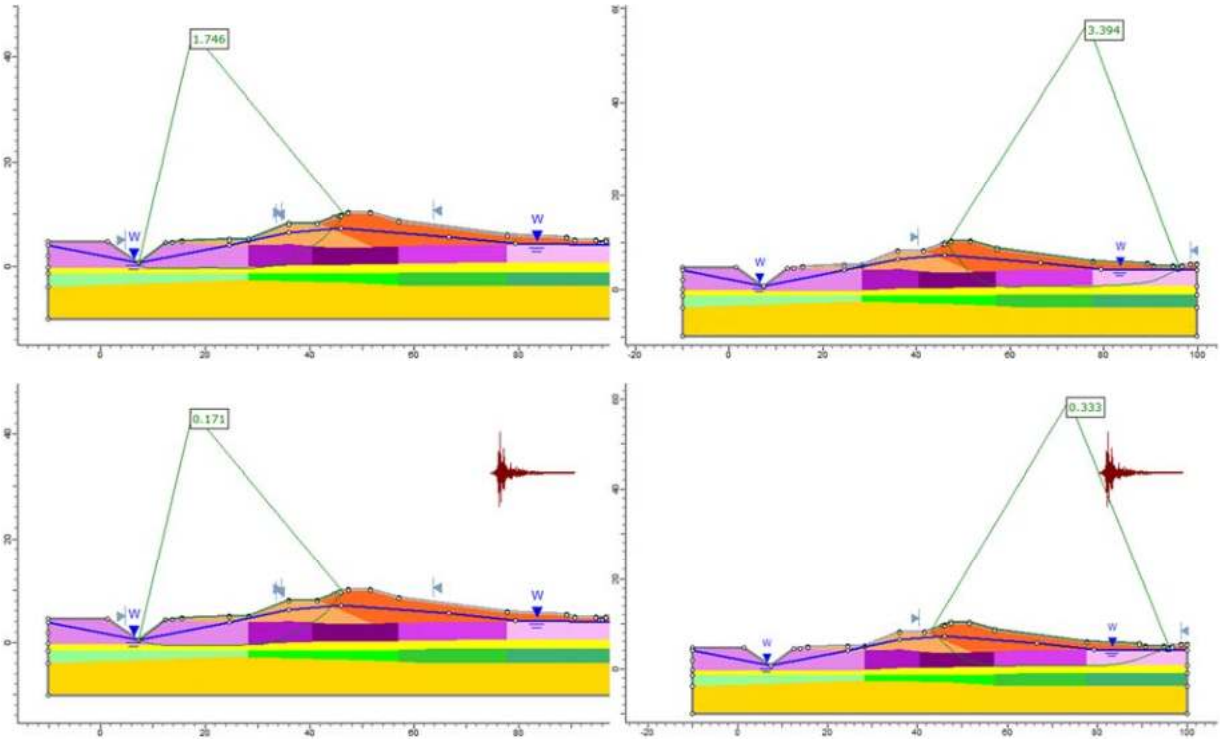

Material Name	Color	Unit Weight (kN/m3)	Sat. Unit Weight (kN/m3)	Strength Type	Cohesion (kPa)	Phi (deg)	Water Surface	Hu Type	Hu
Fill1		19	20	Mohr-Coulomb	1	42	Water Surface	Custom	1
Fill 2		19	20	Mohr-Coulomb	1	38	Water Surface	Custom	1
Peat 1		10	11	Mohr-Coulomb	51.7	0	Water Surface	Custom	1
Peat 2L		10	11	Mohr-Coulomb	31.3	0	Water Surface	Custom	1
Peat 2R		10	11	Mohr-Coulomb	38.9	0	Water Surface	Custom	1
Peat 3L		10	11	Mohr-Coulomb	21.3	0	Water Surface	Custom	1
Peat 3R		10	11	Mohr-Coulomb	26	0	Water Surface	Custom	1
Ac 1		16	18	Mohr-Coulomb	83.1	0	Water Surface	Custom	1
Ac 2R		16	18	Mohr-Coulomb	93.9	0	Water Surface	Custom	1
Ac 3R		16	18	Mohr-Coulomb	104.9	0	Water Surface	Custom	1
Ac 3L		16	18	Mohr-Coulomb	60.5	0	Water Surface	Custom	1
As1		19	20	Mohr-Coulomb	1	38	Water Surface	Custom	1
As2		19	20	Mohr-Coulomb	1	43	Water Surface	Custom	1

Section 7 – Post-earthquake

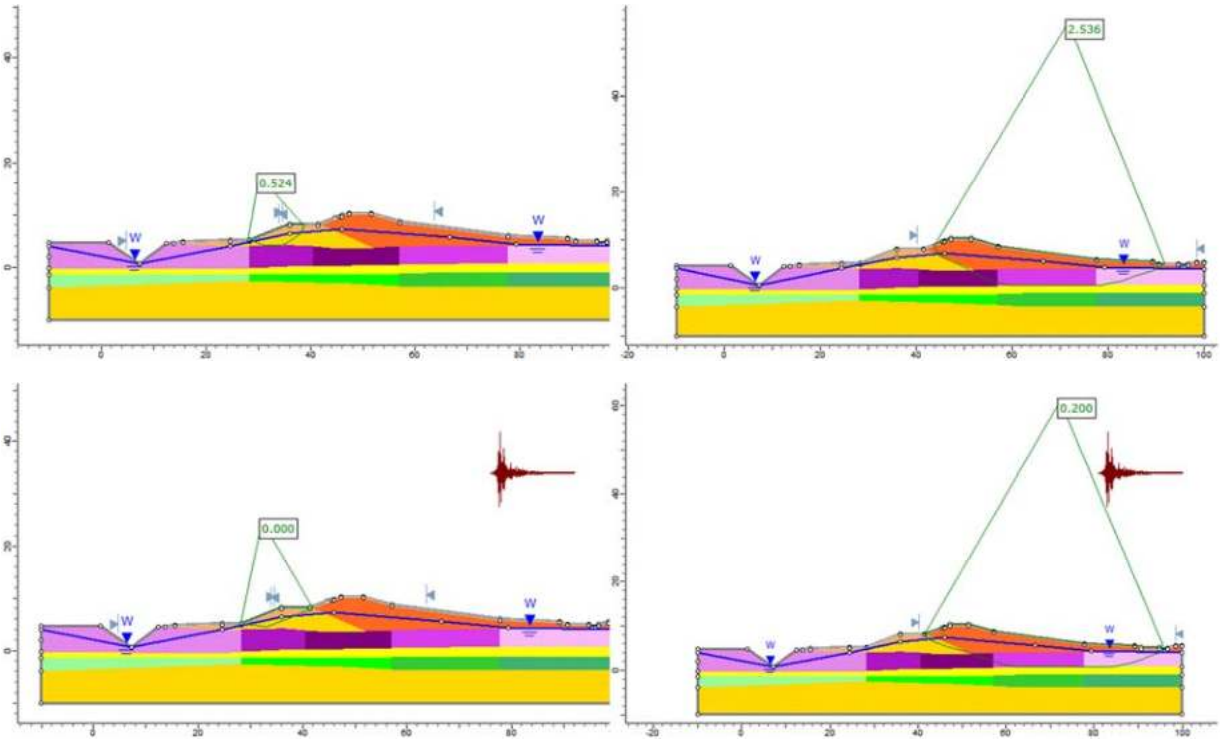

Material Name	Color	Unit Weight (kN/m3)	Sat. Unit Weight (kN/m3)	Strength Type	Cohesion (kPa)	Phi (deg)	Cohesion Type	Water Surface	Hu Type	Hu
Fill1		19	20	Mohr-Coulomb	1	42		Water Surface	Custom	1
Fill 2		19	20	Mohr-Coulomb	1	38		Water Surface	Custom	1
Peat 1 (soften)		10	11	Undrained	41.4		Constant	Water Surface	Custom	1
Peat 2L (soften)		10	11	Undrained	25		Constant	Water Surface	Custom	1
Peat 2R (soften)		10	11	Undrained	31.1		Constant	Water Surface	Custom	1
Peat 3L (soften)		10	11	Undrained	17		Constant	Water Surface	Custom	1
Peat 3R (soften)		10	11	Undrained	20.8		Constant	Water Surface	Custom	1
Ac 1 (soften)		16	18	Undrained	74.7		Constant	Water Surface	Custom	1
Ac 2R (soften)		16	18	Undrained	84.5		Constant	Water Surface	Custom	1
Ac 3R		16	18	Undrained	104.9		Constant	Water Surface	Custom	1
Ac 3L		16	18	Undrained	54.5		Constant	Water Surface	Custom	1
As1		19	20	Mohr-Coulomb	1	38		Water Surface	Custom	1
As2		19	20	Mohr-Coulomb	1	43		Water Surface	Custom	1
Fill 2 (liq)		19	20	Mohr-Coulomb	4.1	0		Water Surface	Custom	1

Section 8 – Pre-earthquake

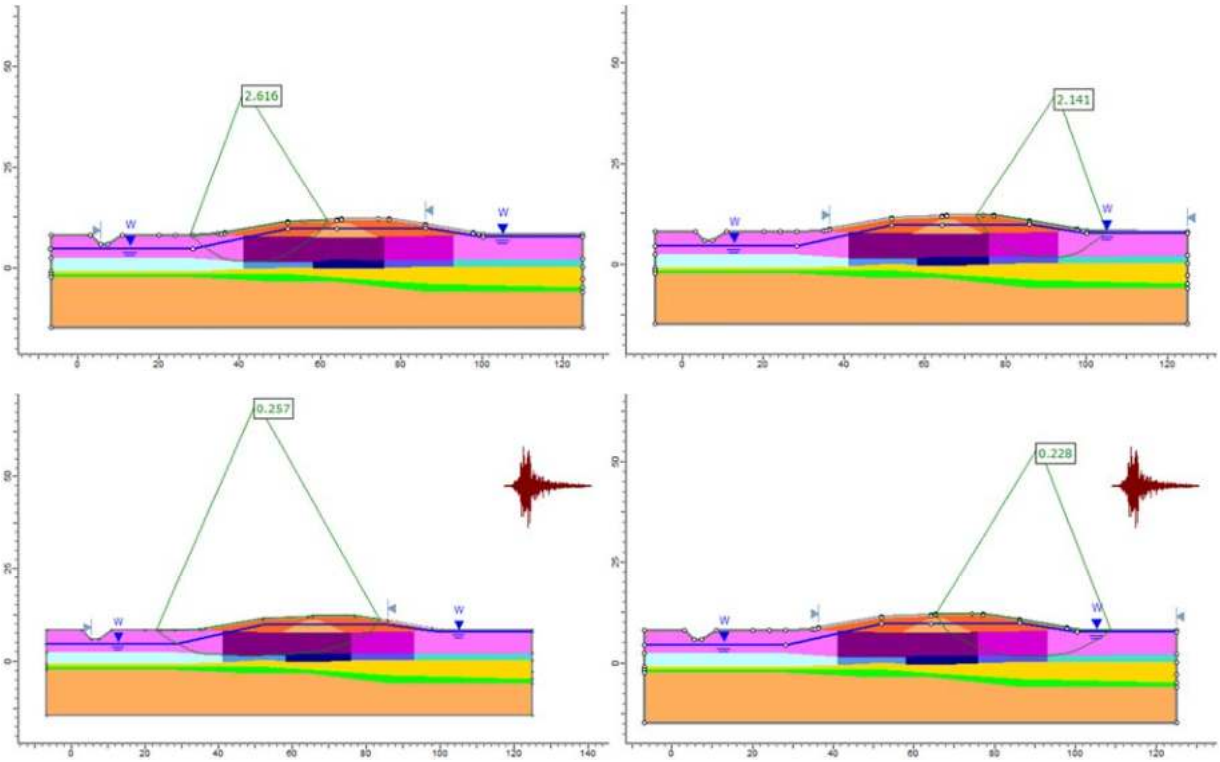

Material Name	Color	Unit Weight (kN/m3)	Sat. Unit Weight (kN/m3)	Strength Type	Cohesion (kPa)	Phi (deg)	Cohesion Type	Water Surface	Hu Type	Hu
Fill 1		19	20	Mohr-Coulomb	1	40		Water Surface	Custom	1
Fill 2		19	20	Mohr-Coulomb	1	37		Water Surface	Custom	1
Peat 1		10	11	Undrained	37		Constant	Water Surface	Custom	1
Peat 2		10	11	Undrained	28.2		Constant	Water Surface	Custom	1
Peat 3		10	11	Undrained	22.9		Constant	Water Surface	Custom	1
Sand 1		19	20	Mohr-Coulomb	1	38		Water Surface	Custom	1
Sandy Silt		16	18	Mohr-Coulomb	1	35		Water Surface	Custom	1
Clay 1		16	18	Undrained	86.1		Constant	Water Surface	Custom	1
Clay 2L		16	18	Undrained	80.8		Constant	Water Surface	Custom	1
Clay 2R		16	18	Undrained	72.3		Constant	Water Surface	Custom	1
Clay 3L		16	18	Undrained	73.7		Constant	Water Surface	Custom	1
Clay 3R		16	18	Undrained	59.7		Constant	Water Surface	Custom	1
Sand 2		19	20	Mohr-Coulomb	1	41		Water Surface	Custom	1

Section 8 – Post-earthquake

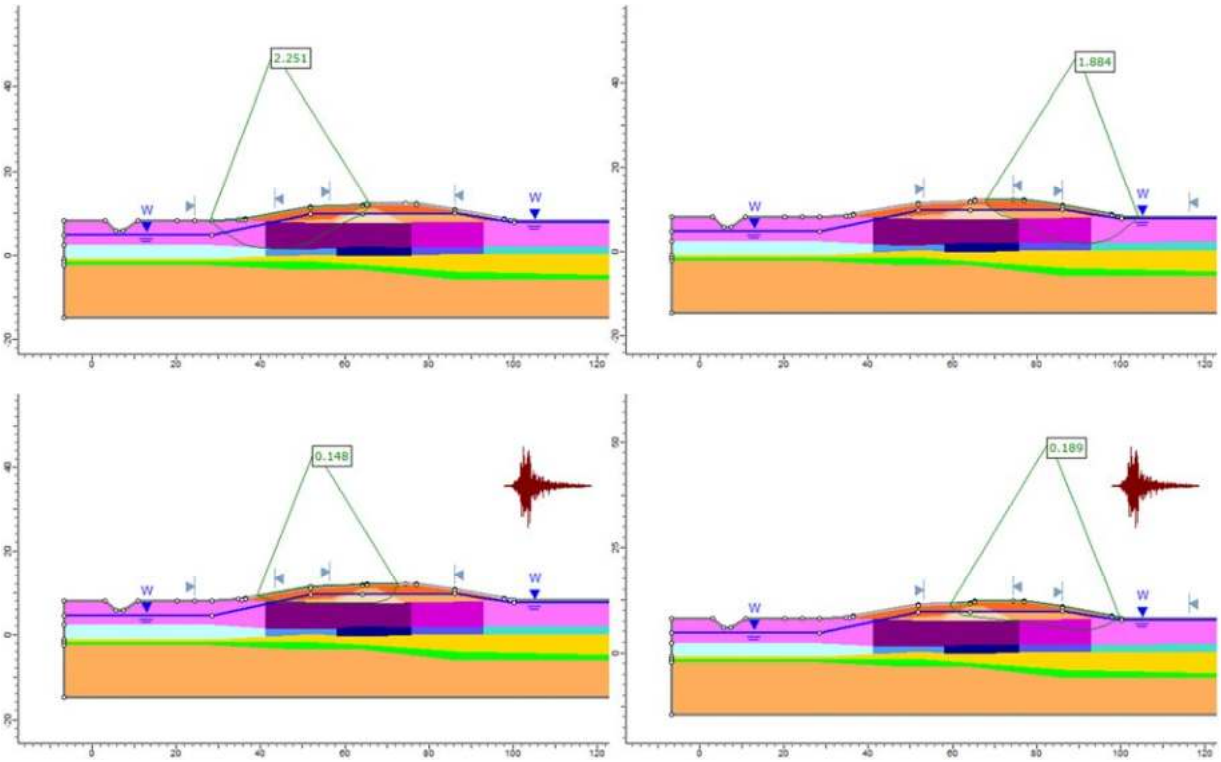

Material Name	Color	Unit Weight (kN/m3)	Sat. Unit Weight (kN/m3)	Strength Type	Cohesion (kPa)	Phi (deg)	Cohesion Type	Water Surface	Hu Type	Hu
Fill 1		19	20	Mohr-Coulomb	1	40		Water Surface	Custom	1
Fill 2		19	20	Mohr-Coulomb	1	37		Water Surface	Custom	1
Peat 1 (soften)		10	11	Undrained	33.3		Constant	Water Surface	Custom	1
Peat 2 (soften)		10	11	Undrained	25.4		Constant	Water Surface	Custom	1
Peat 3		10	11	Undrained	22.9		Constant	Water Surface	Custom	1
Sand 1		19	20	Mohr-Coulomb	1	38		Water Surface	Custom	1
Sandy Silt		16	18	Mohr-Coulomb	1	35		Water Surface	Custom	1
Fill S27 (liq)		19	20	Undrained	3.5		Constant	Water Surface	Custom	1
Fill S53 (liq)		19	20	Undrained	15.7		Constant	Water Surface	Custom	1
Clay 1		16	18	Undrained	86.1		Constant	Water Surface	Custom	1
Clay 2L		16	18	Undrained	80.8		Constant	Water Surface	Custom	1
Clay 2R		16	18	Undrained	72.3		Constant	Water Surface	Custom	1
Clay 3L		16	18	Undrained	73.7		Constant	Water Surface	Custom	1
Clay 3R		16	18	Undrained	59.7		Constant	Water Surface	Custom	1
Sand 2		19	20	Mohr-Coulomb	1	41		Water Surface	Custom	1

Section 9 – Pre-earthquake

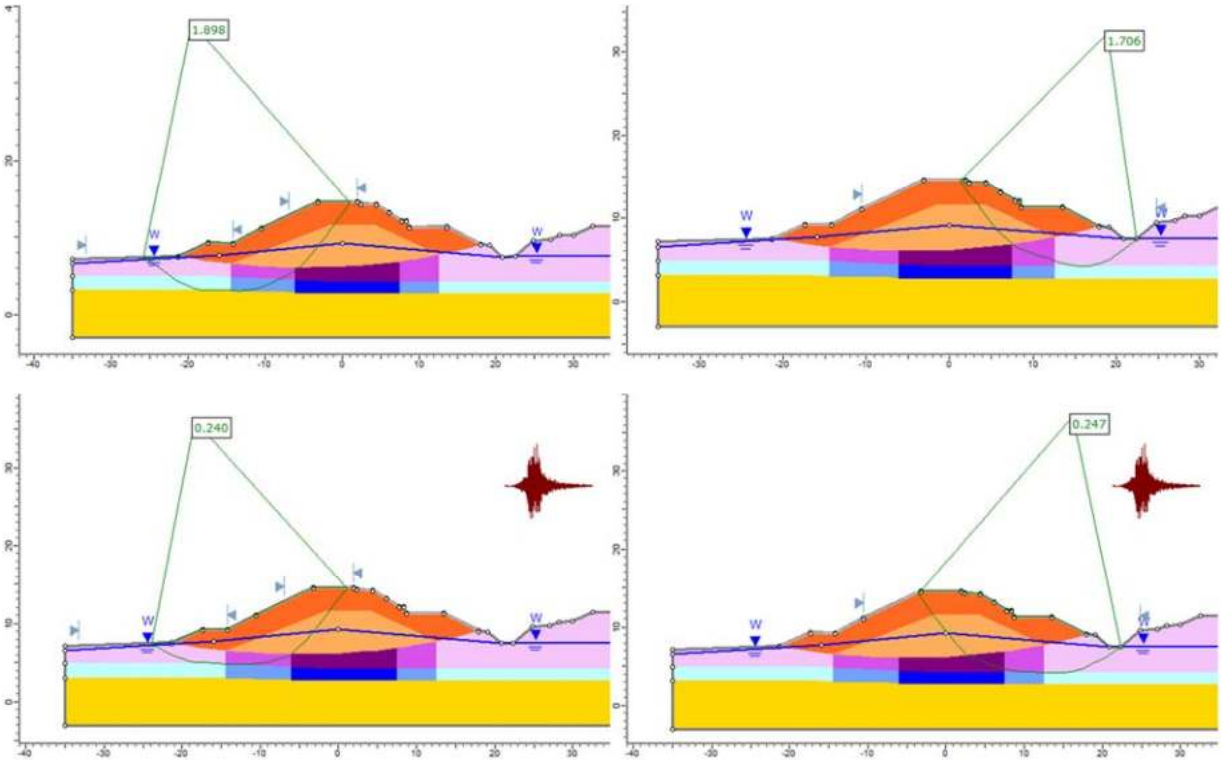

Material Name	Color	Unit Weight (kN/m3)	Sat. Unit Weight (kN/m3)	Strength Type	Cohesion (kPa)	Phi (deg)	Cohesion Type	Water Surface	Hu Type	Hu
Fill 1		19	20	Mohr-Coulomb	1	44		Water Surface	Custom	1
Fill 2		19	20	Mohr-Coulomb	1	40		Water Surface	Custom	1
Peat 1		10	11	Undrained	61.3		Constant	Water Surface	Custom	1
Peat 2		10	11	Undrained	41.8		Constant	Water Surface	Custom	1
Peat 3		10	11	Undrained	22.3		Constant	Water Surface	Custom	1
Clay 1		14	16	Undrained	70.8		Constant	Water Surface	Custom	1
Clay 2		14	16	Undrained	52.1		Constant	Water Surface	Custom	1
Clay 3		14	16	Undrained	33.3		Constant	Water Surface	Custom	1
Sand 1		20	21	Mohr-Coulomb	1	46		Water Surface	Custom	1

Section 9 – Post-earthquake

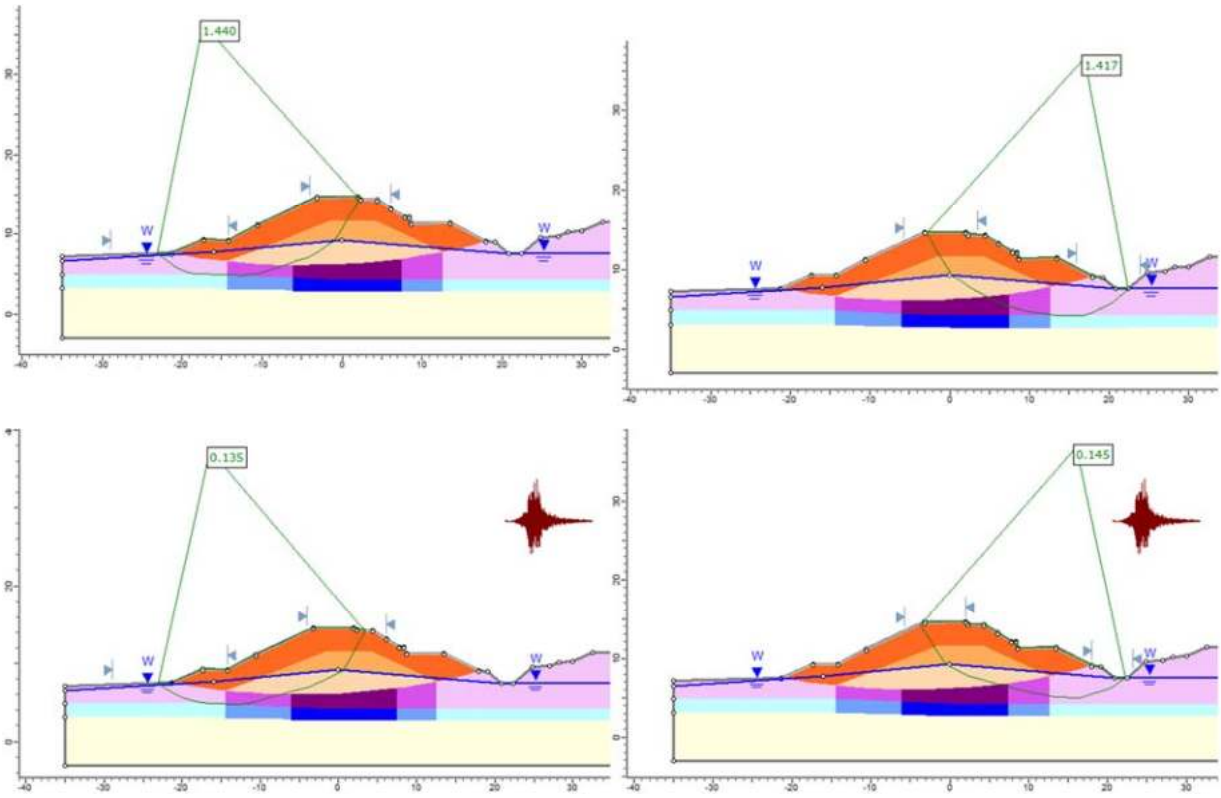

Material Name	Color	Unit Weight (kN/m3)	Sat. Unit Weight (kN/m3)	Strength Type	Cohesion (kPa)	Phi (deg)	Cohesion Type	Water Surface	Hu Type	Hu
Fill 1		19	20	Mohr-Coulomb	1	44		Water Surface	Custom	1
Fill 2		19	20	Mohr-Coulomb	1	40		Water Surface	Custom	1
Peat 1 (soften)		10	11	Undrained	49		Constant	Water Surface	Custom	1
Peat 2		10	11	Undrained	41.8		Constant	Water Surface	Custom	1
Peat 3		10	11	Undrained	22.3		Constant	Water Surface	Custom	1
Clay 1 (soften)		14	16	Undrained	56.6		Constant	Water Surface	Custom	1
Clay 2		14	16	Undrained	52.1		Constant	Water Surface	Custom	1
Clay 3		14	16	Undrained	33.3		Constant	Water Surface	Custom	1
Fill 2 (liq)		19	20	Undrained	24		Constant	Water Surface	Custom	1
Sand 2 (liq)		19	20	Undrained	104		Constant	Water Surface	Custom	1

Section 10 – Pre-earthquake

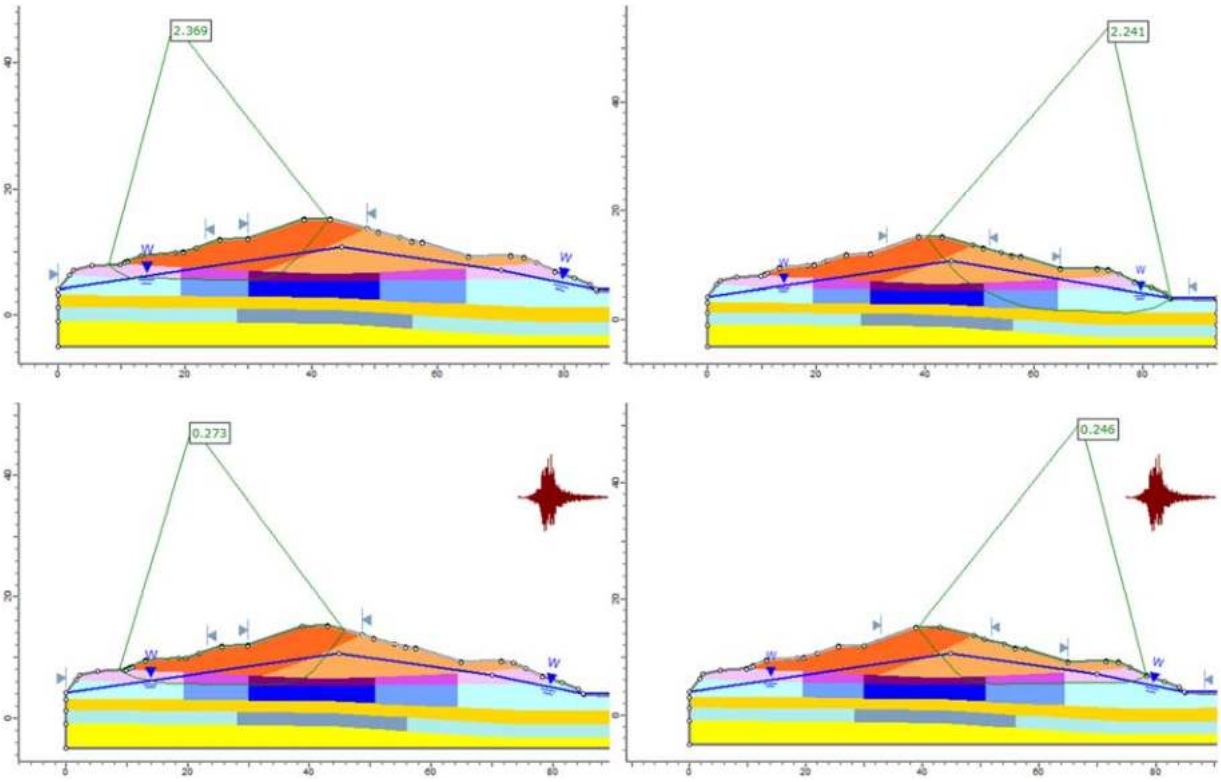

Material Name	Color	Unit Weight (kN/m3)	Sat. Unit Weight (kN/m3)	Strength Type	Cohesion (kPa)	Phi (deg)	Cohesion Type	Water Surface	Hu Type
Fill 1		19	20	Mohr-Coulomb	1	40		Water Surface	Custom
Fill 2		19	20	Mohr-Coulomb	1	40		Water Surface	Custom
Peat 1		10	11	Undrained	50.7		Constant	Water Surface	Custom
Peat 2		10	11	Undrained	35.8		Constant	Water Surface	Custom
Peat 3		10	11	Undrained	20.8		Constant	Water Surface	Custom
Clay 1A		14	16	Undrained	85.6		Constant	Water Surface	Custom
Clay 1B		14	16	Undrained	63.3		Constant	Water Surface	Custom
Clay 1C		14	16	Undrained	40.9		Constant	Water Surface	Custom
Sand 1		20	21	Mohr-Coulomb	1	46		Water Surface	Custom
Sand 2		19	20	Mohr-Coulomb	1	38		Water Surface	Custom
Clay 2A		14	16	Mohr-Coulomb	113.3	0		Water Surface	Custom
Clay 2B		14	16	Mohr-Coulomb	102.7	0		Water Surface	Custom

Section 10 – Post-earthquake

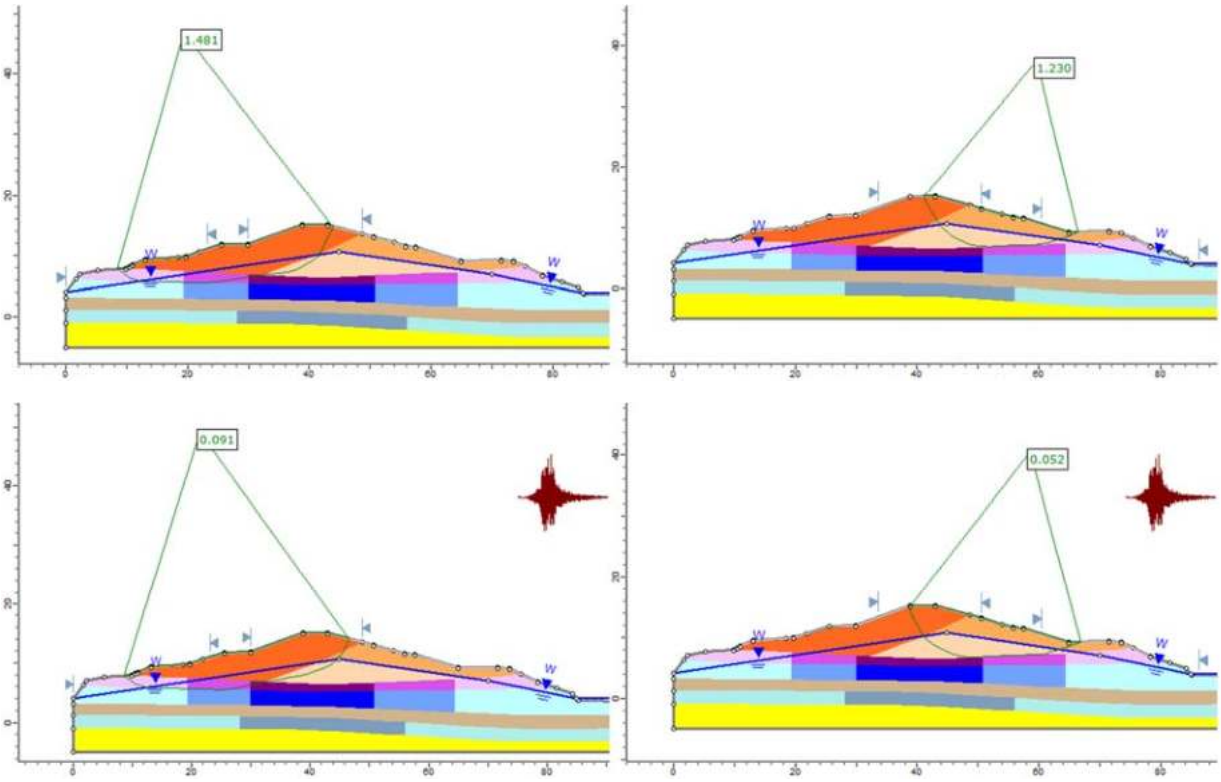

Material Name	Color	Unit Weight (kN/m3)	Sat. Unit Weight (kN/m3)	Strength Type	Cohesion (kPa)	Phi (deg)	Cohesion Type	Water Surface	Hu Type	Hu
Fill 1		19	20	Mohr-Coulomb	1	40		Water Surface	Custom	1
Fill 2		19	20	Mohr-Coulomb	1	40		Water Surface	Custom	1
Peat 1 (soften)		10	11	Undrained	40.6		Constant	Water Surface	Custom	1
Peat 2 (soften)		10	11	Undrained	28.6		Constant	Water Surface	Custom	1
Peat 3 (soften)		10	11	Undrained	16.6		Constant	Water Surface	Custom	1
Clay 1A (soften)		14	16	Undrained	77		Constant	Water Surface	Custom	1
Clay 1B (soften)		14	16	Undrained	56.9		Constant	Water Surface	Custom	1
Clay 1C (soften)		14	16	Undrained	36.8		Constant	Water Surface	Custom	1
Sand 2		19	20	Mohr-Coulomb	1	38		Water Surface	Custom	1
Fill 2 (liq)		19	20	Undrained	14.4		Constant	Water Surface	Custom	1
Sand 1 (liq)		19	20	Undrained	104.4		Constant	Water Surface	Custom	1
Clay 2A (soften)		14	16	Undrained	102		Constant	Water Surface	Custom	1
Clay 2B		14	16	Mohr-Coulomb	102.7	0		Water Surface	Custom	1

Section 11 – Pre-earthquake

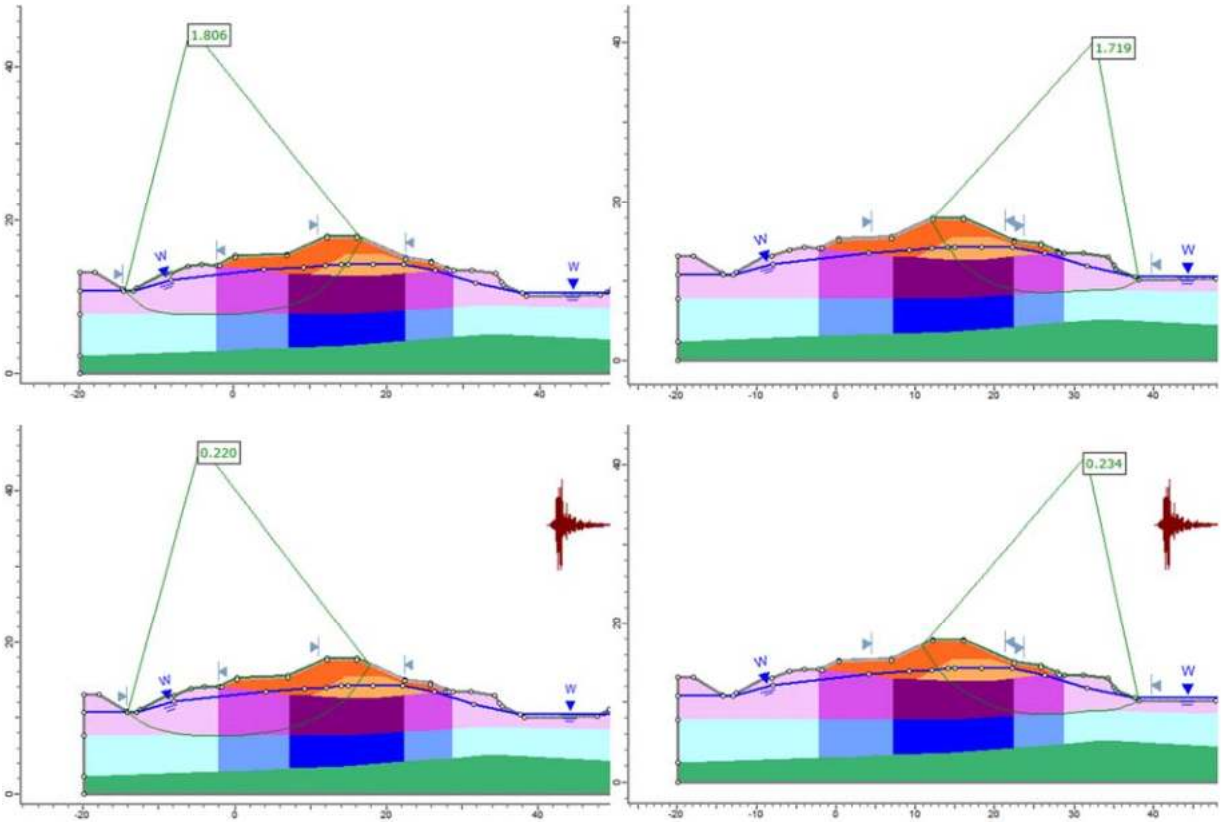

Material Name	Color	Unit Weight (kN/m3)	Sat. Unit Weight (kN/m3)	Strength Type	Cohesion (kPa)	Phi (deg)	Cohesion Type	Water Surface	Hu Type	Hu
Fill 1		19	20	Mohr-Coulomb	1	42		Water Surface	Custom	1
Fill 2		19	20	Mohr-Coulomb	1	38		Water Surface	Custom	1
Peat 1		10	11	Undrained	44.6		Constant	Water Surface	Custom	1
Peat 2		10	11	Undrained	30.5		Constant	Water Surface	Custom	1
Peat 3		10	11	Undrained	16.4		Constant	Water Surface	Custom	1
Silty Clay		14	16	Undrained	63		Constant	Water Surface	Custom	1
Clay 1		14	16	Undrained	58.3		Constant	Water Surface	Custom	1
Clay 2		14	16	Undrained	50.2		Constant	Water Surface	Custom	1
Clay 3		14	16	Undrained	42.1		Constant	Water Surface	Custom	1

Section 11 – Post-earthquake

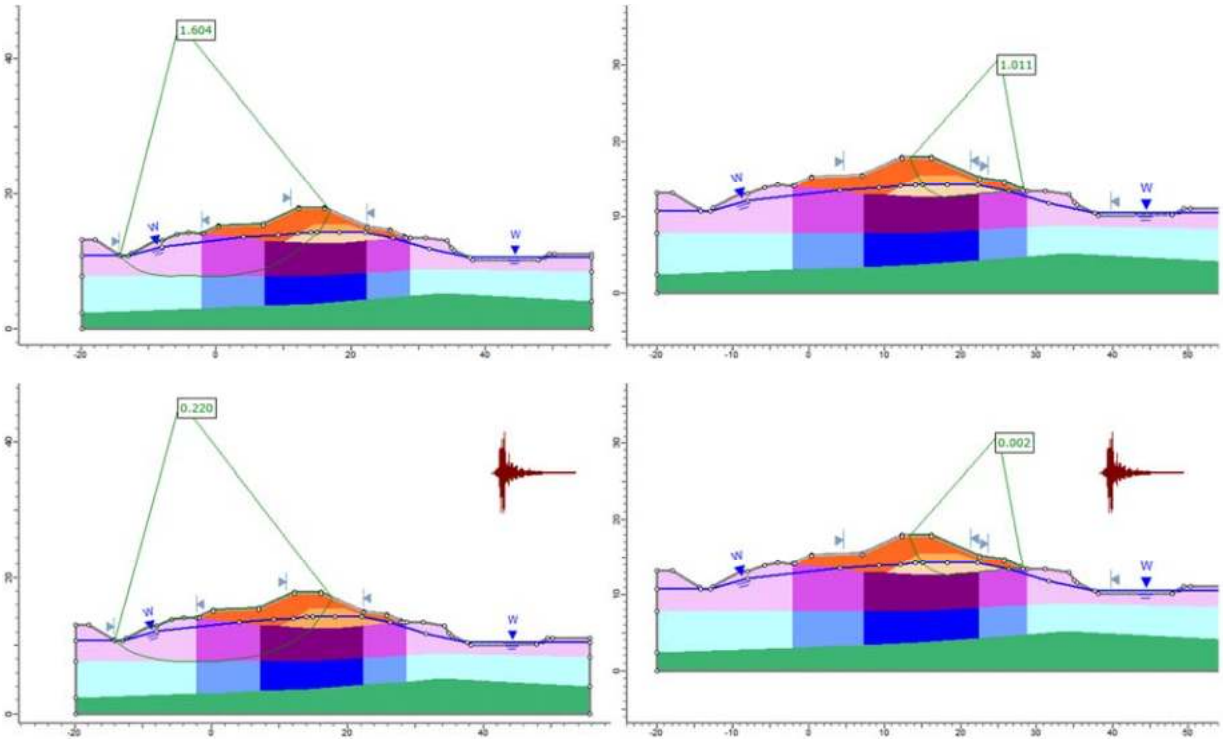

Material Name	Color	Unit Weight (kN/m3)	Sat. Unit Weight (kN/m3)	Strength Type	Cohesion (kPa)	Phi (deg)	Cohesion Type	Water Surface	Hu Type	Hu
Fill 1		19	20	Mohr-Coulomb	1	42		Water Surface	Custom	1
Fill 2		19	20	Mohr-Coulomb	1	38		Water Surface	Custom	1
Fill 2 (liq)		19	20	Mohr-Coulomb	6.1	0		Water Surface	Custom	1
Peat 1		10	11	Mohr-Coulomb	44.6	0		Water Surface	Custom	1
Peat 2 (soften)		10	11	Undrained	28.5		Constant	Water Surface	Custom	0
Peat 3 (soften)		10	11	Undrained	15.2		Constant	Water Surface	Custom	0
Silty Clay		14	16	Undrained	63		Constant	Water Surface	Custom	0
Clay 1		14	16	Undrained	58.3		Constant	Water Surface	Custom	0
Clay 2		14	16	Undrained	50.2		Constant	Water Surface	Custom	0
Clay 3		14	16	Undrained	42.1		Constant	Water Surface	Custom	0

Section 12 – Pre-earthquake

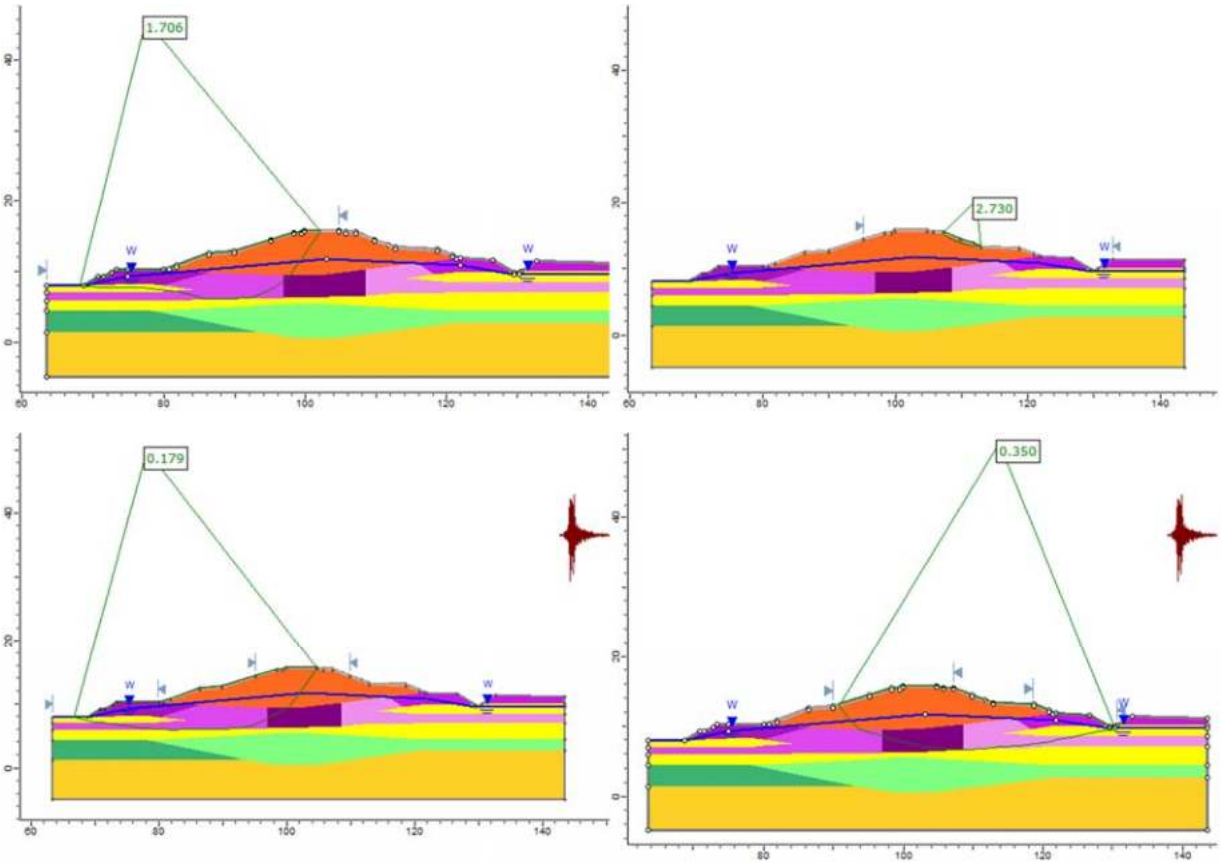

Material Name	Color	Unit Weight (kN/m3)	Sat. Unit Weight (kN/m3)	Strength Type	Cohesion (kPa)	Phi (deg)	Cohesion Type	Water Surface	Hu Type	Hu
Fill 1		19	20	Mohr-Coulomb	1	40		Water Surface	Custom	1
Peat 1		10	11	Undrained	40		Constant	Water Surface	Custom	0
Peat 1L		10	11	Undrained	17.9		Constant	Water Surface	Custom	0
Peat 1R		10	11	Undrained	30.3		Constant	Water Surface	Custom	0
Peat 2L		10	11	Undrained	25.1		Constant	Water Surface	Custom	0
Peat 2R		10	11	Undrained	39.6		Constant	Water Surface	Custom	0
Silty Clay		14	16	Undrained	78.6		Constant	Water Surface	Custom	0
Sandy Silt		16	18	Undrained	94.6		Constant	Water Surface	Custom	0
Sand 1		19	20	Mohr-Coulomb	1	40		Water Surface	Custom	1
Sand 2		19	20	Mohr-Coulomb	1	44		Water Surface	Custom	1

Section 12 – Post-earthquake

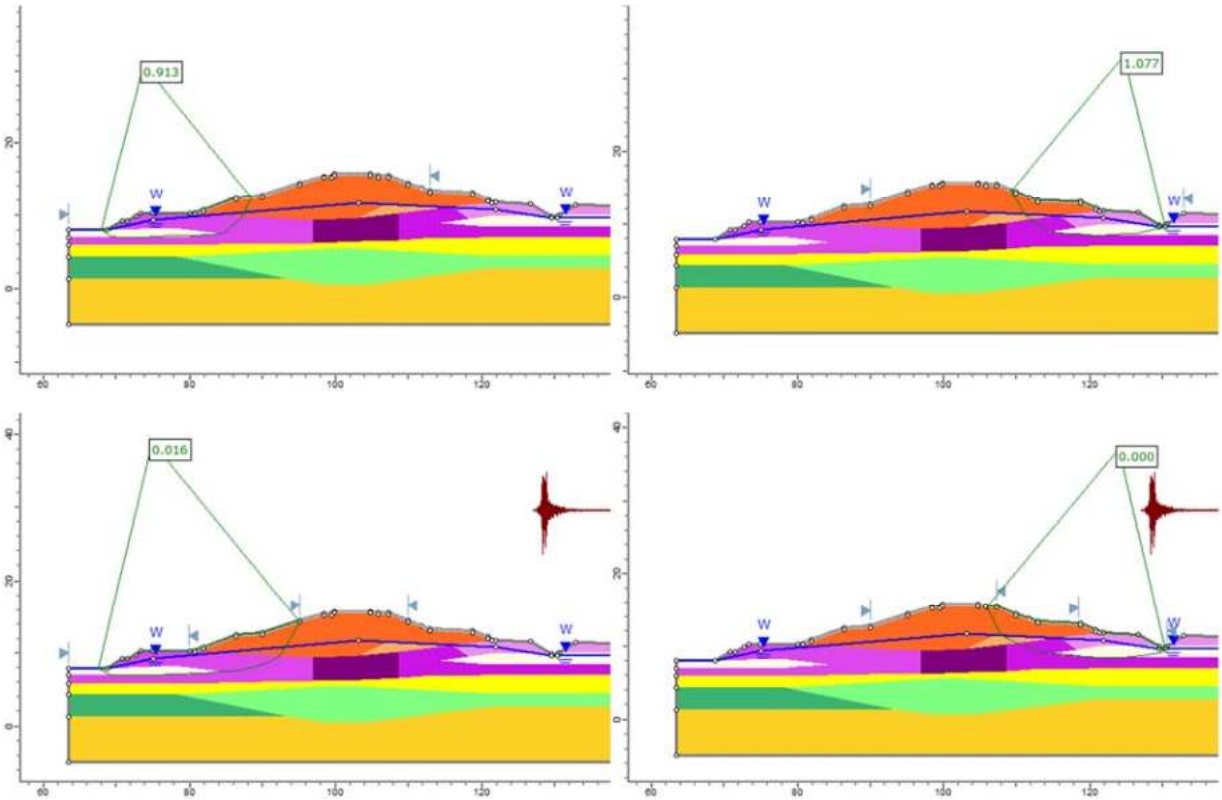

Material Name	Color	Unit Weight (kN/m3)	Sat. Unit Weight (kN/m3)	Strength Type	Cohesion (kPa)	Phi (deg)	Cohesion Type	Water Surface	Hu Type	Hu
Fill 1		19	20	Mohr-Coulomb	1	40		Water Surface	Custom	1
Fill (liq)		19	20	Mohr-Coulomb	9.1	0		Water Surface	Custom	1
Peat 1		10	11	Undrained	40		Constant	Water Surface	Custom	0
Peat 1R		10	11	Undrained	30.3		Constant	Water Surface	Custom	0
Peat 2L (soften)		10	11	Undrained	20.1		Constant	Water Surface	Custom	1
Peat 2R		10	11	Undrained	39.6		Constant	Water Surface	Custom	0
As1 (liq)		19	20	Undrained	2.7		Constant	Water Surface	Custom	1
Silty Clay		14	16	Undrained	78.6		Constant	Water Surface	Custom	0
Sandy Silt		16	18	Undrained	94.6		Constant	Water Surface	Custom	0
Sand 1		19	20	Mohr-Coulomb	1	40		Water Surface	Custom	1
Sand 2		19	20	Mohr-Coulomb	1	44		Water Surface	Custom	1

Section 13 – Pre-earthquake

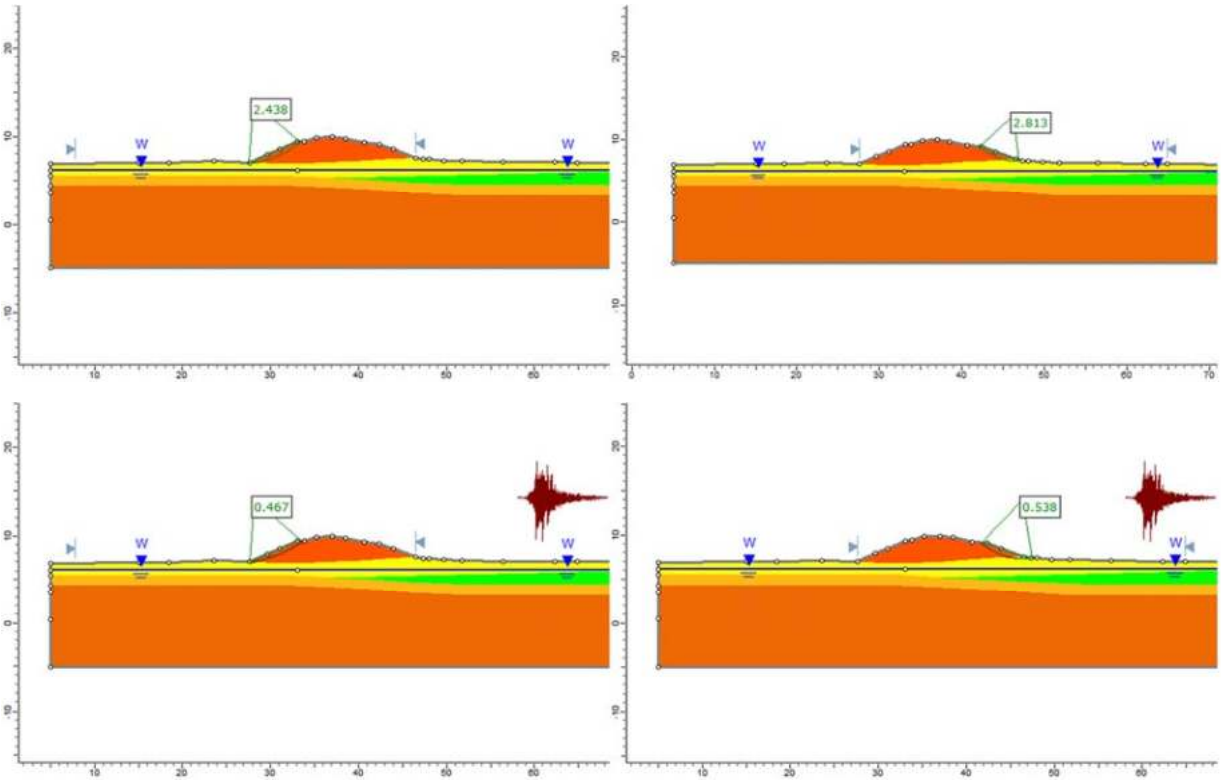

Material Name	Color	Unit Weight (kN/m3)	Sat. Unit Weight (kN/m3)	Strength Type	Cohesion (kPa)	Phi (deg)	Cohesion Type	Water Surface	Hu Type	Hu
Fill 1		19	20	Mohr-Coulomb	1	41		Water Surface	Custom	1
Sandy Silt		16	18	Undrained	67		Constant	Water Surface	Custom	0
Sand 1		19	20	Mohr-Coulomb	1	37.1		Water Surface	Custom	1
Sand 2		14	16	Mohr-Coulomb	1	39.4		Water Surface	Custom	1
Sand 3		16	18	Mohr-Coulomb	1	40		Water Surface	Custom	1

Section 13 – Post-earthquake

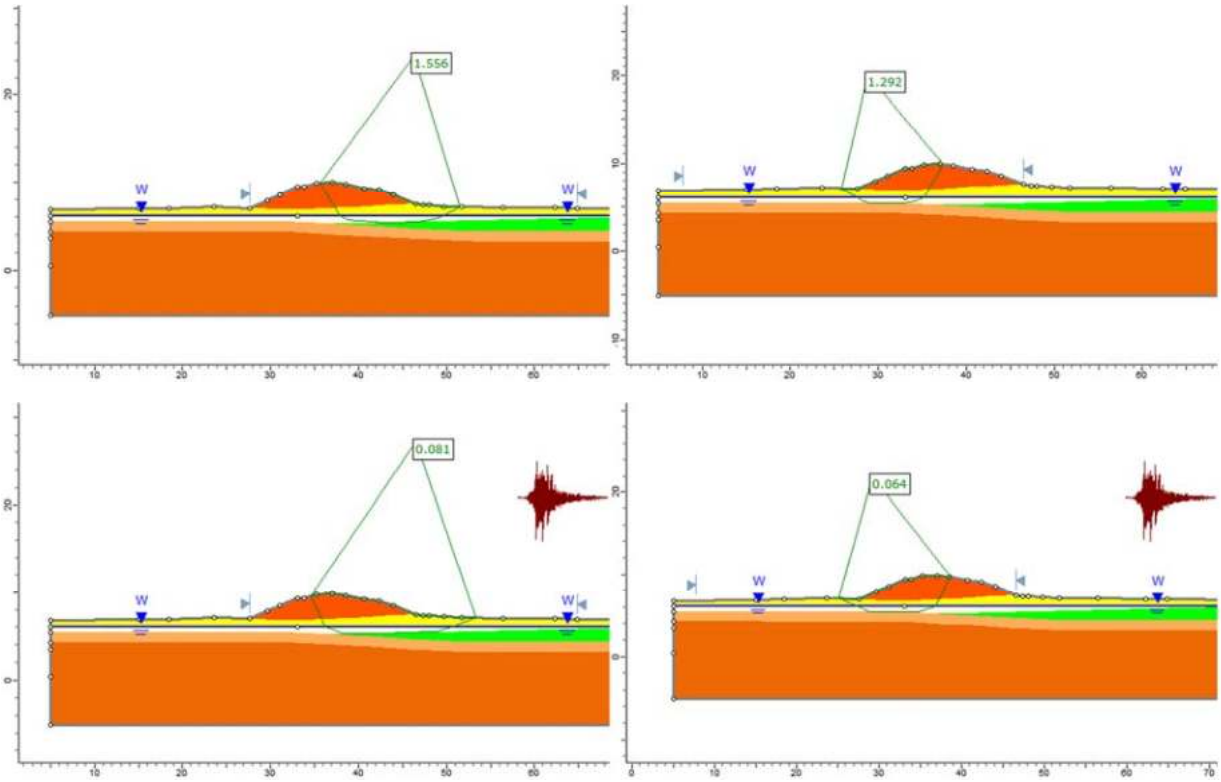

Material Name	Color	Unit Weight (kN/m3)	Sat. Unit Weight (kN/m3)	Strength Type	Cohesion (kPa)	Phi (deg)	Cohesion Type	Water Surface	Hu Type	Hu
Fill 1		19	20	Mohr-Coulomb	1	41		Water Surface	Custom	1
Sandy Silt		16	18	Undrained	67		Constant	Water Surface	Custom	0
Sand 1		19	20	Mohr-Coulomb	1	37.1		Water Surface	Custom	1
Sand 3		16	18	Mohr-Coulomb	1	40		Water Surface	Custom	1
Sand 1 (liq)		19	20	Mohr-Coulomb	5.2	0		Water Surface	Custom	1
Sand 2A (liq)		19	20	Mohr-Coulomb	11.8	0		Water Surface	Custom	1

Section 14 – Pre-earthquake

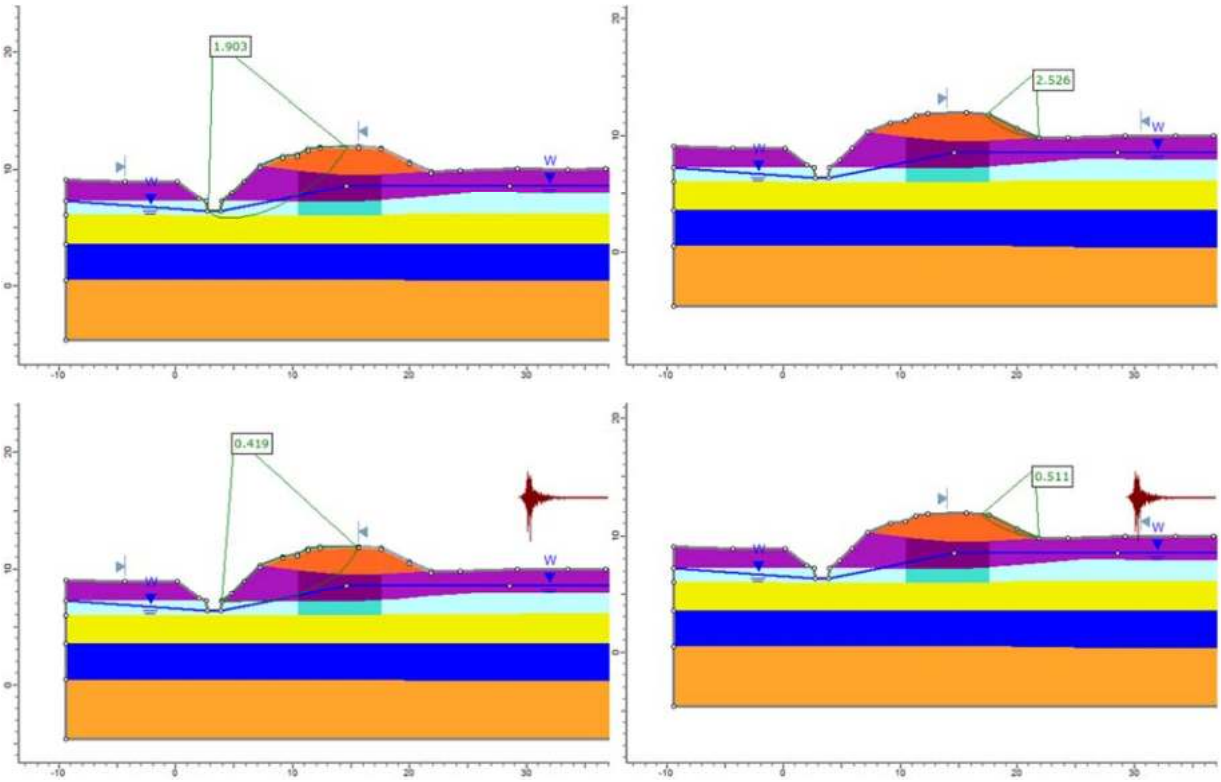

Material Name	Color	Unit Weight (kN/m3)	Sat. Unit Weight (kN/m3)	Strength Type	Cohesion (kPa)	Phi (deg)	Water Surface	Hu Type	Hu
Fill 1		19	20	Mohr-Coulomb	1	43	Water Surface	Custom	1
Peat 1		10	11	Undrained	31.2		Water Surface	Custom	1
Peat 2		10	11	Undrained	20.1		Water Surface	Custom	1
Clay 1A		14	16	Undrained	39.4		Water Surface	Custom	1
Clay 1B		14	16	Undrained	31.1		Water Surface	Custom	1
Clay 2		14	16	Undrained	64.7		Water Surface	Custom	1
Sand 1		19	20	Mohr-Coulomb	1	40	Water Surface	Custom	1
Sand 2		19	20	Mohr-Coulomb	1	40	Water Surface	Custom	1

Section 14 – Post-earthquake

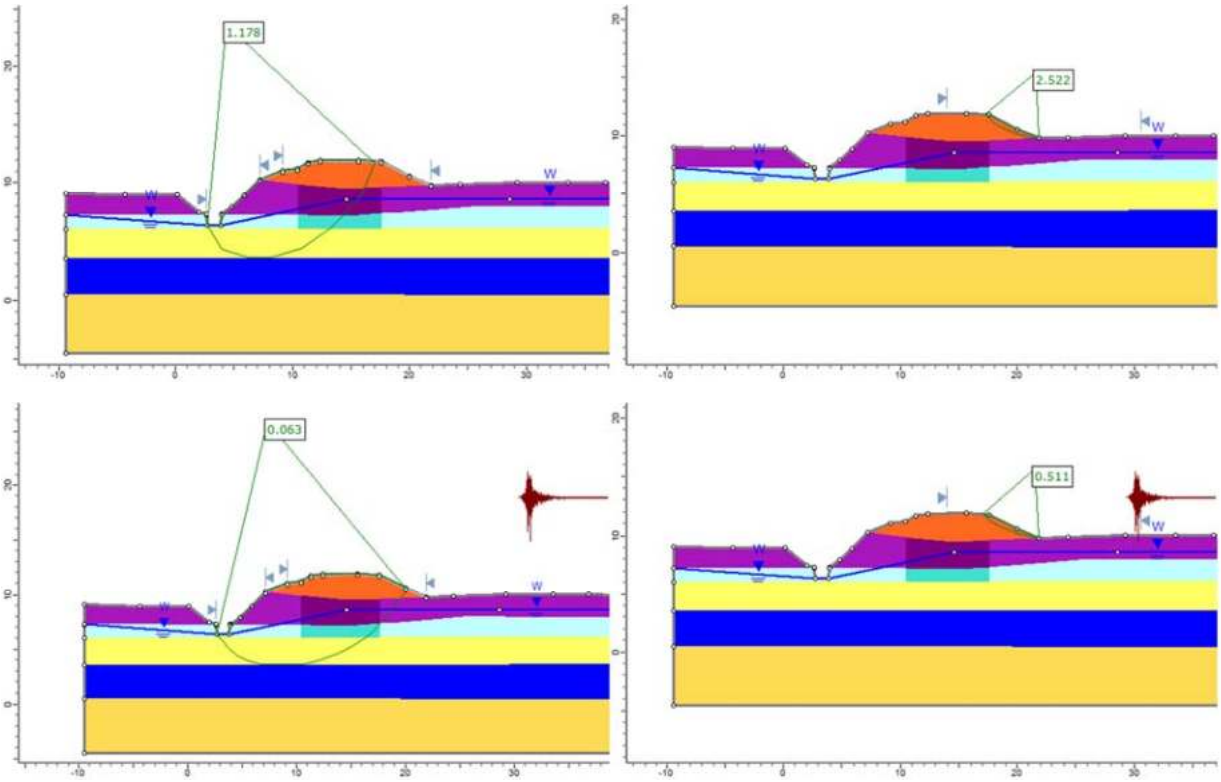

Material Name	Color	Unit Weight (kN/m3)	Sat. Unit Weight (kN/m3)	Strength Type	Cohesion (kPa)	Phi (deg)	Water Surface	Hu Type	Hu
Fill 1		19	20	Mohr-Coulomb	1	43	Water Surface	Custom	1
Peat 1		10	11	Undrained	31.2		Water Surface	Custom	1
Peat 2		10	11	Undrained	20.1		Water Surface	Custom	1
Clay 1A		14	16	Undrained	39.4		Water Surface	Custom	1
Clay 1B		14	16	Undrained	31.1		Water Surface	Custom	1
Clay 2		14	16	Undrained	64.7		Water Surface	Custom	1
Sand 1 (liq)		19	20	Mohr-Coulomb	12.7	0	Water Surface	Custom	1
Sand 2 (liq)		19	20	Mohr-Coulomb	18.4	0	Water Surface	Custom	1

REFERENCES

Abrahamson, N., Kuehn, N., Gulerce, Z., Gregor, N., Bozorgnia, Y., Parker, G., Stewart, J., Chiou, B., Idriss, I.M., Campbell, K., Youngs, R. Update of the BC Hydro Subduction Ground-Motion Model using the NGA-Subduction Dataset. 2018. *Pacific Earthquake Engineering Research Center,* June. Volume 02.

Ahdi, S.K., Stewart, J.P., Ancheta, T.D., Kwak, D.Y., Mitra, D., 2017. Development of *VS* profile database and proxy-based models for *VS30* prediction in the Pacific Northwest region of North America. *Bulletin of the Seismological Society of America,* Volume 107, pp. 1781-1801.

Al Atik, L., 2015. NGA-East: Ground-Motion Standard Deviation Models for Central and Eastern North America. *Pacific Earthquake Engineering Research Center,* June. Volume 07.

Ancheta, T.D., Darragh, R.B., Stewart, J.P., Seyhan E., Silva, W.J., Chiou B. S.-J., Wooddell, K.E., Graves, R. W., Kottke, A. R., Boore, D. M., Kishida, T., Donahue, J. L., 2014. NGA-West2 Database. *Earthquake Spectra,* August. 30(3), pp. 989-1005.

Baker, J.W., 2015. Efficient analytical fragility function fitting using dynamic structural analysis. Earthquake Spectra, 31(1), pp.579–599.

Baker, J.W., Lin, T. & Shahi, S.K., 2011. New Ground Motion Selection Procedures and Selected Motions for the PEER Transportation Research Program *Pacific Earthquake Engineering Research Center*, March, Volume 03.

Van Ballegooy, S., Malan, P., Lacrosse, V., Jacka, M.E., Cubrinovski, M., Bray, J.D., O'Rourke, T.D., Crawford, S.A., Cowan, H., 2014. Assessment of liquefaction-induced land damage for residential Christchurch. *Earthquake Spectra*.

Bolton M.D. (1986). The strength and dilitancy of sands, *Géotechnique*, 36(1): 65-78.

Bonilla, L. F., Steidl, J.H., Gariel, J.-C., Archuleta , R.J., 2002. Borehole Response Studies at the Garner Valley Downhole Array, Southern California. *Bulletin of the Seismological Society of America,* 92(8), pp. 3165-3179.

Boore, D. M., 2010. Orientation-Independent, Nongeometric-Mean Measures of Seismic Intensity from Two Horizontal Components of Motion. *Bulletin of the Seismological Society of America,* August, 100(4), pp. 1830-1835.

Boore, D.M., Stewart, J.P., Seyhan, E., Atkinson, G. M., 2014. NGA-West2 Equations for Predicting PGA, PGV, and 5% Damped PSA for Shallow Crustal Earthquakes. *Earthquake Spectra,* 30(3), pp. 1057-1085.

Boulanger, R.W. & Idriss, I.M., 2006. Liquefaction Susceptibility Criteria for Silts and Clays. *Journal of Geotechnical and Geoenvironmental Engineering*, 132(11), pp.1413–1426.

Boulanger, R.W. & Idriss, I.M., 2007. Evaluation of Cyclic Softening in Silts and Clays. *Journal of Geotechnical and Geoenvironmental Engineering*, 133(6), pp.641–652.

Boulanger, R.W., and Idriss, I. M. 2016. "CPT-based liquefaction triggering procedure." *Journal of Geotechnical and Geoenvironmental Engineering*, ASCE, 04015065, 10.1061/(ASCE)GT.1943-5606.0001388.

Boulanger, R.W., Wilson, D.W. & Idriss, I.M., 2012. Examination and Re-evalaution of SPT-Based Liquefaction Triggering Case Histories, *Journal of Geotechnical and Geoenvironmental Engineering*, 138(8), pp 898-909.

Cadet, H., Bard, P.-Y., Duval, A.-M., Bertrand, E., 2012. Site effect assessment using KiK-net data: part 2—site amplification prediction equation based on f0 and Vsz. *Bulletin of Earthquake Engineering,* April, 10(2), pp. 451-489.

Cook, R.D., and Weiberg, S., 1999. Applied regression including computing and graphics. *Wiley & Sons*, New York.

Darendeli, M., 2001. Development of a new family of normalized modulus reduction and material damping curves. Ph.D. Thesis, Department of Civil Engineering, University of Texas, Austin.

Duncan, M., Wright, S. & Brandon, T., 2014. Soils Strength and Slope Stability. John Wiley and Sons Inc.

Eslami, M., 2017. Experimental Mapping of Elastoplastic Surfaces for Sand and Cyclic Failure of Low- Plasticity Fine-Grained Soils. Ph.D Thesis, Department of Civil and Environmental Engineering, University of California - Los Angeles.

Ghofrani, H., Atkinson, G., 2011. Forearc versus backarc attenuation of earthquake ground motion. *Bulletin of the Seismological Society of America,* December, 101(6), pp. 3032-3045.

Ghofrani, H., Atkinson, G.M., Goda, K., 2013. Implications of the 2011 M9.0 Tohoku Japan earthquake for the treatment of site effects in large earthquakes. *Bulletin of Earthquake Engineering,* January, 11(1), pp. 171-203.

Ghofrani, H., Atkinson, G. M., 2014. Site condition evaluation using horizontal-to-vertical response spectral ratios of earthquakes in the NGA-West 2 and Japanese databases. *Soil Dynamics and Earthquake Engineering*, Volume 67, pp. 30–43.

Groholski, D.R. et al., 2016. Simplified Model for Small-Strain Nonlinearity and Strength in 1D Seismic Site Response Analysis. *Journal of Geotechnical and Geoenvironmental Engineering*, 142(9),

Hashash, Y.M.A. et al., 2016. DEEPSOIL V6.1, User Manual, Urbana, IL: Board of Trustees of University of Illinois at Urbana-Champaign.

Hassani, B., Atkinson, G.M., 2018a. Site-effects model for Central and Eastern North America based on peak frequency and average shear-wave velocity. *Bulletin of the Seismological Society of America*, Volume 108.

Hassani, B., Atkinson, G.M., 2018b. Application of a site-effects model based on peak frequency and average shear-wave velocity to California. *Bulletin of the Seismological Society of America*, Volume 108.

Hayashi, H. Yamanashi, T., Hashimoto, H., Yamaki, M., 2018. Shear Modulus and Damping Ratio for Normally Consolidated Peat and Organic Clay in Hokkaido Area. Geotechnical and Geological Engineering.

Hayashi, H. & Hayashi, T., 1991. Estimation of undrained shear strength for peat using CPT, pp.1159–1160. *Australian Geomechanics Society, Sydney, Australia. (ISBN 978-0-9946261-2-7)*

Hokkaido River Disaster Prevention Research Center, 2004. H15 Tokachi-Oki River Disaster Investigation Report [Japanese]

Hokkaido River Disaster Prevention Research Center, 2005. H16 Tokachi-Oki River Disaster Investigation Report [Japanese]

Ide, S. & Minoru, T., 1996. The dynamic rupture process of the 1993 Kushiro-oki earthquake. *Journal of Geophysical Research*, 101, pp.5661–5675.

Idriss, I. M., 2011. Use of *VS30* to represent local site conditions. *4th LASPEI/IAEE International Symposium Effects of Surface Geology on Strong Ground Motions*, Santa Barbara, CA.

Idriss, I.M. & Boulanger, R.W., 2007. Residual shear strength of liquefied soils. USSD 2007 Modernization and Optimization of Existing Dams and Reservoirs.

Idriss, I.M. & Boulanger, R.W., 2008. Soil liquefaction during earthquakes. *Earthquake Engineering Research Institute*, 136(6), p.755.

Ishihara, K., 1985a. Stability of natural deposits during earthquakes. In Proceedings of the Eleventh International Conference on Soil Mechanics and Foundation Engineering.

Ishihara, K. & Yoshimine, M., 1992. Evaluation of Settlements In Sand Deposits Following Liquefaction During Earthquakes. *Soils and Foundations*.

Jaky, J., 1948. Pressure in silos. In Proceedings of the 2nd International Conference on Soil Mechanics and Foundation Engineering. pp. 103–107.

Japan Highway Public Corporation (JHPC), 2005. Guidelines for Electronic Delivery of Surveys: Appendix of Geological Survey Part [Japanese].

Jayaram, N. & Baker, J., 2009. Correlation model for spatially distributed ground-motion intensities. *Earthquake Engineering & Structural Dynamics*.

Kawase, H., Sánchez-Sesma, F. J., Matsushima, S., 2011. The Optimal Use of Horizontal-to-Vertical Spectral Ratios of Earthquake Motions for Velocity Inversions Based on Diffuse-Field Theory for Plane Waves. *Bulletin of the Seismological Society of America,* 101(5), pp. 2001-2014.

Kayen, R. Moss, R. E. S., Thompson, E. M., Seed, R. B., Cetin, K. O., Der Kiureghian, A., Tanaka, Y., Tokimatsu, K., 2004. Global Shear Wave Velocity Database for Probabilistic Assessment of the Initiation of Seismic-soil Liquefaction. Proc. 11th International Conference on Soil Dynamics & Earthquake Engineering, pp.506–512.

Kim, B., Hashash, Y.M.A., Stewart, J.P., Rathje, E.M., Harmon, J.A., Musgrove, M.I., Campbell, K. W., Silva, W.J., 2016. Relative differences between nonlinear and equivalent-linear 1-D site response analyses. *Earthquake Spectra*, 32(3), pp. 1845-1865.

Kishida, T., Boulanger, R.W., Abrahamson, N.A., Wehling, T. M., Driller, M. W., 2009. Regression Models for Dynamic Properties of Highly Organic Soils. *Journal of Geotechnical and Geoenvironmental Engineering*, 135(4), pp.533–543.

Kishida, T., Boulanger, R.W., Abrahamson, N.A., Driller, M.W., Wehling, T.M. et al., 2009. Seismic response of levees in the Sacramento-San Joaquin Delta. *Earthquake Spectra*, 25(3), pp.557–582.

Kishida,T., Bozorogina, Y., Abrahamson, N.A., Ahdi, S.K., Ancheta, T.D., Boore, D.M., Campbell, K.W., Darragh, R.B., Magistrale, H., Stewart, J.P., 2017. Development of the NGA-Subduction Database. *Proc. 16th World Conf. on Earthquake Eng.*, Santiago, Chile (Paper No. 3452).

Koketsu, K. Hikima, K., Miyazaki, S., Ide, S., 2004. Joint inversion of strong motion and geodetic data for the source process of the 2003 Tokachi-oki, Hokkaido, earthquake. *Earth, Planets and Space*, 56(3), pp.329–334.

Konno, K., & Ohmachi, T., 1998. Ground-motion characteristics estimated from spectral ratio between horizontal and vertical components of microtremor. *Bulletin of the Seismological Society of America,* Volume 88, pp. 228–241.

Kramer, S.L. & Wang, C.-H., 2015. Empirical Model for Estimation of the Residual Strength of Liquefied Soil. *Journal of Geotechnical and Geoenvironmental Engineering*.

Kwak, D.Y. Stewart, J.P., Brandenberg, S.J., Mikami, A., 2016. Characterization of Seismic Levee Fragility using Field Performance Data. Earthquake Spectra, 32(1), pp.193–215.

Kwak, D.Y., Stewart, J.P., Mandokhail, S.-J., Park, D., 2017. Supplementing *VS30* with H/V Spectral Ratios for Predicting Site Effects. *Bulletin of the Seismological Society of America,* October, 107(5), pp. 2028-2042

Kwak, D.Y., Brandenberg, S.J., Mikami, 2015. Prediction Equations for Estimating Shear Wave Velocity from Combined Geotechnical and Geomorphic Indexes Based on Japanese Data Set. *Bulletin of the Seismological Society of America*, 105(4), pp.1919–1930.

Lachet, C., Hatzfeld, D., Bard, P.-Y., Theodulidis, N., Papaioannou, C., Savvaidis, A., 1996. Site effects and microzonation in the city of Thessaloniki (Greece) comparison of different approaches. *Bulletin of the Seismological Society of America,* 86(6), pp. 1692-1703.

Ladd, C.C., 1991. Stability Evaluation during Staged Construction. Journal of Geotechnical Engineering.

Lermo, J. & Chávez-García, F. J., 1993. Site effect evaluation using spectral ratios with only one station. *Bulletin of the Seismological Society of America,* 83(5), pp. 1574-1594.

Lunne, T., Christoffersen, H.P. & Tjelta, T.I., 1985. Engineering Use of Piezocone Data in North Sea Clays. In Proc. ICSMFE-11. pp. 907–912.

Maurer, B.W., Green, R.A. & Oliver-Denzil, S.T., 2015. Moving towards an improved index for assessing liquefaction hazard: Lessons from historical data. Soils and Foundations, 55(4), pp.778–787.

Mayne, P.W. & Kulhawy, F.H., 1982. K-OCR relationships in soil. Journal of the Geotechnical Engineering Division.

Menq, F.Y. (2003). *Dynamic properties of sandy and gravelly soils*. Ph.D. Dissertation, Department of Civil Engineering, University of Texas, Austin.

Midorikawa, S. & Nogi, Y., 2015. Estimation of *VS30* from Shallow Velocity Profile (in Japanese). Journal of Japan Association of Earthquake Engineering, 15(2), pp.91–96.

Moehle, J. & Deierlein, G.G., 2004. A framework for performance-based earthquake engineering. In 13th World Conference on Earthquake Engineering. Vancouver, B.C., Canada.

Montgomery, J. & Boulanger, R.W., 2017. Effects of Spatial Variability on Liquefaction-Induced Settlement and Lateral Spreading. *Journal of Geotechnical and Geoenvironmental Engineering*, 143(1)

National Research Institute for Earth Science and Disaster Prevention (NIED), 2018. (Japan Seismic Hazard Information Station (J-SHIS). Available at: http://www.j-shis.bosai.go.jp/en/ [Accessed December 4, 2018].

Negussey, D., Wijewickreme, W.K.D. & Vaid, Y.P., 1988. Constant-volume friction angle of granular materials. Canadian Geotechnical Journal, 25(1), pp.50–55.

Newmark, N.M., 1965. Effects of Earthquakes on Dams and Embankments. *Géotechnique*, 15(2), pp.139–160.

Olson, S.M. & Stark, T.D., 2002. Liquefied strength ratio from liquefaction flow failure case histories. Canadian Geotechnical Journal.

Pelekis, P.C. & Athanasopoulos, G.A., 2011. An overview of surface wave methods and a reliability study of a simplified inversion technique. *Soil Dynamics and Earthquake Engineering*, 31(12), pp.1654–1668.

Porter, K., Kennedy, R. & Bachman, R., 2007. Creating fragility functions for performance-based earthquake engineering. *Earthquake Spectra*, 23(2), pp.471–489.

Rocscience Inc. 2017, *Slide 7.0 - 2D Limit Equilibrium Slope Stability Analysis.* www.rocscience.com, Toronto, Ontario, Canada.

Rodriguez-Marek, A., Montalva, G.A., Cotton, F., Bonilla, F., 2011. Analysis of Single-Station standard deviation using the KiK-net Data. *Bulletin of the Seismological Society of America,* 101(3), pp. 1242-1258.

Sasaki, Y., 2009. River dike failures during the 1993 Kushiro-oki earthquake and the 2003 Tokachi-oki earthquake. Earthquake Geotechnical Case Histories for Performance-based Design, pp.131–157.

Seyhan, E. & Stewart, J.P., 2014. Semi-Empirical nonlinear site amplification from NGA-West2 data and simulations. *Earthquake Spectra*, August, 30(3), pp. 1241-1256.

Shafiee, A., 2016. Cyclic and Post-Cyclic Behavior of Sherman Island Peat. Ph.D Dissertation, University of California - Los Angeles.

Sheahan, T.C., Ladd, C.C. & Germaine, J.T., 1996. Rate-Dependent Undrained Shear Behavior of Saturated Clay. *Journal of Geotechnical Engineering.*

Stewart, J.P., Afshari, K. & Hashash, Y.M.A., 2014. Guidelines for Performing Hazard-Consistent One-Dimensional Ground Response Analysis for Ground Motion Prediction. *Pacific Earthquake Engineering Research Center,* October. Volume 16

Stewart, J.P., Afshari, K. & Goulet, C.A., 2017. Non-Ergodic Site Response in Seismic Hazard Analysis. *Earthquake Spectra,* November, 33(4), pp. 1385-1414.

Stewart, J.P., Liu, A.H., & Choi, Y., 2003. Amplification factors for spectral acceleration in tectonically active regions. *Bulletin of the Seismological Society of America*, 93(1), pp. 332-352.

Terronez, A., 2017. Non-Linear Ground Motion Amplification Functions for Fine Grained and Highly Organic Soils. M.S. Thesis, University of California - Los Angeles.

Theodulidis, N., Bard, P.-Y., Archuleta, R. & Bouchon, M., 1996. Horizontal-to-vertical spectral ratio and geological conditions: The case of Garner Valley Downhole Array in southern California. *Bulletin of the Seismological Society of America,* 86(2), pp. 306-319.

Tokimatsu, K. & Sekiguchi, T., 2006. Effects of nonlinear properties of surface soils on strong ground motions recorded in Ojiya during 2004 Mid Niigata Prefecture Earthquake. *Soils and Foundations*, 46(6), pp.765–775.

Vorogushyn, S., Merz, B. & Apel, H., 2009. Development of dike fragility curves for piping and micro-instability breach mechanisms. *Natural Hazards and Earth System Science*, 9(4), pp.1383–1401.

Wakamatsu, K. & Matsuoka, M., 2011. Developing a 7.5-sec site-condition map for Japan based on geomorphologic classification. *WIT Transactions on the Built Environment*, 120, pp.101–112.

Wakamatsu, K. & Matsuoka, M., 2013. Nationwide 7.5-arc-second Japan engineering geomorphologic classification map and *VS30* zoning. *Journal of Disaster Research*, 8(5), pp.904–911.

Wang, P., Stewart, J.P., Bozorgnia, Y., Boore, D.M., Kishida, T., 2017. "R" Package for Computation of Earthquake Ground-Motion Response Spectra. *Pacific Earthquake Engineering Research Center,* Volume 9.

Wehling, T.M. Boulanger, R.W., Arulnathan, R., Harder Jr, L.F.,Driller, M.W., 2003. Nonlinear Dynamic Properties of a Fibrous Organic Soil. *Journal of Geotechnical and Geoenvironmental Engineering*, 129(10), pp.929–939.

Yasuhara, K., 1994. Postcyclic Undrained Strength for Cohesive Soils. *Journal of Geotechnical Engineering*, 120(11), pp.1961–1979.

Yoshimine, M. Nishizaki, H., Amano, K., Hosono, Y., 2006. Flow deformation of liquefied sand under constant shear load and its application to analysis of flow slide of infinite slope. *Soil Dynamics and Earthquake Engineering*, 26(2–4 SPEC. ISS.), pp.253–264.

Zhao, J.X. & Hua, X., 2013. A Comparison of *VS30* and Site Period as Site-Effect Parameters in Response Spectral Ground-Motion Prediction Equations. *Bulletin of the Seismological Society of America,* 103(1), pp. 1-18.

Zhao, J.X. Liang, X., Jiang, F., Xing, H., Zhu, M., Hou, R., Zhang, Y., Lan, X., Rhoades, D.A., Irikura, K., Fukushima, Y., Somerville, P.G., 2016a. Ground-Motion Prediction Equations for Subduction Interface Earthquakes in Japan Using Site Class and Simple Geometric Attenuation Functions. *Bulletin of the Seismological Society of America,* August, 106(4), pp. 1518-1534.

Zhao, J. X. Jiang, F., Shi, P., Xing, H., Huang, H., Hou, R., Zhang, Y., Yu, P., Lan, X., Rhoades, D.A., Somerville, P.G., Irikura, K., Fukushima, Y., 2016b. Ground-Motion Prediction Equations for Subduction Slab Earthquakes in Japan Using Site Class and Simple Geometric Attenuation Functions. *Bulletin of the Seismological Society of America,* August, 106(4), pp. 1535-1551